Julius-Maximilians-Universität

Würzburg

Aminotroponiminate:

Koordinationschemie, Reaktivität und Redoxverhalten von Alkalimetall-, Silber- und Bismut-Komplexen

Dissertation zur Erlangung des

naturwissenschaftlichen Doktorgrades

Anna Hanft

Würzburg 2021

AMINOTROPONIMINATES:

COORDINATION CHEMISTRY, REACTIVITY AND REDOX BEHAVIOUR OF ALKALI METAL, SILVER AND BISMUTH COMPLEXES

Dissertation zur Erlangung
des naturwissenschaftlichen Doktorgrades
der
Julius-Maximilians-Universität Würzburg

vorgelegt von

Anna Hanft
aus
Coburg

Würzburg 2021

Eingereicht bei der Fakultät für Chemie und Pharmazie der Julius-Maximilians-Universität Würzburg am: 01.02.2021

Gutachter der schriftlichen Arbeit:

1. Gutachter: Priv.-Doz. Dr. Crispin Lichtenberg

2. Gutachter: Prof. Dr. Maik Finze

Prüfer des öffentlichen Promotionskolloquiums:

1. Prüfer: Priv.-Doz. Dr. Crispin Lichtenberg

2. Prüfer:

3. Prüfer:

Tag des öffentlichen Promotionskolloquiums:

Doktorurkunde ausgehändigt am:

Die Experimente zur vorliegenden Arbeit wurden in der Zeit von August 2017 bis Januar 2021 unter Anleitung von Dr. Crispin Lichtenberg am Institut für Anorganische Chemie der Fakultät für Chemie und Pharmazie der Julius-Maximilians-Universität Würzburg durchgeführt.

für Tizi

&

für meine Eltern

Danksagung

Mein ganz besonderer Dank gilt *Dr. Crispin Lichtenberg*. Danke dafür, dass ich mit meiner Arbeit an dieser Dissertation einen Beitrag zum Aufbau Deines Arbeitskreises leisten durfte. Danke auch, für die Unterstützung, die wertvollen Tipps und hilfreichen Gespräche, die mich immer wieder angespornt und dazu beigetragen haben, dass ich zu einer besseren Wissenschaftlerin wurde. Danke für alles, was Du in mich investiert und was Du mir ermöglicht hast.

Außerdem möchte ich *Prof. Dr. Holger Braunschweig* für die bereitgestellte Infrastruktur danken, die es uns als Nachwuchsgruppe ermöglicht hat, unter hervorragenden Arbeitsbedinungen zu forschen.

Dr. Ivo Krummenacher danke ich für die sehr gute Zusammenarbeit, die Aufnahme von EPR-Spektren, sowie die Hilfe bei Fragen zur Cyclovoltammetrie. Bei *Dr. Krzysztof Radacki* möchte ich mich ebenfalls für die hervorragende Zusammenarbeit und die Aufnahme von Einkristallröntgenstrukturdaten bedanken.

Danken möchte ich auch den Service Abteilungen des Instituts. Der NMR-Abteilung *Dr. Rüdiger Bertermann, Marie-Luise Schäfer* und *Laura Wolz* gilt mein Dank für die ausgezeichnete Zusammenarbeit, die vielen NMR-Messungen und die Erfüllung sämtlicher Sonderwünsche. Außerdem danke ich dem Team der Elementaranalyse *Sabine Timmroth* und *Liselotte Michels*, für das Anfertigen der Elementaranalysen. Danke auch *Christoph Mahler*, für alle massenspektrometrischen Messungen. Auch den restlichen Abteilungen des Instituts, der Verwaltung, dem Glasbläser, der Werkstatt, der Haustechnik und der guten Fee, *Gertrud Wunderling (Gerdi)*, sei gedankt, ohne euch würde der Laden nicht laufen. Über Eure fachliche Expertise hinaus bin ich Euch allen auch für jeden netten Plausch, der mir den Arbeitsalltag erleichtert hat, sehr dankbar.

Für ihren Fleiß und das Mitwirken an dieser Arbeit im Rahmen einer Bachelorarbeit oder eines Forschungspraktikums bedanke ich mich bei allen Studenten, die ich betreuen durfte, *Malte Jürgensen*, *Pascal Weinberger*, *Peter Endres*, *Victoria Müller*, *Nele Wieprecht*, *Felix Geist* und *Florian Martens*.

Ein großer Dank gilt allen Mitgliedern des Arbeitskreises Lichtenberg und Braunschweig, für die tolle Arbeitsatmosphäre, überragende Zusammenarbeit und stete Hilfsbereitschaft, die Diskussionen chemischer und nicht-chemischer Art, die vielen gemeinsamen Aktivitäten und die Freundschaften, die während der Zeit hier entstanden sind. Vor allem an die *Skifahrer*, die *Spielegruppe* und die *Girls* geht ein herzlicher Dank. *Krzys*, danke Dir, nicht nur für Deine Hilfe bei kristallographischen Problemen, ohne Dich wäre ich verloren gewesen, sondern auch für Deine Unterstützung in sämtlichen Arbeits- und Lebenslagen.

Ganz besonders möchte ich mich bei den besten Arbeitskollegen *Jacky*, *Kai* und *Malte* bedanken. *Jacky*, es war mir eine Ehre, mit Dir diesen Arbeitskreis aufzubauen, mit Deinem Wissen und Deiner effektiven und zielstrebigen Arbeitsweise bist Du für mich ein Vorbild. Danke, dass wir das gemeinsam gemacht haben. *Kai*, Du hast zwar die Frauenquote zerstört, aber es sei Dir verziehen, da Du den Arbeitskreis in jeglicher Hinsicht bereichert hast. Außerdem fällt die Arbeit mit ein paar Pöbeleien auch gleich nicht mehr ganz so schwer. Danke, dass ich von Dir so einiges chemisches und nicht-chemisches lernen durfte. *Malte,* Du hattest es als mein erster Bachelor mit Sicherheit nicht leicht, aber Du hast es gerockt, weil Du ein kluger Kopf bist. Mit deiner gutmütigen, wohlwollenden, hilfsbereiten Art, bist Du nicht umsonst das *Mäuschen* im Arbeitskreis. Danke, für deine Unterstützung über meine ganze Doktorandenzeit hinweg. Danke, dass jeder von Euch, sowohl innerhalb als auch außerhalb der Uni, zum Gelingen dieser Arbeit beigetragen hat und nicht zuletzt danke, für eure Freundschaft.

Ein großer Dank gilt auch „meinen Jungs", die mich seit Beginn des Studiums begleitet und dafür gesorgt haben, dass ich nicht alles hingeschmissen und lieber Theologie studiert habe, oder *Julian*, *Brüggi*, *Benny*, *Bischi*, *Lukas* und *Magnus*? Ohne Euch würde ich diese Danksagung heute nicht brauchen.

Allen *Freunden* mit chemischem oder nicht-chemischem Background bin ich unendlich dankbar dafür, dass sie für die nötige Ablenkung während des Studiums und der Promotion gesorgt und mich dadurch immer wieder zum Weitermachen motiviert haben. Danke, für die unzählbaren, unbezahlbaren, epischen Momente. Ihr seid die Besten.

Der größte Dank gilt meiner *Familie*, die mich immer in allen Bestrebungen unterstützt hat, die mir den nötigen Rückhalt gegeben hat, die mich in schwierigen Zeiten aufgebaut und nie an meinem Können zweifeln lassen hat. Danke, für alles.

Publikationsliste

Teile der vorliegenden Arbeit wurden bereits veröffentlicht unter:

Aminotroponiminates: ligand-centred, reversible redox events under oxidative conditions in sodium and bismuth complexes

Anna Hanft, Crispin Lichtenberg

Dalton Trans. **2018**, *47,* 10578-10589.

Sodium Aminotroponiminates: Ligand-Induced Disproportionation, Mixed-Metal Compounds, and Exceptional Activity in Polymerization Catalysis

Anna Hanft, Malte Jürgensen, Rüdiger Bertermann, Crispin Lichtenberg

ChemCatChem **2018**, *10,* 4018-4027.

Rationalizing the Effect of Ligand Substitution Patterns on Coordination and Reactivity of Alkali Metal Aminotroponiminates

Anna Hanft, Crispin Lichtenberg

Organometallics **2018**, *37*, 1781-1787.

New Perspectives for Aminotroponiminates: Coordination Chemistry, Redox Behavior, Cooperativity, and Catalysis

Anna Hanft, Crispin Lichtenberg

Eur. J. Inorg. Chem. **2018**, 3361-3373.

Alkali Metal Aminotroponiminates: Selectivities and Equilibria in Reversible Radical Coupling of Delocalized π-Electron Systems

Anna Hanft, Ivo Krummenacher, Crispin Lichtenberg

Chem. Eur. J. **2019***, 25,* 11883-11891.

Dimerization of 2-[(2-((2-aminophenyl)thio)phenyl)amino]-cyclohepta-2,4,6-trien-1-one through hydrogen bonding

Anna Hanft, Crispin Lichtenberg

Z. Kristallogr. NCS **2020**, *235*, 963-966.

Salicylaldimines: Formation via Ring Contraction and Synthesis of Mono- and Heterobimetallic Alkali Metal Heterocubanes

Anna Hanft, Malte Jürgensen, Laura Wolz, Krzysztof Radacki, Crispin Lichtenberg

Inorg. Chem. **2020**, *51*, 17678-17688.

Cationic Bismuth Aminotroponiminates: Charge Controls Redox Properties

Anna Hanft, Krzysztof Radacki, Crispin Lichtenberg

Chem. Eur. J. **2021**, DOI: 10.1002/chem.202005186.

Der Nachdruck von Texten/Tabellen/Abbildungen erfolgt mit Genehmigung des jeweiligen Verlages. Das Copyright liegt weiterhin bei dem entsprechenden Verlag.

Außerdem wurden Teile der Arbeit in folgenden Abschlussarbeiten beschrieben:

P. Weinberger, **2018**, Alkalimetall-Aminotroponiminate: Synthese und Einfluss der Rückgratsubstitution auf die Redoxchemie, Julius-Maximilians-Universität, Würzburg.

N. Wieprecht, **2020**, Aminotroponiminate mit Nitrofunktionalität: Synthese, Charakterisierung und Redoxverhalten, Julius-Maximilians-Universität, Würzburg.

Abkürzungsverzeichnis

Å	Angström = 10^{-10} m
Äq.	Äquivalente
arom.	aromatisch
Ar	Aryl
AT	Aminotropon
ATI	Aminotroponimin oder Aminotroponiminat
BAr^F	Tetrakis-[3,5-bis-(trifluormethyl)-phenyl]-borat
br.	breit (NMR)
Bu	Butyl
bzw.	beziehungsweise
°C	Grad Celsius
cis	auf der gleichen Seite liegend
d	Dublett (NMR)
DFT	Dichtefunktionaltheorie
DMSO	*N*,*N*-Dimethylsulfoxid
EPR	Elektronenspinresonanz
Et	Ethyl
g	Gramm
°	Grad
h	Stunde(n)
HOMO	Höchstes, besetztes Molekülorbital (engl.: highest occupied molecular orbital)
Hz	Hertz
J	Kopplungskonstante (NMR)
K	Kelvin
kcal	Kilokalorien
KZ	Koordinationszahl
L	Neutralligand
LUMO	Niedrigstes, unbesetztes Molekülorbital (engl.: lowest unoccupied molecular orbital)
m	Multiplett (NMR)
m	*meta*
Me	Methyl

mg	Milligramm
MHz	Megahertz
min	Minute(n)
mL	Milliliter
mmol	Millimol
n	normal
MTBE	Methyl-*tert*-butylether
NMR	Kernresonanzspektroskopie (engl. nuclear magnetic resonance spectroscopy)
o	*ortho*
p	*para*
Ph	Phenyl
PMDTA	*N,N,N‘,N“,N“*-Pentamethyldiethylentriamin
*i*Pr	*Iso*propyl
R	beliebiger organischer Substituent (sofern nicht anders angegeben)
RT	Raumtemperatur
s	Singulett (NMR)
sept	Septett (NMR)
t	Triplett (NMR)
TEMPO	2,2,6,6-Tetramethylpiperidinyloxyl
*t*Bu	*tert*-Butyl
tert	tertiär
THF	Tetrahydrofuran
TMEDA	*N,N,N‘,N‘*-Tetramethylethylendiamin
trans	auf der entgegengesetzten Seite liegend
vs.	versus (lat. gegen)
VT	Variable Temperatur (engl. variable temperature)
Z	Zahl der Formeleinheiten in der Elementarzelle
z. B.	zum Beispiel
δ	chemische Verschiebung
µmol	Mikromol
[Atom–Atom]	Ebene durch die genannten Atome

Inhaltsverzeichnis

I Einleitung

1 Redox-aktive Liganden

Liganden, welche an definierten Redox-Prozessen teilnehmen können, werden als redox-aktive Liganden bezeichnet und sind seit langer Zeit aus der Koordinationschemie bekannt.[1] Dithiolen-Liganden wurden zum Beispiel bereits Anfang der 1960er Jahre in Koordinationskomplexen von Nickel, Palladium und Platin untersucht (Schema 3).[2] Die Bezeichnung redox nicht-unschuldig (non innocent) wird synonym verwendet und trägt der von *Jørgensen* 1966 eingeführten Beschreibung der Unschuldigkeit (innocence) bzw. Nicht-Unschuldigkeit (non innocence) von Liganden Rechnung.[3] Er beschreibt unschuldige (innocent) Liganden als solche, die eine eindeutige Bestimmung der Oxidationsstufe des Metalls, an das sie koordinieren, zulassen.[4] Dagegen unterliegt die Bestimmung der Oxidationsstufe von Metallen mit „non-innocent“ Liganden einer gewissen Ungenauigkeit.[3-4] Diese Definition bezieht sich allerdings auf das Zusammenspiel bestimmter Liganden und Metalle. Ein redox-aktiver Ligand kann sowohl in Komplexen vorkommen, in welchen die Oxidationsstufenbestimmung des Metalls ambivalent ist, als auch in solchen, in welchen die Bestimmung eindeutig ist.[1a] Es sollte somit von einem unschuldigen oder nicht-unschuldigen Verhalten eines redox-aktiven Liganden gesprochen werden.[1a] Das archetypische Beispiel eines redox-aktiven Liganden ist der Nitrosyl-Ligand (NO), der eine große Rolle im biochemischen Informationstransfer spielt.[1b, 3, 5] In Koordinationskomplexen mit Übergangsmetallen kann der Ligand als NO^+ in einer linearen Struktur, oder als neutrales $NO^{\bullet}$-Radikal bzw. NO^--Anion in einer gewinkelten Struktur vorliegen (Schema 1).[1b, 5-6] Die Schwierigkeit der Oxidationsstufenbestimmung in diesen Komplexen ist dabei auf die kovalenten Eigenschaften von Metall-Ligand π^*-Bindungen zurückzuführen.[5, 7]

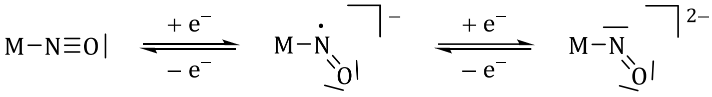

Schema 1: Bindungsmodi des Nitrosyl-Liganden in Übergangsmetall-NO-Komplexen.

Zu Beginn der Untersuchung von Komplexen mit redox-aktiven Liganden stand vor allem die Ambivalenz in der Bestimmung von Oxidationsstufen und die Analyse der elektronischen Struktur der Übergangsmetall-Komplexe im Mittelpunkt.[1a, 2, 8] Mit der Verbesserung analytischer Methoden zur Untersuchung ligandzentrierter Radikale, wie beispielsweise der Einkristall-röntgenstrukturanalyse, Kernresonanz- und Elektronenspinresonanz-Spektroskopie sowie der Mößbauer-Spektroskopie und dem Fortschritt in der theoretischen Berechnung von spektroskopischen Daten, entwickelte sich die Forschung an dieser Ligandklasse zu einem breiten Feld in der Synthese- und Koordinationschemie.[1c, 1d, 1f, 9] Die Eigenschaft redox-aktiver Liganden, im Zusammenspiel mit dem Zentral-Atom oder unabhängig von diesem, an Redox-Prozessen teilzunehmen, eröffnete neue Gestaltungskonzepte für verschiedene Metall-Komplexe und ermöglichte den Zugang zu neuen Anwendungsbereichen für diese Komplexe vor allem in der Katalyse.[1e-g, 9c, 10] Ein wesentliches Ziel war es, das Redox-Verhalten von Edelmetallen auf günstigere, häufiger vorkommende, unedlere Metalle zu übertragen. Dabei sollten redox-aktive Liganden Komplexen mit unedlen Metallen, die zu Einelektronenübertragungsreaktionen neigen, ermöglichen, an reversiblen Mehrelektronenübertragungen teilzunehmen, was die Komplexe für katalytische Prozesse attraktiv macht.[1e] Im Allgemeinen kann die Aktivität und Selektivität von Übergangsmetall-Komplexen in der Katalyse durch redox-aktive Liganden kontrollierten werden. Die Liganden können dabei sowohl eine aktive Rolle einnehmen, indem sie direkt an katalytischen Prozessen beteiligt sind, wobei zum Beispiel Ligand-Substrat Bindungen ausgebildet werden,[11] oder das Substrat selbst einen redox-aktiven Liganden darstellt,[12] als auch weniger aktiv sein, indem sie durch Veränderung ihres Oxidationszustandes die Lewis-Acidität/Basizität des Metall-Atoms beeinflussen,[13] oder als Elektronenreservoir dienen.[14] Indem der redox-aktive Bis(imino)-Pyridin Ligand als Elektronenreservoir diente, konnte beispielsweise von *Chirik* und Mitarbeitern eine Eisen-katalysierte [2π + 2π] Cycloaddition von α,ω-Dienen realisiert werden.[15] Durch ligandzentrierte Elektronenübertragungen in dieser Katalyse konnte die energetisch günstige Oxidationsstufe des Fe(II)-Metallzentrums über den gesamten Katalysezyklus hinweg beibehalten werden.[15]

In neueren Konzepten werden redox-aktive Liganden für Einelektronenübertragungen direkt vom Liganden auf das Substrat oder vom Substrat auf den Liganden genutzt.[10h] Damit wird ein metalloradikalbasierter Elektronentransfer, für welchen ein redox-aktives Metall benötigt wird, umgangen. Einelektronenübertragungen vom Liganden auf das Substrat können einerseits stöchiometrisch ablaufen, wie durch die Gruppe um *Soper* an einem Rhenium-Oxo-Komplex mit zusätzlichen redox-aktiven Iminosemiquinon-Liganden beobachtet wurde.[10h, 16] Andererseits sind katalytische Einelektronenübertragungen vom Liganden auf ein Substrat möglich, wie beispielsweise anhand der intramolekularen C(sp^3)–H Aminierung von Aziden unter Zuhilfenahme eines Fe(III)-Pyridin-aminophenol-Komplexes gezeigt wurde.[10h, 17] Die Übertragung eines Elektrons vom Substrat auf den Liganden ist dagegen selten.[18] Aktuelle Forschung beschäftigt sich außerdem mit einer katalytisch nutzbaren Kombination von Redox- und chemischer Nicht-Unschuldigkeit in Form von kombinierten Elektronen- und Protonenübertragungen.[19] Chemische Nicht-Unschuldigkeit beschreibt dabei die Fähigkeit des Liganden, an reversiblen chemischen Transformationen teilzunehmen.[20] Liganden, die aufgrund dieser Eigenschaft eine Synergie zum komplexierten Zentral-Atom eingehen können, werden auch als kooperative Liganden bezeichnet.[20-21] Nicht selten wurde die Natur als Vorbild für katalytisch aktive Komplexe mit redox-aktiven Liganden herangezogen.[10f] Ein Beispiel, das die

Forschung an redox-aktiven Liganden in der Koordinationssphäre von Übergangsmetallen mitinitiierte, ist das Enzym Galactose-Oxidase, welches die Oxidation von primären Alkoholen zu Aldehyden katalysiert.[22] Bei der Katalyse werden die redox-aktiven und kooperativen Eigenschaften eines Tyrosinyl-Liganden im Enzym genutzt. Durch Nachahmung von Metalloproteinen konnten in der Vergangenheit bereits eine Reihe effizienter Katalysen entwickelt werden.[10a, 23] Über katalytische Anwendungen hinaus macht die Fähigkeit redox-aktiver Liganden, verschiedene Oxidationsstufen anzunehmen und in einer oder mehreren dieser Stufen in ihrer offenschaligen Konfiguration vorzuliegen, diese zu vielseitig nutzbaren Werkzeugen in der Materialwissenschaft.[24] Beispielsweise können in diesem Feld relevante Komplexe durch reversiblen, intramolekularen Elektronentransfer zwischen Ligand und Metall als Valenztautomere oder Redoxisomere vorliegen.[25] Definitionsgemäß enthalten zu Valenztautomerie fähige Komplexe redox-aktive Liganden, für die offenschalige Konfigurationen zugänglich sind.[25] Eine häufig auftretende, offenschalige Konfiguration redox-aktiver Liganden stellt die radikalisch monoanionische Form dar, welche durch Einelektronenreduktion neutraler Vorläufer oder Einelektronenoxidation von Dianionen erhalten werden kann.[1c, 26] Beispielhaft ist dafür das Redox-System von α-Diiminen (dad) dargestellt, welche in Koordinationskomplexen drei verschiedene Redox-Zustände annehmen können (Schema 2). Die neutrale geschlossenschalige Form [dad^0], die offenschalige radikal-monoanionische Form [dad$^{\bullet-}$], sowie die geschlossenschalige dianionische Form [dad^{2-}] sind für diese Art von Liganden typisch.[9e]

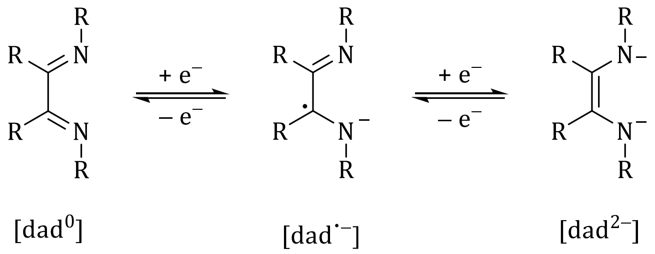

Schema 2: Redoxzustände eines α-Diimins (dad).

Außerdem sind Liganden in offenschaligen Konfigurationen als radikalische Dianionen,[27] Trianionen[28] und sogar als Radikal-Kationen bekannt.[29] Neutrale Ligand-Radikale existieren zum Beispiel in Form von NO$^\bullet$ (Schema 1).[30] Neben den Nitrosyl-Liganden und den bereits erwähnten Dithiolenen[9b, 31] sind zum Beispiel Redox-Systeme von Diketonen wie *o*-Quinon/*o*-Semiquinon/Catecholat biochemisch relevant (Schema 3).[32] Weitere bekannte Beispiele redox-aktiver Liganden sind Imino- und Bis(imino)-Pyridine,[9c, 33] welche zu den α-Diiminen[9d, 34] gehören, Dipyrine[35] und Porphyrine[36], sowie Carbene[37] in Fischer-Carben-Komplexen (Schema 3). Neuere Vertreter redox-aktiver Liganden stellen β-Diketimine[38] und Aminotroponimine (ATIs) dar (Schema 3).[39]

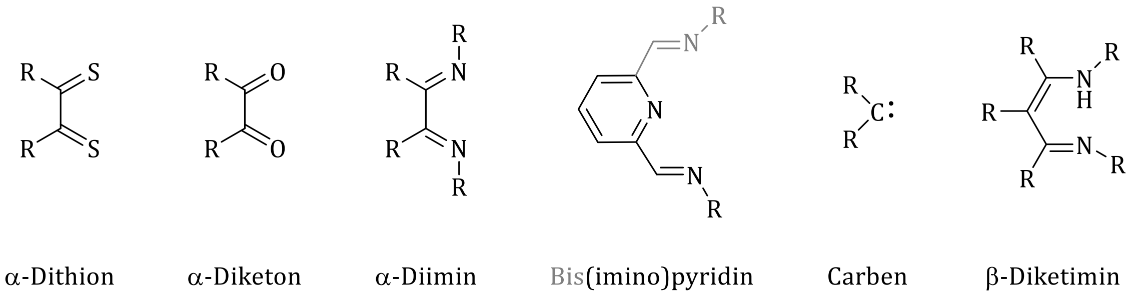

Schema 3: Ausgewählte Beispiele redox-aktiver Liganden. R = beliebiger Rest.

Für letztere konnte die Redox-Aktivität anhand elektrochemischer Untersuchungen eines Neutralliganden, eines Alkalimetall-Komplexes und eines Rhodium-Komplexes nachgewiesen werden.[39] Das Metall in der Aminotroponiminat(ATI)-Bindungstasche hatte dabei einen maßgeblichen Einfluss auf das ligandzentrierte Redox-Ereignis. Unter elektrochemischen Bedingungen war für den Rhodium-Komplex ein reversibler Elektronentransfer möglich, wohingegen die hohe Spindichte auf dem Liganden für den Natrium-ATI-Komplex zu einer reduktiv induzierten Dimerisierung führte.[39]

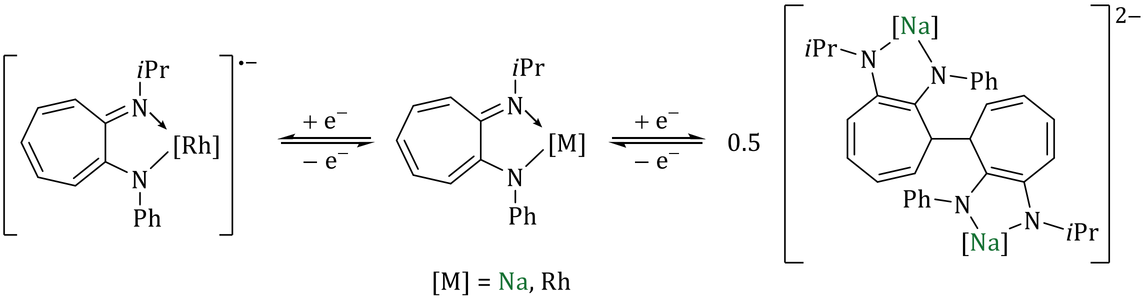

Schema 4: Verhalten eines Natrium- und Rhodium-ATI-Komplexes unter reduktiven Bedingungen.[39]

2 Redox-aktive Liganden in der Hauptgruppenchemie

In der Hauptgruppenchemie haben redox-aktive Liganden eine weit zurückreichende Geschichte.[40] Häufig werden sie verwendet, um niedrige Oxidationsstufen in Hauptgruppenmetall-Komplexen zu stabilisieren. Prominente Beispiele sind hier Magnesium(I)- und Aluminium(I)-Spezies mit β-Diketiminat-Liganden.[41] Mit der Entwicklung solcher hochreaktiver Spezies war es möglich, Reaktionen wie σ-Bindungsspaltungen in Form von oxidativen Additionen, die Aktivierung von Mehrfachbindungen sowie die reversible Aktivierung von Einfachbindungen und reduktive Eliminierungen, die lange Zeit Übergangsmetall-Komplexen vorbehalten waren, auch für Hauptgruppenmetall-Verbindungen zu realisieren.[40d] Meist besitzen die redox-aktiven Liganden in Hauptgruppenmetall-Komplexen nur einen (Ladungs)Zustand. Es sind allerdings eine Reihe an Hauptgruppenmetall-Komplexen bekannt, in welchen redox-aktive Liganden an einem Protonentransfer beteiligt sind, der mit einer (Ladungs)Zustandsänderung des Liganden einhergeht.[19d, 19e] Zwei Beispiele sind die ligandvermittelte, katalytische Dehydrogenierung von Ameisensäure oder die dehydrogenative Kopplung von Aminen mit Aluminium(III)-Komplexen.[19e] Die reduzierte Form des redox-aktiven Bis(imino)-Pyridin Liganden in diesen Komplexen ermöglichte die selektive Spaltung von X−H Bindungen der Substrate, sowie die Stabilisierung von Übergangszuständen bei der β-Hydridabstraktion während der Katalyse.[19e, 42] Eine Änderung des Ladungszustandes von redox-aktiven Liganden in Hauptgruppenmetall-Komplexen, die durch einen ligandzentrierten Elektronentransfer bedingt ist, wird weniger häufig beobachtet.[19d] Durch Einelektronenoxidation des redox-aktiven 1,2-Bis(arylimino)acenaphthen (BIAN) Liganden in einem Magnesium-Komplex kann beispielsweise 2,2,6,6-Tetramethylpiperidinyloxyl (TEMPO) reduziert werden.[43] Ein Aluminium-Komplex des BIAN-Liganden ist in der Lage, durch Ligandoxidation Ketone zu reduzieren.[44] Auch weitere Aluminium-Komplexe mit Liganden wie Diphenolaminen,[45] α-Diiminen[46] und α-Iminopyridinen[33a, 47] zeigen ligandbasierte Elektronenübertragungen. In der Radikalchemie verhalfen redox-aktive Liganden Hauptgruppenmetall-Komplexen außerdem zu deren Einsatz in selektiven, über Radikalreaktionen ablaufenden, Bindungsknüpfungsreaktionen.[48] Dies konnte zum Beispiel an einem Magnesium-Komplex mit einem redox-aktiven BIAN Liganden gezeigt werden. Die Reaktion des untersuchten Komplexes mit Benzophenon führte zu C−C und H−H Bindungsknüpfungen die mit der Änderung des Oxidationszustandes des Liganden von einer dianionischen Form zur radikal monoanionischen Form einhergingen.[48-49] Kontrollierte radikalische C−C Bindungsbildungen, die, aufgrund der hohen Spindichte an bestimmten Positionen des Liganden, am Liganden selbst stattfinden, sind ebenfalls bekannt. Beispielhaft ist hierfür die bereits beschriebene reversible reduktive Dimersierung eines Natrium-ATI-Komplexes zu nennen (Schema 4).[39] Ähnlich dazu führte Einelektronenreduktion des Aluminium-Komplexes $[\mathrm{AlCl(IP^{\bullet})}]_2$ mit zwei monoanionischen α-Iminopyridin Liganden ($\mathrm{IP^{-}}$) nicht zum Komplex $[\mathrm{Al(IP^{\bullet})(IP)^{2-}}]$, sondern zu einer Rekombination zweier *in situ* gebildeter ligandzentrierter Radikale unter Ausbildung der dimeren Spezies $[(\mathrm{IP^{2-}})\mathrm{Al}\text{-}\mu(\mathrm{IP{-}IP^{2-}})\text{-}\mathrm{Al}(\mathrm{IP^{2-}})]$ (Schema 5, rechts).[50] Dagegen ist der Komplex $[\mathrm{AlCl(IP^{\bullet})_2}]$ selbst mit zwei ligandzentrierten Radikalen stabil und isolierbar, was mit einer antiferromagnetischen Kopplung der ungepaarten Elektronen über das Aluminiumzentrum erklärt wurde (Schema 5, links).[50]

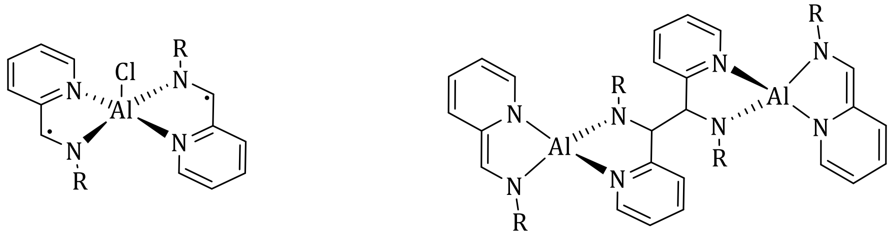

$[AlCl(IP^{\bullet})_2]$ **$[(IP^{2-})Al\text{-}\mu(IP{-}IP^{2-})\text{-}Al(IP^{2-})]$**

Schema 5: Stabiler Biradikalkomplex $[AlCl(IP^{\bullet})_2]$ und durch Rekombination zweier ligandzentrierter Radikale gebildetes Dimer $[(IP^{2-})Al\text{-}\mu(IP{-}IP^{2-})\text{-}Al(IP^{2-})]$. R = 2,6-*i*$Pr_2$-$C_6H_3$.[50]

Ein redox-aktiver Ferrocen-Ligand in der Koordinationssphäre von Indium konnte als Schalter für die Kontrolle der Ringöffnungspolymerisation von 1,3-Dioxan-2-on genutzt werden.[51] Die Veränderung des Oxidationszustandes des Eisenatoms erlaubte dabei den Wechsel zwischen katalytisch aktiver und weniger aktiver Form.[51a] Kürzlich konnte außerdem der erste Hauptgruppenmetall-Komplex isoliert und charakterisiert werden, der redox-isomere Eigenschaften zeigt.[52] Der untersuchte Bis-*o*-Aminophenol-Zinn-Komplex kann in Lösung als diamagnetische Sn(IV)-Spezies und als paramagnetische Sn(II)-Spezies vorliegen, wobei die redox-aktiven Liganden das Metall in ihrer dianionischen Form (AP) pseudotetraedrisch oder in ihrer radikal-monoanionischen Form (imSQ) quadratisch pyramidal (Pseudostruktur) umgeben (Schema 6).

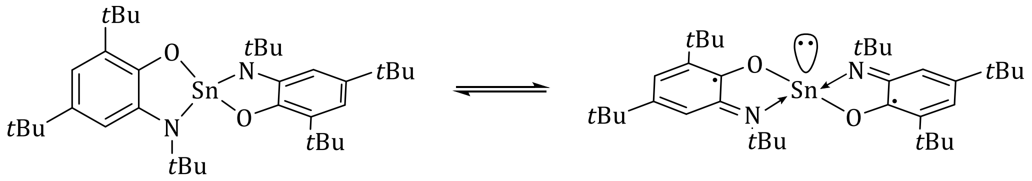

$(AP)_2Sn^{IV}$ **$(imSQ)_2Sn^{II}$**

Schema 6: Redox-Isomere eines Bis-*o*-Aminophenol-Zinn-Komplexes.[52]

Die Gruppe um *Berben* konnte außerdem zeigen, dass eine Kombination von ligandvermittelter Protonen- und Elektronenübertragung möglich ist.[19a, 19d] Dafür wurde die elektrokatalytische Wasserstoffentwicklung aus Aluminium-Komplexen mit redox-aktiven Liganden unterschiedlicher Acidität untersucht. Der beobachtete Reaktionsmechanismus, der zwei Elektronentransfer- und zwei Protonentransfer-Schritte beinhaltet, wurde durch die Acidität der Liganden maßgeblich beeinflusst (Schema 7).[19d]

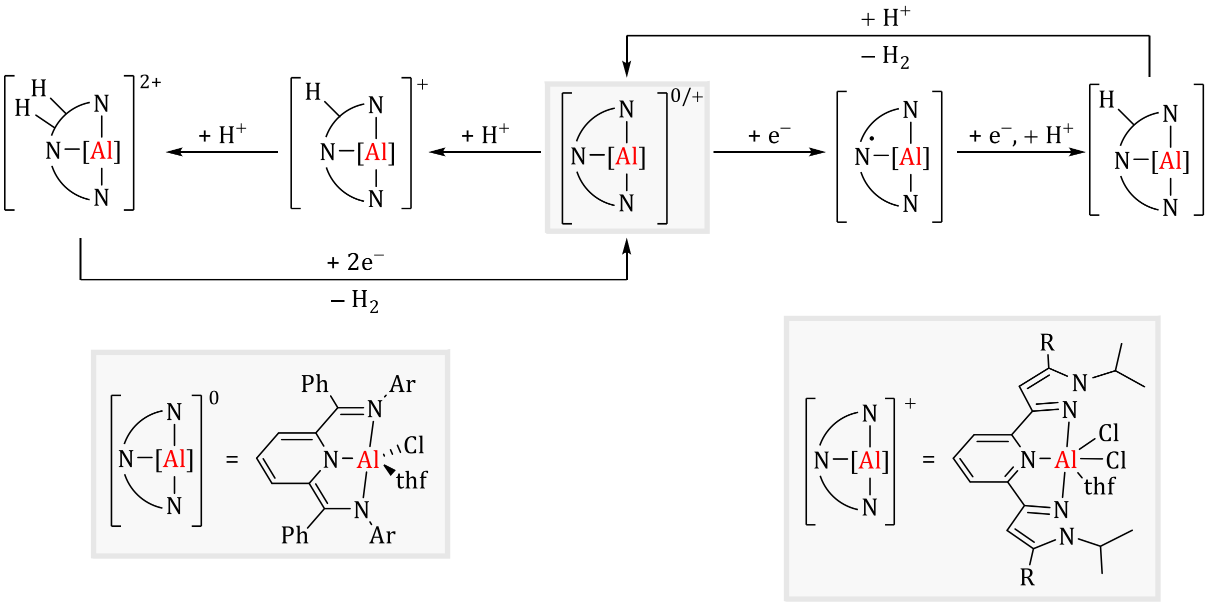

Schema 7: Schematische Darstellung der Reaktionssequenz zur katalytischen Wasserstoffentwicklung mit zwei verschiedenen Aluminium(III)-Komplexen.[19a, 19d]

Im Zuge der Etablierung von redox-aktiven Liganden für Komplexe von Hauptgruppen-Metallen, wurde diese Ligandklasse auch für Koordinationskomplexe von Bismut verwendet. $BiCl_3$ bildet beispielsweise Donor-Akzeptor Komplexe mit redox-aktiven, aryl-substituierten Bis-(imino)acenaphthen Liganden. Die Komplexe wurden allerdings lediglich auf ihre strukturellen Parameter hin untersucht.[53] Eine Reihe weiterer, heteroleptischer Bismut-Halogenid-Komplexe mit prinzipiell redox-aktiven Liganden wie β-Dialdiminaten, β-Diketiminaten und Pyrrol-basierten Liganden sind bekannt, ihre Redox-Eigenschaften wurden aber nicht untersucht.[54] Größtenteils beschränkt sich die Redox-Chemie von Bismut-Komplexen auf metallzentrierte Redox-Prozesse. Die Gruppe um *Cornella* beispielsweise beschäftigte sich kürzlich mit Bi(I)/Bi(III) und Bi(III)/Bi(V) Redox-Paaren, die in der katalytischen Transferhydrierung sowie der Fluorierung von Boronsäurederivaten auftraten.[55] Die Gruppe um *Chitnis* untersuchte ein Bismuttriamid mit T-förmiger Ligandstruktur in welchem das Bismutatom in einem „redox-verwirrten“ Bi(I)/Bi(III) Zustand vorliegt, was mit Hilfe von DFT-Rechnungen sowie Reaktivitätsstudien nachgewiesen werden konnte.[56] Für eine kationische Bismut(III)-Carbamoyl-Spezies wurde unter elektrochemischen Bedingungen ein chemisch reversibler Redox-Prozess zwischen dem Redox-Paar Bi(II)/Bi(III) beobachtet.[57] Isoliert werden konnten niedervalente Bi(I)- bzw. Bi(II)-Spezies zum Beispiel in Form von Dibismutenen oder als monomere Bismutinidene bzw. als Dibismutane oder monomere Bismutinyl-Radikale.[58] Die Verwendung redox-aktiver Liganden in der niedervalenten Bismut-Chemie ist wenig untersucht. Ein Beispiel ist ein Dibismuten mit redox-aktiven Ferrocenyl-Liganden.[59] Die elektrochemische Untersuchung dieses Bi(I)-Systems konnte zeigen, dass die π-Elektronen in der Bi=Bi Bindung als effektive π-Brücken zwischen den beiden Liganden fungieren. *Turner* legte bei der Untersuchung einer radikalischen Bismutinyl-Spezies das Augenmerk auf einen redox-aktiven Pyridin-Dipyrrolid-Liganden.[60] Eine elektronische Stabilisierung der intermediär gebildeten Bi(II)-Spezies durch Übertagung von Elektronendichte vom Metallzentrum auf den Liganden, und damit die Isolierung dieser Spezies, gelang nicht. Die postulierte Radikalspezies konnte allerdings durch eine Abfangreaktion mit dem stabilen organischen Radikal TEMPO indirekt nachgewiesen werden.

II Zielsetzung

Die zunehmende Präsenz redox-aktiver Liganden in der Hauptgruppenchemie und deren Potential in der Stabilisierung niedervalenter Spezies sowie in der Beeinflussung der Reaktivität von Hauptgruppenmetall-Komplexen, zum Beispiel durch das Ermöglichen übergangsmetall-ähnlichen Verhaltens, motivierte zu dieser Dissertation. Ein in diesem Zusammenhang wenig untersuchtes Ligand-System ist das der erst 2016 als redox-aktiv identifizierten Aminotroponiminate (ATIs).[39] Neben ihrer Redox-Aktivität konnte 2016 anhand der strukturellen Charakterisierung eines Natrium-ATI-Komplexes außerdem die vorher in der Literatur nicht diskutierte Fähigkeit des ATI-Liganden zur Ausbildung von Metall-Aren-Wechselwirkungen im Festkörper offengelegt werden, die eine interessante Erweiterung der limitierten Koordinationschemie von ATI-Komplexen darstellte.[61]

Auf Grundlage dieser Ergebnisse sollte im Rahmen dieser Arbeit die Koordinationschemie, die Reaktivität und das Redox-Verhalten von Alkalimetall-ATI-Komplexen tiefergehend untersucht werden. Der Fokus sollte dabei auf der Untersuchung des Einflusses sterischer und elektronischer Eigenschaften des ATI-Liganden sowie auf der Untersuchung des Einflusses des Zentral-Atoms liegen. Die Eigenschaften des Liganden sollten durch verschiedene Substituenten an den Stickstoffatomen sowie am C_7-Rückgrat des Liganden modifiziert werden. Ein Augenmerk sollte anschließend auf der strukturellen Charakterisierung von ATI-Komplexen der Alkalimetall-Reihe Lithium bis Kalium liegen. Insbesondere sollte untersucht werden, welche Faktoren für die Ausbildung von Metall-Aren-Wechselwirkungen verantwortlich sind. Die Kenntnis der Struktur im Festkörper und in Lösung sollte dazu dienen, einen Bezug dieser zur Reaktivität verschiedener Komplexe herzustellen, um die Reaktivität damit gezielt beeinflussen zu können. Ein wesentliches Interesse bei der Untersuchung des Redox-Verhaltens von Alkalimetall-ATI-Komplexen sollte auf der Erforschung des Einflusses der elektronischen und sterischen Eigenschaften der Liganden sowie des Zentral-Atoms auf die Generierung von ligandzentrierten Radikalen bzw. auf die Möglichkeit der Realisierung ligandzentrierter kontrollierter C−C Bindungsknüpfungen liegen.

Da redox-aktive Liganden in der Koordinationssphäre von Bismut bisher wenig untersucht worden sind, sollte der ATI-Ligand auf Bismut als Zentral-Atom übertragen werden. Die Untersuchung der Bismut-ATI-Komplexe sollte dabei neben der strukturellen Charakterisierung vor allem deren Redox-Eigenschaften umfassen. Insbesondere sollte erforscht werden, in wieweit die Ladung der Komplexe das Redox-Verhalten beeinflusst und ob die redox-aktiven Eigenschaften des Liganden zu einer Stabilisierung radikalischer Bismut-Spezies beitragen können.

III New Perspectives for Aminotroponiminates: Coordination Chemistry, Redox Behavior, Cooperativity, and Catalysis

Anna Hanft, Crispin Lichtenberg

Vervielfältigt aus Referenz:

Eur. J. Inorg. Chem. **2018**, 3361-3373.[65]

DOI: 10.1002/ejic.201800465

mit der Erlaubnis von John Wiley and Sons.

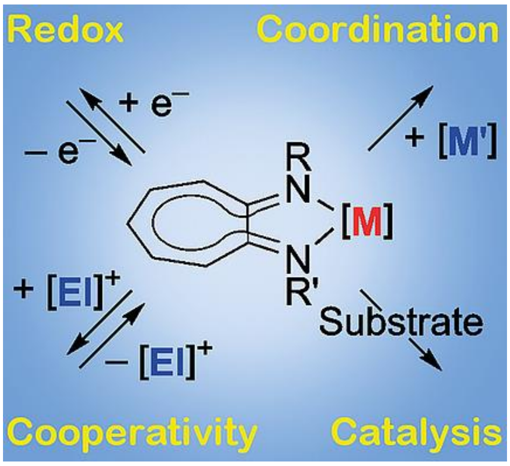

ChemPubSoc Europe
DOI: 10.1002/ejic.201800465
EurJIC European Journal of Inorganic Chemistry
Microreview

Aminotroponiminates | *Very Important Paper* |

New Perspectives for Aminotroponiminates: Coordination Chemistry, Redox Behavior, Cooperativity, and Catalysis

Anna Hanft[a] and Crispin Lichtenberg*[a]

Abstract: Aminotroponiminates (ATIs) are monoanionic ligands with an *N*,*N*-binding pocket and a rigid, planar, unsaturated, C_7-ring as a ligand backbone. Recent findings show that this ligand backbone can play an active role in coordination chemistry, redox reactions, and ligand-centered reactivity of ATI complexes. Based on these results, ATIs have been recognized as redox-active and cooperative ligands, which has implications for existing and potential future applications of ATI compounds in synthesis, catalysis, and materials science. The catalytic applications of ATI complexes are summarized in this Microreview, including results from the fields of hydroamination, epoxidation, cyanosilylation, ε-caprolactone-, olefin-, epoxide-, and epoxide/CO_2 (co-)polymerization as well as electron transfer catalysis. Furthermore, recent advances in the use of ATI ligands for stabilizing heavy analogs of carbon oxo compounds are showcased.

1. Introduction

Aminotroponiminates (ATIs) have garnered extensive interest as easily accessible ligands that readily form complexes with (semi-)metals across large sections of the periodic table. Bearing one amino and one imino functionality, ATIs bridge the gap between the well-established diazadiene and phenylenediamine ligand scaffolds (Scheme 1a). ATIs are structurally related to amidinates and β-diketiminates (Scheme 1b). They are distinguished from these types of ligands by a rigid C_7 ligand backbone, which is a prominent structural feature of the ATI ligand family. ATIs have found application in the stabilization of cationic group 13 complexes,[1] as substitutes for cyclopentadienide ligands in lanthanoid chemistry,[2,3] for the synthesis of hyper- and hypo-valent group 14 compounds,[4,5] in the investigation of spin delocalization of first row-transition metal complexes,[6] and in hydroamination catalysis.[7] These fields have been covered elsewhere by the cited review articles.

Traditionally, ATIs have been exploited as molecules that are:
(i) monoanionic
(ii) *N*,*N*-bidentate
(iii) redox-innocent under reducing conditions
(iv) chemically inert in their C_7 backbone
(v) spectator ligands (exception: chiral induction).

However, this traditional perception of ATI ligands has recently been challenged (Scheme 1c). This is in large part due to insights involving the chemistry of the C_7 ligand backbone.

---

[a] Department of Inorganic Chemistry,
Julius-Maximilians-Universität
Würzburg,
Am Hubland, 97074 Würzburg, Germany
E-mail: crispin.lichtenberg@uni-wuerzburg.de
http://www-anorganik.chemie.uni-wuerzburg.de/startseite

ORCID(s) from the author(s) for this article is/are available on the WWW under https://doi.org/10.1002/ejic.201800465.

Anna Hanft obtained her M. Sc. in chemistry under the supervision of Dr. C. Lichtenberg at the Julius-Maximilians-Universität Würzburg. In 2017, she started her PhD thesis funded by a doctoral fellowship of the Fonds der Chemischen Industrie. Her research interests center around the coordination chemistry, redox-behavior, and catalytic applications of monometallic and mixed-metal ATI compounds.

Crispin Lichtenberg obtained his Diploma in chemistry under the supervision of Prof. J. Sundermeyer (Philipps-Universität Marburg) and his Ph.D. under the guidance of Prof. J. Okuda (RWTH Aachen). Postdoctoral work with Prof. H. Grützmacher led him to the ETH Zurich. Holding a Liebig- and an Emil Fischer fellowship, he currently works as a Junior Group Leader associated with Prof. H. Braunschweig at the Julius-Maximilians-Universität Würzburg. His research interests include new properties of aminotroponiminates and the exploitation of ionic and radical bismuth compounds in synthesis and catalysis.

ChemPubSoc Europe
EurJIC European Journal of Inorganic Chemistry
Microreview

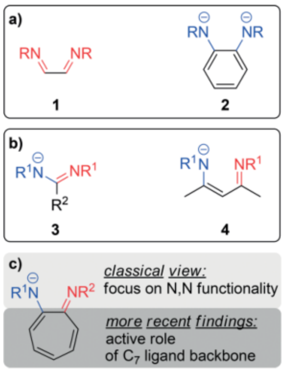

Scheme 1. Comparison of selected *N,N*-chelating ligands: (a) diazadienes and phenylenediamines; (b) amidinates and β-diketiminates; (c) aminotroponiminates (ATIs) with separate view of the *N,N* functionality and the C_7 ligand backbone.

New findings have revealed the potential of the ATI ligand backbone to play an active role in coordination chemistry, redox-reactions, and ligand cooperativity.

This review article highlights these new aspects of the well-established ATI ligand family. In addition, recent findings in the fields of ATI ligand synthesis, catalytic applications based on ATI complexes, and ATI-stabilized heavy analogs of carbon oxo compounds are also covered.

2. Ligand Synthesis

Straightforward protocols for the synthesis of ATIs with different substituents at the two nitrogen atoms are available (Scheme 2).[8,9] The first NR group can be introduced either in transition metal-free protocols[10] or in Pd-catalyzed reactions for less nucleophilic amines.[11] The resulting aminotropones **6** are commonly transformed into the desired ATI ligands by consecutive addition of a Meerwein salt and the desired amine in a one-pot-reaction. Compounds of type **7a** have been isolated and suggested as intermediates in this reaction.[10,12] More recently, a cationic compound **7b** was isolated and shown to react much faster with a given amine than its neutral counterpart **7a** (R^1 = 2,6-diisopropylphenyl).[13] In one-pot-reactions (and also when isolated **7b** is used as a starting material), intermediates of type **7a** and **7b** may coexist in equilibrium reactions.

Using the protocols shown in Scheme 2, a variety of functional groups R^1/R^2 can be introduced, including alkyl and aryl moieties, NR_2 groups, alkyl groups with additional donor functionalities (cf., section 3.8.), chiral substituents, and redox-active substituents (cf., section 4.2.).[10,11,13–15] Since steric protection has been one of the successful strategies for the stabilization of highly reactive species in recent decades, ATIs with bulky aryl groups at the nitrogen atoms can be attractive synthetic targets. Along these lines, the combination of R^1 = sterically demanding aryl group and R^2 = alkyl group can be realized as a substitution pattern in ATI ligands,[11,13] however, the installation of two sterically demanding 2,6-substituted aryl groups has been described as problematic.[16]

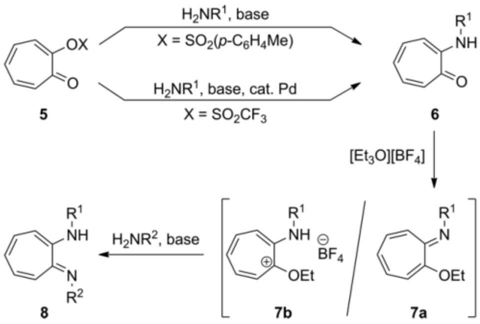

Scheme 2. Synthetic routes to aminotroponiminates (ATIs) **8**.

After initial reports on the functionalization of the C_7 ligand backbone in the 5-position via electrophilic aromatic substitution,[17,18] this type of reaction has recently been investigated in further detail.[19–23] Bromination proceeds smoothly and in excellent yields (90 %),[17,18,20–22] while other substituents can be introduced only with lower yields of 19–43 % [Scheme 3, E = Br, I, N_2Aryl, NO_2, COMe, $C_2(CN)_3$].[19,22,24] The bromo-substituted compound **9-Br** can be subjected to nucleophilic aromatic substitution to give **10-Nu** in excellent yields (92–99 %) {Scheme 3: Nu = SPh, S[3,5-$C_6H_3(CF_3)_2$], SePh, TePh; Nu = S(O)Ph with one additional step}.[22] The electronic parameters of the substituents in the C_7 backbone can affect the performance of ATI complexes as catalysts, as demonstrated for zinc ATIs as catalysts in hydroamination reactions.[7]

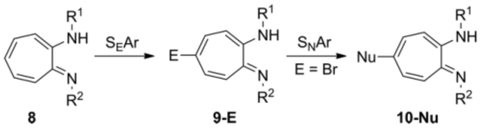

Scheme 3. Functionalization of the C_7 ligand backbone of ATIs in the 5-position by electrophilic and nucleophilic aromatic substitution, respectively.

3. Coordination Chemistry

3.1. Terminal *N,N*-Coordination Mode (A)

The metalacyclic structural motif **A**, with the metal center in the *N,N*-binding pocket of the ligand, represents the archetypical bonding mode of the ATI ligand family (Scheme 4). It was first reported in the early 1960s along with the first ATI metal complexes,[25] and first structurally authenticated by single-crystal X-ray analysis of [Mn($ATI^{Ph/Ph}$)$_2$(acac)] in 1970 (acac = acetylacetonate).[26] Coordination mode **A** predominates in the coordination chemistry of ATI compounds, although new coordination modes have recently been unraveled (vide infra).[27]

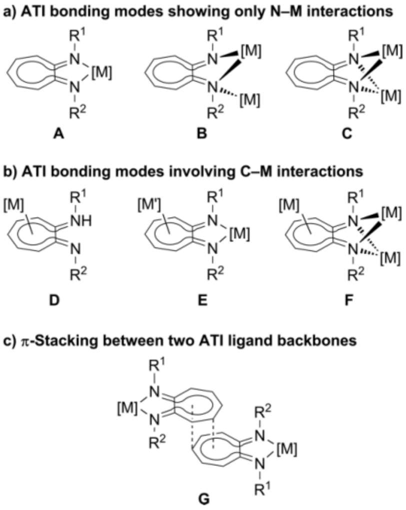

Scheme 4. Coordination modes of ATI ligands.

3.2. Bridging *N,N*-Coordination Modes (B, C)

In coordination modes **B** and **C**, the ATI ligand occupies a bridging position between two metal centers (Scheme 4). Either one (**B**) or two (**C**) nitrogen atoms interact with two metal atoms. These bonding modes are closely related to **A** in that only M–N interactions are present and the ATI ligand acts as a monotopic ligand. Due to the bridging position of the ATI ligand, coordination modes **B** and **C** can in principle be found in small aggregates or in coordination polymers. Type **B** has been reported for a dinuclear, cationic aluminum compound, $[AlEt(\mu_2\text{-}\eta^2,\eta^1\text{-ATI}^{iPr/iPr})(\mu_2\text{-Et})\text{-AlEt}_2][B(C_6F_5)_4]$ (Figure 1a).[28] Coordination mode **C** was first realized for Li and Ca ATI compounds through co-complexation with lithium iodide (Figure 1b).[29] Recently, $[K(ATI^{Ph/iPr})(thf)]$ was described as an example of a monometallic complex with a type **B** bonding mode that leads to a polymeric structure in the solid state (Figure 1c).

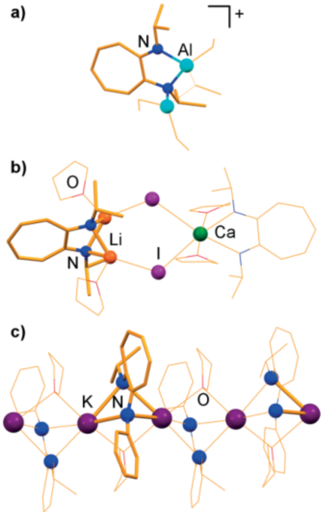

Figure 1. Examples of structurally authenticated molecules with ATI ligands in coordination modes **B** (a) and **C** (b,c) (cf., Scheme 4). (a) molecular structure of the cationic part of $[Al_2(ATI^{iPr/iPr})Et_4][B(C_6F_5)_4]$; (b) molecular structure of $[Li_2Ca(ATI^{iPr/iPr})_2I_2(thf)_2]$; (c) cutout of the solid-state structure of coordination polymer $[K(ATI^{Ph/iPr})(thf)]_\infty$.

3.3. M–C Interactions with Neutral H-ATI Ligands (D)

More recently, the C_7 backbone of ATI ligands has been a focus of considerable research efforts with respect to its role in coordination chemistry. For neutral ATI ligands (H-ATI) that bear a proton in the *N,N*-binding pocket, coordination mode **D** with $M\text{–}C^{\text{ATI–backbone}}$ bonding interactions has been realized (Scheme 4).[30] The arenophilic $[Ru(C_5Me_5)]^+$ group could be coordinated to the ligand backbone of H-ATI$^{iPr/iPr}$ to give the cationic species $[Ru(C_5Me_5)(\text{H-ATI}^{iPr/iPr})]^+$ (Figure 2). NMR spectroscopic investigations revealed an apparent C_S symmetry of the complex in solution and a significant high-field shift of the C^{backbone} resonances, relative to those of the free H-ATI ligand.

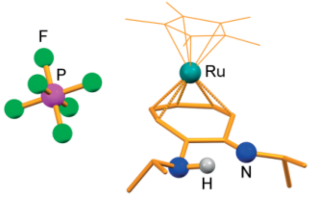

Figure 2. Molecular structure in the solid state of $[Ru(C_5Me_5)(\text{H-ATI}^{iPr/iPr})][PF_6]$ showing coordination mode **D** with a neutral H-ATI ligand (cf., Scheme 4).

3.4. ATIs as Ditopic *N,N*/C_7 Ligands (E)

For ATIs in their monoanionic form, the analogous coordination mode **E** has been reported, making this ligand ditopic (Scheme 4). Whereas the *N,N*-binding site can be considered as relatively hard, the C_7 binding site is classified as relatively soft. The coordination mode **E** was first analyzed in detail for the sodium complex $[Na(ATI^{Ph/iPr})(thf)]$, for which it leads to a one-dimensional coordination polymer in the solid state (Figure 3).[31,32] Related ATI complexes of Na and K have been shown to adopt the same coordination mode in the solid state.[33]

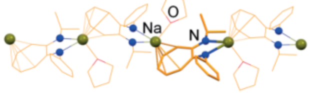

Figure 3. Cutout of the solid-state structure of coordination polymer $[Na(ATI^{Ph/iPr})(thf)]_\infty$ with a type **E** coordination mode (cf., Scheme 4).

A frontier orbital analysis of model compounds $[Na(ATI^{R/R'})(thf)_2]$ revealed strong contributions of p_z-type orbitals of the carbon atoms in the ligand backbone to the HOMO and the LUMO (Figure 4, top).[31,34] Thus, ligand-to-metal (L→M) bonding and metal-to-ligand (M→L) backbonding involving the ATI C_7 backbone appear to be possible.[31] The substitution pattern at the nitrogen atoms of the ATI ligands was shown to have a significant influence on the HOMO/LUMO energies (Figure 4, bottom). This makes ATI ligands with electron donating substituents at nitrogen more suitable for ligand-to-metal (L→M) bonding of type **E**, which was confirmed experimentally.[33] DFT calculations and NMR spectroscopic studies suggest that the coordination mode **E** is not only relevant in the solid state, but also in solution {e.g. dinuclear complexes in equilibrium reactions: 2 $[Na(ATI)(thf)_2] \rightleftarrows [Na_2(ATI)_2(thf)_3]$ + THF}.[31]

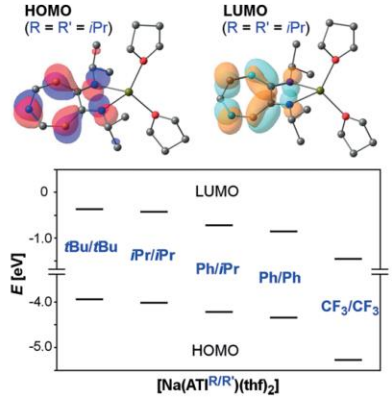

Figure 4. Top: HOMO (left) and LUMO (right) of $[Na(ATI^{iPr/iPr})(thf)_2]$. Bottom: HOMO and LUMO energies of $[Na(ATI^{R/R'})(thf)_2]$ (R/R′ = tBu/tBu; iPr/iPr, Ph/iPr, Ph/Ph, CF_3/CF_3). Reprinted with permission from ref.[34] Copyright 2018 American Chemical Society.

The different properties of the *N*,*N* and the C_7 binding sites of ATI ligands suggest that the synthesis of well-defined mixed-metal compounds should be possible. Indeed, potassium/sodium compounds of type $[KNa(ATI)_2(thf)_2]$ with coordination mode **E** were recently reported as the first representatives of these species. These compounds form coordination polymers in the solid state (Figure 5). According to the hard/soft acid/base principle, potassium ions interact with the softer ligand backbone and sodium atoms are found in the harder *N*,*N*-binding pocket.[33]

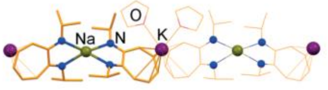

Figure 5. Cutout of the solid-state structure of coordination polymer $[KNa(ATI^{iPr/iPr})_2(thf)_2]_\infty$ with a type **E** coordination mode (cf., Scheme 4).

3.5. ATIs Interacting with Three Metal Centers (F)

Whereas ATI ligands in coordination modes **A**–**E** show interactions with one (**A**, **D**) or two metal centers (**B**, **C**, **E**), the interaction of one ATI ligand with three metal ions is also possible. This has been demonstrated for the potassium compound $[K(ATI^{Ph/Ph})]$, which crystallized free of any neutral donor ligands as a coordination polymer, resulting in coordination mode **F** (Figure 6).[34]

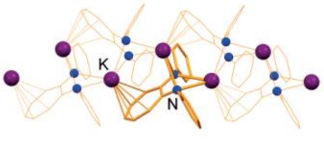

Figure 6. Cutout of the solid-state structure of coordination polymer $[K(ATI^{Ph/Ph})]_\infty$ with a type **F** coordination mode (cf., Scheme 4).

3.6. Stacking between ATI Ligand Backbones (G)

An aromatic character has been suggested for ATI ligands with their characteristic C_7N_2 moiety bearing 10 π-electrons.[78] Thus, it was almost surprising that only recently the first example of arene•••arene interactions with this functional group have been reported. In this specific example, parallel-displaced π•••π-interactions are realized between two ATI ligands, each of which also hosts a metal atom in its *N*,*N*-binding pocket (Figure 7).[15] These interactions were observed in the bismuth compound $[BiCl_2(ATI^{Fc/iPr})]$, which shows additional weak Bi•••Cl interactions, leading to formation of an organic/inorganic coordination polymer in the solid state.

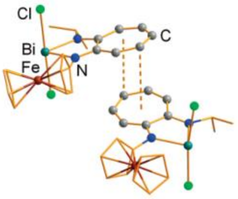

Figure 7. Cutout of the solid-state structure of coordination polymer $[BiCl_2(ATI^{Fc/iPr})]_\infty$ with a type **G** coordination mode (additional intermolecular Bi•••Cl interactions not shown; Fc = ferrocenyl; also see Scheme 4).

The coordination modes of type **B**–**G** exemplify the rich coordination chemistry of the ATI ligand family, which goes far beyond the archetypical and most frequently observed bonding mode **A**. In addition to molecular compounds and small aggregates, coordination polymers are also accessible, especially for bonding modes **E**, **F**, and **G**, which confer a ditopic character to the ATI ligand.

3.7. Flexibility of the C_7N_2 Core of ATI Ligands

ATIs are classified as relatively rigid ligands due to their seven-membered ring consisting exclusively of sp^2 hybridized carbon atoms.[2] Nevertheless, this structural motif shows a certain degree of flexibility. The C_7N_2 unit, which is the core of every ATI ligand, can deviate significantly from the expected planarity in two ways. The first possibility is the puckering of the ligand, which has been quantified by the dihedral angle between the mean planes defined by the atoms [C1–7] and [C1–2,N1–2,M] (Scheme 5a, b).[35,36] Values ranging from 0° to ca. 25° are commonly observed for almost perfectly planar and significantly twisted ring motifs, respectively.[37,38] Analyses of the factors leading to puckering of ATI ligands show that the nature of the (semi-)metal in the ATI binding pocket and the steric bulk of the substituents at nitrogen have to be taken into account.[35,36] A certain degree of puckering is a common phenomenon in ATI complexes. The second possibility for the C_7N_2 unit of ATI ligands to deviate from planarity is bending about the C3/C7 axis (Scheme 5a, c). This deformation may be quantified using the angle between the mean planes defined by the atoms [C3–C7] on the one hand and [C1–3,C7] on the other hand (Scheme 5a, c). This bending mode of the ATI ligand is rare, but has been observed for the previously mentioned complex $[Ru(C_5Me_5)(H\text{-}ATI^{iPr/iPr})]^+$, which shows a type **D** bonding mode.[30] The bending angle of the H-ATI ligand in this compound amounts to 28.2°. Bending of the ATI ligand has so far not been described as a general phenomenon for compounds with ATI ligands in bonding mode **E**.

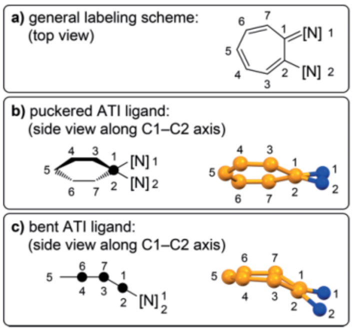

Scheme 5. Conformations of ATI ligands in which the C_7N_2 motif deviates significantly from planarity. (a) general labeling scheme; (b) puckering of ATI ligand {structural data taken from $[Ge(ATI^{tBu/tBu})F]$[36]}; (c) bending of ATI ligand {structural data taken from $[Ru(C_5Me_5)(H\text{-}ATI^{iPr/iPr})][PF_6]$[30]}.

3.8. ATI Ligands with Additional Donor Groups at N

In order to increase the denticity of ATI compounds, substituents with additional donor functionalities can be installed at the nitrogen atoms of these ligands. In this respect, bridged ATI compounds and tropocoronands have been investigated in some detail, and most of this work has previously been reviewed.[2,4] Apart from such ligands containing two ATI moieties, there are relatively few examples of ATIs with additional donor groups in the substituents bound to N. However, most of these compounds were only used as starting materials for ligands containing two or more ATI groups.[39–46] Other examples were investigated more from a heterocyclic chemistry viewpoint than that of coordination chemistry.[47,48]

Examples of ATIs that bear donor functionalities within the substituents at nitrogen and have been ligated to metal centers are shown in Figure 8a. Two zinc complexes, $[Zn(ATI^{R/R})_2]$ {R = $(CH_2)_nOMe$, n = 2, 3}, were isolated and fully characterized, but do not show any interactions between the metal center and the ether groups that are part of the substituents at nitrogen.[49] The same has been suggested for a range of nickel complexes of type $[Ni(ATI)_2]$.[50] For the nickel complex **11**, the structure shown in Figure 8b has been assigned on the basis of NMR spectroscopic studies, but was not unequivocally proven by methods such as single-crystal X-ray diffraction.[51] In this context, the lithium complex $Li(ATI^{Ph/Ph})$ should be mentioned, since an unusual Li–Ph contact was detected for this compound in the solid state (Figure 8b, bottom).[34] Finally, bridged ATIs and tropocoronands should formally also be mentioned in the category of ATI ligands with additional donor groups at N (Figure 8c).[2–4,52–57]

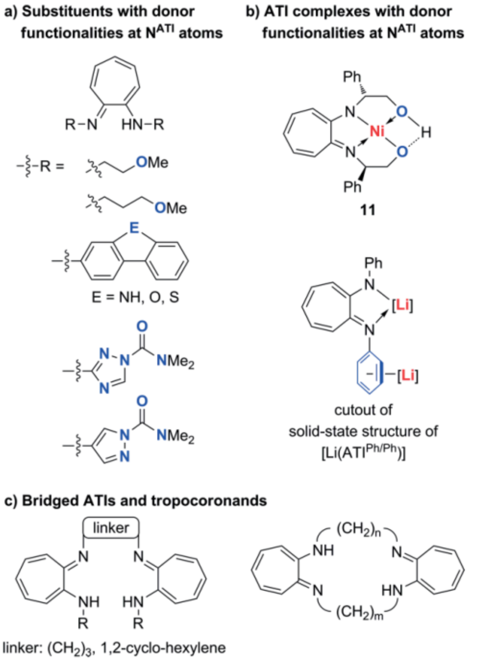

Figure 8. Examples of (a) H-ATI ligands that bear donor functionalities in the substituents at the N^{ATI} atoms; (b) ATI complexes with substituents at N^{ATI} atoms that are involved in donor•••M interactions; (c) bridged ATIs and tropocoronands.

4. Redox Chemistry

4.1. Metal-Centered Redox Chemistry

ATI and tropocoronand complexes of cobalt show (quasi-) reversible redox events in a potential range of –0.05 V to –2.6 V vs. $Fe(C_5H_5)_2/[Fe(C_5H_5)_2]^+$ (Scheme 6).[54–56] Based on comparison with structurally related zinc and gallium compounds, these redox events were ascribed to metal-centered processes (Co^I/

Co^{II} and Co^{II}/Co^{III} couples).[56,57] In tropocoronand complexes, the electrochemical properties can be tuned by the angle Θ between the two C_7 planes of the macrocyclic ligands, which in turn is controlled by the length of the $(CH_2)_{n/m}$ linkers between the ATI moieties (Scheme 6). With larger Θ values, the potentials for oxidation and reduction are shifted to more positive and negative values, respectively, i.e. oxidation and reduction become more difficult. Shifts of electrochemical potentials of up to +0.23 V and –0.34 V were observed, when Θ was varied from 9° to 84°. In a series of cobalt tropocoronands, a linear correlation was observed between the angle Θ and the redox potentials for oxidation/reduction.

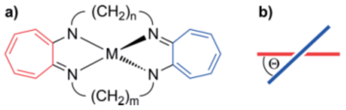

Scheme 6. (a) A tropocoronand complex with its two C_7 groups highlighted (*n*, *m* = 3–6). (b) Angle Θ between the two planes that are defined by the two C_7 groups of tropocoronands; the color code is according to (a).

The ruthenium compound $[Ru(C_5Me_5)(H\text{-}ATI^{iPr/iPr})][PF_6]$ shows an irreversible oxidation and reduction wave with peak potentials of +0.9 V and –1.8 V, respectively.[30,58] The analogous aminotropone and tropolone complexes show a similar electrochemical behavior. The redox events were classified as metal-based processes based on comparison with trorucene compounds[59] and EPR spectroscopic measurements.

4.2. Ligand-Centered Redox Chemistry under Oxidative Conditions

Under oxidative conditions (+0.5 to +0.9 V),[58] irreversible electron transfer has been observed for H-ATI ligands and ATI or tropocoronand complexes of Na, Ga, Zn, Co, and Rh.[54–57,60] These redox events were reasoned to be ligand-centered, since they were observed for the ligands themselves or for complexes of metals that can be regarded as redox-inactive under the applied conditions (Na, Ga, Zn). Ligand-centered oxidations of cationic gallium compounds, $[Ga(tropocoronand)]^+$, occurred at more positive potentials than those of the neutral zinc analogs, which can be attributed to the higher Lewis acidity of the Ga species.[56] For compounds containing more than one ATI ligand and sulfonyl groups at the N^{ATI} atoms, up to two additional irreversible, presumably ligand-centered oxidation waves were reported in the range of +0.8 V to +1.1 V vs. $Fe(C_5H_5)_2/[Fe(C_5H_5)_2]^+$.[55] For all these cases, the products of the reactions induced by irreversible electron transfer have not been characterized.

The behavior of ATI-related species under oxidative conditions has been investigated in more detail. For the cyclohepta[*b*]quinoxalinium cation **12**, which is structurally related to ATI compounds, but shows different electronic properties due to its tricyclic structure, a dimerization has been observed upon double deprotonation under atmospheric conditions (Scheme 7).[61] This oxidatively induced dimerization is chemically reversible as shown by reductive cleavage of **13** to regenerate **12** in acidic media.

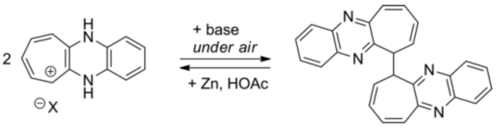

Scheme 7. Behavior of ATI-related species under oxidative conditions: Release of two protons and an electron from **12** gives C–C coupling product **13** in a chemically reversible reaction.

The redox-properties described above are directly related to the properties of the C_7N_2 structural core motif of ATI ligands. In addition, an ATI ligand with a ferrocenyl group as a redox-active substituent at one of the N^{ATI} atoms has recently been reported.[15] The half-wave potential of this $H\text{-}ATI^{Fc/iPr}$ ligand amounts to –0.18 V vs. $Fe(C_5H_5)_2/[Fe(C_5H_5)_2]^+$. In the bismuth compound $[Bi(ATI^{Fc/iPr})_3]$ (**14**), three reversible redox events are detected in the range of –0.23 to +0.09 V (Figure 9).[58] The peak separation in the cyclic voltammogram indicates weak electronic communication between the three ferrocenyl substituents in this compound.

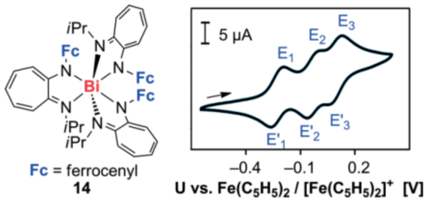

Figure 9. Lewis formula and cyclic voltammogram $\{CH_2Cl_2/0.1\ \text{M}\ [N(nBu)_4][PF_6], 23\ °C\}$ of bismuth ATI compound **14** with ferrocenyl substituents (Fc = ferrocenyl). Adapted from ref.[15] with permission of The Royal Society of Chemistry.

4.3. Ligand-Centered Redox Chemistry under Reductive Conditions

Under strongly reducing conditions, ATIs can act as redox-active ligands. This was unequivocally demonstrated by cyclic voltammetric measurements of the ligand $H\text{-}ATI^{Ph/iPr}$, which reveal a partially reversible redox wave at –2.7 V vs. $Fe(C_5H_5)_2/[Fe(C_5H_5)_2]^+$.[60] Fully reversible electron transfer at very similar potentials (–2.7 V)[58] can be realized for the related rhodium complex $[Rh(ATI^{Ph/iPr})(cod)]$ (cod = cyclooctadiene) (Figure 10a). This redox process was suggested to be ligand-centered based on DFT calculations of the spin density distribution in the radical anion $[Rh(ATI^{Ph/iPr})(cod)]^{•-}$ that is generated upon reduction (Figure 11a).

The nature of the metal center in ATI complexes can have a significant impact on the ligand-based redox chemistry of these species under reducing conditions. The sodium compound $[Na(ATI^{Ph/iPr})(thf)]$ (**15**) (an analog of the Rh species discussed before) is susceptible to a reductively induced dimerization to give compound **16** (Scheme 8; CV: Figure 10b).[60] This reaction presumably involves a delocalized, ligand-centered, persistent

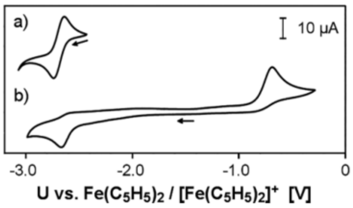

Figure 10. Cyclic voltammograms of ligand-based redox events in ATI compounds. (a) fully reversible electron transfer for [Rh(ATI$^{Ph/iPr}$)(cod)]; (b) chemically reversible, reductively induced dimerization of [Na(ATI$^{Ph/iPr}$)(thf)]. Adapted from ref.[60] with permission of The Royal Society of Chemistry.

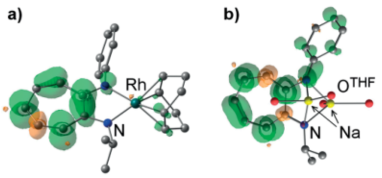

Figure 11. Spin density plots of (a) radical anion [Rh(ATI$^{Ph/iPr}$)(cod)]$^{\cdot-}$ and (b) radical intermediate [Na$_2$(ATI$^{Ph/iPr}$)(thf)$_4$] as determined by DFT calculations; isovalue: 0.0025. Adapted from ref.[60] with permission of The Royal Society of Chemistry.

radical as an intermediate, as determined by DFT calculations (Figure 11b) and EPR spectroscopy. Nevertheless, it proceeds with high chemo-, regio-, and diastereoselectivity. Moreover, this transformation is chemically reversible (Scheme 8).

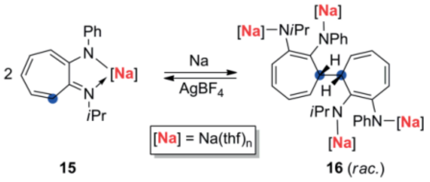

Scheme 8. Chemically reversible, reductively induced dimerization of [Na(ATI$^{Ph/iPr}$)(thf)] (**15**) to give [Na$_4$(di-ATI$^{Ph/iPr}$)(thf)$_6$] (**16**).

The reversibility of the redox processes shown in Figures 9 and 10 opens up possibilities for applications of ATI species in the fields of redox-switchable materials and electron transfer catalysis (cf. section 6.5.).

4.4. Stabilization of (Semi-)Metals in Low Oxidation States

Since the redox-activity of ATI ligands under reducing conditions sets in at strongly negative potentials {typically below −2.5 V vs. Fe(C$_5$H$_5$)$_2$/[Fe(C$_5$H$_5$)$_2$]$^+$},[60,62] ATI ligands can still act as redox-innocent ligands for the stabilization of low-valent metal centers. This has been exemplified for complexes containing central atoms such as Ti^{III}, Zn^{I}, Ge^{II}, or Sn^{II}.[5,35,36,63–66] Notably, these Ge^{II} and Sn^{II} ATI complexes can engage in Ge^{II}/Sn^{II}–M interactions with coinage metal cations M = Cu$^+$, Ag$^+$, Au$^+$.[65–72]

5. Ligand Cooperativity

Ligand cooperativity has recently emerged as a powerful tool in synthesis and catalysis.[73–75] Cooperative ligands participate directly in bond breaking/forming events: a functional group is transferred to the ligand and released at a later stage of the reaction. This reversible reactivity facilitates an overall chemical process due to synergistic effects between the ligand and the metal center.

5.1. Reactions with Electrophiles

The reactivity of ATI ligands towards electrophiles or nucleophiles is considered to be lower than that of the related diazadiene ligands, for instance.[2] Nevertheless, cooperative behavior has been reported for ATI ligands in the coordination sphere of group 13 metals (Scheme 9).[28,76,77] Reaction of compounds [M(ATI$^{iPr/iPr}$)R$_2$] (**17-M**; M = Al–In; R = alkyl) with a tritylium salt did not proceed via initial abstraction of the alkyl group R. An electrophilic attack in the C-5 position of the ligand was observed instead, resulting in formation of compounds **18-M**, which can be detected spectroscopically at low temperature (−90 to −45 °C) for M = Al or even isolated in the case of M = Ga, In. In these compounds, the formerly monoanionic ATI ligand has been transformed into a neutral diimine ligand. At temperatures of −40 to −30 °C (M = Al) or 80 °C (M = Ga, In), the intermediates **18-M** undergo elimination of RCPh$_3$ (or HCPh$_3$ + olefin for R-groups with β-hydrogen atoms) to give the cationic species **19-M** with regeneration of the monoanionic ATI ligand motif. This type of reactivity has explicitly been observed for R = Me, Et and has been suggested for R = Pr, *i*Bu, cyclohexyl, benzyl.

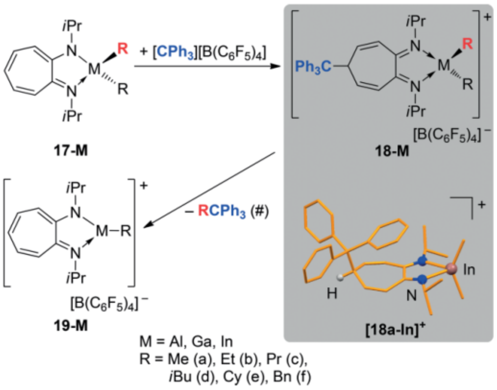

Scheme 9. Cooperative behavior of ATI ligands in the coordination sphere of Al, Ga, or In with (CPh$_3$)$^+$ as an electrophile. Cy = cyclohexyl; Bn = benzyl. #: depending on R, either RCPh$_3$ or [HCPh$_3$ + olefin] is eliminated.

De-aromatization of the C$_7$N$_2$ moiety[78] has also been reported with a proton as the electrophile: stirring H-ATI$^{iPr/iPr}$ with W(CO)$_3$(NCMe)$_3$ in heptane at 65 °C gave compound **20** (Scheme 10).[79] This reaction involves migration of a proton from the nitrogen atom to the C3 position of the ATI ligand.

The ligand in compound **20** shows a diimine structural motif, which can be transformed into an ATI moiety by deprotonation with KH to give compound **21**.

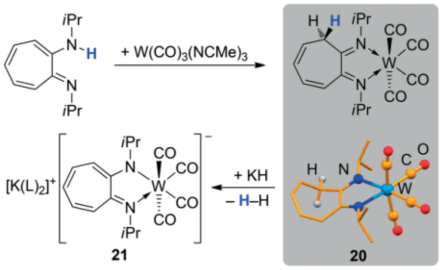

Scheme 10. Cooperative behavior of ATI ligand with a proton as an electrophile. L = thf, dimethoxyethane.

5.2. Reactions with Nucleophiles

De-aromatization of the C_7N_2 group[78] by nucleophilic attack has recently been mentioned for the reaction of H-ATI$^{Ph/Ph}$ with *n*BuLi, which gives **22** as one of the products (Scheme 11).[34] However, the reverse process has not yet been realized.

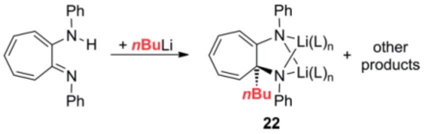

Scheme 11. Nucleophilic attack of $(n\mathrm{Bu})^-$ at the ATI ligand backbone; L = neutral donor ligand.

6. Catalysis

6.1. Hydroamination of Alkenes and Alkynes

ATI complexes have been intensively investigated as catalysts in hydroamination reactions with a strong focus on lanthanoid and zinc compounds. These fields of research have been covered in recent review articles.[2,3,7] Thus, only more recent advances and contributions based on ATI complexes of other elements are included here.

ATI complexes $[M(ATI^{iPr/iPr})\{N(SiMe_3)_2(thf)_2\}]$ (**25-M**) of the heavier alkaline earth metals Ca and Sr have been tested as catalysts in intramolecular hydroamination reactions and compared to their Yb^{II} analogs (Scheme 12).[80–82] The ATI ligand presumably serves as a spectator ligand in these transformations, while the $\{N(SiMe_3)_2\}^-$ group undergoes transamination with the substrate **23**.[81] Near quantitative yields of regioselectively cyclized products **24** were observed in most cases, with catalyst loadings of 2–10 %, reaction times of 0.25–40 h and reaction temperatures of 23–60 °C, depending on the substrate. Generally, the calcium compound **25-Ca** showed a higher catalytic activity than the strontium congener **25-Sr**. This is remarkable, since the opposite trend (i.e. increasing activity with increasing ionic radius of the metal center) has been reported for lanthanoid complexes as olefin hydroamination catalysts.[81,83] For more challenging substrates **23** (e.g. R^1, R^3 = H, R^2 = Me, *n* = 0 or R^1, R^2 = H, R^3 = Me, *n* = 0) the calcium catalyst **25-Ca** was found to be more active than the ytterbium(II) analog **25-Yb**, with oxidations to Yb^{III} species being observed as side reactions.[81] The properties of ATI complex **25-Ca** as a hydroamination catalyst were also compared to those of the related β-diketiminate compound $[\{\{HC(CMe)_2N\text{-}2,6\text{-}iPr_2C_6H_3\}_2\}Ca\text{-}\{N(SiMe_3)_2\}(thf)]$. Whereas **25-Ca** showed higher activities in the formation of products **24** with six-membered rings (*n* = 1), the β-diketiminate was more active for substrates that give products **24** with five-membered rings (*n* = 0; Scheme 12).[80]

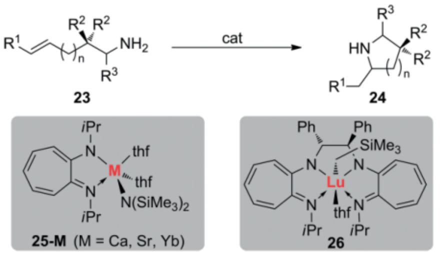

Scheme 12. General scheme for intramolecular hydroamination reactions of alkenes catalyzed by $[M(ATI^{iPr/iPr})\{N(SiMe_3)_2(thf)_2\}]$ (M = Ca, Sr, Yb). Scheme applies analogously for alkynes as substrates; *n* = 0, 1; R^1 = H, Ph, R^2 = H, Me, Ph or $(R_2)_2 = (CH_2)_5$; R^3 = H, Me.

Stereoselective intramolecular hydroaminations were realized with the lutetium ATI complex **26** (Scheme 12). However, the highest enantiomeric excess observed in these reactions was 44 % at full conversion for substrate **23** with R^1 = R^3 = H, R^2 = Me and *n* = 1.[84–86]

Zinc ATI complexes can be covalently attached to mesoporous silica, resulting in a recyclable, heterogeneous catalyst for intramolecular hydroamination. The properties of this catalyst material have recently been investigated in detail (e.g. determination of surface area, pore size distribution, pore volume).[87] Furthermore, the synthesis of this catalyst species was improved by accounting for the fact that Et_3OBF_4, which is used in the synthesis of H-ATI ligands, can edge the silica surface (leading to the presence of unwanted Zn–O bond motifs in the final product). The immobilized Zn ATI catalysts were shown in most cases to be slightly more active than the related, immobilized zinc aminotroponate complexes [Δ(TOF) of up to 0.15 h^{-1}].

6.2. Alkyne Oligomerization and Olefin (Co-)Polymerization

Low-coordinate, cationic aluminum ATI compounds such as $[Al(ATI^{iPr/iPr})R][B(C_6F_5)_4]$ (**27-R**) are strongly Lewis acidic and potent catalysts for a range of oligo- and polymerization reactions (Scheme 13, R = alkyl, also see section 6.3). Compounds **27-R** catalyze the head-to-tail dimerization of *tert*-butylacetylene (**28**) to give **29** in > 90 % selectivity with a turnover frequency of ca. 4 h⁻¹ at 23 °C (Scheme 13a).[1,28,88] With ethylene, **27-Et** undergoes chain transfer reactions as demonstrated in deuteration experiments (Scheme 13b), but no pronounced polymerization activity was observed. In contrast, isobutylene polymerization is readily initiated by **27-Et** and presumably proceeds via a cationic mechanism (Scheme 13c).

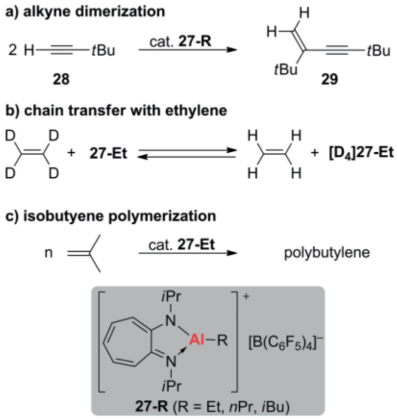

Scheme 13. Stoichiometric and catalytic reactions of cationic aluminium ATI complex **27** with an alkyne and olefins.

Zirconium and hafnium ATIs **30-M** and **31-M** (M = Zr, Hf) are active as pre-catalysts for the copolymerization of ethylene and 1-octene in the presence of $[HNMe(C_{18}H_{37})_2][B(C_6F_5)_4]$ as an activator (Scheme 14a).[13] The hafnium ATIs were generally more active than their zirconium analogs. Within this series of catalysts, **30-Hf** showed the highest catalyst efficiency (2.4×10^4 g of polymer/mmol catalyst) to give the polymer with the highest weight-averaged molecular weight (M_W = 5.0×10^5 g mol⁻¹) and 1-octene content (7.7 mol-%). High polydispersity indices of 1.8 to 12.8 suggest the presence of multiple active species under catalytic conditions. Compounds **30-M** and **31-M** were developed in an attempt to further improve the performance of promising imino-enamido pre-catalysts of type **32** (Scheme 14b). However, the original pre-catalyst proved to show a higher efficiency (1.1×10^5 g of polymer/mmol catalyst), producing a polymeric material with a higher molecular weight (M_W = 1.3×10^6 g mol⁻¹) and higher 1-octene content (8.6 mol-%).[89,90]

Scheme 14. Pre-catalysts for ethylene/1-octene copolymerization: (a) ATI complexes with M = Zr, Hf and (b) a structurally related Hf imino-enamido complex. Bn = benzyl.

6.3. (Co-)Polymerization of Polar Monomers

The ionic sodium ATI complexes **33-R** and **34-R**, each of which contain the complex anion $[Na(ATI)_2]^-$ (Scheme 15a), have been reported to be highly active as initiators for the polymerization of ε-caprolactone (full conversion after 1 min at –30 °C with 0.04–0.1 mol-% catalyst loading).[33] They exhibit synergistic effects, i.e. their activity exceeds that of their monometallic components [M(ATI)] (M = Na, K), which may be ascribed to the increased nucleophilicity of the $[Na(ATI)_2]^-$ anion. Unfortunately, the high activity of these initiators goes along with a relatively poor molecular weight control at low catalyst loadings (M_w/M_n = 2.6–7.7). Excellent molecular weight control was obtained at lower monomer/initiator ratios between 125:1 and 500:1.

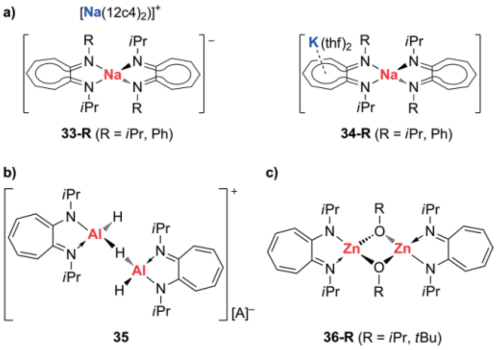

Scheme 15. Dinuclear ATI complexes as catalysts for (a) the polymerization of ε-caprolactone, (b) the polymerization of MMA or (c) the copolymerization of epoxides with CO_2. $[A]^-$ = $[B(C_6F_5)_4]^-$. 12c4 = 12crown4.

Cationic aluminum ATI compounds may be utilized as catalysts for the polymerization of polar monomers such as methylmethacrylate (MMA) and propylene oxide (PO). Poly-MMA with a moderate syndiotacticity (*mm*/*mr*/*rr* = 1:22:77) was obtained by treating MMA with 0.2 mol-% of the ATI-supported, cationic, dinuclear aluminum hydride **35** as an initiator (Scheme 15b).[28] Similarly, atactic poly-PO was obtained in an exothermic reaction with 0.2 mol-% of **27-*i*Bu** as an initiator, showing a turnover frequency of 240 h⁻¹.[28]

The dinuclear zinc ATI compounds **36-R** have been synthesized and tested as catalysts for the copolymerization of PO and/or cyclohexene oxide with CO_2 (Scheme 15c).[91] Moderate activities and up to 67 % yields of polymeric material were observed with catalyst **36-*i*Pr** at 80 °C and 25 bar CO_2 pressure within 2 h in the presence of tetrahexylammonium benzoate as a co-catalyst. Structurally related β-diketiminate complexes showed higher activities, which was ascribed to the steric and electronic properties of the complexes influencing monomer/dimer equilibria of (potentially) active species in solution.[91,92]

6.4. Epoxidation and Cyanosilylation

Zinc peroxides stabilized by *N*,*N*-chelating ligands have recently been introduced as well-defined reagents for the epoxidation of electron deficient alkenes.[93] The catalytic version of these reactions was first realized with zinc ATI catalysts **39** and **40** (or their β-diketiminate analogs) using *trans*-chalcone (**37**) as a model substrate (Scheme 16).[94] Quantitative conversion was reached in 4–8 h at 0 °C. With the zinc ATI catalyst (*S*,*S*)-**40**, enantioselective reactions were achieved, although only moderate enantiomeric excesses of up to 29 % of the 2S-3R-enantiomer **38** were obtained. In this context, it is interesting to note that a magnesium analog of the zinc compound **39** has been suggested as an intermediate in the reaction of magnesium alkyl ATI compounds, [Mg(ATI)R], with molecular oxygen to give magnesium ATI alkoxides, [Mg(ATI)OR].[95]

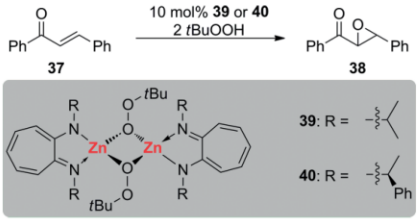

Scheme 16. (Enantioselective) epoxidation of *trans*-chalcone (**37**) with *t*BuOOH to give **38** using zinc ATI catalysts **39** or **40**.

Low-valent germanium ATI compounds have been investigated in quite some detail with respect to structure, bonding, and reactivity (cf., section 7).[5] The ATI-supported germanium cyanide **43** reacts with aldehydes with insertion of the substrate into the Ge–C bond.[96] The resulting Ge^{II} alcoholate reacts with Me_3Si–CN to regenerate compound **43**. These reactions are the key steps for realization of a Ge^{II}-catalyzed cyanosilylation of aldehydes. Indeed, a range of aldehydes **41-R** could be transformed into the cyanohydrins **42-R** with 1 mol-% of the germanium ATI **43** as a catalyst.[96,97] The reactions proceed at 0 °C in ca. 1–2 h in near quantitative yields. The oxidation state of the germanium center seems to play an important role in this catalytic transformation, since the related Ge^{IV} compound **44** did not react with aldehydes in a 1:1 stoichiometry, even under more forcing reaction conditions (Scheme 17).

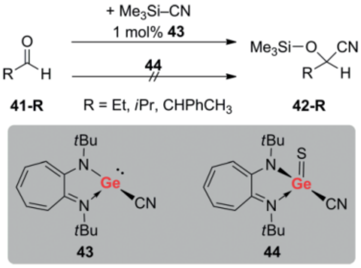

Scheme 17. Cyanosilylation of aldehydes with Me_3SiCN using the Ge^{II} ATI catalyst **43**.

6.5. Electron Transfer Catalysis

The redox-active character of ATI ligands under strongly reducing conditions suggests the possibility that ATI complexes may act as electron transfer catalysts under suitable reaction conditions (cf., section 4).[60] The reaction of 2-bromonaphthalene with MgPhBr has been reported to proceed only in the presence of a suitable electron transfer catalyst.[98] In a proof-of-principle study, it was demonstrated that Rh or in-situ-formed Mg ATI complexes catalyze this and related C–C coupling reactions in moderate to good yields.[60]

7. Heavy Analogs of Carbon Oxo Compounds

There has recently been an increased interest in heavy analogs of carbon oxo compounds.[99–103] In these compounds, the oxygen and/or the carbon atom(s) of ketones and carboxylic acid derivatives (esters, amides, anhydrides and acid chlorides) have been exchanged for atoms of heavier group 14/16 elements. These studies mainly aim at understanding the fundamental differences between the carbon oxo compounds and their analogs involving heavier group 14/16 elements.

7.1. Synthesis and Characteristics of ATI-Supported Heavy Analogs of Carbon Oxo Compounds

In recent years, it has been demonstrated that ATI ligands are well-suited for stabilizing heavy analogs of carbon oxo compounds. With the Ge^{IV} complexes [GeO(ATI$^{iBu/iBu}$)*i*Pr(LA)] (**45-LA**) were the first Lewis acid adducts of a heavy ketone analog isolated and fully characterized (Scheme 18a; LA = Lewis acid).[104] DFT calculations confirmed a decreased ^{ATI}Ge–O bond order for **45-LA** [Wiberg bond indices (WBI): 0.60–0.72] compared to that in the theoretically investigated parent germanone **45** (WBI: 1.08). This was accompanied by higher ionicity of the ^{ATI}Ge–O bond in **45-LA** (71–72 %) compared to that in **45** (60 %). The thio- and selenogermanones [GeX(ATI$^{tBu/tBu}$)Ph] were shown to also act as ligands towards Lewis-acidic moieties (X = S, Se).[105] In specific, the dinuclear silver iodide complexes [GeX(ATI$^{tBu/tBu}$)Ph(AgI)]$_2$ were synthesized and characterized. Stronger intramolecular argentophilic interactions were observed for the selenogermanone-AgI complexes.

A series of germaester complexes of type [GeX(ATI)O*t*Bu] (**46-X-O*t*Bu** and **47-X-O*t*Bu**, Scheme 18b) have been synthesized by oxidation of the germylene ATI alkoxides, [Ge(ATI)O*t*Bu], with elemental sulfur (X = S), selenium (X = Se) or tellurium (X = Te).[106,107] The *O*-silylated derivatives **46-X-OSiR′$_3$** are accessible in an analogous approach for X = S, Se and R′ = Me, Ph.[108] They underwent transesterification with MeOH to give **46-X-OMe**. Attempts to isolate ATI-supported germaesters of type **46-X-Z** with X = O led to compounds containing Ge–O single bonds via rearrangement or dimerization.[108]

The oxidation of ATI-supported germylenes proved to be a successful strategy for the synthesis of heavy analogs of carboxylic acid amides,[107,109] halides,[36,110] and anhydrides[107,111] as well. Thus, reaction of [Ge(ATI)Z] with elemental sulfur, selenium, or tellurium gave compounds [GeX(ATI)Z] (**46-X-Z**, **47-X-Z**) with X = S, Se, Te and Z = N(SiMe$_3$)$_2$, pyrrolyl F, Cl, Br (Scheme 18b). In the case of anhydride analogs, the digermylene oxide complexes [{Ge(ATI)}$_2$O] (**48**, **49**) were oxidized with

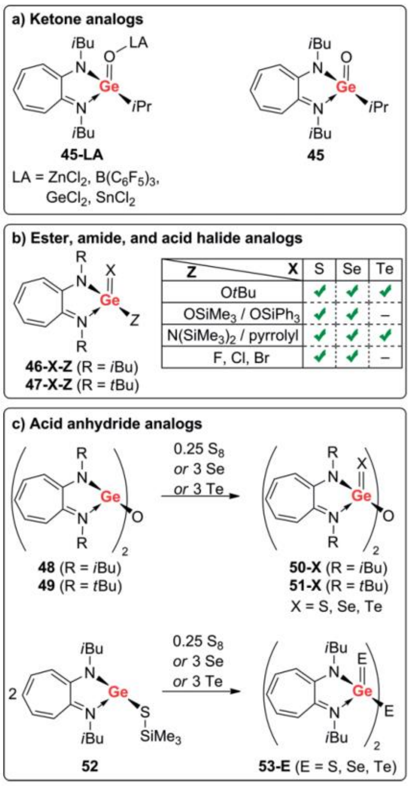

Scheme 18. ATI-supported heavy analogs of ketones as well as carboxylic acid esters, amides, halides, and anhydrides.

elemental sulfur, selenium, or tellurium to give [{GeX(ATI)}$_2$O] (**50-X**, **51-X**, X = S, Se, Te; Scheme 18c, top).

Heavy analogs of carboxylic acid anhydrides could also be obtained in an unusual reaction of the silathiogermylene **52** with group 16 elements to give compounds **53-E** (E = S, Se, Te; Scheme 18c).[112] $(Me_3Si)_2S$ was detected as a byproduct (in addition to elemental sulfur in the case of E = Se, Te), classifying these transformations as condensation reactions.

The Ge=Te bonding interactions in a series of three tellurium compounds, **46-Te-OtBu**, **46-Te-N(SiMe$_3$)$_2$**, and **50-Te**, were analyzed in detail using DFT methods.[107] Moderate ionicities of ca. 7 % were reported in all cases, with a polarization towards the Te atoms. Bonding σ-type orbitals and antibonding π-type orbitals were identified for the Ge=Te interaction in all cases. In the case of the amide analog **46-Te-N(SiMe$_3$)$_2$**, a Ge-Te-centered bonding π-type orbital was also localized. Wiberg bond indices of 1.4–1.5 were found. These analyses confirm the nature of the Ge=Te interaction to be between that of a single and a double bond, as suggested on the basis of distance criteria derived from single-crystal X-ray diffraction measurements.

7.2. Reactivity of ATI-Supported Heavy Analogs of Carbon Oxo Compounds

The fundamental differences in ground state properties between carboxylic acid derivatives and their heavy analogs also leads to marked differences in reactivity. This has been exemplified by the interconversion of some of these heavy analogs, in which the conventional reactivity trend of acid halide > ester > amide are not necessarily maintained. Reactions of the germaacid amides [GeX(ATI)Z] {**46-X-Z**; X = S, Se, Z = N(SiMe$_3$)$_2$, pyrrolyl} with Me_3SiBr led to the germaacid bromides [GeX(ATI)Br] (**46-X-Br**) in high yields of 88–94 %.[110] Similarly, reactions of [GeX(ATI)Z] (**46-X-Z**; X = S, Se, Z = pyrrolyl) with PhEH (E = S, Se) gave the heavy ester analogs [GeX(ATI)Z] (**46-X-Z**; X = S, Se, Z = SPh, SePh) in 92–96 % yield.[109]

8. Summary and Conclusion

Aminotroponiminates (ATIs) are a well-established class of ligands that readily form complexes with elements across large sections of the periodic table.

Over the last 25 years or so, the versatility of ATI complexes has been demonstrated by catalytic applications spanning a wide range of chemical transformations (e.g. hydroaminations, epoxidations, polymerization catalysis, electron transfer catalysis). Furthermore, the use of ATI ligands for the stabilization of Ge-analogs of ketones and carboxylic acid derivatives has been impressively demonstrated.

In recent years, research on ATIs has changed our understanding of some of the fundamental properties of these ligands. It has been demonstrated that their coordination chemistry is not limited to the well-known chelating *N*,*N*-binding mode; it now includes the ATI ligand backbone as a potential binding site and is thus much richer than previously reported. Furthermore, ATIs can act as tunable, redox-active ligands under strongly reducing conditions. Depending on the metal bound to the ATI moiety, reversible electron transfer or reductively induced, chemically reversible dimerizations can be realized. The reduced radical species show a large spin density on the C_7 ligand backbone. The ligand backbones of ATIs are also responsible for the potentially cooperative behavior of these ligands. Functional groups such as $(CPh_3)^+$ or H^+ can be covalently bound to the C_7 ring and selectively removed at a later stage of the reaction (or under modified reaction conditions). These properties of ATI complexes will have implications for their use in stoichiometric and catalytic transformations. A deeper understanding of this class of compounds will contribute to the rational design of ATIs for future applications. Previously described reactivity patterns might be rationalized and further exploited by taking these new insights into account.

Acknowledgments

The authors thank Dr. Rian Dewhurst for helpful discussions and Prof. Holger Braunschweig for continuous support. Financial support by the Fonds der Chemischen Industrie (doctoral fellowship to A. H. and Liebig fellowship to C. L.) is gratefully acknowledged.

Keywords: Coordination modes · Redox chemistry · Cooperative ligands · Homogeneous catalysis · Heavy carbon oxo analogs

[1] S. Dagorne, D. A. Atwood, *Chem. Rev.* **2008**, *108*, 4037–4071.

[2] P. W. Roesky, *Chem. Soc. Rev.* **2000**, *29*, 335–345.

[3] P. W. Roesky, *Z. Anorg. Allg. Chem.* **2003**, *629*, 1881–1894.

[4] H. V. R. Dias, Z. Wang, W. Jin, *Coord. Chem. Rev.* **1998**, *176*, 67–86.

[5] O. Kühl, *Coord. Chem. Rev.* **2004**, *248*, 411–427.

[6] R. H. Holm, M. J. O'Connor, *Prog. Inorg. Chem.* **1971**, *14*, 241–401.

[7] J. Jenter, A. Lühl, P. W. Roesky, S. Blechert, *J. Organomet. Chem.* **2011**, *696*, 406–418.

[8] Different groups have contributed over a number of decades to the development of the synthetic route that is commonly used today (see ref.[4]).

[9] For the traditional synthesis of ATI ligands starting from cyclopentadiene and C_2F_4, see: a) J. J. Drysdale, W. W. Gilbert, H. K. Sinclair, W. H. Sharkey, *J. Am. Chem. Soc.* **1958**, *80*, 3672–3675; b) ref.[17] c) ref.[4]

[10] For common protocols without Pd catalysis see, for instance: a) R. M. Claramunt, D. Sanz, M. Pérez-Torralba, E. Pinilla, M. R. Torres, J. Elguero, *Eur. J. Org. Chem.* **2004**, 4452–4466; b) also see ref.[49]

[11] For a protocol based on Pd catalysis see: F. A. Hicks, M. Brookhart, *Org. Lett.* **2000**, *2*, 219–221.

[12] The methyl analog of **7a** was isolated using Me_2SO_4 instead of $[Et_3O][BF_4]$ as the alkylating agent: G. M. Villacorta, C. P. Rao, S. J. Lippard, *J. Am. Chem. Soc.* **1988**, *110*, 3175–3182.

[13] E. Szuromi, J. Klosin, K. A. Abboud, *Organometallics* **2011**, *30*, 4589–4597.

[14] P. W. Roesky, *J. Organomet. Chem.* **2001**, *621*, 277–283.

[15] A. Hanft, C. Lichtenberg, *Dalton Trans.* **2018**, https://doi.org/10.1039/C8DT01019F.

[16] D. Zhu, P. H. M. Budzelaar, *Dalton Trans.* **2013**, *42*, 11343–11354.

[17] W. R. Brasen, H. E. Holmquist, R. E. Benson, *J. Am. Chem. Soc.* **1960**, *82*, 995–956.

[18] W. R. Brasen, H. E. Holmquist, R. E. Benson, *J. Am. Chem. Soc.* **1961**, *83*, 3125–3135.

[19] W. F. Richter, K. Hartke, W. Massa, G. Münninghoff, *Chem. Ber.* **1989**, *122*, 1133–1137.

[20] M. Dochnahl, K. Löhnwitz, J.-W. Pissarek, P. W. Roesky, S. Blechert, *Dalton Trans.* **2008**, 2844–2848.

[21] K. Löhnwitz, M. J. Molski, A. Lühl, P. W. Roesky, M. Dochnahl, S. Blechert, *Eur. J. Inorg. Chem.* **2009**, 1369–1375.

[22] M. Dochnahl, K. Lähnwitz, A. Lühl, J. W. Pissarek, M. Biyikal, P. W. Roesky, S. Blechert, *Organometallics* **2010**, *29*, 2637–2645.

[23] An early report also describes the synthesis of a 5-amino-ATI starting from 5-nitro-tropolone: T. Nozoe, M. Sato, S. Ito, K. Matsui, T. Matsuda, *Proc. Jpn. Acad.* **1953**, *39*, 565–569.

[24] D. R. Eaton, A. D. Josry, R. E. Benson, W. D. Philips, T. L. Cairns, *J. Am. Chem. Soc.* **1962**, *84*, 4100–4106.

[25] a) Ref.[18] b) R. A. Benkeser, R. F. Grossman, G. M. Stanton, *J. Am. Chem. Soc.* **1961**, *83*, 3714–3716; c) also see ref.[6]

[26] M. Bartlett, G. J. Palenik, *J. Chem. Soc., D* **1970**, 416.

[27] A search of the CCDC database in January **2018** revealed >95 % of the more than 350 structurally characterized ATI complexes to show coordination mode **A**.

[28] A. V. Korolev, E. Ihara, I. A. Guzei, V. G. Young Jr., R. F. Jordan, *J. Am. Chem. Soc.* **2001**, *123*, 8291–8309.

[29] H. V. R. Dias, W. Jin, *J. Chem. Crystallogr.* **1997**, *27*, 353–358.

[30] M. Pittracher, U. Frisch, H. Kopacka, K. Wurst, T. Müller, L. Oehninger, I. Ott, E. Wuttke, S. Scheerer, R. F. Winter, B. Bildstein, *Organometallics* **2014**, *33*, 1630–1643.

[31] C. Lichtenberg, *Organometallics* **2016**, *35*, 894–902.

[32] The results of single-crystal XRD studies on $[K(ATI^{iPr/iPr})(thf)]$ have been mentioned previously (ref.[4]), but no crystallographic details were given, and this study is thus not listed in common databases such as SciFinder or CCDC.

[33] A. Hanft, M. Jürgensen, R. Bertermann, C. Lichtenberg, *ChemCatChem* **2018**, https://doi.org/10.1002/cctc.201800580.

[34] A. Hanft, C. Lichtenberg, *Organometallics* **2018**, *37*, 1781–1787.

[35] R. K. Siwatch, S. Kundu, D. Kumar, S. Nagendran, *Organometallics* **2011**, *30*, 1998–2005.

[36] S. Sinhababu, R. K. Siwatch, G. Mukherjee, G. Rajaraman, S. Nagendran, *Inorg. Chem.* **2012**, *51*, 9240–9248.

[37] A dihedral angle of 0° was observed for $[M(ATI^{nPr/nPr})][OTf]$ with M = Ge, Sn: A. E. Ayers, H. V. R. Dias, *Inorg. Chem.* **2002**, *41*, 3259–3268.

[38] A dihedral angle of 25.3° was observed for $[Ca(ATI^{iPr/iPr})I(thf)_3]$; see reference in ref.[81]

[39] K. Shindo, H. Wakabayashi, S. Ishikawa, T. Nozoe, *Bull. Chem. Soc. Jpn.* **1993**, *66*, 2941–2948.

[40] K. Shindo, H. Wakabayashi, H. Miyamae, S. Ishikawa, T. Nozoe, *Heterocycles* **1994**, *37*, 943–54.

[41] K. Shindo, L.-C. Zhang, H. Wakabayashi, H. Miyame, S. Ishikawa, T. Nozoe, *Heterocycles* **1995**, *40*, 913–924.

[42] O. Sato, Y. Koshiba, S. Sagara, K. Okada, *Heterocycles* **2006**, *67*, 529–533.

[43] K. Shindo, H. Wakabayashi, L.-C. Zhang, S. Ishikawa, T. Nozoe, *Heterocycles* **1994**, *39*, 639–648.

[44] T. Nozoe, K. Shindo, H. Wakabayashi, S. Ishikawa, *Heterocycles* **1992**, *34*, 881–884.

[45] A. Zask, N. Gonnella, K. Nakanishi, C. J. Turner, S. Imajo, T. Nozoe, *Inorg. Chem.* **1986**, *25*, 3400–3407.

[46] S. A. Hilderbrand, S. J. Lippard, *Inorg. Chem.* **2004**, *43*, 4674–4682.

[47] T. Nozoe, K. Shindo, S. Ishikawa, *Chem. Lett.* **1988**, *17*, 1593–1596.

[48] T. Nozoe, H. Okai, T. Someya, *Bull. Chem. Soc. Jpn.* **1978**, *51*, 2185–2186.

[49] M. Dochnahl, K. Löhnwitz, J.-W. Pissarek, M. Biyikal, S. R. Schulz, S. Schön, N. Meyer, P. W. Roesky, S. Blechert, *Chem. Eur. J.* **2007**, *13*, 6654–6666.

[50] D. R. Eaton, R. E. Benson, C. G. Bottomley, A. D. Josey, *J. Am. Chem. Soc.* **1972**, *94*, 5996–6004.

[51] S. Choi, K.-H. Ahn, *Bull. Korean Chem. Soc.* **1995**, *16*, 1–2.

[52] P. W. Roesky, *Inorg. Chem.* **1998**, *37*, 4509–4511.

[53] D. P. Steinhuebel, S. J. Lippard, *Organometallics* **1999**, *18*, 3959–3961.

[54] L. H. Doerrer, M. T. Bautista, S. J. Lippard, *Inorg. Chem.* **1997**, *36*, 3578–3579.

[55] K. J. Franz, N. Singh, B. Spingler, S. J. Lippard, *Inorg. Chem.* **2000**, *39*, 4081–4092.

[56] J. Kozhukh, M. A. Minier, S. J. Lippard, *Inorg. Chem.* **2015**, *54*, 418–424.

[57] L. H. Doerrer, S. J. Lippard, *Inorg. Chem.* **1997**, *36*, 2554–2563.

[58] Electrochemical potentials are reported vs. the $Fe(C_5H_5)_2/[Fe(C_5H_5)_2]^+$ couple.

[59] A. M. McNair, D. C. Boyd, D. A. Bohling, T. P. Gill, K. R. Mann, *Inorg. Chem.* **1987**, *26*, 1182–1185.

[60] C. Lichtenberg, I. Krummenacher, *Chem. Commun.* **2016**, *52*, 10044–10047; https://doi.org/10.1039/c6cc05762d.

[61] K. Shindo, S. Ishikawa, T. Nozoe, *Bull. Chem. Soc. Jpn.* **1989**, *62*, 1158–1166.

[62] A tunability of the electrochemical window, in which ATIs act as redox-active ligands, is to be expected, but has not yet been established.

[63] D. P. Steinhuebel, S. J. Lippard, *Inorg. Chem.* **1999**, *38*, 6225–6233.

[64] H. P. Nayek, A. Lühl, S. Schulz, R. Köppe, P. W. Roesky, *Chem. Eur. J.* **2011**, *17*, 1773–1777.

[65] H. V. R. Dias, X. Wang, H. V. K. Diyabalanage, *Inorg. Chem.* **2005**, *44*, 7322–7324.

[66] H. V. R. Dias, W. Jin, *J. Am. Chem. Soc.* **1996**, *118*, 9123–9126.

[67] See literature cited in ref.[37]

[68] H. V. R. Dias, Z. Wang, *Inorg. Chem.* **2000**, *39*, 3890–3893.

[69] H. V. R. Dias, A. E. Ayers, *Polyhedron* **2002**, *21*, 611–618.

[70] D. Yadav, R. K. Siwatch, S. Sinhababu, S. Nagendran, *Inorg. Chem.* **2014**, *53*, 600–606.

[71] D. Yadav, R. K. Siwatch, S. Sinhababu, S. Karwasara, D. Singh, G. Rajaraman, S. Nagendran, *Inorg. Chem.* **2015**, *54*, 11067–11076.

[72] ATI-supported Ge^{IV} complexes have also been ligated to Ag^+ centers. See ref.[105]

[73] H. Grützmacher, *Angew. Chem. Int. Ed.* **2008**, *47*, 1814–1818; *Angew. Chem.* **2008**, *120*, 1838–1842.

[74] Cooperative behavior has also been observed for diazadiene ligands, which are structurally related to ATIs. For example: R. E. Rodríguez-Lugo, M. Trincado, M. Vogt, F. Tewes, G. Santiso-Quinones, H. Grützmacher, *Nat. Chem.* **2013**, *5*, 342–347.

[75] Cooperative behavior has also been observed for β-diketiminate ligands, which are structurally related to ATIs. For a recent review article see: C. Camp, J. Arnold, *Dalton Trans.* **2016**, *45*, 14462–14498.

[76] A. V. Korolev, F. Delpech, S. Dagorne, I. A. Guzei, R. F. Jordan, *Organometallics* **2001**, *20*, 3367–3369.

[77] F. Delpech, I. A. Guzei, R. F. Jordan, *Organometallics* **2002**, *21*, 1167–1176.

[78] ATI ligands have been described as 10-electron aromatic compounds, e.g.: ref.[2,4,5] Also see [22] and references cited therein.

[79] V. Kirin, P. W. Roesky, *Z. Anorg. Allg. Chem.* **2004**, *630*, 466–469.

[80] S. Datta, P. W. Roesky, S. Blechert, *Organometallics* **2007**, *26*, 4392–4394.

[81] S. Datta, M. T. Gamer, P. W. Roesky, *Organometallics* **2008**, *27*, 1207–1213.

[82] For the synthesis and properties of structurally related ATI compounds of Ca and Sr see: S. Datta, M. T. Gamer, P. W. Roesky, *Dalton Trans.* **2008**, 2839–2843.

[83] For example: a) M. A. Giardello, V. P. Conticello, L. Brard, M. R. Gagné, T. J. Marks, *J. Am. Chem. Soc.* **1994**, *116*, 10241–10254; b) M. R. Gagné, C. L. Stern, T. J. Marks, *J. Am. Chem. Soc.* **1992**, *114*, 275–294.

[84] N. Meyer, A. Zulys, P. W. Roesky, *Organometallics* **2006**, *25*, 4179–4182.

[85] For the synthesis and properties of related enantiomerically pure Yb- and Lu-bridged ATI complexes, see: N. Meyer, P. W. Roesky, *Dalton Trans.* **2007**, 2652–2657.

[86] For an example of a Lu catalyst giving higher enantiomeric excesses of up to 90 % in intramolecular hydroamination reactions, see: D. V. Gribkov, K. C. Hultzsch, F. Hampel, *J. Am. Chem. Soc.* **2006**, *128*, 3748–3759.

[87] C. Duncan, A. V. Biradar, T. Asefa, *ACS Catal.* **2011**, *1*, 736–750.

[88] A. V. Korolev, I. A. Guzei, R. F. Jordan, *J. Am. Chem. Soc.* **1999**, *121*, 11605–11606.

[89] R. Figueroa, R. D. Froese, Y. He, J. Klosin, C. N. Theriault, K. A. Abboud, *Organometallics* **2011**, *30*, 1695–1709.

[90] R. Figueroa, J. Klosin, Int. Pat. *Appl.* 2010022228, **2010**.

[91] J.-S. Herrmann, G. A. Luinstra, P. W. Roesky, *J. Organomet. Chem.* **2004**, *689*, 2720–2725.

[92] E.g.: M. Cheng, D. R. Moore, J. J. Reczek, B. M. Chamberlain, E. B. Lobkosvsky, G. W. Coates, *J. Am. Chem. Soc.* **2001**, *123*, 8738–8749.

[93] J. Lewiński, Z. Ochal, E. Bojarski, E. Tratkiewicz, I. Justyniak, J. Lipkowski, *Angew. Chem. Int. Ed.* **2003**, *42*, 4643–4646; *Angew. Chem.* **2003**, *115*, 4791.

[94] M. Kubisiak, K. Zelga, I. Justyniak, E. Tratkiewicz, T. Pietrzak, A. R. Keeri, Z. Ochal, L. Hartenstein, P. W. Roesky, J. Lewiński, *Organometallics* **2013**, *32*, 5263–5265.

[95] P. J. Bailey, C. M. E. Dick, S. Fabre, S. Parsons, *J. Chem. Soc., Dalton Trans.* **2000**, 1655–1661.

[96] R. K. Siwatch, S. Nagendran, *Chem. Eur. J.* **2014**, *20*, 13551–13556.

[97] For a recent review on cyanhydrin synthesis, see, for example: M. North, D. L. Usanov, C. Young, *Chem. Rev.* **2008**, *108*, 5146–5226.

[98] E. Shirakawa, Y. Hayashi, K. Itoh, R. Watabe, N. Uchiyama, W. Konagaya, S. Masui, T. Hayashi, *Angew. Chem. Int. Ed.* **2012**, *51*, 218–221; *Angew. Chem.* **2012**, *124*, 222.

[99] P. P. Power, *Chem. Rev.* **1999**, *99*, 3463–3503.

[100] R. C. Fischer, P. P. Power, *Chem. Rev.* **2010**, *110*, 3877–3923.

[101] M. Asay, C. Jones, M. Driess, *Chem. Rev.* **2011**, *111*, 354–396.

[102] Y. Xiong, S. Yao, M. Driess, *Angew. Chem. Int. Ed.* **2013**, *52*, 4302–4311; *Angew. Chem.* **2013**, *125*, 4398.

[103] J. Barrau, G. Rima, *Coord. Chem. Rev.* **1998**, *178–180*, 593–622.

[104] S. Sinhababu, D. Yadav, S. Karwasara, M. K. Sharma, G. Mukherjee, G. Rajaraman, S. Nagendran, *Angew. Chem. Int. Ed.* **2016**, *55*, 7742–7746; *Angew. Chem.* **2016**, *128*, 7873.

[105] D. Yadav, R. K. Siwatch, G. Mukherjee, G. Rajaraman, S. Nagendran, *Inorg. Chem.* **2014**, *53*, 10054–10059.

[106] R. K. Siwatch, S. Nagendran, *Organometallics* **2012**, *31*, 3389–3394.

[107] R. K. Siwatch, D. Yadav, G. Mukherjee, G. Rajaraman, S. Nagendran, *Inorg. Chem.* **2014**, *53*, 5073–5079.

[108] S. Karwasara, R. K. Siwatch, C. K. Jha, S. Nagendran, *Organometallics* **2015**, *34*, 3246–3254.

[109] S. Karwasara, M. K. Sharma, R. Tripathi, S. Nagendran, *Organometallics* **2013**, *32*, 3830–3836.

[110] R. K. Siwatch, S. Karwasara, M. K. Sharma, S. Mondal, G. Mukherjee, G. Rajaraman, S. Nagendran, *Organometallics* **2016**, *35*, 429–438.

[111] R. K. Siwatch, D. Yadav, G. Mukherjee, G. Rajaraman, S. Nagendran, *Organometallics* **2013**, *32*, 13384–13391.

[112] S. Karwasara, D. Yadav, C. K. Jha, G. Rajaraman, S. Nagendran, *Chem. Commun.* **2015**, *51*, 4310–4313.

Received: April 13, 2018

IV Aminotroponiminates: ligand-centred, reversible redox events under oxidative conditions in sodium and bismuth complexes

Anna Hanft, Crispin Lichtenberg

Vervielfältigt aus Referenz:

Dalton Trans. **2018**, *47,* 10578-10589.[62]

DOI: 10.1039/C8DT01019F

mit der Erlaubnis von The Royal Society of Chemistry.

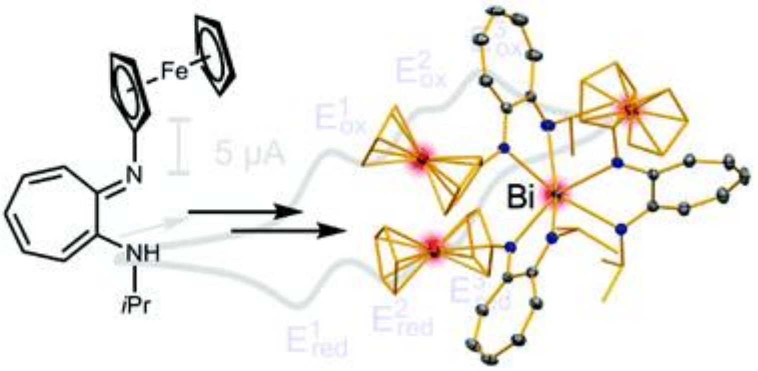

Dalton Transactions

ROYAL SOCIETY OF CHEMISTRY

PAPER

View Article Online
View Journal | View Issue

Cite this: *Dalton Trans.*, 2018, **47**, 10578

Aminotroponiminates: ligand-centred, reversible redox events under oxidative conditions in sodium and bismuth complexes†

Anna Hanft and Crispin Lichtenberg *

Received 16th March 2018,
Accepted 1st May 2018

DOI: 10.1039/c8dt01019f

rsc.li/dalton

A straightforward synthetic route to aminotroponate (AT) and aminotroponiminate (ATI) ligands with a ferrocenyl substituent at nitrogen is presented. Sodium derivatives have been synthesised and the first synthetic access to bismuth AT and ATI species has been demonstrated. All compounds show reversible ligand-centered redox events under oxidising conditions. In a homoleptic bismuth ATI complex, weak electronic communication between three ATI ligands was observed. The coordination chemistry and redox properties of AT and ATI compounds have been investigated by methods including NMR and UV/vis spectroscopy, single-crystal X-ray diffraction, cyclic voltammetry, and DFT calculations.

Introduction

In recent years, redox-active ligands have emerged as valuable tools in synthesis, catalysis, and materials science.[1] This is due to their ability to generate transition metal and main group complexes with unique properties. In such compounds, metal centres with unusual oxidation or spin states can be stabilized,[2] main group species with open-shell electronic structures become accessible,[3] and switching between two distinct electronic structures can be realised.[4] These properties have been turned into a number of remarkable synthetic applications. Prominent examples include the use of base metal complexes with redox-active ligands as substitutes for noble metal catalysts[5] as well as the exploitation of redox-active ligands in redox-switchable catalysis,[6] in the catalytic reduction of H^+ to H_2,[7] and in electrochemically controlled gas purification.[8]

Whereas some redox-active ligands have been developed deliberately,[9] the redox activity of other ligand sets was only recognized long after they had first been used for the synthesis of coordination compounds.[1h] We have recently uncovered the redox-active behaviour of the well-established aminotroponiminate (ATI) ligand family[10] under strongly reducing conditions (Scheme 1a and b).[11] Depending on the choice of the central atom, reversible electron transfer (Scheme 1a) or a chemically reversible, reductively induced dimerization can be realised (Scheme 1b). In the key (intermediate) radical species, considerable spin density is located on the C_7 ligand backbone, providing evidence for the redox-active nature of ATI ligands under these conditions.[11b] Under oxidative conditions, however, (quasi-)reversible redox events have thus far only be detected for metal-centred processes in a range of cobalt ATI complexes.[12] Ligand-centred oxidations of ATI species have been reported, but are irreversible processes.[13,14] Examples include certain cobalt ATIs,[12] complexes of Na,[11b] Ga,[12b] and Zn,[12b,c] as well as free H-ATI ligands.[11b,12] These irreversible ligand oxidations take place at potentials ranging from *ca.*

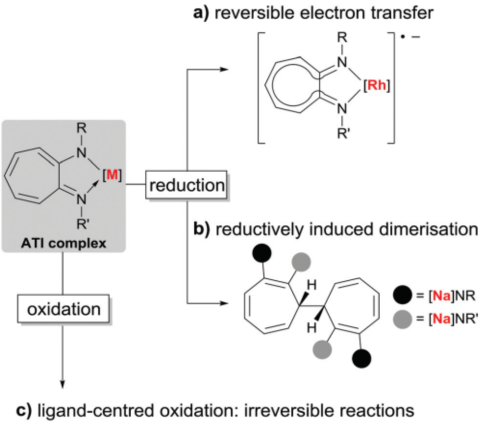

Scheme 1 Ligand-centred redox chemistry of ATI compounds.

Department of Inorganic Chemistry, Julius-Maximilians-Universität Würzburg, Am Hubland, D-97074 Würzburg, Germany.
E-mail: crispin.lichtenberg@uni-wuerzburg.de

† Electronic supplementary information (ESI) available. CCDC 1825483–1825488. For ESI and crystallographic data in CIF or other electronic format see DOI: 10.1039/c8dt01019f

+0.20 to +0.92 V *vs.* $Fe(C_5H_5)_2/[Fe(C_5H_5)_2]^+$.[11b,12,15] Products of these oxidation reactions have not been described to date, suggesting the possibility of unselective consecutive reactions.

ATI complexes have found various applications in catalysis,[10d] including the hydroamination of olefins,[16] the cyanosilylation of aldehydes,[17] or the (co-)polymerisation of olefins,[18,19] epoxides,[18b] and epoxide/CO_2.[20,21] For the ATI species, the electronic parameters of the ligands have been shown to strongly influence the catalyst performance in some of these reactions.[22] Along these lines, it would be desirable to design ATI ligands with ligand-centred redox-activity under moderately oxidative conditions, thereby offering an additional possibility for tuning their electronic properties. In view of the reluctance of the ATI ligand framework to undergo reversible electron transfer under oxidative conditions, the installation of a redox-active substituent may be considered in order to achieve this goal.

Here we present the synthesis and characterisation of an aminotropone and an aminotroponimine ligand featuring a ferrocenyl substituent as a redox-active functional group, along with complexes of sodium and bismuth. The redox properties of all compounds have been investigated.

Results and discussion

In order to synthesize an ATI ligand susceptible to reversible electron transfer under oxidising conditions, the redox-active group should be chemically robust and easy to introduce. Most importantly however, it must undergo oxidation at a potential lower than that of irreversible ligand oxidation, which can set it at *ca.* +0.20 V *vs.* $Fe(C_5H_5)_2/[Fe(C_5H_5)_2]^+$ (*vide supra*). These requirements make the aminoferrocenyl group an attractive candidate, since aromatic amines are standard reagents for the synthesis of ATI ligands[16b,23] and the parent H_2NFc shows a redox potential of −0.37 V (Fc = ferrocenyl).[24]

Aminotroponates: synthesis and structural characterisation

Starting from tosyloxytropone **1**, the ferrocenyl-aminotropone **2** (H-AT^{Fc}) was synthesised in a straightforward substitution reaction (Scheme 2). Metalation of compound **2** with NaHMDS gave the sodium aminotroponate Na(AT^{Fc}) (**3**), which could be transformed into the bismuth aminotroponate, Bi(AT^{Fc})$_3$ (**4**) in a salt elimination reaction with $BiCl_3$ (HMDS = hexamethyldisilazide). Whereas AT complexes of main group elements such as Na,[31] Ca,[21a] Al,[21c] or As[41] have been investigated, compound **4** is the first example of an aminotroponate in the coordination sphere of a heavy p-block element.[25]

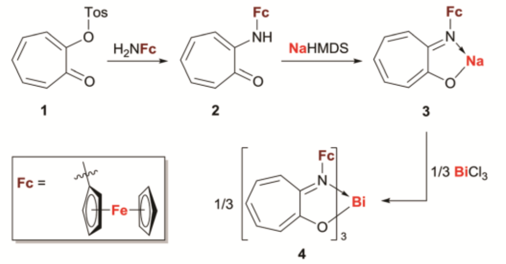

Scheme 2 Synthesis of ferrocenyl-substituted aminotropone H-AT^{Fc} (**2**), its sodium complex Na(AT^{Fc}) (**3**) and its bismuth complex Bi(AT^{Fc})$_3$ (**4**); Tos = SO_2-*p*-(C_6H_4Me).

Compounds **2–4** show signal patterns in ^1H and ^{13}C NMR spectra that are typical for unsymmetrically substituted tropone derivatives and ferrocenyl groups. The acidic proton in compound **2** is located at the nitrogen atom as indicated by a ^{15}N NMR chemical shift of −282.1 ppm and ^{13}C NMR chemical shifts of 155 ppm ($CN^{Fc}H$) and 177 ppm (*C*O), respectively, for the quaternary carbon atoms in the C_7 ring. In ^{13}C NMR spectra of compounds **3** and **4**, the resonances for the diagnostic $CN^{Fc}M$ moieties are low-field-shifted by *ca.* 10 ppm compared to that of **2**, which suggests a stronger electron delocalisation in these complexes. Whereas sharp sets of resonances were observed for compounds **2** and **4**, significant signal broadening was observed for the sodium species **3**, especially when using low-polarity solvents such as benzene. Aggregation phenomena, which are commonly observed for sodium aryloxide complexes, are likely to account for these observations.[26]

Single crystal X-ray diffraction analysis of H-AT^{Fc} (**2**) confirmed the structural assignments from solution NMR spectroscopic experiments (Fig. 1; monoclinic space group $P2_1/c$; $Z = 4$). The hydrogen H1 atom was located in the difference Fourier map near the nitrogen atom N1. A short C1–O1 (1.25 Å) and a relatively long C2–N1 distance (1.35 Å) also indicate an α-amino-ketone structure for **2**. No intermolecular hydrogen bonding was observed for **2** in the solid state.

Slow diffusion of pentane into a THF solution of **3** yielded crystals suitable for single crystal X-ray diffraction analysis. Compound **3** crystallised as a thf-ligated, tetranuclear species with an Na_4O_4 heterocubane core structure (**3·(thf)$_{1.5}$**, triclinic space group $P\bar{1}$ with $Z = 2$; Fig. 2). The heterocubane motif has previously been reported for sodium aryloxides and imine-functionalised derivatives thereof.[26,27] Compound **3·(thf)$_{1.5}$** differs from these examples in that the ligand sphere around its Na_4O_4 moiety is highly irregular. This is due to the interaction of the sodium centres with either one thf ligand (Na2, Na3) or two thf ligands (Na1, Na4). In addition, one of the NFcR functionalities is located above a Na_2O_2 face and adopts

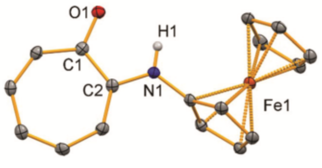

Fig. 1 Molecular structure of H-AT^{Fc} (**2**) in the solid state. Displacement ellipsoids are shown at the 50% probability level. Hydrogen atoms except for H1 are omitted for clarity. Selected bond lengths (Å): C1–O1, 1.253(4); C2–N1, 1.348(4).

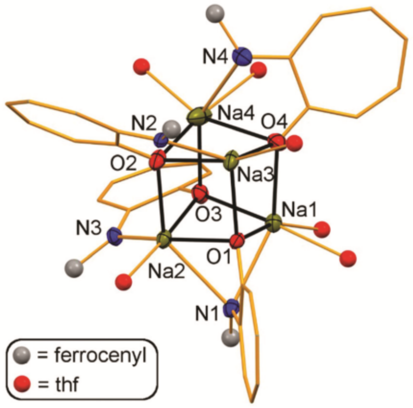

Fig. 2 Molecular structure of $[Na_4(AT^{Fc})_4(thf)_6]$ ($\mathbf{3}\cdot(thf)_{1.5}$) in the solid state. Heteroatoms are represented by displacement ellipsoids at the 50% probability level; carbon atoms are shown as wireframe; ferrocenyl substituents and thf ligands are represented by the *ipso*-C atoms and the oxygen atoms respectively. Bonds of the N_4O_4 core are shown in black for better visual distinction. Hydrogen atoms and lattice-bound solvent molecules are omitted for clarity. Selected bond lengths (Å) and angles (°): Na1–N1, 2.598(3); Na2–N1, 2.651(3); Na2–N3, 2.428(3); Na3–N2, 2.437(3); Na4–N4, 2.490(4); Na(1–4)–O(1–4), 2.295(3)–2.426(3); C^{AT}–O, 1.268(5)–1.280(4); C^{AT}–N, 1.307(5)–1.321(5); angles O(1–4)–Na(1–4)–O(1–4) in Na_4O_4 motif, 79.98(9)–95.93(10).

a bridging coordination mode between Na1 and Na2, which is unprecedented in sodium aryloxide heterocubanes. The remaining three AT^{Fc} ligands are located along the Na–O edges of the cubane, as commonly observed in Na_4O_4 heterocubanes based on chelating aryloxide ligands with appropriate bite angles. The sodium atoms in $\mathbf{3}\cdot\mathbf{(thf)_{1.5}}$ adopt slightly (Na4) or strongly (Na1, Na2) distorted octahedral coordination geometries or a slightly distorted square pyramidal coordination geometry (Na3; $\tau_5 = 0.26$, O1 in the apical position).[28] The coordination chemistry of each sodium site can be correlated with the Na–O distances in the Na_4O_4 core: the shortest Na–O bond (2.295(3) Å) is found for pentacoordinate Na3, whereas the longest one (2.426(3) Å) is associated with hexacoordinate Na2, which is the only sodium atom in this structure to interact with two strong nitrogen donors. The C–O (1.268(5)–1.280(4) Å) distances in the aminotroponate moieties of $\mathbf{3}\cdot\mathbf{(thf)_{1.5}}$ are marginally longer than those in the free ligand, whereas the C–N (1.307(5)–1.321(5) Å) distances are slightly shorter. The C–O/N bond lengths in $\mathbf{3}\cdot\mathbf{(thf)_{1.5}}$ range between values expected for single and double bonds, respectively. These observations suggest considerable delocalisation of electron density between these functional groups and a shift of electron density from the nitrogen to the oxygen atom when compared to neutral H-AT^{Aryl} ligands.[29–31] This is in analogy with the bonding situation in the only other structurally characterised sodium aminotroponate.[31,32]

Aminotroponiminates: synthesis and structural characterisation

Following the established one-pot-protocol for ATI synthesis, the ferrocenyl-aminotroponimine **5** (H-$ATI^{Fc/iPr}$) was obtained in good yield after activation of aminotropone **2** with a Meerwein salt (Scheme 3). The sodium complex [Na($ATI^{Fc/iPr}$)(thf)] (**6-thf**) was synthesised by metalation of **5** with NaHMDS. Addition of the strong neutral donor ligand $OPPh_3$ gave **6-OPPh$_3$** in quantitative isolated yield, demonstrating that the thf ligand in **6-thf** is substitutionally labile. Salt elimination reactions between **6-thf** and $BiCl_3$ in a 1 : 1 or 3 : 1 stoichiometry gave the first bismuth ATI complexes Bi($ATI^{Fc/iPr}$)Cl_2 (**7**) and Bi($ATI^{Fc/iPr}$)$_3$ (**8**).[33]

The H-ATI ligand **5** was found to form only a single amine/imine tautomer in solution with the proton localised at the N-iPr group as shown in the Lewis formula in Scheme 3. This is evidenced by ^{15}N NMR chemical shifts of −263.7 ppm and −131.6 ppm for the H*N*iPr and the *N*Fc group, respectively, as determined in short- and long-range $^1H^{15}N$ correlation NMR spectroscopic experiments.[34] DFT calculations in the gas phase confirmed the compound with the proton bound to the N-iPr group to be the lower energy tautomer (ESI†). Compounds **5**, **6-L**, and **7** show signal patterns in their ^1H and ^{13}C NMR spectra that are typical for iPr and ferrocenyl moieties as well as unsymmetrically substituted ATI ligands. For each compound, similar ^{13}C NMR chemical shifts were observed for the two quarternary C_7 ring carbon atoms ($\Delta\delta$ = 0.4–3.7 ppm), suggesting electron delocalisation in the $[C_7N_2]$ moieties. The homoleptic bismuth ATI complex **8** shows a set of broad resonances in ^1H NMR spectra at ambient temperature in toluene solution. These signals gradually sharpen with increasing temperature, and one set of sharp resonances was obtained at +80 °C.[35] However, compound **8** slowly degraded

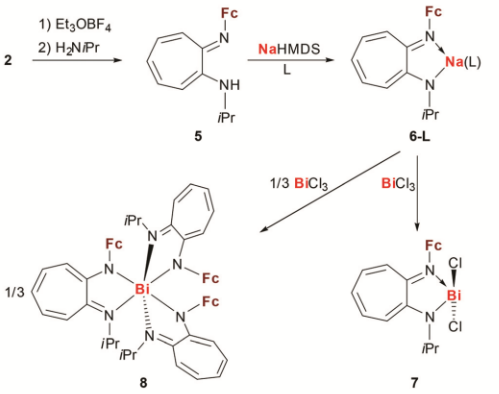

Scheme 3 Synthesis of ferrocenyl-substituted aminotroponimine H-$ATI^{Fc/iPr}$ (**5**), its sodium complexes [Na($ATI^{Fc/iPr}$)(L)] (**6-L**) (L = thf, $OPPh_3$) as well as its bismuth complexes Bi($ATI^{Fc/iPr}$)Cl_2 (**7**) and Bi($ATI^{Fc/iPr}$)$_3$ (**8**).

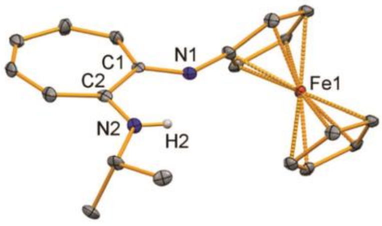

Fig. 3 Molecular structure of H-ATI$^{Fc/iPr}$ (5) in the solid state. Displacement ellipsoids are shown at the 50% probability level. Hydrogen atoms except for H2, which was located in the difference Fourier map, are omitted for clarity. Selected bond lengths (Å): C1–N1, 1.314(13); C2–N2, 1.348(13).

under these conditions, prohibiting ^{13}C NMR spectra to be recorded. The dynamic behaviour of this octahedral M(A–B)$_3$ type complex in solution was ascribed to a *cis*/*trans* isomerism. DFT calculations confirm a small energy difference of $\Delta\Delta H$ = 4.1 kcal mol^{-1} between these two complexes, the *trans* isomer being lower in energy.

The ATI compounds **5**, **6-OPPh$_3$**, **7**, and **8** were investigated by single-crystal X-ray diffraction analyses. Compound **5** crystallised in the orthorhombic space group $P2_12_12_1$ with Z = 4 (Fig. 3). No intermolecular hydrogen bonds were detected for **5** in the solid state. In congruency with the bonding situation in solution, the bonding parameters obtained from XRD analysis suggest the presence of an isopropyl-substituted amine (C2–N2, 1.35 Å) and a ferrocenyl-substituted imine moiety (C1–N1, 1.31 Å) with 1σ-significance.

The sodium ATI compound **6-OPPh$_3$** crystallised as a dinuclear species in the monoclinic space group $P2_1/c$ with Z = 4 (Fig. 4). The sodium atoms Na1 and Na1′ are related by a centre of inversion. Each of them is part of a five-membered C$_2$N$_2$Na ring and a four-membered Na$_2$O$_2$ ring, which leads to highly distorted tetrahedral coordination geometries around these metal atoms (bond angles around Na1: 69°–140°). The central four-membered Na$_2$O$_2$ ring is planar by symmetry. The Na–O bonds of 2.28 and 2.30 Å in this ring are similar to those found in a dicationic complex with the same structural motif, [Na$_2$(μ$_2$-OPPh$_3$)$_2$(OPPh$_3$)$_2$]$^{2+}$ (2.28–2.32 Å).[36] The five-membered C$_2$N$_2$Na rings deviate slightly from planarity (Na–(C$_2$N$_2$ plane): 0.33 Å), whereas the C$_7$N$_2$ moiety shows significant puckering (dihedral angle between C$_7$ plane and C$_2$N$_2$Na plane: 17°). The Na1–N1/2 (2.32 Å) and the C1/2–N1/2 bond lengths (1.32–1.33 Å) in **6-OPPh$_3$** are identical within the limits of error, indicating a high degree of electron delocalization in the C$_7$N$_2$ unit. In contrast to the related compound [Na(ATI$^{Ph/iPr}$)(thf)], no bonding interactions are observed between the sodium atom and the π-electrons of the C$_7$ ligand backbone.[11a] This was ascribed to the presence of the strongly σ-donating phosphane oxide ligands.

The bismuth compound Bi(ATI$^{Fc/iPr}$)Cl$_2$ (**7**) forms a weakly aggregated dinuclear species in the solid state (Fig. 5a; triclinic

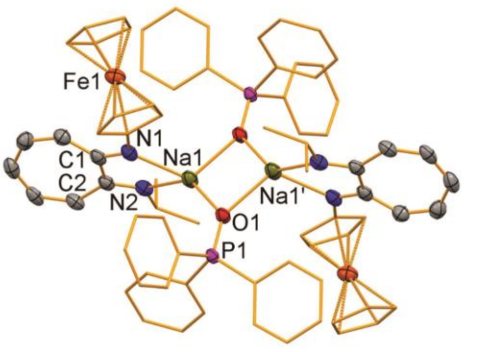

Fig. 4 Molecular structure of [Na(ATI$^{Fc/iPr}$)(OPPh$_3$)] (**6-OPPh$_3$**) in the solid state. Displacement ellipsoids are shown at the 50% probability level. Carbon atoms of Fc, iPr, and Ph groups are shown as wireframe. Hydrogen atoms, split position of a disordered iPr group and lattice bound solvent molecules are omitted for clarity. Selected bond lengths (Å) and angles (°): Na1–N1, 2.318(4); Na1–N2, 2.322(4); Na1–O1, 2.283(3); Na1–O1′, 2.300(3); C1–N1, 1.325(6); C2–N2, 1.320(6); N1–Na1–N2, 69.14(14); N2–Na1–O1′, 139.65(14); O1–Na1–O1′, 94.15(11); Na1–O1–Na1′, 85.86(11).

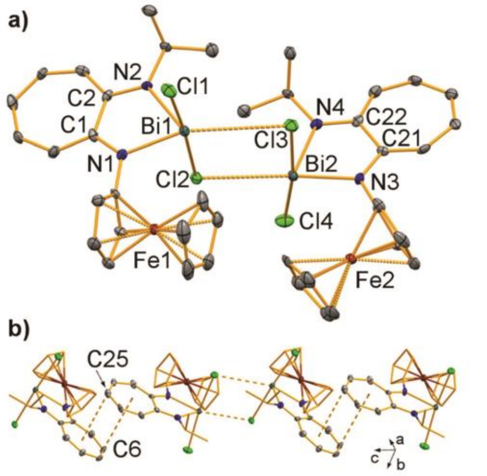

Fig. 5 (a) Molecular structure of dinuclear subunit [Bi(ATI$^{Fc/iPr}$)Cl$_2$]$_2$ (**7**)$_2$ in the solid state. Displacement ellipsoids are shown at the 50% probability level. Hydrogen atoms are omitted for clarity. (b) Cut out of coordination polymer (**7**)$_\infty$. Selected bond lengths (Å) and angles (°): Bi1–N1, 2.163(7); Bi1–N2, 2.214(7); Bi1–Cl1, 2.637(2); Bi1–Cl2, 2.744(2); Bi1···Cl3, 3.603(2); Bi2–N3, 2.159(6); Bi2–N4, 2.205(7); Bi2–Cl3, 2.713(2); Bi2–Cl4, 2.669(2); Bi2···Cl2, 3.259(2); C1–N1, 1.327(10); C2–N2, 1.347(10); C21–N3, 1.342(10); C22–N4, 1.343(10); C6–centroid, 3.758(17); C6–plane(C21–27), 3.625(17); C25–centroid′, 3.369(17); C25–plane (C1–7), 3.301(17); N1–Bi1–N2, 73.1(3); N1–Bi1···Cl3, 155.27(19); N2–Bi1···Cl3, 110.79(17); Cl1–Bi1–Cl2, 175.33(7); Bi1···Cl2···Bi2, 110.44(7); Bi2···Cl3···Bi1, 102.01(6); Cl2–Bi1···Cl3, 70.66(5); Cl3–Bi2···Cl2, 76.86(6).

space group $P\bar{1}$; $Z = 2$). The intermolecular interactions are realised *via* two Bi⋯Cl contacts (Bi1⋯Cl3, 3.60 Å and Bi2⋯Cl2, 3.26 Å). These values are below the sum of the van der Waals radii (3.82 Å)[37] and at the upper limit of distances associated with weak bismuth chloride bonding.[38] The Bi_2Cl_2 four-membered ring is essentially planar (sum of internal angles: 360°). The bismuth atoms are found in distorted square pyramidal coordination geometries with N2 and N4 in the apical positions (τ_5 (Bi1) = 0.33; τ_5 (Bi2) = 0.17).[28] The intramolecular Bi–Cl bonds with terminal chlorido ligands (Bi1–Cl1, 2.64 Å; Bi2–Cl4, 2.67 Å) are shorter than those involving bridging Cl atoms (Bi1–Cl2, 2.74 Å; Bi2–Cl3, 2.71 Å). The Bi–N bond lengths in **7** differ slightly, the Bi–N^{Fc} bonds (2.16 Å) being shorter than the Bi–N^{iPr} bonds (2.21 Å). However, these differences in metal–nitrogen bonding are not pronounced enough to be reflected by differences in the respective $C^{tropone}$–N bond lengths, which are identical within limits of error (1.33–1.35 Å) and intermediate between those expected for C–N single and double bonds. In addition to the intermolecular Bi⋯Cl contacts in **7**, there are also intermolecular, parallel-displaced arene⋯arene interactions between the C_7 backbones of the ATI ligands in **7** (Fig. 5b). The C6/25–C_7(centroid) distances amount to 3.37 Å and 3.76 Å, respectively.[39] These findings demonstrate that the ATI ligand backbone can undergo bonding interactions not only with main group[11] and transition metals,[47] but also with organic moieties. Taken together, the C_7⋯C_7 and Bi⋯Cl interactions in **7** lead to formation of an organic/inorganic coordination polymer in the solid state, which extends along the crystallographic *c*-axis (Fig. 5b, ESI†).[40] Compound **7** represents the first example of a bismuth ATI complex and may thus be compared to the related arsenic species $As(ATI^{iPr/iPr})Cl_2$, which forms a mononuclear complex in the solid state.[41] The higher degree of aggregation in **7** evidences the higher Lewis acidity of the bismuth compound compared to the related arsenic species.

The homoleptic bismuth complex $Bi(ATI^{Fc/iPr})_3$ (**8**) crystallised as a typical molecular compound without any directed intermolecular bonding interactions in the solid state (Fig. 6; triclinic space group $P\bar{1}$; $Z = 2$). The bismuth atom is found in a strongly distorted octahedral coordination geometry (N–Bi–N angles between *cis*-oriented sites: 62–121°). The distortion is due to the small bite angle of the ATI ligand (62–67°) and possibly further promoted by the bulky ferrocenyl substituents and the stereochemical activity of the bismuth-centred lone pair (ESI†). Compound **8** is only the second example of a structurally characterised $Bi(AB)_3$ type complex based on nitrogen donors and the first one to crystallise as the *trans* isomer.[42] The Bi–N bonds in **8** (2.33–2.61 Å) are 0.12 to 0.45 Å longer than those in **7**, which was ascribed to the lower coordination number, the presence of electronegative chlorido ligands, and the weak Bi⋯Cl bonding in **7**. The pronounced alteration of Bi–N lengths in **8** (Δ(Bi–N) = 0.28 Å) results from one ATI ligand showing shorter bonds to the central atom (Bi1–N1/2, 2.33–2.39 Å) than the other two (Bi–N3/4, 2.47–2.61 Å; Bi1–N5/6, 2.48–2.55 Å); *i.e.* it is not due to a lack of electron delocalisation within the ATI ligands. In fact, the $C^{tropone}$–N bond lengths in all three ATI ligands of compound **8** (1.30–1.36 Å) are between those expected for C–N single and double bonds. Each ferrocenyl substituent in **8** is moderately twisted against the mean plane of the C_7 ring to which it is connected through a nitrogen atom. The angles between the mean planes defined by the five carbon atoms of the NC_5H_4 groups and the seven carbon atoms of the C_7 rings amount to 41–49°, which in principle allows for electron delocalisation through the BiN(NFc)C_7H_5 moieties.

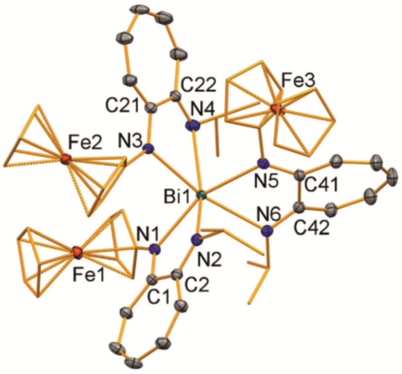

Fig. 6 Molecular structure of $Bi(ATI^{Fc/iPr})_3$ (**8**) in the solid state. Displacement ellipsoids are shown at the 50% probability level. Carbon atoms of Fc and iPr unit are shown as wireframe for better visibility. Hydrogen atoms and lattice bound THF molecules are omitted for clarity. Selected bond lengths (Å), bond angles (°), and angles between planes defined by C_7 rings and nitrogen-bound C_5 rings (°): Bi1–N1, 2.386(3); Bi1–N2, 2.328(3); Bi1–N3, 2.470(3); Bi1–N4, 2.608(3); Bi1–N5, 2.476(3); Bi1–N6, 2.548(3); C1–N1, 1.336(5); C2–N2, 1.338(5); C21–N3, 1.355(5); C22–N4, 1.298(5); C41–N5, 1.342(5); C42–N6, 1.308(5); N3–Bi1–N4, 62.40(11); N1–Bi1–N4, 120.71(11); N1–Bi1–N5, 155.21(11); N3–Bi1–N6, 166.70(11); plane(C1–C7)/plane(C_5), 41.7; plane(C21–C27)/plane(C_5), 48.9; plane(C41–C47)/plane(C_5), 40.8.

Electrochemical behaviour

The ligands and complexes presented in this work were investigated by cyclic voltammetry (CV) at 23 °C in THF or CH_2Cl_2 containing 0.1 M $[N(nBu)_4][PF_6]$ at scan rates in the range of 50 to 1000 mV s^{-1} (for details see ESI†). All potentials are reported *versus* the ferrocene/ferrocenium couple.

Oxidative conditions. Under oxidative conditions, the aminotropone ligand **2**, its sodium salt **3**, and its bismuth derivative **4** each showed one reversible redox wave. Half-wave potentials of $E^1(\mathbf{2}) = -0.03$ V, $E^1(\mathbf{3}) = -0.08$ V, and $E^{1-3}(\mathbf{4}) = -0.01$ V were recorded with THF as a solvent (Table 1). Thus, the nature of the element situated in the N,O binding pocket (H *vs.* Na *vs.* Bi) has only a minor effect on the redox potential of the ferrocenyl substituent. Compared to the parent ferrocenyl amine, the redox potentials of **2–4** are anodically shifted by *ca.* 0.29 to 0.36 V. Notably, only one broad redox wave was detected for the electron transfer events of the three ferrocenyl groups

Table 1 Redox potentials of compounds **2–8** under oxidative conditions at 23 °C in THF/0.1 M $[N(nBu)_4][PF_6]$. Potentials of reversible redox events E^1–E^3 are reported *vs.* that of $Fe(C_5H_5)_2/[Fe(C_5H_5)_2]^+$

Cpd	Ligand	M	E^1 [V]	E^2 [V]	E^3 [V]
2	AT	—	−0.03	—	—
3	AT	Na	−0.08	—	—
4	AT	Bi	−0.01	−0.01	−0.01
5	ATI	—	−0.18	—	—
6-thf	ATI	Na	−0.19	—	—
6-OPPh$_3$	ATI	Na	−0.17	—	—
7	ATI	Bi	−0.21	—	—
8	ATI	Bi	−0.16[a]	−0.05[a]	+0.09[a]

[a] Potentials determined from square wave voltammogram (redox waves not fully resolved in cyclic voltammogram); when recorded in CH_2Cl_2/0.1 M $[N(nBu)_4][PF_6]$, the three redox waves E^1–E^3 were fully resolved in the cyclic voltammogram: E^1 = −0.23 V; E^2 = −0.03 V; E^3 = +0.09 V (*cf.*, Fig. 7).

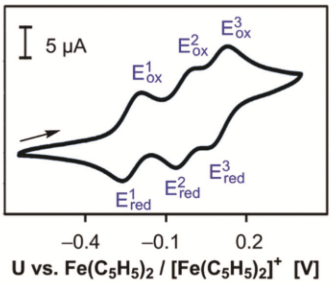

Fig. 7 Cyclic voltammogram of **8** at 23 °C in CH_2Cl_2/0.1 M $[N(nBu)_4][PF_6]$ at a scan rate of 50 mV s^{-1}.

of $Bi(AT^{Fc})_3$ (**4**), *i.e.* there is no (or only very weak) electronic communication between the ferrocenyl substituents.[43] Similarly, in a $Cu^{II}(AT)_2$ complex with ferrocenyl substituents in the 5-position of the C_7 ligand backbone, only one redox wave was detected by CV for the two Fe^{II}/Fe^{III} couples.[44–46] A remarkable ferromagnetic coupling between the two Fe^{III} centres and the Cu^{II} centre *via* a spin polarisation mechanism was demonstrated for the oxidised form of this complex on the basis of magnetic susceptibility measurements, EPR spectroscopy, and DFT calculations. For a Cu^{II} AT complex without ferrocenyl substituents, $Cu(AT^{iPr})_2$, only a partially reversible redox event has been reported.[47]

The aminotroponimine ligand **5**, its sodium complexes **6-thf** and **6-OPPh$_3$**, as well as its bismuth derivatives **7** and **8**, show reversible redox events at similar potentials in the range of −0.16 V to −0.21 V (Table 1). Thus, substitution of the oxygen atom in compounds **2–4** for an N-iPr group in compounds **5–8** leads to a cathodic shift of the first ferrocenyl-based redox events by 80–200 mV. In the small series of ATI complexes **5–8**, the element bound to the ATI ligand (H *vs.* Na *vs.* Bi) and the neutral or anionic ligand bound to the metal centre (thf *vs.* $OPPh_3$; ATI *vs.* Cl) have only a minor effect on the potential of the first oxidation. However, electron transfer involving the second and the third ferrocenyl group of the homoleptic bismuth complex $Bi(ATI^{Fc/iPr})_3$ (**8**) was observed at half-wave potentials that are anodically shifted by up to 250 mV (E^1(**8**) = −0.16 V, E^2(**8**) = −0.05 V, and E^3(**8**) = +0.09 V). When recorded in CH_2Cl_2/0.1 M $[N(nBu)_4][PF_6]$, this potential difference slightly increases ($\Delta(E^1,E^3)$ = 320 mV) and the redox waves are clearly separated in the cyclic voltammogram (Fig. 7). In contrast to the situation observed for the analogous bismuth aminotroponate **4**, the peak separation detected in CV experiments with aminotroponiminate **8** indicates weak electronic communication between the three ferrocenyl substituents in this compound. In principle, intramolecular electronic communication may proceed *via* a through-bond or a through-space mechanism, both of which can also be operative simultaneously.[44,48,49] DFT calculations on the singly oxidised compound $[Bi(ATI^{Fc/iPr})_3]^+$ (**8$^+$**) revealed that its singly occupied molecular orbital (SOMO) extends over two $ATI^{Fc/iPr}$ ligands and that the shortest Fe⋯Fe distance amounts to 5.796 Å (ESI†). Based on these criteria, both mechanisms appear to be viable in **8$^+$**.[50] In contrast, the SOMO in $[Bi(AT^{Fc})_3]^+$ (**4$^+$**) is predominantly localized on one AT^{Fc} ligand and the shortest Fe⋯Fe distance in this species amounts to 6.051 Å (ESI†), which is in line with the weaker electronic communication in the bismuth AT complex **4** as compared to the bismuth ATI complex **8**.

The AT and ATI complexes **4**, **7**, and **8** are rare examples of redox-active bismuth compounds. In recent years, a number of mononuclear bismuth compounds with the metal centre in oxidation states of +1 and +2 have been reported, some of which have been shown to undergo well-defined redox reactions.[51–53] In addition, a dibismuthene, $[Bi((2,5\text{-}Ar_2\text{-}C_5H_2)Fe(C_5H_5))]_2$ (Ar = 3,5-tBu_2-C_6H_3), with bismuth-bound ferrocenyl groups has been shown to be susceptible to reversible electron transfer under oxidising and reducing conditions at −78 °C and +23 °C, respectively.[54] In this case, electronic communication between the two Fe^{II}/Fe^{III} redox couples was evidenced by a peak separation of 480 mV in the cyclic voltammogram.

Reducing conditions. The aminotroponate ligand **2** shows a quasi-reversible redox event at −2.38 V. DFT calculations of the radical species $[H\text{-}AT^{Fc}]^{\bullet-}$ (**2-red**) led us to suggest that the spin density in this species is located on the C_7 ligand backbone, as opposed to that of the oxidised species $[H\text{-}AT^{Fc}]^{\bullet+}$ (**2-ox**), which expectedly bears the spin density at the Fe centre (Fig. 8a). Whereas the sodium complex **3** does not show a redox event under reducing conditions in the accessible potential window, the bismuth complex **4** shows a quasi-reversible redox event at −2.38 V, similar to the neutral ligand. These results are in line with recent findings that established related aminotroponiminates as redox-active ligands.[11] Similarly, a heterobimetallic Cu/Ru complex, $[Cu(AT^{iPr})_2(Ru(C_5Me_5))_2][PF_6]_2$, has been reported to show a quasi-reversible two-electron reduction, which is at least partially ligand-centred according to EPR spectroscopy.[47] However, this redox event was detected at −0.53 V, which corresponds to a dramatic anodic shift of more than 1.8 V compared to compounds **2** and **4**.

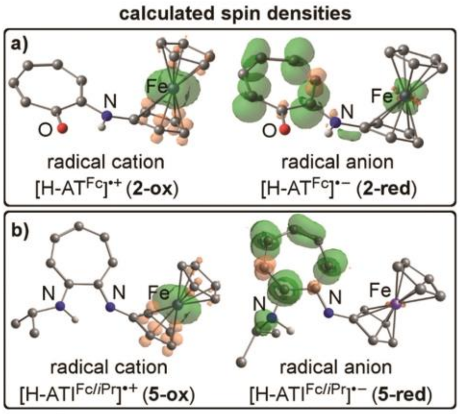

Fig. 8 Mulliken spin densities of radical ions obtained by one-electron oxidation and -reduction of ligands **2** (a) and **5** (b) as determined by DFT calculations (iso-value 0.004). Carbon-bound hydrogen atoms are omitted for clarity. (a) $[\text{H-AT}^{\text{Fc}}]^{\bullet+}$ (**2-ox**) and $[\text{H-AT}^{\text{Fc}}]^{\bullet-}$ (**2-red**); (b) $[\text{H-ATI}^{\text{Fc/iPr}}]^{\bullet+}$ (**5-ox**) and $[\text{H-ATI}^{\text{Fc/iPr}}]^{\bullet-}$ (**5-red**).

The aminotroponiminate ligand **5** shows a chemically reversible redox event at −2.64 V. This is in agreement with the recently reported redox behaviour of H-ATI$^{\text{Ph/iPr}}$ and corresponds to a cathodic shift of 260 mV compared to the aminotropone analogue **2**.[11] The calculated spin density distributions for the radical cation $[\text{H-ATI}^{\text{Fc}}]^{\bullet+}$ (**5-ox**) and the radical anion $[\text{H-ATI}^{\text{Fc}}]^{\bullet-}$ (**5-red**) follow the same trend as those in the aminotropone analogs **2-ox** and **2-red** (Fig. 8b). That is, the spin density in the oxidised and reduced species is mainly centred at the Fe atom and the C_7 ligand backbone, respectively (for details see ESI†). Cyclic voltammograms of the sodium complex **6-OPPh$_3$** suggest a reductively induced dimerisation, as recently revealed for [Na(ATI$^{\text{Ph/iPr}}$)(thf)] with a reduction wave at −2.69 V and a corresponding oxidation wave at −0.82 V. Qualitatively, the same electrochemical behaviour was observed for the homoleptic bismuth compound **8** with the potentials being shifted to −2.01 V and −1.20 V for the reduction and the oxidation wave, respectively. However, the three ATI ligands of **8** do not undergo a quantitative reductive dimerization under these conditions, since an additional quasi-reversible redox event is detected at −2.65 V (ESI†).[55] As could be expected due to the presence of two chlorido ligands, the bismuth ATI complex **7** showed ill-defined redox events under reducing conditions, which was attributed to degradation of electrochemically generated species such as $[\text{Bi}(\text{ATI}^{\text{Fc/iPr}})\text{Cl}]^{\bullet}$.[56]

Conclusions

We have presented new aminotroponate (AT) and aminotroponiminate (ATI) ligands bearing a ferrocenyl substituent at the nitrogen atom. Sodium complexes and the first bismuth AT and ATI complexes were isolated and characterised. Structural analyses revealed the formation of an unusual *trans* isomer for $\text{Bi}(\text{ATI}^{\text{Fc/iPr}})_3$ and the Lewis-acidity of $\text{Bi}(\text{ATI}^{\text{Fc/iPr}})\text{Cl}_2$ (indicated by weak intermolecular interactions in the solid state). The latter compound also gave evidence for parallel-displaced π-stacking of ATI ligand backbones, demonstrating that the ATI ligand backbone can engage in π–π interactions with organic moieties. This has potential relevance for the pre-coordination of substrates and the stabilization of transition states in stoichiometric and catalytic transformations of ATI compounds. Reversible, ferrocenyl-based redox-events were detected for all AT and ATI species under investigation, giving evidence for the first ligand-centred, reversible electron transfer of ATI compounds under oxidative conditions. Furthermore, we have demonstrated that reversible electron transfer in bismuth compounds is possible under oxidative conditions at ambient temperature. In the homoleptic bismuth ATI complex, three oxidation steps can be realised with electronic communication between the metal centres as indicated by cyclic voltammetry, which is unprecedented for mononuclear bismuth complexes. Under reducing conditions, both the AT and the ATI compounds show well-defined, ligand-centred redox events. These studies open up perspectives for the use of AT and ATI ligands in redox- or electrochemically controlled applications such as redox-switchable catalysis.

Experimental section

General considerations

All air- and moisture-sensitive manipulations were carried out using standard vacuum line Schlenk techniques or in an MBraun inert atmosphere dry-box containing an atmosphere of purified argon. Solvents were degassed and purified according to standard laboratory procedures. Starting materials were synthesised according to the literature. NMR spectra were recorded on Bruker instruments operating at 200, 400 or 500 MHz with respect to ^{1}H. ^{1}H and ^{13}C NMR chemical shifts are reported relative to SiMe$_4$ using the residual ^{1}H and ^{13}C chemical shifts of the solvent as a secondary standard. ^{15}N NMR chemical shifts are reported relative to CH_3NO_2 (90% in $CDCl_3$) and were determined by two-dimensional ^{1}H–^{15}N correlation NMR spectroscopic experiments. If not otherwise noted, NMR spectra were recorded at 23 °C. In the NMR spectroscopic characterisation, the *C*O (in AT compounds) and the *C*N$^{\text{Fc}}$ carbon atoms (in ATI compounds) are referred to as 1-C. Elemental analyses were performed on a Leco or a Carlo Erba instrument. Cyclic voltammograms were recorded using a Gamry Instruments Reference 600 potentiostat at 23 °C in THF containing 0.1 M $[\text{N}(n\text{Bu})_4][\text{PF}_6]$ unless otherwise noted. A standard three-electrode cell configuration was employed using a platinum disk working electrode, a platinum wire counter electrode, and a silver wire, separated by a Vycor tip, serving as the reference electrode. Formal redox potentials are referenced to the ferrocene/ferrocenium redox couple. UV-vis spectra were recorded with a Jasco V-660 UV-vis spectrometer in THF solution. Mass spectrometric data were recorded using an Exactive Plus instrument by Thermo Scientific. Single crystals suitable for X-ray diffraction were coated with polyisobutylene or perfluorinated polyether oil in a glovebox, transferred to a nylon loop and then transferred to the goniometer of a diffractometer equipped with a molybdenum X-ray tube (λ = 0.71073 Å). The structures were solved using direct methods (SHELXS) completed by Fourier synthesis and refined by full-matrix least-squares procedures. CCDC 1825483–1825488† contain the crystallographic information for this work.

H-AT^{Fc} (2). Ethanol (40 mL) and NEt_3 (5.53 g, 5.47 mmol) were added to a mixture of 2-tosyloxy-tropone (**1**) (1.37 g, 4.97 mmol) and aminoferrocene (1.00 g, 4.97 mmol). The reaction mixture was heated under reflux for 24 h. All volatiles were removed *in vacuo*. The crude reaction product was purified by column chromatography. The product was obtained as a dark orange solid. Yield: 1.14 g, 3.74 mmol, 75%.

^{1}H NMR (500 MHz, $CDCl_3$): δ = 4.20 (t, 2H, $^{3}J_{HH}$ = 1.9 Hz, 3,4-(C_5H_4NHR)), 4.27 (s, 5H, C_5H_5), 4.41 (t, 2H, $^{3}J_{HH}$ = 1.9 Hz, 2,5-(C_5H_4NHR)), 6.71–6.78 (m, 1H, 5-H), 7.19–7.22 (m, 2H, 6,7-H (overlapping)), 7.23 (dd, 1H, $^{3}J_{HH}$ = 11.7 Hz, $^{4}J_{HH}$ = 1.1 Hz, 3-H), 7.30 (ddd, 1H, $^{3}J_{HH}$ = 11.7 Hz, $^{3}J_{HH}$ = 8.9 Hz, $^{4}J_{HH}$ = 0.8 Hz, 4-H), 8.26 (br s, 1H, NH) ppm. ^{13}C NMR (126 MHz, $CDCl_3$) δ = 64.38 (s, 2,5-(C_5H_4NHR)), 66.15 (s, 3,4-(C_5H_4NHR)), 69.54 (s, C_5H_5), 94.36 (s, 1-(C_5H_4NHR)), 111.33 (s, 6/7-C), 123.69 (s, 5-C), 129.76 (s, 3-C), 135.97 (s, 7/6-C), 137.56 (s, 4-C), 155.05 (s, 2-C), 176.90 (s, 1-C) ppm. ^{15}N NMR (51 MHz, $CDCl_3$): δ = −282.1 (HNFcR) ppm. UV-vis (THF): λ_{max} = 346, 409, 476 (shoulder) nm. Anal. calc. for $C_{17}H_{15}NOFe$ (305.16 g mol^{-1}): C, 66.91; H, 4.95; N, 4.59; found: C, 66.84; H, 4.82; N, 4.68. M. p.: 81 °C.

Na-AT^{Fc} (3). $Na(N(SiMe_3)_2)$ (120 mg, 65.5 µmol) was added to a solution of (2-ferrocenylamino)tropone (**2**) (200 mg, 65.5 µmol) in THF/toluene/pentane (1 : 1 : 1, 3 mL). After 20 min, all volatiles were removed from the reaction mixture under reduced pressure. The resulting red oil was washed with pentane (3 × 3 mL) and dried *in vacuo* to give a red foamy solid. Yield: 133 mg, 38.9 µmol, 59%. Residual amounts of pentane could not be removed by exposing **3** to reduced pressure, even at slightly elevated temperature of up to 60 °C.

^{1}H NMR (500 MHz, THF-d_8): δ = 4.04 (br s, 2H, 3,4-(C_5H_4NR)), 4.15 (br s, 5H, C_5H_5), 4.21 (br s, 2H, 2,5-(C_5H_4NR)), 5.98–6.01 (m, 1H, 5-H), 6.47–6.50 (m, 1H, 7-H), 6.64–6.68 (m, 1H, 6-H), 6.81–6.85 (m, 1H, 4-H), 8.03 (d, 1H, $^{3}J_{HH}$ = 10.2 Hz, 3-H) ppm. ^{13}C NMR (126 MHz, THF-d_8): δ = 63.33 (s, 2,5-(C_5H_4NR)), 64.98 (s, 3,4-(C_5H_4NR)), 68.64 (s, C_5H_5), 108.15 (s, 1-(C_5H_4NR)), 115.11 (s, 5-C), 119.00 (s, 3-C, 7-C), 131.90 (s, 4-C), 134.68 (s, 6-C), 164.67 (s, 2-C), 181.41 (s, 1-C) ppm. Resonances due to residual amounts of pentane were also detected. UV-vis (THF): λ_{max} = 415, 443, 500 (shoulder) nm. Anal. calc. for $C_{17}H_{14}NOFeNa\cdot(C_5H_{12})_{0.2}$ (341.57 g mol^{-1}): C, 63.30; H, 4.84; N, 4.10; found: C,63.31; H, 4.77; N, 4.33.

Bi(AT^{Fc})$_3$ (4). A solution of $Na(N(SiMe_3)_2)$ (30.0 mg, 0.16 mmol) in THF (1 mL) was added to a solution of H-AT^{Fc} (**2**) (50.0 mg, 0.163 mmol) in THF (1 mL). Subsequently, a solution of $BiCl_3$ (17.2 mg, 54.6 µmol) in THF (1 mL) was added. After 5 minutes, the resulting deep red suspension was filtered. All volatiles were removed from the filtrate under reduced pressure. The resulting red solid was washed with Et_2O (2 × 3 mL) and dried *in vacuo*. Yield: 28.0 mg, 23.7 µmol, 43%.

^{1}H-NMR (400 MHz, C_6D_6): δ = 3.92–3.93 (m, 6H, 3,4-(C_5H_4NR)), 4.17 (br s, 15H, C_5H_5), 4.36–4.37 (m, 6H, 2,5-(C_5H_4NR)), 6.17–6.21 (t, 3H, $^{3}J_{HH}$ = 9.3 Hz 5-H), 6.68–6.73 (m, 3H, 6-H), 6.81–6.86 (m, 3H, 4-H), 6.91–6.93 (d, 3H, $^{3}J_{HH}$ = 10.4 Hz, 7-H), 7.85–7.88 (d, 1H, $^{3}J_{HH}$ = 12.0 Hz, 3-H) ppm. ^{13}C-NMR (101 MHz, C_6D_6): δ = 63.68 (s, 2,5-(C_5H_4NR)), 66.23 (s, 3,4-(C_5H_4NR)), 69.36 (s, C_5H_5), 103.44 (s, 1-(C_5H_4NR)), 122.99 (s, 5-C), 123.43 (s, 3-C), 124.08 (s, 7-C), 133.97 (s, 4-C), 135.63 (s, 6-C), 164.99 (s, 2-C), 176.32 (s, 1-C) ppm. UV-vis (THF): λ_{max} = 348, 410, 482 (shoulder) nm. ESI-MS (THF), found: *m*/*z* (%) = 817.064 (45), calc. for $[Bi(AT^{Fc})_2]^+$: *m*/*z* = 817.065. ESI-MS (toluene), found: *m*/*z* (%) = 1121.081 (1), calc. for $[Bi(AT^{Fc})_3]^{\bullet+}$: *m*/*z* = 1121.107.[57]

H-ATI$^{Fc/iPr}$ (5). A solution of (2-ferrocenylamino)tropone (**2**) (170 mg, 557 µmol) in dichloromethane (15 mL) was added to a solution of Et_3OBF_4 in dichloromethane (250 mg, 1.32 mmol) to give a dark brown solution. After 4 h, iso-propylamine (1 mL) was added at 0 °C. The reaction mixture was warmed to ambient temperature overnight. All volatiles were removed *in vacuo*. The crude reaction product was purified by column chromatography. The product was obtained as a red oil that solidified upon standing: yield: 121 mg, 349 µmol, 63%.

^{1}H NMR (500 MHz, $CDCl_3$): δ = 1.35 (d, 6H, $^{3}J_{HH}$ = 6.4 Hz, Me), 3.84 (sept, 1H, $^{3}J_{HH}$ = 6.4 Hz, C*H*Me$_2$), 4.15 (t, 2H, $^{3}J_{HH}$ = 1.9 Hz, 3,4-(C_5H_4NHR)), 4.20 (s, 5H, C_5H_5), 4.28 (t, 2H, $^{3}J_{HH}$ = 1.9 Hz, 2,5-(C_5H_4NHR)), 6.14 (d, 1H, $^{3}J_{HH}$ = 10.1 Hz, 3-H), 6.21 (dd, 1H, $^{3}J_{HH}$ = 8.4 Hz, $^{3}J_{HH}$ = 9.9 Hz, 5-H), 6.77 (ddd, 1H, $^{3}J_{HH}$ = 8.4 Hz, $^{3}J_{HH}$ = 11.9 Hz, $^{4}J_{HH}$ = 1.3 Hz, 6-H), 6.85 (dd, 1H, $^{3}J_{HH}$ = 10.1 Hz, $^{3}J_{HH}$ = 9.9 Hz, 4-H), 7.50 (d, 1H, $^{3}J_{HH}$ = 11.9 Hz, 7-H), 7.69 (br s, 1H, NH) ppm. ^{1}H NMR (300 MHz, CD_2Cl_2): δ = 1.34 (d, 6H, $^{3}J_{HH}$ = 6.4 Hz, Me), 3.85 (sept, 1H, $^{3}J_{HH}$ = 6.4 Hz, C*H*Me$_2$), 4.15 (t, 2H, $^{3}J_{HH}$ = 1.9 Hz, 3,4-(C_5H_4NHR)), 4.19 (s, 5H, C_5H_5), 4.27 (t, 2H, $^{3}J_{HH}$ = 1.9 Hz, 2,5-(C_5H_4NHR)), 6.16 (d, 1H, $^{3}J_{HH}$ = 10.2 Hz, 3-H), 6.20 (br dd, 1H, $^{3}J_{HH}$ = 8.4 Hz, $^{3}J_{HH}$ = 10.1 Hz, 5-H), 6.78 (ddd, 1H, $^{3}J_{HH}$ = 8.4 Hz, $^{3}J_{HH}$ = 12.0 Hz, $^{4}J_{HH}$ = 1.2 Hz, 6-H), 6.85 (ddd, 1H, $^{3}J_{HH}$ = 10.1 Hz, $^{3}J_{HH}$ = 10.2 Hz, $^{4}J_{HH}$ = 1.2 Hz, 4-H), 7.48 (d, 1H, $^{3}J_{HH}$ = 12.0 Hz, 7-H), 7.68 (br s, 1H, NH) ppm. ^{13}C NMR (126 MHz, $CDCl_3$) δ = 22.48 (s, Me), 43.90 (s, *C*HMe$_2$), 63.51 (s, 2,5-(C_5H_4NHR)), 65.48 (s, 3,4-(C_5H_4NHR)), 69.19 (s, C_5H_5), 104.69 (s, 3-C), 105.15 (s, 1-(C_5H_4NHR)), 118.85 (s, 5-C), 120.95 (s, 7-C), 131.95 (s, 6-C), 134.09 (s, 4-C), 151.11 (s, 2-C), 154.81 (1-C) ppm. ^{15}N NMR (51 MHz, $CDCl_3$): δ = −263.7 (HNiPrR), −131.6 (NFcR) ppm. UV-vis (THF): λ_{max} = 366, 408, 489 (shoulder) nm. Anal. calc. for $C_{20}H_{22}N_2Fe$ (346.25 g mol^{-1}): C, 69.38; H, 6.40; N, 8.09; found: C, 69.35; H, 6.56; N, 7.97. HR-MALDI-MS, *m*/*z* (%): calcd for $(C_{20}H_{22}FeN_2)^+$ 346.1127, found: 346.1126; $[M^{\bullet}]^+$; m. p. = 100–102 °C.

[Na(ATI$^{\mathrm{Fc/iPr}}$)(thf)] (6-thf). Na(N(SiMe$_3$)$_2$) (66 mg, 0.36 mmol) was added to a solution of H-ATI$^{\mathrm{Fc/iPr}}$ (**5**) (125 mg, 0.36 mmol) in THF (2 mL) to give a deep red solution. After 5 min, all volatiles were removed from the reaction mixture under reduced pressure. The resulting red oil was washed with hexanes (2 × 3 mL) and dried *in vacuo* to give a red foamy solid. Yield: 135 mg, 0.34 mmol, 94%.

^{1}H NMR (200 MHz, C$_6$D$_6$): δ = 1.00 (d, 6H, $^{3}J_{\mathrm{HH}}$ = 6.1 Hz, Me), 1.24–1.29 (m, n × 4H, β-THF), 3.29–3.33 (m, n × 4H, α-THF), 3.69 (sept, 1H, $^{3}J_{\mathrm{HH}}$ = 6.1 Hz, C*H*Me$_2$), 3.91 (t, 2H, $^{3}J_{\mathrm{HH}}$ = 1.5 Hz, 2,5/3,4-(C$_5$H$_4$NR)), 4.27 (t, 2H, $^{3}J_{\mathrm{HH}}$ = 1.5 Hz, 3,4/2,5-(C$_5$H$_4$NR)), 4.34 (s, 5H, C$_5$H$_5$), 6.18 (dd, 1H, $^{3}J_{\mathrm{HH}}$ = 8.5 Hz, $^{3}J_{\mathrm{HH}}$ = 9.2 Hz, 5-H), 6.41 (d, 1H, $^{3}J_{\mathrm{HH}}$ = 11.7 Hz, 3-H), 6.88 (ddd, 1H, $^{3}J_{\mathrm{HH}}$ = 11.7 Hz, $^{3}J_{\mathrm{HH}}$ = 8.5 Hz, $^{4}J_{\mathrm{HH}}$ = 1.4 Hz, 4-H), 6.99 (ddd, 1H, $^{3}J_{\mathrm{HH}}$ = 11.1 Hz, $^{3}J_{\mathrm{HH}}$ = 9.2, $^{4}J_{\mathrm{HH}}$ = 1.4 Hz, 6-H), 7.73 (d, 1H, $^{3}J_{\mathrm{HH}}$ = 11.1 Hz, 7-H) ppm. ^{13}C NMR (50 MHz, C$_6$D$_6$): δ = 24.26 (s, CH*Me*$_2$), 25.53 (s, β-THF), 48.39 (s, *C*HMe$_2$), 62.31 (s, 3,4/2,5-(C$_5$H$_4$NR)), 64.23 (s, 2,5/3,4-(C$_5$H$_4$NR)), 67.99 (s, α-THF), 69.19 (s, C$_5$H$_5$), 110.92 (s, 1-(C$_5$H$_4$NHR)), 112.07 (s, 3-C), 112.33 (s, 7-C), 112.94 (s, 5-C), 132.45 (s, 6-C), 133.38 (s, 4-C), 162.11 (s, 1-C), 163.82 (s, 2-C) ppm. The exact amount of THF in the sample should be determined for every batch individually (typically n = 0.4 to 1.0 equivalents). The data presented here was obtained for a sample containing n = 0.4 equiv. of THF per formula unit. UV-vis (THF): $\lambda_{\max}$ = 410, 476, 506 (shoulder) nm. Anal. calc. for C$_{20}$H$_{21}$FeN$_2$Na·(C$_4$H$_8$)$_{0.4}$ (397.08 g mol^{-1}): C, 65.34; H, 6.14; N, 7.06; found: C, 64.94; H, 6.16; N, 7.03.

[Na(ATI$^{\mathrm{Fc/iPr}}$)(OPPh$_3$)] (6-OPPh$_3$). OPPh$_3$ (33 mg, 0.12 mmol) was added to a solution of [Na(ATI$^{\mathrm{Fc}}$)(thf)$_{0.5}$] (49 mg, 0.12 mmol) in toluene (1 mL). The red solution was layered with hexanes (8 mL) and cooled to −30 °C. After 24 h, the precipitated red solid was isolated by filtration and dried under a stream of argon. Yield: 84 mg, 0.12 mmol, quantitative.

^{1}H NMR (200 MHz, C$_6$D$_6$/MeCN-d_3 (10 : 1)): δ = 1.24 (d, 6H, $^{3}J_{\mathrm{HH}}$ = 6.1 Hz, Me), 3.92 (sept, 1H, $^{3}J_{\mathrm{HH}}$ = 6.1 Hz, C*H*Me$_2$), 3.98 (br s, 2H, 3,4-(C$_5$H$_4$NR)), 4.18 (s, 5H, C$_5$H$_5$), 4.31 (br s, 2H, 2,5-(C$_5$H$_4$NR)), 5.88 (br dd, 1H, $^{3}J_{\mathrm{HH}}$ = 7.4 Hz, $^{3}J_{\mathrm{HH}}$ = 9.4 Hz, 5-H), 6.32 (d, 1H, $^{3}J_{\mathrm{HH}}$ = 11.5 Hz, 3-H), 6.75 (br dd, 1H, $^{3}J_{\mathrm{HH}}$ = 7.4 Hz, $^{3}J_{\mathrm{HH}}$ = 11.2 Hz, 6-H), 6.78 (br dd, 1H, $^{3}J_{\mathrm{HH}}$ = 9.4 Hz, $^{3}J_{\mathrm{HH}}$ = 11.5 Hz, 4-H), 7.01–7.05 (d, 1H, 7-H, partially covered by resonances due to OPPh$_3$), 7.05–7.15 (m, 9H, *m*/*o*-Ph, *p*-Ph), 7.57–7.64 (m, 6H, *o*/*m*-Ph) ppm. ^{13}C NMR (50 MHz, C$_6$D$_6$/MeCN-d_3 (10 : 1)): δ = 24.31 (s, CH*Me*$_2$), 48.90 (s, *C*HMe$_2$), 62.74 (s, 2,5-(C$_5$H$_4$NR)), 64.37 (s, 3,4-(C$_5$H$_4$NR)), 68.70 (s, C$_5$H$_5$), 108.92 (s, 5-C), 109.15 (s, 3-C), 110.33 (s, 7-C), 112.77 (s, 1-(C$_5$H$_4$NR)), 128.82 (d, $^{3/2}J_{\mathrm{CP}}$ = 12.2 Hz, *m*/*o*-Ph), 131.78 (s, 6-C), 132.13 (d, $^{4}J_{\mathrm{CP}}$ = 2.8 Hz, *p*-Ph), 132.19 (s, 4-C), 132.36 (d, $^{2/3}J_{\mathrm{CP}}$ = 10.1 Hz, *o*/*m*-Ph), 132.91 (d, $^{1}J_{\mathrm{CP}}$ = 114.9 Hz, *ipso*-Ph), 162.23 (s, 2-C), 163.67 (s, 1-C) ppm. Resonances for *n*-hexane (0.5 equiv.) were also detected. ^{31}P NMR (121 MHz, C$_6$D$_6$/MeCN-d_3 (10 : 1)): δ = 28.57 (s, OPPh$_3$) ppm. UV-vis (THF): $\lambda_{\max}$ = 410, 476, 508 (shoulder) nm. Anal. calc. for C$_{38}$H$_{36}$FeN$_2$NaOP·(C$_6$H$_{14}$)$_{0.5}$ (689.62 g mol^{-1}): C, 71.41; H, 6.28; N, 4.06; found: C, 71.37; H, 6.05; N, 3.82. M. p.: 105–107 °C (decomp.).

Bi(ATI$^{\mathrm{Fc/iPr}}$)Cl$_2$ (7). Na(N(SiMe$_3$)$_2$) (26.5 mg, 144 µmol) was added to a solution of H-ATI$^{\mathrm{Fc/iPr}}$ (**5**) (50 mg, 144 µmol) in THF (2 mL) to give a deep red solution. A solution of BiCl$_3$ (15.2 mg, 48 µmol) in THF (1 mL) was added. After 5 min, the suspension was filtered. A solution of BiCl$_3$ (30.4 mg, 96.2 µmol) in THF (1 mL) was added to the resulting filtrate. After 5 min, the dark suspension was filtered. After 1 h the precipitated deep red needles were isolated by filtration and washed with THF (3 × 3 mL). The needles were dried *in vacuo*. Yield: 60 mg, 96 µmol, 67%.

^{1}H-NMR (500 MHz, pyridine-d_5): δ = 1.84 (d, 6H, $^{3}J_{\mathrm{HH}}$ = 6.4 Hz, Me), 4.01 (dd, 4H, $^{4}J_{\mathrm{HH}}$ = 1.9 Hz, 3,4-(C$_5$H$_4$NR)), 4.45 (s, 10H, C$_5$H$_5$), 4.86 (dd, 4H, $^{4}J_{\mathrm{HH}}$ = 1.9 Hz, 2,5-(C$_5$H$_4$NR)), 5.46–5.54 (sept, 1H, $^{3}J_{\mathrm{HH}}$ = 6.4 Hz, C*H*Me$_2$), 6.68 (dd, 1H, $^{3}J_{\mathrm{HH}}$ = 9.2 Hz, 5-H), 6.95 (d, 1H, $^{3}J_{\mathrm{HH}}$ = 11.6 Hz, 7-H), 7.45 (dd, 1H, $^{3}J_{\mathrm{HH}}$ = 9.6 Hz, 4-H), 7.55–7.60 (m, 1H, 6-H, overlapping with resonance due to pyridine-d_5), 7.70 (d, 1H, $^{3}J_{\mathrm{HH}}$ = 11.1 Hz, 3-H) ppm. ^{13}C-NMR (126 MHz, pyridine-d_5): δ = 23.90 (s, CH*Me*$_2$), 51.97 (s, C*H*Me$_2$), 67.33 (s, 3,4-(C$_5$H$_4$NR)), 67.83 (s, 2,5-(C$_5$H$_4$NR)), 70.35 (s, C$_5$H$_5$), 103.13 (s, 1-(C$_5$H$_4$NR)), 124.26 (s, 7-C), 124.77 (s, 3-C), 126.75 (s, 5-C), 134.98 (s, 4-C), 135.53 (s, 6-C), 169.56 (s, 2-C), 169.96 (s, 1-C) ppm. UV-vis (THF): $\lambda_{\max}$ = 364, 382, 443 (shoulder) nm. Anal. calc. for C$_{20}$H$_{21}$N$_2$FeBiCl$_2$ (625.13 g mol^{-1}): C, 38.43; H, 3.39; N, 4.48; found: C, 38.69; H, 3.48; N, 4.54.

Bi(ATI$^{\mathrm{Fc/iPr}}$)$_3$ (8). Method A: BiCl$_3$ (49 mg, 155 µmol) was added to a solution of **6-thf** (187 mg, 463 µmol (the sample of **6-thf** contained 0.5 equiv. THF)) in THF (3.0 mL). After 30 min, all volatiles were removed under reduced pressure. The dark red residue was extracted with toluene (4 × 1.0 mL). The combined toluene phases were filtered. All volatiles were removed from the filtrate under reduced pressure to give a dark red solid, which was washed with hexanes (3 × 3 mL) and dried *in vacuo*. Yield (given for **8**·(C$_7$H$_8$)$_{1.5}$ (*vide infra*)): 184 mg, 133 µmol, 86%.

Method B: NaHMDS (42 mg, 229 µmol) was added to a solution of H-ATI$^{\mathrm{Fc/iPr}}$ (**5**) (79 mg, 228 µmol) in THF (2 mL). BiCl$_3$ (24 mg, 76 µmol) was added after 5 min. All volatiles were removed from the reaction mixture under reduced pressure after 30 min. The residue was extracted with toluene (3 × 1 mL). The combined toluene phases were filtered. All volatiles were removed from the filtrate under reduced pressure. The dark red residue was recrystallised from THF/hexanes at −30 °C to give dark red crystals, which were isolated by filtration and dried *in vacuo*. Yield (given for of **8**·(thf)$_4$ (*vide infra*)): 53 mg, 35 µmol, 46%.

Samples of **8** contained lattice-bound solvent molecules, which could not be removed under reduced pressure. The exact amount of toluene (Method A) or THF (Method B) should individually be determined for every batch (typically 1.5–4.0 equiv. per formula unit).

^{1}H NMR (400 MHz, C$_7$D$_8$, 353 K): δ = 1.10 (br d, 18H, $^{3}J_{\mathrm{HH}}$ = 6.2 Hz, Me), 3.88 (br s, 6H, 2,5/3,4-(C$_5$H$_4$NR)), 4.16 (br s, 21H, 3,4/2,5-(C$_5$H$_4$NR); C$_5$H$_5$ (overlapping)), 4.43 (br sept, 3H, $^{3}J_{\mathrm{HH}}$ = 6.2 Hz, C*H*Me$_2$), 6.15 (br dd, 3H, $^{3}J_{\mathrm{HH}}$ = 9.4 Hz, $^{3}J_{\mathrm{HH}}$ = 8.5 Hz, 5-H), 6.45 (d, 3H, $^{3}J_{\mathrm{HH}}$ = 11.7 Hz, 3-H), 6.88 (ddd, 3H, $^{3}J_{\mathrm{HH}}$ = 11.7 Hz, $^{3}J_{\mathrm{HH}}$ = 8.5 Hz, $^{4}J_{\mathrm{HH}}$ = 1.4 Hz, 4-H), 7.09 (br dd, 3H, $^{3}J_{\mathrm{HH}}$ = 11.2 Hz, $^{3}J_{\mathrm{HH}}$ = 9.4, 6-H, partially overlapping with

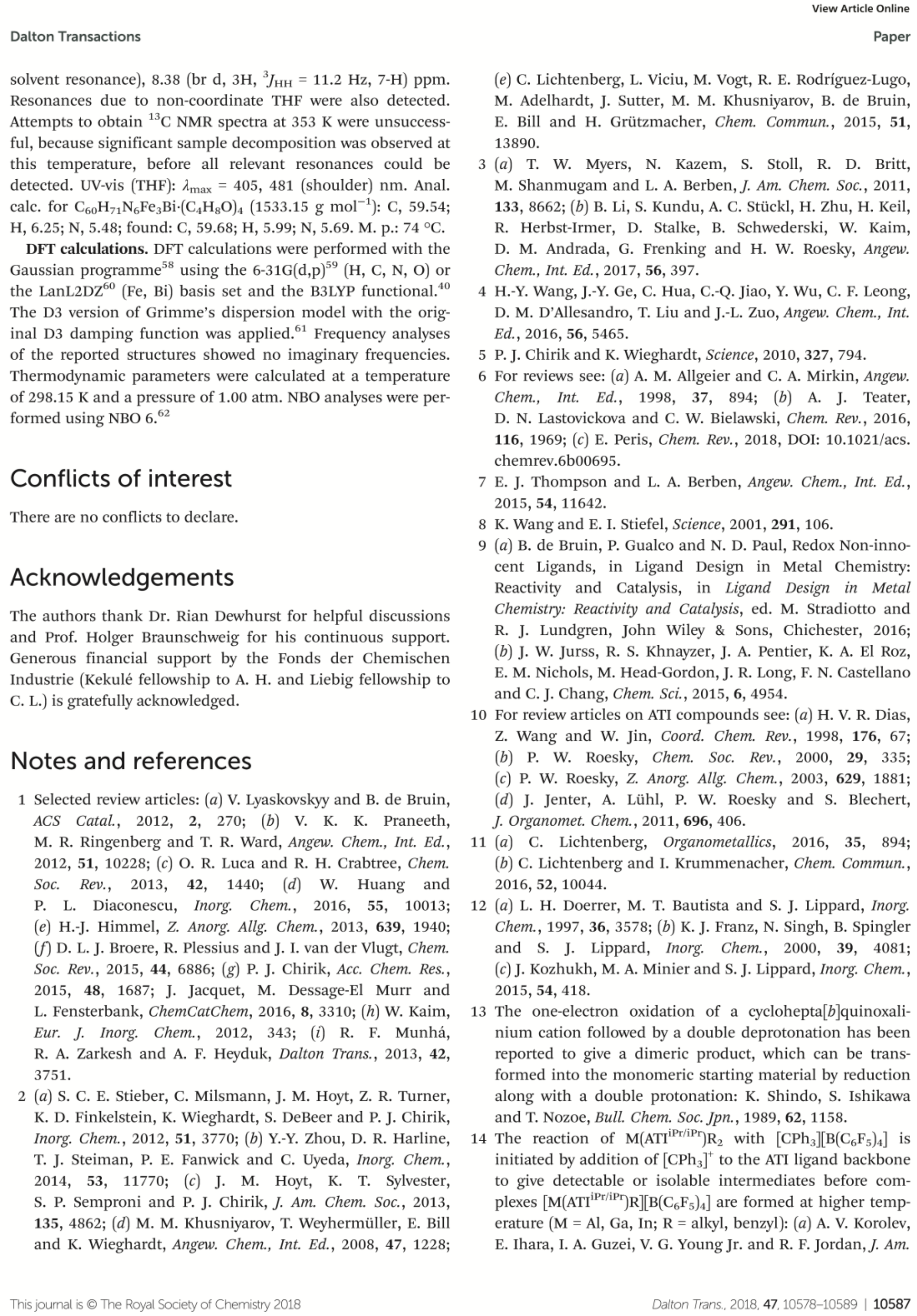

solvent resonance), 8.38 (br d, 3H, $^{3}J_{\mathrm{HH}}$ = 11.2 Hz, 7-H) ppm. Resonances due to non-coordinate THF were also detected. Attempts to obtain ^{13}C NMR spectra at 353 K were unsuccessful, because significant sample decomposition was observed at this temperature, before all relevant resonances could be detected. UV-vis (THF): $\lambda_{\max}$ = 405, 481 (shoulder) nm. Anal. calc. for $C_{60}H_{71}N_6Fe_3Bi\cdot(C_4H_8O)_4$ (1533.15 g mol^{-1}): C, 59.54; H, 6.25; N, 5.48; found: C, 59.68; H, 5.99; N, 5.69. M. p.: 74 °C.

DFT calculations. DFT calculations were performed with the Gaussian programme[58] using the 6-31G(d,p)[59] (H, C, N, O) or the LanL2DZ[60] (Fe, Bi) basis set and the B3LYP functional.[40] The D3 version of Grimme's dispersion model with the original D3 damping function was applied.[61] Frequency analyses of the reported structures showed no imaginary frequencies. Thermodynamic parameters were calculated at a temperature of 298.15 K and a pressure of 1.00 atm. NBO analyses were performed using NBO 6.[62]

Conflicts of interest

There are no conflicts to declare.

Acknowledgements

The authors thank Dr. Rian Dewhurst for helpful discussions and Prof. Holger Braunschweig for his continuous support. Generous financial support by the Fonds der Chemischen Industrie (Kekulé fellowship to A. H. and Liebig fellowship to C. L.) is gratefully acknowledged.

Notes and references

1 Selected review articles: (*a*) V. Lyaskovskyy and B. de Bruin, *ACS Catal.*, 2012, **2**, 270; (*b*) V. K. K. Praneeth, M. R. Ringenberg and T. R. Ward, *Angew. Chem., Int. Ed.*, 2012, **51**, 10228; (*c*) O. R. Luca and R. H. Crabtree, *Chem. Soc. Rev.*, 2013, **42**, 1440; (*d*) W. Huang and P. L. Diaconescu, *Inorg. Chem.*, 2016, **55**, 10013; (*e*) H.-J. Himmel, *Z. Anorg. Allg. Chem.*, 2013, **639**, 1940; (*f*) D. L. J. Broere, R. Plessius and J. I. van der Vlugt, *Chem. Soc. Rev.*, 2015, **44**, 6886; (*g*) P. J. Chirik, *Acc. Chem. Res.*, 2015, **48**, 1687; J. Jacquet, M. Dessage-El Murr and L. Fensterbank, *ChemCatChem*, 2016, **8**, 3310; (*h*) W. Kaim, *Eur. J. Inorg. Chem.*, 2012, 343; (*i*) R. F. Munhá, R. A. Zarkesh and A. F. Heyduk, *Dalton Trans.*, 2013, **42**, 3751.

2 (*a*) S. C. E. Stieber, C. Milsmann, J. M. Hoyt, Z. R. Turner, K. D. Finkelstein, K. Wieghardt, S. DeBeer and P. J. Chirik, *Inorg. Chem.*, 2012, **51**, 3770; (*b*) Y.-Y. Zhou, D. R. Harline, T. J. Steiman, P. E. Fanwick and C. Uyeda, *Inorg. Chem.*, 2014, **53**, 11770; (*c*) J. M. Hoyt, K. T. Sylvester, S. P. Semproni and P. J. Chirik, *J. Am. Chem. Soc.*, 2013, **135**, 4862; (*d*) M. M. Khusniyarov, T. Weyhermüller, E. Bill and K. Wieghardt, *Angew. Chem., Int. Ed.*, 2008, **47**, 1228; (*e*) C. Lichtenberg, L. Viciu, M. Vogt, R. E. Rodríguez-Lugo, M. Adelhardt, J. Sutter, M. M. Khusniyarov, B. de Bruin, E. Bill and H. Grützmacher, *Chem. Commun.*, 2015, **51**, 13890.

3 (*a*) T. W. Myers, N. Kazem, S. Stoll, R. D. Britt, M. Shanmugam and L. A. Berben, *J. Am. Chem. Soc.*, 2011, **133**, 8662; (*b*) B. Li, S. Kundu, A. C. Stückl, H. Zhu, H. Keil, R. Herbst-Irmer, D. Stalke, B. Schwederski, W. Kaim, D. M. Andrada, G. Frenking and H. W. Roesky, *Angew. Chem., Int. Ed.*, 2017, **56**, 397.

4 H.-Y. Wang, J.-Y. Ge, C. Hua, C.-Q. Jiao, Y. Wu, C. F. Leong, D. M. D'Allesandro, T. Liu and J.-L. Zuo, *Angew. Chem., Int. Ed.*, 2016, **56**, 5465.

5 P. J. Chirik and K. Wieghardt, *Science*, 2010, **327**, 794.

6 For reviews see: (*a*) A. M. Allgeier and C. A. Mirkin, *Angew. Chem., Int. Ed.*, 1998, **37**, 894; (*b*) A. J. Teater, D. N. Lastovickova and C. W. Bielawski, *Chem. Rev.*, 2016, **116**, 1969; (*c*) E. Peris, *Chem. Rev.*, 2018, DOI: 10.1021/acs.chemrev.6b00695.

7 E. J. Thompson and L. A. Berben, *Angew. Chem., Int. Ed.*, 2015, **54**, 11642.

8 K. Wang and E. I. Stiefel, *Science*, 2001, **291**, 106.

9 (*a*) B. de Bruin, P. Gualco and N. D. Paul, Redox Non-innocent Ligands, in Ligand Design in Metal Chemistry: Reactivity and Catalysis, in *Ligand Design in Metal Chemistry: Reactivity and Catalysis*, ed. M. Stradiotto and R. J. Lundgren, John Wiley & Sons, Chichester, 2016; (*b*) J. W. Jurss, R. S. Khnayzer, J. A. Pentier, K. A. El Roz, E. M. Nichols, M. Head-Gordon, J. R. Long, F. N. Castellano and C. J. Chang, *Chem. Sci.*, 2015, **6**, 4954.

10 For review articles on ATI compounds see: (*a*) H. V. R. Dias, Z. Wang and W. Jin, *Coord. Chem. Rev.*, 1998, **176**, 67; (*b*) P. W. Roesky, *Chem. Soc. Rev.*, 2000, **29**, 335; (*c*) P. W. Roesky, *Z. Anorg. Allg. Chem.*, 2003, **629**, 1881; (*d*) J. Jenter, A. Lühl, P. W. Roesky and S. Blechert, *J. Organomet. Chem.*, 2011, **696**, 406.

11 (*a*) C. Lichtenberg, *Organometallics*, 2016, **35**, 894; (*b*) C. Lichtenberg and I. Krummenacher, *Chem. Commun.*, 2016, **52**, 10044.

12 (*a*) L. H. Doerrer, M. T. Bautista and S. J. Lippard, *Inorg. Chem.*, 1997, **36**, 3578; (*b*) K. J. Franz, N. Singh, B. Spingler and S. J. Lippard, *Inorg. Chem.*, 2000, **39**, 4081; (*c*) J. Kozhukh, M. A. Minier and S. J. Lippard, *Inorg. Chem.*, 2015, **54**, 418.

13 The one-electron oxidation of a cyclohepta[*b*]quinoxalinium cation followed by a double deprotonation has been reported to give a dimeric product, which can be transformed into the monomeric starting material by reduction along with a double protonation: K. Shindo, S. Ishikawa and T. Nozoe, *Bull. Chem. Soc. Jpn.*, 1989, **62**, 1158.

14 The reaction of M(ATI$^{\mathrm{iPr/iPr}}$)R$_2$ with [CPh$_3$][B(C$_6$F$_5$)$_4$] is initiated by addition of [CPh$_3$]$^+$ to the ATI ligand backbone to give detectable or isolable intermediates before complexes [M(ATI$^{\mathrm{iPr/iPr}}$)R][B(C$_6$F$_5$)$_4$] are formed at higher temperature (M = Al, Ga, In; R = alkyl, benzyl): (*a*) A. V. Korolev, E. Ihara, I. A. Guzei, V. G. Young Jr. and R. F. Jordan, *J. Am.*

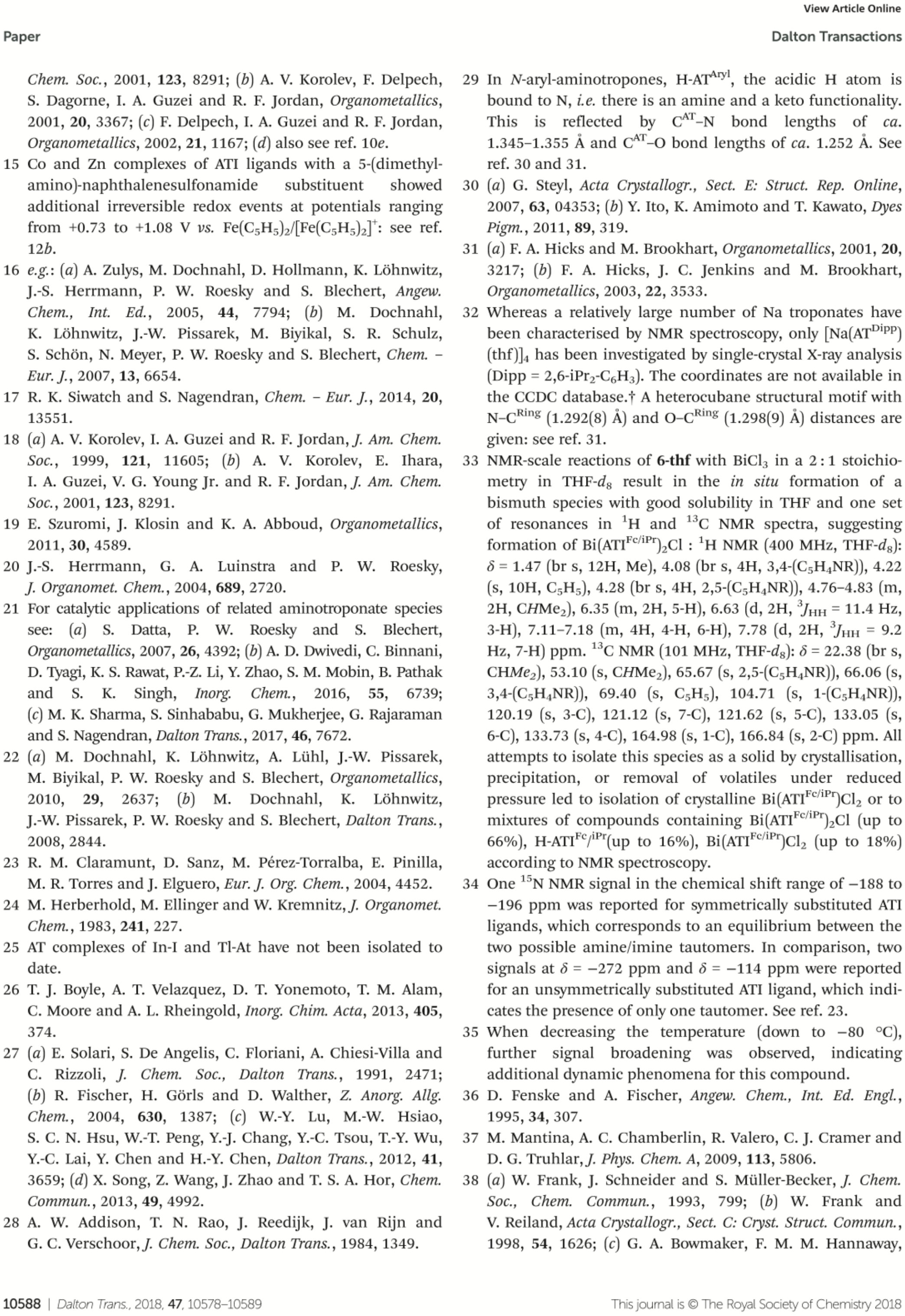

Chem. Soc., 2001, **123**, 8291; (*b*) A. V. Korolev, F. Delpech, S. Dagorne, I. A. Guzei and R. F. Jordan, *Organometallics*, 2001, **20**, 3367; (*c*) F. Delpech, I. A. Guzei and R. F. Jordan, *Organometallics*, 2002, **21**, 1167; (*d*) also see ref. 10*e*.

15 Co and Zn complexes of ATI ligands with a 5-(dimethylamino)-naphthalenesulfonamide substituent showed additional irreversible redox events at potentials ranging from +0.73 to +1.08 V *vs.* $Fe(C_5H_5)_2/[Fe(C_5H_5)_2]^+$: see ref. 12*b*.

16 *e.g.*: (*a*) A. Zulys, M. Dochnahl, D. Hollmann, K. Löhnwitz, J.-S. Herrmann, P. W. Roesky and S. Blechert, *Angew. Chem., Int. Ed.*, 2005, **44**, 7794; (*b*) M. Dochnahl, K. Löhnwitz, J.-W. Pissarek, M. Biyikal, S. R. Schulz, S. Schön, N. Meyer, P. W. Roesky and S. Blechert, *Chem. – Eur. J.*, 2007, **13**, 6654.

17 R. K. Siwatch and S. Nagendran, *Chem. – Eur. J.*, 2014, **20**, 13551.

18 (*a*) A. V. Korolev, I. A. Guzei and R. F. Jordan, *J. Am. Chem. Soc.*, 1999, **121**, 11605; (*b*) A. V. Korolev, E. Ihara, I. A. Guzei, V. G. Young Jr. and R. F. Jordan, *J. Am. Chem. Soc.*, 2001, **123**, 8291.

19 E. Szuromi, J. Klosin and K. A. Abboud, *Organometallics*, 2011, **30**, 4589.

20 J.-S. Herrmann, G. A. Luinstra and P. W. Roesky, *J. Organomet. Chem.*, 2004, **689**, 2720.

21 For catalytic applications of related aminotroponate species see: (*a*) S. Datta, P. W. Roesky and S. Blechert, *Organometallics*, 2007, **26**, 4392; (*b*) A. D. Dwivedi, C. Binnani, D. Tyagi, K. S. Rawat, P.-Z. Li, Y. Zhao, S. M. Mobin, B. Pathak and S. K. Singh, *Inorg. Chem.*, 2016, **55**, 6739; (*c*) M. K. Sharma, S. Sinhababu, G. Mukherjee, G. Rajaraman and S. Nagendran, *Dalton Trans.*, 2017, **46**, 7672.

22 (*a*) M. Dochnahl, K. Löhnwitz, A. Lühl, J.-W. Pissarek, M. Biyikal, P. W. Roesky and S. Blechert, *Organometallics*, 2010, **29**, 2637; (*b*) M. Dochnahl, K. Löhnwitz, J.-W. Pissarek, P. W. Roesky and S. Blechert, *Dalton Trans.*, 2008, 2844.

23 R. M. Claramunt, D. Sanz, M. Pérez-Torralba, E. Pinilla, M. R. Torres and J. Elguero, *Eur. J. Org. Chem.*, 2004, 4452.

24 M. Herberhold, M. Ellinger and W. Kremnitz, *J. Organomet. Chem.*, 1983, **241**, 227.

25 AT complexes of In-I and Tl-At have not been isolated to date.

26 T. J. Boyle, A. T. Velazquez, D. T. Yonemoto, T. M. Alam, C. Moore and A. L. Rheingold, *Inorg. Chim. Acta*, 2013, **405**, 374.

27 (*a*) E. Solari, S. De Angelis, C. Floriani, A. Chiesi-Villa and C. Rizzoli, *J. Chem. Soc., Dalton Trans.*, 1991, 2471; (*b*) R. Fischer, H. Görls and D. Walther, *Z. Anorg. Allg. Chem.*, 2004, **630**, 1387; (*c*) W.-Y. Lu, M.-W. Hsiao, S. C. N. Hsu, W.-T. Peng, Y.-J. Chang, Y.-C. Tsou, T.-Y. Wu, Y.-C. Lai, Y. Chen and H.-Y. Chen, *Dalton Trans.*, 2012, **41**, 3659; (*d*) X. Song, Z. Wang, J. Zhao and T. S. A. Hor, *Chem. Commun.*, 2013, **49**, 4992.

28 A. W. Addison, T. N. Rao, J. Reedijk, J. van Rijn and G. C. Verschoor, *J. Chem. Soc., Dalton Trans.*, 1984, 1349.

29 In *N*-aryl-aminotropones, H-AT^{Aryl}, the acidic H atom is bound to N, *i.e.* there is an amine and a keto functionality. This is reflected by C^{AT}–N bond lengths of *ca.* 1.345–1.355 Å and C^{AT}–O bond lengths of *ca.* 1.252 Å. See ref. 30 and 31.

30 (*a*) G. Steyl, *Acta Crystallogr., Sect. E: Struct. Rep. Online*, 2007, **63**, 04353; (*b*) Y. Ito, K. Amimoto and T. Kawato, *Dyes Pigm.*, 2011, **89**, 319.

31 (*a*) F. A. Hicks and M. Brookhart, *Organometallics*, 2001, **20**, 3217; (*b*) F. A. Hicks, J. C. Jenkins and M. Brookhart, *Organometallics*, 2003, **22**, 3533.

32 Whereas a relatively large number of Na troponates have been characterised by NMR spectroscopy, only [Na(AT^{Dipp})(thf)]$_4$ has been investigated by single-crystal X-ray analysis (Dipp = 2,6-iPr$_2$-C$_6$H$_3$). The coordinates are not available in the CCDC database.† A heterocubane structural motif with N–C^{Ring} (1.292(8) Å) and O–C^{Ring} (1.298(9) Å) distances are given: see ref. 31.

33 NMR-scale reactions of **6-thf** with BiCl$_3$ in a 2 : 1 stoichiometry in THF-*d*$_8$ result in the *in situ* formation of a bismuth species with good solubility in THF and one set of resonances in ^{1}H and ^{13}C NMR spectra, suggesting formation of Bi(ATI$^{Fc/iPr}$)$_2$Cl : ^{1}H NMR (400 MHz, THF-*d*$_8$): δ = 1.47 (br s, 12H, Me), 4.08 (br s, 4H, 3,4-(C$_5$H$_4$NR)), 4.22 (s, 10H, C$_5$H$_5$), 4.28 (br s, 4H, 2,5-(C$_5$H$_4$NR)), 4.76–4.83 (m, 2H, C*H*Me$_2$), 6.35 (m, 2H, 5-H), 6.63 (d, 2H, $^3J_{HH}$ = 11.4 Hz, 3-H), 7.11–7.18 (m, 4H, 4-H, 6-H), 7.78 (d, 2H, $^3J_{HH}$ = 9.2 Hz, 7-H) ppm. ^{13}C NMR (101 MHz, THF-*d*$_8$): δ = 22.38 (br s, CH*Me*$_2$), 53.10 (s, C*H*Me$_2$), 65.67 (s, 2,5-(C$_5$H$_4$NR)), 66.06 (s, 3,4-(C$_5$H$_4$NR)), 69.40 (s, C$_5$H$_5$), 104.71 (s, 1-(C$_5$H$_4$NR)), 120.19 (s, 3-C), 121.12 (s, 7-C), 121.62 (s, 5-C), 133.05 (s, 6-C), 133.73 (s, 4-C), 164.98 (s, 1-C), 166.84 (s, 2-C) ppm. All attempts to isolate this species as a solid by crystallisation, precipitation, or removal of volatiles under reduced pressure led to isolation of crystalline Bi(ATI$^{Fc/iPr}$)Cl$_2$ or to mixtures of compounds containing Bi(ATI$^{Fc/iPr}$)$_2$Cl (up to 66%), H-ATI^{Fc}/^{iPr}(up to 16%), Bi(ATI$^{Fc/iPr}$)Cl$_2$ (up to 18%) according to NMR spectroscopy.

34 One ^{15}N NMR signal in the chemical shift range of −188 to −196 ppm was reported for symmetrically substituted ATI ligands, which corresponds to an equilibrium between the two possible amine/imine tautomers. In comparison, two signals at δ = −272 ppm and δ = −114 ppm were reported for an unsymmetrically substituted ATI ligand, which indicates the presence of only one tautomer. See ref. 23.

35 When decreasing the temperature (down to −80 °C), further signal broadening was observed, indicating additional dynamic phenomena for this compound.

36 D. Fenske and A. Fischer, *Angew. Chem., Int. Ed. Engl.*, 1995, **34**, 307.

37 M. Mantina, A. C. Chamberlin, R. Valero, C. J. Cramer and D. G. Truhlar, *J. Phys. Chem. A*, 2009, **113**, 5806.

38 (*a*) W. Frank, J. Schneider and S. Müller-Becker, *J. Chem. Soc., Chem. Commun.*, 1993, 799; (*b*) W. Frank and V. Reiland, *Acta Crystallogr., Sect. C: Cryst. Struct. Commun.*, 1998, **54**, 1626; (*c*) G. A. Bowmaker, F. M. M. Hannaway,

P. C. Junk, A. M. Lee, B. W. Skelton and A. H. White, *Aust. J. Chem.*, 1998, **51**, 325; (*d*) J. Heine, T. Wehner, R. Bertermann, A. Steffen and K. Müller-Buschbaum, *Inorg. Chem.*, 2014, **53**, 7197.

39 In parallel-displaced benzene dimers, the distance between the two benzene planes has been determined to be approximately 3.5 Å by quantum chemical calculations: E. G. Hohenstein and C. D. Sherrill, *J. Phys. Chem. A*, 2009, **113**, 878.

40 Pairs of strands shown in Fig. 5b are connected *via* additional arene···arene interactions (ESI†).

41 L.-C. Pop, A. Castel, L. Silaghi-Dumitrescu and N. Saffon, *Eur. J. Inorg. Chem.*, 2011, 3357.

42 C. L. Raston, B. W. Skelton, V.-A. Tolhurst and A. H. White, *J. Chem. Soc., Dalton Trans.*, 2000, 1279.

43 CVs and square wave voltammograms of **4** measured in CH_2Cl_2/0.1 m $[N(nBu)_4][PF_6]$ at 23 °C with scan rates ranging from 20–1000 mV s^{-1} did also not allow for resolution of the three redox waves for oxidation/reduction of the ferrocenyl groups. Under these conditions, a reversible redox event was detected at −0.26 V.

44 (*a*) Y. Miyake, S. Watanabe, S. Aono, T. Nishinaga, A. Miyazaki, T. Enoki, H. Miyasaka, H. Otani and M. Iyoda, *Chem. Commun.*, 2008, 6167; (*b*) T. Nishinaga, T. Aono, E. Isomura, S. Watanabe, Y. Miyake, A. Miyazaki, T. Enoki, H. Miyasaka, H. Otani and M. Iyoda, *Dalton Trans.*, 2010, **39**, 2293.

45 M. Iyoda, Private communication.

46 A trinuclear Ru troponate complex shows long range intramolecular electronic communication between the three metal centres and three well-separated redox waves in the cyclic voltammogram: J. Yoshida, K. Kuwahara, K. Suzuki and H. Yuge, *Inorg. Chem.*, 2017, **56**, 1846.

47 M. Pittracher, U. Frisch, H. Kopacka, K. Wurst, T. Müller, L. Oehninger, I. Ott, E. Wuttke, S. Scheerer, R. F. Winter and B. Bildstein, *Organometallics*, 2014, **33**, 1630.

48 E.g.: (*a*) D. M. D'Alessandro and F. R. Keene, *Chem. Rev.*, 2006, **106**, 2270; (*b*) P. Aguirre-Etcheverry and D. O'Hare, *Chem. Rev.*, 2010, **110**, 4839.

49 Z.-L. Gong, Y.-W. Zhong and J. Yao, *Chem. – Eur. J.*, 2015, **21**, 1554.

50 (*a*) D. O. Cowan, P. Shu, F. L. Hedberg, M. Rossi and T. J. Kistenmacher, *J. Am. Chem. Soc.*, 1979, **101**, 1304; (*b*) L. Kaufmann, J.-M. Breunig, H. Vitze, F. Schödel, I. Nowik, M. Pichlmaier, M. Bolte, H.-W. Lerner, R. F. Winter, R. H. Herber and M. Wagner, *Dalton Trans.*, 2009, 2940.

51 (*a*) P. Šimon, F. de Proft, R. Jambor, A. Růžička and L. Dostál, *Angew. Chem., Int. Ed.*, 2010, **49**, 5468; (*b*) M. Alonso, R. Lo, R. Sedlák, R. Jambor, A. Růžička, F. De Proft, P. Hobza and L. Dostál, *Chem. – Eur. J.*, 2016, **21**, 16917.

52 (*a*) S. Ishida, F. Hirakawa, K. Furukawa, K. Yoza and T. Iwamoto, *Angew. Chem., Int. Ed.*, 2014, **53**, 11172; (*b*) R. J. Schwamm, J. R. Harmer, M. Lein, C. M. Fitchett, S. Granville and M. P. Coles, *Angew. Chem., Int. Ed.*, 2015, **54**, 10630.

53 C. Lichtenberg, *Angew. Chem., Int. Ed.*, 2016, **55**, 484.

54 M. Sakagami, T. Sasamori, H. Sakai, Y. Furukawa and N. Tokitoh, *Chem. – Asian J.*, 2013, **8**, 690.

55 The areas under the curves for redox events at −2.01 V and −2.65 V show a ratio of *ca.* 1 : 2 in differential pulse and square wave voltammograms.

56 In specific, an irreversible reduction and a partially reversible redox event were detected at −1.08 V and −1.31 V by cyclic voltammetry (ESI†). Differential pulse voltammetry (DPV) revealed that the broadened feature detected by cyclic voltammetry at −1.31 V (E_{pc} from CV) corresponds to two distinct processes at −1.11 and −1.33 V (peak potentials from DPV run in reductive scan direction).

57 Elemental analysis of this compound gave no satisfactory results, which was ascribed to its sensitivity. The sensitivity of the related species $As(AT^{iPr})Cl_2$ has been mentioned explicitly and no elemental analysis was reported for this compound (ref. 41).

58 *Gaussian 16*; for full reference see ESI.†

59 P. C. Hariharan and J. A. Pople, *Theor. Chim. Acta*, 1973, **28**, 213.

60 (*a*) T. H. Dunning Jr. and P. J. Hay, in *Modern Theoretical Chemistry*, ed. H. F. Schaefer III, Plenum, New York, 1977, vol. 3, pp. 1–28; (*b*) P. J. Hay and W. R. Wadt, *J. Chem. Phys.*, 1985, **82**, 270; (*c*) P. J. Hay and W. R. Wadt, *J. Chem. Phys.*, 1985, **82**, 299.

61 S. Grimme, J. Antony, S. Ehrlich and H. Krieg, *J. Chem. Phys.*, 2010, **132**, 154104.

62 E. D. Glendening, C. R. Landis and F. Weinhold, *J. Comput. Chem.*, 2013, **34**, 1429.

V Sodium Aminotroponiminates: Ligand-Induced Disproportionation, Mixed-Metal Compounds, and Exceptional Activity in Polymerization Catalysis

Anna Hanft, Malte Jürgensen, Rüdiger Bertermann, Crispin Lichtenberg

Vervielfältigt aus Referenz:

ChemCatChem **2018**, *10,* 4018-4027.[63]

DOI: 10.1002/cctc.201800580

mit der Erlaubnis von John Wiley and Sons.

ChemPubSoc Europe
DOI: 10.1002/cctc.201800580
CHEMCATCHEM
Full Papers

Sodium Aminotroponiminates: Ligand-Induced Disproportionation, Mixed-Metal Compounds, and Exceptional Activity in Polymerization Catalysis

Anna Hanft,[a] Malte Jürgensen,[a] Rüdiger Bertermann,[a] and Crispin Lichtenberg*[a]

Sodium complexes of aminotroponiminate (ATI) ligands have been reacted with a range of neutral donor ligands. Upon addition of crown ethers, they undergo an unusual ligand-induced disproportionation reaction with formation of $[Na(ATI)_2]^-$ sodiate complex anions. The same structural motif has also been found in the first well-defined mixed-metal ATI complexes, which have been accessed starting from monometallic sodium and potassium species. The mixed-metal compounds confirm the possibility of ATIs to act as ditopic ligands. Using the polymerization of ε-caprolactone as a model system, structure-reactivity-relationships in sodium and mixed-metal ATI compounds have been studied by comparing the reactivity of [Na(ATI)] and $[Na(ATI)_2]^-$ structural motifs. These studies revealed trends in the catalyst activity depending on the nuclearity of the complex and the substitution pattern at the ATI ligand. Exceptionally high activities were obtained for dinuclear sodium sodiates of type $[Na(crown)_2][Na(ATI)_2]$, making them the most active alkali metal initiators for this reaction. The organometallic and polymeric compounds presented in this work have been characterized by techniques including (VT-)NMR spectroscopy, single-crystal X-ray diffraction, gel permeation chromatography, mass spectrometry, and DFT calculations.

Introduction

The reactivity of alkali metal complexes can be controlled by the use of neutral ligands that differ in parameters such as polarity, denticity, or bite angle. This has been studied extensively for lithium alkyl compounds, showing that the degree of aggregation plays a crucial role in determining their nucleophilicity and basicity.[1] For the heavier congener sodium, the art of tuning the reactivity of its metal complexes by external parameters is much less developed. In a range of case studies, however, it has been demonstrated that factors such as reaction temperature, choice of solvent, or the use of a combination of two different sodium reagents can lead to different chemo-, regio-, and stereoselectivities or catalyst activities.[2] Examples include the dehydrodehalogenation of haloalkanes,[3] the metalation of alkylated pyridine derivatives,[4] the Haller-Bauer reaction,[5] and the polymerization of olefins with so-called Alfin catalysts.[6] These valuable contributions clearly showcase the potential to realize an effective control of the reactivity of sodium amides, but remain largely descriptive, i.e. differences in reactivity have oftentimes not been rationalized on the molecular level.

The reactivity of alkali metal complexes can further be modified by accessing mixed-metal compounds, which contain two or more different types of metal atoms.[7] Mixed-metal compounds containing sodium are mostly limited to cases in which Na is combined with a more electronegative element such as Mg, Mn, Fe, or Zn.[8,9]

Recently, we turned our attention towards the chemistry of aminotroponiminate (ATI) complexes (Scheme 1),[10] which represent a valuable ligand platform for catalytic applications such as the hydroamination of olefins,[11] the cyanosilylation of aldehydes,[12] the (co-)polymerization of methylmetacrylate or cyclohexene oxide/CO_2,[13] as well as electron transfer catalysis.[14] In order to contribute to the understanding of the role of the ATI ligand in such transformations, its coordination chemistry has been investigated in some detail. In particular, it has been demonstrated that ATIs can interact with metal centers and potential substrates not only via their *N,N* binding pocket,[15] but also via the cyclic-conjugated π-electron system of their C_7 ligand backbone (Scheme 1). Interactions of the ATI ligand backbone have recently been reported with a late transition metal cation,[16] an alkali metal cation,[15c,17] or with an arene moiety[18] as the second binding partner. A profound

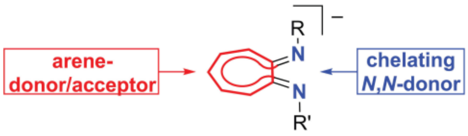

Scheme 1. Aminotroponiminate (ATI) as a ditopic ligand.

---

[a] A. Hanft, M. Jürgensen, Dr. R. Bertermann, Dr. C. Lichtenberg
Department of Inorganic Chemistry
Julius-Maximilians-Universität Würzburg
Am Hubland, 97074 Würzburg, Germany
E-mail: crispin.lichtenberg@uni-wuerzburg.de

Supporting information for this article is available on the WWW under https://doi.org/10.1002/cctc.201800580

This publication is part of the Young Researchers Series. More information regarding these excellent researchers can be found on the ChemCatChem homepage.

understanding of the coordination chemistry of this ligand set will be crucial for rationalizing its reactivity and modes of action in catalysis. Thus, we set out to investigate the influence of neutral donor ligands and the effect of heterobimetallic compounds on the coordination chemistry and reactivity of alkali metal ATIs.

Here we report on sodium ATI complexes, which show an unusual ligand-induced disproportionation and form unprecedented mixed-metal ATIs when combined with potassium derivatives. The effects of these coordination chemistry phenomena on their catalytic performance was investigated using the polymerization of ε-caprolactone as a model system.

Results and Discussion

Synthesis and Characterization

The literature-known and new sodium and potassium ATI complexes [M(ATI$^{R/iPr}$)L$_n$] were synthesized according to the protocols shown in Table 1 (M = Na, K; R = Ph, *i*Pr). NMR spectroscopic analysis indicated electron delocalization between the amide and imine functionalities.[19]

Table 1. Synthesis of known and new alkali metal ATIs.

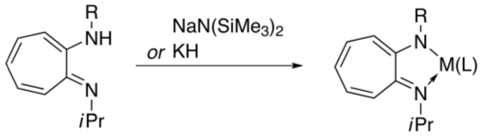

Compound	M	R	L	Reference
1-thf	Na	Ph	thf	17
2-thf	K	Ph	thf	17
3	Na	*i*Pr	none	this work
4	K	*i*Pr	none	20/this work

Compound **3** crystallized from THF/hexanes in the monoclinic space group $P2_1/n$ with $Z = 4$ as the thf-adduct **3-thf** (Figure 1). It shows a μ_2-(M-κ^2N)(M′-κ^5C) coordination mode, as recently reported for its analog **1-thf**. The distorted tetrahedral coordination geometry around Na (angles around Na, 68–136°) as well as the Na1–N1/2 (2.36 Å), Na1–C(3–7) (2.93–3.27 Å), and Na1–O1 (2.34 Å) distances in **3-thf** are similar to those in **1-thf**. The ditopic nature of the ATI ligand in **3-thf** results in formation of a coordination polymer with a twofold screw axis 2_1 along the crystallographic *b*-axis (Figure 1b).

In view of the experimentally observed Na–ATI^{backbone} interactions, K–ATI^{backbone} bonding seems even more likely, because potassium generally shows a higher tendency than sodium to interact with soft arene donors. Somewhat unexpectedly, the potassium complex [K(ATI$^{Ph/iPr}$)(thf)] (**2-thf**) has been reported to form a coordination polymer in the solid state without such K–ATI^{backbone} interactions. However, the thf ligands of this compound can be removed *in vacuo*, suggesting a saturation of the coordination sphere of potassium by arene moieties in thf-free **2**.[17] We subjected the literature-known compound [K(ATI$^{iPr/iPr}$)] (**4**) to single-crystal X-ray diffraction analysis (monoclinic space group $P2_1/c$ with $Z = 4$). Indeed, a previously mentioned μ_2-(M-κ^2N)(M′-κ^7C) coordination mode could be confirmed for the thf-adduct **4-thf** (Figure 2).[21] The potassium ion is found in a strongly distorted tetrahedral coordination geometry (angles around K: 59–150°). The terminal K–N and K–O bonds in **4-thf** (K–N, 2.70–2.71 Å; K–O, 2.64 Å) are significantly shorter than those in hexacoordinate **2-thf** with its bridging nitrogen and oxygen atoms (K–N, 2.79–2.97 Å; K–O, 2.85–2.86 Å).[17] The K–C(1–7) distances range from 3.16 to 3.53 Å indicating significant K–C(π) bonding.[22] **4-thf** forms a coordination polymer in the solid state, which extends with a screw axis 2_1 along the crystallographic *a*-axis.

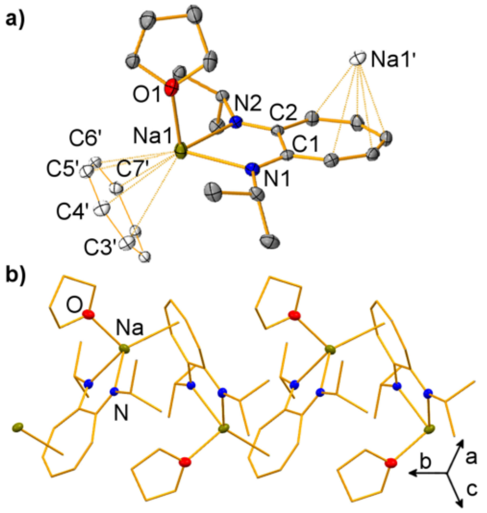

Figure 1. a) Cut-out of solid state structure of coordination polymer [Na(ATI$^{iPr/iPr}$)(thf)]$_\infty$ (**3-thf**)$_\infty$. Displacement ellipsoids are shown at the 50% probability level. Hydrogen atoms are omitted for clarity; ct represents the centroid of C(3–7). Atoms exceeding one asymmetric unit are shown as white ellipsoids. b) Representation showing the arrangement of (**3-thf**)$_\infty$ as a one-dimensional coordination polymer. Selected bond lengths (Å) and angles (°) for: Na1–N1, 2.3592(15); Na1–N2, 2.3598(14); Na1–O1, 2.3387(14); Na1–C3′, 3.2720(17); Na1–C4′, 3.0554(19); Na1–C5′, 2.9279(18); Na1–C6′, 2.9575(18); Na1–C7′, 3.2369(16); N1–C1, 1.307(2); N2–C2, 1.305(2); N1–Na1–N2, 67.70(5); N1–Na1–O1, 98.03(5); N2–Na1–O1, 97.11(5); O1–Na1–ct, 114.75(5); N1–Na1–ct, 135.83(5); N2–Na1–ct, 131.18(5).

Addition of Neutral Ligands to Na ATIs

The sodium complexes **1-thf** and **3-thf** form polymeric structures in the solid state via Na–C(π) bonding. In order to evaluate the persistency of Na–C(π) interactions in these compounds, the effect of neutral donor ligands on their coordination chemistry was studied. Remarkably, **1-thf** crystallized as the known coordination polymer (**1-thf**)$_\infty$ even in the presence of one equivalent of tmeda as a chelating ligand

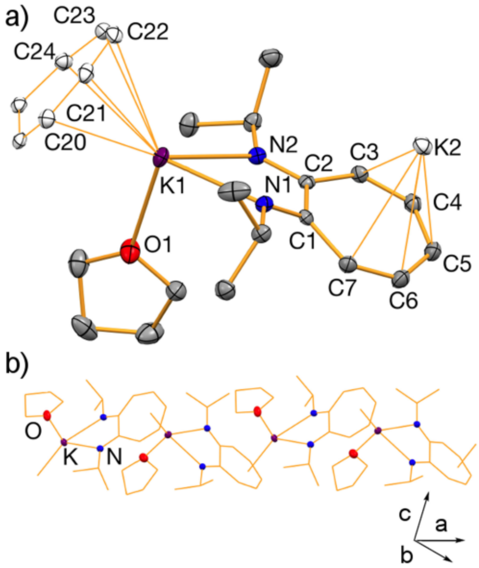

Figure 2. a) Cut-out of solid state structure of coordination polymer $[K(ATI^{iPr/iPr})(thf)]_\infty$ (**4-thf**)$_\infty$. Displacement ellipsoids are shown at the 50 % probability level. Hydrogen atoms are omitted for clarity; ct represents the centroid of C(1–7). Atoms exceeding one formula unit are shown as white ellipsoids. Only one of two chemically equivalent but crystallographically distinct formula units is depicted. b) Representation showing the arrangement of (**4-thf**)$_\infty$ as a one-dimensional coordination polymer in the solid state. Selected bond lengths (Å) and angles (°): K1–N1 2.7134(15); K1–N2 2.6978(16); K1–O1, 2.6433(15); K1–C18, 3.5285(18); K1–C19, 3.2680(17); K1–C20, 3.2103(18); K1–C21, 3.2043(18); K1–C22, 3.1710(19); K1–C23, 3.1620(18); K1–C24, 3.2787(18); K1–ct, 2.8260(19); C1–N1, 1.307(2); C2–N2, 1.309(2); N1–K1–N2, 58.97(4); N1–K1–O1, 94.27(5); N2–K1–O1, 85.22(5); N1–K1–ct, 149.82(5); N2–K1–ct, 135.12(5); O1–K1–ct, 111.85(5).

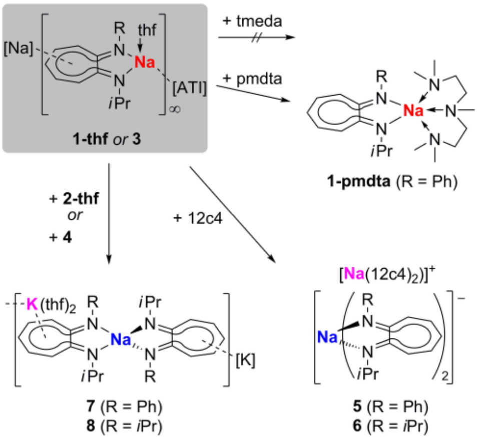

Scheme 2. Effect of multidentate neutral donor ligands on coordination chemistry of sodium ATIs and synthesis of mixed-metal-ATIs; R = Ph, ^{i}Pr; tmeda = tetramethyl-ethylene-diamine; pmdta = pentamethyl-diethylene-triamine; 12c4 = 12-crown-4.

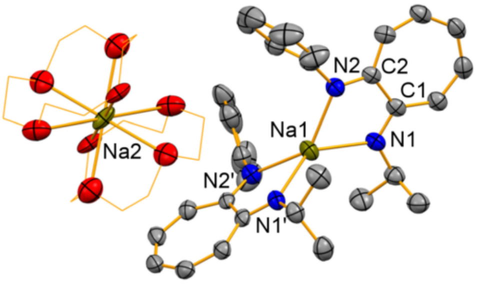

Figure 3. Molecular structure of $[Na(12c4)_2][Na(ATI^{Ph/iPr})_2)]$ (**5**) in the solid state. Displacement ellipsoids are shown at the 50 % probability level. Hydrogen atoms and split positions of disordered 12c4 ligands are omitted for clarity; carbon atoms of 12c4 ligands are drawn as wire frame. Selected bond lengths (Å) and angles (°): Na1–N1, 2.317(3); Na1–N2, 2.313(3); C1–N1, 1.319(5); C2–N2, 1.314(5); N1–Na1–N2, 68.60(11); N1–Na1–N1′, 134.26(19); N1–Na1–N2′, 130.69(11); N2–Na1–N2′, 136.7(2); plane(N1C1C2N2)–plane (N1′C1′C2′N2′), 86.13.

(Scheme 2; tmeda = tetramethyl-ethylene-diamine). Reaction of **1-thf** with the neutral tridentate ligand pmdta gave the expected molecular complex **1-pmdta** (Scheme 2, pmdta = pentamethyl-diethylene-triamine). This compound was fully characterized, showing the expected signal patterns in its ^{1}H and ^{13}C NMR spectra and unexceptional bonding parameters as determined by single-crystal X-ray analysis (Supp. Inf.). In ^{1}H^{1}H-NOESY NMR experiments, cross signals are observed between protons bound to the ATI ligand and protons bound to the pmdta ligand. This indicates close interactions of the anionic *and* the neutral ligand with the Na center in solution, suggesting that the molecular structure of **1-pmdta** in the solid state is maintained in solution.

Surprisingly, reactions of the sodium ATIs with crown ethers 12c4 or 15c5 did not give simple adducts of type [Na(ATI)(crown)], but led to sodium sodiate compounds of type $[Na(crown)_2][Na(ATI)_2]$ in ligand induced disproportionations (Scheme 2). The connectivity of compounds $[Na(12c4)_2][Na(ATI^{Ph/iPr})_2]$ (**5**) and $[Na(12c4)_2][Na(ATI^{iPr/iPr})_2]$ (**6**) was unambiguously determined by single-crystal X-ray diffraction analysis (data for compound **6** was not sufficient for a discussion of bond lengths and angles (see Supp. Inf.)). Compound **5** crystallized in the monoclinic space group *C2/c* with $Z = 4$ (Figure 3). The sodium atom Na2 of the complex cation is coordinated by two 12c4 ligands excluding any direct bonding interactions with the ATI ligands. The sodium atom Na1 of the sodiate complex anion is coordinated by two κ^{2}N-ATI ligands. This results in a distorted tetrahedral coordination geometry around Na1, the distortion being due to the small bite angle of the ATI ligand (N–Na–N, 69–137°). The Na1–N1/2 bond lengths of 2.31–2.32 Å are slightly shorter than those in the parent compound (**1-thf**)$_\infty$ (Na–N, 2.36 Å), in which each ATI ligand interacts with two Na atoms.

In THF solution, the ATI ligands of $[Na(12c4)_2][Na(ATI^{Ph/iPr})_2]$ (**5**) and $[Na(12c4)_2][Na(ATI^{iPr/iPr})_2]$ (**6**) show one set of resonances in ^1H and ^{13}C NMR spectra, respectively. No cross signals between protons of the crown ether and the ATI ligands were detected in $^1H^1H$-NOESY NMR spectra. This suggests that the solid-state structure of "solvent-separated" ion pairs **5** and **6** is essentially maintained in solution. This was corroborated by a ^1H-DOSY NMR experiment with **6**, which showed two sets of signals in the diffusion dimension, one for the crown ether and one for the ATI ligand. These were ascribed to $[Na(12c4)_2]^+$ and $[Na(ATI^{iPr/iPr})_2]^-$, respectively. Using an external calibration curve, the experimentally determined diffusion constants were translated into molecular weights, which are in good agreement with those of the suggested species (for details see Supp. Inf.).[23] DFT calculations on sodium compounds based on the $(ATI^{Ph/iPr})^-$ ligand with a THF solvent model further support this interpretation (Scheme 3). The ligand substitution reaction shown in Eq. [1] leads to the adduct, which was not observed experimentally, and is endothermic ($\Delta H^{rel} = +6.7$ kcal mol^{-1}) and only slightly exergonic ($\Delta G^{rel} = -0.5$ kcal mol^{-1}). The reaction shown in Eq. [2] (ligand substitution followed by disproportionation) leads to the experimentally observed product **6** and was calculated to be clearly exothermic and exergonic ($\Delta H^{rel} = -24.6$ kcal mol^{-1}; $\Delta G^{rel} = -28.3$ kcal mol^{-1}).

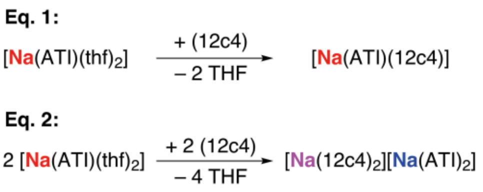

Scheme 3. Thermodynamic parameters determined by DFT calculations [kcal mol^{-1}]: Eq. [1]: ΔH^{rel}: +6.7; ΔG^{rel}: −0.5. Eq. [2]: ΔH^{rel}: −24.6; ΔG^{rel}: −28.3.

Ligand-induced disproportionations as observed for compounds **1-thf** and **3** have only rarely been reported for other sodium complexes.[24] The solid-state structure of $[Na(15c5)][Na(C_5H_5)_2]$ has been described in a private communication.[25] Sodium carbazolide forms an adduct with 15-crown-5, but a mixture of ion pairs, $[Na(crypt)][Na(NC_{12}H_8)_2(thf)_2]$ and $[Na(crypt)]_2[Na(NC_{12}H_8)_3]$, is obtained in the presence of a cryptand (crypt = 2,2,1-cryptand).[26] These ion pairs could not be separated on the preparative scale and were analyzed only by single-crystal X-ray analysis, i.e. no information about the coordination chemistry in solution was reported. Other sodium compounds form ion pairs in the solid state, but their mononuclear parent compounds remain elusive to date.[27,28] Our results on the sodium ATIs demonstrate that the addition of crown ethers induces a disproportionation into ion pairs, which persist not only in the solid state but also in solution.

Mixed-metal Compounds

Based on the above findings, Na/K mixed-metal ATIs containing sodium-complex-anions should be accessible. Indeed, reaction of sodium ATIs **1-thf** or **3** with potassium ATIs **2-thf** or **4**, respectively, gave the targeted potassium sodiate compounds $[K(thf)_2][Na(ATI^{Ph/iPr})_2]$ (**7**) and $[K(thf)_2][Na(ATI^{iPr/iPr})_2]$ (**8**) (Scheme 2). Both compounds were analyzed by single-crystal X-ray diffraction. Only one of the compounds is discussed in the main text, because they show essentially the same coordination chemistry in the solid state (for details see Supp. Inf.). Compound **7** crystallized in the monoclinic space group *C*2/*c* with *Z* = 4 (Figure 4). The diffraction experiment confirms coordination of two ATI ligands to the sodium atom Na1 in a κ^2*N* coordination mode. The resulting $[Na(ATI)_2]^-$ complex anions are linked by $[K(thf)_2]^+$ complex cations via K–ATI^{backbone} interactions. Overall, this results in formation of a one-dimensional coordination polymer along the crystallographic *a*-axis (Figure 4b). Thus, compounds **7** and **8** represent the first structurally authenticated examples of heterobimetallic ATI species, in which metals of two different kinds interact with the same ATI ligand.[29] Both ATI ligands in the unit cell of **7** are crystallographically equivalent as are both THF ligands. The potassium ion K1 is found in a distorted tetrahedral coordination geometry. The K–O distances (2.62 Å) are 0.07 Å shorter

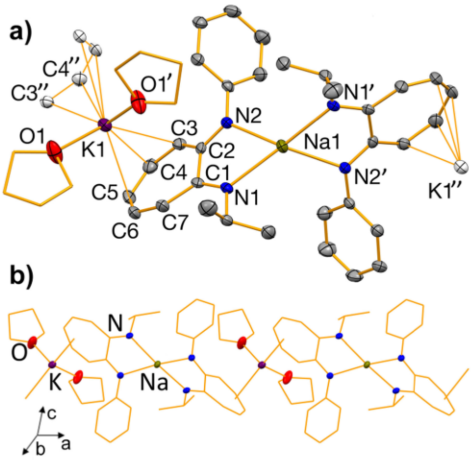

Figure 4. a) Cut-out of the solid-state structure of $[K(thf)_2][Na(ATI^{Ph/iPr})_2]_\infty$ $(\mathbf{7})_\infty$. Displacement ellipsoids are shown at the 50% probability level. Hydrogen atoms and one split position of a disordered thf molecule are omitted for clarity; ct represents the centroid of C(3–7); carbon atoms of thf ligands are drawn as wire frame. b) Representation showing the arrangement of $(\mathbf{7})_\infty$ as a one-dimensional coordination polymer in the solid state. Selected bond lengths (Å) and angles (°): K1–O1, 2.621(3); K1–C3, 3.145(4); K1–C4, 3.107(4); K1–C5, 3.167(4); K1–C6, 3.237(4); K1–C7, 3.461(4); Na1–N1, 2.397(3); Na1–N2, 2.379(3); N1–C1, 1.307(4); N2–C2, 1.314(4); O1–K1–O1′, 81.00(13); O1–K1–ct, 117.62; O1′–K1–ct′, 117.62; ct–K1–ct′, 108.11; N1–Na1–N2, 66.82(9); N1–Na1–N1′, 156.50(16); plane(N1C1C2N2)–plane(N1′C1′C2′N2′), 85.26.

than that in compound **4-thf**, which was ascribed to the presence of K–N interactions in the latter compound. The K–C distances in **7** (3.11–3.46 Å) are similar to those observed in **4-thf** (3.16–3.53 Å) and indicate significant bonding interactions.[22] The sodium atom Na1 in the complex anion adopts a strongly distorted tetrahedral coordination geometry (N–Na–N, 67–157°). The Na–N bonds in **7** are elongated by an average of 0.07 Å compared to those in compound **5**, which contains the same complex anion, but does not exhibit additional K–C interactions. Thus, the K–$ATI^{backbone}$ interactions have a significant impact on the electron donating ability of the nitrogen atoms in the *N,N*-binding pocket of this ligand.

^1H- and ^{13}C NMR spectroscopic analysis of compounds **7** and **8** revealed one set of signals indicating apparent C_i symmetry in solution. Low temperature ^1H NMR spectra of **8** in THF-d_8 at −40 °C revealed no significant alterations. In specific, splitting of the single set of resonances of **8** into two sets of resonances of the starting materials **3** and **4** was not observed, suggesting an ionic structure in solution. This assumption is supported by DFT calculations: the model reaction $[K(ATI^{Ph/iPr})(thf)_2]+[Na(ATI^{Ph/iPr})(thf)_2]\rightarrow[K(thf)_3][Na(ATI^{Ph/iPr})_2]+THF$ was calculated to be exothermic and exergonic ($\Delta H^{rel}=-19.9$ kcal mol^{-1}; $\Delta G^{rel}=-13.5$ kcal mol^{-1}; for details see Supp. Inf.).

Polymerization of ε-caprolactone

The formation of sodiate complex anions, $[Na(ATI)_2]^-$, by ligand-induced disproportionations or in mixed-metal compounds is a coordination chemistry phenomenon, but should have implications for the reactivity of these complexes. The $[Na(ATI)_2]^-$ anion is expected to show a higher nucleophilicity than its neutral counterpart $Na(ATI)L_n$. In order to validate this hypothesis, the polymerization of ε-caprolactone (ε-CL) was chosen as a model system, since the catalyst activity can be expected to depend on the nucleophilicity/basicity of the catalyst in these reactions.[30,31] Surprisingly little is known about the polymerization of ε-CL using alkali metal complexes as initiators. $Li(NiPr_2)$,[32] LiPh,[33] a pentanuclear complex $[Li_5L_2(OCHCH_2)]$,[34] $Na(C_5H_5)$,[35] NaH,[36] $Na(O\text{-}2,6\text{-}tBu_2C_6H_3)$,[37] and KOtBu[38] have been reported to initiate ε-CL polymerization at monomer/initiator ratios ranging from 49:1 to 400:1 (Table 2, entries 1–8).[39] For sodium and potassium compounds in particular, relatively high reaction temperatures of 20–110 °C were necessary (entries 4–8), low conversions were reported (entries 7,8), long reaction times of 60–300 min were obligatory to reach full conversion (entries 4,5), or a high polydispersity index (PDI) of 5.2 was reported for a bulk polymerization that gave poly-ε-CL in 89% yield after 5 min reaction time (entry 6). Remarkably, the initiator $Na(O\text{-}2,6\text{-}iPr_2C_6H_3)$ was inactive (entry 7), and $Na(C_5H_5)$ did not give any polymeric material when THF was used as a solvent.[35]

The ATI compounds **1**–**8** were tested as initiators for the polymerization of ε-CL in THF at −30 °C. All compounds based on the $(ATI^{iPr/iPr})^-$ ligand (**3**, **4**, **6**, **8**) led to full conversion of 250 equivalents of monomer per ATI ligand within reaction times of ≤1 min (Table 3, entries 1–4). With the mononuclear sodium compound $[Na(ATI^{iPr/iPr})]$ (**3**), even 500 equivalents of ε-CL were fully converted within 1 min (entry 5), whereas the potassium compound $[K(ATI^{iPr/iPr})]$ (**4**) was inactive under these conditions (entry 6). This was ascribed to the high sensitivity of the potassium complex. The mixed-metal compound $[NaK(ATI^{iPr/iPr})_2(thf)_2]$ (**8**) led to full conversion of 1000 equivalents of ε-CL, i.e. its activity exceeds that of the mononuclear components **3** and **4** simply added together (entry 7). The highest activity, however, was observed for the sodium sodiate $[Na(12c4)_2]^+[Na(ATI^{iPr/iPr})_2]^-$ (**6**), which led to full conversion of 2500 equivalents of ε-CL within 1 min (entry 8). Thus, the nucleophilicity of the sodium ATI compounds can be increased by exploiting the unusual ligand induced disproportionation reaction leading to formation of **6**. Compound **6** successfully combines the robustness of the sodium species **3** with the high activity of the sodium complex anion $[Na(ATI^{iPr/iPr})_2]^-$, which is also present in mixed-metal compound **8**.

These results make the sodium compounds presented in this work the most active alkali metal initiators for ε-CL polymerization. Their activity is even similar to that of exceptional catalysts such as the ytterbium complex $[Yb(NPh_2)$

Table 2. Results of literature-reported ε-caprolactone (ε-CL) polymerization reactions.

Entry	Initiator	[ε-CL]/[cat]	Conditions	*t* [min]	Yield [%]	M_n [g/mol]	M_w/M_n	Ref.
1	$Li(NiPr_2)$	50	dioxane, r.t.[a]	5	100	–	–	32
2	LiPh	300	bulk, 170 °C	120	49	78000[b]	-	33
3	$Li_5L_2(OCHCH_2)$[c]	400	toluene, r.t.	30	94	51000[d]	1.37	34
4	$Na(C_5H_5)$	250	toluene, 20 °C	60	98	11600[b]	–	35
5	NaH	190	THF, 70 °C	300	88	10200[e]	1.2	36
6	NaH	280	bulk, 70 °C	5	89	47600[e]	5.2	36
7	NaOAr[f]	1500	toluene, 20 °C	3	0	–	–	37
8	KOtBu	49	toluene, 110 °C	15	35	17500	2.0	38
9	$Yb(NPh_2)L'$[g]	2000	toluene, 25 °C	1	99	96400	2.58	40
10	$Nd_2Na_8L''_{12}(OH)_2$[h]	15000	toluene, 20 °C	1	100	90000	1.58	41
11	$Nd_2Na_8L''_{12}(OH)_2$[h]	8000	THF, 20 °C	1	20	21000	1.77	41

[a] The reaction temperature is implied to be r.t., but is not explicitly mentioned in ref. 32. [b] The viscosity average molecular weight, M_η, was reported instead of the number average molecular weight, M_n. [c] L = 2,2′-ethylidene-bis(4,6-di-tert-butyl-phenolate). [d] The value was corrected by a factor of 0.56. [e] The weight average molecular weight, M_w, was reported instead of the number average molecular weight, M_n. The value was corrected by a factor of 0.58. [f] OAr = $O\text{-}2,6\text{-}tBu_2C_6H_3$. [g] L′ = $Me_2NCH_2CH_2N\{CH_2\text{-}(2\text{-}O\text{-}C_6H_2\text{-}3,5\text{-}tBu_2)\}_2$. [h] L″ = $OCH_2CH_2NMe_2$.

Table 3. ε-Caprolactone (ε-CL) polymerization with sodium, potassium, and mixed-metal initiators based on the $(ATI^{iPr/iPr})^-$ ligand.

Entry	Initiator	[ε-CL]/[cat]	Conditions	*t* [min]	Yield [%]	M_n [g/mol]	M_w/M_n
1	$[Na(ATI^{iPr/iPr})]$ (**3**)	250	THF, −30 °C	1	>95	9700	5.6
2	$[K(ATI^{iPr/iPr})]$ (**4**)	250	THF, −30 °C	1	>95	6900	4.5
3	$[KNa(ATI^{iPr/iPr})_2(thf)_2]$ (**8**)	500	THF, −30 °C	1	>95	9300	6.3
4	$[Na(12c4)_2]^+[Na(ATI^{iPr/iPr})_2]^-$ (**6**)	500	THF, −30 °C	1	>95	8500	5.9
5	$[Na(ATI^{iPr/iPr})]$ (**3**)	500	THF, −30 °C	1	>95	9300	5.5
6	$[K(ATI^{iPr/iPr})]$ (**4**)	500	THF, −30 °C	1	<5	–	–
7	$[KNa(ATI^{iPr/iPr})_2(thf)_2]$ (**8**)	1000	THF, −30 °C	1	>95	46000	6.9
8	$[Na(12c4)_2]^+[Na(ATI^{iPr/iPr})_2]^-$ (**6**)	2500	THF, −30 °C	1	>95	10400	5.2

$Me_2NCH_2CH_2N\{CH_2\text{-}(2\text{-}O\text{-}C_6H_2\text{-}3,5\text{-}tBu_2)\}_2]$ or the neodymium cluster $Nd_2Na_8(OCH_2CH_2NMe_2)_{12}(OH)_2$ (Table 2, entries 9–11).[40–43] Remarkably, the high polymerization activities of the sodium ATI species were obtained in THF as a solvent, which is commonly observed to be detrimental for the performance of catalysts in ε-CL polymerization (*cf*, Table 2 entries 5,6,10,11).

In addition to the catalyst activity, molecular weight control is one of the key parameters in ε-CL polymerization.[30] Unfortunately, the high activity of the alkali metal ATI complexes is associated with a relatively poor molecular weight control, especially when very high monomer/catalyst ratios are applied. At full conversion, polymeric materials with broad molecular weight distributions of $M_w/M_n = 4.5–6.9$ were obtained, (entries 1–8). When the polymerization of ε-CL with ATI initiators was performed at lower monomer/initiator ratios, polymer samples with narrow molecular weight distributions were obtained (Supp. Inf., e.g.: 125 equiv. ε-CL, initiator **3**, THF, −30 °C, 1 min, >95 % conversion, $M_w/M_n = 1.16$).

For ATI compounds based on the unsymmetrically substituted $(ATI^{Ph/iPr})^-$ ligand (**1-thf**, **2-thf**, **5**, **7**), the same trend in overall activities (i.e. the combination of activity and robustness) was observed. The initial activities of these catalysts follow the trend **1-thf**≈**5**>**7** >**2-thf** (Supp. Inf.). However, they showed a generally slightly lower activity than the initiators based on the $(ATI^{iPr/iPr})^-$ ligand, as reaction times of up to 5 min were required to reach full conversion (Table 4 and Supp. Inf.). This was attributed to the potential −M (mesomeric) effect and the weaker inductive effect of the phenyl group, as compared to the *iso*-propyl group in the symmetrically substituted $(ATI^{iPr/iPr})^-$ ligand.

The lower activity of the $ATI^{Ph/iPr}$ complexes was accompanied by a dramatically improved molecular weight control compared to the $ATI^{iPr/iPr}$ complexes ($M_w/M_n = 1.14–1.35$, entries 1–4 Table 4; *cf.* Table 3). Only with higher monomer/initiator ratios, the PDIs increase (Table 4, entry 5 and Supp. Inf.). It is interesting to note that the choice of solvent also had a strong influence on the PDI of the polymer sample. With the only toluene-soluble catalyst **1-thf**, a much narrower molecular weight distribution ($M_w/M_n = 1.17$) was observed in toluene at a similar catalyst activity, when compared to results obtained with THF as the solvent (Table 4, entries 5,6 and Supp. Inf.).

Overall, the dinuclear sodiate complexes **6** and **8** show an extraordinary catalyst activity, whereas the toluene-soluble mononuclear compound **1-thf** combines a good catalyst activity with an excellent molecular weight control. When compared to literature-known alkali metal catalysts for ε-CL polymerization, compound **1-thf** shows the highest activity (outperformed only by catalysts reported in this work) and matches the best molecular weight control reported to date (*cf.* Table 2).

The isolated polymer samples obtained from reactions with ATI initiators showed cyclic structures according to mass spectrometric investigations, indicating back-biting processes to be operative (Supp. Inf.).[44] Back-biting processes are suggested to also play a major role in prohibiting a good molecular weight control, when polymerizations are performed at high monomer/initiator ratios. For initiator **6**, a polymerization reaction was carried out as indicated in Table 3 (entry 8) and analyzed at different stages of the reaction. Whereas good molecular weight control was observed up to conversions of ca. 17 % ($M_w/M_n = 1.78$), the polydispersity index increased at higher conversions up to the value detected at full conversion (Table 3, entry 8). It should be noted that PDIs did not significantly increase when monomer/initiator mixtures were left to react longer than necessary to reach full conversion. For instance, reaction of **3** with 250 equiv. ε-CL gave full conversion and a high PDI of 5.6 after 1 min (Table 3, entry 1). Under identical conditions, 125 equiv. ε-CL were converted to a polymer sample with an excellent PDI of 1.16 (Table S1, entry 7). Thus, transesterification processes seem to be most relevant

Table 4. ε-Caprolactone (ε-CL) polymerization with sodium, potassium, and mixed-metal initiators based on the $(ATI^{Ph/iPr})^-$ ligand.

Entry	Initiator	[ε-CL]/[cat]	Conditions	*t* [min]	Yield [%]	M_n [g/mol]	M_w/M_n
1	$[Na(ATI^{Ph/iPr})(thf)]$ (**1-thf**)	250	THF, −30 °C	5	>95	79500	1.35
2	$[K(ATI^{Ph/iPr})(thf)]$ (**2-thf**)	250	THF, −30 °C	5	>95	162000	1.16
3	$[K(thf)_2][Na(ATI^{Ph/iPr})_2]$ (**7**)	500	THF, −30 °C	5	>95	138100	1.15
4	$[Na(12c4)_2]^+[Na(ATI^{Ph/iPr})_2]^-$ (**5**)	500	THF, −30 °C	5	>95	1600	1.14
5	$[Na(ATI^{Ph/iPr})(thf)]$ (**1-thf**)	500	THF, −30 °C	5	>95	9400	6.4
6	$[Na(ATI^{Ph/iPr})(thf)]$ (**1-thf**)	500	Toluene, −30 °C	5	>95	235200	1.17

during polymerization at high monomer/initiator ratios, with post-polymerization events being less decisive.

For the initiation of the polymerization reactions, a nucleophilic attack of an ATI ligand at the carbonyl group of the monomer or the deprotonation of the monomer may be considered. Since back-biting processes make the determination of the initiation mechanism by end group analysis less reliable, reactions of initiators of type **1**–**8** with 5–7 equiv. ε-CL were performed and analyzed by ^{1}H NMR spectroscopy. In all cases, formation of the free ligand H-ATI$^{R/iPr}$ (R = Ph, *i*Pr) was detected along with corresponding amounts of deprotonated ε-CL moieties (Supp. Inf.).[45] A deprotonative initiation mechanism has previously been suggested for reactions with $Na(C_5H_5)$ on the basis of end group analysis.[35] This is also in line with reports of $NaNH_2$ and $LiN(iPr)_2$ reacting with enolizable organic esters (including ε-CL) via deprotonation rather than nucleophilic substitution (i.e. amide formation).[2,46]

Conclusions

In conclusion, we have synthesized and fully characterized a set of new alkali metal aminotroponiminate (ATI) complexes. These studies confirm an active role of the ATI ligand backbone in coordination chemistry. In addition, the coordination chemistry of sodium ATIs was found to be strongly affected by the presence of chelating neutral ligands. Crown ethers induce unusual disproportionation reactions of the type: $2\ Na(ATI) + 2\ L \rightarrow [NaL_2]^{+}[Na(ATI)_2]^{-}$, the products of which may be described as sodium sodiate complexes. By combining sodium and potassium ATI complexes, synthetic access to the first well-defined mixed-metal ATI compounds was generated. In these potassium sodiate compounds, the harder Lewis-acid Na^{+} occupies the harder *N,N* binding site of the ATI ligand, whereas the softer K^{+} ion prefers the softer C_7 ligand backbone as a binding site. The coordination chemistry of sodium ATI complexes was shown to influence their reactivity, which was exemplified using the polymerization of ε-caprolactone (ε-CL) as a model reaction. Sodium ATI compounds with anionic $[Na(ATI)_2]^{-}$ moieties were overall more active as initiators in this reaction than those containing neutral [Na(ATI)] moieties. The ATI compounds reported here were found to be the most active alkali metal initiators for ε-CL polymerization and show activities that are similar to exceptional literature-known lanthanoid catalysts. Whereas the most active catalysts showed a relatively poor molecular weight control in THF, the only toluene-soluble catalyst [Na(ATI$^{Ph/iPr}$)(thf)] showed a good catalyst activity and excellent molecular weight control, outperforming literature-known alkali metal catalysts for ε-CL polymerization. These results suggest alkali metal ATI complexes with a good solubility in moderately polar solvents as promising target catalysts for the efficient and controlled polymerization of polar monomers. Overall, these studies contribute to the development of design principles and structure-reactivity-relationships of ATI complexes.

Experimental Section

General considerations. All air- and moisture-sensitive manipulations were carried out using standard vacuum line Schlenk techniques or in inert atmosphere gloveboxes containing an atmosphere of purified argon. Solvents were degassed and purified according to standard laboratory procedures. NMR spectra were recorded on Bruker instruments operating at 300, 400, or 500 MHz with respect to ^{1}H. ^{1}H and ^{13}C NMR chemical shifts are reported relative to $SiMe_4$ using the residual ^{1}H and ^{13}C chemical shifts of the solvent as a secondary standard. ^{7}Li and ^{23}Na NMR chemical shifts are reported relative to 1 M LiCl in D_2O and 1 M NaCl in D_2O, respectively. NMR spectroscopic experiments were performed at ambient temperature (typically 25 °C), if not otherwise noted. In the NMR spectroscopic characterization of ATI compounds, the CN^{iPr} carbon atom is referred to as 1-C. Elemental analyses were performed on a Leco or a Carlo Erba instrument. For mass spectrometric analyses, an Exactive plus instrument (Thermo Scientific) was used. Single-crystals suitable for X-ray diffraction were coated with perfluorinated polyether oil in a glovebox, transferred to a nylon loop and then transferred to the goniometer of a diffractometer equipped with a molybdenum X-ray tube (λ = 0.71073 Å). The structures were solved using direct methods (SHELXS) completed by Fourier synthesis and refined by full-matrix least-squares procedures. CCDC 1822672–1822674 and 1822678–1822680 contain the crystallographic information for this work. Gel permeation chromatography (GPC) experiments were performed using an Agilent SECcurity GPC System (1260 Infinity) with a refractive index and a UV detector. THF was used as the eluent at a flow rate of 1.0 mL·min^{-1}. All molecular weights are reported relative to a monodisperse polystyrene standard. The columns were contained within an oven (35 °C) and consisted of styrene/divinylbenzene gels with pore sizes ranging from 500 to 100 000 Å.

DFT calculations. DFT calculations were performed with the Gaussian program[47] using the 6-31G(d,p)[48] (H, C, N, O) or the 6-311G(d,p) (Na) basis set[49] and the B3LYP functional.[50] A solvent model (smd,solvent = thf) was used for all calculations.[51] The D3 version of Grimme's dispersion model with the original D3 damping function was applied.[52] Frequency analyses of the reported structures showed no imaginary frequencies for ground states. Thermodynamic parameters were calculated at a temperature of 298.15 K and a pressure of 1.00 atm.

[Na(ATI$^{Ph/iPr}$)(pmdta)] (1-pmdta). A solution of pmdta (5.5 mg, 32 μmol) in C_6D_6 (0.25 mL) was added to a solution of **1-thf** (10 mg, 32 μmol) in C_6D_6 (0.25 mL). Quantitative formation of **1-pmdta** was indicated by ^{1}H NMR spectroscopy. Upon removal of all volatiles under reduced pressure a yellow solid was obtained, which was washed with pentane. Yield: 12.3 mg, 28 μmol, 88%. The reaction can also be performed on a 50–100 mg scale.

^{1}H-NMR (400 MHz, THF-d_8): δ = 1.15 (d, 6H, $^{3}J_{HH}$ = 6.2 Hz, CH*Me*$_2$), 2.14 (s, 12H, $N(CH_3)_2$), 2.18 (s, 3H, NCH_3), 2.28–2.32 (m, 4H, CH_2), 2.39–2.43 (m, 4H, CH_2), 3.79 (sept, 1H, $^{3}J_{HH}$ = 6.2 Hz, C*H*Me$_2$), 5.41 (t, 1H, $^{3}J_{HH}$ = 8.7 Hz, 5-H), 5.86 (d, 1H, $^{3}J_{HH}$ = 11.1 Hz, 3-H), 6.03 (d, 1H, $^{3}J_{HH}$ = 11.7 Hz, 7-H),6.15–6.21 (m, 1H, 4-H), 6.37–6.42 (m, 1H, 6-H), 6.71–6.75 (m, 3H, *o*-Ph, *p*-Ph), 7.11–7.15 (m, 2H, *m*-Ph) ppm. ^{1}H-NMR (400 MHz, C_6D_6): δ = 1.24 (d, 6H, $^{3}J_{HH}$ = 6.2 Hz, CH*Me*$_2$), 1.51 (s, 3H, NCH_3), 1.71 (br. s, 8H, CH_2), 1.84 (s, 12H, $N(CH_3)_2$), 4.07 (sept, 1H, $^{3}J_{HH}$ = 6.2 Hz, C*H*Me$_2$), 6.07 (t, 1H, $^{3}J_{HH}$ = 8.8 Hz, 5-H), 6.54 (d, 1H, $^{3}J_{HH}$ = 8.7 Hz, 7-H), 6.57 (d, 1H, $^{3}J_{HH}$ = 9.2 Hz, 3-H), 6.77–6.82 (m, 1H, 4-H), 6.93 (t, 1H, $^{3}J_{HH}$ = 7.2 Hz, *p*-Ph), 6.98–7.03 (m, 3H, *o*-Ph, 6-H), 7.28–7.32 (m, 2H, *m*-Ph) ppm. ^{13}C-NMR (101 MHz, THF-d_8): δ = 24.32 (CH*Me*$_2$), 43.34 (NCH_3), 46.22 ($N(CH_3)_2$), 49.15 ($CHMe_2$), 57.43 (CH_2), 58.89 (CH_2), 108.82 (5-C), 109.31 (7-C), 110.02 (3-C), 120.15 (*p*-Ph), 123.40 (*o*-Ph), 129.50 (*m*-Ph), 132.07 (6-C), 132.44 (4-C), 158.05 (*ipso*-Ph), 161.96 (1-C), 163.55 (2-C) ppm. ^{13}C-NMR (101 MHz, C_6D_6): δ =

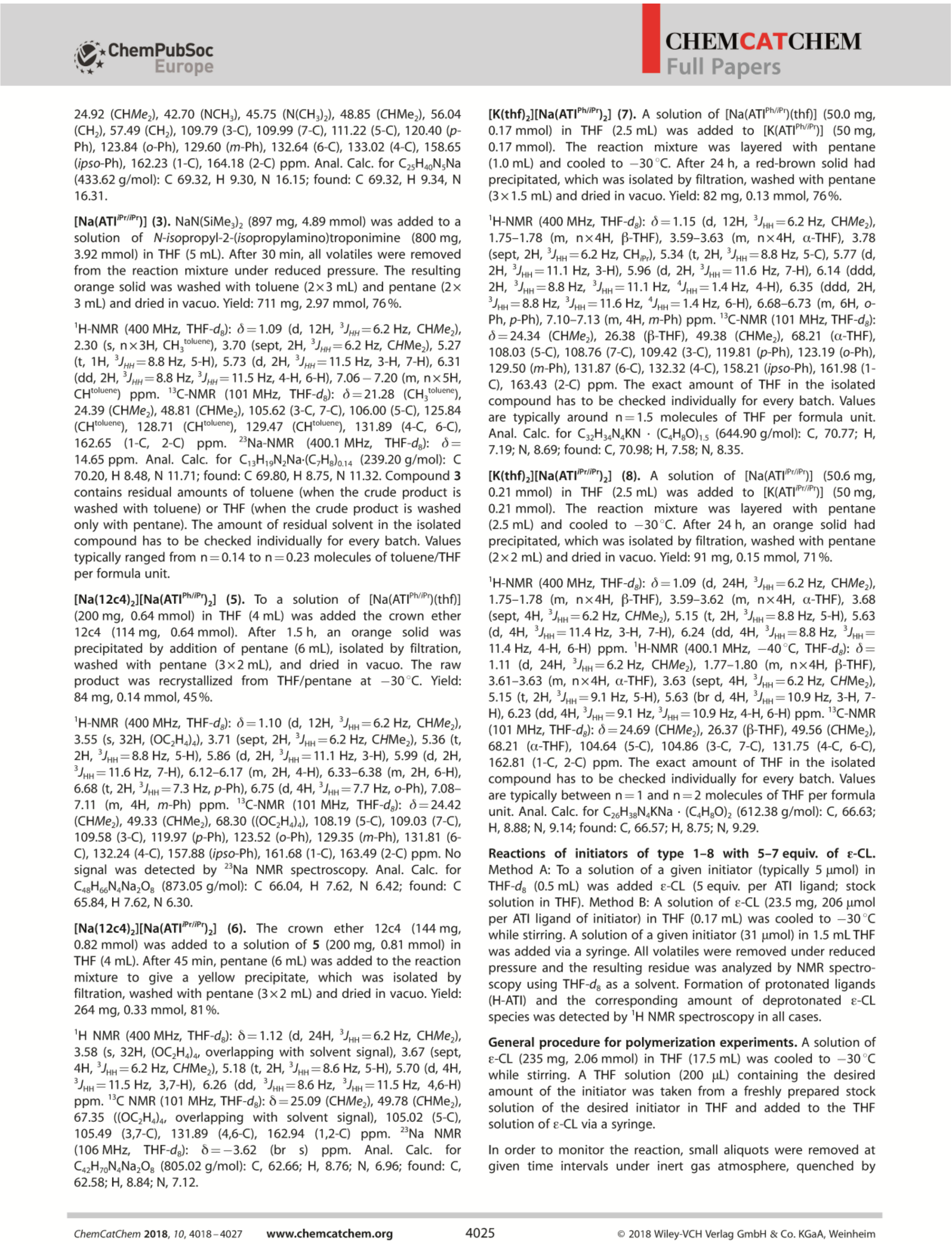

24.92 (CH*Me*$_2$), 42.70 (NCH$_3$), 45.75 (N(CH$_3$)$_2$), 48.85 (*C*HMe$_2$), 56.04 (CH$_2$), 57.49 (CH$_2$), 109.79 (3-C), 109.99 (7-C), 111.22 (5-C), 120.40 (*p*-Ph), 123.84 (*o*-Ph), 129.60 (*m*-Ph), 132.64 (6-C), 133.02 (4-C), 158.65 (*ipso*-Ph), 162.23 (1-C), 164.18 (2-C) ppm. Anal. Calc. for $C_{25}H_{40}N_5Na$ (433.62 g/mol): C 69.32, H 9.30, N 16.15; found: C 69.32, H 9.34, N 16.31.

[Na(ATI$^{iPr/iPr}$)] (3). NaN(SiMe$_3$)$_2$ (897 mg, 4.89 mmol) was added to a solution of *N-iso*propyl-2-(*iso*propylamino)troponimine (800 mg, 3.92 mmol) in THF (5 mL). After 30 min, all volatiles were removed from the reaction mixture under reduced pressure. The resulting orange solid was washed with toluene (2×3 mL) and pentane (2×3 mL) and dried in vacuo. Yield: 711 mg, 2.97 mmol, 76 %.

^{1}H-NMR (400 MHz, THF-d_8): $\delta = 1.09$ (d, 12H, $^{3}J_{HH} = 6.2$ Hz, CH*Me*$_2$), 2.30 (s, n×3H, $CH_3^{toluene}$), 3.70 (sept, 2H, $^{3}J_{HH} = 6.2$ Hz, C*H*Me$_2$), 5.27 (t, 1H, $^{3}J_{HH} = 8.8$ Hz, 5-H), 5.73 (d, 2H, $^{3}J_{HH} = 11.5$ Hz, 3-H, 7-H), 6.31 (dd, 2H, $^{3}J_{HH} = 8.8$ Hz, $^{3}J_{HH} = 11.5$ Hz, 4-H, 6-H), 7.06 – 7.20 (m, n×5H, $CH^{toluene}$) ppm. ^{13}C-NMR (101 MHz, THF-d_8): $\delta = 21.28$ ($CH_3^{toluene}$), 24.39 (CH*Me*$_2$), 48.81 (*C*HMe$_2$), 105.62 (3-C, 7-C), 106.00 (5-C), 125.84 ($CH^{toluene}$), 128.71 ($CH^{toluene}$), 129.47 ($CH^{toluene}$), 131.89 (4-C, 6-C), 162.65 (1-C, 2-C) ppm. ^{23}Na-NMR (400.1 MHz, THF-d_8): $\delta =$ 14.65 ppm. Anal. Calc. for $C_{13}H_{19}N_2Na{\cdot}(C_7H_8)_{0.14}$ (239.20 g/mol): C 70.20, H 8.48, N 11.71; found: C 69.80, H 8.75, N 11.32. Compound **3** contains residual amounts of toluene (when the crude product is washed with toluene) or THF (when the crude product is washed only with pentane). The amount of residual solvent in the isolated compound has to be checked individually for every batch. Values typically ranged from n = 0.14 to n = 0.23 molecules of toluene/THF per formula unit.

[Na(12c4)$_2$][Na(ATI$^{Ph/iPr}$)$_2$] (5). To a solution of [Na(ATI$^{Ph/iPr}$)(thf)] (200 mg, 0.64 mmol) in THF (4 mL) was added the crown ether 12c4 (114 mg, 0.64 mmol). After 1.5 h, an orange solid was precipitated by addition of pentane (6 mL), isolated by filtration, washed with pentane (3×2 mL), and dried in vacuo. The raw product was recrystallized from THF/pentane at −30 °C. Yield: 84 mg, 0.14 mmol, 45 %.

^{1}H-NMR (400 MHz, THF-d_8): $\delta = 1.10$ (d, 12H, $^{3}J_{HH} = 6.2$ Hz, CH*Me*$_2$), 3.55 (s, 32H, $(OC_2H_4)_4$), 3.71 (sept, 2H, $^{3}J_{HH} = 6.2$ Hz, C*H*Me$_2$), 5.36 (t, 2H, $^{3}J_{HH} = 8.8$ Hz, 5-H), 5.86 (d, 2H, $^{3}J_{HH} = 11.1$ Hz, 3-H), 5.99 (d, 2H, $^{3}J_{HH} = 11.6$ Hz, 7-H), 6.12–6.17 (m, 2H, 4-H), 6.33–6.38 (m, 2H, 6-H), 6.68 (t, 2H, $^{3}J_{HH} = 7.3$ Hz, *p*-Ph), 6.75 (d, 4H, $^{3}J_{HH} = 7.7$ Hz, *o*-Ph), 7.08–7.11 (m, 4H, *m*-Ph) ppm. ^{13}C-NMR (101 MHz, THF-d_8): $\delta = 24.42$ (CH*Me*$_2$), 49.33 (*C*HMe$_2$), 68.30 ($(OC_2H_4)_4$), 108.19 (5-C), 109.03 (7-C), 109.58 (3-C), 119.97 (*p*-Ph), 123.52 (*o*-Ph), 129.35 (*m*-Ph), 131.81 (6-C), 132.24 (4-C), 157.88 (*ipso*-Ph), 161.68 (1-C), 163.49 (2-C) ppm. No signal was detected by ^{23}Na NMR spectroscopy. Anal. Calc. for $C_{48}H_{66}N_4Na_2O_8$ (873.05 g/mol): C 66.04, H 7.62, N 6.42; found: C 65.84, H 7.62, N 6.30.

[Na(12c4)$_2$][Na(ATI$^{iPr/iPr}$)$_2$] (6). The crown ether 12c4 (144 mg, 0.82 mmol) was added to a solution of **5** (200 mg, 0.81 mmol) in THF (4 mL). After 45 min, pentane (6 mL) was added to the reaction mixture to give a yellow precipitate, which was isolated by filtration, washed with pentane (3×2 mL) and dried in vacuo. Yield: 264 mg, 0.33 mmol, 81 %.

^{1}H NMR (400 MHz, THF-d_8): $\delta = 1.12$ (d, 24H, $^{3}J_{HH} = 6.2$ Hz, CH*Me*$_2$), 3.58 (s, 32H, $(OC_2H_4)_4$, overlapping with solvent signal), 3.67 (sept, 4H, $^{3}J_{HH} = 6.2$ Hz, C*H*Me$_2$), 5.18 (t, 2H, $^{3}J_{HH} = 8.6$ Hz, 5-H), 5.70 (d, 4H, $^{3}J_{HH} = 11.5$ Hz, 3,7-H), 6.26 (dd, $^{3}J_{HH} = 8.6$ Hz, $^{3}J_{HH} = 11.5$ Hz, 4,6-H) ppm. ^{13}C NMR (101 MHz, THF-d_8): $\delta = 25.09$ (CH*Me*$_2$), 49.78 (*C*HMe$_2$), 67.35 ($(OC_2H_4)_4$, overlapping with solvent signal), 105.02 (5-C), 105.49 (3,7-C), 131.89 (4,6-C), 162.94 (1,2-C) ppm. ^{23}Na NMR (106 MHz, THF-d_8): $\delta = -3.62$ (br s) ppm. Anal. Calc. for $C_{42}H_{70}N_4Na_2O_8$ (805.02 g/mol): C, 62.66; H, 8.76; N, 6.96; found: C, 62.58; H, 8.84; N, 7.12.

[K(thf)$_2$][Na(ATI$^{Ph/iPr}$)$_2$] (7). A solution of [Na(ATI$^{Ph/iPr}$)(thf)] (50.0 mg, 0.17 mmol) in THF (2.5 mL) was added to [K(ATI$^{Ph/iPr}$)] (50 mg, 0.17 mmol). The reaction mixture was layered with pentane (1.0 mL) and cooled to −30 °C. After 24 h, a red-brown solid had precipitated, which was isolated by filtration, washed with pentane (3×1.5 mL) and dried in vacuo. Yield: 82 mg, 0.13 mmol, 76 %.

^{1}H-NMR (400 MHz, THF-d_8): $\delta = 1.15$ (d, 12H, $^{3}J_{HH} = 6.2$ Hz, CH*Me*$_2$), 1.75–1.78 (m, n×4H, β-THF), 3.59–3.63 (m, n×4H, α-THF), 3.78 (sept, 2H, $^{3}J_{HH} = 6.2$ Hz, CH_{iPr}), 5.34 (t, 2H, $^{3}J_{HH} = 8.8$ Hz, 5-C), 5.77 (d, 2H, $^{3}J_{HH} = 11.1$ Hz, 3-H), 5.96 (d, 2H, $^{3}J_{HH} = 11.6$ Hz, 7-H), 6.14 (ddd, 2H, $^{3}J_{HH} = 8.8$ Hz, $^{3}J_{HH} = 11.1$ Hz, $^{4}J_{HH} = 1.4$ Hz, 4-H), 6.35 (ddd, 2H, $^{3}J_{HH} = 8.8$ Hz, $^{3}J_{HH} = 11.6$ Hz, $^{4}J_{HH} = 1.4$ Hz, 6-H), 6.68–6.73 (m, 6H, *o*-Ph, *p*-Ph), 7.10–7.13 (m, 4H, *m*-Ph) ppm. ^{13}C-NMR (101 MHz, THF-d_8): $\delta = 24.34$ (CH*Me*$_2$), 26.38 (β-THF), 49.38 (*C*HMe$_2$), 68.21 (α-THF), 108.03 (5-C), 108.76 (7-C), 109.42 (3-C), 119.81 (*p*-Ph), 123.19 (*o*-Ph), 129.50 (*m*-Ph), 131.87 (6-C), 132.32 (4-C), 158.21 (*ipso*-Ph), 161.98 (1-C), 163.43 (2-C) ppm. The exact amount of THF in the isolated compound has to be checked individually for every batch. Values are typically around n = 1.5 molecules of THF per formula unit. Anal. Calc. for $C_{32}H_{34}N_4KN \cdot (C_4H_8O)_{1.5}$ (644.90 g/mol): C, 70.77; H, 7.19; N, 8.69; found: C, 70.98; H, 7.58; N, 8.35.

[K(thf)$_2$][Na(ATI$^{iPr/iPr}$)$_2$] (8). A solution of [Na(ATI$^{iPr/iPr}$)] (50.6 mg, 0.21 mmol) in THF (2.5 mL) was added to [K(ATI$^{iPr/iPr}$)] (50 mg, 0.21 mmol). The reaction mixture was layered with pentane (2.5 mL) and cooled to −30 °C. After 24 h, an orange solid had precipitated, which was isolated by filtration, washed with pentane (2×2 mL) and dried in vacuo. Yield: 91 mg, 0.15 mmol, 71 %.

^{1}H-NMR (400 MHz, THF-d_8): $\delta = 1.09$ (d, 24H, $^{3}J_{HH} = 6.2$ Hz, CH*Me*$_2$), 1.75–1.78 (m, n×4H, β-THF), 3.59–3.62 (m, n×4H, α-THF), 3.68 (sept, 4H, $^{3}J_{HH} = 6.2$ Hz, C*H*Me$_2$), 5.15 (t, 2H, $^{3}J_{HH} = 8.8$ Hz, 5-H), 5.63 (d, 4H, $^{3}J_{HH} = 11.4$ Hz, 3-H, 7-H), 6.24 (dd, 4H, $^{3}J_{HH} = 8.8$ Hz, $^{3}J_{HH} = 11.4$ Hz, 4-H, 6-H) ppm. ^{1}H-NMR (400.1 MHz, −40 °C, THF-d_8): $\delta = 1.11$ (d, 24H, $^{3}J_{HH} = 6.2$ Hz, CH*Me*$_2$), 1.77–1.80 (m, n×4H, β-THF), 3.61–3.63 (m, n×4H, α-THF), 3.63 (sept, 4H, $^{3}J_{HH} = 6.2$ Hz, C*H*Me$_2$), 5.15 (t, 2H, $^{3}J_{HH} = 9.1$ Hz, 5-H), 5.63 (br d, 4H, $^{3}J_{HH} = 10.9$ Hz, 3-H, 7-H), 6.23 (dd, 4H, $^{3}J_{HH} = 9.1$ Hz, $^{3}J_{HH} = 10.9$ Hz, 4-H, 6-H) ppm. ^{13}C-NMR (101 MHz, THF-d_8): $\delta = 24.69$ (CH*Me*$_2$), 26.37 (β-THF), 49.56 (*C*HMe$_2$), 68.21 (α-THF), 104.64 (5-C), 104.86 (3-C, 7-C), 131.75 (4-C, 6-C), 162.81 (1-C, 2-C) ppm. The exact amount of THF in the isolated compound has to be checked individually for every batch. Values are typically between n = 1 and n = 2 molecules of THF per formula unit. Anal. Calc. for $C_{26}H_{38}N_4KNa \cdot (C_4H_8O)_2$ (612.38 g/mol): C, 66.63; H, 8.88; N, 9.14; found: C, 66.57; H, 8.75; N, 9.29.

Reactions of initiators of type 1–8 with 5–7 equiv. of ε-CL. Method A: To a solution of a given initiator (typically 5 μmol) in THF-d_8 (0.5 mL) was added ε-CL (5 equiv. per ATI ligand; stock solution in THF). Method B: A solution of ε-CL (23.5 mg, 206 μmol per ATI ligand of initiator) in THF (0.17 mL) was cooled to −30 °C while stirring. A solution of a given initiator (31 μmol) in 1.5 mL THF was added via a syringe. All volatiles were removed under reduced pressure and the resulting residue was analyzed by NMR spectroscopy using THF-d_8 as a solvent. Formation of protonated ligands (H-ATI) and the corresponding amount of deprotonated ε-CL species was detected by ^{1}H NMR spectroscopy in all cases.

General procedure for polymerization experiments. A solution of ε-CL (235 mg, 2.06 mmol) in THF (17.5 mL) was cooled to −30 °C while stirring. A THF solution (200 μL) containing the desired amount of the initiator was taken from a freshly prepared stock solution of the desired initiator in THF and added to the THF solution of ε-CL via a syringe.

In order to monitor the reaction, small aliquots were removed at given time intervals under inert gas atmosphere, quenched by

addition of $CDCl_3$ containing traces of water, and analyzed by NMR spectroscopy.

For isolation of the polymer sample, the reaction was stopped at a given time by addition of an excess of wet pentane (typically 20 mL). The precipitated polymer was isolated by filtration, washed with pentane (typically 3×5 mL) and dried in vacuo.

Acknowledgements

The authors thank Dr. R. Dewhurst for helpful discussions, Prof. H. Braunschweig for generous support, and the Fonds der Chemischen Industrie for a doctoral scholarship (A. H.) and a Liebig Fellowship (C. L.).

Conflict of Interest

The authors declare no conflict of interest.

Keywords: Sodium · Ligand-induced Disproportionation · Mixed-Metal Compounds · Caprolactone · Polymerization

[1] a) T. P. Hanusa, *The Lightest Metals: Science and Technology from Lithium to Calcium*, Wiley **2015**; b) K. Ruhlandt-Senge, K. W. Henderson, P. C. Andrews, *Alkali Metal Organometallics – Structure and Bonding in Comprehensive Organometallic Chemistry III*, Eds.: R. H. Crabtree, D. M. Mingos, Vol. 2, Elsevier, **2007**; c) D. Hoffmann, W. Bauer, P. von Ragué Schleyer, U. Pieper, D. Stalke, *Organometallics* **1993**, *12*, 1193–1200; d) C. Schade, P. von Ragué Schleyer, *Adv. Organomet. Chem.* **1987**, *27*, 169–278; e) Z. Rappoport, I. Marek, (Eds.) *The Chemistry of Organolithium Compounds*, Wiley, New York, **2004**.

[2] J.-M. Poirier, *Sodium Amide in Organic Synthesis in Industrial Chemistry Library*, Eds.: J.-R. Desmuirs, S. Ratton, Vol. 8, Elsevier, **1996**, p. 445–468.

[3] F. Fisher, D. E. Applequist, *J. Org. Chem.* **1965**, *30*, 2089–2090; b) J. R. Salaun, J. Champion, J. M. Conia, *Org. Synth.* **1977**, *57*, 36; c) R. Köster, S. Arora, P. Binger, *Liebigs Ann. Chem.* **1973**, 1219–1235; d) P. Caubère, *Top. Curr. Chem.* **1978**, *73*, 49–103.

[4] a) E. M. Kaiser, G. J. Bartling, W. R. Thomas, S. B. Nichols, D. R. Nash, *J. Org. Chem.* **1973**, *38*, 71–75; b) R. Levine, D. A. Dimmig, W. M. Kadunce, *J. Org. Chem.* **1974**, *39*, 3834–3837; c) P. L. Compagnon, T. Kimny, *J. Organomet. Chem.* **1980**, *184*, 297–308.

[5] a) E. M. Kaiser, C. D. Warner, *Synthesis* **1973**, 395–396; b) L. A. Paquette, J. P. Gilday, *J. Org. Chem.* **1988**, *53*, 4972–4978; c) L. A. Paquette, C. S. Ra, *J. Org. Chem.* **1988**, *53*, 4978–4985.

[6] a) K. Komatsu, K. Itoyama, J. Hirota, A. Nishijima, US patent 4,097,661, **1978**; b) A. A. Morton, F. D. Marsh, R. D. Coombs, A. L. Lyons, S. E. Penner, H. E. Ramsden, V. B. Baker, E. L. Little, R. L. Letsinger, *J. Am. Chem. Soc.* **1950**, *72*, 3785–3792; c) A. A. Morton, E. E. Magat, R. L. Letsinger, *J. Am. Chem. Soc.* **1947**, *69*, 950–961.

[7] a) R. E. Mulvey, *Organometallics* **2006**, *25*, 1060–1075; b) R. E. Mulvey, *Acc. Chem. Res.* **2009**, *42*, 743–755; c) R. E. Mulvey, F. Mongin, M. Uchiyama, Y. Kondo, *Angew. Chem. Int. Ed.* **2007**, 46, 3802–3824; *Angew. Chem.* **2007**, *119*, 3876–3899; d) R. E. Mulvey, S. D. Robertson, *Top. Organomet. Chem.* **2014**, *47*, 129–158; e) R. E. Mulvey, *Dalton Trans.* **2013**, *42*, 6676–6693.

[8] E.g.: a) A. J. Martínez-Martínez, A. R. Kennedy, R. E. Mulvey, C. T. O'Hara, *Science* **2014**, *346*, 834–837; b) R. E. Mulvey, V. L. Blair, W. Clegg, A. R. Kennedy, J. Klett, L. Russo, *Nat. Chem.* **2010**, *2*, 588–591; c) C. Lichtenberg, L. Viciu, M. Adelhardt, J. Sutter, K. Meyer, B. de Bruin, H. Grützmacher, *Angew. Chem. Int. Ed.* **2015**, *54*, 5766–5771; *Angew. Chem.* **2015**, *127*, 5858–5863; d) A. R. Kennedy, J. Klett, R. E. Mulvey, D. S. Wright, *Science* **2009**, *326*, 706–708.

[9] Lochmann-Schlosser superbases can also be prepared by combining lithium and sodium compounds, but the combination of lithium and potassium compounds is usually more effective: L. Lochmann, M. Janata, *Cent. Eur. J. Chem.* **2014**, *12*, 537–548.

[10] For review articles see: a) P. W. Roesky, *Chem. Soc. Rev.* **2000**, *29*, 335–345; b) P. W. Roesky, *Z. Anorg. Allg. Chem.* **2003**, *629*, 1881–1894; c) H. V. R. Dias, Z. Wang, W. Jin, *Coord. Chem. Rev.* **1998**, *176*, 67–86; d) O. Kühl, *Coord. Chem. Rev.* **2004**, *248*, 411–427; e) A. Hanft, C. Lichtenberg, *Eur. J. Inorg. Chem.* **2018**, DOI: 10.1002/ejic.201800465; f) also see [11].

[11] J. Jenter, A. Lühl, P. W. Roesky, S. Blechert, *J. Organomet. Chem.* **2011**, *696*, 406–418.

[12] R. K. Siwatch, S. Nagendran, *Chem. Eur. J.* **2014**, *20*, 13551–13556.

[13] a) A. V. Korolev, E. Ihara, I. A. Guzei, V. G. Young Jr., R. F. Jordan, *J. Am. Chem. Soc.* **2001**, *123*, 8291–8309; b) J.-S. Herrmann, G. A. Luinstra, P. W. Roesky, *J. Organomet. Chem.* **2004**, *689*, 2720–2725.

[14] C. Lichtenberg, I. Krummenacher, *Chem. Commun.* **2016**, *52*, 10044–10046.

[15] a) P. W. Roesky, *Chem. Soc. Rev.* **2000**, *29*, 335–345; b) P. W. Roesky, *Z. Anorg. Allg. Chem.* **2003**, *629*, 1881–1894; c) H. V. R. Dias, Z. Wang, W. Jin, *Coord. Chem. Rev.* **1998**, *176*, 67–86.

[16] M. Pittracher, U. Frisch, H. Kopacka, K. Wurst, T. Müller, L. Oehninger, I. Ott, E. Wuttke, S. Scheerer, R. F. Winter, B. Bildstein, *Organometallics* **2014**, *33*, 1630–1643.

[17] C. Lichtenberg, *Organometallics* **2016**, *35*, 894–902.

[18] A. Hanft, C. Lichtenberg, *Dalton Trans.* **2018**, DOI: 10.1039/C8DT01019F.

[19] It should be noted that **3** and **4** require an excess of donor solvents such as THF for sufficient solubilization. Thus, the coordination geometry of their THF adducts **3-thf** and **4-thf** is considered to be most relevant for their chemistry in solution. Nevertheless, the coordination chemistry of **3** and **4** in the absence of neutral ligands may be discussed: Single-crystal X-ray diffraction studies of $K(ATI^{Ph/Ph})$ show that in the absence of neutral donor ligands, one ATI ligand can interact with three different metal centers in the solid state (two potassium ions interact with the N atoms, one potassium ion interacts with the C_7 ligand backbone). These results are part of a manuscript, which has recently been submitted for publication. A similar coordination behavior is suggested for THF-free **3** and **4**.

[20] a) P. W. Roesky, *Chem. Ber.* **1997**, *130*, 859–862; b) also see ref. [17].

[21] The results of single-crystal XRD studies on **6-thf** have previously been mentioned (ref. [10c]); however, no crystallographic details were given and this study is thus not listed in common data bases such as SciFinder or CCDC.

[22] A cut-off value of 3.57 Å has been suggested for K–C(π) contacts: A. Torvisco, K. Decker, F. Uhlig, K. Ruhlandt-Senge, *Inorg. Chem.* **2009**, *48*, 11459–11465.

[23] R. Neufeld, D. Stalke, *Chem. Sci.* **2015**, *6*, 3354–3364.

[24] For related work on lithiate and potassiate compounds as well as a complex anion containing sodium and aluminum ions, see: a) H. Gornitzka, D. Stalke, *Angew. Chem. Int. Ed.* **1994**, *33*, 693–695; *Angew. Chem.* **1994**, *106*, 695–698; b) A. R. Kennedy, R. E. Mulvey, C. T. O'Hara, G. M. Robertson, S. D. Robertson, *Angew. Chem. Int. Ed.* **2011**, *50*, 8375–8378; *Angew. Chem.* **2011**, *123*, 8525–8528; c) W. Clegg, L. Horsburgh, R. E. Mulvey, M. J. Ross, *J. Chem. Soc. Chem. Commun.* **1994**, 2393–2394; d) M. Niemeyer, P. P. Power, *Organometallics* **1996**, *15*, 4107–4109.

[25] T. Kähler, F. Olbrich, CCDC 184336.

[26] H. Bock, C. Arad, C. Näther, Z. Havlas, *Helv. Chim. Acta* **1997**, *80*, 606–620.

[27] For $[Na(tmeda)_2(Et_2O)][Na(C(SiMe_3)_3)_2]$ see: S. S. Al-Juaid, C. Eaborn, P. B. Hitchcock, K. Izod, M. Mallien, J. D. Smith, *Angew. Chem. Ind. Ed.* **1994**, *33*, 1268–1270.

[28] For $[Na(dme)_3][Na(C_5H_4(BMe_2pz))_2Fe]$ (pz = pyrazol-1-yl) see: A. H. Ilkhechi, J. M. Mercero, I. Silanes, M. Bolte, M. Scheibitz, H.-W. Lerner, J. M. Ugalde, M. Wagner, *J. Am. Chem. Soc.* **2005**, *127*, 10656–10666.

[29] For heterobimetallic molecular complexes based on the related tropolonate and aminotropolonate ligands see ref. [16].

[30] For review articles see: a) M. Labet, W. Thielemans, *Chem. Soc. Rev.* **2009**, *38*, 3484–34504; b) O. Nuyken, S. D. Pask, *Polymers* **2013**, *5*, 361–403; c) A. Arbaoui, C. Redshaw, *Polym. Chem.* **2010**, *1*, 801–826.

[31] For examples of alkali metal complexes used as initiators for the polymerization of polar monomers such as *rac*-lactide, see: a) C. Chen, Y. Cui, X. Mao, X. Pan, J. Wu, *Macromolecules* **2017**, *50*, 83–96; b) J. Zhang, J. Xiong, Y. Sun, N. Tang, J. Wu, *Macromolecules* **2014**, *47*, 7789–7796.

[32] A. Bhaw-Luximon, D. Jhurry, S. Motala-Timol, Y. Lochee, *Macromol. Symp.* **2006**, *231*, 60–68.

[33] X. Deng, M. Yuan, C. Xiong, X. Li, *J. Appl. Pol. Sci.* **1999**, *73*, 1401–1408.

[34] L = 2,2′-ethylidene-bis(4,6-di-tert-butyl-phenolate). Z. Liang, M. Zhang, X. Ni, X. Li, Z. Shen, *Inorg. Chem. Commun.* **2013**, *29*, 145–147.
[35] M. Yuan, C. Xiong, X. Deng, *J. Appl. Polym. Sci.* **1998**, *67*, 1273–1276.
[36] G. Gorrasi, D. Pappalardo, C. Pellecchia, *React. Funct. Polym.* **2012**, *72*, 752–756.
[37] H. Sheng, L. Zhou, Y. Zhang, Y. Yao, Q. Shen, *J. Polym. Sci. A* **2007**, *45*, 1210–1218.
[38] A.-F. Mingotaud, F. Dargelas, F. Cansell, *Macromol. Symp.* **2000**, *153*, 77–86.
[39] For an example of a mixed-metal sodium/aluminum complex that initiates ε-CL polymerization in refluxing toluene see: X. Pan, A. Liu, L. Yao, L. Wang, J. Zhang, J. Wu. X. Zhao, C.-C. Lin, *Inorg. Chem. Commun.* **2011**, *14*, 763–766.
[40] Y. Yao, M. Ma, X. Xu, Y. Zhang, Q. Shen, W.-T. Wong, *Organometallics* **2005**, *24*, 4014–4020.
[41] H. Sheng, F. Xu, Y. Yao, Y. Zhang, Q. Shen, *Inorg. Chem.* **2007**, *46*, 7722–7724.
[42] The cluster $Nd_2Na_8(OCH_2CH_2NMe_2)_{12}(OH)_2$ converts 1071 equivalents of ε-CL per anionic ligand in 1 min at 20 °C in toluene and is significantly less active in THF (Table 2, entries 9, 10), whereas compound **6** converts 1250 equivalents of ε-CL per anionic ligand in 1 min at −30 °C in THF.
[43] During revision of this manuscript, a magnesium complex based on a tetradentate, monoanionic aryloxide ligand has been reported to be highly active as an initiator of ε-CL polymerization in the presence of benzyl alcohol: T. Rosen, I. Goldberg, W. Navarra, V. Venditto, M. Kol, *Angew. Chem. Int. Ed.* **2018**, *57*, 7191–7195; *Angew. Chem.* **2018**, *130*, 7309–7313.
[44] The relevance of backbiting processes during polymerization of ε-CL with initiators **1–8** is also indicated by experimental M_n values (obtained from GPC measurements in THF vs. polystyrene standards) being significantly lower than theoretically expected M_n values. The M_n values are uncorrected (a correcting coefficient of 0.56 has been suggested, *cf.* M. Save, M. Schappacher, A. Soum, *Macromol. Chem. Phys.* **2002**, *203*, 889–899).
[45] When these reactions were performed under conditions analogous to those used for the polymerization reactions (experimental part; method B), stoichiometric amounts of free ligand were formed indicating the dominant role of a deprotonative initiation mechanism.
[46] G. L. Larson, V. C. de Maldanado, L. M. Fuentes, L. E. Torres, *J. Org. Chem.* **1988**, *53*, 633–639.
[47] For full reference see Supp. Inf..
[48] P. C. Hariharan, J. A. Pople, *Theor. Chim. Acta* **1973**, *28*, 213–222.
[49] a) A. D. McLean, G. S. Chandler, *J. Chem. Phys.* **1980**, 72, 5639–5648; b) K. Raghavachari, J. S. Binkley, R. Seeger, J. A. Pople, *J. Chem. Phys.* **1980**, *72*, 650–654.
[50] A. D. Becke, *J. Chem. Phys.* **1993**, *98*, 5648–5652.
[51] A. V. Marenich, C. J. Cramer, D. G. Truhlar, *J. Phys. Chem. B* **2009**, *113*, 6378–6396.
[52] S. Grimme, J. Antony, S. Ehrlich, H. Krieg, *J. Chem. Phys.* **2010**, *132*, 154104–154119.

Manuscript received: April 6, 2018
Accepted Article published: June 25, 2018
Version of record online: July 17, 2018

VI Rationalizing the Effect of Ligand Substitution Patterns on Coordination and Reactivity of Alkali Metal Aminotroponiminates

Anna Hanft, Crispin Lichtenberg

Vervielfältigt aus Referenz:

Organometallics **2018**, *37*, 1781-1787.[64]

DOI:10.1021/acs.organomet.8b00208

mit der Erlaubnis American Chemical Society.

ORGANOMETALLICS
Article
Cite This: Organometallics 2018, 37, 1781−1787

Rationalizing the Effect of Ligand Substitution Patterns on Coordination and Reactivity of Alkali Metal Aminotroponiminates

Anna Hanft and Crispin Lichtenberg*

Department of Inorganic Chemistry, Julius-Maximilians-Universität Würzburg, Am Hubland, 97074 Germany

Supporting Information

ABSTRACT: A small series of alkali metal aminotroponiminates (ATIs), [M-(ATI$^{Ph/Ph}$)(thf)$_n$], have been synthesized and fully characterized (M = Li, Na, K). All of these compounds adopt coordination modes that differ from those reported for derivatives with a slightly varied substitution pattern at the ATI ligand (one or two of the N-bound Ph groups substituted by *i*Pr groups). This leads to an unprecedented ATI coordination mode for the potassium compound [K(ATI$^{Ph/Ph}$)] and an unusual Li···Ph interaction for the lithium compound [Li(ATI$^{Ph/Ph}$)]. The influence of the substitution pattern at the ATI ligand on the shape and energy of the frontier orbitals of its sodium complexes has been rationalized by theoretical methods and correlated with experimental results. Analytical techniques applied in this work include NMR spectroscopy, single crystal X-ray diffraction, and DFT calculations.

INTRODUCTION

The alkali metals Li, Na, and K show a multifaceted coordination chemistry. This is largely due to the relatively high ionic character of their bonding interactions, which results in a pronounced flexibility in terms of coordination numbers and geometries.[1] In addition, these metals have only a moderate preference for bonding interactions with either hard or soft donor functionalities (e.g., *O*- or *N*-based donors vs arenes).[2,3] Consequently, the coordination chemistry of alkali metal complexes of monoanionic, ditopic ligands with hard and soft binding sites can be challenging to predict. This is especially true, when factors such as solvent, concentration, and temperature dependency or the presence of additional (multidentate) neutral ligands are taken into account.[2,4,9]

Recently, we turned our attention toward the coordination chemistry of aminotroponiminates (ATIs, Scheme 1, **A**).[5] This well-established ligand scaffold is characterized by the rigidity of its C_7 ligand backbone and its substantial chemical robustness.[6] Consequently, ATIs have found various applications in synthesis and catalysis. Examples include hydroamination catalysis,[6f,7] propylene oxide,[8] and *ε*-caprolactone polymerization,[9] and the stabilization of low-valent main group species and heavy analogues of carbon compounds.[10] For hydroamination catalysis and *ε*-caprolactone polymerization, a significant impact of the ATI substitution pattern on the catalyst activity has been reported.[6f,7,9]

Scheme 1. Coordination Modes of ATI Ligands[a]

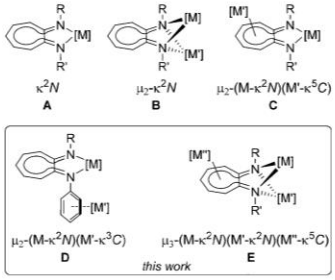

[a] ATI ligands are monoanionic; charges of metal ions are not reflected in graphic representation.[14]

By studying a set of alkali metal ATI complexes, new coordination modes of this ligand have been revealed. Specifically, it has been demonstrated that not only the *N,N* binding pocket of the anionic ligand but also its cyclic C_7 backbone can play an active role in coordination chemistry (Scheme 1, **C**).[5a,11,12] On the basis of coordination mode **C**, the first mixed-metal ATI complexes have recently been reported (M = Na, M′ = K).[9] Differences in the ionic radius and the valence orbitals of the metal center can have a significant impact on the coordination chemistry of ATI compounds. Experimental results backed-up by DFT calculations on a single compound suggest that the ligand backbone can contribute to both, L→M bonding and M→L backbonding.[13] In these respects, the coordination chemistry of monoanionic ATIs parallels that of the neutral H-ATI ligand, which can bind to a ruthenium atom via its C_7 backbone, as reported for the complex [Ru(C_5Me_5)(H-ATI$^{iPr/iPr}$)][PF_6].[11]

Here, we show that subtle differences in the nitrogen-bound substituents of ATI ligands can significantly affect the coordination chemistry and reactivity of alkali metal aminotroponiminates. These effects are rationalized by correlation of results from DFT calculations with experimental observations. Along these lines, the investigation of compounds M(ATI$^{Ph/Ph}$) (M = Li, Na, K) revealed two unprecedented coordination modes of ATI ligands (Scheme 1, **D**,**E**).

Received: April 9, 2018
Published: May 31, 2018

DOI: 10.1021/acs.organomet.8b00208
Organometallics 2018, 37, 1781−1787

■ RESULTS AND DISCUSSION

The coordination chemistry of alkali metal ATIs M(ATI$^{R/R'}$) and their remarkable catalytic activity in the polymerization of ε-caprolactone have recently been reported (M = Li, Na, K, R/R′ = *i*Pr/*i*Pr, Ph/*i*Pr).[5,9] In order to understand the influence of the nitrogen-bound substituents of ATI ligands on their coordination chemistry, we set out to synthesize, isolate, and characterize compounds M(ATI$^{Ph/Ph}$) (M = Li, Na, K), completing the above-mentioned series.[15]

In the original protocol for the synthesis of Li-ATIs, which was first established for [Li(ATI$^{iPr/iPr}$)(thf)$_2$], *n*BuLi is used as a base.[16a] When this procedure was applied for the synthesis of [Li(ATI$^{Ph/Ph}$)(thf)$_2$] (**1-(thf)$_2$**), however, *n*BuLi reacted not only as a base but also as a nucleophile toward the desired product (Scheme 2, top). In the resulting mixture of compounds, the desired complex **1-(Et$_2$O)$_n$** and the product of the nucleophilic attack, [Li$_2$(1-*n*Bu-ATI$^{Ph/Ph}$)(Et$_2$O)$_n$] (**4**), were obtained in a 77:23 ratio. Compound **4** was identified by one- and two-dimensional NMR spectroscopic experiments. Whereas aromatic substitution reactions at the ATI ligand backbone as well as migration of H atoms and the electrophilic addition of (CPh$_3$)$^+$ to the ATI ligand backbone have been reported,[7d,8,16b,17−19] a nucleophilic addition as a side reaction is unprecedented and adds a new facet to the chemistry of ATI ligands. Remarkably, a reaction of the *i*Pr/Ph-substituted ligand H-ATI$^{Ph/iPr}$ with *n*BuLi under identical reaction conditions cleanly generated the literature-known compound [Li(ATI$^{Ph/iPr}$)(L)$_n$].[5a] This observation gives initial evidence for the influence of the substitution pattern in ATI compounds on the energy of their frontier orbitals (*vide infra*) and thus on their reactivity. The use of the less nucleophilic base LiN(SiMe$_3$)$_2$ or LiCH$_2$SiMe$_3$ instead of *n*BuLi allowed for the selective synthesis of **1-(thf)$_2$** (Scheme 2, bottom).[20] Compounds [Na(ATI$^{Ph/Ph}$)(thf)] (**2-thf**) and [K(ATI$^{Ph/Ph}$)] (**3**) could be synthesized analogously to published procedures (Scheme 2).[5a,21]

Scheme 2. Top: Nucleophilic Attack of *n*BuLi at the ATI Ligand Backbone of ATI Ligand as a Side Reaction. Bottom: Synthesis of Alkali Metal ATIs [M(ATI$^{Ph/Ph}$)(thf)$_n$] (M = Li, Na, K, *n* = 0−2)[a]

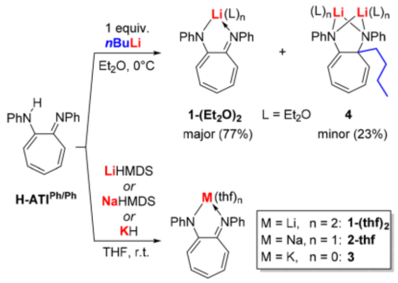

[a] HMDS = hexamethyldisilazide.

In order to obtain solubilities sufficient for solution NMR spectroscopic analysis, compounds of type **1**−**3** require the presence of stoichiometric (for **1-(thf)$_2$**) or super-stoichiometric (**2-thf**, **3**) amounts of monodentate neutral donor ligands such as THF. ^{1}H and ^{13}C NMR spectra of these ATI complexes revealed signal patterns in agreement with an apparent C_{2v} symmetry in solution. This indicates electron delocalization between the formal amide and imine functionalities of the ATI ligands.

In the solid state, the literature-known lithium compounds [Li(ATI$^{Ph/iPr}$)(thf)(OPPh$_3$)] and [Li(ATI$^{iPr/iPr}$)(thf)$_2$] bear two neutral donor ligands and show the expected tetrahedral coordination geometry with a κ^2N coordination mode of the ATI ligand (cf., Scheme 1, **A**).[5a,16] The thf ligands of [Li(ATI$^{Ph/Ph}$)(thf)$_2$] (**1-(thf)$_2$**) could not be removed under reduced pressure. However, crystallization of **1-(thf)$_2$** from benzene/pentane solutions yielded donor ligand-free crystals of [Li(ATI$^{Ph/Ph}$)] (**1**).[22] Single crystal X-ray analysis revealed an asymmetric unit containing two formula units of **1** (Figure 1).

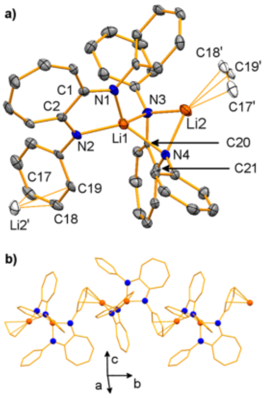

Figure 1. (a) Cut-out of the solid state structure of the coordination polymer [Li(ATI$^{Ph/Ph}$)]$_\infty$ (**1**)$_\infty$. Displacement ellipsoids are shown at the 50% probability level. Hydrogen atoms and lattice-bound benzene molecules are omitted for clarity. Atoms exceeding one asymmetric unit are shown as white ellipsoids. (b) Representation showing the arrangement of (**1**)$_\infty$ as a one-dimensional coordination polymer in the solid state. Selected bond lengths (Å) and angles (deg): Li1−N1, 1.944(6); Li1−N2, 1.956(6); Li1−N3, 2.103(5); Li1−N4, 2.117(6); Li2−N3, 2.035(6); Li2−N4, 2.015(6); Li2−C14′, 2.810(6); Li2−C15′, 2.884(6); Li2−C16′, 2.746(6); Li2−C17′, 2.503(6); Li2−C18′, 2.366(6); Li2−C19′, 2.511(6); N1−C1, 1.322(4); N2−C2, 1.340(4); N1−Li1−N2, 82.5(2); N1−Li1−N3, 122.0(3); N1−Li1−N4, 127.2(3); N2−Li1−N3, 128.5(3); N2−Li1−N4, 130.3(3); N3−Li1−N4, 73.4(2); N3−Li2−ct, 139.68(3); N4−Li2−ct, 128.08(3); ($\sum$(N/(ct)−Li2−N/(ct)), 358.9.

One ATI ligand adopts a bridging μ_2-κ^2N coordination mode; the second shows a new μ_2-(M-κ^2N)(M′-κ^3C) coordination, in which a phenyl substituent rather than the ATI ligand backbone realizes a Li−arene interaction (**D**, Scheme 1). As expected, the Li−N bonds involving bridging N atoms (Li1/2−N3/4, 2.015(6)−2.117(6) Å) are longer than Li−N bonds with terminal N atoms (Li1−N1/2, 1.944(6)−1.956(6) Å). The Li2−C(17′−19′) distances of 2.37−2.51 Å are in the range of those reported for the other few cases of Li−arene^{Ph} interactions.[23] Overall, the bridging coordination modes of the ATI ligands in [Li(ATI$^{Ph/Ph}$)] lead to a coordination polymer with a two-fold screw-axis 2_1 along the crystallographic *b*-axis. Thus, intermolecular Li−Ph interactions can compete

DOI: 10.1021/acs.organomet.8b00208
Organometallics 2018, 37, 1781−1787

with Li−thf interactions in the solid state and in dilute solutions of [Li(ATI$^{Ph/Ph}$)(thf)$_2$] (**1-(thf)$_2$**) in nonpolar solvents.

The sodium complex [Na(ATI$^{Ph/Ph}$)(thf)] (**2-thf**) crystallized from a concentrated solution in Et$_2$O upon cooling to −30 °C as a *bis*-Et$_2$O-adduct, **2-(Et$_2$O)$_2$** (Figure 2; triclinic space group $P\bar{1}$, $Z = 4$). The ATI ligand adopts the κ^2N bonding mode, which is commonly observed for this ligand family (cf., Scheme 1, **A**). That is, compound **2-(Et$_2$O)$_2$** forms a typical molecular structure without any directed intermolecular bonding interactions in the solid state. This is in contrast to the coordination chemistry of recently reported sodium ATIs [Na(ATI$^{iPr/iPr}$)(thf)] and [Na(ATI$^{Ph/iPr}$)(thf)], in which the ATI ligands show bridging coordination modes of type **C** (Scheme 1), resulting in the formation of one-dimensional coordination polymers in the solid state.[5a,9] The sodium atom is found in a distorted tetrahedral coordination geometry (O/N−Na−O/N, 66−135°), which is due to the small bite angle of the ATI ligand (N1−Na−N2, 66°). The Na1−N1/2 distances of 2.36−2.37 Å are similar to those found in [Na(ATI$^{iPr/iPr}$)(thf)] and [Na(ATI$^{Ph/iPr}$)(thf)] (2.36 Å).[5a,9] Due to the weaker donor properties of Et$_2$O compared to thf, the Na−O bond lengths in **2-(Et$_2$O)$_2$** (2.34−2.35 Å) are at the upper limit of those in [Na(ATI$^{iPr/iPr}$)(thf)] and [Na(ATI$^{Ph/iPr}$)(thf)] (2.30−2.34 Å).[5a,9]

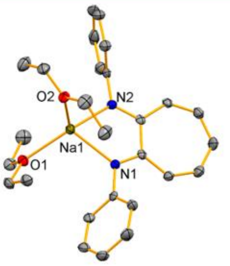

Figure 2. Molecular structure of [Na(ATI$^{Ph/Ph}$)(Et$_2$O)$_2$] (**2-(Et$_2$O)$_2$**) in the solid state. Displacement ellipsoids are shown at the 50% probability level. Hydrogen atoms are omitted for clarity. Selected bond lengths (Å) and angles (deg): Na1−N1, 2.3606(18); Na1−N2, 2.3682(19); Na1−O1, 2.3441(18); Na1−O2, 2.3547(16); N1−C1, 1.318(3); N2−C2, 1.326(3); N1−Na1−N2, 66.30(6); N1−Na−O1, 105.28(6); N1−Na1−O2, 125.10(7); N2−Na1−O1, 134.80(7); N2−Na1−O2, 108.07(6); O1−Na−O2, 111.66(6).

Whereas the thf ligands of potassium compounds [K(ATI$^{iPr/iPr}$)] and [K(ATI$^{Ph/iPr}$)] could only be removed under reduced pressure,[5a,9] compound **3** crystallized from THF/Et$_2$O without any neutral donor ligands and was analyzed by single crystal X-ray diffraction (Figure 3, orthorhombic space group $Cmc2_1$ with $Z = 4$). The potassium ion is coordinated by four nitrogen atoms of two different ATI ligands and by the C$_7$-backbone of a third ATI ligand. This leads to a distorted square pyramidal coordination geometry around K1 with the arene unit in the apical position (ct−K−N, 114−122°; *cis*-(N−K−N), 53−98°). The nitrogen atoms of the ATI ligand occupy bridging positions between two potassium ions, as reported for compound [K(ATI$^{Ph/iPr}$)(thf)],[5a] whereas the ATI ligand backbone adopts a terminal coordination mode as observed in [K(ATI$^{iPr/iPr}$)(thf)].[6b,9] The K1−N and K1−C(2−4) and distances in **3** (K−N, 2.81−2.89 Å; K−C, 3.12−3.42 Å) are similar to those in [K(ATI$^{Ph/iPr}$)(thf)] (K−N, 2.79−2.92 Å) and [K(ATI$^{iPr/iPr}$)(thf)] (K−C, 3.16−3.53 Å), respectively.[24] Every ATI ligand in **3** interacts with a total of three different potassium centers (two via K−N and one via K−C bonding); i.e., an unprecedented μ_3-(M-κ^2N)(M′-κ^2N)(M′′-κ^5C) coordination mode is realized (Scheme 2, **E**). This results in a one-dimensional coordination polymer of compound **3** in the solid state with a two-fold screw axis 2_1 along the crystallographic *c*-axis (Figure 3b).

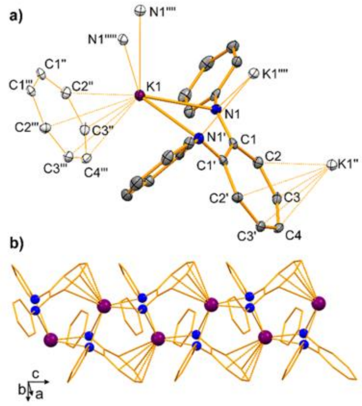

Figure 3. (a) Cut-out of solid state structure of coordination polymer [K(ATI$^{Ph/Ph}$)]$_\infty$ (**3**)$_\infty$. Displacement ellipsoids are shown at the 50% probability level. Hydrogen atoms are omitted for clarity; ct represents the centroid of C(2−4). Atoms exceeding one asymmetric unit are shown as white ellipsoids. (b) Representation showing the arrangement of (**3**)$_\infty$ as a one-dimensional coordination polymer in the solid state. Selected bond lengths (Å) and angles (deg): K1−N1, 2.809(2); K1−N1′′′′, 2.890(2); K1−ct, 2.920(4); K1′′−C2, 3.421(3); K1′′−C3, 3.202(3); K1′′−C4, 3.123(4); N1−C1, 1.321(4); N1−K1−N1′, 54.53(9); N1−K1−ct, 122.10; N1−K1−N1′′′′, 98.17(7); N1−K1−N1′′′′′, 123.37(6); N1−K1′′′′−N1′, 52.88(9); N1−K1′′′′−N1′, 114.44.

In order to rationalize and quantify the influence of nitrogen-bound substituents in ATI ligands on the coordination chemistry and reactivity of the corresponding metal complexes, a range of model compounds were investigated by DFT calculations. A frontier orbital analysis of model compounds [Na(ATI$^{R/R'}$)(thf)$_2$] (**5-R/R′**) confirmed that, for all complexes, the HOMO and the LUMO show considerable contributions by p_z type orbitals of the carbon atoms in the C$_7$ ligand backbone (Figure 4 (top) and the Supporting Information; R/R′ = *t*Bu/*t*Bu, *i*Pr/*i*Pr, Ph/*i*Pr, Ph/Ph, CF$_3$/CF$_3$, SiMe$_3$/SiMe$_3$, NMe$_2$/NMe$_2$).[5a] The frontier orbital energies are significantly influenced by the substitution pattern at the nitrogen atoms: the exchange of electron donating substituents (such as *t*Bu or *i*Pr) for electron withdrawing substituents (such as Ph or CF$_3$) successively lowers the HOMO and LUMO energies. In this series of compounds, the HOMO/LUMO energies vary from −3.94 eV/−0.37 eV for R = R′ = *t*Bu to −5.27 eV/−1.46 eV for R = R′ = CF$_3$, covering a range of 1.33 and 1.09 eV, respectively. Since the effect of the nitrogen-bound substituents on the HOMO and LUMO energies is qualitatively the same and quantitatively similar,

DOI: 10.1021/acs.organomet.8b00208
Organometallics 2018, 37, 1781−1787

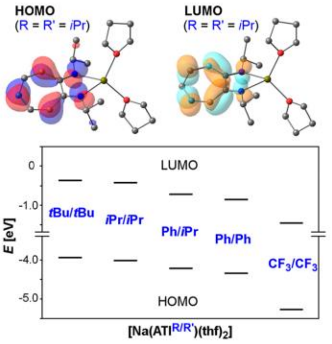

Figure 4. Top: HOMO and LUMO of model compounds $[Na(ATI^{R/R'})(thf)_2]$ (**5-R/R′**) shown for R = R′ = *i*Pr at an isovalue of 0.04. Bottom: HOMO and LUMO energies of model compounds $[Na(ATI^{R/R'})(thf)_2]$ (**5-R/R′**) (R/R′ = *t*Bu/*t*Bu, *i*Pr/*i*Pr, Ph/*i*Pr, Ph/Ph, CF_3/CF_3) as determined by DFT calculations. All HOMOs and LUMOs show considerable contributions from p_z type orbitals of the carbon atoms in the C_7 ligand backbone (Supporting Information).

the HOMO/LUMO gaps show little variation (ΔE(HOMO/LUMO) = 3.48−3.82 eV).

The sum of the Hammett parameters of the nitrogen-bound substituents in model compounds $[Na(ATI^{R/R'})(thf)_2]$ ($\sigma(R) + \sigma(R')$) was plotted against their HOMO and LUMO energies (Figure 5 and the Supporting Information). In both cases, a linear correlation is obtained, which thus allows easy estimation of the frontier orbital energies for unknown ATI complexes based on tabulated Hammett parameters (Supporting Information).

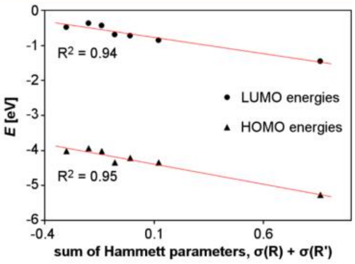

Figure 5. Correlation of the sum of the Hammett parameters of substituents R and R′ in model compounds $[Na(ATI^{R/R'})(thf)_2]$ ($\sigma(R) + \sigma(R')$) with their HOMO and LUMO energies.

In order to correlate the differences in frontier orbital energies of ATI complexes with their ability to interact with Lewis acidic complex fragments via their C_7 ligand backbone, model compounds $[Na(diglyme)Na(ATI^{R/R'})(thf)_2]^+$ (**6-R/R′**) were investigated by DFT calculations (Table 1; diglyme = $MeO(C_2H_4)O(C_2H_4)OMe$). For all compounds **6-R/R′** with hydrocarbon-based substituents R/R′, the general structure shown in Table 1 corresponds to a minimum on the potential energy surface. In contrast, all attempts to locate a minimum structure of this type for **6-CF_3/CF_3** failed, since geometry optimizations for this compound converged to an isomer **7-CF_3/CF_3** with the ATI ligand in a type **B** coordination mode (cf., Scheme 1; for details, see the Supporting Information). This is a first indication for the relatively poor electron donating properties of the C_7 ligand backbone of this species. For comparison with the other compounds of the series **6-R/R′**, a single-point calculation was performed for **6-CF_3/CF_3**, in which all coordinates except for those of the CF_3 groups were taken from the optimized structure of **6-Ph/Ph**.

A natural bond orbital (NBO) analysis of **6-R/R′** was performed in order to evaluate the bonding interactions between the sodium atom in $[Na(diglyme)]^+$ and the complex fragment $[Na(ATI^{R/R'})(thf)_2]$. The deletion energies[25] of C→Na bonding were determined; i.e., dative bonding from natural bond orbitals involving carbon atoms of the C_7 ATI ligand backbone to sodium-centered natural bond orbitals were analyzed (Table 1). These deletion energies range from 30.5 to 44.9 kJ·mol^{-1} and follow the trend that is suggested by the HOMO energies of compounds **5-R/R′**. In agreement with these analyses, free reaction enthalpies associated with the adduct formation leading to compounds **6-R/R′** follow the same trend (Table 1).[26]

These theoretical investigations help to rationalize experimental observations concerning the coordination chemistry and reactivity of ATI compounds. Sodium complexes of $(ATI^{R/iPr})^-$ ligands (R = *i*Pr, Ph) form coordination polymers in the solid state,[5a,9] whereas $[Na(ATI^{Ph/Ph})(thf)]$ (**2-thf**), with its energetically lower-lying HOMO, forms a molecular structure in the solid state (*vide supra*). In reactions with *n*BuLi, (H-$ATI^{iPr/iPr}$) is cleanly metalated,[16a] whereas (H-$ATI^{Ph/Ph}$), with its energetically lower-lying LUMO, is also susceptible to a nucleophilic attack at the ATI ligand backbone (*vide supra*).

■ CONCLUSIONS

The alkali metal aminotroponiminates (ATIs) $[M(ATI^{Ph/Ph})(L)_n]$ (M = Li, Na, K) have been synthesized and fully characterized. In the solid state, the lithium compound shows an unusual Li···Ph interaction. The potassium compound reveals a μ_3-(M-κ^2N)(M′-κ^2N)(M′′-κ^5C) coordination mode, in which one ATI ligand interacts with three different metal atoms, which is unprecedented in ATI chemistry. The sodium compound shows a commonly observed κ^2N coordination mode. This is in contrast with literature-known sodium ATIs $[Na(ATI^{iPr/iPr})(thf)]$ and $[Na(ATI^{Ph/iPr})(thf)]$, for which interactions between the sodium atom and the π-electron cloud of the ATI ligand backbone are observed. These differences have been rationalized on the basis of DFT calculations, which reveal a significant influence of the nitrogen-bound substituents of ATI ligands on their HOMO/LUMO energies and on their ability to efficiently bind to a Lewis acid via their ligand backbone. Specifically, electron donating substituents at nitrogen increase the energy of the HOMO and the LUMO, both of which are in large parts made up by p-type atomic orbitals of the carbon atoms in the ligand backbone. Electron withdrawing substituents at nitrogen decrease the HOMO/LUMO energies. Thus, the ability of the C_7 ligand backbone to act as an electron donating (L→M) or electron accepting (M→L) ligand can be tuned by choice of the nitrogen-bound substituents. A correlation of Hammett parameters with HOMO/LUMO energies has been established

DOI: 10.1021/acs.organomet.8b00208
Organometallics 2018, 37, 1781−1787

Table 1. Deletion Energies for C→Na Interactions in Model Compounds 6-R/R′ and Reaction Enthalpy Associated with Formation of 6-R/R′

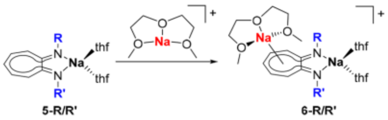

	R/R′				
	tBu/tBu	iPr/iPr	iPr/Ph	Ph/Ph	CF_3/CF_3
Na−C deletion energy [kJ·mol^{-1}][a]	+44.9	+41.3	+39.8	+36.2	+30.5[b]
ΔG [kJ·mol^{-1}]	−145	−135	−128	−120	+26.3[b,c]

[a] Deletion energies of dative bonding from natural bond orbitals involving carbon atoms of the C_7 ATI ligand backbone to sodium-centered natural bond orbitals in model compounds **6-R/R′**. [b] Value based on single-point calculation (see text). [c] Also see ref 26.

and should help to predict the characteristics (and potential reactivity) of yet unknown ATI ligands and complexes.

EXPERIMENTAL SECTION

General Considerations. All air- and moisture-sensitive manipulations were carried out using standard vacuum line Schlenk techniques or in inert atmosphere gloveboxes containing an atmosphere of purified argon. Solvents were degassed and purified according to standard laboratory procedures. NMR spectra were recorded on Bruker instruments operating at 400 or 500 MHz with respect to ^{1}H. ^{1}H and ^{13}C NMR chemical shifts are reported relative to $SiMe_4$ using the residual ^{1}H and ^{13}C chemical shifts of the solvent as a secondary standard. ^{7}Li and ^{23}Na NMR chemical shifts are reported relative to 1 M LiCl in D_2O and 1 M NaCl in D_2O, respectively. NMR spectroscopic experiments were performed at ambient temperature (typically 25 °C). In the NMR spectroscopic characterization of ATI compounds, the CN^{Ph} carbon atom is referred to as 1-C. Elemental analyses were performed on a Leco or a Carlo Erba instrument. Single crystals suitable for X-ray diffraction were coated with perfluorinated polyether oil in a glovebox, transferred to a nylon loop, and then transferred to the goniometer of a diffractometer equipped with a molybdenum X-ray tube (λ = 0.71073 Å). The structures were solved using direct methods (SHELXS) completed by Fourier synthesis and refined by full-matrix least-squares procedures. CCDC 1822675–1822677 contain the crystallographic information for this work.

DFT Calculations. DFT calculations were performed with the Gaussian program[27] using the 6-31G(d,p)[28] (H, C, N, O) or the 6-311G(d,p) (Na) basis set[29] and the B3LYP functional.[30] A solvent model (smd, solvent = thf) was used for the frontier orbital analyses of $[Na(ATI^{R/R'})(thf)_2]$.[31] The D3 version of Grimme's dispersion model with the original D3 damping function was applied.[32] Frequency analyses of the reported structures showed no imaginary frequencies for ground states. Thermodynamic parameters were calculated at a temperature of 298.15 K and a pressure of 1.00 atm.

$[Li(ATI^{Ph/Ph})(thf)_2]$ ***(1-(thf)$_2$)***. $LiN(SiMe_3)_2$ (61.4 mg, 367 μmol) was added to a solution of *N*-phenyl-2-(phenylamino)troponimine (100 mg, 367 μmol) in THF (3 mL). After 30 min, all volatiles were removed from the reaction mixture under reduced pressure. The resulting orange solid was washed with pentane (3 × 3 mL) and dried in vacuo. The crude product was recrystallized at room temperature from toluene/pentane (3:1) by solvent diffusion, isolated by filtration and dried in vacuo. Yield: 100 mg, 247 μmol, 67%.

Single crystals of **1** were obtained by layering a solution of **1-(thf)$_2$** (10 mg, 25 μmol) in benzene (3 mL) with pentane (1 mL). After 2 days, a crystalline material had formed, which was isolated by filtration.

^{1}H NMR (500 MHz, C_6D_6): δ = 1.16–1.19 (m, $n \times 4$H, β-THF), 3.30–3.32 (m, $n \times 4$H, α-THF), 6.15 (t, 1H, $^3J_{HH}$ = 9.0 Hz, 5-H), 6.74 (t, 2H, $^3J_{HH}$ = 9.0 Hz, 4-H, 6-H), 6.97–7.01 (m, 4H, 3-H, 7-H, *p*-Ph), 7.12 (d, 4H, $^3J_{HH}$ = 7.7 Hz, *o*-Ph), 7.32 (t, 4H, $^3J_{HH}$ = 7.7 Hz, *m*-Ph) ppm. ^{13}C NMR (126 MHz, C_6D_6): δ = 25.40 (s, β-THF), 68.15 (s, α-THF), 114.36 (s, 3-C, 7-C), 115.39 (br. s, 5-C), 121.97 (br. s, *o*-Ph), 123.47 (s, *m*-Ph), 129.71 (s, *p*-Ph), 133.67 (s, 4-C, 6-C), 154.80 (br. s, *ipso*-Ph), 163.71 (br. s, 1-C, 2-C) ppm. ^{7}Li NMR (194 MHz, C_6D_6): δ = 1.78 (s) ppm. Anal. Calc. for $C_{19}H_{15}LiN_2{\cdot}(C_4H_8O)_{1.75}$ (404.46 g/mol): C 77.21, H 7.23, N 6.93; found: C 77.37, H 7.39, N 7.19. The amount of THF in the isolated complex is n = 1.75 molecules per formula unit.

$[Na(ATI^{Ph/Ph})(thf)]$ ***(2-thf)***. $NaN(SiMe_3)_2$ (67.3 mg, 367 μmol) was added to a solution of *N*-phenyl-2-(phenylamino)troponimine (100 mg, 367 μmol) in THF (2 mL). After 30 min, all volatiles were removed from the reaction mixture under reduced pressure. The resulting orange solid was washed with pentane (3 × 2 mL) and dried in vacuo. Yield: 68.0 mg, 196 μmol, 53%.

Single crystals of **2-(Et$_2$O)$_2$** were obtained by cooling a solution of **2-thf** (20 mg, 58 μmol) in Et_2O (1 mL) to −30 °C. After 2 days, a crystalline material had formed, which was isolated by filtration.

^{1}H NMR (400 MHz, THF-d_8): δ = 1.76–1.79 (m, $n \times 4$H, β-THF), 3.60–3.63 (m, $n \times 4$H, α-THF), 5.52 (t, 1H, $^3J_{HH}$ = 8.8 Hz, 5-H), 6.10 (d, 2H, $^3J_{HH}$ = 10.8 Hz, 3-H, 7-H), 6.31 (dd, 2H, $^3J_{HH}$ = 8.8 Hz, $^3J_{HH}$ = 11.7 Hz, 4-H, 6-H), 6.78–6.83 (m, 6H, *o*-Ph, *p*-Ph), 7.17–7.22 (m, 4H, *m*-Ph) ppm. ^{13}C NMR (101 MHz, THF-d_8): δ = 26.55 (s, β-THF), 68.39 (s, α-THF), 110.59 (br. s, 5-C), 112.84 (s, 3-C, 7-C), 120.52 (s, *p*-Ph), 123.21 (s, *o*-Ph), 129.42 (s, *m*-Ph), 132.20 (s, 4-C, 6-C), 157.80 (s, *ipso*-Ph), 162.89 (s, 1-C, 2-C) ppm. ^{23}Na-NMR (132 MHz, THF-d_8): δ = 3.69 ppm. Anal. Calc. for (%) $C_{19}H_{15}N_2Na{\cdot}(C_4H_8O)_{0.7}$ (344.80 g/mol): C 75.94, H 6.02, N 8.12; found: C 75.72, H 5.89, N 8.22. The amount of THF in the isolated compound has to be checked individually for every batch. Values typically ranged from n = 0.4 to n = 0.7 molecules of THF per formula unit.

$[K(ATI^{Ph/Ph})]$ ***(3)***. A solution of *N*-phenyl-2-(phenylamino)-troponimine (150 mg, 551 μmol) in THF (3 mL) was added slowly to a suspension of KH (44.2 mg, 1.10 mmol) in THF at −78 °C. The mixture was warmed to room temperature, stirred for 4 h, and then filtered. All volatiles were removed from the filtrate under reduced pressure. The resulting orange solid was washed with pentane (2 × 4 mL) and dried in vacuo. Yield: 123 mg, 370 μmol, 67%.

Single crystals of **3** were obtained by layering a solution of **3** (10 mg, 30 μmol) in THF (1 mL) with Et_2O (1 mL). After 3 days, a crystalline material had formed, which was isolated by filtration.

^{1}H NMR (400 MHz, THF-d_8): δ = 1.77 (m, $n \times 4$H, β-THF), 3.61 (m, $n \times 4$H, α-THF), 5.45 (t, 1H, $^3J_{HH}$ = 8.7 Hz, 5-H), 6.02 (d, 2H, $^3J_{HH}$ = 11.4 Hz, 3-H, 7-H), 6.23 (m, 2H, 4-H, 6-H), 6.74–6.78 (m, 6H, *o*-Ph, *p*-Ph), 7.16–7.20 (m, 4H, *m*-Ph) ppm. ^{13}C NMR (101 MHz, THF-d_8): δ = 26.55 (s, β-THF), 68.39 (s, α-THF), 109.85 (s, 5-C), 112.01 (s, 3-C, 7-C), 119.93 (s, *p*-Ph), 122.49 (s, *o*-Ph), 129.52 (s, *m*-Ph), 132.16 (s, 4-C, 6-C), 157.72 (s, *ipso*-Ph), 162.65 (s, 1-C, 2-C) ppm. Anal. Calc. for $C_{19}H_{15}KN_2{\cdot}(C_4H_8O)_{0.3}$ (332.07 g/mol): C 73.06, H 5.28, N 8.44; found: C 72.73, H 5.15, N 8.73. Residual amounts of THF could not be removed from the isolated compound under reduced pressure. The amount of THF in the isolated compound has to be checked individually for every batch. Values typically ranged from n = 0.1 to n = 0.3 molecules of THF per formula unit.

DOI: 10.1021/acs.organomet.8b00208
Organometallics 2018, 37, 1781–1787

Reaction of H-ATI$^{Ph/Ph}$ with *n*BuLi. The following procedure describes a representative experiment: A solution of *n*BuLi in hexanes (1.6 M, 360 μL) was slowly added to a solution of H-ATI$^{Ph/Ph}$ (150 mg, 0.55 mmol) in Et_2O (3.0 mL) at 0 °C. The reaction mixture was warmed to ambient temperature over a period of 2.5 h, after which all volatiles were removed under reduced pressure. The solid residue was washed with pentane (3 × 3.0 mL) to give an orange solid, which was dried in vacuo. Yield: 51 mg.

^{1}H NMR (400 MHz, C_6D_6): δ = 0.85 (t, 3H, $^3J_{HH}$ = 7.4 Hz, δ-CH_3), 1.21–1.30 (m, 2H, γ-CH_2), 1.43–1.53 (m, 2H, β-CH_2), 2.66 (t, 2H, $^3J_{HH}$ = 7.4 Hz, α-CH_2), 5.76 (dd, 1H, $^3J_{HH}$ = 7.5 Hz, $^4J_{HH}$ = 12.0 Hz, 4-H), 5.86–5.91 (m, 1H, 5-H), 5.99–6.03 (m, 1H, 6-H), 6.22 (d, 2H, $^3J_{HH}$ = 10.0 Hz, 7-H), 6.25 (d, $^3J_{HH}$ = 12.0 Hz, 3-H), 6.65–6.70 (m, *o*-Ph, overlapping with signal due to [Li(ATI$^{Ph/Ph}$)]), 6.87–6.91 (m, 2H, *p*-Ph, overlapping with signal due to [Li(ATI$^{Ph/Ph}$)]), 7.01–7.11 (m, 4H, *m*-Ph) ppm. Resonances due to **1-(Et_2O)$_n$** and Et_2O are not listed. ^{13}C NMR (101 MHz, C_6D_6): δ = 14.18 (s, δ-C), 22.83 (s, γ-C), 30.77 (s, β-C), 36.41 (s, α-C), 121.06 (s, *o*-Ph), 124.65 (s, *p*-Ph), 129.40 (s, 3-C), 130.20 (s, *m*-Ph), 130.48 (s, 5-C), 131.59 (s, 7-C), 132.52 (s, 4-C), 132.66 (s, 6-C), 149.57 (s, *ipso*-Ph), 165 (s, 2-C, detected only in ^{1}H^{13}C-HMBC experiment) ppm. A resonance of the quarternary carbon atom C-1 could not be detected. Resonances due to **1-(Et_2O)$_n$** and Et_2O are not listed. ^{7}Li NMR (194 MHz, C_6D_6): δ = 2.08–3.35 (two broad, overlapping resonances) ppm.

Reaction of H-ATI$^{Ph/Ph}$ with $LiCH_2SiMe_3$. $LiCH_2SiMe_3$ (3.5 mg, 37 μmol) was added to a solution of H-ATI$^{Ph/Ph}$ (5 mg, 18 μmol) in THF-*d*$_8$ (0.5 mL). NMR spectroscopic analysis revealed the formation of a 1:1 mixture of [Li(ATI$^{Ph/Ph}$)(thf)$_n$] and $LiCH_2SiMe_3$. No changes were observed in the ^{1}H NMR spectrum after heating this reaction mixture to 60 °C for 24 h.

Reaction of H-ATI$^{Ph/iPr}$ with *n*BuLi. The following procedure describes a representative experiment: A solution of *n*BuLi in hexanes (1.6 M, 1.11 mL) was slowly added to a solution of H-ATI$^{Ph/iPr}$ (400 mg, 1.68 mmol) in Et_2O (10 mL) at 0 °C. The reaction mixture was warmed to ambient temperature over a period of 2.5 h, after which all volatiles were removed under reduced pressure. The solid residue was washed with pentane (3 × 5.0 mL) to give an orange solid, which was dried in vacuo. Yield: 240 mg, 0.76 mmol, 45%. The product was identified as [Li(ATI$^{Ph/iPr}$)(Et_2O)$_{0.5}$] by NMR spectroscopic analyses.[5a]

■ ASSOCIATED CONTENT

Ⓢ Supporting Information

The Supporting Information is available free of charge on the ACS Publications website at DOI: 10.1021/acs.organomet.8b00208.

Further experimental and computational details, NMR spectra of isolated compounds (PDF)

Cartesian coordinates of compounds investigated by DFT calculations (XYZ)

Accession Codes

CCDC 1822675–1822677 contain the supplementary crystallographic data for this paper. These data can be obtained free of charge via www.ccdc.cam.ac.uk/data_request/cif, or by emailing data_request@ccdc.cam.ac.uk, or by contacting The Cambridge Crystallographic Data Centre, 12 Union Road, Cambridge CB2 1EZ, UK; fax: +44 1223 336033.

■ AUTHOR INFORMATION

Corresponding Author

*E-mail: crispin.lichtenberg@uni-wuerzburg.de.

ORCID

Crispin Lichtenberg: 0000-0002-0176-0939

Notes

The authors declare no competing financial interest.

■ ACKNOWLEDGMENTS

The authors thank Dr. K. Radacki and Dr. R. Dewhurst for helpful discussions, Prof. H. Braunschweig for generous support, and the Fonds der Chemischen Industrie for a doctoral scholarship (A.H.) and a Liebig Fellowship (C.L.).

■ REFERENCES

(1) (a) Hanusa, T. P. *The Lightest Metals: Science and Technology from Lithium to Calcium*; Wiley: Chichester, U.K., 2015. (b) Ruhlandt-Senge, K.; Henderson, K. W.; Andrews, P. C. Alkali Metal Organometallics – Structure and Bonding. In *Comprehensive Organometallic Chemistry III*; Crabtree, R. H., Mingos, D. M. P., Eds.; Elsevier: Amsterdam, 2007; Vol. 2. (c) Hoffmann, D.; Bauer, W.; v. R. Schleyer, P.; Pieper, U.; Stalke, D. *Organometallics* **1993**, *12*, 1193–1200. (d) Schade, C.; von Ragué Schleyer, P. *Adv. Organomet. Chem.* **1987**, *27*, 169–278. (e) Rappoport, Z., Marek, I., Eds. *The Chemistry of Organolithium Compounds*; Wiley: New York, 2004.

(2) For examples of M–C(π) interactions (M = Li, Na, K), see: (a) Gren, C. K.; Hanusa, T. P.; Rheingold, A. L. *Organometallics* **2007**, *26*, 1643–1649. (b) Evans, W. J.; Ansari, M. A.; Khan, S. I. *Organometallics* **1995**, *14*, 558–560. (c) Clark, D. L.; Watkin, J. G.; Huffman, J. C. *Inorg. Chem.* **1992**, *31*, 1554–1556. (d) Kroesen, U.; Knauer, L.; Strohmann, C. *Angew. Chem., Int. Ed.* **2017**, *56*, 6232–6235. (e) Lichtenberg, C.; Spaniol, T. P.; Peckermann, I.; Hanusa, T. P.; Okuda, J. *J. Am. Chem. Soc.* **2013**, *135*, 811–821. (f) Lichtenberg, C.; Viciu, L.; Adelhardt, M.; Sutter, J.; Meyer, K.; de Bruin, B.; Grützmacher, H. *Angew. Chem.* **2015**, *127*, 5858–5863. (g) Also see ref 24.

(3) The tendency of alkali metal cations to interact with delocalized π-electrons increases with increasing atomic number of the alkali metal, e.g., for alkyl and aryl compounds (refs 1c–e and references therein) or for amidinates (ref 4d and references therein).

(4) (a) Fuentes, M. A.; Zabala, A.; Kennedy, A. R.; Mulvey, R. E. *Chem. - Eur. J.* **2016**, *22*, 14968–14978. (b) Davidson, M. G.; Garcia-Vivo, D.; Kennedy, A. R.; Mulvey, R. E.; Robertson, S. D. *Chem. - Eur. J.* **2011**, *17*, 3364–3369. (c) Travieso-Puente, R.; Chang, M.-C.; Otten, E. *Dalton Trans.* **2014**, *43*, 18035–18041. (d) Lichtenberg, C.; Adelhardt, M.; Wörle, M.; Büttner, T.; Meyer, K.; Grützmacher, H. *Organometallics* **2015**, *34*, 3079–3089. (e) Bock, H.; Arad, C.; Näther, C.; Havlas, Z. *Helv. Chim. Acta* **1997**, *80*, 606–620.

(5) (a) Lichtenberg, C. *Organometallics* **2016**, *35*, 894–902. (b) Lichtenberg, C.; Krummenacher, I. *Chem. Commun.* **2016**, *52*, 10044–10046.

(6) For reviews, see: (a) Holm, R. H.; O'Connor, M. J. *The Stereochemistry of Bis-Chelate Metal(II) Complexes in Progress in Inorganic Chemistry*; Lippard, S. J., Ed.; Wiley: New York, 1971; Vol. *14*, pp 241–401. (b) Dias, H. V. R.; Wang, Z.; Jin, W. *Coord. Chem. Rev.* **1998**, *176*, 67–86. (c) Roesky, P. W. *Chem. Soc. Rev.* **2000**, *29*, 335–345. (d) Roesky, P. W. *Z. Anorg. Allg. Chem.* **2003**, *629*, 1881–1894. (e) Kühl, O. *Coord. Chem. Rev.* **2004**, *248*, 411–427. (f) Jenter, J.; Lühl, A.; Roesky, P. W.; Blechert, S. *J. Organomet. Chem.* **2011**, *696*, 406–418. (g) Hanft, A.; Lichtenberg, C.*Eur. J. Inorg. Chem.* **2018**, DOI: 10.1002/ejic.201800465.

(7) For example: (a) Datta, S.; Roesky, P. W.; Blechert, S. *Organometallics* **2007**, *26*, 4392–4394. (b) Bürgstein, M. R.; Berberich, H.; Roesky, P. W. *Organometallics* **1998**, *17*, 1452–1454. (c) Dochnahl, M.; Löhnwitz, K.; Pissarek, J.-W.; Biyikal, M.; Schulz, S. R.; Schön, S.; Meyer, N.; Roesky, P. W.; Blechert, S. *Chem. - Eur. J.* **2007**, *13*, 6654–6666. (d) Dochnahl, M.; Löhnwitz, K.; Pissarek, J.-W.; Roesky, P. W.; Blechert, S. *Dalton Trans.* **2008**, 2844–2848.

(8) For example: (a) Korolev, A. V.; Guzei, I. A.; Jordan, R. F. *J. Am. Chem. Soc.* **1999**, *121*, 11605–11606. (b) Korolev, A. V.; Ihara, E.; Guzei, I. A.; Young, V. G.; Jordan, R. F. *J. Am. Chem. Soc.* **2001**, *123*, 8291–8309.

(9) Hanft, A.; Jürgensen, M.; Bertermann, R.; Lichtenberg, C.*ChemCatChem* **2018**, DOI: 10.1002/cctc.201800580.

(10) For example: (a) Yadav, D.; Siwatch, R. K.; Sinhababu, S.; Nagendran, S. *Inorg. Chem.* **2014**, *53*, 600–606. (b) Siwatch, R. K.;

Kundu, S.; Kumar, D.; Nagendran, S. *Organometallics* **2011**, *30*, 1998–2005. (c) Karwasara, S.; Yadav, D.; Jha, C. K.; Rajaraman, G.; Nagendran, S. *Chem. Commun.* **2015**, *51*, 4310–4313. (d) Sinhababu, S.; Yadav, D.; Karwasara, S.; Sharma, M. K.; Mukherjee, G.; Rajaraman, G.; Nagendran, S. *Angew. Chem., Int. Ed.* **2016**, *55*, 7742–7746.

(11) Pittracher, M.; Frisch, U.; Kopacka, H.; Wurst, K.; Müller, T.; Oehninger, L.; Ott, I.; Wuttke, E.; Scheerer, S.; Winter, R. F.; Bildstein, B. *Organometallics* **2014**, *33*, 1630–1643.

(12) Hanft, A.; Lichtenberg, C. *Dalton Trans.* **2018**, DOI: 10.1039/C8DT01019F.

(13) The potential π-acceptor character of the α-amino-imine functionality in ATIs has not yet been investigated in detail.

(14) The notation used in Scheme 1 and throughout the paper is slightly simplified for the sake of readability. Formal coordination modes are **A**: κ^2N,N'; **B**: μ_2-(M-κ^2N,N')(M′-κ^2N,N'); **C**: μ_2-(M-κ^2N,N')(M′-$\kappa^5C,C',C'',C''',C''''$); **D**: μ_2-(M-κ^2N,N')(M′-κ^3C,C',C''); **E**: μ_3-(M-κ^2N,N')(M′-κ^2N,N')(M″-$\kappa^5C,C',C'',C''',C''''$).

(15) For the synthesis of the H-ATI$^{Ph/Ph}$ ligand, see: (a) Reference 7c. (b) Claramunt, R. M.; Sanz, D.; Pérez-Torralba, M.; Pinilla, E.; Torres, M. R.; Elguero, J. *Eur. J. Org. Chem.* **2004**, *2004*, 4452–4466.

(16) (a) Dias, H. V. R.; Jin, W.; Wang, Z. *Inorg. Chem.* **1996**, *35*, 6074–6079. (b) Delpech, F.; Guzei, I. A.; Jordan, R. F. *Organometallics* **2002**, *21*, 1167–1176.

(17) (a) Richter, W. F.; Hartke, K.; Massa, W.; Münninghoff, G. *Chem. Ber.* **1989**, *122*, 1133–1137. (b) Löhnwitz, K.; Molski, M. J.; Lühl, A.; Roesky, P. W.; Dochnahl, M.; Blechert, S. *Eur. J. Inorg. Chem.* **2009**, *2009*, 1369–1375. (c) Dochnahl, M.; Löhnwitz, K.; Lühl, A.; Pissarek, J. W.; Biyikal, M.; Roesky, P. W.; Blechert, S. *Organometallics* **2010**, *29*, 2637–2645.

(18) Kirin, V.; Roesky, P. W. *Z. Anorg. Allg. Chem.* **2004**, *630*, 466–469.

(19) Korolev, A. V.; Delpech, F.; Dagorne, S.; Guzei, I. A.; Jordan, R. F. *Organometallics* **2001**, *20*, 3367–3369.

(20) Even the reaction of H-ATI$^{Ph/Ph}$ with 2 equivalents of $LiCH_2SiMe_3$ in THF gave a 1:1 mixture of Li(ATI$^{Ph/Ph}$) and $LiCH_2SiMe_3$ at 23 °C due to the lower nucleophilicity of this lithium base as compared to *n*BuLi. No further reaction occurred, when the reaction mixture was heated to 60 °C for 24 h.

(21) (a) Roesky, P. W. *Chem. Ber.* **1997**, *130*, 859–862. (b) Meiners, J.; Herrmann, J.-S.; Roesky, P. W. *Inorg. Chem.* **2007**, *46*, 4599–4604.

(22) Entirely donor ligand free [Li(ATI$^{Ph/Ph}$)] is only poorly soluble in weakly coordinating solvents such as C_6D_6, so that only [Li(ATI$^{Ph/Ph}$)(thf)$_n$] could be analyzed by solution NMR spectroscopy.

(23) (a) Hellmann, K. W.; Galka, C.; Gade, L. H.; Kottke, T.; Stalke, D. *Chem. Commun.* **1998**, 549–550. (b) Schiemenz, B.; Power, P. P. *Angew. Chem., Int. Ed. Engl.* **1996**, *35*, 2150–2152. (c) Ruhlandt-Senge, K.; Ellison, J. J.; Wehmschulte, R. J.; Pauer, F.; Power, P. P. *J. Am. Chem. Soc.* **1993**, *115*, 11353–11357. (d) Kurz, S.; Hey-Hawkins, E. *Organometallics* **1992**, *11*, 2729–2732.

(24) A cutoff value of 3.57 Å has been suggested for K–C(π) contacts: Torvisco, A.; Decker, K.; Uhlig, F.; Ruhlandt-Senge, K. *Inorg. Chem.* **2009**, *48*, 11459–11465.

(25) In NBO analyses, deletion energies are used to assess bonding energies by deleting specific elements of the Fock matrix. The energy obtained after rediagonalization and applying SCF routines is then compared to that obtained with the original matrix: Weinhold, F.; Landis, C. R. *Valency and Bonding: A Natural Bond Orbital Donor-Acceptor Perspective*; Cambridge University Press: Cambridge, U.K., 2005.

(26) The reaction of [Na(diglyme)]$^+$ with **5-CF$_3$/CF$_3$** to give **7-CF$_3$/CF$_3$** with both Na atoms in the *N,N* binding pocket of the ATI ligand is clearly exothermal ($\Delta H = -177$ kJ·mol^{-1}) and exergonic ($\Delta G = -123$ kJ·mol^{-1}).

(27) For full reference, see the Supporting Information.

(28) Hariharan, P. C.; Pople, J. A. *Theor. Chim. Acta* **1973**, *28*, 213–222.

(29) (a) McLean, A. D.; Chandler, G. S. *J. Chem. Phys.* **1980**, *72*, 5639–5648. (b) Krishnan, R.; Binkley, J. S.; Seeger, R.; Pople, J. A. *J. Chem. Phys.* **1980**, *72*, 650–654.

(30) Becke, A. D. *J. Chem. Phys.* **1993**, *98*, 5648–5652.

(31) Marenich, A. V.; Cramer, C. J.; Truhlar, D. G. *J. Phys. Chem. B* **2009**, *113*, 6378–6396.

(32) Grimme, S.; Antony, J.; Ehrlich, S.; Krieg, H. *J. Chem. Phys.* **2010**, *132*, 154104–154119.

VII Alkali Metal Aminotroponiminates: Selectivities and Equilibria in Reversible Radical Coupling of Delocalized π-Electron Systems

Anna Hanft, Ivo Krummenacher, Crispin Lichtenberg

Vervielfältigt aus Referenz:

Chem. Eur. J. **2019**, *25*, 11883-11891.[66]

DOI:10.1002/chem.201901962

mit der Erlaubnis von John Wiley and Sons.

ChemPubSoc Europe
DOI: 10.1002/chem.201901962
CHEMISTRY
A European Journal
Full Paper

Alkali Metals |*Hot Paper*|

Alkali-Metal Aminotroponiminates: Selectivities and Equilibria in Reversible Radical Coupling of Delocalized π-Electron Systems

Anna Hanft, Ivo Krummenacher, and Crispin Lichtenberg*[a]

Abstract: Aminotroponiminates (ATIs) have recently been shown to belong to the growing class of redox-active ligands. The choice of the metal center allowed to switch between reversible electron transfer (M=Rh) and reductively induced dimerization (M=Na). Here, we investigate if the reductively induced dimerization of ATIs is a more general phenomenon for their alkali-metal complexes. Lithium ATI complexes are shown to undergo reductively induced dimerizations, which are equilibrium reactions and chemically reversible. The choice of the metal center (Li vs. Na), the substitution pattern at the nitrogen atoms of the ATI ligands, and the solvent critically influence the regioselectivity and diastereoselectivity of the radical-dimerization reactions. Potassium ATIs are shown to be susceptible to side reactions, more specifically a reduction accompanied by hydrogen-atom transfer. Products and intermediates of the reductively induced dimerizations were characterized by techniques including NMR and EPR spectroscopy, cyclic voltammetry, DFT calculations, single-crystal X-ray diffraction, and mass spectrometry.

Introduction

Organic and organometallic carbon-centered radicals are key species in various fields of synthetic chemistry, including organic radical synthesis, radical polymerization of olefins, and one-electron-transfer reagents. One strategy to stabilize these compounds and to control their reactivity is to aim for a delocalization of the spin density. This approach has been exploited in the investigation of radical species that are obtained by reduction of cyclic conjugated π-electron systems. Examples include naphthalene, anthracene, tropylium ions, azulene, guaiazulene, and related compounds, from which persistent and in special cases even isolable radicals can be generated.[1] These species can be applied as reducing agents and electron-transfer catalysts with adjustable redox potentials that operate under homogeneous conditions (common examples being naphthalene and anthracene radical anions).[2] A promising, but yet underdeveloped strategy targets the exploitation of bond-forming events from such delocalized radical species by radical coupling. A range of case studies has been reported in which radicals that are generated by reduction of cyclic conjugated π-electron systems undergo dimerization with C–C bond formation (Scheme 1). Prominent examples include the dimerization of radicals generated from benzene,[3] tropylium ions,[4] azulene,[5] and acenaphthylene[6] (derivatives).

The latter cases are especially noteworthy because chiral *ansa*-metallocene complexes that are competent as olefin polymerization catalysts can be synthesized in a single step (Scheme 1 b,c).[5–7]

The stabilization of radicals by delocalization of spin density through a conjugated π-electron system helps to minimize side reactions of otherwise highly reactive radical compounds, thus it can be a powerful strategy to increase chemoselectivity. In contrast, controlling the regioselectivity of reactions involving delocalized radical species becomes a major challenge,

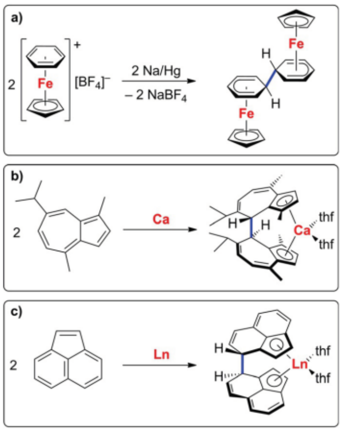

Scheme 1. Radical dimerization reactions involving cyclic conjugated π-electron systems that proceed with formation of a new C–C bond (highlighted in blue). Ln = Sm, Yb.

---

[a] A. Hanft, Dr. I. Krummenacher, Dr. C. Lichtenberg
Institute of Inorganic Chemistry, Julius-Maximilians-University Würzburg
Am Hubland, 97074 Würzburg (Germany)
E-mail: crispin.lichtenberg@uni-wuerzburg.de

Supporting information and the ORCID identification number(s) for the author(s) of this article can be found under: https://doi.org/10.1002/chem.201901962.

because every atom that carries a significant amount of spin density may be considered as a potentially reactive site. In the dimerization of radicals that are delocalized through a cyclic conjugated π-electron system, the number of regioisomers that may be formed equals $0.5\cdot[n\cdot(n+1)]$ with n being the number of chemically inequivalent reactive sites (for details see the Supporting Information). In addition, two diastereomeric forms of each regioisomer may be formed: the *R,S* (*meso*) compound or a racemic mixture of the *R,R* and the *S,S* compound, which sums up to a total number of $n\cdot(n+1)$ different compounds in the above-mentioned example of a radical dimerization.

In practice, some dimerizations of delocalized radical species indeed yield a large number of different isomers, which sometimes cannot be separated due to their similar physical and physicochemical properties.[5a,e,8] In contrast, there are also cases which proceed with remarkable selectivity despite the presence of a larger number of chemically inequivalent potentially reactive sites.[4b,5c–e,6a,b,d] In some of these reports, possible reasons for the observed selectivities have not been discussed in detail.[5a,6a] In other standalone case studies, steric protection and reversibility of radical recombination have been discussed as possible driving forces for unexpectedly high selectivities.[4b,5d,9] However, contributions towards a more systematic investigation of the reasons that influence regio- and diastereoselectivities in the dimerization of delocalized radical species under reducing conditions have not been reported to date.

We recently demonstrated that aminotroponiminate (ATI) complexes can undergo a one-electron reduction with the extra electron being delocalized in the π-electron system of the ligand (Scheme 2).[10,11] Depending on the choice of the metal atom, reversible electron transfer (M = Rh) or dimerization of the radical species is observed (M = Na). Remarkably, the reductively induced dimerization of ATIs was found to be chemically reversible.

We now set out to investigate the general validity of the (reversible) reductively induced dimerization of alkali-metal ATIs and the factors influencing the selectivity of these transformations.

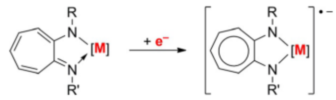

Scheme 2. Generation of an ATI radical anion by one-electron reduction of an ATI complex.

Results and Discussion

Reductively induced dimerizations of lithium ATIs

The regio- and diastereoselective reductively induced dimerization of the sodium ATI complex [Na(ATI$^{Ph/iPr}$)(thf)] (**1-Na**) to give the coupling product ***rac*-2-Na** has recently been reported (Scheme 3 a). The C–C bond formation takes place through the 7/7′-positions and a racemic mixture of the *R,R* and *S,S* isomers is formed exclusively, whereas the *meso* (*R,S*) compound is not observed. To test if the reductively induced dimerization is a more general reaction pathway for alkali-metal ATIs, the analogous lithium compound [Li(ATI$^{Ph/iPr}$)] (**1-Li**) was reacted with elemental lithium in dimethoxyethane (DME) at ambient temperature (Scheme 3 b).[12] Indeed, the product of a reductively induced dimerization was isolated from this reaction as a mixture of the *rac*- and the *meso*-form, ***rac*-2-Li** and ***meso*-2-Li** (3.0:2.0). Remarkably, the selective C–C bond formation does not take place through the 7/7′-position in this case, but through the 4/4′-position instead. Thus, the formal exchange of Na for Li atoms in these reactions maintains the chemoselectivity, but switches the regioselectivity (from 100 % 7/7′ to 100 % 4/4′), and also influences the diastereoselectivity.[13] The mixture of ***rac*/*meso*-2-Li** was obtained in the form of an air-sensitive slightly yellow solid, which is stable in THF at 23 °C,[14] but decomposes upon heating to 60 °C. In the NMR spectroscopic analysis of **2-Li**, the resonances of the CH group at

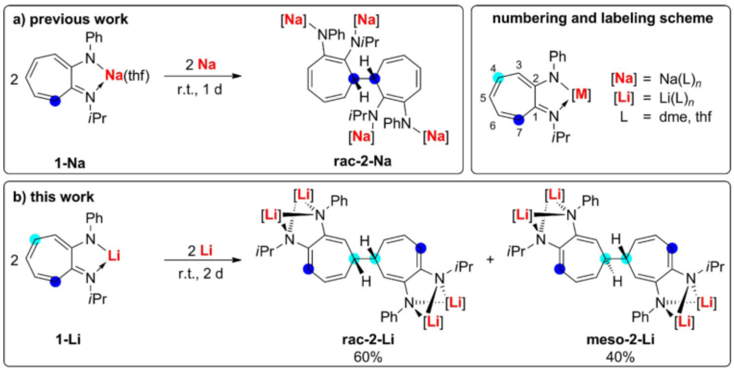

Scheme 3. Reductive dimerization of sodium ATI complex [Na(ATI$^{Ph/iPr}$)(thf)] (a, previous work) and its lithium analog [Li(ATI$^{Ph/iPr}$)] (b, this work); dme = dimethoxyethane.

which the C–C coupling takes place serve as a valuable spectroscopic handle, because the resonances for the two diastereomers are baseline separated and show characteristic chemical shifts (^{1}H NMR: $\delta = 2.16$ (*rac*), 2.32 ppm (*meso*); ^{13}C NMR: 42.3 (*rac*), 42.5 ppm (*meso*)). This allows for the ^{1}H NMR spectroscopic determination of the ***rac*-2-Li** to ***meso*-2-Li** ratio.

Isolated samples of the two diastereomers ***rac*-2-Li** and ***meso*-2-Li** were obtained in small amounts by careful crystallization from DME/pentane and THF/pentane (for details see the Experimental Section). Single-crystal X-ray diffraction analysis of these samples allowed for the unequivocal assignment of NMR spectroscopic resonances to each of the two isomers. Compounds ***rac*-2-Li** and ***meso*-2-Li** crystallized in the orthorhombic space group $P2_12_12$ with $Z = 2$ and the monoclinic space group $P2_1/n$ with $Z = 2$, respectively (Figure 1). The racemic mixture of the *R,R* and the *S,S* isomer, ***rac*-2-Li**, crystallized with one chelating DME ligand coordinated to each Li center, *rac*-[Li$_4$(di-ATI$^{Ph/iPr}$)(dme)$_4$] (Figure 1 a). Monomeric subunits of ***rac*-2-Li** are crystallographically related by a twofold screw axis, which runs through the C4–C4′ bond and is perpendicular to the mean plane defined by the atoms H4,C4,C4′,H4′. The nitrogen atoms of the di-ATI ligand adopt a bridging coordination mode between two Li atoms, as previously observed for ATI complexes of lithium and potassium.[10,11,15] This results in a distorted-tetrahedral coordination geometry around Li1 and Li2, the distortion being due to the chelating nature of the ligands (O-Li-O 81–85°, N-Li-N 79–82°, O-Li-N 117–134°).

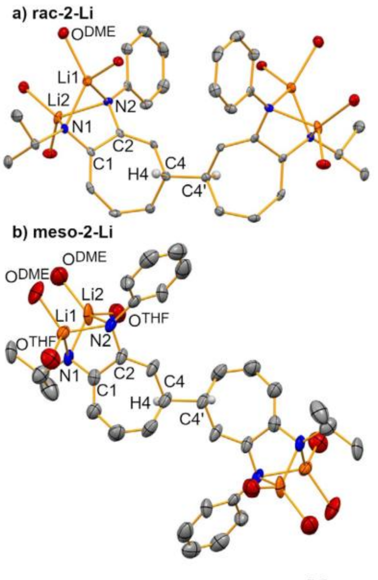

Figure 1. Molecular structures of *rac*- and *meso*-[Li$_4$(di-ATI$^{Ph/iPr}$)(thf)$_n$(dme)$_m$] (a: ***rac*-2-Li**, $n = 0$, $m = 4$; b: ***meso*-2-Li**, $n = 4$, $m = 2$) in the solid state. Displacement ellipsoids are shown at the 50 % probability level. Hydrogen atoms except for H4 and carbon atoms of THF and DME ligands are omitted for clarity. Selected bond lengths (Å) and angles (°): **a)** Li1–N1 1.994(8), Li1–N2 1.994(9), Li1–O^{DME} 1.971(9)–2.030(8), Li2–N1 2.087(9), Li2–N2 2.006(9), Li2–O^{DME} 1.975(9)–2.014(8), N1–C1 1.377(6), N2–C2 1.409(6); O^{DME}-Li1-O^{DME} 81.4(3), O^{DME}-Li1-N1/2 120.2(4)–128.2(4), N1-Li1-N2 81.7(3), O^{DME}-Li2-O^{DME} 85.3(3), O^{DME}-Li2-N1/2 116.5(4)–134.4(4), N1-Li2-N2 79.2(3). **b)** Bond lengths and angles are not discussed (see text); for structure of *meso*-[Li$_4$(di-ATI$^{Ph/iPr}$)(tmeda)$_3$] see the Supporting Information.

The Li–N bonds in ***rac*-2-Li** (1.99–2.09 Å) are on average shorter than those in lithium complexes of nonreduced ATI ligands in a bridging coordination mode (2.04–2.16 Å),[15b] reflecting the larger negative charge of the reduced species. The reductive C–C coupling of two ATI ligands strongly decreases the delocalization of π-electron density in the C_7N_2 core units. As a result, the C_7 backbones in ***rac*-2-Li** show a stronger alternation between smaller and larger C–C distances than those of nonreduced ATI ligands.[10b,11,16a] In agreement with these observations, the C1/2–N1/2 bonds (1.38–1.41 Å) are longer than typically observed in nonreduced ATI complexes.[10b,11,16a] Despite ***rac*-2-Li** crystallizing in a chiral space group (see above), the determination of its absolute stereochemistry by X-ray diffraction was not successful, because the compound proved to be a weak anomalous scatterer.

Crystals of ***meso*-2-Li** showed low diffraction intensities at high diffraction angles; therefore, bond lengths and angles are not discussed, but the diffraction data serve as a proof of connectivity (Figure 1 b). In the presence of *N,N,N′,N′*-tetramethylethylenediamine (tmeda), samples of the analogous species *meso*-[Li$_4$(di-ATI$^{Ph/iPr}$)(thf)$_2$(tmeda)$_3$] suitable for single-crystal X-ray analysis were obtained (for a more detailed discussion see the Supporting Information).

As a next step, the influence of the substituents at the nitrogen atoms of the ATI ligands on the feasibility of reductively induced dimerizations was investigated. Given that small changes in the properties of the central atom (Na vs. Li) had a dramatic impact on the regioselectivity of this type of reaction, only a small variation in the characteristics of the substituents was targeted. Thus, [Li(ATI$^{iPr/iPr}$)] (**3-Li**)[16] was chosen as a substrate, in which one of the phenyl groups is exchanged for an *iso*-propyl group, when compared with **1-Li**. Reduction of **3-Li** with lithium gave the dimerization product **4-Li** in quantitative spectroscopic and was isolated as a pale-yellow solid.[12] In this case, the C–C bond formation occurs in 4/4′-position exclusively (Scheme 4).[17] Again, the diastereoselectivity of the reaction can be determined by NMR spectroscopy, using the resonances of the CH group in 4-position as a diagnostic tool (^{1}H NMR: $\delta = 2.19$ (*rac*), 2.23 ppm (*meso*); ^{13}C NMR: $\delta = 43.15$ (*rac*), 43.43 ppm (*meso*)). Reaction monitoring with NMR spectroscopy revealed a ***rac*-4-Li** to ***meso*-4-Li** ratio of 1:1 when using polar solvents such as THF. This ratio can be modified to 13:1 in favor of the *meso*-isomer, when using a less polar solvent mixture such as benzene/THF (*V/V* 6:1; small amounts of THF are needed to dissolve the starting material **3-Li** and the product, for details see the Experimental Section). From reactions in THF (initially giving a ratio of *rac*/*meso* = 1:1), ***meso*-4-Li** was isolated in 41 % yield by crystallization over a period of 2 d. Surprisingly, pure ***meso*-4-Li** was isolated in 71 % yield from samples that originally showed a *rac*/*meso* ratio of 1:1 after prolonged crystallization (14 d). Thus, a very slow isomerization of **4-Li** takes place at 23 °C. To further support this hypothesis, a THF solution of *rac*-enriched **4-Li** was heated to 60 °C. Under

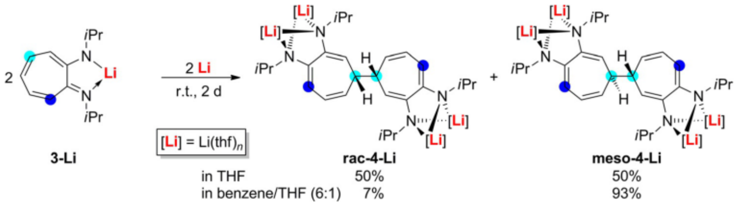

Scheme 4. Reductive dimerization of [Li(ATI$^{iPr/iPr}$)].

these conditions, the *rac*/*meso* ratio changed from 2.5:1.0 to 1.0:1.3 over the course of 1 d, as determined by ^{1}H NMR spectroscopy along with slow decomposition of **4-Li**.[18]

Single crystals suitable for X-ray diffraction analysis of both diastereomers, ***rac*-4-Li** and ***meso*-4-Li**, were obtained. In addition, preparative separation of the *meso*-compound was achieved by fractional crystallization, thus allowing for the unequivocal assignment of the spectroscopic signatures of both diastereomers. Compounds ***rac*-4-Li** and ***meso*-4-Li** crystallized in the tetragonal space group $I4_1/a$ with $Z=8$ and the triclinic space group $P\bar{1}$ with $Z=2$, respectively (Figure 2). In the *meso*-isomer, two of the lithium atoms, Li1, Li1′, bear only one instead of two THF ligands, resulting in a somewhat unusual distorted trigonal-planar coordination geometry (N-Li-N 83°, O-Li-N 126–150°). Other than that, bonding parameters in ***rac*-4-Li** and ***meso*-4-Li** are similar to those of the related species ***rac*-2-Li**, which have been discussed above (for detailed discussion, see the Supporting Information).

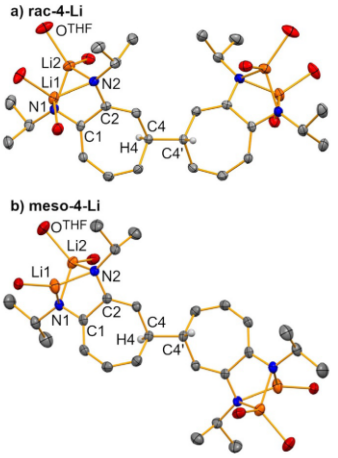

Figure 2. Molecular structures of *rac*- and *meso*-[Li$_4$(di-ATI$^{iPr/iPr}$)(thf)$_n$] (a: ***rac*-4-Li**, $n=8$; b: ***meso*-4-Li**, $n=6$) in the solid state. Displacement ellipsoids are shown at the 50% probability level. Hydrogen atoms except for H4, carbon atoms of THF ligands, and one set of split positions of a disordered thf ligand at Li1 in ***meso*-4-Li** are omitted for clarity. The asymmetric unit of ***meso*-4-Li** contains two chemically identical, but crystallographically independent molecules of ***meso*-4-Li**, only one of which is discussed. Selected bond lengths (Å) and angles (°): **a)** Li1–N1 2.115(4), Li1–N2 1.967(4), Li1–O^{THF} 1.949(4)–2.000(4), Li2–N1 1.986(4), Li2–N2 2.065(4), Li2–O^{THF} 1.987(4)–2.007(4), N1–C1 1.376(3), N2–C2 1.393(3); O^{THF}-Li1-O^{THF} 96.03(17), O^{THF}-Li1-N1/2 110.89(18)–127.3(2), N1-Li1-N2 79.59(14), O^{THF}-Li2-O^{THF} 96.71(17), O^{THF}-Li2-N1/2 108.36(18)–128.1(2), N1-Li2-N2 80.39(15). **b)** Li1–N1 2.030(5), Li1–N2 1.937(4), Li1–O^{THF} 1.91(2), Li2–N1 2.002(5), Li2–N2 2.071(4), Li2–O^{THF} 1.976(4)–2.016(4), N1–C1 1.388(3), N2–C2 1.399(3); O^{THF}-Li1-N1/2 125.5(7)–149.7(7), N1-Li1-N2 82.61(17), O^{THF}-Li2-O^{THF} 105.81(19), O^{THF}-Li2-N1/2 111.0(2)–123.8(2), N1-Li2-N2 80.01(16).

Reduction of sodium and potassium ATIs.

^{1}H NMR spectroscopic experiments concerning the reductive dimerization of [Na(ATI$^{iPr/iPr}$)] (**Na-3**)[19] with sodium suggest that C–C coupling also takes place at the 4/4′-position. However, attempts to obtain full spectroscopic data or to isolate the product of this reaction were hampered by its high sensitivity and very poor solubility in common aprotic solvents. Attempts to reduce potassium species [K(ATI$^{Ph/iPr}$)] and [K(ATI$^{iPr/iPr}$)] with elemental potassium or KC$_8$ led to complex product mixtures. Trace amounts of decomposition product **5** were obtained and unambiguously identified by single-crystal X-ray diffraction analysis (Scheme 5, for details see the Supporting Information). Compound **5** is a 1:1 adduct of starting material [K(ATI$^{Ph/iPr}$)] and its (formally) hydrogenated derivative. The latter is suggested to result from twofold reduction and protonation of [K(ATI$^{Ph/iPr}$)], which is in line with a very high reactivity and sensitivity of the targeted radical species [K(ATI$^{Ph/iPr}$)]$^{\bullet}$.

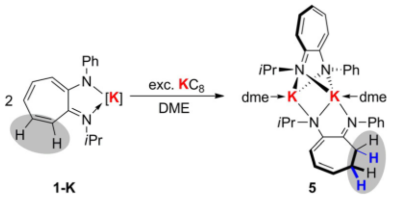

Scheme 5. Side reaction in the reduction of potassium ATI **1-K** to give **5**. [K] = K(thf)$_{0.5}$.

EPR spectroscopy and DFT calculations

To detect potential radical intermediates in the reductively induced dimerization of **1-Li** and **3-Li**, the reactions were monitored by EPR spectroscopy. Indeed, an isotropic resonance ascribed to a single radical compound was detected during the reduction of **1-Li** with Li ($g_{iso}=2.003$). The spectrum resembles that obtained for the reduction of **1-Na** with Na, but is not as well resolved, precluding the detailed analysis of hyperfine splittings (for details see the Supporting Information).[10a]

In contrast, the EPR spectrum obtained from monitoring the reduction of **3-Li** with lithium in DME showed an isotropic signal with $g_{iso}=2.003$ and distinctly resolved hyperfine splittings (Figure 3). Simulation of the experimental spectrum together with DFT calculations (see below) revealed coupling of the unpaired electron with all protons of the ATI ligand backbone as well as both nitrogen atoms and both *CH*Me$_2$ groups. In particular, one very large coupling constant of $a(^1H, 2H)=22.7$ MHz suggests that the spin density is predominantly located at two magnetically equivalent positions of the C$_7$ ring (C4,C6-position).[20] A second medium coupling constant of $a(^1H, 1H)=11.0$ MHz hints at additional substantial spin density at a single CH group, that is most likely in the C5-position. In addition, smaller coupling constants of $a(^1H, 2H$; C3,C7-position$)=3.80$, $a(^{14}N, 2N)=1.87$, and $a(^1H, 2H$; $2\times$*CH*Me$_2)=0.93$ MHz were obtained from the simulation. Importantly, solutions of isolated samples of **2-Li** and **4-Li** in THF were found to show very weak EPR signals close to the detection limit.[21] The signal detected from solutions of **4-Li** was approximately twice as intensive as that obtained from **2-Li**. Together with the experiments on the isomerization of racemic mixtures of **4-Li** (see above), this indicates the radical dimerization of [Li$_2$(ATI$^{iPr/iPr}$)(L)$_n$]$^\bullet$ to be an equilibrium reaction that is far on the product (i.e. dimer) side at 23 °C in solution (L = thf, dme).[22]

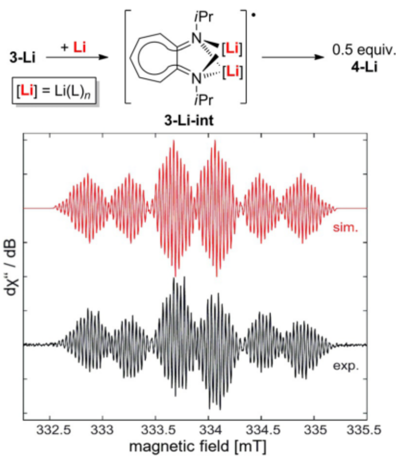

Figure 3. EPR spectrum of suggested intermediate [Li$_2$(ATI$^{iPr/iPr}$)(L)$_n$]$^\bullet$ (**3-Li-int**) obtained by in situ reduction of [Li(ATI$^{iPr/iPr}$)] (**3-Li**) with Li in DME at 23 °C; L = dme.

The molecular geometries of potential radical intermediates were optimized using DFT calculations (for details, see the Experimental Section and the Supporting Information). In these calculations, the coordination spheres of the metal centers were saturated by THF ligands. Although bonding between the π-electron cloud of the C$_7$ ligand backbone and the metal center plays an important role in diamagnetic alkali-metal ATIs,[10b,11a,15a,19] DFT calculations suggest that this is not the case for the radical intermediates discussed in this work (for details see the Supporting Information). In agreement with the results from EPR spectroscopy, the spin density in the calculated radical intermediates **1-Li-int** and **3-Li-int** is delocalized through the π-electron system of the ATI ligands (Figure 4, Table 1). The unsymmetrical substitution pattern of **1-Li-int** induces an unsymmetrical distribution of spin density over the C$_7$N$_2$ framework. Somewhat counterintuitively, only one of the two nitrogen atoms bears significant spin density, as previously observed for the sodium analog, [Na$_2$(ATI$^{Ph/iPr}$)(thf)$_4$]$^\bullet$ (**1-Na-int**).[10a] The highest spin density is located at the C2 carbon atom bearing the NPh substituent, but this position can be expected not to be relevant for effective radical dimerization for steric reasons.[23] Out of the five CH groups in the ATI ligand backbone which should be accessible for radical coupling (C3–7), one shows a significantly higher spin density than the others. This is exactly the 4-position at which the C–C bond formation of the reductively induced dimerization was exclusively observed. In the radical species **3-Li-int**, the spin density distribution shows an apparent C_{2v} symmetry (in agreement

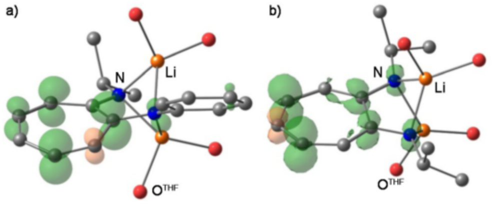

Figure 4. Spin-density plots of [Li$_2$(ATI$^{Ph/iPr}$)(L)$_n$]$^\bullet$ (**1-Li-int**) (a) and [Li$_2$(ATI$^{iPr/iPr}$)(L)$_n$] (**3-Li-int**) (b) for L = thf, $n=2$. Carbon atoms of thf ligands and hydrogen atoms are omitted for clarity; positive and negative spin density shown in green and orange, respectively, at an iso-value of 0.008.

Table 1. Calculated spin densities of **1-Li-int**, **3-Li-int**, and **1-Na-int** at individual positions of the C$_7$N$_2$ backbone. Highest spin density of sterically accessible carbon atom (C3-7) is printed in bold. Position at which C–C coupling was experimentally observed is underlined.

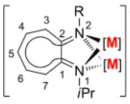

1-Li-int: [M] = Li(thf)$_2$; R = Ph
3-Li-int: [M] = Li(thf)$_2$; R = *i*Pr
1-Na-int: [M] = Na(thf)$_2$; R = Ph

	1-Li-int	**3-Li-int**	**1-Na-int**
N1	0.00	0.07	0.00
N2	0.04	0.07	0.04
C1	−0.05	0.11	−0.08
C2	0.39	0.13	0.42
C3	−0.17	−0.01	−0.14
C4	**0.36**	**0.41**	**0.29**
C5	−0.04	−0.18	0.06
C6	0.14	**0.40**	0.04
C7	0.22	0.01	**0.29**

with the apparent symmetry of the symmetrically substituted ATI ligand in this molecule). The spin-density distribution within the C_7N_2 unit of **3-Li-int** clearly differs from that observed for **1-Li-int**: The largest share of the spin density is localized at the chemically equivalent 4- and 6-position, at which the reductively induced C–C coupling was experimentally observed (Table 1). Minor contributions to the overall spin density were found at carbon atoms in the 1-, 2-, and 5-position. Altogether, there is an excellent agreement between the sterically accessible position with highest spin density in suggested intermediates **1-Li-int** and **3-Li-int** and the experimentally observed position of C–C coupling in their reductively induced dimerizations. This prompted us to comparatively analyze the spin density distribution in the previously reported intermediate **1-Na-int**, which undergoes reductive C–C coupling in the 7/7′-position. Indeed, the spin density in the 4-position is smaller and that in the 7-position is larger than those in the lithium analog **1-Li-int** (Table 1). This corroborates the significant impact of the alkali metal in the N,N-binding pocket of the ATI ligand on the spin density distribution in the radical intermediate. Additional calculations on related ATI radical species with and without alkali-metal ions in different coordination modes further support these findings (Supporting Information). The fact that **1-Na-int** selectively coupled through the 7-position, although the spin density in the 4- and 7-position are equally high, suggests that other factors such as aggregation phenomena of radical species prior to coupling events may also play an important role.

The overall thermodynamics of the ATI radical-dimerization reactions are significantly affected by the choice of the central atoms and the ligand substitution patterns. DFT calculations together with experimental observations indicate that dimerizations are more exergonic for Na than for Li complexes. Exchanging one *i*Pr substituent at nitrogen for a Ph group also increases the exergonic character of these reactions (for details see the Supporting Information). This results in an equilibrium reaction for the radical dimerization of $[Li_2(ATI^{iPr/iPr})(thf)_2]^{\bullet}$ (**3-Li-int**), which is far on the dimer side at ambient temperature in THF solution.

Oxidatively induced C–C bond cleavage and cyclic voltammetry

The dimerization products **2-Li** and **4-Li** were reacted with oxidizing agents such as $AgBF_4$, because previously reported **2-Na** underwent clean oxidative C–C bond cleavage to regenerate starting material **1-Na** (Scheme 6). For compound **2-Li**, this oxidation resulted in quantitative formation of starting material **1-Li** (Scheme 6). In the case of **4-Li**, starting material **3-Li** was generated as the only THF-soluble species according to ^1H NMR spectroscopy. Using resonances of the deuterated solvent as an internal reference, however, indicated a spectroscopic yield of only 35 % at full conversion, suggesting the formation of insoluble side products due to unselective oxidation or complex formation with $AgBF_4$ (Scheme 6).

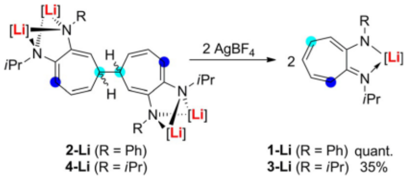

Scheme 6. Oxidatively induced C–C bond cleavage in compounds **2-Li** and **4-Li**. [Li] = Li(solv)$_n$.

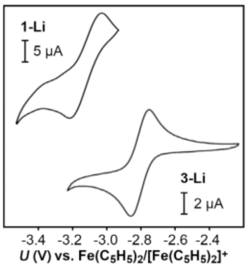

Figure 5. Cyclic voltammograms of **1-Li** and **3-Li** in THF/ 0.1 M $[nBu_4N][PF_6]$ at 23 °C with a scan rate of 250 mV s^{-1}.

Compounds **1-Li** and **3-Li** were further investigated by cyclic voltammetry (CV) in THF/ 0.1 M $[nBu_4N][PF_6]$ at 23 °C (Figure 5, for details, see the Supporting Information). A partially reversible redox event was detected for **1-Li** at −3.23 V (vs. Fc/Fc$^+$, Fc = ferrocene), indicating that the radical dimerization is relevant under the conditions of the CV experiment.

Compound **3-Li** showed a quasi-reversible redox event at −2.81 V (vs. Fc/Fc$^+$), which is in agreement with a slower and less exergonic dimerization process of **3-Li-int** as compared with **1-Li-int**. In contrast, the reductive dimerization of the sodium species **1-Na** was fast on the time scale of the CV experiment.[10a] Somewhat unexpectedly, the reduction of **1-Li** (−3.23 V) occurs at more negative potentials than that of the sodium analog **1-Na** (−2.67 V) and the lithium derivative **3-Li** (−2.81), in which one Ph group of the ATI ligand is substituted for an *i*Pr moiety.[24] This demonstrates that the choice of the alkali-metal atom and the substitution pattern in ATI complexes can significantly affect their redox potentials.

Conclusions

To shed some more light on the factors influencing the reactivity of radical species containing a delocalized π-electron system, a previous single case report of a sodium aminotroponiminate (ATI) radical complex was extended. We have demonstrated that the chemically reversible, reductively induced dimerization of alkali-metal ATIs is a more general reaction pathway. For lithium and sodium ATIs, a high chemoselectivity with chemically reversible C–C bond formation/cleavage is maintained. The regioselectivity is generally very high (up to 100 %, determined by ^1H NMR spectroscopy). Importantly, the position of the delocalized π-electron system at which radical coupling occurs can be controlled by choice of the central atom (Li vs.

Na) and the ATI substitution pattern (Ph vs. *i*Pr). The regioselectivity correlates with the spin-density distribution of the radical intermediates which were characterized by EPR spectroscopy and DFT calculations. Although the spin density of radical intermediates appears to be the most important parameter to control the regioselectivity of reductively induced dimerizations, other factors such as the aggregation of radical intermediates in solution may also play a significant role. The diastereoselectivity was found to be tunable by modifying the reaction conditions. The thermodynamic parameters of the exothermic dimerization reactions also depend on the choice of the central atom and the ligand substitution pattern, with one example of an experimentally exploitable equilibrium between the *rac*- and the *meso*-isomers. These findings contribute to the understanding of redox-active ATI ligands and the reactivity of radicals featuring delocalized π-electron systems.

Experimental Section

General considerations

All air- and moisture-sensitive manipulations were carried out using standard vacuum-line Schlenk techniques or in an MBraun inert-atmosphere dry-box containing an atmosphere of purified argon. Solvents were degassed and purified according to standard laboratory procedures. Lithium sand was prepared from lithium rod purchased from Merck as follows: pieces of lithium were heated to 250 °C in paraffin oil under an argon atmosphere. The molten lithium was dispersed with an overhead homogenizer (ultra turrax). The lithium sand was filtered, washed with hexane, and dried in vacuo. NMR spectra were recorded on Bruker instruments operating at 400 or 500 MHz with respect to ^{1}H. ^{1}H and ^{13}C NMR chemical shifts are reported relative to SiMe$_4$ using the residual ^{1}H and ^{13}C chemical shifts of the solvent as a secondary standard. ^{7}Li NMR chemical shifts are reported relative to 1 M LiCl in D$_2$O. In the NMR spectroscopic characterization of ATI and *di*-ATI compounds, the CN^{iPr} carbon atom is referred to as 1-C. Satisfactory elemental analyses of dimerization products **2-Li** and **4-Li** were not obtained due to the sensitivity of these compounds (analyses were performed on a Leco or a Carlo Erba instrument). High-resolution mass-spectrometric analyses of these compounds gave signals corresponding the species that have undergone partial oxidation and protonolysis, providing evidence for their dimeric nature and their sensitivity. For mass-spectrometric analyses, an Exactive plus instrument (Thermo Scientific) was used. Cyclic voltammograms were recorded using a Gamry Instruments Reference 600 potentiostat. A standard three-electrode cell configuration was employed using a platinum-disk working electrode, a platinum-wire counter electrode, and a silver wire, separated by a *Vycor* tip, serving as the reference electrode. Formal redox potentials are referenced to the ferrocene/ferrocenium (Fc/Fc$^+$) redox couple. EPR measurements at X-band (9.37 GHz) were carried out at 298 K using a Bruker ELEXSYS E580 CW/FT EPR spectrometer. CW EPR spectra were measured using 0.6 mW microwave power and 0.1 G field modulation at 100 kHz, with a conversion time of 80 ms. The spectral simulations were performed using MATLAB 8.6 and the EasySpin 5.0.18 toolbox.[25] Single crystals suitable for X-ray diffraction were coated with polyisobutylene or perfluorinated polyether oil in a glove box, transferred to a nylon loop and then transferred to the goniometer of a diffractometer equipped with a molybdenum X-ray tube (λ = 0.71073 Å). The structures were solved using direct methods (SHELXS) completed by Fourier synthesis and refined by full-matrix least-squares procedures. CCDC 1910098, 1910099, 1910100, 1910101, 1910102, and 1910103 contain the supplementary crystallographic data for this paper. These data are provided free of charge by The Cambridge Crystallographic Data Centre.

Computational Details

DFT calculations were performed with the Gaussian program[26] using the 6-31G(d,p)[27] (H, Li, C, N, O) and the 6-311G(d,p)[28] (Na) basis set and the B3LYP functional.[29] A THF solvent model and dispersion corrections were applied for all calculations.[30,31] Frequency analyses of the reported structures showed no imaginary frequencies. Thermodynamic parameters were calculated at a temperature of 298.15 K and a pressure of 1.00 atm. Cartesian coordinates of optimized structures are provided in the Supporting Information.

[Li$_4$(4,4′-di-ATI$^{Ph/iPr}$)(dme)$_4$] (2-Li)

Lithium sand (4.3 mg, 620 μmol) was added to a solution of [Li(ATI$^{Ph/iPr}$)] (**1-Li**, 50 mg, 205 μmol) in dimethoxyethane (4 mL). The red suspension was stirred for 3 d and then filtered to give "solid A" and "filtrate B". THF (2 mL) was added to the remaining beige "solid A" to give a suspension, which was filtered. The solvent was evaporated in a stream of argon to give an off-white solid, which was washed with pentane (3×2 mL) and dried in a stream of argon. Exposure to high vacuum leads to decomposition of the compound. The amount of THF and DME in the isolated compound has to be checked individually for every batch. Values typically ranged from $n = 0.8$ to $n = 6$ molecules of THF or DME per formula unit. A 3:2 mixture of *rac*- and *meso*-compound was obtained. Yield: 30 mg (35 μmol (with $n = 4$ equiv of dme), 34%).

Procedure for isolation of ***rac*-2-Li**: Using 123 μmol of **1-Li** as a starting material, the volume of "filtrate B" was reduced to 1 mL and layered with pentane (0.3 mL). After 2 d, a crystalline material had precipitated, which was isolated by filtration and dried in a stream of argon. Yield: 14 mg (16.2 μmol, with $n = 4$ equiv DME, 26%).

Procedure for isolation of ***meso*-2-Li**: Using 123 μmol of **1-Li** as a starting material, THF (1 mL) was added to "solid A" to give a suspension, which was filtered. The filtrate was layered with the same volume of pentane to give a precipitate after 1 d, which was isolated by filtration and dried in a stream of argon. Yield: 7 mg (8 μmol with $n = 2.0$ equiv dme and $n = 3.4$ equiv THF 13%).

NMR spectroscopic data for ***rac*-2-Li**: ^{1}H NMR (400 MHz, [D$_8$]THF): δ = 1.07 (d, 6H, $^3J_{HH} = 6.0$ Hz, CH*Me*$_2^a$), 1.10 (d, 6H, $^3J_{HH} = 6.0$ Hz, CH*Me*$_2^b$), 2.16 (br. s, 2H, 4-H, 4′-H), 3.27 (s, n×6H, DME-*Me*), 3.32–3.37 (m, 4H, C*H*Me$_2$), 3.43 (n×4H, DME-C*H*$_2$), 4.57 (d, 2H, $^3J_{HH} = 7.5$ Hz, 7-H, 7′-H), 4.63 (d, 2H, $^3J_{HH} = 9.7$ Hz, 5-H, 5′-H), 5.17 (s, 2H, 3-H, 3′-H), 5.75 (dd, 2H, $^3J_{HH} = 8.9$ Hz, $^3J_{HH} = 7.4$ Hz, 6-H, 6′-H), 5.95 (t, 2H, $^3J_{HH} = 7.0$ Hz, *p*-Ph), 6.66 (dd, 4H, $^3J_{HH} = 8.5$ Hz, $^3J_{HH} = 7.1$ Hz, *m*-Ph), 6.94 ppm (d, 4H, $^3J_{HH} = 7.5$ Hz, *o*-Ph); ^{13}C NMR (101, [D$_8$]THF): δ = 25.25–25.79 (overlapping with the signal of [D$_8$]THF, CH*Me*$_2$), 42.29 (s, 4-C, 4′-C), 47.19 (s, CHMe$_2$), 58.71 (s, DME-*Me*), 72.56 (s, DME-C*H*$_2$), 93.14 (s, 7-C, 7′-C), 100.27 (s, 3-C, 3′-C), 111.01 (s, *p*-Ph), 116.96 (s, 5-C, 5′-C), 120.96 (s, *o*-Ph), 126.52 (s, 6-C, 6′-C), 128.56 (*m*-Ph), 148.20 (s, 2-C, 2′-C), 160.11 (s, *ipso*-Ph), 161.14 ppm (s, 1-C,1′-C); resonances of THF ligands may be detected (see above); ^{7}Li NMR (155 MHz, [D$_8$]THF): δ = 0.53 ppm (br. s).

NMR spectroscopic data for ***meso*-2-Li**. ^{1}H NMR (400 MHz, [D$_8$]THF): δ = 1.07 (d, 6H, $^3J_{HH} = 6.0$ Hz, CH*Me*$_2^A$) 1.11 (d, 6H, $^3J_{HH} = 6.1$ Hz, CH*Me*$_2^B$), 1.76–1.79 (m, n×4H, α-THF), 2.30–2.35 (br. m, 2H, 4-H, 4′-

H), 3.27 (s, $n\times$6 H, DME-*Me*), 3.32–3.38 (m, 4 H, C*H*Me$_2$), 3.43 ($n\times$4 H, DME-C*H*$_2$), 3.60–3.63 (m, $n\times$4 H, β-THF), 4.54 (d, 2 H, $^{3}J_{HH}$ = 7.6 Hz, 7-H, 7′-H), 4.84 (dd, 2 H, $^{3}J_{HH}$ = 9.3 Hz, $^{4}J_{HH}$ = 3.7 Hz, 5-H, 5′-H), 5.38 (d, 2 H, $^{3}J_{HH}$ = 4.3 Hz, 3-H, 3′-H), 5.73 (dd, 2 H, $^{3}J_{HH}$ = 8.5 Hz, $^{3}J_{HH}$ = 7.7 Hz, 6-H, 6′-H), 6.01–6.05 (t, 2 H, $^{3}J_{HH}$ = 7.0 Hz, *p*-Ph), 6.83 (dd, 4 H, $^{3}J_{HH}$ = 8.4 Hz, $^{3}J_{HH}$ = 7.1 Hz, *m*-Ph), 7.07 ppm (d, 4 H, $^{3}J_{HH}$ = 7.5 Hz, *o*-Ph); ^{13}C NMR (101 MHz, [D$_8$]THF): δ = 25.25–25.79 (s, CH*Me*$_2$^{A,B}, overlapping with the signal of [D$_8$]THF), 26.19 (s, α-THF), 42.52 (s, 4-C, 4′-C), 47.12 (s, CH), 58.71 (s, DME-*Me*), 68.03 (s, β-THF), 72.58 (s, DME-CH$_2$), 92.78 (s, 7-C, 7′-C), 99.15 (s, 3-C, 3′-C), 111.39 (s, *p*-Ph), 116.34 (s, 5-C, 5′-C), 121.40 (s, *o*-Ph), 126.77 (s, 6-C, 6′-C), 128.39 (s, *m*-Ph), 147.90 (s, 2-C, 2′-C), 159.77 (s, *ipso*-Ph), 160.97 ppm (s, 1-C, 1′-C); ^{7}Li NMR (156 MHz, [D$_8$]THF): δ = 0.50 (br. s), 0.70 ppm (br. s); ESI(+)-MS: calc. for $[C_{32}H_{36}N_4]^{+\bullet}$, *m/z* = 476.2934; found: *m/z* = 476.2932.

NMR spectroscopic monitoring of reduction of ***3-Li*** *with lithium to give* ***4-Li***

Lithium sand (0.5 mg, 76 μmol) was added to a solution of [Li(ATI$^{iPr/iPr}$)] (**3-Li**) (10 mg, 38 μmol) in the solvent of choice (0.5 mL, a: [D$_8$]THF; b: C$_6$D$_6$/[D$_8$]THF (6:1)). The course of the reaction was monitored by ^{1}H NMR spectroscopy. After a given reaction time (a: 3 d; b: 3 d), quantitative conversion to **4-Li** was detected with a *rac/meso* ratio of 1:1 (a) and 4:1 (b). In reaction b, a solid precipitated during the course of the reaction, which was isolated by filtration. It was dissolved in [D$_8$]THF and filtered (to remove excess Li). ^{1}H NMR spectroscopy revealed exclusively resonances for ***meso*-4-Li**. To evaluate the overall diastereoselectivity of reaction b, all volatiles were removed from the reaction mixture after the reaction had reached full conversion. [D$_8$]THF was added to dissolve all **4-Li**. NMR spectroscopy revealed a *rac/meso* ratio of 13:1.

[Li$_4$(4,4′-di-ATI$^{iPr/iPr}$)(thf)$_6$] (4-Li)

Lithium sand (4.0 mg, 576 μmol) was added to a solution of [Li(ATI$^{iPr/iPr}$)(Et$_2$O)] (**3-Li**, (50 mg, 191 μmol) in THF (4 mL). The yellow suspension was stirred for 3 d and then filtered. Under reduced pressure, the volume of the filtrate was reduced to half. Then the filtrate was layered with pentane (2 mL). The sample was left to crystallize for a defined period of time (a: 2 d; b: 14 d). After that yellow crystals had formed, which were isolated by filtration and dried in a stream of argon. Exposure to high vacuum leads to decomposition of the compound. The amount of THF in the isolated compound has to be checked individually for every batch; values typically ranged from *n* = 2.5 to *n* = 6 molecules of THF per formula unit. Yield: conditions a): 29 mg of pure ***meso*-4-Li** (36 μmol, with *n* = 5 equiv of THF, 41 %). Conditions b: 50 mg of pure ***meso*-4-Li** (63 μmol, with *n* = 5 equiv of THF, 71 %).

Procedure for enrichment of ***rac*-4-Li**: Using benzene/THF (6:1) as a solvent mixture for the reduction of **3-Li** with Li gave a suspension, the liquid phase of which contained **4-Li** with a *rac/meso* ratio of 4:1 (see reaction b in "NMR spectroscopic monitoring of reduction of **3-Li** with lithium to give **4-Li**.").

NMR spectroscopic data for ***meso*-4-Li**. ^{1}H NMR (400 MHz, [D$_8$]THF): δ = 0.94 (d, 6 H, $^{3}J_{HH}$ = 5.9 Hz, 2,2′-N(CH(*Me*$_2$))), 1.05 (d, 6 H, $^{3}J_{HH}$ = 5.9 Hz, 2,2′-N(CH*Me*$_2$)), 1.06 (d, 6 H, $^{3}J_{HH}$ = 6.1 Hz, 1,1′-N(CH*Me*$_2$)), 1.09 (d, 6 H, $^{3}J_{HH}$ = 6.1 Hz, 1,1′-N(CH(*Me*$_2$))), 1.76–1.79 (m, $n\times$4 H, β-THF), 2.23 (br. s, 2 H, 4-H, 4′-H), 3.18 (sept, 2 H, $^{3}J_{HH}$ = 6.1 Hz,1,1′-N(C*H*Me$_2$)), 3.35 (sept, 2 H, $^{3}J_{HH}$ = 6.3 Hz, 2,2′- N(C*H*Me$_2$)), 3.60–3.63 (m, $n\times$4 H, α-THF), 3.67 (br. s, 2 H, 3-H, 3′-H), 4.40 (d, 2 H, $^{3}J_{HH}$ = 6.9 Hz, 7-H, 7′-H), 4.92 (br. d, 2 H, 5-H, 5′-H), 5.59–5.63 ppm (m, 2 H, 6-H, 6′-H); ^{13}C NMR (101 MHz, [D$_8$]THF): δ = 25.43–26.15 (partially overlapped with THF and [D$_8$]THF, 1,1′,2,2′-N(CH*Me*$_2$)), 43.43 (s, 4-C, 4′-C), 47.20 (s, 2,2′-N(C*H*Me$_2$)), 47.34 (s, 1,1′-N(*CH*Me$_2$)), 91.58 (s, 7-C, 7′-C), 92.92 (s, 3-C, 3′-C), 118.83 (s, 5-C, 5′-C), 125.37 (s, 6-C, 6′-C), 152.70 (s, 2,2′-C), 161.61 ppm (s, 1,1′-C); ^{7}Li NMR (155 MHz, [D$_8$]THF): δ = 0.66 (br. s), 1.01 ppm (br. s).

NMR spectroscopic data for ***rac*-4-Li** (extracted from samples containing ***rac*-4-Li** and ***meso*-4-Li**). ^{1}H NMR (400 MHz, [D$_8$]THF): δ = 0.94 (d, 12 H, $^{3}J_{HH}$ = 5.9 Hz, 2,2′-N(CH(*Me*$_2$)), overlapping with 2,2′-N(CH(*Me*$_2$)) of *meso*-compound), 1.05 (d, 12 H, $^{3}J_{HH}$ = 5.9 Hz, 2,2′-N(CH(*Me*$_2$)), overlapping with 2,2′-N(CH(*Me*$_2$)) of *meso*-compound), 1.06 (d, 12 H, $^{3}J_{HH}$ = 6.1 Hz, 1,1′-N(CH(*Me*$_2$)), overlapping with 1,1′-N(CH(*Me*$_2$)) of *meso*-compound), 1.09 (d, 12 H, $^{3}J_{HH}$ = 6.1 Hz, 1,1′-N(CH(*Me*$_2$)), overlapping with 1,1′-N(CH(*Me*$_2$)) of *meso*-compound), 2.19 (br. s, 2 H, 4-H, 4′-H), 3.18 (sept, 4 H, $^{3}J_{HH}$ = 6.1 Hz, 1,1′-N(C*H*(Me$_2$)), overlapped with 1,1′-N(CH(*Me*$_2$)) of *meso*-compound), 3.35 (sept, 9 H, $^{3}J_{HH}$ = 6.3 Hz, 2,2′- N(C*H*(Me$_2$)), overlapping with 2,2′-N(CH(*Me*$_2$)) of *meso*-compound and and O(C*H*$_2$Me)$_2$), 3.71 (br. s, 2 H, 3-H, 3′-H), 4.40 (d, 4 H, $^{3}J_{HH}$ = 6.9 Hz, 7-H, 7′-H, overlapping with 7-H, 7′-H of *meso*-compound), 4.72 (br. d, 2 H, 5-H, 5′-H), 5.59–5.63 ppm (m, 4 H, 6-H, 6′-H, overlapped with 6-H, 6′-H of *meso*-compound); ^{13}C NMR (101 MHz, [D$_8$]THF): δ = 25.61–26.12 (1,1′,2,2′-N(CH(*Me*$_2$)) overlapping with THF and 1,1′,2,2′-N(CH(*Me*$_2$)) of *meso*-compound), 43.15 (s, 4-C, 4′-C), 47.21 (s, 2,2′-N(C*H*(Me$_2$)), 47.29 (s, 1,1′-N(*CH*(Me$_2$)), 91.77 (s, 7-C, 7′-C), 92.80 (s, 3-C, 3′-C), 119.30 (s, 5-C, 5′-C), 125.34 (s, 6-C, 6′-C), 152.82 (s, 2,2′-C), 161.56 ppm (s, 1,1′-C); ^{7}Li NMR (155 MHz, [D$_8$]THF): δ = 0.66 (br. s), 1.01 ppm (br. s).ESI(+)-MS: calc. for $[C_{26}H_{40}N_4]^{+\bullet}$, *m/z* = 408.3247; found: *m/z* = 408.3246.

Oxidation of 2-Li

AgBF$_4$ (2.0 mg, 10.4 μmol) was added to a solution of [Li$_4$(4,4′-di-ATI$^{Ph/iPr}$)(dme)$_4$] (9.0 mg 10.4 μmol) in [D$_8$]THF (0.5 mL). The color of the reaction mixture changed from yellow to dark brown and precipitation of dark solid was observed. ^{1}H NMR spectroscopic analysis of the reaction mixture indicated full conversion to [Li(ATI$^{Ph/iPr}$)] (**1-Li**) as only THF-soluble species. Quantitative conversion to **1-Li** was corroborated by using the resonances of [D$_8$]THF as an internal standard.

Oxidation of 4-Li

Compound **4-Li** was generated in situ from **3-Li** (10 mg, 38 μmol) and lithium sand (1.0 mg, 144 μmol) in [D$_8$]THF (0.5 mL). When full conversion to **4-Li** was detected by NMR spectroscopy, the lithium sand was filtered off and AgBF$_4$ (5.4 mg, 38 μmol) was added to the solution containing **4-Li** (19 μmol). The color of the reaction mixture changed from yellow to dark brown and precipitation of a dark solid was observed. ^{1}H NMR spectroscopic analysis of the reaction mixture indicated full conversion of **4-Li. 3-Li** was detected as the only THF-soluble species. Using the resonances of [D$_8$]THF as an internal standard, a spectroscopic yield of 35 % was determined.

Acknowledgements

The authors thank Prof. Dr. Holger Braunschweig for continuous support. Generous financial support by the Fonds der Chemischen Industrie and the DFG are gratefully acknowledged.

Conflict of interest

The authors declare no conflict of interest.

Keywords: alkali metals · aminotroponiminates · persistent radicals · radical chemistry · redox-active ligands

[1] a) H. Bock, C. Arad, C. Näther, Z. Havlas, *J. Chem. Soc. Chem. Commun.* **1995**, 2393 – 2394; b) H. Bock, K. Gharagozloo-Hubmann, M. Sievert, T. Prisner, Z. Havlas, *Nature* **2000**, *404*, 267 – 269; c) A. H. Reddoch, *J. Chem. Phys.* **1965**, *43*, 225 – 234; d) A. H. Reddoch, *J. Chem. Phys.* **1964**, *41*, 444 – 447; e) A. Carrington, I. C. P. Smith, *Mol. Phys.* **1964**, *7*, 99 – 100; f) D. E. Wood, H. M. McConnell, *J. Chem. Phys.* **1962**, *37*, 1150 – 1151; g) J. dos Santos-Veiga, *Mol. Phys.* **1962**, *5*, 639 – 641.

[2] a) N. G. Connelly, W. E. Geiger, *Chem. Rev.* **1996**, *96*, 877 – 910; b) G. A. Molander, C. R. Harris, "Sodium Naphthalenide" in *Encyclopedia of Reagents for Organic Synthesis*, **2001**, https://doi.org/10.1002/047084289X.rs091; c) E. Shirakawa, Y. Hayashi, K.-I. Itoh, R. Watabe, N. Uchiyama, W. Konagaya, S. Masui, T. Hayashi, *Angew. Chem. Int. Ed.* **2012**, *51*, 218 – 221; *Angew. Chem.* **2012**, *124*, 222 – 225.

[3] a) A. N. Nesmeyanov, N. A. Vol'kenau, V. A. Petrakova, *J. Organomet. Chem.* **1977**, *136*, 363 – 370; b) J.-R. Hamon, D. Astruc, P. Michaud, *J. Am. Chem. Soc.* **1981**, *103*, 758 – 766; c) M. D. Fryzuk, C. M. Kozak, P. Mehrkhodavandi, L. Morello, B. O. Patrick, S. J. Rettig, *J. Am. Chem. Soc.* **2002**, *124*, 516 – 517.

[4] a) M. Su, S. L. Gipson, D. F. Mullica, E. L. Sappenfield, D. H. Leschnitzer, *J. Chem. Soc. Dalton Trans.* **1993**, 3323 – 3328; b) M. Tamm, T. Bannenberg, R. Fröhlich, S. Grimme, M. Gerenkamp, *Dalton Trans.* **2004**, 482 – 491; c) U. Friedrich, N. Korber, *Z. Kristallogr. New Cryst. Struct.* **2012**, *227*, 455 – 456.

[5] a) M. Hoch, D. Rehder, *Chem. Ber.* **1988**, *121*, 1541 – 1552; b) P. Burger, H.-U. Hund, K. Evertz, H.-H. Brintzinger, *J. Organomet. Chem.* **1989**, *378*, 153 – 161; c) I. L. Fedushkin, M. N. Bochkarev, S. Dechert, H. Schumann, *Chem. Eur. J.* **2001**, *7*, 3558 – 3563; d) P.-J. Sinnema, P. J. Shapiro, B. Höhn, B. Twamley, *J. Organomet. Chem.* **2003**, *676*, 73 – 79; e) I. L. Fedushkin, Y. A. Kurskii, T. V. Balashova, M. N. Bochkarev, S. Dechert, S. Mühler, H. Schumann, *Russ. Chem. Bull.* **2003**, *52*, 1363 – 1371.

[6] a) I. L. Fedushkin, S. Cechert, H. Schumann, *Angew. Chem. Int. Ed.* **2001**, *40*, 561 – 563; *Angew. Chem.* **2001**, *113*, 584 – 586; b) I. L. Fedushkin, T. V. Petrovskaya, M. N. Bochkarev, S. Dechert, H. Schumann, *Angew. Chem. Int. Ed.* **2001**, *40*, 2474 – 2477; *Angew. Chem.* **2001**, *113*, 2540 – 2543; c) D. Rehder, M. Hoch, M. Link, *Organometallics* **1988**, *7*, 233 – 235; d) P.-J. Sinnema, B. Twamley, P. J. Shapiro, *Acta Crystallogr. Sect. E* **2001**, *57*, m438 – m440.

[7] Y. Hu, G. M. Miyake, B. Wang, D. Cui, E. Y.-X. Chen, *Chem. Eur. J.* **2012**, *18*, 3345 – 3354.

[8] In oxidatively induced dimerizations of heptafulvenes, at least seven different dimerization products were obtained in some cases: see Ref. [9].

[9] In oxidatively induced dimerizations of heptafulvene, results from the Hückel Molecular Orbital (HMO) method were also used to account for experimentally observed selectivities. However, the HMO method was applied to the starting material used for the generation of a radical species, not to the radical species itself: W. Bauer, J. Daub, E. Eibler, A. Gieren, V. Lamm, H. Lotter, *Chem. Ber.* **1984**, *117*, 809 – 826.

[10] a) C. Lichtenberg, I. Krummenacher, *Chem. Commun.* **2016**, *52*, 10044 – 10046; b) C. Lichtenberg, *Organometallics* **2016**, *35*, 894 – 902; c) A. Hanft, C. Lichtenberg, *Dalton Trans.* **2018**, *47*, 10578 – 1010589.

[11] For review articles about the properties of ATI complexes see: a) A. Hanft, C. Lichtenberg, *Eur. J. Inorg. Chem.* **2018**, 3361 – 3373; b) P. W. Roesky, *Chem. Soc. Rev.* **2000**, *29*, 335 – 345; c) P. W. Roesky, *Z. Anorg. Allg. Chem.* **2003**, *629*, 1881 – 1894; d) H. V. R. Dias, Z. Wang, W. Jin, *Coord. Chem. Rev.* **1998**, *176*, 67 – 86; e) O. Kühl, *Coord. Chem. Rev.* **2004**, *248*, 411 – 427; f) J. Jenter, A. Luhl, P. W. Roesky, S. Blechert, *J. Organomet. Chem.* **2011**, *696*, 406 – 418.

[12] The reduction of **1-Li** with **Li** was more selective in DME than in THF, in which unidentified side products were obtained that could not quantitatively be separated. The reduction of **3-Li** with Li gave similar results, when DME or THF was used as the solvent.

[13] When the reaction of **1-Li** with **Li** was performed in $[D_8]$THF, that is, under the same conditions as the analogous reaction of **1-Na** with **Na**, the dimer with C–C coupling in the 4/4′-position was the main product, but other species were also detected, which could not unambiguously be identified so far.

[14] The *rac/meso* ratio of pure ***rac*-2-Li** and pure ***meso*-2-Li** did not change in THF solution at 23 °C over a period of 3 d as determined by ^{1}H NMR spectroscopy.

[15] a) A. Hanft, C. Lichtenberg, *Organometallics* **2018**, *37*, 1781 – 1787; b) H. V. R. Dias, W. Jin, *J. Chem. Crystallogr.* **1997**, *27*, 353 – 358.

[16] a) H. V. R. Dias, W. Jin, Z. Wang, *Inorg. Chem.* **1996**, *35*, 6074 – 6079; b) F. Delpech, I. A. Guzei, R. F. Jordan, *Organometallics* **2002**, *21*, 1167 – 1176.

[17] The same regioselectivity is assigned to the reductively induced dimerization of $[\mathrm{Na(ATI}^{i\mathrm{Pr}/i\mathrm{Pr}})\mathrm{(thf)}]$ with Na based on in situ NMR spectroscopic investigations, but the product of this reaction could so far not be isolated and fully characterized due to poor solubility and high sensitivity.

[18] Under these conditions, partial decomposition to **3-Li** was also observed (15 % after 1 d at 60 °C). After 4 d at 60 °C, the *rac/meso* ratio was 1.0: 5.0 and 21 % **3-Li** were detected. A very slow isomerization from the *rac* to the *meso* isomer was observed at 23 °C in THF solution: *rac/meso* = 2.5:1.0 changed to *rac/meso* = 2.4:1.0 in 3 d.

[19] A. Hanft, M. Jürgensen, R. Bertermann, C. Lichtenberg, *ChemCatChem* **2018**, *10*, 4018 – 4027.

[20] For comparison: coupling constants in the EPR spectrum of $[C_7H_6R]^{\bullet}$ radicals of up to $a(^1\mathrm{H}, 2\,\mathrm{H}) = 0.91$ mT (translating to 25.5 MHz) have been reported for $R = NMe_2$: F. MacCorquodale, J. C. Walton, *Magn. Reson. Chem.* **1990**, *28*, 364 – 369.

[21] As expected, neat THF did not show any resonance in the EPR spectrum under identical conditions.

[22] The *rac/meso* ratio in isolated samples of ***rac*-2-Li** or ***meso*-2-Li** does not change in THF solution at 23 °C (see Ref. [13]). Thus, the concentration and/or the life time of radicals in solutions of **2-Li** is too low to change the ratio of diastereomers.

[23] It should be noted, however, that a nucleophilic attack of a primary lithium alkyl at the carbon atom bearing an NPh substituent of an $[\mathrm{ATI}^{\mathrm{Ph/Ph}}]^-$ ligand has been reported: see Ref. [15a].

[24] Taking only the electronegativity of the central atom (Li vs. Na) and the group electronegativity of the substituents at the $\mathrm{N}^{\mathrm{ATI}}$ atoms (Ph vs. *i*Pr) into account, a less negative redox potential would be expected for **1-Li**. Thus, other factors such as solvation and aggregation phenomena are suggested to also play a significant role in determining the redox potentials of these complexes.

[25] S. Stoll, A. Schweiger, *J. Magn. Reson.* **2006**, *178*, 42 – 55.

[26] For full reference of Gaussian program, see the Supporting Information.

[27] P. C. Hariharan, J. A. Pople, *Theor. Chim. Acta* **1973**, *28*, 213 – 222.

[28] a) A. D. McLean, G. S. Chandler, *J. Chem. Phys.* **1980**, *72*, 5639 – 5648; b) K. Raghavachari, J. S. Binkley, R. Seeger, J. A. Pople, *J. Chem. Phys.* **1980**, *72*, 650 – 654.

[29] A. D. Becke, *J. Chem. Phys.* **1993**, *98*, 5648 – 5652.

[30] A. V. Marenich, C. J. Cramer, D. G. Truhlar, *J. Phys. Chem. B* **2009**, *113*, 6378 – 6396.

[31] S. Grimme, J. Antony, S. Ehrlich, H. Krieg, *J. Chem. Phys.* **2010**, *132*, 154104.

Manuscript received: April 29, 2019
Accepted manuscript online: May 29, 2019
Version of record online: July 11, 2019

VIII Dimerization of 2-[(2-((2-aminophenyl)thio)phenyl)amino]-cyclohepta-2,4,6-trien-1-one through hydrogen bonding

Anna Hanft, Crispin Lichtenberg

Vervielfältigt aus Referenz:

Z. Kristallogr. NCS **2020**, *235*, 963-966.[67]

DOI: https://doi.org/10.1515/ncrs-2020-0124.

DE GRUYTER Z. Kristallogr. NCS 2020; 235(4): 963–966

Anna Hanft and Crispin Lichtenberg*

Dimerization of 2-[(2-((2-aminophenyl)thio) phenyl)amino]-cyclohepta-2,4,6-trien-1-one through hydrogen bonding, $C_{19}H_{16}N_2OS$

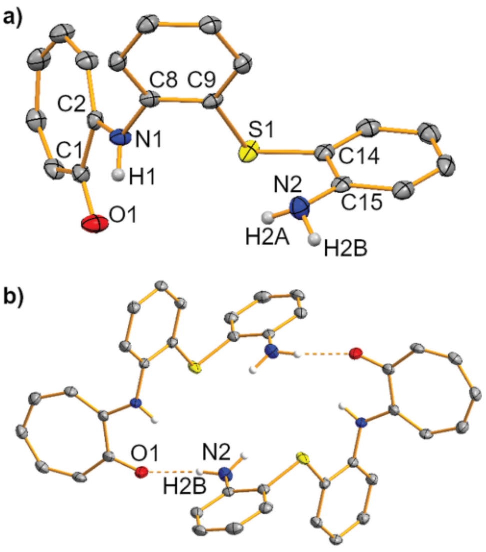

https://doi.org/10.1515/ncrs-2020-0124
Received March 5, 2020; accepted April 23, 2020; available online May 5, 2020

Abstract

$C_{19}H_{16}N_2OS$, triclinic, $P\bar{1}$ (no. 2), $a = 8.1510(3)$ Å, $b = 8.8021(3)$ Å, $c = 11.3953(5)$ Å, $\alpha = 72.546(2)°$, $\beta = 84.568(2)°$, $\gamma = 80.760(2)°$, $V = 768.86(5)$ Å^3, $Z = 2$, $R_{gt}(F) = 0.0491$, $wR_{ref}(F^2) = 0.1494$, $T = 100$ K.

CCDC no.: 1998662

The molecular structure is shown in the figure. Table 1 contains crystallographic data and Table 2 contains the list of the atoms including atomic coordinates and displacement parameters.

Table 1: Data collection and handling.

Crystal:	Colourless plate
Size:	$0.21 \times 0.16 \times 0.04$ mm
Wavelength:	Mo $K\alpha$ radiation (0.71073 Å)
μ:	0.22 mm^{-1}
Diffractometer, scan mode:	Bruker SMART APEX, φ and ω
θ_{max}, completeness:	28.0°, 99%
$N(hkl)_{measured}$, $N(hkl)_{unique}$, R_{int}:	9366, 3619, 0.040
Criterion for I_{obs}, $N(hkl)_{gt}$:	$I_{obs} > 2\ \sigma(I_{obs})$, 2625
$N(param)_{refined}$:	220
Programs:	Bruker [1, 2], SHELX [3, 4], Mercury [5], Olex2 [6]

Comment

Aminotroponiminates (ATIs) are monoanionic ligands with applications in fields such as hydroamination and polymerization catalysis and the stabilization of low-valent main group species [7–12]. Their potential to act as redox-active ligands has recently been demonstrated [13–15]. In the coordination chemistry of ATIs, it has been shown that not only their *N*,*N*′-binding pocket, but also their C_7-ligand backbone can undergo directed bonding interactions with metal centers [16–19]. Thus, ATIs can effectively act as ditopic, tridentate ligands. A strategy to further increase the denticity of this class of ligands is to connect two ATI ligands *via* linkers, generating so-called tropocoronands. These macrocyclic ligands have been employed for the chelation of metal atoms including Co, Ni, Cu, and Rh [20–28]. We became interested in tropocoronands containing unsaturated linker units. Reaction of 2,2′-thio-dianiline (**1**) with *O*-tosyltropone (**2**) in a 1.0:2.5 stoichiometry gave the title compound 2-((2-((2-aminophenyl)thio)phenyl)amino)-cyclohepta-2,4,6-trien-1-one (**3**) as the main product, which was isolated and fully characterized. The isolation of compound **3** shows that functionalization of the first N atom in **1** hampers functionalization of the second nitrogen atom in this substrate in the protocol that was employed. The asymmetric unit of the

---

***Corresponding author: Crispin Lichtenberg,** Institut für Anorganische Chemie, Julius-Maximilians-Universität Würzburg, Am Hubland, 97074 Würzburg, Germany, e-mail: crispin.lichtenberg@uni-wuerzburg.de. https://orcid.org/0000-0002-0176-0939
Anna Hanft: Institut für Anorganische Chemie, Julius-Maximilians-Universität Würzburg, Am Hubland, 97074 Würzburg, Germany

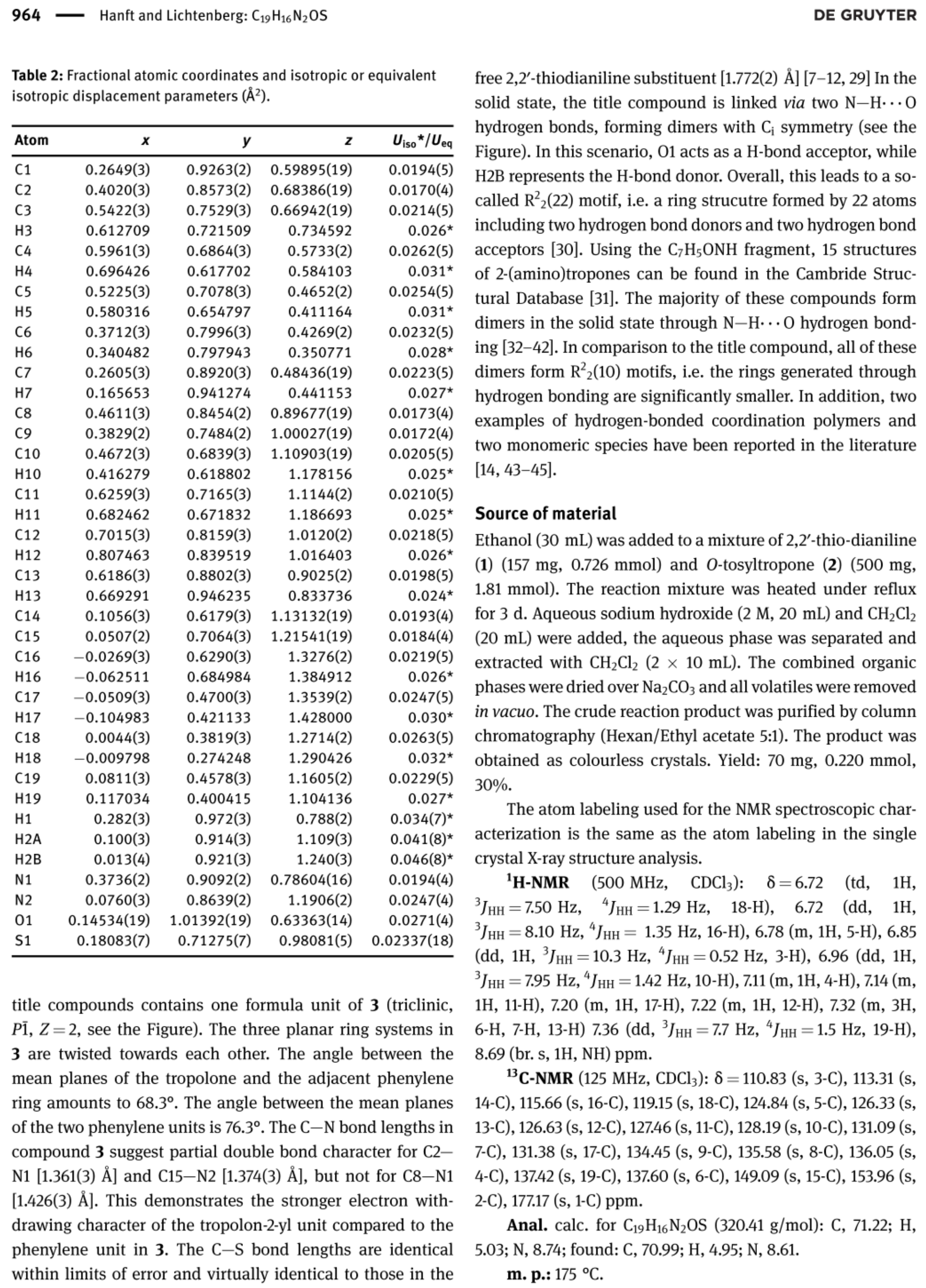

Table 2: Fractional atomic coordinates and isotropic or equivalent isotropic displacement parameters (Å^2).

Atom	*x*	*y*	*z*	$U_{iso}*/U_{eq}$
C1	0.2649(3)	0.9263(2)	0.59895(19)	0.0194(5)
C2	0.4020(3)	0.8573(2)	0.68386(19)	0.0170(4)
C3	0.5422(3)	0.7529(3)	0.66942(19)	0.0214(5)
H3	0.612709	0.721509	0.734592	0.026*
C4	0.5961(3)	0.6864(3)	0.5733(2)	0.0262(5)
H4	0.696426	0.617702	0.584103	0.031*
C5	0.5225(3)	0.7078(3)	0.4652(2)	0.0254(5)
H5	0.580316	0.654797	0.411164	0.031*
C6	0.3712(3)	0.7996(3)	0.4269(2)	0.0232(5)
H6	0.340482	0.797943	0.350771	0.028*
C7	0.2605(3)	0.8920(3)	0.48436(19)	0.0223(5)
H7	0.165653	0.941274	0.441153	0.027*
C8	0.4611(3)	0.8454(2)	0.89677(19)	0.0173(4)
C9	0.3829(2)	0.7484(2)	1.00027(19)	0.0172(4)
C10	0.4672(3)	0.6839(3)	1.10903(19)	0.0205(5)
H10	0.416279	0.618802	1.178156	0.025*
C11	0.6259(3)	0.7165(3)	1.1144(2)	0.0210(5)
H11	0.682462	0.671832	1.186693	0.025*
C12	0.7015(3)	0.8159(3)	1.0120(2)	0.0218(5)
H12	0.807463	0.839519	1.016403	0.026*
C13	0.6186(3)	0.8802(3)	0.9025(2)	0.0198(5)
H13	0.669291	0.946235	0.833736	0.024*
C14	0.1056(3)	0.6179(3)	1.13132(19)	0.0193(4)
C15	0.0507(2)	0.7064(3)	1.21541(19)	0.0184(4)
C16	−0.0269(3)	0.6290(3)	1.3276(2)	0.0219(5)
H16	−0.062511	0.684984	1.384912	0.026*
C17	−0.0509(3)	0.4700(3)	1.3539(2)	0.0247(5)
H17	−0.104983	0.421133	1.428000	0.030*
C18	0.0044(3)	0.3819(3)	1.2714(2)	0.0263(5)
H18	−0.009798	0.274248	1.290426	0.032*
C19	0.0811(3)	0.4578(3)	1.1605(2)	0.0229(5)
H19	0.117034	0.400415	1.104136	0.027*
H1	0.282(3)	0.972(3)	0.788(2)	0.034(7)*
H2A	0.100(3)	0.914(3)	1.109(3)	0.041(8)*
H2B	0.013(4)	0.921(3)	1.240(3)	0.046(8)*
N1	0.3736(2)	0.9092(2)	0.78604(16)	0.0194(4)
N2	0.0760(3)	0.8639(2)	1.1906(2)	0.0247(4)
O1	0.14534(19)	1.01392(19)	0.63363(14)	0.0271(4)
S1	0.18083(7)	0.71275(7)	0.98081(5)	0.02337(18)

title compounds contains one formula unit of **3** (triclinic, $P\bar{1}$, $Z=2$, see the Figure). The three planar ring systems in **3** are twisted towards each other. The angle between the mean planes of the tropolone and the adjacent phenylene ring amounts to 68.3°. The angle between the mean planes of the two phenylene units is 76.3°. The C—N bond lengths in compound **3** suggest partial double bond character for C2—N1 [1.361(3) Å] and C15—N2 [1.374(3) Å], but not for C8—N1 [1.426(3) Å]. This demonstrates the stronger electron withdrawing character of the tropolon-2-yl unit compared to the phenylene unit in **3**. The C—S bond lengths are identical within limits of error and virtually identical to those in the free 2,2′-thiodianiline substituent [1.772(2) Å] [7–12, 29] In the solid state, the title compound is linked *via* two N—H···O hydrogen bonds, forming dimers with C_i symmetry (see the Figure). In this scenario, O1 acts as a H-bond acceptor, while H2B represents the H-bond donor. Overall, this leads to a so-called $R^2_2(22)$ motif, i.e. a ring strucutre formed by 22 atoms including two hydrogen bond donors and two hydrogen bond acceptors [30]. Using the C_7H_5ONH fragment, 15 structures of 2-(amino)tropones can be found in the Cambridge Structural Database [31]. The majority of these compounds form dimers in the solid state through N—H···O hydrogen bonding [32–42]. In comparison to the title compound, all of these dimers form $R^2_2(10)$ motifs, i.e. the rings generated through hydrogen bonding are significantly smaller. In addition, two examples of hydrogen-bonded coordination polymers and two monomeric species have been reported in the literature [14, 43–45].

Source of material

Ethanol (30 mL) was added to a mixture of 2,2′-thio-dianiline (**1**) (157 mg, 0.726 mmol) and *O*-tosyltropone (**2**) (500 mg, 1.81 mmol). The reaction mixture was heated under reflux for 3 d. Aqueous sodium hydroxide (2 M, 20 mL) and CH_2Cl_2 (20 mL) were added, the aqueous phase was separated and extracted with CH_2Cl_2 (2 × 10 mL). The combined organic phases were dried over Na_2CO_3 and all volatiles were removed *in vacuo*. The crude reaction product was purified by column chromatography (Hexan/Ethyl acetate 5:1). The product was obtained as colourless crystals. Yield: 70 mg, 0.220 mmol, 30%.

The atom labeling used for the NMR spectroscopic characterization is the same as the atom labeling in the single crystal X-ray structure analysis.

^{1}H-NMR (500 MHz, $CDCl_3$): $\delta = 6.72$ (td, 1H, $^3J_{HH} = 7.50$ Hz, $^4J_{HH} = 1.29$ Hz, 18-H), 6.72 (dd, 1H, $^3J_{HH} = 8.10$ Hz, $^4J_{HH} = 1.35$ Hz, 16-H), 6.78 (m, 1H, 5-H), 6.85 (dd, 1H, $^3J_{HH} = 10.3$ Hz, $^4J_{HH} = 0.52$ Hz, 3-H), 6.96 (dd, 1H, $^3J_{HH} = 7.95$ Hz, $^4J_{HH} = 1.42$ Hz, 10-H), 7.11 (m, 1H, 4-H), 7.14 (m, 1H, 11-H), 7.20 (m, 1H, 17-H), 7.22 (m, 1H, 12-H), 7.32 (m, 3H, 6-H, 7-H, 13-H) 7.36 (dd, $^3J_{HH} = 7.7$ Hz, $^4J_{HH} = 1.5$ Hz, 19-H), 8.69 (br. s, 1H, NH) ppm.

^{13}C-NMR (125 MHz, $CDCl_3$): $\delta = 110.83$ (s, 3-C), 113.31 (s, 14-C), 115.66 (s, 16-C), 119.15 (s, 18-C), 124.84 (s, 5-C), 126.33 (s, 13-C), 126.63 (s, 12-C), 127.46 (s, 11-C), 128.19 (s, 10-C), 131.09 (s, 7-C), 131.38 (s, 17-C), 134.45 (s, 9-C), 135.58 (s, 8-C), 136.05 (s, 4-C), 137.42 (s, 19-C), 137.60 (s, 6-C), 149.09 (s, 15-C), 153.96 (s, 2-C), 177.17 (s, 1-C) ppm.

Anal. calc. for $C_{19}H_{16}N_2OS$ (320.41 g/mol): C, 71.22; H, 5.03; N, 8.74; found: C, 70.99; H, 4.95; N, 8.61.

m. p.: 175 °C.

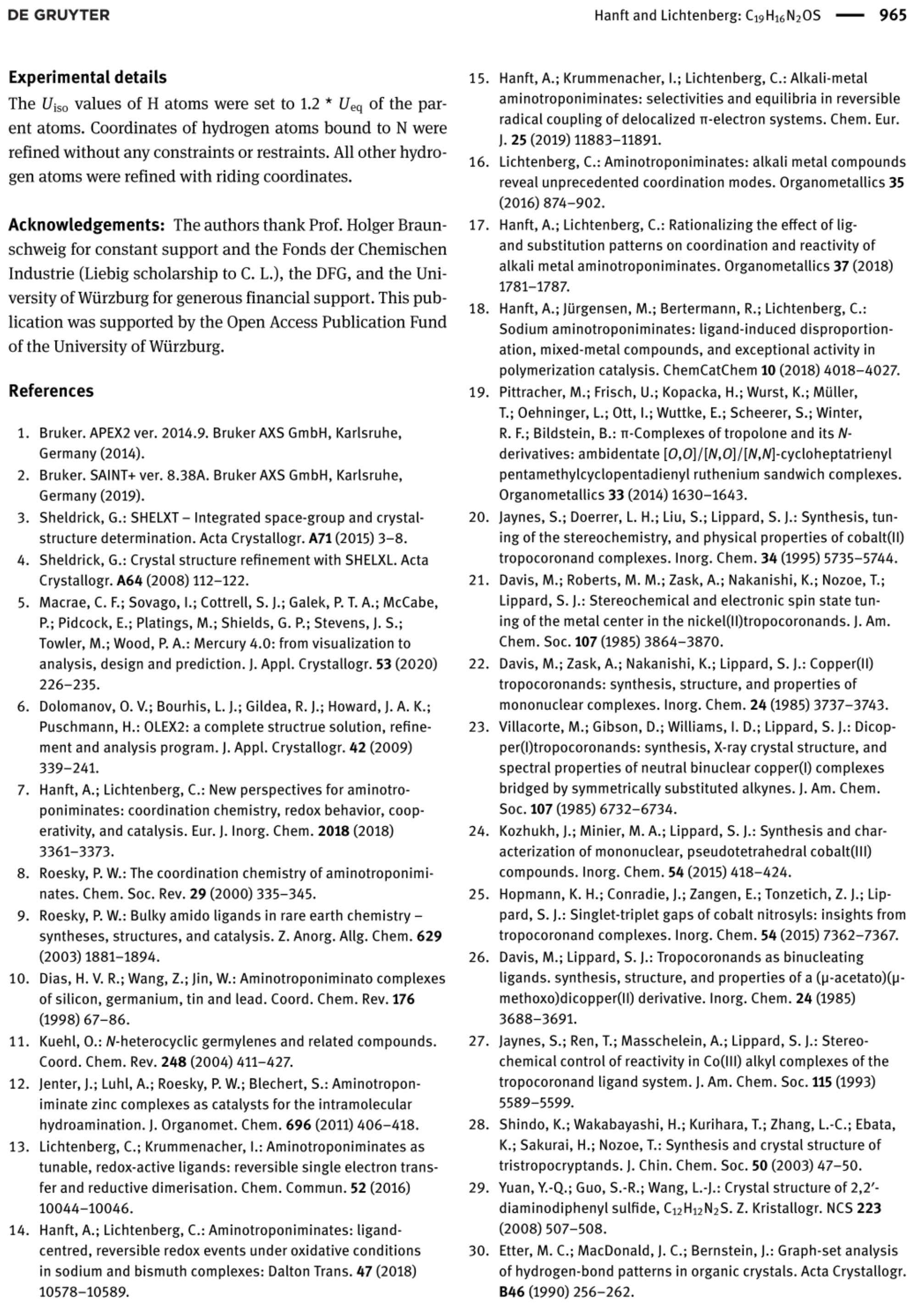

Experimental details

The U_{iso} values of H atoms were set to 1.2 * U_{eq} of the parent atoms. Coordinates of hydrogen atoms bound to N were refined without any constraints or restraints. All other hydrogen atoms were refined with riding coordinates.

Acknowledgements: The authors thank Prof. Holger Braunschweig for constant support and the Fonds der Chemischen Industrie (Liebig scholarship to C. L.), the DFG, and the University of Würzburg for generous financial support. This publication was supported by the Open Access Publication Fund of the University of Würzburg.

References

1. Bruker. APEX2 ver. 2014.9. Bruker AXS GmbH, Karlsruhe, Germany (2014).
2. Bruker. SAINT+ ver. 8.38A. Bruker AXS GmbH, Karlsruhe, Germany (2019).
3. Sheldrick, G.: SHELXT – Integrated space-group and crystal-structure determination. Acta Crystallogr. **A71** (2015) 3–8.
4. Sheldrick, G.: Crystal structure refinement with SHELXL. Acta Crystallogr. **A64** (2008) 112–122.
5. Macrae, C. F.; Sovago, I.; Cottrell, S. J.; Galek, P. T. A.; McCabe, P.; Pidcock, E.; Platings, M.; Shields, G. P.; Stevens, J. S.; Towler, M.; Wood, P. A.: Mercury 4.0: from visualization to analysis, design and prediction. J. Appl. Crystallogr. **53** (2020) 226–235.
6. Dolomanov, O. V.; Bourhis, L. J.; Gildea, R. J.; Howard, J. A. K.; Puschmann, H.: OLEX2: a complete structrue solution, refinement and analysis program. J. Appl. Crystallogr. **42** (2009) 339–241.
7. Hanft, A.; Lichtenberg, C.: New perspectives for aminotroponiminates: coordination chemistry, redox behavior, cooperativity, and catalysis. Eur. J. Inorg. Chem. **2018** (2018) 3361–3373.
8. Roesky, P. W.: The coordination chemistry of aminotroponiminates. Chem. Soc. Rev. **29** (2000) 335–345.
9. Roesky, P. W.: Bulky amido ligands in rare earth chemistry – syntheses, structures, and catalysis. Z. Anorg. Allg. Chem. **629** (2003) 1881–1894.
10. Dias, H. V. R.; Wang, Z.; Jin, W.: Aminotroponiminato complexes of silicon, germanium, tin and lead. Coord. Chem. Rev. **176** (1998) 67–86.
11. Kuehl, O.: *N*-heterocyclic germylenes and related compounds. Coord. Chem. Rev. **248** (2004) 411–427.
12. Jenter, J.; Luhl, A.; Roesky, P. W.; Blechert, S.: Aminotroponiminate zinc complexes as catalysts for the intramolecular hydroamination. J. Organomet. Chem. **696** (2011) 406–418.
13. Lichtenberg, C.; Krummenacher, I.: Aminotroponiminates as tunable, redox-active ligands: reversible single electron transfer and reductive dimerisation. Chem. Commun. **52** (2016) 10044–10046.
14. Hanft, A.; Lichtenberg, C.: Aminotroponiminates: ligand-centred, reversible redox events under oxidative conditions in sodium and bismuth complexes: Dalton Trans. **47** (2018) 10578–10589.
15. Hanft, A.; Krummenacher, I.; Lichtenberg, C.: Alkali-metal aminotroponiminates: selectivities and equilibria in reversible radical coupling of delocalized π-electron systems. Chem. Eur. J. **25** (2019) 11883–11891.
16. Lichtenberg, C.: Aminotroponiminates: alkali metal compounds reveal unprecedented coordination modes. Organometallics **35** (2016) 874–902.
17. Hanft, A.; Lichtenberg, C.: Rationalizing the effect of lig- and substitution patterns on coordination and reactivity of alkali metal aminotroponiminates. Organometallics **37** (2018) 1781–1787.
18. Hanft, A.; Jürgensen, M.; Bertermann, R.; Lichtenberg, C.: Sodium aminotroponiminates: ligand-induced disproportionation, mixed-metal compounds, and exceptional activity in polymerization catalysis. ChemCatChem **10** (2018) 4018–4027.
19. Pittracher, M.; Frisch, U.; Kopacka, H.; Wurst, K.; Müller, T.; Oehninger, L.; Ott, I.; Wuttke, E.; Scheerer, S.; Winter, R. F.; Bildstein, B.: π-Complexes of tropolone and its *N*-derivatives: ambidentate [*O*,*O*]/[*N*,*O*]/[*N*,*N*]-cycloheptatrienyl pentamethylcyclopentadienyl ruthenium sandwich complexes. Organometallics **33** (2014) 1630–1643.
20. Jaynes, S.; Doerrer, L. H.; Liu, S.; Lippard, S. J.: Synthesis, tuning of the stereochemistry, and physical properties of cobalt(II) tropocoronand complexes. Inorg. Chem. **34** (1995) 5735–5744.
21. Davis, M.; Roberts, M. M.; Zask, A.; Nakanishi, K.; Nozoe, T.; Lippard, S. J.: Stereochemical and electronic spin state tuning of the metal center in the nickel(II)tropocoronands. J. Am. Chem. Soc. **107** (1985) 3864–3870.
22. Davis, M.; Zask, A.; Nakanishi, K.; Lippard, S. J.: Copper(II) tropocoronands: synthesis, structure, and properties of mononuclear complexes. Inorg. Chem. **24** (1985) 3737–3743.
23. Villacorte, M.; Gibson, D.; Williams, I. D.; Lippard, S. J.: Dicopper(I)tropocoronands: synthesis, X-ray crystal structure, and spectral properties of neutral binuclear copper(I) complexes bridged by symmetrically substituted alkynes. J. Am. Chem. Soc. **107** (1985) 6732–6734.
24. Kozhukh, J.; Minier, M. A.; Lippard, S. J.: Synthesis and characterization of mononuclear, pseudotetrahedral cobalt(III) compounds. Inorg. Chem. **54** (2015) 418–424.
25. Hopmann, K. H.; Conradie, J.; Zangen, E.; Tonzetich, Z. J.; Lippard, S. J.: Singlet-triplet gaps of cobalt nitrosyls: insights from tropocoronand complexes. Inorg. Chem. **54** (2015) 7362–7367.
26. Davis, M.; Lippard, S. J.: Tropocoronands as binucleating ligands. synthesis, structure, and properties of a (μ-acetato)(μ-methoxo)dicopper(II) derivative. Inorg. Chem. **24** (1985) 3688–3691.
27. Jaynes, S.; Ren, T.; Masschelein, A.; Lippard, S. J.: Stereochemical control of reactivity in Co(III) alkyl complexes of the tropocoronand ligand system. J. Am. Chem. Soc. **115** (1993) 5589–5599.
28. Shindo, K.; Wakabayashi, H.; Kurihara, T.; Zhang, L.-C.; Ebata, K.; Sakurai, H.; Nozoe, T.: Synthesis and crystal structure of tristropocryptands. J. Chin. Chem. Soc. **50** (2003) 47–50.
29. Yuan, Y.-Q.; Guo, S.-R.; Wang, L.-J.: Crystal structure of 2,2′-diaminodiphenyl sulfide, $C_{12}H_{12}N_2S$. Z. Kristallogr. NCS **223** (2008) 507–508.
30. Etter, M. C.; MacDonald, J. C.; Bernstein, J.: Graph-set analysis of hydrogen-bond patterns in organic crystals. Acta Crystallogr. **B46** (1990) 256–262.

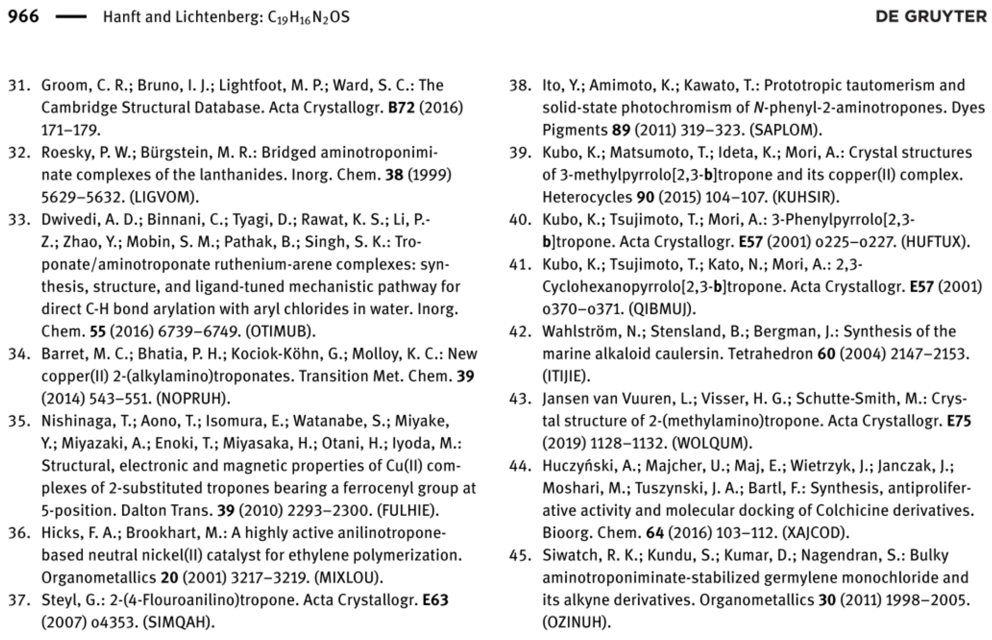

31. Groom, C. R.; Bruno, I. J.; Lightfoot, M. P.; Ward, S. C.: The Cambridge Structural Database. Acta Crystallogr. **B72** (2016) 171–179.
32. Roesky, P. W.; Bürgstein, M. R.: Bridged aminotroponiminate complexes of the lanthanides. Inorg. Chem. **38** (1999) 5629–5632. (LIGVOM).
33. Dwivedi, A. D.; Binnani, C.; Tyagi, D.; Rawat, K. S.; Li, P.-Z.; Zhao, Y.; Mobin, S. M.; Pathak, B.; Singh, S. K.: Troponate/aminotroponate ruthenium-arene complexes: synthesis, structure, and ligand-tuned mechanistic pathway for direct C-H bond arylation with aryl chlorides in water. Inorg. Chem. **55** (2016) 6739–6749. (OTIMUB).
34. Barret, M. C.; Bhatia, P. H.; Kociok-Köhn, G.; Molloy, K. C.: New copper(II) 2-(alkylamino)troponates. Transition Met. Chem. **39** (2014) 543–551. (NOPRUH).
35. Nishinaga, T.; Aono, T.; Isomura, E.; Watanabe, S.; Miyake, Y.; Miyazaki, A.; Enoki, T.; Miyasaka, H.; Otani, H.; Iyoda, M.: Structural, electronic and magnetic properties of Cu(II) complexes of 2-substituted tropones bearing a ferrocenyl group at 5-position. Dalton Trans. **39** (2010) 2293–2300. (FULHIE).
36. Hicks, F. A.; Brookhart, M.: A highly active anilinotropone-based neutral nickel(II) catalyst for ethylene polymerization. Organometallics **20** (2001) 3217–3219. (MIXLOU).
37. Steyl, G.: 2-(4-Flouroanilino)tropone. Acta Crystallogr. **E63** (2007) o4353. (SIMQAH).
38. Ito, Y.; Amimoto, K.; Kawato, T.: Prototropic tautomerism and solid-state photochromism of *N*-phenyl-2-aminotropones. Dyes Pigments **89** (2011) 319–323. (SAPLOM).
39. Kubo, K.; Matsumoto, T.; Ideta, K.; Mori, A.: Crystal structures of 3-methylpyrrolo[2,3-**b**]tropone and its copper(II) complex. Heterocycles **90** (2015) 104–107. (KUHSIR).
40. Kubo, K.; Tsujimoto, T.; Mori, A.: 3-Phenylpyrrolo[2,3-**b**]tropone. Acta Crystallogr. **E57** (2001) o225–o227. (HUFTUX).
41. Kubo, K.; Tsujimoto, T.; Kato, N.; Mori, A.: 2,3-Cyclohexanopyrrolo[2,3-**b**]tropone. Acta Crystallogr. **E57** (2001) o370–o371. (QIBMUJ).
42. Wahlström, N.; Stensland, B.; Bergman, J.: Synthesis of the marine alkaloid caulersin. Tetrahedron **60** (2004) 2147–2153. (ITIJIE).
43. Jansen van Vuuren, L.; Visser, H. G.; Schutte-Smith, M.: Crystal structure of 2-(methylamino)tropone. Acta Crystallogr. **E75** (2019) 1128–1132. (WOLQUM).
44. Huczyński, A.; Majcher, U.; Maj, E.; Wietrzyk, J.; Janczak, J.; Moshari, M.; Tuszynski, J. A.; Bartl, F.: Synthesis, antiproliferative activity and molecular docking of Colchicine derivatives. Bioorg. Chem. **64** (2016) 103–112. (XAJCOD).
45. Siwatch, R. K.; Kundu, S.; Kumar, D.; Nagendran, S.: Bulky aminotroponiminate-stabilized germylene monochloride and its alkyne derivatives. Organometallics **30** (2011) 1998–2005. (OZINUH).

IX Salicylaldimines: Formation via Ring Contraction and Synthesis of Mono- and Heterobimetallic Alkali Metal Heterocubanes

Anna Hanft, Malte Jürgensen, Laura Wolz, Krzysztof Radacki, Crispin Lichtenberg

Vervielfältigt aus Referenz:

Inorg. Chem. **2020**, *51*, 17678-17688.[68]

https://doi.org/10.1021/acs.inorgchem.0c02920

mit Erlaubnis von American Chemical Society.

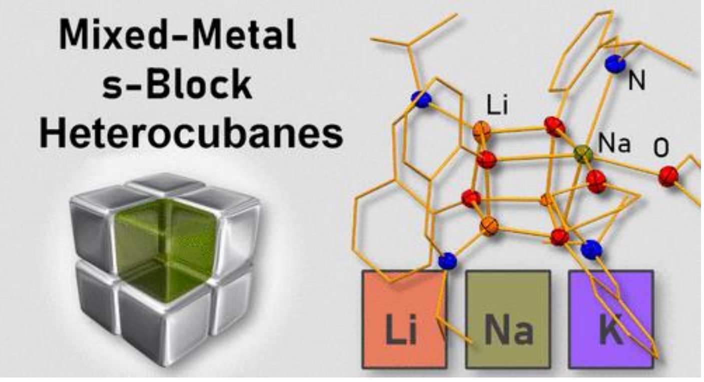

Inorganic Chemistry

pubs.acs.org/IC Article

Salicylaldimines: Formation via Ring Contraction and Synthesis of Mono- and Heterobimetallic Alkali Metal Heterocubanes

Anna Hanft, Malte Jürgensen, Laura Wolz, Krzysztof Radacki, and Crispin Lichtenberg*

Cite This: *Inorg. Chem.* 2020, 59, 17678−17688 Read Online

ABSTRACT: The formation of salicylaldimine derivatives via ring contraction as byproducts in 2-aminotropone syntheses has been investigated. Salicylaldiminate (SAI) complexes of the alkali metals Li−K have been synthesized and transformed into heterobimetallic complexes. Important findings include an unusual double heterocubane structure of the homometallic sodium SAI, an unprecedented ligand-induced *E*/*Z* isomerization of the aldimine functional group in the homometallic potassium SAI, and the first example of a structurally authenticated mixed-metal SAI based on s-block central atoms. Rapid equilibria have been shown to play a crucial role in the solution phase chemistry of mixed-metal SAIs. Analytical techniques applied in this work include (heteronuclear) NMR spectroscopy, VT- and DOSY NMR spectroscopy, high-resolution mass spectrometry, single-crystal X-ray diffraction analysis, and DFT calculations.

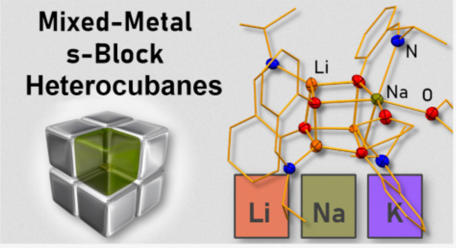

■ INTRODUCTION

Aminotroponiminates (ATIs) are a well-established ligand family[1] with a rich coordination chemistry,[2] a multi-faceted redox chemistry,[3] ligand cooperativity,[4] and a variety of catalytic applications (e.g., alkyne oligomerization,[4a] olefin hydroamination,[5] and polymerization of cyclic esters[2d]). A range of approaches have been developed for the generation of various types of ATI ligands.[1a,d] The synthetic route to ATIs with aryl and alkyl substituents at nitrogen (without excessive steric bulk) and without further substituents in the ATI backbone is robust, high-yielding, and probably the one that has been applied most frequently (Scheme 1a).[1a,d,6]

The first step of this reaction (**1** → **A**) reflects a substitution reaction transforming the tropone into an aminotropone. Ring contraction reactions may compete with this transformation, when additional substituents are present in the tropone backbone,[7] when transition metal complexes are present,[7h] or when high reaction temperatures in combination with bulky amines are employed (Scheme 1b).[8] The nature of the leaving group X and the substituents in the tropone backbone as well as the nature of the amine employed as a nucleophile can have a dramatic impact on the chemo- and regioselectivity of these reactions.[7e] By using tropones with bromo substituents in the backbone, for instance, a substitution-rearrangement pathway has been addressed deliberately in order to generate bromo-substituted salen-type ligands for hydroamination catalysis (Scheme 1c).[9] In the widely applied standard protocol for the synthesis of 2-aminotropones **A**, however, such rearrangements have not been reported to date.[1a,d,6]

Salicylaldimines of type **D** have a long-standing history as ligands in coordination chemistry and catalysis.[10] For example, transition metal salicylaldiminate (SAI) complexes show antimicrobial activity[11] and have been exploited as catalysts[12] for the polymerization of ethylene[13] and cyclic esters,[14] in olefin metathesis,[15] and in hydroamination reactions.[9b]

Main group complexes and especially alkali metal derivatives of SAIs are less explored. They have been utilized as SAI transfer reagents in the synthesis of transition metal complexes,[13b,16] as bases in carboxylation reactions,[17] and as catalysts in ring opening polymerizations (ROP) of cyclic esters.[14c,18] In the last type of reactions, the ligand architecture and the coordination chemistry of the metal complexes have been shown to critically influence the catalytic performance of SAI complexes and have thus been studied in some detail. In the solid state, alkali metal SAIs may aggregate to give dinuclear,[18e,f,l] tetranuclear, and hexanuclear species, corresponding to planar, cubic,[13b,14c,17,18b,e,f] and double cubic[19] core structures, respectively (Scheme 2a). These structural features may be rationalized in analogy with the ring stacking principle that has originally been proposed for the analysis of the solid state structures of lithium compounds.[20]

Received: October 1, 2020
Published: November 23, 2020

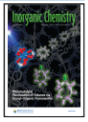

ACS Publications

https://dx.doi.org/10.1021/acs.inorgchem.0c02920
Inorg. Chem. 2020, 59, 17678−17688

Scheme 1. (a) Synthetic Route to Aminotroponimines (H-ATIs). (b) Substitution Reaction of Tropone Derivatives with Amines, Followed by Ring Contraction to Give Salicylaldimines (H-SAIs). (c) Example of a Double Substitution at a Brominated Tropone Derivative, Followed by a Ring Contraction[a]

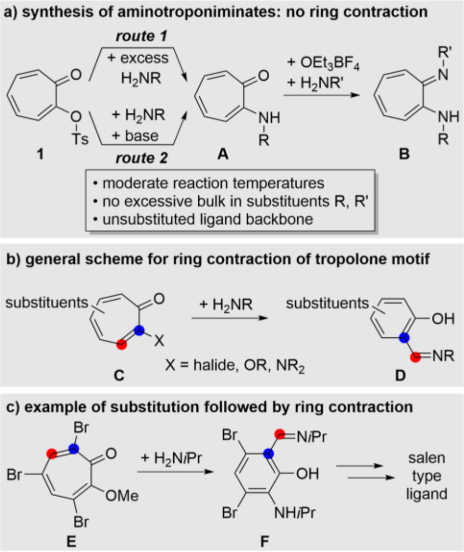

[a]OTs = tosylate.

Scheme 2. (a) Schematic Presentation of Structural Motifs Reported for Alkali Metal SAI Complexes. (b, c) Examples of Heterobimetallic SAI Complexes[a]

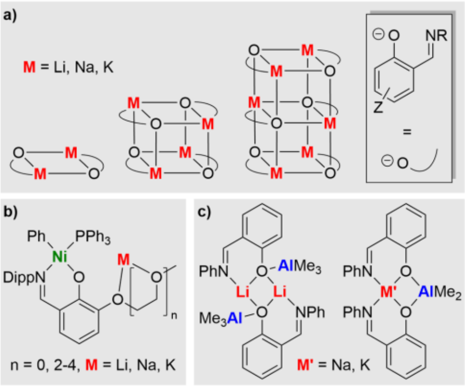

[a]R = alkyl, aryl; Z = substituent(s) in the aromatic backbone.

Heterobimetallic SAI complexes are rare and comprise transition metal complexes linked to alkali metals by additional donor substituents in the ligand periphery (e.g., Scheme 2b).[18g,21,22] In olefin polymerization, the heterobimetallic species show enhanced catalytic activities or improved molecular weight control compared to their monometallic counterparts.[21c,22] Heterobimetallic complexes with both metals being main group metals have so far only been realized in a series of alkali metal aluminate complexes (Scheme 2c).[23] The intriguing cubic and double cubic structural motifs found in alkali metal SAI complexes (Scheme 2a) have so far not been authenticated for heterobimetallic SAI species.

We herein report the formation of salicylaldimines during the synthesis of unsubstituted 2-aminotropones **B** (Scheme 1a) and factors influencing the chemoselectivity of this reaction. Mono- and heterobimetallic alkali metal SAI complexes were synthesized, and their structure in the solid state and in solution was investigated.

■ RESULTS AND DISCUSSION

Salicylaldimines. In the standard protocol for the synthesis of 2-aminotropones **B**, the tosyl-oxy-tropone **1** can simply be stirred in an excess of amine, if the amine is sufficiently nucleophilic, liquid at room temperature, and affordable in the required quantities (Scheme 1, route 1). Alternatively, stoichiometric amounts of an amine are used in the presence of a base, if the amine is valuable and/or solid at room temperature (route 2).[1a,d,6,24] Many primary alkylamines fulfill the requirements for the more facile route 1, isopropylamine being one of the archetypical examples. Consequently, the reaction of **1** to give **2** is one of the most common reactions in the preparation of aminotropones and aminotroponimines (Scheme 3a, left).[25] We were therefore surprised to detect a side product in this frequently used synthetic procedure, which—to the best of our knowledge—had never been identified in any literature reports. This species was obtained in small, but reproducible, quantities and could be isolated by column chromatography. Elemental analysis and high-resolution mass spectrometry indicated the composition $C_{10}H_{13}N_1O_1$; i.e., it is an isomer of compound **2** (for details, see the Experimental Section). This left the possibilities of a ring contraction to give literature-known **3a**[26] or a *cine*-substitution pathway[27] to give the unknown seven-membered ring **3b**.

Scheme 3. Isolation of Ring Contraction Products 3a and 5 from Reactions of 1 with H$_2$N*i*Pr and H$_2$NFc, Respectively[a]

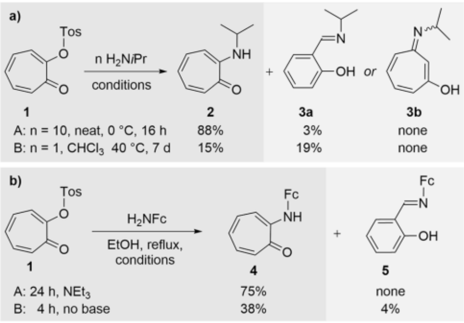

[a]Tos = SO$_2$-*p*-(C$_6$H$_4$Me); Fc = ferrocenyl; results from conditions A in part (b) have been reported in ref 3b.

Evaluation of the NMR data of the sample strongly suggested the formation of **3a**,[26] which was verified by transformation of **3a** into metalated derivatives and their detailed analysis (*vide infra*).

The unprecedented observation of a ring contraction in a standard protocol for the synthesis of 2-aminotropones prompted us to perform a short survey on the factors influencing the selectivity of these reactions. As a result, reaction of **1** with only 1 equiv of isopropylamine at extended reaction times of 7 d and in the absence of an additional base gave selectivities of >50% toward **3a** at moderate overall conversions (for details, see the Supporting Information). It should be noted that, under the applied reaction conditions, isolated **2** did not rearrange to give compound **3a** (for details, see the Supporting Information).

In the light of these findings on the occurrence of ring contractions during the synthesis of 2-aminotropones via route 1, ferrocenylamine (H_2NFc) was also investigated in this reaction as a typical representative of a less nucleophilic and more valuable primary amine (route 2). In this case, the product of a ring contraction (compound **5**[28]) was obtained in low yield, only when the reaction was performed in the absence of an external base (Scheme 3b; for details, see the Experimental Section and, for NMR spectroscopic reaction monitoring, see the Supporting Information).

These results show that the ring contraction reactions identified here only play a minor role under standard conditions for the synthesis of aminotropones, but may become reaction pathways of significant importance when the reaction conditions are slightly modified. This is an important point to keep in mind (i) for the synthesis of yet unknown aminotropones (and ATIs derived thereof) and (ii) for the exploitation of synthetic strategies that deliberately address such ring contraction reactions in order to generate salicylaldimines that may be more difficult to synthesize via more established synthetic routes.[9]

Alkali Metal Salicylaldiminates (SAIs). The synthesis of alkali metal salicylaldiminates (SAIs) was targeted in order to explore their potential in the generation of mixed-metal compounds. Thus, compound **3a** was reacted with alkali metal bases MHMDS (Scheme 4; M = Li−K; HMDS = hexamethyldisilazide). Isolation and characterization of the literature-known lithium species **6**[13b] confirmed the structural assignment of starting material **3a** obtained from the ring contraction reaction of **1** (*cf.* Scheme 3a). The sodium and the potassium compounds **7** and **8** were isolated as colorless solids in good yields. NMR spectroscopic analysis of **6**−**8** in pyridine-d_5 revealed the expected signal patterns for the isopropyl, the aldimine, and the 1,2-substituted aryl functional groups with clearly distinct chemical shifts for each of the complexes.[29]

Scheme 4. Synthesis of Alkali Metal Salicylaldiminate Complexes 6, 7, 8, and 8-crown[a]

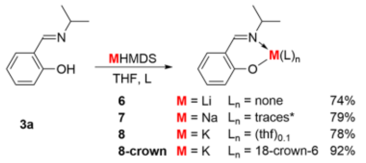

[a] *: Traces of THF (0.02 equiv) and toluene (0.04 equiv) were detected.

For the potassium SAI crown ether complex **8-crown**, NMR spectroscopy revealed the presence of a second signal set of minor intensity (3% upon solvation of the sample). This was ascribed to an *E*/*Z* isomerism of the aldimine functional group with the main species being the *E*-isomer.[30] This is supported by analysis of the $^1H^1H$-NOESY NMR spectrum of this compound: a cross signal between the CH moiety of the isopropyl group and the aromatic CH group in the 3-position is absent for the major isomer, but present for the minor isomer. A *trans* configuration of the $C^{aryl}-C^{aldimine}$ group was tentatively assigned to both isomers based on cross signals between the aldimine CH group and the ethylene groups of the crown ether.

For aldimines in general, *E*/*Z* isomerism is a well-known phenomenon, with the isomer distribution depending on electronic and steric factors as well as solvent effects.[31] Transformations between the two isomers can be triggered thermally or photochemically.[32] However, *E*/*Z* isomerism has only rarely been discussed for salicylaldiminate complexes and not been unambiguously identified.[33] Most importantly, the isomerism was not observed for compounds **6**−**8**; in other words, it can be triggered by addition of the strong chelating ligand 18-crown-6. This is most likely due to a switch of the SAI ligand from a chelating coordination mode in the absence of 18-crown-6 to a κ^1O coordination mode in the presence of 18-crown-6 (*vide infra*). In agreement with these findings, irradiating solutions of **8-crown** with a mercury vapor lamp for 2 h increased the amount of the *Z*-isomer to 11%. Storing the same sample at ambient light for 2 d gave back the initial 3% of the *Z*-isomer. Heating the sample to 60 °C for 2 h or shielding from ambient light for 7 d resulted in formation of the *E*-isomer, exclusively. No decomposition of the sample was observed during the above-mentioned manipulations.

Single-crystal X-ray analysis of the lithium complex **6** revealed the literature-known Li_4SAI_4 structural motif,[13b] although single crystals were grown under various conditions, including the use of polar solvents such as pyridine.

Slow diffusion of pentane into a THF solution of the sodium compound **7** yielded crystals suitable for single-crystal X-ray diffraction analysis. Compound **7** crystallized as a hexanuclear species with a Na_6O_6 core structure, which is built of two face-fused Na_4O_4 heterocubanes (triclinic space group $P\bar{1}$ with $Z = 2$; Figure 1). The structure can be thought of as being composed of three Na_2SAI_2 units, which are equivalent to two outer faces and one inner face of the double heterocubane. The outer face units are linked to the inner face unit only through Na−O interactions (not through Na−N bonding). The SAI ligands adopt chelating coordination modes with a sodium atom in the N/O binding pocket. At the same time, the oxygen atoms of the ligands that are part of the outer face units bridge three sodium atoms, while each of the oxygen atoms that is part of the central Na_2SAI_2 unit bridges four sodium atoms. As a result, the sodium atoms of the outer faces are four-coordinate and adopt a strongly distorted tetrahedral coordination geometry (O−Na(1/2/4/5)−O/N, 81.4−154.1°).[34] The inner face sodium atoms are five-coordinate and adopt a slightly distorted square pyramidal coordination geometry (Na3, $\tau = 0.06$, O3 in the apical position; Na6, $\tau = 0.05$, O6 in the apical position). The four-coordinate sodium atoms (Na1, Na2, Na4, and Na5) show short Na−O and Na−N bond lengths (Na−O, 2.23−2.38 Å; Na−N, 2.32−2.36 Å) as compared to the five-coordinate sodium atoms Na3 and Na6 (Na−O, 2.33−2.46 Å; Na−N, 2.44 Å).

While heterocubane structures of sodium SAIs have been reported in several instances,[14c,17,18b,e,35] double heterocubane

https://dx.doi.org/10.1021/acs.inorgchem.0c02920
Inorg. Chem. 2020, 59, 17678−17688

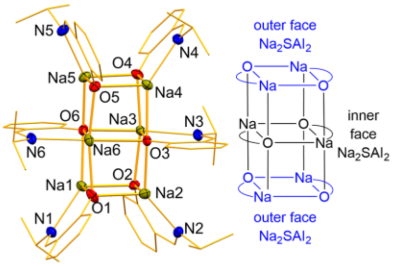

Figure 1. Molecular structure of $[Na_6(SAI)_6]$ **7** in the solid state (left) and schematic presentation (right). Heteroatoms are represented by displacement ellipsoids at the 50% probability level; carbon atoms are shown as wireframe. Hydrogen atoms and a lattice bound solvent molecule are omitted for clarity. Selected bond lengths (Å) and angles (deg): Na1−N1, 2.3305(13); Na1−O1, 2.2284(11); Na1−O2, 2.2844(11); Na1−O6, 2.3835(11); Na2−N2, 2.355(3); Na2−O1, 2.2773(12); Na2−O2, 2.2375(11); Na2−O3, 2.3178(11); Na3−N3, 2.4416(13); Na3−O2, 2.3659(11); Na3−O3, 2.3252(11); Na3−O4, 2.4019(11); Na3−O6, 2.4324(11); Na4−N4, 2.3181(13); Na4−O3, 2.3636(11); Na4−O4, 2.2287(13); Na4−O5, 2.2799(12); Na5−N5, 2.3371(19); Na5−O4, 2.2852(12); Na5−O5, 2.2364(11); Na5−O6, 2.3276(11); Na6−N6, 2.437(2); Na6−O1, 2.3688(13); Na6−O3, 2.4621(11); Na6−O5, 2.3382(11); Na6−O6, 2.3289(11); O1−C1, 1.3019(18); O2−C11, 1.3067(17); O3−C21, 1.3176(17); O4−C31, 1.3044(17); O5−C41, 1.3061(17); O6−C51, 1.3211(18); O(1−6)−Na(1/2/4/5)−O(1−6), 88.98(4)−96.84(4); O(1−6)−Na(1/2/4/5)−N(1/2/4/5), 81.44(8)−154.13(7); O(1−6)−Na(3/6)−O(1−6), 84.84(4)−169.95(4); O(1−6)−Na(3/6)−N(5/6), 76.61(4)−166.82(7).

structural motifs are extremely rare for sodium SAIs.[36] In fact, only one such example has been reported in the literature, but contains additional thioether functional groups, which leads to larger coordination numbers of the sodium atoms (CN = 5−6) and larger Na−O bond lengths of up to 2.62 Å (as compared to an upper limit of 2.46 Å for the Na−O bond lengths in **7**).[19] Thus, the structural analysis of **7** proves that the unusual double heterocubane structural motif can be realized for sodium SAIs without the aid of additional chelating functional groups.[37]

Potassium SAI complexes have been reported to be mono-, di-, or tetranuclear in the solid state.[18e,f,h] Mononuclear species can be obtained, for instance, by complexation of the potassium atom with 18-crown-6. Since our attempts to obtain single crystals of compound **8** were unsuccessful under various conditions, crystallization in the presence of 18-crown-6 was performed. Slow diffusion of pentane into a THF solution containing **8** and 1 equiv of 18-crown-6 led to crystals suitable for single-crystal X-ray diffraction analysis. **8-crown** crystallized in the monoclinic space group $P2_1$ with $Z = 2$ (Figure 2). In accordance with the literature, a mononuclear complex is formed, and the coordination sphere of the potassium atom is saturated by the crown ether and the oxygen atom of the SAI ligand, which coordinates in a κ^1O fashion.

The C^{aryl}−$C^{aldimine}$ group shows a *trans* configuration, which minimizes steric repulsion between the *i*Pr substituent and the K(18-crown-6) moiety. The C═N double bond shows an *E*-configuration. These findings confirm the structure suggested for the main isomer of **8-crown** in solution (*vide supra*). The K1−O1 bond length of 2.50 Å is significantly smaller, and the C1−O1−K1 angle of 164.1° is much larger than the corresponding values in the closely related species $[K(SAI^{Ph})(18\text{-crown-6})]$, where the *i*Pr group of **8-crown** is formally substituted by a Ph group (K−O, 2.62 Å; C−O−K, 130.9°).[18h] This was ascribed to the electron-donating character of the *i*Pr group in **8-crown**.

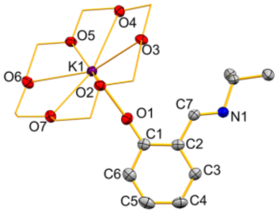

Figure 2. Molecular structure of [K(SAI)(18-crown-6)] **8-crown** in the solid state. All atoms except the ethylene units of the crown ether, which are shown as wire frame, are represented by displacement ellipsoids at the 50% probability level. Hydrogen atoms are omitted for clarity. Selected bond lengths (Å) and angles (deg): K1−O1, 2.501(3); K1−O2, 2.847(3); K1−O3, 2.841(2); K1−O4, 2.874(3); K1−O5, 2.808(3); K1−O6, 2.863(3); K1−O7, 2.866(3); O1−C1, 1.282(4); C2−C7, 1.458(5); N1−C7, 1.271(4); C1−C2, 1.428(5); C2−C3, 1.406(5); C3−C4, 1.379(5); C4−C5, 1.394(5); C5−C6, 1.364(5); C1−C6, 1.430(5); O(1−7)−K1−O(1−7), 58.35(7)−161.49(7); C1−O1−K1, 164.1(2).

Mixed-Metal Salicylaldiminates (SAIs). Mixed-metal compounds, in general,[38] and mixed-metal compounds of s-block elements, in particular, have been shown to display a complex coordination chemistry in solution and in the solid state, with high potential for applications such as metalation reactions,[39] cyclization reactions,[40] (reversible) de-aromatization reactions,[41] olefin oligomerization[30] as well as the polymerization of olefins[30,42] and cyclic esters.[2d,42b] We aimed to evaluate the potential of simple SAI ligands without additional functional groups for the synthesis of heterobimetallic complexes. Thus, two series of reactions were performed with compounds **6−8**: (i) reactions of two alkali metal SAIs in a 1:1 stoichiometry (Table 1, entries 1−3) and (ii) reactions of the lithium compound **6** and the sodium compound **7** in 1:3, and 3:1 stoichiometries (entries 4 and 5). The products **9−13** of these reactions were isolated as colorless solids. In all cases, NMR spectroscopic analysis (^1H, ^{13}C; ^7Li, ^{23}Na where appropriate) at 23 °C revealed one set of well-resolved signals with the expected multiplicities and with chemical shifts, which did not correspond to the weighted average of the chemical shifts recorded for the pure monometallic complexes. The NMR spectra of all

Table 1. Synthesis of Heterobimetallic Complexes 9−13

$$x\,M(SAI) + y\,M'(SAI) \xrightarrow[THF]{} M_xM'_y(SAI)_{(x+y)}(thf)_n$$

Entry	Compound	M	M’	x	y	n	Yield[a]
1	**9**	Li	Na	1	1	0	61%
2	**10**	Li	K	1	1	0	96%
3	**11**	Na	K	1	1	0.15	79%
4	**12**	Li	Na	3	1	0	59%
5	**13**	Li	Na	1	3	0.18	65%

[a] Isolated yield, conversion quantitative.

compounds **9**−**13** remained unchanged, when solutions of these complexes were kept under inert conditions for several days.

Slow evaporation of the solvent of a THF solution of complex **9** with its Li/Na = 1:1 stoichiometry led to the formation of crystals suitable for single-crystal X-ray diffraction analysis (orthorhombic space group *Pna*2_1 with $Z = 4$). Unexpectedly, the structural analysis revealed a complex with a Li/Na = 3:1 stoichiometry, $[Li_3(SAI)_3Na(SAI)(thf)_2]$ (**12·(thf)$_2$**).[43] Compound **12·(thf)$_2$** shows a heterocubane core structure (Figure 3), confirming the formation of the first mixed alkali metal SAI complex.

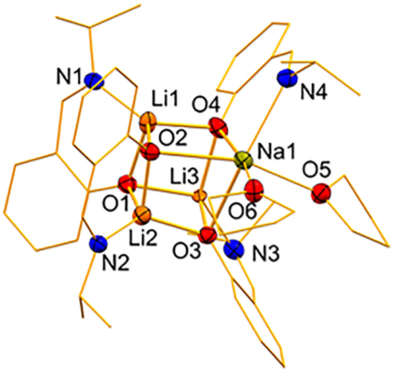

Figure 3. Molecular structure of $[Li_3Na(SAI)_4(thf)_2]$ (**12·(thf)$_2$**) in the solid state. Heteroatoms are represented by displacement ellipsoids at the 50% probability level; carbon atoms are shown as wireframe. Hydrogen atoms are omitted for clarity. Selected bond lengths (Å) and angles (deg): Na1−O2, 2.545(2); Na1−O3, 2.469(2); Na1−O4, 2.3270(19); Na1−O5, 2.400(2); Na1−O6, 2.453(14); Na1−N4, 2.514(2); Li1−O1, 1.943(5); Li1−O2, 1.962(4); Li1−O4, 1.974(4); Li1−N1, 2.037(4); Li2−O1, 2.029(4); Li2−O2, 1.930(5); Li2−O3, 1.914(4); Li2−N2, 2.030(5); Li3−O1, 2.005(4); Li3−O3, 1.995(5); Li3−O4, 2.020(4); Li3−N3, 2.049(4); O1−C1, 1.310(3); O2−C11, 1.298(3); O3−C21, 1.306(3); O4−C31, 1.316(3); N1−C7, 1.282(3); N2−C17, 1.277(4); N3−C27, 1.279(4); N4−C37, 1.275(4); O(2−6)−Na1−(O2−6), 74.67(6)−169.0(3); O(2−6)−Na1−N4, 76.88(7)−152.84(7); O(1−4)−Li(1−3)−O(1−4), 92.21(19)−104.6(2); O(1−4)−Li(1−3)−N(1−3), 91.77(18)−135.4(2).

The coordination geometries are distorted tetrahedral for lithium atoms and distorted octahedral for the sodium center with its two thf ligands. The structure of **12·(thf)$_2$** is related to that of the parent homometallic lithium complex **6**[13b] by exchange of one Li atom for one $[Na(thf)_2]$ unit. This leads to a significant distortion of the M_4O_4 cube in **12·(thf)$_2$** due to the larger Na−O bond lengths. In addition, the incorporation of a sodium atom into the heterocubane also increases the Li···Li interatomic distances to 2.68−2.72 Å, as compared to 2.55−2.69 Å in homometallic **6**.[13b] The Li−O (1.91−2.03 Å) and Li−N bond lengths (2.03−2.05 Å) in **12·(thf)$_2$** are only marginally larger than those in **6** (Li−O, 1.89−2.00 Å; Li−N, 1.97−2.00 Å).[13b] The Na1−O^{SAI} (2.33−2.55 Å) and Na1−N4 (2.51 Å) bonds in **12·(thf)$_2$** are longer than those in homometallic **7** (CN = 4: Na−O, 2.23−2.38 Å; Na−N, 2.32−2.36 Å; CN = 5: Na−O, 2.33−2.46 Å; Na−N, 2.44 Å), which was ascribed to the higher coordination number of the sodium atom in the heterobimetallic species.

The isolation of **12·(thf)$_2$** from a solution of compound **9** raised the question of dynamic exchange reactions in such heterobimetallic species. In order to gain first insights into the aggregation behavior of and potential interconversion between these compounds, DFT calculations were performed (for details, see the Experimental Section and Supporting Information). According to these studies, the addition of 2 equiv of THF to **9** and **12**, respectively, is exothermal and exergonic in both cases (Scheme 5a). The dissociations of tetranuclear species **9·(thf)$_2$** and **12·(thf)$_2$** into dinuclear species are thermoneutral (for **9·(thf)$_2$**) and exothermic (for **12·(thf)$_2$**) as well as slightly endergonic in both cases (Scheme 5b). Thus, these transformations represent a potential entry into rearrangement reactions of this type of heterocubanes. The formation of "lithium-rich" compound **12·(thf)$_2$** from compound **9·(thf)$_2$** requires the appearance of one or more "sodium-rich" byproducts. The formation of isolable homometallic sodium complex **7** fulfills this requirement and results in the reaction equation given in Scheme 5c. This reaction is marginally endothermic and exergonic, demonstrating that such rearrangement reactions are thermodynamically feasible.

Scheme 5. Thermodynamic Data for Reactions of Heterocubanes $[Li_2Na_2(SAI)_4]$ (9) and $[Li_3Na_1(SAI)_4]$ (12) As Determined by DFT Calculations[a]

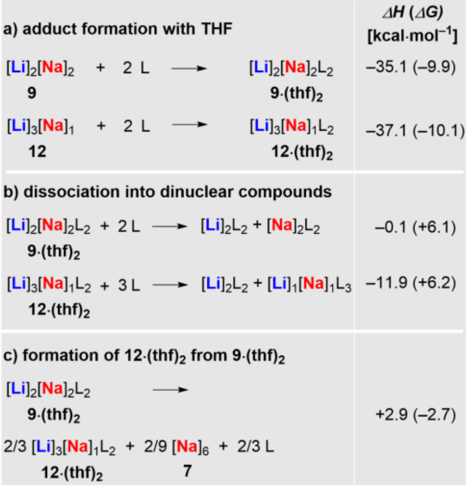

[a] [Li] = Li(SAI); [Na] = Na(SAI); L = thf.

The potential of compound **9** to be susceptible to dynamic exchange reactions in solution motivated more detailed investigations of the solution behavior of lithium/sodium mixed-metal SAI complexes (all of which were performed in THF). Low-temperature NMR spectroscopy on compound **9** revealed one sharp set of signals even at −100 °C, suggesting the exchange indicated by the isolation of **12·(thf)$_2$** from solutions of **9** and by DFT calculations (*vide supra*) to be fast on the time scale of the NMR spectroscopic experiment (Figure S23). In contrast, the mixed-metal complexes **12** and **13** revealed significant broadening of all resonances in THF solution at

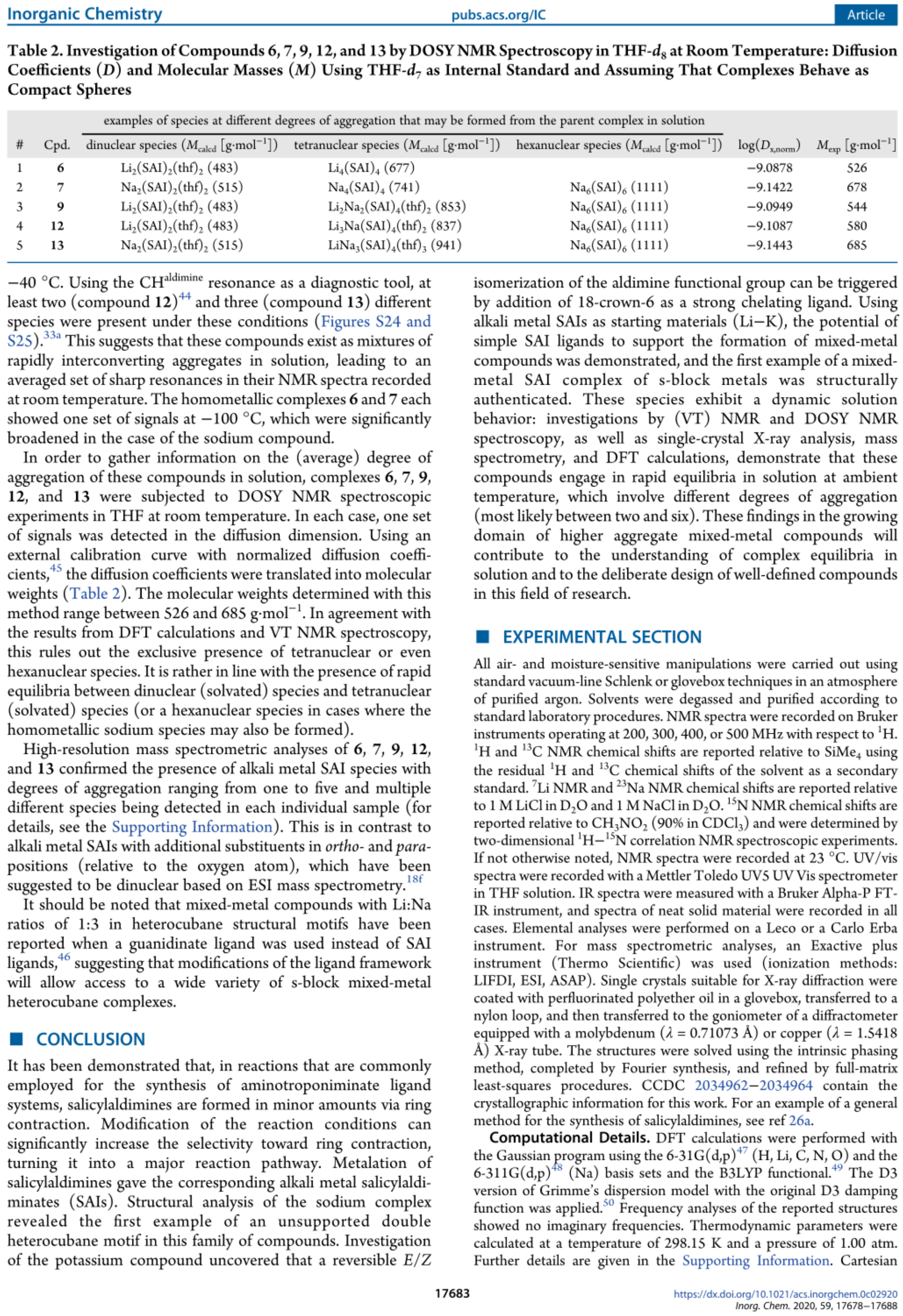

Table 2. Investigation of Compounds 6, 7, 9, 12, and 13 by DOSY NMR Spectroscopy in THF-d_8 at Room Temperature: Diffusion Coefficients (D) and Molecular Masses (M) Using THF-d_7 as Internal Standard and Assuming That Complexes Behave as Compact Spheres

		examples of species at different degrees of aggregation that may be formed from the parent complex in solution				
#	Cpd.	dinuclear species (M_{calcd} [g·mol^{-1}])	tetranuclear species (M_{calcd} [g·mol^{-1}])	hexanuclear species (M_{calcd} [g·mol^{-1}])	log($D_{x,norm}$)	M_{exp} [g·mol^{-1}]
1	**6**	$Li_2(SAI)_2(thf)_2$ (483)	$Li_4(SAI)_4$ (677)		−9.0878	526
2	**7**	$Na_2(SAI)_2(thf)_2$ (515)	$Na_4(SAI)_4$ (741)	$Na_6(SAI)_6$ (1111)	−9.1422	678
3	**9**	$Li_2(SAI)_2(thf)_2$ (483)	$Li_2Na_2(SAI)_4(thf)_2$ (853)	$Na_6(SAI)_6$ (1111)	−9.0949	544
4	**12**	$Li_2(SAI)_2(thf)_2$ (483)	$Li_3Na(SAI)_4(thf)_2$ (837)	$Na_6(SAI)_6$ (1111)	−9.1087	580
5	**13**	$Na_2(SAI)_2(thf)_2$ (515)	$LiNa_3(SAI)_4(thf)_3$ (941)	$Na_6(SAI)_6$ (1111)	−9.1443	685

−40 °C. Using the CH^{aldimine} resonance as a diagnostic tool, at least two (compound **12**)[44] and three (compound **13**) different species were present under these conditions (Figures S24 and S25).[33a] This suggests that these compounds exist as mixtures of rapidly interconverting aggregates in solution, leading to an averaged set of sharp resonances in their NMR spectra recorded at room temperature. The homometallic complexes **6** and **7** each showed one set of signals at −100 °C, which were significantly broadened in the case of the sodium compound.

In order to gather information on the (average) degree of aggregation of these compounds in solution, complexes **6**, **7**, **9**, **12**, and **13** were subjected to DOSY NMR spectroscopic experiments in THF at room temperature. In each case, one set of signals was detected in the diffusion dimension. Using an external calibration curve with normalized diffusion coefficients,[45] the diffusion coefficients were translated into molecular weights (Table 2). The molecular weights determined with this method range between 526 and 685 g·mol^{-1}. In agreement with the results from DFT calculations and VT NMR spectroscopy, this rules out the exclusive presence of tetranuclear or even hexanuclear species. It is rather in line with the presence of rapid equilibria between dinuclear (solvated) species and tetranuclear (solvated) species (or a hexanuclear species in cases where the homometallic sodium species may also be formed).

High-resolution mass spectrometric analyses of **6**, **7**, **9**, **12**, and **13** confirmed the presence of alkali metal SAI species with degrees of aggregation ranging from one to five and multiple different species being detected in each individual sample (for details, see the Supporting Information). This is in contrast to alkali metal SAIs with additional substituents in *ortho*- and *para*-positions (relative to the oxygen atom), which have been suggested to be dinuclear based on ESI mass spectrometry.[18f]

It should be noted that mixed-metal compounds with Li:Na ratios of 1:3 in heterocubane structural motifs have been reported when a guanidinate ligand was used instead of SAI ligands,[46] suggesting that modifications of the ligand framework will allow access to a wide variety of s-block mixed-metal heterocubane complexes.

■ CONCLUSION

It has been demonstrated that, in reactions that are commonly employed for the synthesis of aminotroponiminate ligand systems, salicylaldimines are formed in minor amounts via ring contraction. Modification of the reaction conditions can significantly increase the selectivity toward ring contraction, turning it into a major reaction pathway. Metalation of salicylaldimines gave the corresponding alkali metal salicylaldiminates (SAIs). Structural analysis of the sodium complex revealed the first example of an unsupported double heterocubane motif in this family of compounds. Investigation of the potassium compound uncovered that a reversible *E*/*Z* isomerization of the aldimine functional group can be triggered by addition of 18-crown-6 as a strong chelating ligand. Using alkali metal SAIs as starting materials (Li−K), the potential of simple SAI ligands to support the formation of mixed-metal compounds was demonstrated, and the first example of a mixed-metal SAI complex of s-block metals was structurally authenticated. These species exhibit a dynamic solution behavior: investigations by (VT) NMR and DOSY NMR spectroscopy, as well as single-crystal X-ray analysis, mass spectrometry, and DFT calculations, demonstrate that these compounds engage in rapid equilibria in solution at ambient temperature, which involve different degrees of aggregation (most likely between two and six). These findings in the growing domain of higher aggregate mixed-metal compounds will contribute to the understanding of complex equilibria in solution and to the deliberate design of well-defined compounds in this field of research.

■ EXPERIMENTAL SECTION

All air- and moisture-sensitive manipulations were carried out using standard vacuum-line Schlenk or glovebox techniques in an atmosphere of purified argon. Solvents were degassed and purified according to standard laboratory procedures. NMR spectra were recorded on Bruker instruments operating at 200, 300, 400, or 500 MHz with respect to ^{1}H. ^{1}H and ^{13}C NMR chemical shifts are reported relative to $SiMe_4$ using the residual ^{1}H and ^{13}C chemical shifts of the solvent as a secondary standard. ^{7}Li NMR and ^{23}Na NMR chemical shifts are reported relative to 1 M LiCl in D_2O and 1 M NaCl in D_2O. ^{15}N NMR chemical shifts are reported relative to CH_3NO_2 (90% in $CDCl_3$) and were determined by two-dimensional ^{1}H−^{15}N correlation NMR spectroscopic experiments. If not otherwise noted, NMR spectra were recorded at 23 °C. UV/vis spectra were recorded with a Mettler Toledo UV5 UV Vis spectrometer in THF solution. IR spectra were measured with a Bruker Alpha-P FT-IR instrument, and spectra of neat solid material were recorded in all cases. Elemental analyses were performed on a Leco or a Carlo Erba instrument. For mass spectrometric analyses, an Exactive plus instrument (Thermo Scientific) was used (ionization methods: LIFDI, ESI, ASAP). Single crystals suitable for X-ray diffraction were coated with perfluorinated polyether oil in a glovebox, transferred to a nylon loop, and then transferred to the goniometer of a diffractometer equipped with a molybdenum (λ = 0.71073 Å) or copper (λ = 1.5418 Å) X-ray tube. The structures were solved using the intrinsic phasing method, completed by Fourier synthesis, and refined by full-matrix least-squares procedures. CCDC 2034962−2034964 contain the crystallographic information for this work. For an example of a general method for the synthesis of salicylaldimines, see ref 26a.

Computational Details. DFT calculations were performed with the Gaussian program using the 6-31G(d,p)[47] (H, Li, C, N, O) and the 6-311G(d,p)[48] (Na) basis sets and the B3LYP functional.[49] The D3 version of Grimme's dispersion model with the original D3 damping function was applied.[50] Frequency analyses of the reported structures showed no imaginary frequencies. Thermodynamic parameters were calculated at a temperature of 298.15 K and a pressure of 1.00 atm. Further details are given in the Supporting Information. Cartesian

https://dx.doi.org/10.1021/acs.inorgchem.0c02920
Inorg. Chem. 2020, 59, 17678−17688

coordinates of optimized structures are provided in .xyz format (Supporting Information).

Compounds 2 and 3a.[6a] Isopropylamine (27.8 g, 470 mmol, 40.3 mL) was cooled to 0 °C. 2-Tosyloxytropone (10.0 g, 36.2 mmol) was added in small portions while stirring. The mixture was allowed to warm to room temperature and was stirred at room temperature overnight. All volatiles were removed under reduced pressure, and the crude product was purified by column chromatography (silica; EtOAc:Pentane 1:4, 3 vol % NEt_3). The product **2** was obtained as a yellow crystalline solid. Yield: 5.19 g, 31.8 mmol, 88%. Analytical data were in agreement with the literature.[6a]

During column chromatography, compound **3a** was isolated as a brown oil. Yield: 183 mg, 1.1 mmol, 3%.

^{1}H NMR (300 MHz, $CDCl_3$): $\delta = 1.29$ (d, 6H, $^{3}J_{HH} = 6.4$ Hz, CH_3), 3.55 (sept, 1H, $^{3}J_{HH} = 6.4$ Hz, CH_{iPr}), 6.86 (dt, 1H, $^{4}J_{HH} = 1.1$ Hz, $^{3}J_{HH} = 7.4$ Hz, 4-H), 6.95 (td, 1H, $^{3}J_{HH} = 8.3$ Hz, 6-H), 7.23 (dd, 1H, $^{4}J_{HH} = 1.7$ Hz, $^{3}J_{HH} = 7.6$ Hz, 3-H), 7.27–7.31 (m, 1H, 5-H), 8.35 (s, 1H, $H_{Aldimine}$), 13.68 (s, 1H, OH) ppm. ^{13}C NMR (76 MHz, $CDCl_3$): $\delta = 24.31$ (s, CH_3), 60.14 (s, CH_{iPr}), 117.13 (s, 6-C), 118.52 (s, 4-C), 118.96 (s, 2-C), 131.18 (s, 3-C), 132.09 (s, 5-C), 161.43 (s, 1-C), 162.12 (s, $C_{Aldimine}$) ppm. Elemental analysis: calcd (%) for $C_{10}H_{13}NO$ (163.22 g/mol): C 73.59, H 8.03, N 8.58; found: C 73.69, H 8.32, N 8.64. ASAP-MS, positive mode (%): calcd for $[C_{10}H_{13}NO + H^+]^+$, $m/z = 164.1070$; found: $m/z = 164.1064$.

Compounds 4 and 5. (In contrast to the literature protocol for the synthesis of **4**, no NEt_3 was used here).[3b]

Ethanol (40 mL) was added to a mixture of 2-tosyloxytropone (3.03 g, 10.9 mmol) and aminoferrocene (2.20 g, 10.9 mmol). The reaction mixture was heated under reflux for 4 h. All volatiles were removed *in vacuo*. The crude reaction product was purified by column chromatography. The product **4** was obtained as a dark orange solid. Yield: 1.27 g, 4.16 mmol, 38%. Analytical data were in agreement with the literature.[3b]

During column chromatography, compound **5** was isolated as a red solid. Yield: 140 mg, 457 μmol, 4%.

^{1}H NMR (200 MHz, $CDCl_3$): $\delta = 4.19$ (s, 5H, C_5H_5), 4.29 (t, 2H,$^{3}J_{HH} = 1.9$ Hz, 3,4-(C_5H_4NHR)), 4.60 (t, 2H,$^{3}J_{HH} = 1.9$ Hz, 2,5-(C_5H_4NHR)), 6.87–6.95 (dd, $^{3}J_{HH} = 8.1$ Hz, $^{3}J_{HH} = 6.8$ Hz, 1H, 4-H), 6.99 (d, 1H, $^{3}J_{HH} = 8.1$ Hz, 6-H), 7.29–7.39 (m, 2H, 3-H, 5-H (overlapping)), 8.63 (s, 1H, $H_{Aldimine}$), 13.37 (s, 1H, OH) ppm. ^{13}C NMR (50 MHz, $CDCl_3$): $\delta = 62.60$ (s, 2,5-(C_5H_4NHR)), 67.73 (s, 3,4-(C_5H_4NHR)), 70.00 (s, C_5H_5), 102.37 (s, 1-(C_5H_4NHR), 117.31 (s, 6-C), 119.10 (s, 4-C), 119.85 (s, 2-C), 131.16 (s, 3-C), 132.19 (s, 5-C), 160.20 (s, 1-C), 160.93 (s, $C_{Aldimine}$) ppm. ESI, positive mode (%): calcd for $[C_{17}H_{16}FeNO + H^+]^+$, $m/z = 306.0576$; found: $m/z = 306.0578$.

Compound 6.[13b] 2-Isopropyliminomethylphenol (**3a**) (115 mg, 0.71 mmol) and lithium HMDS (117 mg, 0.71 mmol) were dissolved in THF (1 mL) and stirred for 10 min. All volatiles were removed *in vacuo*, and the remaining white solid was washed with a mixture of toluene and pentane (1:1, 2 × 4 mL) and dried *in vacuo*. The product was obtained as a white solid. Yield: 88 mg, 0.52 mmol, 74%.

^{1}H NMR (400 MHz, pyridine-d_5): $\delta = 1.17$ (d, 6H, $^{3}J_{HH} = 6.4$ Hz, CH_3), 3.25–3.34 (sept, 1H, $^{3}J_{HH} = 6.3$ Hz, CH_{iPr}), 6.67 (dd, 1H, $^{3}J_{HH} = 7.8$ Hz, $^{3}J_{HH} = 6.5$ Hz, 4-H), 7.15 (d, 1H, $^{3}J_{HH} = 8.5$ Hz, 6-H), 7.40–7.43 (m, 2H, 3-H, 5-H), 8.28 (s, 1H, $H_{Aldimine}$) ppm. ^{13}C NMR (100 MHz, pyridine-d_5): $\delta = 25.36$ (s, CH_3), 62.98 (s, CH_{iPr}), 112.01 (s, 4-C), 123.53 (s, 6-C), 123.77 (s, 2-C), 133.35 (s, 5-C), 136.47 (s, 3-C), 165.17 (s, $C_{Aldimine}$), 171.59 (s, 1-C) ppm. ^{7}Li NMR (155.7 MHz, pyridine-d_5): $\delta = 2.64$ ppm. Further analytical data were in agreement with the literature.[13b]

Compound 7. 2-Isopropyliminomethylphenol (**3a**) (100 mg, 0.61 mmol) and sodium HMDS (112 mg, 0.61 mmol) were dissolved in THF (1 mL) and stirred for 10 min. All volatiles were removed *in vacuo*, and the remaining white solid was washed with a mixture of toluene and pentane (1:1, 2 × 4 mL) and dried *in vacuo*. The product was obtained as a white solid. The amount of THF in the isolated compound has to be checked individually for every batch. Yield: 90 mg, 0.49 mmol (with n = 0.02 equiv of THF and m = 0.04 equiv of toluene), 79%.

^{1}H NMR (400 MHz, THF-d_8): $\delta = 1.06$ (d, 6H, $^{3}J_{HH} = 6.4$ Hz, CH_3), 1.76–1.79 (m, $n \times 4$H, β-THF), 3.26 (sept, 1H, $^{3}J_{HH} = 6.4$ Hz, CH_{iPr}), 3.60–3.63 (m, $n \times 4$H, α-THF), 6.19 (dd, 1H, $^{3}J_{HH} = 8.2$ Hz, $^{3}J_{HH} = 6.2$ Hz, 4-H), 6.46 (d, 1H, $^{3}J_{HH} = 8.3$ Hz, 6-H), 6.89–6.93 (m, 1H, 5-H), 7.03 (dd, 1H, $^{3}J_{HH} = 7.7$ Hz, $^{4}J_{HH} = 1.7$ Hz, 3-H), 8.19 (s, 1H, $H_{Aldimine}$) ppm. ^{1}H NMR (400 MHz, pyridine-d_5): $\delta = 1.17$ (d, 6H, $^{3}J_{HH} = 6.4$ Hz, CH_3), 1.60–1.64 (m, $n \times 4$H, β-THF), 3.28 (sept, 1H, $^{3}J_{HH} = 6.3$ Hz, CH_{iPr}), 3.65–3.68 (m, $n \times 4$H, α-THF), 6.54 (dd, 1H, $^{3}J_{HH} = 8.4$ Hz, $^{3}J_{HH} = 7.2$ Hz, 4-H), 6.96 (d, 1H, $^{3}J_{HH} = 8.4$ Hz, 6-H), 7.24–7.28 (m, 1H, 5-H), 7.03 (dd, 1H, $^{3}J_{HH} = 7.6$ Hz, $^{4}J_{HH} = 2.1$ Hz, 3-H), 8.55 (s, 1H, $H_{Aldimine}$) ppm. ^{13}C NMR (100 MHz, THF-d_8): $\delta = 24.59$ (s, CH_3), 63.36 (s, CH_{iPr}), 110.64 (s, 4-C), 123.09 (s, 6-C), 123.86 (s, 2-C), 131.91 (s, 5-C), 135.54 (s, 3-C), 164.64 (s, $C_{Aldimine}$), 172.71 (s, 1-C) ppm. ^{23}Na NMR (106 MHz, THF-d_8): $\delta = 5.93$ ppm.

Elemental analysis: calcd (%) for $C_{10}H_{12}NaNO{\cdot}(C_4H_8O)_{0.1}$ (192.41 g/mol): C 64.92, H 6.71, N 7.21; found: C 64.85, H 6.84, N 7.00.

Compound 8. 2-Isopropyliminomethylphenol (**3a**) (60 mg, 0.37 mmol) and potassium HMDS (74 mg, 0.37 mmol) were dissolved in THF (1 mL). Immediately, a white precipitate was formed. Pentane (6 mL) was added, and the precipitate was isolated by filtration. The white solid was washed with pentane (4 × 5 mL) and dried *in vacuo*. The product was obtained as a white solid. The amount of THF in the isolated compound has to be checked individually for every batch.

Yield: 60 mg, 0.29 mmol (with n = 0.1 equiv of THF), 78%.

^{1}H NMR (400 MHz, pyridine-d_5): $\delta = 1.24$ (d, 6H, $^{3}J_{HH} = 6.4$ Hz, CH_3), 1.61–1.64 (m, $n \times 4$ H, β-THF), 3.29–3.35 (sept, 1H, $^{3}J_{HH} = 6.1$ Hz, CH_{iPr}), 3.65–3.68 (m, $n \times 4$ H, α-THF), 6.50 (dd, 1H, $^{3}J_{HH} = 7.9$ Hz, $^{3}J_{HH} = 6.2$ Hz, 4-H), 7.01 (d, 1H, $^{3}J_{HH} = 8.0$ Hz, 6-H), 7.25–7.30 (m, 1H, 5-H), 8.00 (d, 1H, $^{3}J_{HH} = 7.5$ Hz, 3-H) 9.04 (s, 1H, $H_{Aldimine}$) ppm. ^{13}C NMR (100 MHz, pyridine-d_5): $\delta = 25.73$ (s, CH_3), 26.26 (s, β-THF), 63.29 (s, CH_{iPr}), 68.29 (s, α-THF), 109.09 (s, 4-C), 123.78 (s, overlay with signal of pyridine-d_5, 6-C),124.95 (s, 2-C), 132.17 (s, 3-C), 132.74 (s, 5-C), 162.03 (s, $C_{Aldimine}$), 174.76 (s, 1-C) ppm. Elemental analysis: calcd (%) for $C_{10}H_{12}KNO{\cdot}(C_4H_8O)_{0.1}$ (208.52 g/mol): C 59.90, H 6.19, N 6.72; found: C 59.71, H 6.12, N 6.72.

Compound 8-crown. 2-Isopropyliminomethylphenol (**3a**) (50 mg, 0.31 mmol) and potassium HMDS (61 mg, 0.31 mmol) were dissolved in THF (3 mL). Immediately, a white precipitate was formed. 18-crown-6 was added, and the resulting light yellow solution was layered with pentane (1 mL). After 24 h, a beige solid had precipitated, was isolated by filtration, washed with pentane (4 × 2 mL), and dried *in vacuo*. The product was obtained as a beige solid. Yield: 131 mg, 0.28 mmol, 92%.

Signals of the *E*-isomer (97%): ^{1}H NMR (500 MHz, pyridine-d_5): $\delta = 1.34$ (d, 6H, $^{3}J_{HH} = 6.3$ Hz, CH_3), 3.48 (s, 24H, CH_2 crown), 3.60–3.68 (sept, 1H, $^{3}J_{HH} = 6.3$ Hz, CH_{iPr}), 6.41–6.44 (m, 1H, 4-H), 7.05–7.08 (m, 1H, 6-H), 7.34–7.38 (m, 1H, 5-H), 8.50 (m, 1H, 3-H) 9.74 (s, 1H, $H_{Aldimine}$) ppm. ^{13}C NMR (126 MHz, pyridine-d_5): $\delta = 26.10$ (s, CH_3), 62.73 (s, CH_{iPr}), 70.71 (s, CH_2 crown), 107.31 (s, 4-C),124.50 (s, 6-C), 125.21 (s, 2-C),128.38 (s, 3-C), 132.58 (s, 5-C), 160.75 (s, $C_{Aldimine}$), 176.25 (s, 1-C) ppm.

Signals of the *Z*-isomer (3%): ^{1}H NMR (500 MHz, pyridine-d_5): $\delta = 1.36$ (d, 6H, $^{3}J_{HH} = 6.1$ Hz, CH_3), 3.48 (s, 24H, CH_2 crown), 4.76–4.83 (sept, 1H, $^{3}J_{HH} = 6.1$ Hz, CH_{iPr}), 6.39–6.42 (m, 1H, 4-H), 7.05–7.08 (m, 1H, 6-H), 7.35–7.40 (m, 1H, 5-H), 7.58 (m, 1H, 3-H (overlapping with signal of pyridine-d_5)) 9.38 (s, 1H, $H_{Aldimine}$) ppm. ^{13}C NMR (126 MHz, pyridine-d_5): $\delta = 25.79$ (s, CH_3), 51.02 (s, CH_{iPr}), 68.29 (s, CH_2 crown), 105.93 (s, 4-C),124.17 (s, overlay with signal of pyridine-d_5, 6-C), 124.64 (s, 2-C), 130.08 (s, 3-C),131.90 (s, 5-C), 161.84 (s, $C_{Aldimine}$), 175.98 (s, 1-C) ppm.

Elemental analysis: calcd (%) for $C_{23}H_{36}KNO_7$ (465.63 g/mol): C 56.75, H 7.79, N 3.01; found: C 56.93, H 8.00, N 2.94.

Compound 9. A solution of **6** (8.7 mg, 51 μmol) in THF (1 mL) was added to a solution of $\mathbf{7{\cdot}(thf)_{0.14}}$ (10 mg, 51 μmol) in THF (1 mL). All volatiles were removed *in vacuo*. The product was obtained as a white solid, which was washed with pentane (2 × 2 mL) and dried *in vacuo*.

Yield: 11 mg, 31 μmol, 61%.

^{1}H NMR (400 MHz, pyridine-d_5): $\delta = 1.17$ (d, 12H, $^{3}J_{HH} = 6.4$ Hz, CH_3), 3.26–3.32 (sept, 2H, $^{3}J_{HH} = 6.3$ Hz, CH_{iPr}), 6.55 (dd, 2H, $^{3}J_{HH}$ =

8.6 Hz, $^{3}J_{HH}$ = 7.0 Hz, 4-H), 6.85 (d, 2H, $^{3}J_{HH}$ = 8.1 Hz, 6-H), 7.19 (m, overlay with signal of pyridine-d_5, 2H,5-H), 7.35 (d, 2H, $^{3}J_{HH}$ = 7.6 Hz, 3-H) 8.27 (s, 2H, $H_{Aldimine}$) ppm. ^{13}C NMR (100 MHz, pyridine-d_5): δ = 25.28 (s, CH_3), 63.10 (s, CH_{iPr}), 110.89 (s, 4-C), 123.79 (s, overlay with signals of pyridine-d_5, 6-C),124.03 (s, overlay with signals of pyridine-d_5, 2-C), 132.70 (s, 5-C), 136.03 (s, overlay with signals of pyridine-d_5, 3-C), 164.51 (s, $C_{Aldimine}$), 172.66 (s, 1-C) ppm. ^{7}Li NMR (156 MHz, pyridine-d_5): δ = 2.78 (s) ppm. ^{23}Na NMR (106 MHz, pyridine-d_5): δ = 3.79 (br. s) ppm.

Elemental analysis: calcd (%) for $C_{20}H_{24}LiNaN_2O_2$ (354.35 g/mol): C 67.79, H 6.83, N 7.91; found: C 67.81, H 6.99, N 7.87.

Compound 10. A solution of **6** (8 mg, 48 μmol) in THF (2 mL) was added to a solution of **8·(thf)$_{0.08}$** (10 mg, 48 μmol) in THF (2 mL). All volatiles were removed *in vacuo*. The product was obtained as a white solid, which was washed with pentane (2 × 2 mL) and dried *in vacuo*. Yield: 17 mg, 46 μmol, 96%.

^{1}H NMR (400 MHz, pyridine-d_5): δ = 1.22 (d, 12H, $^{3}J_{HH}$ = 6.3 Hz, CH_3), 3.24−3.34 (sept, 2H, $^{3}J_{HH}$ = 6.3 Hz, CH_{iPr}), 6.54 (dd, 2H, $^{3}J_{HH}$ = 7.5 Hz, $^{3}J_{HH}$ = 5.8 Hz, 4-H), 6.91 (d, 2H, $^{3}J_{HH}$ = 8.4 Hz, 6-H), 7.25 (dd, overlay with signal of pyridine-d_5, 2H, $^{3}J_{HH}$ = 10.2 Hz, $^{3}J_{HH}$ = 6.9 Hz 5-H), 7.39 (d, 2H, $^{3}J_{HH}$ = 7.5 Hz, 3-H) 8.32 (s, 2H, $H_{Aldimine}$) ppm. ^{13}C NMR(100 MHz, pyridine-d_5): δ = 25.29 (s, CH_3), 63.47 (s, CH_{iPr}), 110.46 (s, 4-C), 123.85 (s, overlay with signals of pyridine-d_5, 6-C),123.87 (s, overlay with signals of pyridine-d_5, 2-C), 132.83 (s, 5-C), 135.71 (s, overlay with signals of pyridine-d_5, 3-C), 164.24 (s, $C_{Aldimine}$), 172.89 (s, 1-C) ppm. ^{7}Li NMR (156 MHz, pyridine-d_5): δ = 3.99 (s) ppm. Elemental analysis: calcd (%) for $C_{20}H_{24}KLiN_2O_2$ (370.46 g/mol): C 64.84, H 6.53, N 7.56; found: C 64.66, H 6.56, N 7.38.

Compound 11. A solution of **7·(thf)$_{0.02}$(toluene)$_{0.04}$** (9.0 mg, 48 μmol) in THF (1 mL) was added to a solution of **8·(thf)$_{0.08}$** (10 mg, 48 μmol) in THF (1 mL). All volatiles were removed *in vacuo*. The product was obtained as a white solid, which was washed with pentane (2 × 2 mL) and dried *in vacuo*. The amount of THF in the isolated compound has to be checked individually for every batch. Yield: 15 mg, 38 μmol (with n = 0.15 equiv of THF), 79%.

^{1}H NMR (400.1 MHz, pyridine-d_5): δ = 1.18 (d, 12H, $^{3}J_{HH}$ = 6.4 Hz, CH_3), 1.61−1.64 (m, $n \times 4$ H, β-THF), 3.23−3.32 (sept, 2H, $^{3}J_{HH}$ = 6.3 Hz, CH_{iPr}), 3.65−3.68 (m, $n \times 4$ H, α-THF), 6.53 (dd, 2H, $^{3}J_{HH}$ = 7.8 Hz, $^{3}J_{HH}$ = 6.6 Hz, 4-H), 6.93 (d, 2H, $^{3}J_{HH}$ = 8.4 Hz, 6-H), 7.19 (dd, overlay with signal of pyridine-d_5, 2H, $^{3}J_{HH}$ = 8.7 Hz, $^{3}J_{HH}$ = 6.8 Hz 5-H), 7.60 (d, overlay with signal of pyridine-d_5, 2H, $^{3}J_{HH}$ = 7.7 Hz, 3-H) 8.59 (s, 2H, $H_{Aldimine}$) ppm. ^{13}C NMR (100 MHz, pyridine-d_5): δ = 25.41 (s, CH_3), 26.26 (s, β-THF), 63.41 (s, CH_{iPr}), 68.29 (s, α-THF), 110.46 (s, 4-C), 123.94 (s, overlay with signals of pyridine-d_5, 6-C),124.49 (s, 2-C), 132.74 (s, 3-C), 134.94 (s, 5-C), 163.93 (s, $C_{Aldimine}$), 173.68 (s, 1-C) ppm. ^{23}Na NMR (106 MHz, pyridine-d_5): δ = 8.79 (br. s) ppm. Elemental analysis: calcd (%) for $C_{20}H_{24}KNaN_2O_2 \cdot (C_4H_8O)_{0.08}$ (392.28 g/mol): C 62.23, H 6.35, N 7.12; found: C 62.23, H 6.39, N 6.95.

Compound 12. Compound **6** (30 mg, 177 μmol) was added to a solution of compound **7·(toluene)$_{0.13}$** (12 mg, 59 μmol) in THF (2 mL). All volatiles were removed *in vacuo*. The product was obtained as a white solid, which was washed with pentane (2 × 2 mL) and dried *in vacuo*. Yield: 24 mg, 35 μmol, 59%.

^{1}H NMR (400 MHz, pyridine-d_5): δ = 1.17 (d, 24H, $^{3}J_{HH}$ = 6.0 Hz, CH_3), 3.25−3.34 (sept, 4H, $^{3}J_{HH}$ = 6.2 Hz, CH_{iPr}), 6.61 (m, 4H, 4-H), 6.96 (br. s, 4H, 6-H), 7.29 (br. m, 4H,5-H), 7.36 (d, 4H, $^{3}J_{HH}$ = 7.4 Hz, 3-H) 8.26 (s, 4H, $H_{Aldimine}$) ppm. ^{13}C NMR (100 MHz, pyridine-d_5): δ = 25.28 (s, CH_3), 63.01 (s, CH_{iPr}), 111.45 (s, 4-C), 123.74 (s, overlay with signals of pyridine-d_5, 6-C),123.91 (s, overlay with signals of pyridine-d_5, 2-C), 132.96 (s, 5-C), 136.24 (s, overlay with signals of pyridine-d_5, 3-C), 164.83 (s, $C_{Aldimine}$), 172.09 (s, 1-C) ppm. ^{7}Li NMR (156 MHz, pyridine-d_5): δ = 2.66 (s) ppm. ^{23}Na NMR (106 MHz, pyridine-d_5): δ = 3.12 (br. s) ppm.

Elemental analysis: calcd (%) for $C_{40}H_{48}Li_3NaN_4O_4$ (692.66 g/mol): C 69.36, H 6.99, N 8.09; found: C 69.67, H 7.20, N 7.99.

Compound 13. Compound **6** (10 mg, 59 μmol) was added to a solution of compound **7·(toluene)$_{0.13}$** (33 mg, 177 μmol) in THF (2 mL). All volatiles were removed *in vacuo*. The product was obtained as a white solid, which was washed with pentane (3 × 5 mL) and dried *in vacuo*. The amount of THF in the isolated compound has to be checked individually for every batch. Yield: 32 mg, 43 μmol (with n = 0.06 equiv of THF and 0.13 equiv of pentane), 73%.

^{1}H NMR (400 MHz, pyridine-d_5): δ = 1.17 (d, 24H, $^{3}J_{HH}$ = 6.4 Hz, CH_3), 1.61−1.64 (m, $n \times 4$ H, β-THF), 3.24−3.33 (sept, 4H, $^{3}J_{HH}$ = 6.3 Hz, CH_{iPr}), 3.65−3.68 (m, $n \times 4$ H, α-THF), 6.52−6.56 (dd, 4H, $^{3}J_{HH}$ = 8.6 Hz, $^{3}J_{HH}$ = 7.0 Hz, 4-H), 6.90 (d, 4H, $^{3}J_{HH}$ = 7.8 Hz, 6-H), 7.22−7.26 (m, overlay with signals of pyridine-d_5, 5-H,), 7.44 (d, 4H, $^{3}J_{HH}$ = 7.7 Hz, 3-H) 8.39 (s, 4H, $H_{Aldimine}$) ppm. ^{13}C NMR (100 MHz, pyridine-d_5): δ = 25.33 (s, CH_3), 26.26 (s, β-THF), 63.20 (s, CH_{iPr}), 68.29 (s, α-THF), 110.59 (s, 4-C), 124.13 (s, 6-C),124.24 (s, overlay with signals of pyridine-d_5, 2-C), 132.66 (s, 5-C), 135.8 (s, overlay with signals of pyridine-d_5, 3-C), 164.51 (s, $C_{Aldimine}$), 173.29 (s, 1-C) ppm. ^{7}Li NMR (156 MHz, pyridine-d_5): δ = 2.80 (s) ppm. ^{23}Na NMR (106 MHz, pyridine-d_5): δ = 5.68 (br. s) ppm. Elemental analysis: calcd (%) for $C_{40}H_{48}LiNa_3N_4O_4 \cdot (C_4H_8O)_{0.1}$ (731.97 g/mol): C 66.29, H 6.72, N 7.65; found: C 66.34, H 6.87, N 7.36.

■ ASSOCIATED CONTENT

Supporting Information

The Supporting Information is available free of charge at https://pubs.acs.org/doi/10.1021/acs.inorgchem.0c02920.

Experimental and computational details, as well as NMR spectra (PDF)

Coordinates of optimized structures obtained from DFT calculations (XYZ)

Accession Codes

CCDC 2034962−2034964 contain the supplementary crystallographic data for this paper. These data can be obtained free of charge via www.ccdc.cam.ac.uk/data_request/cif, or by emailing data_request@ccdc.cam.ac.uk, or by contacting The Cambridge Crystallographic Data Centre, 12 Union Road, Cambridge CB2 1EZ, UK; fax: +44 1223 336033.

■ AUTHOR INFORMATION

Corresponding Author

Crispin Lichtenberg − *Department of Inorganic Chemistry, Julius-Maximilians Universität, Würzburg, 97074 Würzburg, Germany;* orcid.org/0000-0002-0176-0939;
Email: crispin.lichtenberg@uni-wuerzburg.de

Authors

Anna Hanft − *Department of Inorganic Chemistry, Julius-Maximilians Universität, Würzburg, 97074 Würzburg, Germany*

Malte Jürgensen − *Department of Inorganic Chemistry, Julius-Maximilians Universität, Würzburg, 97074 Würzburg, Germany*

Laura Wolz − *Department of Inorganic Chemistry, Julius-Maximilians Universität, Würzburg, 97074 Würzburg, Germany*

Krzysztof Radacki − *Department of Inorganic Chemistry, Julius-Maximilians Universität, Würzburg, 97074 Würzburg, Germany*

Complete contact information is available at:
https://pubs.acs.org/10.1021/acs.inorgchem.0c02920

Author Contributions

The manuscript was written through contributions of all authors. All authors have given approval to the final version of the manuscript.

Notes

The authors declare no competing financial interest.

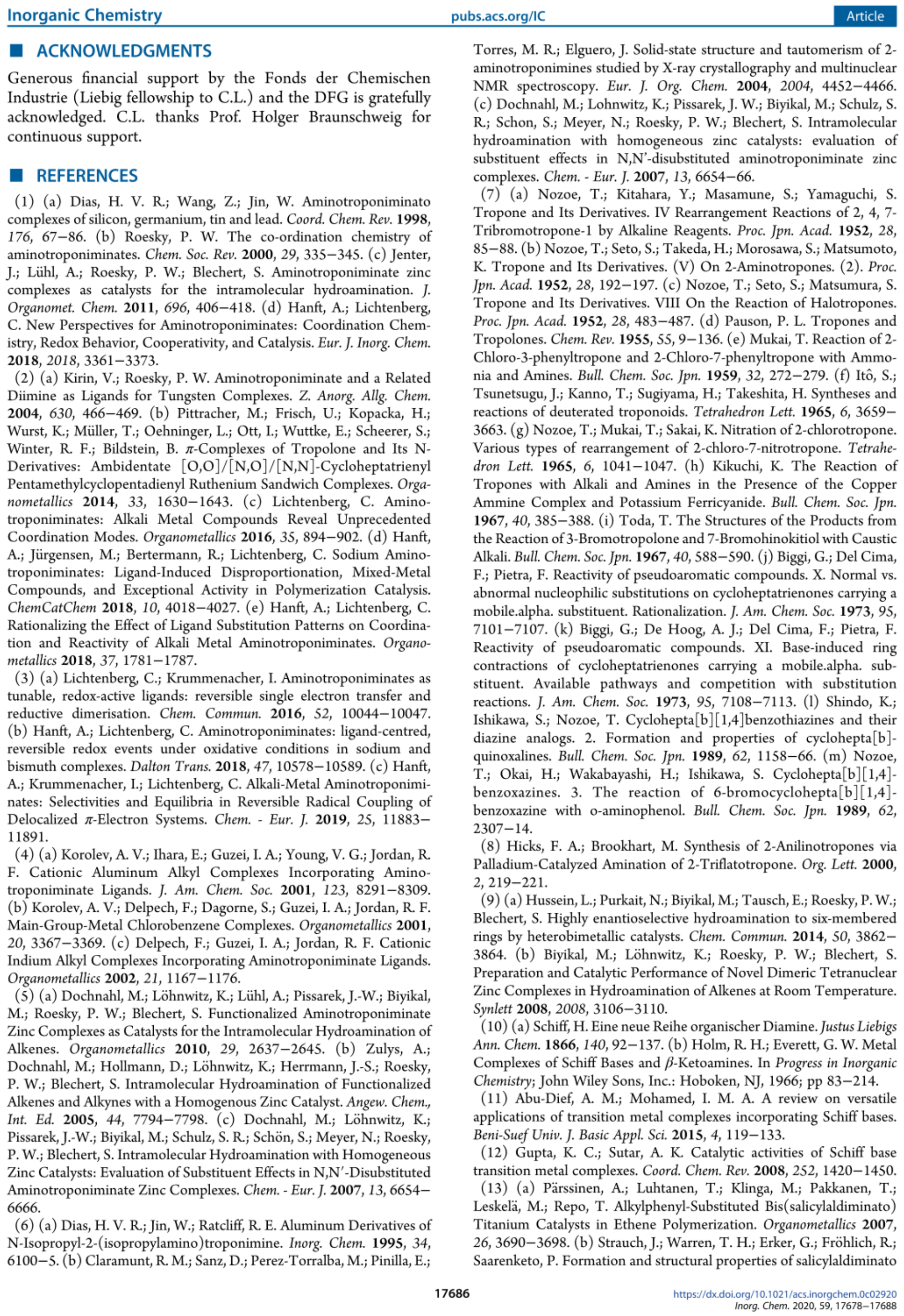

■ ACKNOWLEDGMENTS

Generous financial support by the Fonds der Chemischen Industrie (Liebig fellowship to C.L.) and the DFG is gratefully acknowledged. C.L. thanks Prof. Holger Braunschweig for continuous support.

■ REFERENCES

(1) (a) Dias, H. V. R.; Wang, Z.; Jin, W. Aminotroponiminato complexes of silicon, germanium, tin and lead. *Coord. Chem. Rev.* **1998**, *176*, 67−86. (b) Roesky, P. W. The co-ordination chemistry of aminotroponiminates. *Chem. Soc. Rev.* **2000**, *29*, 335−345. (c) Jenter, J.; Lühl, A.; Roesky, P. W.; Blechert, S. Aminotroponiminate zinc complexes as catalysts for the intramolecular hydroamination. *J. Organomet. Chem.* **2011**, *696*, 406−418. (d) Hanft, A.; Lichtenberg, C. New Perspectives for Aminotroponiminates: Coordination Chemistry, Redox Behavior, Cooperativity, and Catalysis. *Eur. J. Inorg. Chem.* **2018**, *2018*, 3361−3373.

(2) (a) Kirin, V.; Roesky, P. W. Aminotroponiminate and a Related Diimine as Ligands for Tungsten Complexes. *Z. Anorg. Allg. Chem.* **2004**, *630*, 466−469. (b) Pittracher, M.; Frisch, U.; Kopacka, H.; Wurst, K.; Müller, T.; Oehninger, L.; Ott, I.; Wuttke, E.; Scheerer, S.; Winter, R. F.; Bildstein, B. π-Complexes of Tropolone and Its N-Derivatives: Ambidentate [O,O]/[N,O]/[N,N]-Cycloheptatrienyl Pentamethylcyclopentadienyl Ruthenium Sandwich Complexes. *Organometallics* **2014**, *33*, 1630−1643. (c) Lichtenberg, C. Aminotroponiminates: Alkali Metal Compounds Reveal Unprecedented Coordination Modes. *Organometallics* **2016**, *35*, 894−902. (d) Hanft, A.; Jürgensen, M.; Bertermann, R.; Lichtenberg, C. Sodium Aminotroponiminates: Ligand-Induced Disproportionation, Mixed-Metal Compounds, and Exceptional Activity in Polymerization Catalysis. *ChemCatChem* **2018**, *10*, 4018−4027. (e) Hanft, A.; Lichtenberg, C. Rationalizing the Effect of Ligand Substitution Patterns on Coordination and Reactivity of Alkali Metal Aminotroponiminates. *Organometallics* **2018**, *37*, 1781−1787.

(3) (a) Lichtenberg, C.; Krummenacher, I. Aminotroponiminates as tunable, redox-active ligands: reversible single electron transfer and reductive dimerisation. *Chem. Commun.* **2016**, *52*, 10044−10047. (b) Hanft, A.; Lichtenberg, C. Aminotroponiminates: ligand-centred, reversible redox events under oxidative conditions in sodium and bismuth complexes. *Dalton Trans.* **2018**, *47*, 10578−10589. (c) Hanft, A.; Krummenacher, I.; Lichtenberg, C. Alkali-Metal Aminotroponiminates: Selectivities and Equilibria in Reversible Radical Coupling of Delocalized π-Electron Systems. *Chem. - Eur. J.* **2019**, *25*, 11883−11891.

(4) (a) Korolev, A. V.; Ihara, E.; Guzei, I. A.; Young, V. G.; Jordan, R. F. Cationic Aluminum Alkyl Complexes Incorporating Aminotroponiminate Ligands. *J. Am. Chem. Soc.* **2001**, *123*, 8291−8309. (b) Korolev, A. V.; Delpech, F.; Dagorne, S.; Guzei, I. A.; Jordan, R. F. Main-Group-Metal Chlorobenzene Complexes. *Organometallics* **2001**, *20*, 3367−3369. (c) Delpech, F.; Guzei, I. A.; Jordan, R. F. Cationic Indium Alkyl Complexes Incorporating Aminotroponiminate Ligands. *Organometallics* **2002**, *21*, 1167−1176.

(5) (a) Dochnahl, M.; Löhnwitz, K.; Lühl, A.; Pissarek, J.-W.; Biyikal, M.; Roesky, P. W.; Blechert, S. Functionalized Aminotroponiminate Zinc Complexes as Catalysts for the Intramolecular Hydroamination of Alkenes. *Organometallics* **2010**, *29*, 2637−2645. (b) Zulys, A.; Dochnahl, M.; Hollmann, D.; Löhnwitz, K.; Herrmann, J.-S.; Roesky, P. W.; Blechert, S. Intramolecular Hydroamination of Functionalized Alkenes and Alkynes with a Homogenous Zinc Catalyst. *Angew. Chem., Int. Ed.* **2005**, *44*, 7794−7798. (c) Dochnahl, M.; Löhnwitz, K.; Pissarek, J.-W.; Biyikal, M.; Schulz, S. R.; Schön, S.; Meyer, N.; Roesky, P. W.; Blechert, S. Intramolecular Hydroamination with Homogeneous Zinc Catalysts: Evaluation of Substituent Effects in N,N′-Disubstituted Aminotroponiminate Zinc Complexes. *Chem. - Eur. J.* **2007**, *13*, 6654−6666.

(6) (a) Dias, H. V. R.; Jin, W.; Ratcliff, R. E. Aluminum Derivatives of N-Isopropyl-2-(isopropylamino)troponimine. *Inorg. Chem.* **1995**, *34*, 6100−5. (b) Claramunt, R. M.; Sanz, D.; Perez-Torralba, M.; Pinilla, E.; Torres, M. R.; Elguero, J. Solid-state structure and tautomerism of 2-aminotroponimines studied by X-ray crystallography and multinuclear NMR spectroscopy. *Eur. J. Org. Chem.* **2004**, *2004*, 4452−4466. (c) Dochnahl, M.; Lohnwitz, K.; Pissarek, J. W.; Biyikal, M.; Schulz, S. R.; Schon, S.; Meyer, N.; Roesky, P. W.; Blechert, S. Intramolecular hydroamination with homogeneous zinc catalysts: evaluation of substituent effects in N,N'-disubstituted aminotroponiminate zinc complexes. *Chem. - Eur. J.* **2007**, *13*, 6654−66.

(7) (a) Nozoe, T.; Kitahara, Y.; Masamune, S.; Yamaguchi, S. Tropone and Its Derivatives. IV Rearrangement Reactions of 2, 4, 7-Tribromotropone-1 by Alkaline Reagents. *Proc. Jpn. Acad.* **1952**, *28*, 85−88. (b) Nozoe, T.; Seto, S.; Takeda, H.; Morosawa, S.; Matsumoto, K. Tropone and Its Derivatives. (V) On 2-Aminotropones. (2). *Proc. Jpn. Acad.* **1952**, *28*, 192−197. (c) Nozoe, T.; Seto, S.; Matsumura, S. Tropone and Its Derivatives. VIII On the Reaction of Halotropones. *Proc. Jpn. Acad.* **1952**, *28*, 483−487. (d) Pauson, P. L. Tropones and Tropolones. *Chem. Rev.* **1955**, *55*, 9−136. (e) Mukai, T. Reaction of 2-Chloro-3-phenyltropone and 2-Chloro-7-phenyltropone with Ammonia and Amines. *Bull. Chem. Soc. Jpn.* **1959**, *32*, 272−279. (f) Itô, S.; Tsunetsugu, J.; Kanno, T.; Sugiyama, H.; Takeshita, H. Syntheses and reactions of deuterated troponoids. *Tetrahedron Lett.* **1965**, *6*, 3659−3663. (g) Nozoe, T.; Mukai, T.; Sakai, K. Nitration of 2-chlorotropone. Various types of rearrangement of 2-chloro-7-nitrotropone. *Tetrahedron Lett.* **1965**, *6*, 1041−1047. (h) Kikuchi, K. The Reaction of Tropones with Alkali and Amines in the Presence of the Copper Ammine Complex and Potassium Ferricyanide. *Bull. Chem. Soc. Jpn.* **1967**, *40*, 385−388. (i) Toda, T. The Structures of the Products from the Reaction of 3-Bromotropolone and 7-Bromohinokitiol with Caustic Alkali. *Bull. Chem. Soc. Jpn.* **1967**, *40*, 588−590. (j) Biggi, G.; Del Cima, F.; Pietra, F. Reactivity of pseudoaromatic compounds. X. Normal vs. abnormal nucleophilic substitutions on cycloheptatrienones carrying a mobile.alpha. substituent. Rationalization. *J. Am. Chem. Soc.* **1973**, *95*, 7101−7107. (k) Biggi, G.; De Hoog, A. J.; Del Cima, F.; Pietra, F. Reactivity of pseudoaromatic compounds. XI. Base-induced ring contractions of cycloheptatrienones carrying a mobile.alpha. substituent. Available pathways and competition with substitution reactions. *J. Am. Chem. Soc.* **1973**, *95*, 7108−7113. (l) Shindo, K.; Ishikawa, S.; Nozoe, T. Cyclohepta[b][1,4]benzothiazines and their diazine analogs. 2. Formation and properties of cyclohepta[b]-quinoxalines. *Bull. Chem. Soc. Jpn.* **1989**, *62*, 1158−66. (m) Nozoe, T.; Okai, H.; Wakabayashi, H.; Ishikawa, S. Cyclohepta[b][1,4]-benzoxazines. 3. The reaction of 6-bromocyclohepta[b][1,4]-benzoxazine with o-aminophenol. *Bull. Chem. Soc. Jpn.* **1989**, *62*, 2307−14.

(8) Hicks, F. A.; Brookhart, M. Synthesis of 2-Anilinotropones via Palladium-Catalyzed Amination of 2-Triflatotropone. *Org. Lett.* **2000**, *2*, 219−221.

(9) (a) Hussein, L.; Purkait, N.; Biyikal, M.; Tausch, E.; Roesky, P. W.; Blechert, S. Highly enantioselective hydroamination to six-membered rings by heterobimetallic catalysts. *Chem. Commun.* **2014**, *50*, 3862−3864. (b) Biyikal, M.; Löhnwitz, K.; Roesky, P. W.; Blechert, S. Preparation and Catalytic Performance of Novel Dimeric Tetranuclear Zinc Complexes in Hydroamination of Alkenes at Room Temperature. *Synlett* **2008**, *2008*, 3106−3110.

(10) (a) Schiff, H. Eine neue Reihe organischer Diamine. *Justus Liebigs Ann. Chem.* **1866**, *140*, 92−137. (b) Holm, R. H.; Everett, G. W. Metal Complexes of Schiff Bases and β-Ketoamines. In *Progress in Inorganic Chemistry*; John Wiley Sons, Inc.: Hoboken, NJ, 1966; pp 83−214.

(11) Abu-Dief, A. M.; Mohamed, I. M. A. A review on versatile applications of transition metal complexes incorporating Schiff bases. *Beni-Suef Univ. J. Basic Appl. Sci.* **2015**, *4*, 119−133.

(12) Gupta, K. C.; Sutar, A. K. Catalytic activities of Schiff base transition metal complexes. *Coord. Chem. Rev.* **2008**, *252*, 1420−1450.

(13) (a) Pärssinen, A.; Luhtanen, T.; Klinga, M.; Pakkanen, T.; Leskelä, M.; Repo, T. Alkylphenyl-Substituted Bis(salicylaldiminato) Titanium Catalysts in Ethene Polymerization. *Organometallics* **2007**, *26*, 3690−3698. (b) Strauch, J.; Warren, T. H.; Erker, G.; Fröhlich, R.; Saarenketo, P. Formation and structural properties of salicylaldiminato

complexes of zirconium and titanium. *Inorg. Chim. Acta* **2000**, *300−302*, 810−821.

(14) (a) Routaray, A.; Nath, N.; Maharana, T.; Sahoo, P. K.; Das, J. P.; Sutar, A. K. Salicylaldimine Copper(II) complex catalyst: Pioneer for ring opening Polymerization of Lactide. *J. Chem. Sci.* **2016**, *128*, 883−891. (b) Clowes, L.; Walton, M.; Redshaw, C.; Chao, Y.; Walton, A.; Elo, P.; Sumerin, V.; Hughes, D. L. Vanadium(iii) phenoxyimine complexes for ethylene or ε-caprolactone polymerization: mononuclear versus binuclear pre-catalysts. *Catal. Sci. Technol.* **2013**, *3*, 152−160. (c) Pastor, M. F.; Whitehorne, T. J. J.; Oguadinma, P. O.; Schaper, F. Zinc complexes of chiral ligands obtained from methylbenzylamine. *Inorg. Chem. Commun.* **2011**, *14*, 1737−1741.

(15) Chang, S.; Jones, L.; Wang, C.; Henling, L. M.; Grubbs, R. H. Synthesis and Characterization of New Ruthenium-Based Olefin Metathesis Catalysts Coordinated with Bidentate Schiff-Base Ligands. *Organometallics* **1998**, *17*, 3460−3465.

(16) Al-Shboul, T. M. A.; Ziemann, S.; Görls, H.; Jazzazi, T. M. A.; Krieck, S.; Westerhausen, M. Synthesis of Dipotassium 2,2′-Bis(2-oxidobenzylideneamino)-4,4′-dimethyl-1,1′-biphenyl Derivatives and Use as Ligand Transfer Reagent. *Eur. J. Inorg. Chem.* **2018**, *2018*, 1563−1570.

(17) Fischer, R.; Görls, H.; Walther, D. Natriumkomplexe mit Salicylideniminen: Synthesen, Strukturen, CO_2-Aufnahme und Carboxylierung von 2-Fluorpropiophenon bzw. Estronmethylether. *Z. Anorg. Allg. Chem.* **2004**, *630*, 1387−1394.

(18) (a) Liu, J.; Iwasa, N.; Nomura, K. Synthesis of Al complexes containing phenoxy-imine ligands and their use as the catalyst precursors for efficient living ring-opening polymerisation of ε-caprolactone. *Dalton Trans.* **2008**, 3978−3988. (b) Lu, W.-Y.; Hsiao, M.-W.; Hsu, S. C. N.; Peng, W.-T.; Chang, Y.-J.; Tsou, Y.-C.; Wu, T.-Y.; Lai, Y.-C.; Chen, Y.; Chen, H.-Y. Synthesis, characterization and catalytic activity of lithium and sodium iminophenoxide complexes towards ring-opening polymerization of l-lactide. *Dalton Trans.* **2012**, *41*, 3659−3667. (c) Gallaway, J. B. L.; McRae, J. R. K.; Decken, A.; Shaver, M. P. Ring-opening polymerization of rac-lactide and ε-caprolactone using zinc and calcium salicylaldiminato complexes. *Can. J. Chem.* **2012**, *90*, 419−426. (d) Yi, W.; Ma, H. Magnesium complexes containing biphenyl-based tridentate imino-phenolate ligands for ring-opening polymerization of rac-lactide and α-methyltrimethylene carbonate. *Dalton Trans.* **2014**, *43*, 5200−5210. (e) García-Valle, F. M.; Estivill, R.; Gallegos, C.; Cuenca, T.; Mosquera, M. E. G.; Tabernero, V.; Cano, J. Metal and Ligand-Substituent Effects in the Immortal Polymerization of rac-Lactide with Li, Na, and K Phenoxo-imine Complexes. *Organometallics* **2015**, *34*, 477−487. (f) Ghosh, S.; Chakraborty, D.; Varghese, B. Group 1 salts of the imino(phenoxide) scaffold: Synthesis, structural characterization and studies as catalysts towards the bulk ring opening polymerization of lactides. *Eur. Polym. J.* **2015**, *62*, 51−65. (g) Lee, C.-L.; Lin, Y.-F.; Jiang, M.-T.; Lu, W.-Y.; Vandavasi, J. K.; Wang, L.-F.; Lai, Y.-C.; Chiang, M. Y.; Chen, H.-Y. Improvement in Aluminum Complexes Bearing Schiff Bases in Ring-Opening Polymerization of ε-Caprolactone: A Five-Membered-Ring System. *Organometallics* **2017**, *36*, 1936−1945. (h) Wu, B.-B.; Tian, L.-L.; Wang, Z.-X. Ring-opening polymerization of rac-lactide catalyzed by crown ether complexes of sodium and potassium iminophenoxides. *RSC Adv.* **2017**, *7*, 24055−24063. (i) Fuoco, T.; Pappalardo, D. Aluminum Alkyl Complexes Bearing Salicylaldiminato Ligands: Versatile Initiators in the Ring-Opening Polymerization of Cyclic Esters. *Catalysts* **2017**, *7*, 64. (j) García-Valle, F. M.; Tabernero, V.; Cuenca, T.; Mosquera, M. E. G.; Cano, J.; Milione, S. Biodegradable PHB from rac-β-Butyrolactone: Highly Controlled ROP Mediated by a Pentacoordinated Aluminum Complex. *Organometallics* **2018**, *37*, 837−840. (k) Huang, T.-W.; Su, R.-R.; Lin, Y.-C.; Lai, H.-Y.; Yang, C.-Y.; Senadi, G. C.; Lai, Y.-C.; Chiang, M. Y.; Chen, H.-Y. Improvement in aluminum complexes bearing a Schiff base in ring-opening polymerization of ε-caprolactone: the synergy of the N,S-Schiff base in a five-membered ring aluminum system. *Dalton Trans.* **2018**, *47*, 15565−15573. (l) García-Valle, F. M.; Muñoz, M. T.; Cuenca, T.; Milione, S.; Mosquera, M. E. G.; Cano, J. Fluorinated alkali metal catalysts for the Ring-Opening Polymerization (ROP) of rac-lactide. Effect of the M···F interactions in the polymerization control. *J. Organomet. Chem.* **2019**, *898*, 120854. (m) García-Valle, F. M.; Cuenca, T.; Mosquera, M. E. G.; Milione, S.; Cano, J. Ring-Opening Polymerization (ROP) of cyclic esters by a versatile aluminum Diphenoxyimine Complex: From polylactide to random copolymers. *Eur. Polym. J.* **2020**, *125*, 109527. (n) Gao, J.; Zhu, D.; Zhang, W.; Solan, G. A.; Ma, Y.; Sun, W.-H. Recent progress in the application of group 1, 2 & 13 metal complexes as catalysts for the ring opening polymerization of cyclic esters. *Inorg. Chem. Front.* **2019**, *6*, 2619−2652.

(19) Song, X.; Wang, Z.; Zhao, J.; Hor, T. S. A. Sodium cubane and double-cubane aggregates of hybridised salicylaldimines and their transmetallation to nickel for catalytic ethylene oligomerisation. *Chem. Commun.* **2013**, *49*, 4992−4994.

(20) (a) Barr, D.; Clegg, W.; Mulvey, R. E.; Snaith, R.; Wade, K. Bonding implications of interatomic distances and ligand orientations in the iminolithium hexamers $[\mathrm{LiN{=}C(Ph)Bu^t}]_6$ and $[\mathrm{LiN{=}C(Ph)NMe_2}]_6$: a stacked-ring approach to these and related oligomeric organolithium systems. *J. Chem. Soc., Chem. Commun.* **1986**, 295−297. (b) Armstrong, D. R.; Barr, D.; Snaith, R.; Clegg, W.; Mulvey, R. E.; Wade, K.; Reed, D. The ring-stacking principle in organolithium chemistry: its development through the isolation and crystal structures of hexameric iminolithium clusters $(\mathrm{RR'C{=}NLi})_6$ (R′= Ph, R = Bu^t or Me$_2$N; R = R′= Me$_2$N or Bu^t). *J. Chem. Soc., Dalton Trans.* **1987**, 1071−1081. (c) Barr, D.; Clegg, W.; Mulvey, R. E.; Snaith, R. Synthesis and crystal structure of the mixed alkali metal imide $\mathrm{Li_{4-x}Na_{2+x}[N{=}C(Ph)Bu^t]}$6: three (metal−nitrogen)$_2$ ring dimers in a triple-layered stack. *J. Chem. Soc., Chem. Commun.* **1989**, 57−58.

(21) (a) Meally, S. T.; Taylor, S. M.; Brechin, E. K.; Piligkos, S.; Jones, L. F. Homo- and heterometallic planes, chains and cubanes. *Dalton Trans.* **2013**, *42*, 10315−10325. (b) Upadhyay, A.; Das, C.; Meera, S. N.; Langley, S. K.; Murray, K. S.; Shanmugam, M. Synthesis and magnetic properties of a 1-D helical chain derived from a Nickel-Sodium Schiff base complex. *J. Chem. Sci.* **2014**, *126*, 1443−1449. (c) Cai, Z.; Xiao, D.; Do, L. H. Fine-Tuning Nickel Phenoxyimine Olefin Polymerization Catalysts: Performance Boosting by Alkali Cations. *J. Am. Chem. Soc.* **2015**, *137*, 15501−15510. (d) Griffiths, K.; Escuer, A.; Kostakis, G. E. Topological insights in polynuclear Ni/Na coordination clusters derived from a schiff base ligand. *Struct. Chem.* **2016**, *27*, 1703−1714.

(22) Roitershtein, D. M.; Minashina, K. I.; Minyaev, M. E.; Ananyev, I. V.; Lyssenko, K. A.; Tavtorkin, A. N.; Nifant'ev, I. E. Different coordination modes of trans-2-{[(2-methoxyphenyl)imino]methyl}-phenoxide in rare-earth complexes: influence of the metal cation radius and the number of ligands on steric congestion and ligand coordination modes. *Acta Crystallogr., Sect. C: Struct. Chem.* **2018**, *74*, 1105−1115.

(23) García-Valle, F. M.; Tabernero, V.; Cuenca, T.; Cano, J.; Mosquera, M. E. G. Schiff-base -ate derivatives with main group metals: generation of a tripodal aluminate metalloligand. *Dalton Trans.* **2018**, *47*, 6499−6506.

(24) It may be noted that problems have been encountered, when using route 2 toward the synthesis of compounds bearing two 2-aminotropolone units: Hanft, A.; Lichtenberg, C. Dimerization of 2-[(2-((2-Aminophenyl)thio)phenyl)amino]-cyclohepta-2,4,6-trien-1-one through Hydrogen Bonding. *Z. Kristallogr. - New Cryst. Struct.* **2020**, *235*, 963−966.

(25) For instance, a SciFinder search on compounds featuring an aminotroponiminate motif with at least one isopropyl group at a nitrogen atom gives more than 350 hits.

(26) (a) Torzilli, M. A.; Colquhoun, S.; Kim, J.; Beer, R. H. Structural and ^{1}H NMR spectroscopic characterization of bis(N-isopropylsalicylaldiminato)iron(II). *Polyhedron* **2002**, *21*, 705−713. (b) Tripathi, S. M.; Tandon, J. P. Acetoxyboron derivatives of N-substituted salicylaldimines. *J. Inorg. Nucl. Chem.* **1978**, *40*, 983−985.

(27) (a) Hobson, J. D.; Malpass, J. R. The chemistry of azidotropones. Part II. 3- and 4-Azidotropones and related compounds. *J. Chem. Soc. C* **1969**, 1499−1503. (b) Iriarte, J.; Camargo, C.; Crabbé, P. Reaction of 6-bromobenzocyclohepten-5-one with amines. *J. Chem. Soc., Perkin Trans. 1* **1980**, 2077−2080.

(28) Bracci, M.; Ercolani, C.; Floris, B.; Bassetti, M.; Chiesi-Villa, A.; Guastini, C. Molecular and electronic structure of the complexes formed by the Schiff base N-(o-hydroxybenzylidene)ferroceneamine with Co, Ni, Cu, and Zn. *J. Chem. Soc., Dalton Trans.* **1990**, 1357−1363.

(29) In solutions of the strong donor pyridine, compounds **6**−**8** are likely to exist as solvates.

(30) Lichtenberg, C.; Spaniol, T. P.; Peckermann, I.; Hanusa, T. P.; Okuda, J. Cationic, Neutral, and Anionic Allyl Magnesium Compounds: Unprecedented Ligand Conformations and Reactivity Toward Unsaturated Hydrocarbons. *J. Am. Chem. Soc.* **2013**, *135*, 811−821.

(31) (a) Bjørgo, J.; Boyd, D. R.; Watson, C. G.; Jennings, W. B.; Jerina, D. M. E−Z-isomerism in aldimines. *J. Chem. Soc., Perkin Trans. 2* **1974**, 1081−1084. (b) Paetzold, R.; Reichenbächer, M.; Appenroth, K. Die Kohlenstoff-Stickstoff-Doppelbindung: Spektren, Struktur, thermische und photochemische E/Z-Isomerisierung. *Z. Chem.* **1981**, *21*, 421−430. (c) Zhao, L.; Liu, J.; Zhou, P. New Insight into the Photoisomerization Process of the Salicylidene Methylamine under Vacuum. *J. Phys. Chem. A* **2016**, *120*, 7419−7426.

(32) (a) Yeh, H. J. C.; Ziffer, H.; Jerina, D. M.; Boyd, D. R. Stereochemical dependence of the sign and magnitude of coupling constants on geometry in nitrogen-15 (E)- and (Z)-aldimines. *J. Am. Chem. Soc.* **1973**, *95*, 2741−2743. (b) Kessler, H. Thermal isomerization about double bonds: Rotation and inversion. *Tetrahedron* **1974**, *30*, 1861−1870. (c) Osamura, Y.; Yamabe, S.; Nishimoto, K. MO Study of the photochemical behavior of the imine bond. *Int. J. Quantum Chem.* **1980**, *18*, 457−462.

(33) (a) Güngör, Ö.; Gürkan, P. Synthesis and characterization of higher amino acid Schiff bases, as monosodium salts and neutral forms. Investigation of the intramolecular hydrogen bonding in all Schiff bases, antibacterial and antifungal activities of neutral forms. *J. Mol. Struct.* **2014**, *1074*, 62−70. (b) Hayvali, Z.; Yardimci, D. Synthesis and spectroscopic characterization of asymmetric Schiff bases derived from 4′-formylbenzo-15-crown-5 containing recognition sites for alkali and transition metal guest cations. *Transition Met. Chem.* **2008**, *33*, 421−429.

(34) Additionally, weak Na···C interactions between the outer face sodium atoms and the ipso-carbon atoms of the ligands coordinated to the inner face sodium atoms may be discussed based on distance criteria (Na···C, 2.70−2.84 Å; sum of the van der Waals radii: 3.97 Å).

(35) (a) García-Valle, F. M.; Tabernero, V.; Cuenca, T.; Mosquera, M. E. G.; Cano, J. Intramolecular C−F Activation in Schiff-Base Alkali Metal Complexes. *Organometallics* **2019**, *38*, 894−904. (b) Solari, E.; De Angelis, S.; Floriani, C.; Chiesi-Villa, A.; Rizzoli, C. Cubane structure of sodium derivatives of tetradentate Schiff bases. *J. Chem. Soc., Dalton Trans.* **1991**, 2471−2476.

(36) The aryl oxide [Na(1-O,2-(CH$_2$NMe$_2$)-C$_6$H$_4$]$_4$ is structurally related to **7**. It also forms a double heterocubane in the solid state. Contrary to **7**, however, outer and inner faces of the double heterocubane are linked through Na-O and Na-N interactions and additional Na-arene interactions are present: Hogerheide, M. P.; Ringelberg, S. N.; Janssen, M. D.; Boersma, J.; Spek, A. L.; van Koten, G. Influence of Intramolecular Coordination on the Aggregation of Sodium Phenolate Complexes. X-ray Structures of [NaOC$_6$H$_4$(CH$_2$NMe$_2$)-$_2$]$_6$ and [Na(OC$_6$H$_2$(CH$_2$NMe$_2$)$_2$-2,6-Me-4)(HOC$_6$H$_2$(CH$_2$NMe$_2$)$_2$-2,6-Me-4)]$_2$. *Inorg. Chem.* **1996**, *35*, 1195−1200.

(37) Thus, the solid state structure of compound **7** can be put into context with the ring stacking principle that has originally been proposed for the description of lithium compounds (cf. ref 20).

(38) Campos, J. Bimetallic cooperation across the periodic table. *Nat. Rev. Chem.* **2020**. DOI: 10.1038/s41570-020-00226-5.

(39) (a) Martínez-Martínez, A. J.; Kennedy, A. R.; Mulvey, R. E.; O'Hara, C. T. Directed ortho-meta′- and meta-meta′-dimetalations: A template base approach to deprotonation. *Science* **2014**, *346*, 834−837. (b) Mulvey, R. E. Modern Ate Chemistry: Applications of Synergic Mixed Alkali-Metal-Magnesium or -Zinc Reagents in Synthesis and Structure Building. *Organometallics* **2006**, *25*, 1060−1075. (c) Haag, B.; Mosrin, M.; Ila, H.; Malakhov, V.; Knochel, P. Regio- and Chemoselective Metalation of Arenes and Heteroarenes Using Hindered Metal Amide Bases. *Angew. Chem., Int. Ed.* **2011**, *50*, 9794−9824. (d) Mulvey, R. E. Avant-Garde Metalating Agents: Structural Basis of Alkali-Metal-Mediated Metalation. *Acc. Chem. Res.* **2009**, *42*, 743−755. (e) Mulvey, R. E.; Mongin, F.; Uchiyama, M.; Kondo, Y. Deprotonative Metalation Using Ate Compounds: Synergy, Synthesis, and Structure Building. *Angew. Chem., Int. Ed.* **2007**, *46*, 3802−3824. (f) Mulvey, R. E. s-Block metal inverse crowns: synthetic and structural synergism in mixed alkali metal−magnesium (or zinc) amide chemistry. *Chem. Commun.* **2001**, 1049−1056. (g) Benrath, P.; Kaiser, M.; Limbach, T.; Mondeshki, M.; Klett, J. Combining Neopentyllithium with Potassium tert-Butoxide: Formation of an Alkane-Soluble Lochmann−Schlosser Superbase. *Angew. Chem., Int. Ed.* **2016**, *55*, 10886−10889. (h) Mulvey, R. E.; Robertson, S. D. Synthetically Important Alkali-Metal Utility Amides: Lithium, Sodium, and Potassium Hexamethyldisilazides, Diisopropylamides, and Tetramethylpiperidides. *Angew. Chem., Int. Ed.* **2013**, *52*, 11470−11487. (i) Robertson, S. D.; Uzelac, M.; Mulvey, R. E. Alkali-Metal-Mediated Synergistic Effects in Polar Main Group Organometallic Chemistry. *Chem. Rev.* **2019**, *119*, 8332−8405.

(40) Fairley, M.; Davin, L.; Hernán-Gómez, A.; García-Álvarez, J.; O'Hara, C. T.; Hevia, E. s-Block cooperative catalysis: alkali metal magnesiate-catalysed cyclisation of alkynols. *Chem. Sci.* **2019**, *10*, 5821−5831.

(41) Lichtenberg, C.; Spaniol, T. P.; Perrin, L.; Maron, L.; Okuda, J. Reversible 1,4-Insertion of Pyridine Into a Highly Polar Metal−Carbon Bond: Effect of the Second Metal. *Chem. - Eur. J.* **2012**, *18*, 6448−6452.

(42) (a) Deffieux, A.; Shcheglova, L.; Barabanova, A.; Maréchal, J. M.; Carlotti, S. Aluminate and Magnesiate Complexes as Propagating Species in the Anionic Polymerization of Styrene and Dienes. *Macromol. Symp.* **2004**, *215*, 17−28. (b) Honeyman, G. W.; Kennedy, A. R.; Mulvey, R. E.; Sherrington, D. C. Synthesis, Structure, and Methyl Methacrylate Polymerization Activity of a Mixed π-Ferrocene π-Toluene Complex of Potassium Tris-(hexamethyldisilazide)magnesiate. *Organometallics* **2004**, *23*, 1197−1199.

(43) The ^{1}H NMR spectrum of the crystalline material, which was obtained in small amounts, was identical with that of compound **12** (and thus clearly different from those of **9**).

(44) Two main and two minor resonances were detected for the aldimine protons (see the Supporting Information).

(45) Neufeld, R.; Stalke, D. Accurate molecular weight determination of small molecules via DOSY-NMR by using external calibration curves with normalized diffusion coefficients. *Chem. Sci.* **2015**, *6*, 3354−3364.

(46) Clegg, W.; Mulvey, R. E.; Snaith, R.; Toogood, G. E.; Wade, K. The synthesis and X-ray structural characterisation of the first mixed alkali metal organonitrogen molecular cluster LiNa$_3$[O=P-(NMe$_2$)$_3$]$_3$[N=C(NMe$_2$)$_2$]$_4$. *J. Chem. Soc., Chem. Commun.* **1986**, 1740−1742.

(47) Hariharan, P. C.; Pople, J. A. The influence of polarization functions on molecular orbital hydrogenation energies. *Theor. Chim. Acta* **1973**, *28*, 213−222.

(48) (a) McLean, A. D.; Chandler, G. S. Contracted Gaussian basis sets for molecular calculations. I. Second row atoms, Z=11−18. *J. Chem. Phys.* **1980**, *72*, 5639−5648. (b) Krishnan, R.; Binkley, J. S.; Seeger, R.; Pople, J. A. Self-consistent molecular orbital methods. XX. A basis set for correlated wave functions. *J. Chem. Phys.* **1980**, *72*, 650−654.

(49) Becke, A. D. Density-functional thermochemistry. III. The role of exact exchange. *J. Chem. Phys.* **1993**, *98*, 5648−5652.

(50) Grimme, S.; Antony, J.; Ehrlich, S.; Krieg, H. A consistent and accurate ab initio parametrization of density functional dispersion correction (DFT-D) for the 94 elements H-Pu. *J. Chem. Phys.* **2010**, *132*, 154104.

X Cationic Bismuth Aminotroponiminates: Charge Controls Redox Properties

Anna Hanft, Krzysztof Radacki, Crispin Lichtenberg

Vervielfältigt aus Referenz:

Chem. Eur. J. **2021**, DOI: 10.1002/chem.202005186.[69]

mit Erlaubnis von John Wiley and Sons.

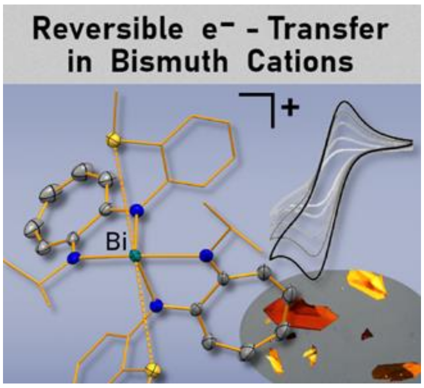

Chemistry–A European Journal
Full Paper
doi.org/10.1002/chem.202005186

Coordination Chemistry

Cationic Bismuth Aminotroponiminates: Charge Controls Redox Properties

Anna Hanft, Krzysztof Radacki, and Crispin Lichtenberg*[a]

Dedicated to Professor Wolfgang Kaim on the occasion of his 70th birthday

Abstract: The behavior of the redox-active aminotroponiminate (ATI) ligand in the coordination sphere of bismuth has been investigated in neutral and cationic compounds, [Bi(ATI)$_3$] and [Bi(ATI)$_2$L$_n$][A] (L = neutral ligand; $n = 0, 1$; A = counteranion). Their coordination chemistry in solution and in the solid state has been analyzed through (variable-temperature) NMR spectroscopy, line-shape analysis, and single-crystal X-ray diffraction analyses, and their Lewis acidity has been evaluated by using the Gutmann–Beckett method (and modifications thereof). Cyclic voltammetry, in combination with DFT calculations, indicates that switching between ligand- and metal-centered redox events is possible by altering the charge of the compounds from 0 in neutral species to +1 in cationic compounds. This adds important facets to the rich redox chemistry of ATIs and to the redox chemistry of bismuth compounds, which is, so far, largely unexplored.

Introduction

In recent years, redox-active ligands have been established as a versatile and valuable tool to diversify and control the properties and reactivity of coordination entities.[1] In compounds of first-row transition metals, for instance, redox-active ligands have been used to stabilize unusual oxidation states of the central atom[2] or to foster reactions that involve two-electron processes rather than single-electron transfer.[3] In compounds of p-block elements, redox-active ligands have been used to enable facile and reversible electron transfer and to open up reaction pathways for controlled radical reactions.[1c,g,4]

It has been demonstrated that redox-active ligands may also be directly involved in selective bond-forming events, such as the dimerization of radical species, which result from a high spin density at specific sites of the redox-active entity.[5] However, strategies to control such reactivity remain rare. Aluminum complex **A** has been reported to undergo dimerization through C–C bond formation to give **A$_2$** (Scheme 1 a, left), whereas the closely related species **B** is isolable in the monomeric form (Scheme 1 a, right).[4a] This has been ascribed to intramolecular ferromagnetic coupling between the radical ligands in **B**, which leads to a reduced effective spin density in these compounds. We have demonstrated that rhodium compounds of aminotroponiminates (ATIs) are susceptible to reversible (ligand-centered) electron transfer (Scheme 1 b (left), **C**→**D**), whereas the corresponding alkali-metal complexes readily undergo reductively induced dimerization (Scheme 1 b (right), **C**→0.5 **E**).[6] Thus, modifying the metal bound to a redox-active ligand can have a dramatic influence on ligand-centered redox events and reactivity.

Although the chemistry of redox-active ligands is well developed for central atoms across large parts of the periodic table,[1] the redox chemistry of heavier Group 15 elements, and the heaviest congener bismuth, in particular, has been focused on metal(oid)-centered radical species and redox-shuttling.[5,7] Remarkable advances in the field include the incorporation of Bi^{V}/Bi^{III} and proposed Bi^{III}/Bi^{I} redox couples in catalytic cycles,[8] the first examples of persistent and isolable bismuth radical complexes,[9] the generation of an organometallic biradical,[10] unusual reactivity patterns (e.g., towards P$_4$ and S$_8$),[11] and catalytic applications in cycloisomerization and dehydrocoupling reactions,[12] olefin polymerization,[13] and photochemistry.[12c] These findings were largely based on strategies in which the radical center (if present) was stabilized through bulky ligands or through reversible radical recombination reactions. In contrast, the use of (potentially) redox-active ligands in the field of bismuth chemistry is only little explored. Examples include bismuth(I) and bismuth(III) complexes with ferrocenyl groups in the ligand backbone (**F**, **G**),[14] as well as bismuth(III) pyridine dipyrrolide complexes **H** (Scheme 2).[15]

---

[a] A. Hanft, Dr. K. Radacki, Priv.-Doz. Dr. C. Lichtenberg
Department of Inorganic Chemistry
Julius-Maximilians-University Würzburg
Am Hubland, 97074 Würzburg (Germany)
E-mail: crispin.lichtenberg@uni-wuerzburg.de

Supporting information and the ORCID identification number(s) for the author(s) of this article can be found under: https://doi.org/10.1002/chem.202005186.

Chemistry–A European Journal | Full Paper
doi.org/10.1002/chem.202005186
Chemistry Europe
European Chemical Societies Publishing

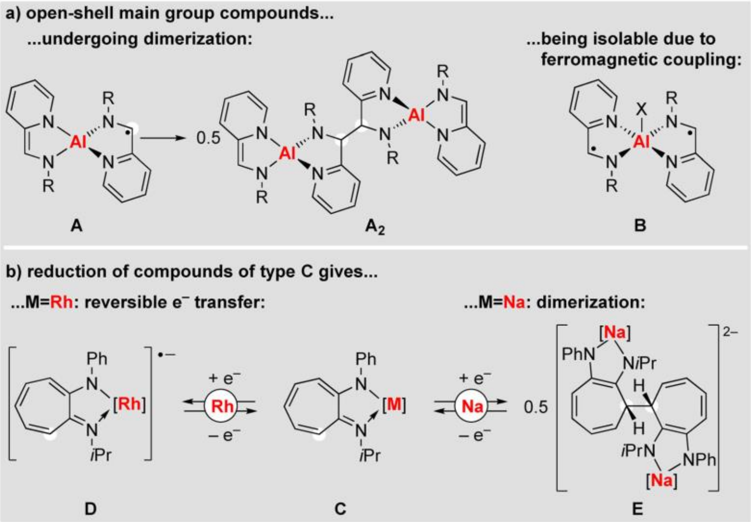

Scheme 1. Controlling the properties of open-shell main-group compounds: a) through magnetic coupling (dimerization vs. isolable species); b) through the choice of the central atom (reversible electron transfer vs. dimerization). X = Cl, O_3SCF_3; R = 2,6-*i*Pr_2-C_6H_3.

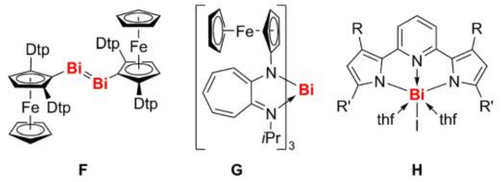

Scheme 2. Bismuth complexes with redox-active ligands (**F**, **G**) and potentially redox-active ligands (**H**). R/R' = *t*Bu/*t*Bu, Ph/mesityl; Dtp = 3,5-*t*Bu_2-C_6H_3.

Herein, we report on the synthesis, isolation, characterization, and redox properties of the first series of cationic bismuth ATI complexes.

Results and Discussion

Synthesis and structure

Starting from a reported sodium ATI compound [Na(ATI$^{Ph/iPr}$)(thf)], with its unsymmetric Ph/*i*Pr substitution pattern, neutral and cationic bismuth ATIs **1** and **2**-X were synthesized in straightforward salt elimination protocols (Scheme 3; X = OTf, SbF_6, BAr^F; OTf = O_3SCF_3; BAr^F = B(3,5-$(CF_3)_2C_6H_3)_4$). Following the same synthetic approach, cationic bismuth ATIs **3**-X and **4**-X based on ATI$^{iPr/iPr}$, which has been reported in the literature, and the new ATI$^{PhSMe/iPr}$ ligand were obtained (Scheme 3; for details on the synthesis and characterization of [Na(ATI$^{PhSMe/iPr}$)(thf)] and related species, see the Experimental Section and the Supporting Information). The products were isolated as red to orange solids.

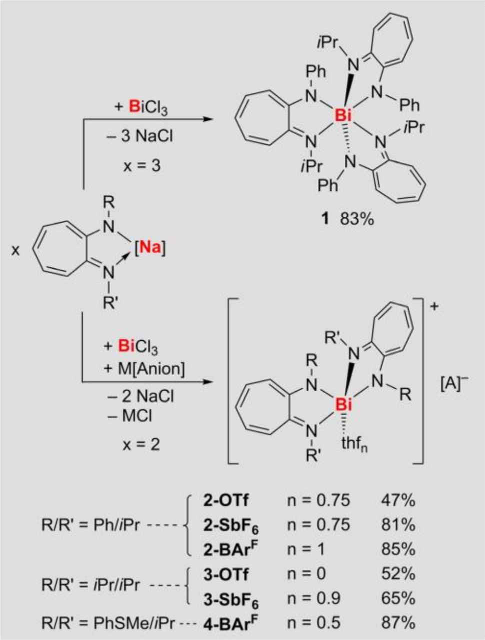

Scheme 3. Synthesis of neutral and cationic bismuth ATI complexes.

NMR spectroscopic analysis in solution revealed the expected signal patterns for bismuth complexes with one set of magnetically equivalent ATI ligands in all cases. In the case of neutral **1**, a second set of resonances with minor intensities of 6% was detected. This was ascribed to *fac*/*mer* isomerism in this $M(AB)_3$-type compound;[14b,16] the main isomer is the *fac* species, according to DFT calculations (ΔG (*fac*-**1**→*mer*-**1**) = +1.9 kcal mol^{-1}) and structural analysis of **1** in the solid state (see below). In all compounds with the $[ATI^{Ph/iPr}]^-$ ligand, the resonances for all protons of the phenyl groups were significantly broadened at room temperature. Variable-temperature (VT) ^1H NMR spectroscopy revealed coalescence temperatures of 40 °C for neutral **1** and 15–25 °C for cationic **2**-X and five well-resolved signals for the phenyl groups in the low-temperature scenario. This indicates a hindered rotation of the phenyl groups around the N^{ATI}–C^{Ph} bond. Line-shape analyses and Eyring plots revealed activation parameters of $\Delta G^{\neq}(298\ K) = 14.9$ kcal mol^{-1} for neutral **1** and $\Delta G^{\neq}(298\ K) = 13.6–13.9$ kcal mol^{-1} for cationic **2**-X (for details, see the Supporting Information). Thus, the ATI ligands in neutral and cationic complexes experience similar steric clash in the coordination sphere of bismuth, although a significantly less crowded coordination environment and a more easily accessible metal center is found for the cationic species (see below). This was ascribed to the coordination geometry of the cationic species being dictated by orbital interactions rather than Coulomb interactions.

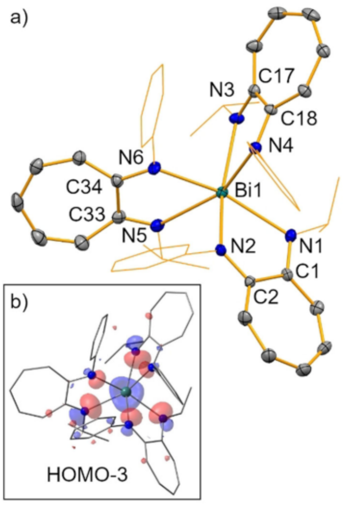

Figure 1. a) Molecular structure of $[Bi(ATI^{Ph/iPr})_3]$ (**1**) in the solid state. Displacement ellipsoids are shown at the 50% probability level. Carbon atoms of Ph and *i*Pr groups are shown in the wireframe model and hydrogen atoms are omitted for clarity. Bi1–N1 2.552(4), Bi1–N2 2.384(4), Bi1–N3 2.531(4), Bi1–N4 2.354(4), Bi1–N5 2.581(4), Bi1–N6 2.368(4), N1–C1 1.313(6), N2–C2 1.349(6), N3–C17 1.326(6), N4–C18 1.354(6), N5–C33 1.319(7), N6–C34 1.342(6) Å; N1-Bi1-N6 155.87(14), N2-Bi1-N3 158.65(13), N4-Bi1-N5 154.62(14), N1-Bi1-N2 64.89(12), N3-Bi1-N4 67.16(13), N5-Bi1-N6 64.89(13), N1-Bi1-N5 117.64(13)°. b) HOMO-3 of compound **1** (isovalue = 0.05), as determined by DFT calculations. This molecular orbital (MO) shows contributions by an s-type bismuth atomic orbital that is polarized towards the hemisphere in which the N*i*Pr groups are localized and may be associated with a stereochemically active lone pair (for details, see the Supporting Information).

Compounds **1**, **2**-X, **3**-X, and **4**-BAr^F were characterized by single-crystal X-ray diffraction analyses. Compound **1** crystallized in the monoclinic space group $P2_1/n$ with $Z = 4$ and shows a *fac* configuration (Figure 1 a). The central atom is found in a distorted octahedral coordination geometry: angles of ligands in *cis* orientation range from 65 to 118°. Strong deviations from ideal symmetry are due to the small bite angle of the ATI ligand (chelating: N-Bi-N, 65–67°). In addition, the HOMO-3 shows significant contributions from an s-type bismuth atomic orbital, which is polarized towards the empty space created by deviations from an octahedral symmetry, as determined by DFT calculations (Figure 1 b; for details, see the Supporting Information). This may be associated with a stereochemically active lone pair at bismuth. Due to its *fac* configuration, compound **1** bears three pairs of *trans*-oriented NPh and N*i*Pr groups. Delocalization of electron density in the ATI ligands prohibits the unequivocal assignment of amido and imino groups. Nevertheless, it is apparent that the C–N*i*Pr bonds (1.31–1.33 Å) are, on average, slightly shorter than the C–NPh bonds (1.34–1.35 Å). In agreement with this observation, the Bi–N*i*Pr bonds (2.53–2.58 Å) are significantly longer than the Bi–NPh bonds (2.35–2.38 Å). This is further supported by the Wiberg bond indices (WBIs), which are considerably smaller for the Bi–N*i*Pr bonds (WBI = 0.22–0.23) than for the Bi-NPh bonds (WBI = 0.32–0.33). This is in contrast to the only other homoleptic bismuth ATI complex $[Bi(ATI^{Fc/iPr})_3]$, which crystallizes in a *mer* configuration, leading to an even more pronounced variation in Bi–N bond lengths (2.33–2.61 Å).[14b]

The molecular structures of the cationic bismuth ATIs **2**-X, **3**-X, and **4**-BAr^F are shown in Figure 2. Selected crystallographic and structural information are summarized in Table 1. The coordination geometries of the cationic species are bisphenoidal (**2**-BAr^F, **3**-OTf, **4**-BAr^F) or square pyramidal (**2**-OTf, **2**-SbF_6, **3**-SbF_6; $\tau_5 = 0.18–0.28$), if only the ATI and thf ligands are considered. If additional weak bonding interactions with counteranions or the thioether group in **4**-BAr^F are also taken into account, the coordination geometries are best described as square pyramidal (**2**-BAr^F; $\tau_5 = 0.22$), distorted octahedral (**3**-OTf, **3**-SbF_6), and irregular (**2**-OTf, **2**-SbF_6, **4**-BAr^F). The Bi–N bond lengths of the cationic species (2.21–2.38 Å) are, on average, significantly shorter than those in neutral **1** (2.35–2.58 Å), although the same or even higher coordination numbers are reached in the cationic species. This is due to the interactions between the bismuth atoms of the cationic species and their counteranions or neutral donor groups (thf or thioether) being weak compared with the Bi–N^{ATI} interactions in neutral **1**. In all cationic species, the Bi–N bonds that face another Bi–N bond in the *trans* position (2.31–2.38 Å) are significantly longer than those that have a Bi–X bond or a free coordination site in the *trans* position (2.21–2.25 Å; X = O^{THF}, O^{OTf}, $S^{thioether}$, F^{BArF}), that is, there is a considerable thermodynamic *trans* effect in these compounds.[14b,17] Notably, this is also observed in compounds **3**-X, in which the substituents at nitrogen are identical and any

Chemistry–A European Journal
Full Paper
doi.org/10.1002/chem.202005186
Chemistry Europe
European Chemical Societies Publishing

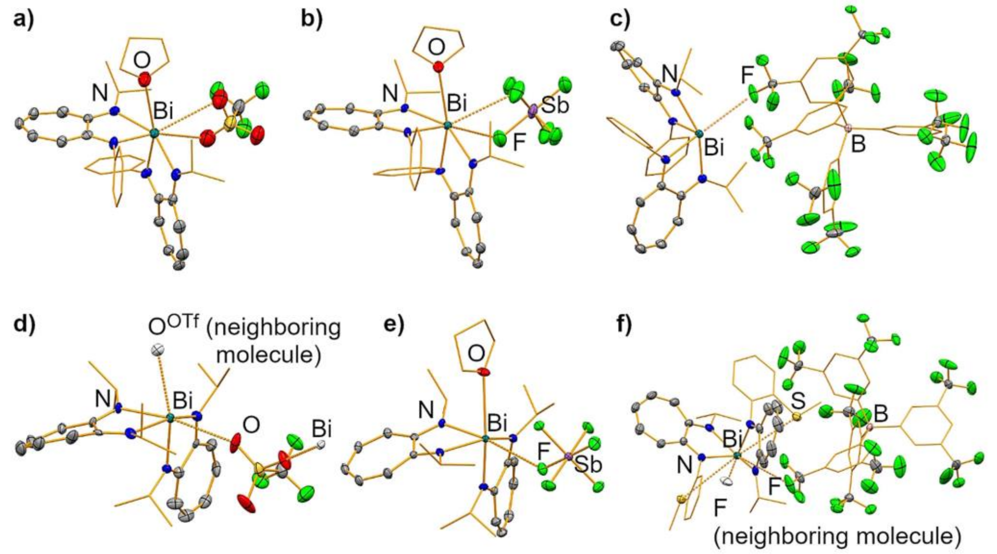

Figure 2. Molecular structures of compounds **2**-X (a–c), **3**-X (d, e), and **4**-BAr^F (f) in the solid state. Displacement ellipsoids are shown at the 50 % probability level. Carbon atoms, except for those of the ATI backbone, are shown as wireframe. Hydrogen atoms and lattice-bound solvent molecules are omitted for clarity. Only one of the six crystallographically independent, but chemically identical, formula units is shown in d). Atoms that exceed one formula unit are shown as colorless ellipsoids (d, f). For details, see the Supporting Information.

Table 1. Selected crystallographic information and structural parameters of compounds **1**, **2**-X, **3**-X, and **4**-BAr^F. For details, see the Supporting Information.

	1	**2**-OTf	**2**-SbF$_6$	**2**-BAr^F	**3**-OTf[a]	**3**-SbF$_6$	**4**-BAr^F
crystal system	monoclinic	monoclinic	monoclinic	triclinic	monoclinic	monoclinic	orthorhombic
space group	$P2_1/n$	$P2_1/n$	$P2_1/n$	$P\bar{1}$	$P2_1$	Cc	$C222_1$
Z	4	4	4	2	2	4	4
R/R′	Ph/*i*Pr	Ph/*i*Pr	Ph/*i*Pr	Ph/*i*Pr	*i*Pr/*i*Pr	*i*Pr/*i*Pr	PhSMe/*i*Pr
coordination number with (without) weak interactions[b]	6	7 (5)	7 (5)	5 (4)	6 (4)	6 (5)	8 (4)
Bi–O^{THF} [Å]	–	2.943(11)	2.809(5)	–	–	2.888(4)	2× Bi···SMeR; 3.8693(15); 3.8693(15)[c]
Bi···anion; [Å]	–	2× Bi···O; 3.120(14); 3.215(13)	2× Bi···F; 3.084(7); 3.437(7)	1× Bi···F; 3.2908(19)	2× Bi···O; 2.873(6); 2.940(6)	1× Bi···F; 3.139(3)	2× Bi···F; 3.470(6); 3.470(6)
Bi–N (other N atom in *trans* position) [Å]	shortest Bi–N: 2.354(4);	2.360(4); 2.383(4)	2.311(5); 2.370(5)	2.327(2); 2.3389(19)	2.336(7); 2.341(8)	2.339(3); 2.376(3)	2.338(5); 2.338(5)
Bi–N (X or free coordination site in *trans* position)[d] [Å]	longest Bi–N: 2.581(4)	2.241(4); 2.250(4)	2.221(4); 2.249(4)	2.2068(19); 2.210(2);	2.195(10); 2.226(6)	2.226(3); 2.243(3)	2.219(5); 2.219(5)

[a] Data for one of the six crystallographically independent, but chemically identical, formula units are presented (for details, see the Supporting Information). [b] For the determination of the coordination number in compounds **2**-X, **3**-X, and **4**-X, Bi···O^{OTf}, Bi···F, and Bi···$S^{thioether}$, interactions were considered to be weak. [c] No thf ligand is present in **4**-BAr^F and the interatomic distance between the Bi atom and S atoms of the thioether functional groups are listed instead. [d] X = O^{THF}, O^{OTf}, $S^{thioether}$, F^{SbF_6}, F^{BAr^F}.

impact of the substitution pattern on Bi–N bond lengths is thus ruled out. The Bi–O^{THF} bond lengths in the cationic bismuth ATIs (2.81–2.94 Å) are within the broad range of Bi–O^{THF} bond lengths reported for other cationic bismuth amides (e.g., 2.57–3.19 Å in [Bi(N*i*Pr$_2$)$_2$(thf)$_3$][BAr^F]).[18] As a trend, a stronger electron-donating ability of the ATI ligand ([ATI$^{iPr/iPr}$]$^-$ in **3**-SbF$_6$ versus [ATI$^{Ph/iPr}$]$^-$ in **2**-SbF$_6$)[19] and the counteranion (OTf$^-$ in **2**-OTf vs. [SbF$_6$]$^-$ in **2**-SbF$_6$) increase the Bi–O^{THF} bond lengths (Table 1). The Bi···$S^{thioether}$ interactions in **4**-BAr^F are very weak (if they exist) based on distance criteria (Bi···S 3.87 Å; identical to the sum of the van der Waals radii), which is ascribed to geometrical constraints in the ligand framework. While bonding interactions between the bismuth atom and the counteranion are significant in the case of the triflate species ($\text{Bi}\cdots\text{O}^{\text{OTf}}$ 2.87–3.22 Å; 10–20% below the sum of the van der Waals radii), they are less pronounced for the hexafluoroantimonates ($\text{Bi}\cdots\text{F}$ 3.08–3.14 Å; 11–13% below the sum of the van der Waals radii),[20] and only minor in the BAr^F species ($\text{Bi}\cdots\text{F}$ 3.29–3.47 Å; 2–7% below the sum of the van der Waals radii). The cationic species generally form typical mononuclear complexes in the solid state. As an exception to this, compound **3**-OTf crystallizes as a coordination polymer due to a bridging coordination mode of the triflate anion (for details, see the Supporting Information). Surprisingly, the cationic species **2**-BAr^F, which forms only very weak interactions with the borate counteranion, crystallizes from solutions of difluorobenzene without any thf ligands bound to the bismuth atom. This shows that the thf adduct (as obtained from the isolation of analytically pure bulk material) may release its neutral ligand in solutions of moderately polar and weakly donating solvents.

Lewis acidity

The Lewis acidity of molecular cationic bismuth compounds can be a crucial factor for the realization of unusual phenomena and reactivity patterns in coordination chemistry,[21] group-transfer reactions,[18] CH activation,[22] small-molecule activation,[23] and catalytic applications.[13b,24] It has recently been quantified by using the Gutmann–Beckett (GB) method, that is, through adduct formation of the bismuth species with OPEt_3.[25] We have recently reported that the use of EPMe_3 (E = S, Se) instead of OPEt_3 can be exploited for the assessment of the soft character of a Lewis acid, which is demonstrated to be especially pronounced for bismuth cations.[26] Because the Lewis acidity of cationic bismuth compounds based on chelating N,N-donor ligands has not been quantified, to date, selected bismuth ATI complexes were investigated with the original and modified GB methods (Table 2).

By using one equivalent of OPEt_3 as a donor in dichloromethane, all bismuth ATIs showed relatively low acceptor numbers of $\text{AN(OPEt}_3) = 21–29$. As a trend, bismuth ATI cations without significant bonding interactions to the counteranion showed slightly larger ANs of 25–29 than those with $\text{Bi}\cdots\text{OTf}$ interactions or neutral **1**[27] ($\text{AN(OPEt}_3) = 21–22$).

Table 2. ^{31}P NMR chemical shifts and acceptor numbers (ANs), according to the original GB method (OPEt_3 as a Lewis base) and modifications thereof (SPMe_3, SePMe_3 as Lewis bases).[a]

Compound	OPEt_3 δ ^{31}P [ppm]	AN	SPMe_3 δ ^{31}P [ppm]	AN	SePMe_3 δ ^{31}P [ppm]	AN
1	50.3	21				
2-OTf	50.4	21				
2-SbF_6	53.4	27				
2-BAr^F	52.4	25				
3-OTf	51.1	22				
4-BAr^F	54.0	29	30.9	11	8.9	6

[a] One equivalent of OPEt_3, SPMe_3, or SePMe_3 was added to solutions of the respective bismuth compound in dichloromethane. For details, see the Experimental Section.

These ANs are larger than that of $\text{B(NMe}_2)_3$ ($\text{AN(OPEt}_3) = 9$) and similar to that of B(OMe)_3 ($\text{AN(OPEt}_3) = 23$).[28] Compound **4**-BAr^F was additionally investigated with the modified GB method, but also showed low ANs if the soft donors EPMe_3 were applied ($\text{AN(SPMe}_3) = 11$; $\text{AN(SePMe}_3) = 6$). Thus, the ATI ligand (an example of a bidentate monoanionic N,N-donor ligand) quenches large parts of the Lewis acidity of the bismuth center towards external Lewis bases, even in cationic species. This raises the question of whether the reduction of cationic bismuth ATIs would predominantly be a ligand- or a metal-centered event (or an intermediate scenario; see below).

Redox properties

The redox-active nature of ATI ligands has recently been established. Specifically, it has been demonstrated that alkali-metal ATI complexes undergo reductively induced dimerization reactions, whereas rhodium ATI species are susceptible to reversible, ligand-centered electron transfer (Scheme 1b).[6] To shed some light on the redox properties of the bismuth complexes presented herein, they were analyzed by cyclic voltammetry (all potentials referenced vs. ferrocene/ferrocenium; for details, see the Experimental Section and the Supporting Information). An irreversible redox event in the range of 0.27–0.39 V was observed for all compounds (see the Supporting Information). Under reducing conditions, neutral bismuth ATI complex **1** showed a reduction wave at −2.26 V, with the corresponding oxidation wave appearing at −1.20 V (Figure 3a and Table 3, entry 1). This indicates that a chemical reaction takes place after electron transfer. The ratio, I_{pc}/I_{pa}, of these redox waves is close to one and the shape of the cyclic voltammogram does not change significantly upon increasing the number of cycles, which indicates the reversibility of the ECEC sequence. This be-

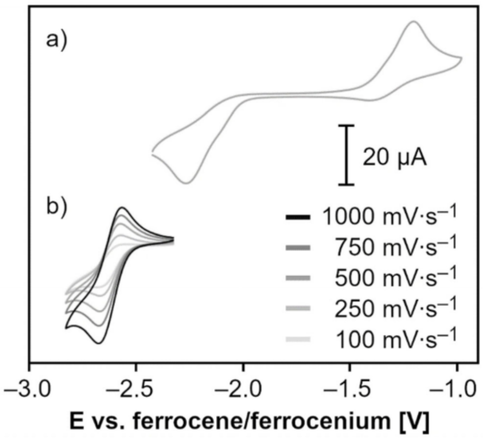

Figure 3. Cyclic voltammograms of **1** (a) and $[\text{Bi(ATI}^{\text{Ph}/i\text{Pr}})_2][\text{BAr}^\text{F}]$ (**2**-BAr^F) (b) in THF/0.1 M $[\text{N}(n\text{Bu})_4][\text{PF}_6]$ at a temperature of 23 °C and scan rates in the range of 100–1000 mV s^{-1}.

Chemistry–A European Journal | Full Paper
doi.org/10.1002/chem.202005186
Chemistry Europe
European Chemical Societies Publishing

Table 3. Redox properties of bismuth ATI complexes under reducing conditions, as deduced from cyclic voltammetry in THF/0.1 M $[N(nBu)_4][PF_6]$ at 23 °C and scan rates of 50–5000 mV s^{-1} (for details, see the Supporting Information).

Entry	Compound	$E_{1/2}$ or E_{pc}/E_{pa} [V][a]	Classification[b]	Reversibility[c]
1	**1**	−2.26/−1.20[d]	ECEC	qr
2	**2**-OTf	−2.63	EE	pr
3	**2**-SbF_6	−2.64	EE	pr
4	**2**-BAr^F	−2.61	EE	qr
5	**3**-OTf	−2.71	EE	pr
6	**3**-SbF_6	−2.80	EE	pr
7	**4**-BAr^F	−2.57	EE	qr

[a] Potentials are referenced versus the ferrocene/ferrocenium couple; entry 1: E_{pc}/E_{pa}; entries 2–7: $E_{1/2}$. [b] E = electron transfer; C = chemical reaction. [c] qr = quasi-reversible; pr = partially reversible. [d] There is an additional redox event at −2.66 V (for details, see the Supporting Information).

havior (as determined from cyclic voltammetry) is strongly reminiscent of the situation found for the corresponding sodium compound, $[\mathrm{Na(ATI}^{Ph/iPr})(thf)]$, which undergoes a highly selective, chemically reversible, reductively induced dimerization with the formation of a C–C bond between two ATI moieties (cf. **C**→**E** in Scheme 1 b).[6b] In contrast, no indications for such redox behavior were obtained in the cyclic voltammetry analyses of the cationic bismuth ATI species **2**-X, **3**-X, and **4**-BAr^F. While complexes with $[OTf]^-$ or $[SbF_6]^-$ counteranions show partially reversible redox events, compounds **2**-BAr^F and **4**-BAr^F show quasi-reversible redox events at strongly negative potentials of −2.61 and −2.57 V, respectively (shown for **2**-BAr^F in Figure 3 b and Table 3, entries 2–7). While the redox potentials of cationic bismuth ATIs with $[\mathrm{ATI}^{Ph/iPr}]^-$ and $[\mathrm{ATI}^{PhSMe/iPr}]^-$ ligands range from −2.57 to −2.64 V, those for complexes with the $[\mathrm{ATI}^{iPr/iPr}]^-$ ligand were found from −2.71 to −2.80 V. This corresponds to a cathodic shift of up to 230 mV and reflects the more electron-donating nature of the $[\mathrm{ATI}^{iPr/iPr}]^-$ ligand, which has previously been discussed in the context of catalytic applications.[19]

Overall, these findings demonstrate that the redox properties of bismuth ATI compounds can be controlled by the choice of the charge of the complex. While the redox behavior of the neutral species resembles that of alkali-metal ATI complexes, the cationic species show a redox behavior reminiscent of the corresponding rhodium compound. DFT calculations were performed to rationalize these differences (for details, see the Experimental Section and the Supporting Information). Frontier orbital analysis of **1** and **2**-BAr^F revealed that the LUMO is exclusively ligand-centered in the neutral compound, but has significant contributions from a bismuth p-type atomic orbital in the cationic species (Figure 4 a,b). These findings are in agreement with an analysis of the spin-density distribution in the reduced species Na-**1**-rad and **2**-rad. Compound Na-**1**-rad shows a negligible spin density of 0.6 % at the bismuth atom, and an overwhelming spin density of 97 % at one ATI ligand, which interacts with the sodium countercation (with spin densities of up to 27 % at individual atoms of this ligand; Figure 4 c). In contrast, compound **2**-rad may be described as a bismuth-centered radical (72 % spin density) supported by two redox-active ATI ligands, each of which has a spin density of 14 % (with up to 3 % spin density at individual atoms of these ligands; Figure 4 d).[29]

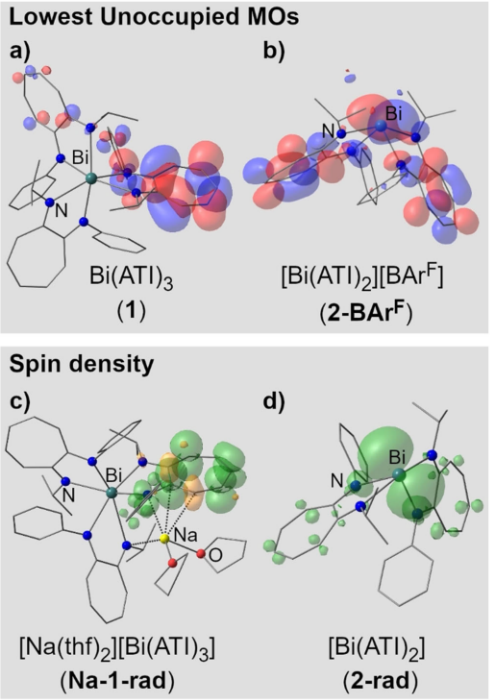

Figure 4. Structures obtained from geometry optimizations by DFT calculations. LUMOs of **1** (a) and **2**-BAr^F (b; the counteranion is included in the calculation, but omitted in the figure for clarity) at isovalues of 0.03. Spin densities of $[\mathrm{Na(thf)_2][Bi(ATI^{Ph/iPr})_3}]$ (Na-**1**-rad) (c) and $[\mathrm{Bi(ATI^{Ph/iPr})_2}]$ (**2**-rad) (d) at isovalues of 0.002.

Conclusion

We have prepared the first examples of cationic bismuth ATIs, $[\mathrm{Bi(ATI)_2}L_n][A]$ (L = neutral ligand; n = 0–1; A = counteranion). Depending on the choice of the counteranion, contact ion pairs, solvent-separated ion pairs, or "naked" bismuth ATI cations with weak Bi⋯[F] interactions were obtained ([F] = fluorine atom of BAr^F). According to VT-NMR spectroscopy studies and line-shape analyses, the ATI ligands in neutral and cationic species experience similar steric clash, which was assigned to a predominantly orbital-controlled coordination chemistry in the cationic compounds. The Lewis acidity of bismuth ATI cations towards hard and soft donors was relatively weak, according to the GB method (and its modifications), which was ascribed to the bidentate nature of the monoanionic ATI ligand. In turn, the empty p orbital of the bismuth atom in cationic species was accessible under reducing conditions and allowed for quasi-reversible electron transfer at bismuth (according to cyclic voltammetry and DFT calculations). In contrast, investigations into the redox chemistry of the neutral bismuth ATI complex [Bi(ATI$^{iPr/iPr}$)$_3$] indicated ligand-centered redox events. Thus, we demonstrated that the choice of the charge in bismuth ATI complexes allowed switching from ligand-centered redox events (as previously reported for alkali-metal complexes) to metal-centered, quasi-reversible redox events. The latter was analogous to Rh ATI compounds in terms of reversibility, but are distinct in terms of the localization of spin density in the reduced species (metal-centered in [Bi(ATI)$_2$]$^{\bullet}$, but ligand-centered in [Rh(ATI)(cod)]$^{\bullet-}$; cod = 1,5-cyclooctadienyl). These findings open up perspectives for switchable redox-catalysis based on the heavy main-group element bismuth.

Experimental Section

General

All air- and moisture-sensitive manipulations were carried out by using standard vacuum-line Schlenk or glove box techniques in an atmosphere of purified argon. Solvents were degassed and purified, according to standard laboratory procedures. NMR spectra were recorded on Bruker instruments operating at 200, 400, or 500 MHz with respect to ^{1}H. ^{19}F and ^{31}P NMR spectra were recorded with proton decoupling. All chemical shifts (δ) are reported in ppm. ^{1}H and ^{13}C NMR chemical shifts are reported relative to $SiMe_4$ by using the residual ^{1}H and ^{13}C chemical shifts of the solvent as a secondary standard. ^{19}F and ^{31}P NMR chemical shifts are reported relative to $CFCl_3$ and 85% aqueous H_3PO_4, respectively, as external standards. Unless stated otherwise, NMR spectra were recorded at 23 °C. Elemental analyses were performed on a Leco or a Carlo Erba instrument. For MS analyses, an Exactive plus instrument (Thermo Scientific) was used. Cyclic voltammograms were recorded by using a Gamry Instruments Reference 600 potentiostat at 23 °C in THF containing 0.1 M [N(nBu)$_4$][PF$_6$], unless otherwise noted. A standard three-electrode cell configuration was employed by using a platinum disk working electrode, a platinum wire counter electrode, and a silver wire separated by a Vycor tip as the reference electrode. Formal redox potentials are referenced to the ferrocene/ferrocenium redox couple. Single crystals suitable for X-ray diffraction were coated with perfluorinated polyether oil in a glove box, transferred to a nylon loop, and then transferred to the goniometer of a diffractometer equipped with a molybdenum (λ = 0.71073 Å) or copper (λ = 1.5418 Å) X-ray tube. The structures were solved using the intrinsic phasing method, completed by Fourier synthesis and refined by full-matrix least-squares procedures. Deposition numbers 2044644, 2044645, 2044646, 2044647, 2044648, 2044649, 2044650, 2044875, and 2044876 contain the supplementary crystallographic data for this paper. These data are provided free of charge by the joint Cambridge Crystallographic Data Centre and Fachinformationszentrum Karlsruhe Access Structures service.

Computational details

DFT calculations were performed with the Gaussian program by using the 6-31G(d,p) (H, B, C, N, O, F),[30] 6-311G(d,p) (Na),[31] and LaNL2DZ (Bi)[32] basis sets and the (U)B3LYP functional.[33] The D3 version of Grimme's dispersion model with the original D3 damping function was applied.[34] Frequency analyses of the reported structures showed no imaginary frequencies. Thermodynamic parameters were calculated at a temperature of 298.15 K and a pressure of 1.00 atm. Further details are given in the Supporting Information. Cartesian coordinates of optimized structures are provided in .xyz format.

General procedure for the original and modified GB methods

Equimolar amounts of the potential Lewis acid (usually 10 mg of the bismuth complex) and the Lewis base ($OPEt_3$, $SPMe_3$, or $SePMe_3$) were dissolved in CD_2Cl_2 (0.5 mL) and ^{1}H and ^{31}P NMR spectra were recorded.

Compound 1

$NaN(SiMe_3)_2$ (42 mg, 0.23 mmol) and $BiCl_3$ (24 mg, 76 μmol) were subsequently added to a solution of *N*-*i*Pr-2-phenylaminotroponimine (54 mg, 0.23 mmol) in THF (2 mL). All volatile compounds were removed from the red reaction mixture under reduced pressure. The residue was suspended in toluene (3 × 1.5 mL) and the resulting suspension was filtered. All volatile compounds were removed from the deep-red filtrate under reduced pressure to give a deep-red solid, which was dried in vacuo (58 mg, 63 μmol, 83%). M.p. 198 °C (dec); ^{1}H NMR (500 MHz, −40 °C, [D$_8$]toluene): δ = 1.23 (d, ^3J(H,H) = 5.5 Hz, 9H; Me^1), 1.32 (d, ^3J(H,H) = 5.8 Hz, 9H; Me^2), 3.96–4.03 (br s, 3H; C*H*Me$_2$), 4.80 (d, ^3J(H,H) = 8.2 Hz, 3H; *o*-Ph^1), 5.83 (d, ^3J(H,H) = 11.2 Hz, 3H; 3-H), 6.00 (br dd, ^3J(H,H) = 8.2, 8.9 Hz, 3H; 5-H), 6.43 (d, ^3J(H,H) = 11.8 Hz, 3H; 7-H), 6.44 (br dd, ^3J(H,H) = 9.8, 11.2 Hz, 3H; 4-H), 6.77–6.80 (m, 3H; *p*-Ph), 6.87 (br dd, ^3J(H,H) = 8.2, 11.8 Hz, 3H; 6-H), 6.97 (d, ^3J(H,H) = 8.2 Hz, 3H; *o*-Ph^2), 6.98–7.02 ppm (m, 6H; *m*-Ph^{1,2}); ^{13}C NMR (126 MHz, −40 °C, [D$_8$]toluene): δ = 23.9 (s, Me^2), 24.1 (s, Me^1), 49.9 (s, CHMe$_2$), 116.8 (s, 7-C), 117.4 (s, 5-C), 117.4 (s, 3-C), 124.7 (s, *p*-Ph), 127.7 (s, *o*-Ph^2), 128.5 (s, *m*-Ph^1/*m*-Ph^2), 129.2 (s, *m*-Ph^2/*m*-Ph^1), 133.3 (s, 6-C), 133.6 (s, 4-C), 151.4 (s, *ipso*-Ph), 163.5 (s, 1-C), 168.0 ppm (s, 2-C); elemental analysis calcd (%) for $C_{48}H_{51}N_6Bi$ (920.95 g mol^{-1}): C 62.60, H 5.58, N 9.13; found: C 62.79, H 5.41, N 9.09.

Compound 2-OTf

A solution of Na(ATI$^{iPr/Ph}$)(thf)$_{0.84}$ (50 mg, 156 μmol) in THF (1 mL) was added dropwise to a suspension of sodium triflate (13.5 mg, 78 μmol) and $BiCl_3$ (25 mg, 78 μmol) under stirring. The red suspension was filtered and layered with pentane (0.5 mL). After 24 h, the red crystalline precipitate was isolated by filtration, washed with pentane (3 × 3 mL), and dried in vacuo. Crystals suitable for single-crystal X-ray analysis were obtained by layering a solution of **2**-OTf (20 mg) in THF (0.5 mL) with pentane (0.1 mL). Yield: 33 mg, 37 μmol (with n = 0.75 equiv of THF), 47%; ^{1}H NMR (500 MHz, −30 °C, [D$_5$]pyridine): δ = 0.70 (d, ^3J(H,H) = 5.9 Hz, 6H; CH*Me*), 1.35 (d, ^3J(H,H) = 6.0 Hz, 6H; CH*Me*), 1.48–1.50 (m, n × 4H; β-THF), 3.26–3.20 (br m, 2H; C*H*Me$_2$), 3.57–3.59 (m, n × 4H; α-THF), 6.30 (d, ^3J(H,H) = 11.0 Hz, 2H; 3-H), 6.35 (d, ^3J(H,H) = 7.8 Hz, 2H; *o*-Ph, partially overlapped by 3-H), 6.37 (d, ^3J(H,H) = 11.7 Hz, 2H; 7-H), 6.73 (dd, ^3J(H,H) = 8.7, 9.8 Hz, 2H; 5-H), 7.13 (d, ^3J(H,H) = 7.6 Hz, 2H; *o*-Ph), 7.18 (m, 2H; 6-H, partially overlapped by [D$_5$]pyridine), 7.22 (m, 2H; *m*-Ph, partially overlapped by [D$_5$]pyridine), 7.27 (dd, ^3J(H,H) = 6.5, 8.3 Hz, 2H; *p*-Ph), 7.45 (m, 2H; *m*-Ph, partially overlapped by 4-H), 7.47 ppm (m, 2H; 4-H); ^{13}C NMR (126 MHz, −30 °C, [D$_5$]pyridine): δ = 21.0 (s, CH*Me*), 26.2 (s, β-THF), 26.7 (s, CH*Me*), 50.0 (s, CHMe$_2$), 68.3 (s, α-THF), 120.6 (s, 3-C), 121.7 (s, 7-C), 124.5 (s, 5-C), 127.8 (s, *m*-Ph), 128.1 (s, *o*-Ph), 129.4 (s, *o*-Ph), 130.7 (s, *p*-Ph), 130.7 (s, *p*-Ph), 148.1 (s, *ipso*-Ph), 165.1 (s, 1-C), 170.3 ppm (s, 2-C); ^{19}F NMR (470 MHz, [D$_5$]pyridine): δ = −76.07 ppm; elemental analysis calcd

(%) for $C_{33}H_{34}N_4BiF_3SO_3{\cdot}(C_4H_8O)$ (904.80 g mol^{-1}): C 49.12, H 4.68, N 6.19, S 3.54; found: C 49.03, H 4.58, N 6.41, S 3.32.

Compound 2-SbF$_6$

A solution of Na(ATI$^{iPr/Ph}$) (25 mg, 96 μmol) in THF (0.5 mL) was added dropwise to a suspension of silver hexafluoroantimonate(V) (17 mg, 48 μmol) and BiCl$_3$ (15 mg, 48 μmol) under stirring. After 10 min, the red suspension was filtered, and the volume of the filtrate was reduced to half. After 24 h, the red crystalline precipitate was isolated by filtration, washed with pentane (3×1 mL), and dried in vacuo (38 mg, 39 μmol (with $n=0.75$ equiv of THF), 81 %). ^{1}H NMR (500 MHz, −35 °C, [D$_5$]pyridine): $\delta=0.59$ (d, ^{3}J(H,H) = 5.9 Hz, 6H; CH*Me*), 1.25 (d, ^{3}J(H,H) = 5.8 Hz, 6H; CH*Me*), 1.46–1.49 (m, $n\times4$H; β-THF), 3.19–3.23 (br m, 2H; C*H*Me$_2$), 3.56–3.59 (m, $n\times4$H; α-THF), 6.33 (d, ^{3}J(H,H) = 7.8 Hz, 2H; *o*-Ph, partially overlapped by 4-H), 6.34 (d, ^{3}J(H,H) = 11.1 Hz, 2H; 3-H), 6.37 (d, ^{3}J(H,H) = 12.1 Hz, 2H; 7-H), 6.78 (dd, ^{3}J(H,H) = 8.8, 9.7 Hz, 2H; 5-H), 7.01 (d, ^{3}J(H,H) = 8.0 Hz, 2H; *o*-Ph), 7.22–7.25 (m, 2H; 6-H, partially overlapped by *m*-Ph), 7.23–7.26 (m, 2H; *m*-Ph, partially overlapped by 6-H), 7.28 (dd, ^{3}J(H,H) = 7.4, 8.3 Hz, 2H; *p*-Ph), 7.45 (dd, ^{3}J(H,H) = 7.2, 8.1 Hz, 2H; *m*-Ph), 7.51 ppm (dd, ^{3}J(H,H) = 9.4, 11.1 Hz, 2H; 4-H); ^{13}C NMR (126 MHz, −35 °C, [D$_5$]pyridine): $\delta=20.9$ (s, CH*Me*), 26.2 (s, β-THF), 26.8 (s, CH*Me*), 49.9 (s, *C*HMe$_2$), 68.3 (s, α-THF), 120.8 (s, 3-C), 124.5 (s, 7-C), 125.0 (s, 5-C), 127.9 (s, *m*-Ph), 129.3 (s, *o*-Ph), 129.5 (s, *o*-Ph), 130.7 (s, *p*-Ph), 130.8 (s, *p*-Ph), 147.8 (s, *ipso*-Ph), 165.0 (s, 1-C), 170.2 ppm (s, 2-C); elemental analysis calcd (%) for $C_{32}H_{34}N_4BiF_6Sb{\cdot}(C_4H_8O)$ (991.49 g mol^{-1}): C 43.61, H 4.27, N 5.65; found: C 43.87, H 4.24, N 5.65.

Compound 2-BAr^F

Na(ATI$^{iPr/Ph}$) (200 mg, 602 μmol) was added dropwise to a solution of sodium tetrakis[3,5-bis(trifluoromethyl)phenyl]borate (267 mg, 301 μmol) and BiCl$_3$ (95 mg, 301 μmol) in THF (4 mL) under stirring. After 1 h, the red suspension was filtered, and all volatile compounds were removed under reduced pressure. The crude product was washed with hexane (2×2 mL) and dried in vacuo (416 mg, 257 μmol (with $n=1$ equiv of THF), 85 %). ^{1}H NMR (500 MHz, −40 °C, [D$_8$]THF): $\delta=1.10$ (d, ^{3}J(H,H) = 6.0 Hz, 6H; CH*Me*), 1.48 (d, ^{3}J(H,H) = 6.3 Hz, 6H; CH*Me*), 1.77–1.79 (m, $n\times4$H; β-THF), 3.39–3.44 (br m, 2H; C*H*Me$_2$), 3.61–3.63 (m, $n\times4$H; α-THF), 6.14 (d, ^{3}J(H,H) = 11.1 Hz, 2H; 3-H), 6.46 (d, ^{3}J(H,H) = 7.8 Hz, 2H; *o*-Ph^1), 6.48 (d, ^{3}J(H,H) = 11.8 Hz, 2H; 7-H), 6.67 (dd, ^{3}J(H,H) = 8.6, 9.8 Hz, 2H; 5-H), 7.15 (dd, ^{3}J(H,H) = 9.8, 11.1 Hz, 2H; 4-H), 7.18 (d, ^{3}J(H,H) = 7.8 Hz, 2H; *o*-Ph^2), 7.28 (ddd, ^{3}J(H,H) = 7.6, 7.6 Hz, ^{4}J(H,H) = 1.7 Hz, 2H; *m*-Ph^1), 7.35 (br dd, ^{3}J(H,H) = 7.3, 7.3 Hz, 2H; *p*-Ph), 7.45 (m, ^{3}J(H,H) = 8.6, 11.8 Hz, ^{4}J(H,H) = 1.5 Hz, 2H; 6-H), 7.59 (ddd, ^{3}J(H,H) = 7.3, 7.8 Hz, ^{4}J(H,H) = 1.7 Hz, 2H; *m*-Ph^2), 7.76 (br s, 4H; 4-$C_6H_3(CF_3)_2$), 7.86 (br s, 8H; 2,6-$C_6H_3(CF_3)_2$) ppm; ^{13}C NMR (126 MHz, −40 °C, [D$_8$]THF): $\delta=21.1$ (s, Me^1), 26.2 (s, β-THF), 26.5 (s, Me^2), 50.2 (s, *C*HMe$_2$), 68.0 (s, α-THF), 118.1 (s, 4-$C_6H_3(CF_3)_2$), 120.8 (s, 3-C), 124.4 (s, 5-C), 125.0 (s, 7-C), 125.2 (quart, ^{1}J(C,F) = 271.9 Hz, CF$_3$), 127.9 (s, *p*-Ph), 128.6 (s, *o*-Ph^2), 129.5 (s, *o*-Ph^1), 129.7 (br quart, ^{2}J(C,F) = 34.5 Hz, 3,5-$C_6H_3(CF_3)_2$), 130.7 (s, *m*-Ph^{1,2}), 135.2 (br s, 4-C, 2,6-$C_6H_3(CF_3)_2$ (overlapping)), 135.4 (s, 6-C), 147.8 (s, *ipso*-Ph), 162.7 (quart, ^{1}J(B,C) = 49.9 Hz, 1-$C_6H_3(CF_3)_2$), 165.0 (s, 1-C), 170.2 ppm (s, 2-C); elemental analysis calcd (%) for $C_{64}H_{46}N_4BF_{24}Bi{\cdot}(C_4H_8O)$ (1618.95 g mol^{-1}): C 50.45, H 3.36, N 3.46; found: C 50.73, H 3.20, N 3.48.

Compound 3-OTf

A solution of Na(ATI$^{iPr/iPr}$) (200 mg, 808 μmol) in THF (1.5 mL) was added dropwise to a suspension of sodium triflate (70 mg, 404 μmol) and BiCl$_3$ (127 mg, 404 μmol) under stirring. The red suspension was filtered and all volatile compounds of the filtrate were removed under reduced pressure to give an orange solid, which was washed with pentane (3×3 mL) and dried in vacuo. Crystals suitable for single-crystal X-ray analysis were obtained by layering a solution of **3**-OTf (20 mg) in THF (0.5 mL) with pentane (0.1 mL). Yield: 162 mg, 210 μmol, 52 %; ^{1}H NMR (500 MHz, [D$_5$]pyridine): $\delta=1.37$ (d, ^{3}J(H,H) = 6.7 Hz, 24H; CH*Me*), 4.73–4.81 (sept, ^{3}J(H,H) = 6.7 Hz, 4H; C*H*Me$_2$), 6.71 (t, ^{3}J(H,H) = 9.1 Hz, 2H; 5-H), 6.92 (d, ^{3}J(H,H) = 11.5 Hz, 4H; 3-H, 7-H), 7.48 ppm (dd, ^{3}J(H,H) = 11.8, 9.1 Hz, 4H; 4-H, 7-H); ^{13}C NMR (126 MHz, [D$_5$]pyridine): $\delta=22.6$ (s, CH*Me*), 52.3 (s, *C*HMe$_2$), 120.86 (s, 3-C, 7-C), 120.87 (s, 3-C, 7-C), 123.5 (s, 5-C), 135.0 (s, 4-C, 6-C), 168.2 ppm (s, 1-C, 2-C); ^{19}F NMR (470 MHz, [D$_5$]pyridine): $\delta=-76.16$ ppm; elemental analysis calcd (%) for $C_{27}H_{38}N_4BiF_3SO_3$ (764.66 g mol^{-1}): C 42.41, H 5.01, N 7.33, S 4.19; found: C 42.61, H 4.98, N 7.49, S 3.96.

Compound 3-SbF$_6$

A solution of Na(ATI$^{iPr/iPr}$) (25 mg, 101 μmol) in THF (1 mL) was added dropwise to a suspension of silver hexafluoroantimonate(V) (17 mg, 51 μmol) and BiCl$_3$ (16 mg, 51 μmol) in a plastic vial under stirring. The red suspension was filtered and hexane was added (5 mL). The brown precipitate was isolated by filtration, washed with hexane (3×3 mL), and dried in vacuo. Drying for prolonged periods of time reproducibly led to the start of decomposition of the compound. Therefore, the amount of THF and residual hexane had to be checked individually for every batch. Typically, *n* equivalents of THF and *m* equivalents of hexane were detected, with $n=0.07$–1.0 and $m=0.0$–0.5. Yield: 31 mg, 33 μmol (with $n=0.9$ equiv of THF and 0.25 equiv of hexane), 65 %; ^{1}H NMR (400 MHz, CD$_2$Cl$_2$): $\delta=1.48$ (d, ^{3}J(H,H) = 6.7 Hz, 24H; CH*Me*), 1.80–1.83 (m, $n\times4$H; β-THF), 3.66–3.70 (m, $n\times4$H; α-THF), 4.77–4.87 (sept, ^{3}J(H,H) = 6.7 Hz, 4H; C*H*Me$_2$), 6.74 (t, ^{3}J(H,H) = 9.2 Hz, 2H; 5-H), 6.88 (d, ^{3}J(H,H) = 11.5 Hz, 4H; 3-H, 7-H), 7.42 ppm (dd, ^{3}J(H,H) = 11.8, 9.2 Hz, 4H; 4-H, 7-H); ^{13}C NMR (101 MHz, CD$_2$Cl$_2$): $\delta=23.0$ (s, CH*Me*), 26.2 (s, β-THF), 52.4 (s, *C*HMe$_2$), 68.3 (s, α-THF), 121.6 (s, 3-C, 7-C), 125.2 (s, 5-C), 135.1 (s, 4-C, 6-C), 167.4 ppm (s, 1-C, 2-C); elemental analysis calcd (%) for $C_{26}H_{38}N_4BiF_6Sb{\cdot}(C_4H_8O)_{0.07}$ (856.40 g mol^{-1}): C 36.86, H 4.54, N 6.54; found: C 36.46, H 4.68, N 6.35. Fast decomposition of **3**-SbF$_6$ was observed in THF at ambient temperature, which was accompanied by the precipitation of a dark solid. According to ^{1}H NMR spectroscopy, 23 % of the free ligand were detected after about 30 min. After 5 d in solution, the complex was fully decomposed and only the free ligand was detected.

Compound 4-BAr^F

Na(ATI$^{iPr/PhSMe}$)(thf)$_{0.5}$(hex)$_{0.5}$ (100 mg, 259 μmol) was added dropwise to a solution of BiCl$_3$ (41 mg, 130 μmol) in THF (4 mL) and sodium tetrakis[3,5-bis(trifluoromethyl)phenyl]borate (115 mg, 130 μmol) was added under stirring. After 20 min, the red suspension was filtered, and all volatile compounds were removed under reduced pressure. The crude product was washed with hexane (4×2 mL) and dried in vacuo (190 mg, 113 μmol (with $n=0.5$ equiv of THF), 87 %); ^{1}H NMR (500 MHz, −40 °C, CD$_2$Cl$_2$): $\delta=1.10$ (d, ^{3}J(H,H) = 6.0 Hz, 6H; CH*Me*), 1.33 (d, ^{3}J(H,H) = 6.3 Hz, 6H; CH*Me*), 2.44 (s, 6H; *Me*), 3.26–3.34 (br m, 2H; C*H*Me$_2$), 5.33 (s, $n\times2$H; CH$_2$Cl$_2$), 6.17 (d, ^{3}J(H,H) = 10.9 Hz, 2H; 3-H), 6.47 (d, ^{3}J(H,H) = 11.9 Hz, 2H; 7-H), 6.50 (d, ^{3}J(H,H) = 7.9 Hz, 2H; 6-H^{arom}), 6.72 (dd, ^{3}J(H,H) = 8.7, 9.7 Hz, 2H;

5-H), 7.07 (dd, ^3J(H,H) = 9.4, 11.4 Hz, 2H; 4-H), 7.22 (dd, ^3J(H,H) = 6.7, 8.3 Hz, 2H; 5-H$^{\mathrm{arom}}$), 7.33 (d, ^3J(H,H) = 7.9 Hz, 2H; 3-H$^{\mathrm{arom}}$), 7.41 (br dd, ^3J(H,H) = 6.5, 8.2 Hz, 2H; 4-H$^{\mathrm{arom}}$), 7.48 (br dd, ^3J(H,H) = 9.3, 11.2 Hz, ^4J(H,H) = 1.5 Hz, 2H; 6-H), 7.55 (br s, 4H; 4-$C_6H_3(CF_3)_2$), 7.72 (br s, 8H; 2,6-$C_6H_3(CF_3)_2$) ppm; ^{13}C NMR (126 MHz, −40 °C, CD_2Cl_2): $\delta = 13.6$ (s, Me), 20.8 (s, Me^1), 25.2 (s, Me^2), 49.7 (s, *C*HMe$_2$), 117.4 (s, 4-$C_6H_3(CF_3)_2$), 117.9 (s, 3-C), 124.3 (s, 3-C$^{\mathrm{arom}}$), 124.4 (quart, ^1J(C,F) = 273.0 Hz, CF_3), 124.5 (s, 7-C), 125.5 (s, 5-C), 125.6 (s, 5-C$^{\mathrm{arom}}$), 128.5 (quart, ^2J(C,F) = 50.0 Hz, 3,5-$C_6H_3(CF_3)_2$ overlapping), 128.6 (s, 6-C$^{\mathrm{arom}}$), 128.9 (s, 4-C$^{\mathrm{arom}}$), 134.6 (s, 2,6-$C_6H_3(CF_3)_2$), 135.1 (s, 4-C), 135.5 (s, 6-C), 137.0 (s, 2-C$^{\mathrm{arom}}$), 141.0 (s, *ipso*-C$^{\mathrm{arom}}$), 161.6 (quart, $^1J_{BC}$ = 50.0 Hz, 1-$C_6H_3(CF_3)_2$), 163.5 (s, 1-C), 168.3 ppm (s, 2-C); ^{19}F NMR (470 MHz, −40 °C, CD_2Cl_2): $\delta = -62.55$ ppm; elemental analysis calcd (%) for $C_{66}H_{50}N_4S_2BF_{24}Bi\cdot(CH_2Cl_2)_{0.5}$ (1681.49 g mol^{-1}; obtained by recrystallization from CH_2Cl_2/pentane): C 47.50, H 3.06, N 3.33; found: C 47.44, H 3.03, N 3.18.

Acknowledgements

Funding through the Fonds der Chemischen Industrie and the Deutsche Forschungsgemeinschaft is gratefully acknowledged. C.L. thanks Prof. Holger Braunschweig for continued support. Open access funding enabled and organized by Projekt DEAL.

Conflict of interest

The authors declare no conflict of interest.

Keywords: aminotroponiminates · bismuth · cationic species · redox chemistry · redox-active ligands

[1] a) O. R. Luca, R. H. Crabtree, *Chem. Soc. Rev.* **2013**, *42*, 1440–1459; b) "Redox Non-innocent Ligands: Reactivity and Catalysis": B. de Bruin, P. Gualco, N. D. Paul, in *Ligand Design in Metal Chemistry: Reactivity and Catalysis*, Wiley, Chichester, **2016**, pp. 176—204; c) L. A. Berben, *Chem. Eur. J.* **2015**, *21*, 2734–2742; d) J. Wei, P. L. Diaconescu, *Acc. Chem. Res.* **2019**, *52*, 415–424; e) V. Lyaskovskyy, B. de Bruin, *ACS Catal.* **2012**, *2*, 270–279; f) J. I. van der Vlugt, *Chem. Eur. J.* **2019**, *25*, 2651–2662; g) A. Hanft, C. Lichtenberg, *Eur. J. Inorg. Chem.* **2018**, 3361–3373; h) W. Kaim, *Inorg. Chem.* **2011**, *50*, 9752–9765; i) W. Kaim, *Eur. J. Inorg. Chem.* **2012**, 343–348.

[2] a) M. Vogt, B. de Bruin, H. Berke, M. Trincado, H. Grützmacher, *Chem. Sci.* **2011**, *2*, 723–727; b) C. Lichtenberg, L. Viciu, M. Adelhardt, J. Sutter, K. Meyer, B. de Bruin, H. Grützmacher, *Angew. Chem. Int. Ed.* **2015**, *54*, 5766–5771; *Angew. Chem.* **2015**, *127*, 5858–5863; c) C. Lichtenberg, L. Viciu, M. Vogt, R. E. Rodríguez-Lugo, M. Adelhardt, J. Sutter, M. M. Khusniyarov, K. Meyer, B. de Bruin, E. Bill, H. Grützmacher, *Chem. Commun.* **2015**, *51*, 13890–13893; d) C. Lichtenberg, M. Adelhardt, T. L. Gianetti, K. Meyer, B. de Bruin, H. Grützmacher, *ACS Catal.* **2015**, *5*, 6230–6240.

[3] a) P. J. Chirik, K. Wieghardt, *Science* **2010**, *327*, 794–795; b) M. W. Bouwkamp, A. C. Bowman, E. Lobkovsky, P. J. Chirik, *J. Am. Chem. Soc.* **2006**, *128*, 13340–13341.

[4] a) T. W. Myers, N. Kazem, S. Stoll, R. D. Britt, M. Shanmugam, L. A. Berben, *J. Am. Chem. Soc.* **2011**, *133*, 8662–8672; b) E. Magdzinski, P. Gobbo, M. S. Workentin, P. J. Ragogna, *Inorg. Chem.* **2013**, *52*, 11311–11319.

[5] C. Lichtenberg, *Chem. Eur. J.* **2020**, *26*, 9674–9687.

[6] a) C. Lichtenberg, *Organometallics* **2016**, *35*, 894–902; b) C. Lichtenberg, I. Krummenacher, *Chem. Commun.* **2016**, *52*, 10044–10047; c) A. Hanft, I. Krummenacher, C. Lichtenberg, *Chem. Eur. J.* **2019**, *25*, 11883–11891.

[7] a) C. Helling, S. Schulz, *Eur. J. Inorg. Chem.* **2020**, 3209–3221; b) C. Lichtenberg, *Radical Compounds of Antimony and Bismuth* in *Encyclopedia of Inorganic and Bioinorganic Chemistry*, Wiley, **2020**.

[8] a) O. Planas, F. Wang, M. Leutzsch, J. Cornella, *Science* **2020**, *367*, 313–317; b) F. Wang, O. Planas, J. Cornella, *J. Am. Chem. Soc.* **2019**, *141*, 4235–4240.

[9] a) S. Ishida, F. Hirakawa, K. Furukawa, K. Yoza, T. Iwamoto, *Angew. Chem. Int. Ed.* **2014**, *53*, 11172–11176; *Angew. Chem.* **2014**, *126*, 11354–11358; b) R. J. Schwamm, J. R. Harmer, M. Lein, C. M. Fitchett, S. Granville, M. P. Coles, *Angew. Chem. Int. Ed.* **2015**, *54*, 10630–10633; *Angew. Chem.* **2015**, *127*, 10776–10779; c) C. Ganesamoorthy, C. Helling, C. Wölper, W. Frank, E. Bill, G. E. Cutsail, S. Schulz, *Nat. Commun.* **2018**, *9*, 87; d) C. Lichtenberg, *Angew. Chem. Int. Ed.* **2016**, *55*, 484–486; *Angew. Chem.* **2016**, *128*, 494–496.

[10] a) D. P. Mukhopadhyay, D. Schleier, S. Wirsing, J. Ramler, D. Kaiser, E. Reusch, P. Hemberger, T. Preitschopf, I. Krummenacher, B. Engels, I. Fischer, C. Lichtenberg, *Chem. Sci.* **2020**, *11*, 7562–7568; b) for the investigation of a dinuclear bismuth biradical see: J. Bresien, A. Hinz, A. Schulz, A. Villinger, *Dalton Trans.* **2018**, *47*, 4433–4436.

[11] a) R. J. Schwamm, M. Lein, M. P. Coles, C. M. Fitchett, *Angew. Chem. Int. Ed.* **2016**, *55*, 14798–14801; *Angew. Chem.* **2016**, *128*, 15018–15021; b) R. J. Schwamm, M. Lein, M. P. Coles, C. M. Fitchett, *J. Am. Chem. Soc.* **2017**, *139*, 16490–16493.

[12] a) J. Ramler, I. Krummenacher, C. Lichtenberg, *Angew. Chem. Int. Ed.* **2019**, *58*, 12924–12929; *Angew. Chem.* **2019**, *131*, 13056–13062; b) R. J. Schwamm, M. Lein, M. P. Coles, C. M. Fitchett, *Chem. Commun.* **2018**, *54*, 916–919; c) J. Ramler, I. Krummenacher, C. Lichtenberg, *Chem. Eur. J.* **2020**, *26*, 14551–14555.

[13] a) S. Yamago, E. Kayahara, M. Kotani, B. Ray, Y. Kwak, A. Goto, T. Fukuda, *Angew. Chem. Int. Ed.* **2007**, *46*, 1304–1306; *Angew. Chem.* **2007**, *119*, 1326–1328; b) C. Lichtenberg, F. Pan, T. P. Spaniol, U. Englert, J. Okuda, *Angew. Chem. Int. Ed.* **2012**, *51*, 13011–13015; *Angew. Chem.* **2012**, *124*, 13186–13190.

[14] a) M. Sakagami, T. Sasamori, H. Sakai, Y. Furukawa, N. Tokitoh, *Chem. Asian J.* **2013**, *8*, 690–693; b) A. Hanft, C. Lichtenberg, *Dalton Trans.* **2018**, *47*, 10578–10589.

[15] Z. R. Turner, *Inorg. Chem.* **2019**, *58*, 14212–14227.

[16] C. L. Raston, B. W. Skelton, V.-A. Tolhurst, A. H. White, *J. Chem. Soc. Dalton Trans.* **2000**, 1279–1285.

[17] S. Balasubramaniam, S. Kumar, A. P. Andrews, E. D. Jemmis, A. Venugopal, *Eur. J. Inorg. Chem.* **2020**, 2530–2536.

[18] H. Dengel, C. Lichtenberg, *Chem. Eur. J.* **2016**, *22*, 18465–18475.

[19] A. Hanft, M. Jürgensen, R. Bertermann, C. Lichtenberg, *ChemCatChem* **2018**, *10*, 4018–4027.

[20] An additional weak Bi⋯F contact with an interatomic distance of 3.44 Å is also present in **2**-SbF_6.

[21] a) C. Tschersich, S. Hoof, N. Frank, C. Herwig, C. Limberg, *Inorg. Chem.* **2016**, *55*, 1837–1842; b) S. S. Chitnis, N. Burford, A. Decken, M. J. Ferguson, *Inorg. Chem.* **2013**, *52*, 7242–7248; c) J. Ramler, K. Radacki, J. Abbenseth, C. Lichtenberg, *Dalton Trans.* **2020**, *49*, 9024–9034.

[22] a) B. Ritschel, J. Poater, H. Dengel, F. M. Bickelhaupt, C. Lichtenberg, *Angew. Chem. Int. Ed.* **2018**, *57*, 3825–3829; *Angew. Chem.* **2018**, *130*, 3887–3891; b) B. Ritschel, C. Lichtenberg, *Synlett* **2018**, *29*, 2213–2217.

[23] J. Ramler, J. Poater, F. Hirsch, B. Ritschel, I. Fischer, F. M. Bickelhaupt, C. Lichtenberg, *Chem. Sci.* **2019**, *10*, 4169–4176.

[24] a) S. Balasubramaniam, S. Kumar, A. P. Andrews, B. Varghese, E. D. Jemmis, A. Venugopal, *Eur. J. Inorg. Chem.* **2019**, 3265–3269; b) R. Kannan, S. Balasubramaniam, S. Kumar, R. Chambenahalli, E. D. Jemmis, A. Venugopal, *Chem. Eur. J.* **2020**, *26*, 12717–12721.

[25] a) J. A. Johnson, A. Venugopal, *J. Chem. Sci.* **2019**, *131*, 114; b) R. Kannan, S. Kumar, A. P. Andrews, E. D. Jemmis, A. Venugopal, *Inorg. Chem.* **2017**, *56*, 9391–9395; c) J. Ramler, K. Hofmann, C. Lichtenberg, *Inorg. Chem.* **2020**, *59*, 3367–3376.

[26] J. Ramler, C. Lichtenberg, *Chem. Eur. J.* **2020**, *26*, 10250–10258.

[27] Coordination of $OPEt_3$ or $EPMe_3$ (E = S, Se) to compound **1** would either result in dissociation of one N*i*Pr group (turning one ATI ligand into a monodentate ligand and keeping a coordination number of six for bismuth) or it would lead to a coordination number of seven at bismuth. For examples of neutral molecular bismuth compounds with a coordination number of seven, see: a) J. N. Murphy, F. M. Kerton, L. N. Dawe, *J. Chem. Crystallogr.* **2014**, *44*, 108–114; b) G. A. Bowmaker, F. M. M. Hannaway, P. C. Junk, A. M. Lee, B. W. Skelton, A. H. White, *Aust. J. Chem.* **1998**, *51*, 331–336.

[28] M. A. Beckett, G. C. Strickland, J. R. Holland, K. Sukumar Varma, *Polymer* **1996**, *37*, 4629–4631.

[29] Although compound **2**-rad has two N*i*Pr groups in the apical positions of the bisphenoidal coordination geometry, an isomer with one N*i*Pr and one NPh group in the apical positions (**2**-rad-isom) was found to be only slightly higher in energy ($\Delta H = +3.0$ kcal mol^{-1}; $\Delta G = +3.6$ kcal mol^{-1}) and showed a very similar spin density distribution (for details, see the Supporting Information).

[30] P. C. Hariharan, J. A. Pople, *Theor. Chim. Acta* **1973**, *28*, 213–222.

[31] a) R. Krishnan, J. S. Binkley, R. Seeger, J. A. Pople, *J. Chem. Phys.* **1980**, *72*, 650–654; b) A. D. McLean, G. S. Chandler, *J. Chem. Phys.* **1980**, *72*, 5639–5648.

[32] a) T. H. Dunning, P. J. Hay, in *Modern Theoretical Chemistry, Vol. 3* (Ed.: H. F. Schaefer), Springer, Boston, **1977**, pp. 1–28; b) W. R. Wadt, P. J. Hay, *J. Chem. Phys.* **1985**, *82*, 284–298.

[33] A. D. Becke, *J. Chem. Phys.* **1993**, *98*, 5648–5652.

[34] S. Grimme, J. Antony, S. Ehrlich, H. Krieg, *J. Chem. Phys.* **2010**, *132*, 154104.

Manuscript received: December 3, 2020
Accepted manuscript online: December 16, 2020
Version of record online: ■■ ■■, 0000

XI Synthese und Struktur rückgratsubstituierter Aminotroponimine

1 Ph(O)S–ATI$^{i\mathrm{Pr}/i\mathrm{Pr}}$

1.1 Synthese des Liganden

Der Ligand *N-Iso*propyl-2-(*iso*propylamino)-5-(phenylsulfinyl)iminotroponimin (Ph(O)S–ATI$^{i\mathrm{Pr}/i\mathrm{Pr}}$ (**1-Ph(O)S**)) wurde in Anlehnung an die Literatur in einer dreistufigen Synthese dargestellt (Schema 8).[70] Ausgehend vom ebenfalls literaturbekannten H–ATI$^{i\mathrm{Pr}/i\mathrm{Pr}}$ (**1**)[71] wurde zuerst über eine elektrophile aromatische Substitution ein Brom-Substituent in 5-Position des C_7-Rings eingeführt. Im zweiten Schritt wurde Br–ATI$^{i\mathrm{Pr}/i\mathrm{Pr}}$ (**1-Br**) über eine nukleophile aromatische Substitution zur Thioetherspezies PhS–ATI$^{i\mathrm{Pr}/i\mathrm{Pr}}$ (**1-PhS**) umgesetzt, welche im letzten Schritt mit *meta*-Chlorperbenzoesäure (*m*CPBA) zum gewünschten Liganden **1-Ph(O)S** oxidiert wurde. Für alle Stufen wurden Ausbeuten entsprechend der Literaturausbeuten erhalten.

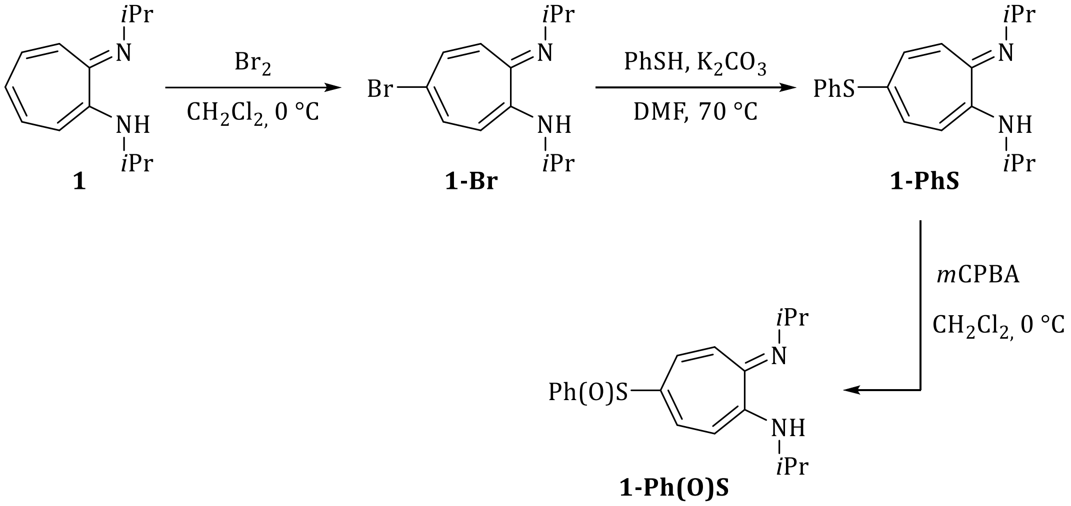

Schema 8: Dreistufige Synthese von Ph(O)S–ATI$^{i\mathrm{Pr}/i\mathrm{Pr}}$ (**1-Ph(O)S**).

2 NO_2–ATI$^{iPr/iPr}$

2.1 Synthese des Liganden

NO_2–ATI$^{iPr/iPr}$ (**1-NO$_2$**) wurde in Anlehnung an die Literatur ausgehend von H–ATI$^{iPr/iPr}$ (**1**) durch Umsetzung mit Nitroniumtetrafluoroborat als Nitrierungsreagenz synthetisiert (Schema 9, unten).[70b] Entsprechend der Literatur konnte eine Ausbeute von 19% erhalten werden. Da eine dünnschichtchromatographische Reaktionskontrolle zeigte, dass unter den in der Literatur beschriebenen Bedingungen kein vollständiger Reaktionsumsatz erreicht wird, wurden verschiedene Reaktionsbedingungen getestet. Eine Verlängerung der Reaktionszeit sowie die erneute Zugabe von 0.5 Äquivalenten NO_2BF_4 nach 16 Stunden führten zu keiner dünnschichtchromatographisch nachweisbaren Umsatzsteigerung und nach Aufarbeitung zu der Literatur entsprechenden Ausbeuten. Um auszuschließen, dass die Stabilität bzw. Reaktivität des Nitrierungsreagenzes unter den gewählten Bedingungen den geringen Umsatz bedingt, wurde die Reaktionstemperatur auf 0 °C bzw. −40 °C verringert, Acetonitril anstatt CH_2Cl_2 als Lösungsmittel verwendet, sowie die Reaktionszeit verkürzt. Allerdings konnte auch unter den veränderten Bedingungen keine Erhöhung des Umsatzes bzw. der Ausbeute erzielt werden. In Anlehnung an die Synthese von **1-PhS** wurde **1-Br** mit Natriumnitrit in *N*,*N*-Dimethylsulfoxid (DMSO) umgesetzt.[70a] Nach einer Reaktionszeit von sieben Tagen bei 100 °C konnte **1-NO$_2$** nach Aufarbeitung und säulenchromatographischer Reinigung in einer Ausbeute von 42% (34% über zwei Stufen) erhalten werden.

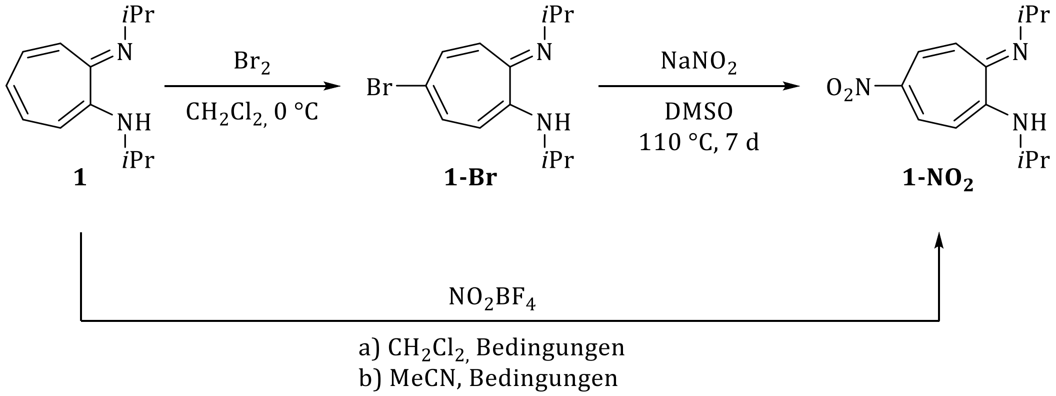

Schema 9: Zweistufige Synthese von NO_2–ATI$^{iPr/iPr}$ (**1-NO$_2$**) (oben), einstufige Synthese von **1-NO$_2$** in a) CH_2Cl_2, RT, 16 h; b) Acetonitril, 0 °C→RT, 16 h oder −40 °C, 1 h→RT, 30 min (unten).

Zur Verbesserung der Ausbeute wurden die Reaktionsbedingungen dieser Syntheseroute variiert (Tabelle 1). In *N*,*N*-Dimethylformamid (DMF) konnte keine Umsetzung zum gewünschten Produkt beobachtet werden (Tabelle 1, I). Die Verwendung von nicht trockenem DMSO als Lösungsmittel führte bei Reaktionen mit 1.05 und fünf Äquivalenten $NaNO_2$ (Tabelle 1, II, III) zu Ausbeuten von

15−16%. Für den äquimolaren Ansatz II konnten 81% des Edukts re-isoliert werden, was auf die geringere Bildung von unerwünschten Nebenprodukten im Vergleich zu Ansatz III (Reisolation von 25% **1-Br**) hindeutet. Die Verwendung von trockenem DMSO sowie eine Reaktionsführung unter Schutzgas lieferte die bestmögliche Ausbeute von 42% (Tabelle 1, V). Allerdings wurden für die Synthese unter diesen Bedingungen schwankende Ausbeuten erhalten. Unter analogen Reaktionsbedingungen wie in Ansatz V konnten in Folgesynthesen lediglich 5−13% **1-NO$_2$** isoliert werden. Eine Verwendung von frisch destilliertem, trocknem DMSO und eine verkürzte Reaktionszeit von fünf Tagen lieferten 29% Ausbeute (Tabelle 1, Ansatz VI).

Tabelle 1: Reaktionsparameter für die Darstellung von **1-NO$_2$**. Wenn nicht anders beschreiben, wurden die Reaktionen unter Argonatmosphäre durchgeführt.

Ansatz	Äq. NaNO$_2$	Lösungsmittel	Reaktionsbedingungen	Ausbeute **1-NO$_2$**	Re-isoliertes **1-Br**	Nebenprodukte
I	1.10	DMF	1) Standardbed. 2 h 2) 115 °C, 1 d	< 5%[a]	> 95%[a]	Nicht isoliert
II	1.05	DMSO	110 °C, 6 d	16%	81%	Nicht isoliert
III	5.00	DMSO	1) 110 °C, 3 d 2) 110 °C, 4 d[b]	15%	25%	Nicht isoliert
IV	1.05	DMSO (trocken)	110 °C, 7 d[b]	26%	9%	Nicht isoliert
V	1.05	DMSO (trocken)	110 °C, 7 d	≤ 42%	≥ 21%	Nicht isoliert
VI	1.05	DMSO (trocken, destilliert)	110 °C, 5 d	29%	36%	Nicht isoliert
VII	1.05	DMSO (trocken)	150 °C, 16 d	< 5%	< 5%	**2**

[a] NMR-spektroskopisch identifiziert, nicht isoliert. [b] Die Reaktion wurde unter Raumluft durchgeführt.

Eine Erhöhung der Reaktionstemperatur auf 150 °C und eine Verlängerung der Reaktionszeit von sieben auf 16 Tage führten lediglich zur Bildung unerwünschter Nebenprodukte (Tabelle 1, VII; Schema 10). Das Nebenprodukt 3,4−Bis(*iso*propylamino)benzaldehyd (**2**) konnte durch säulenchromatographische Reinigung des Rohprodukts isoliert werden. Das nicht literaturbekannte Benzaldehyd-Derivat **2** wurde mit Hilfe von NMR-Spektroskopie, Einkristallröntgenstrukturanalyse sowie über eine Elementaranalyse vollständig charakterisiert.

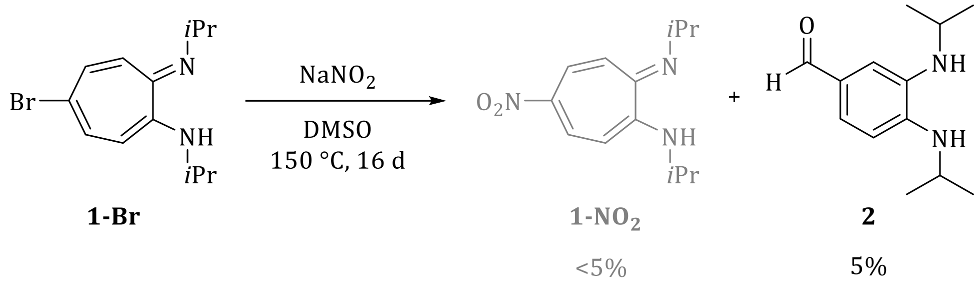

Schema 10: Bildung von 3,4−Bis(*iso*propylamino)benzaldehyd (**2**) als Nebenprodukt.

2 zeigt den zu erwartenden Satz von Resonanzen im ^{1}H- und ^{13}C-NMR Spektrum. Das Signal mit der höchsten chemischen Verschiebung von 9.71 ppm liegt in einem für Aldehyd-Protonen typischen Bereich.[72] Auch das Signal der N*H*-Protonen der beiden Amin-Funktionalitäten bei 4.32 ppm befindet sich im erwarteten Bereich.[72] Für die Bildung von **2** aus **1-Br** wird eine Umlagerung unter Ringverkleinerung vorgeschlagen (Schema 11). Dabei erfolgt zuerst ein nukleophiler Angriff eines Hydroxidions in Nachbarschaft zum Brom-Substituenten. Anschließend wird durch Umlagerung das Norcaradiene-Intermediat **Ncd** gebildet, welches schließlich nach erneuter Umlagerung und Abspaltung eines Bromid Ions als Abgangsgruppe das ringkontrahierte Benzaldehydderivat **2** bildet. Umlagerungen gefolgt von Ringverkleinerungen sind für Halotropon-, -tropolon- und -aminotroponderivate bereits bekannt und werden bei Umsetzungen mit verschiedenen Nukleophilen in Konkurrenz zu Substitutionsreaktionen beobachtet.[73] Eine Umlagerung dieser Art ist für Aminotroponimine dagegen bisher nicht beschrieben worden.

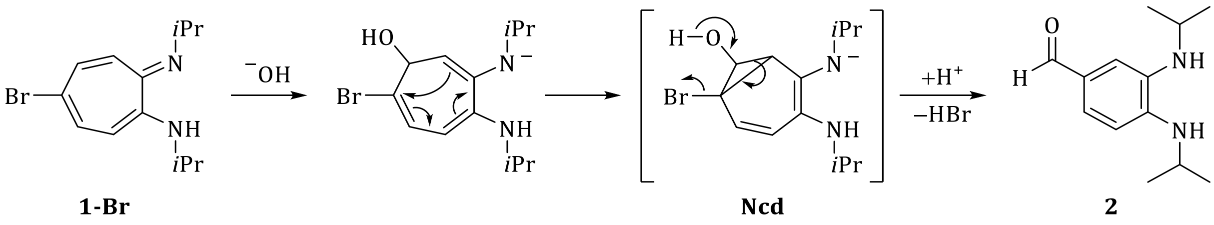

Schema 11: Postulierter Mechanismus zur Bildung von 3,4−Bis(*iso*propylamino)benzaldehyd (**2**) aus **1-Br**.

Das Benzaldehydderivat **2** kristallisiert in der monoklinen Raumgruppe $P2_1/n$ mit $Z = 8$ (Abbildung 1). Die asymmetrische Einheit enthält zwei kristallographisch unabhängige, chemisch identische Formeleinheiten, von welchen nur eine Einheit diskutiert wird. Die C_{Ar}−N Bindungslängen unterscheiden sich geringfügig (1.36 Å bzw. 1.39 Å) und sind im Vergleich zu durchschnittlichen Bindungslängen in Systemen mit einer planaren C_{arom}−NH−C-Substruktur (1.35 Å)[74] leicht verlängert, was auf die direkte Nachbarschaft zweier NH-Funktionalitäten am C_6-Ring und die damit verbundene erhöhte Sterik zurückzuführen ist. Die Alternanz der

C−C Bindungslängen im C_6-Ring deutet auf eine verringerte Delokalisation der Doppel- und Einfachbindungen hin. Die C13−O1 Bindungslänge (1.23 Å) entspricht einer C−O Doppelbindung.

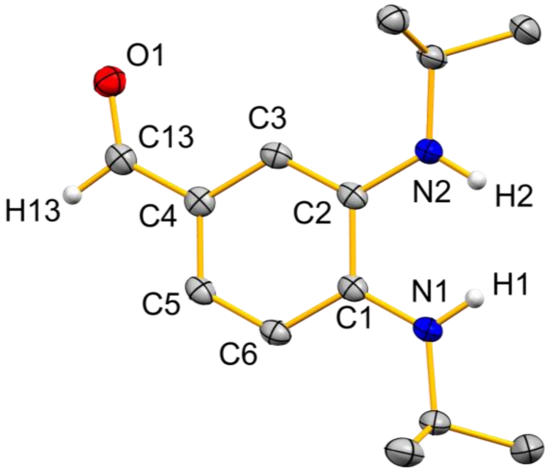

Abbildung 1: Struktur von 3,4−Bis(*iso*propylamino)benzaldehyd (**2**) im Festkörper. Die Ellipsoide repräsentieren 50% der Aufenthaltswahrscheinlichkeit. Wasserstoffatome, außer H13 und die beiden an die Stickstoffatome N1 und N2 gebundenen Wasserstoffatome, wurden aus Gründen der Übersichtlichkeit nicht abgebildet. Ausgewählte Bindungslängen (Å) und -winkel (°): N1−C1, 1.363(2); N2−C2, 1.389(2); C1−C2, 1.445(2); C2−C3, 1.380(2); C3−C4, 1.411(2); C4−C5, 1.393(2); C5−C6, 1.381(2); C1−C6, 1.402(2); C4−C13, 1.437(2); O1−C13, 1.229(2); N1−C1−C2, 119.52(14).

Gründe für die schlechte Reproduzierbarkeit der Synthese von **1-NO₂** ausgehend von **1-Br** konnten nicht weiter eingegrenzt werden. Es wird angenommen, dass sowohl die Reinheit der eingesetzten Bromo-Spezies als auch des verwendeten Lösungsmittels sowie geringe Schwankungen in den Reaktionsbedingungen und der Reaktionsdauer signifikanten Einfluss auf den Umsatz haben.

2.2 Struktur des Liganden

NO_2−ATI$^{iPr/iPr}$ (**1-NO₂**) kristallisiert aus *n*-Pentan in der orthorombischen Raumgruppe *Pbca* (*Z* = 8, Abbildung 2). Die N1/2−C1/2 Bindungen sind mit 1.30 Å bzw. 1.32 Å nur geringfügig kürzer als die analogen Bindungen des im Rückgrat unsubstituierten H−ATI$^{iPr/iPr}$ (**1**) (N1−C1, 1.31 Å; N2−C2, 1.34 Å)[71a] und liegen zwischen typischen N−C Bindungslängen charakteristischer Imin- bzw. Amin-Einheiten (1.28 Å bzw. 1.35 Å).[74] Dies könnte auf eine gesteigerte Delokalisation der π-Elektronen durch den Einfluss der elektronenziehenden Nitro-Gruppe zurückzuführen sein. Mit Bindungslängen von 1.36 Å bis 1.45 Å liegen auch die C−C Bindungen im C_7-Rückgrat zwischen charakteristischen C−C Einfach- und Doppelbindungen. Allerdings ist mit

Bindungslängenunterschieden von Δ_{max}(C–C) = 0.09 Å zweier benachbarter Bindungen eine größere Bindungslängenalternanz als in **1** (Δ_{max}(C–C) = 0.07 Å)[71a] zu beobachten, was auf eine geringere Delokalisation der π-Elektronen bedingt durch den –I- und den –M-Effekt der Nitro-Gruppe hindeutet. Die N3–C5 Bindung liegt mit einer Länge von 1.45 Å im Bereich einer N–C Einfachbindung. Die N3–O Bindungslängen sind im Rahmen der Fehlergrenzen identisch (1.24 Å) und im Vergleich zu Bindungslängen charakteristischer Nitro-Substituenten verlängert (1.22 Å).[74] Ähnlich wie in der Stammverbindung **1** ist der C_7-Ring in **1-NO₂** nahezu planar ([C1–2,N1–2]–[C1–7] = 1.05°). Der Torsionswinkel der Nitro-Gruppe von 8.4(2)° zwischen O2–N3 und C5–C6, sowie der O1–N3–O2 Bindungswinkel (121.5°) liegen in einem ähnlichen Bereich wie analoge Winkel in *para*-substituierten Nitrobenzol-Derivaten.[75]

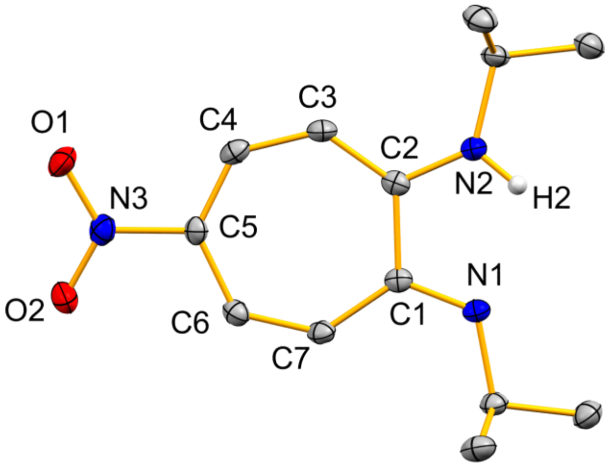

Abbildung 2: Struktur von NO_2–ATI$^{iPr/iPr}$ (**1-NO₂**) im Festkörper. Die Ellipsoide repräsentieren 50% der Aufenthaltswahrscheinlichkeit. Wasserstoffatome, außer das an das Stickstoffatom N2 gebundene Wasserstoffatom, wurden aus Gründen der Übersichtlichkeit nicht abgebildet. Ausgewählte Bindungslängen (Å) und -winkel (°): N1–C1, 1.2960(19); N2–C2, 1.3229(19); O1–N3, 1.2429(17); O2–N3, 1.2402(17); N3–C5, 1.4502(19); C1–C7, 1.448(2); C1–C2, 1.507(2); C2–C3, 1.400(2); C3–C4, 1.385(2); C4–C5, 1.371(2); C5–C6, 1.415(2); C6–C7, 1.357(2); O2–N3–O1, 121.50(13).

XII Synthese und Struktur rückgratsubstituierter Alkalimetall-ATI-Komplexe

1 Alkalimetall-Ph(O)S–ATI$^{i\mathrm{Pr}/i\mathrm{Pr}}$-Komplexe

1.1 Synthese

In Anlehnung an bereits literaturbekannte Syntheserouten wurden die Alkalimetall-Komplexe [Li(Ph(O)S–ATI$^{i\mathrm{Pr}/i\mathrm{Pr}}$)] (**3-Ph(O)S**), [Na(Ph(O)S–ATI$^{i\mathrm{Pr}/i\mathrm{Pr}}$)] (**4-Ph(O)S**) und [K(Ph(O)S–ATI$^{i\mathrm{Pr}/i\mathrm{Pr}}$)] (**5-Ph(O)S**) durch Umsetzung des Liganden Ph(O)S–ATI$^{i\mathrm{Pr}/i\mathrm{Pr}}$ (**1-Ph(O)S**) mit der entsprechenden Metallbase (Trimethylsilylmethyllithium oder Alkalimetall-Hexamethyldisilazid (MHMDS, M = Li, Na, K) dargestellt und in guten Ausbeuten erhalten (Schema 12).[61, 64]

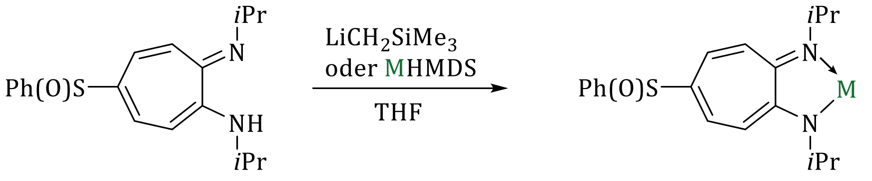

1-Ph(O)S

3-Ph(O)S M = Li 42%[a]
4-Ph(O)S M = Na 74%
5-Ph(O)S M = K 70%

Schema 12: Synthese der Alkalimetall-Aminotroponiminat-Komplexe [Li(Ph(O)S–ATI$^{i\mathrm{Pr}/i\mathrm{Pr}}$)] (**3-Ph(O)S**), [Na(Ph(O)S–ATI$^{i\mathrm{Pr}/i\mathrm{Pr}}$)] (**4-Ph(O)S**) und [K(Ph(O)S–ATI$^{i\mathrm{Pr}/i\mathrm{Pr}}$)] (**5-Ph(O)S**). [a] Spuren von Et_2O (0.05 Äq.) wurden ^{1}H-NMR-spektroskopisch detektiert.

Die ^{1}H- und ^{13}C-NMR-spektroskopische Charakterisierung der Natrium- und Kalium-Komplexe **4-Ph(O)S** und **5-Ph(O)S** deutet auf eine scheinbare C_{2v}-Symmetrie der Verbindungen in Lösung hin. Die Lithium-Verbindung **3-Ph(O)S** dagegen zeigt zwei Dubletts für die CH_3-Gruppen der *Iso*propyl-Reste. Für die CH-Protonen der *Iso*propyl-Reste sowie die Protonen im Ligandrückgrat erhält man für **3-Ph(O)S**, **4-Ph(O)S** und **5-Ph(O)S** Signale, die einer scheinbar C_{2v}-symmetrischen Verbindung entsprechen. Berücksichtigt man, dass das Schwefelatom des Sulfinyl-Rests ein Stereozentrum darstellt, könnte durch die Bildung eines Koordinationspolymers bzw. –oligomers ein Diastereomerengemisch generiert werden. Aufgrund der unterschiedlichen physikalischen und chemischen Eigenschaften könnten für die Diastereomere theoretisch zwei Sätze von Resonanzen mit unterschiedlicher chemischer Verschiebung detektiert werden. Da für **3-Ph(O)S** lediglich die CH_3-Gruppen zwei Signale zeigen, ist die Aufspaltung vermutlich auf eine gehinderte Rotation der *Iso*propyl-Reste um die C–N Bindung zurückzuführen.

1.2 Struktur

Die Struktur von [Li(Ph(O)S–ATI$^{i\mathrm{Pr}/i\mathrm{Pr}}$)] (**3-Ph(O)S**) im Festkörper konnte durch Einkristall-röntgenstrukturanalyse aufgeklärt werden. Geeignete Einkristalle wurden durch langsame Diffusion von *n*-Hexan in eine Lösung von **3-Ph(O)S** in Pyridin erhalten. **[3-Ph(O)S-py]$_\infty$** kristallisiert in der monoklinen Raumgruppe $P2_1/n$ ($Z = 4$, Abbildung 3).

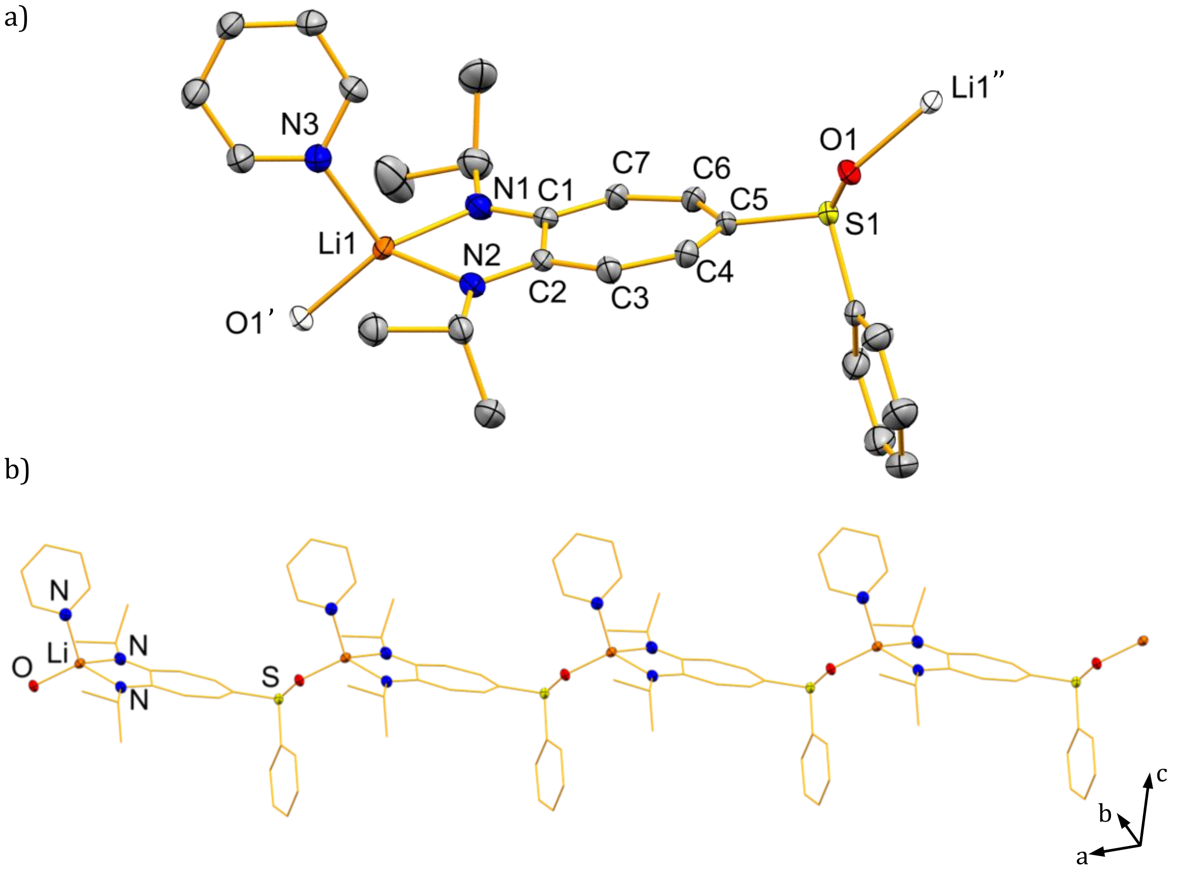

Abbildung 3: a) Ausschnitt der Struktur von [Li(Ph(O)S–ATI$^{i\mathrm{Pr}/i\mathrm{Pr}}$)(py)]$_\infty$ (**[3-Ph(O)S-py]$_\infty$**) im Festkörper. Die Ellipsoide repräsentieren 50% der Aufenthaltswahrscheinlichkeit. Wasserstoffatome wurden aus Gründen der Übersichtlichkeit nicht abgebildet. Atome, die eine Formeleinheit überschreiten, sind als weiße Ellipsoide dargestellt. b) Eindimensionales Koordinationspolymer von **[3-Ph(O)S-py]$_\infty$** im Festkörper. Kohlenstoffatome sind im Drahtmodell dargestellt. Ausgewählte Bindungslängen (Å) und -winkel (°): N1–Li1, 2.025(11); Li1–N2, 2.029(10); Li1–O1‘, 1.955(4); Li1–N3, 2.059(8); N1–C1, 1.256(9); N2–C2, 1.313(7); C1–C2, 1.527(4); C2–C3, 1.441(6); C3–C4, 1.376(4); C4–C5, 1.390(4); C5–C6, 1.391(4); C6–C7, 1.378(3); C1–C7, 1.425(4); N1–Li1–N2, 76.7(3); O1‘–Li1–N1/2, 122.0(5)–131.1(4); O1‘–Li1–N3, 100.6(3); N1/2–Li1–N3, 110.8(5)–115.5(4).

In Übereinstimmung mit dem im Rückgrat unsubstituierten Komplex [Li(ATI$^{i\mathrm{Pr}/i\mathrm{Pr}}$)(thf)$_2$] (**3-(thf)$_2$**)[76] ist das Lithiumatom verzerrt tetraedrisch koordiniert, wobei die Verzerrung auf den kleinen Bisswinkel des ATI-Liganden (N1–Li1–N2, 76.7(3)°) zurückzuführen ist. Im Gegensatz zur

Stammverbindung wird die vierte Koordinationsstelle nicht von einem neutralen Donormolekül abgesättigt, sondern durch das Sauerstoffatom des Sulfinyl-Rests einer benachbarten Monomereinheit (Abbildung 3a). Dies führt zur Ausbildung eines eindimensionalen Koordinationspolymers im Festkörper durch Translation in Richtung der kristallographischen *a*-Achse (Abbildung 3b). Betrachtet man die Li1−N1/2 Bindungslängen (2.03 Å) sind diese im Rahmen der Fehlergrenzen identisch mit jenen der analogen Bindungen in **3-(thf)$_2$** (1.99−2.00 Å).[76] Dies gilt auch für die Li−O Bindungslängen in **[3-Ph(O)S-py]$_\infty$** (1.96 Å) und **3-(thf)$_2$** (1.96−1.97 Å).[76] Die Sulfinyl-Gruppe in **[3-Ph(O)S-py]$_\infty$** und der thf-Ligand im unsubstituierten Komplex weisen somit eine vergleichbare Donorstärke auf. Der Komplex [Li(Ph(O)C−ATI$^{i\mathrm{Pr}/i\mathrm{Pr}}$)(py)]$_\infty$ (**[3-Ph(O)C-py]$_\infty$**) mit einem Benzoyl-Substituenten im Rückgrat, welcher ein analoges Koordinationsverhalten im Festkörper zeigt, besitzt im Vergleich eine geringfügig kürzere Li−O-Bindung (1.91 Å)[77] sowie verlängerte Li−N-Bindungen (2.05−2.07 Å),[77] was auf einen stärkeren Donorcharakter der Benzoyl- im Vergleich zur Sulfinyl-Gruppe hindeutet. Die N−C1/2 und C−C Bindungslängen im ATI-Gerüst von **[3-Ph(O)S-py]$_\infty$** liegen zwischen typischen N/C−C Einfach- und Doppelbindungen und sprechen für eine Delokalisation der π-Elektronendichte über den C$_7$-Ring sowie die beiden Stickstoffatome (N−C, 1.25−1.31 Å, C−C, 1.38−1.44 Å). Dies zeigt sich auch an der nahezu planaren Struktur des ATI-Gerüsts, welche anhand des Winkels zwischen einer Ebene des C$_7$-Rings sowie einer Ebene des C$_2$N$_2$Li-Fünfrings verifiziert wurde ([C1−7]−[C1−2,N1−2,Li], 7.73°). Dagegen ist die Verdrehung aus der Ebene sowie die Lokalisation von π-Elektronen für **[3-Ph(O)C-py]$_\infty$** deutlich gesteigert ([C1−7]−[C1−2,N1−2,Li], 19.6°; Δ_{max}(C−C) = 0.09 Å), was den stärkeren −I- und −M-Effekt der Benzoyl-Gruppe reflektiert.

Durch die Umsetzung des Natrium-Komplexes **4-Ph(O)S** mit zwei Äquivalenten 12-Krone-4 in THF und anschließender Lösungsmitteldiffusion mit *n*-Pentan konnten Einkristalle zur Einkristallröntgenstrukturanalyse gewonnen werden. Entgegen der erwarteten Ausbildung eines monomeren Addukt-Komplexes durch Koordination des Kronenethers an das Natriumatom, kommt es zu einer ligandinduzierten Disproportionierung und der Bildung des Natrium-Natriat-Komplexes [Na(12-Krone-4)$_2$][Na(Ph(O)S−ATI$^{i\mathrm{Pr}/i\mathrm{Pr}}$)$_2$] (**6-Ph(O)S**) (trikline Raumgruppe, $P\bar{1}$, $Z = 2$, Abbildung 4). Ligandinduzierte Disproportionierungen dieser Art konnten bereits für die im Rückgrat unsubstituierte Stammverbindung [Na(ATI$^{i\mathrm{Pr}/i\mathrm{Pr}}$)] sowie [K(ATI$^{i\mathrm{Pr}/i\mathrm{Pr}}$)] und die analogen Natrium und Kalium Verbindungen mit je einem Phenyl- und einem *Iso*propyl-Rest an den Stickstoffatomen des ATI-Liganden beobachtet werden.[63] Der Komplex **6-Ph(O)S** kann als indirekter Strukturbeweis für die Existenz des neutralen Natrium-Komplexes **4-Ph(O)S** gesehen werden.

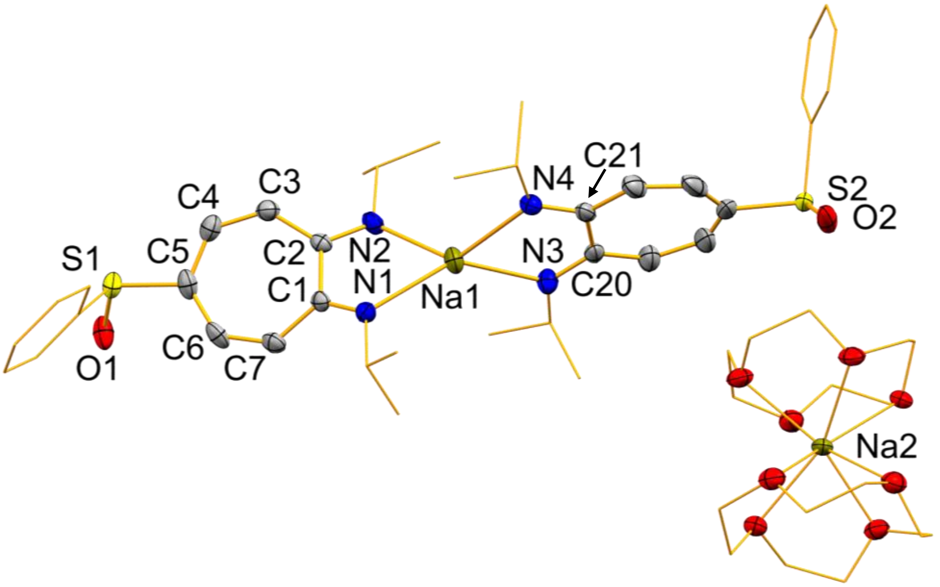

Abbildung 4: Struktur von $[Na(12\text{-Krone-}4)_2][Na(Ph(O)S{-}ATI^{iPr/iPr})_2]$ (**6-Ph(O)S**) im Festkörper. Die Ellipsoide repräsentieren 50% der Aufenthaltswahrscheinlichkeit. Wasserstoffatome wurden aus Gründen der Übersichtlichkeit nicht abgebildet. Die Kohlenstoffatome der *Iso*propyl-Reste sowie die Phenyl-Gruppen der Sulfinyl-Reste und die Ethyleneinheiten der Kronenethermoleküle wurden im Drahtmodell dargestellt. Ausgewählte Bindungslängen (Å) und -winkel (°): Na1–N1, 2.408(3); Na1–N2, 2.356(3); Na1–N3, 2.380(3); Na1–N4, 2.379(3); N1–C1, 1.301(4); N2–C2, 1.303(4); N3–C20, 1.300(4); N4–C21, 1.307(4); C1– C2, 1.515(4); C2–C3, 1.442(4); C3–C4, 1.373(4); C4–C5, 1.387(5); C6–C5, 1.388(5); C6–C7, 1.374(4); C1–C7, 1.450(4); N–Na1–N (chelatisierend), 66.64(9)–69.16(8); N–Na1–N (nicht chelatisierend), 125.56(10)–141.66(10).

Analog zur im Rückgrat unsubstituierten Stammverbindung $[Na(12\text{-Krone-}4)_2][Na(ATI^{iPr/iPr})_2]$ wird Na2 durch zwei Kronenether-Moleküle koordiniert und bildet das Komplex-Kation, welches keine gerichtete Bindungswechselwirkung zum Komplex-Anion eingeht. Das Natriumatom Na1 im $[Na(Ph(O)S{-}ATI^{iPr/iPr})_2]^-$-Fragment ist aufgrund der κ^2N-Koordination zweier ATI-Liganden verzerrt tetraedrisch koordiniert, wobei die Verzerrung durch den kleinen Bisswinkel des ATI-Liganden bedingt ist (N–Na1–N, 66.6–69.2°). Die Na1–N Bindungslängen zu den beiden ATI-Liganden unterscheiden sich geringfügig (Na1–N1/2, 2.36–2.41 Å; Na1–N3/4, 2.38 Å), was vermutlich auf sterische Effekte zurückgeführt werden kann.

Lagerung einer Lösung von Komplex **5-Ph(O)S** in THF/*n*-Pentan (2:1) bei −30 °C lieferte Einkristalle, welche einkristallröntgenstrukturanalytisch untersucht werden konnten. **$[5\text{-Ph(O)S-(thf)}_3]_\infty$** kristallisiert in der monoklinen Raumgruppe $P2_1/c$ ($Z = 4$, Abbildung 5). Ähnlich wie im analogen Lithium-Komplex **$[3\text{-Ph(O)S-py}]_\infty$** ist die Koordinationssphäre des Metall-Atoms durch die κ^2N-Koordination eines ATI-Liganden, eine κ^1O-Koordination des Sauerstoffatoms des Sulfinyl-Restes einer benachbarten ATI-Einheit, sowie durch Koordination dreier thf-Liganden abgesättigt. Es ergibt sich somit ein μ_2-(M-κ^2*N*)-(M‘-κ^1*O*)-Koordinationsmodus in welchem das Kaliumatom verzerrt oktaedrisch umgeben ist (Abbildung 5a). Die Verzerrung ist hierbei wiederum auf den kleinen Bisswinkel des ATI-Liganden zurückzuführen (N1–K1–N2, 58.43°; O(1‘/3)–K1–N1/2, 101.7–165.1°; O2–K1–O4, 169.12°). Die Wechselwirkung des Metall-Atoms mit dem Sauerstoffatom einer benachbarten Formeleinheit führt zur Ausbildung eines eindimensionalen Koordinationspolymers im Festkörper, welches sich durch Translation entlang der kristallographischen *b*-Achse ausbreitet (Abbildung 5b).

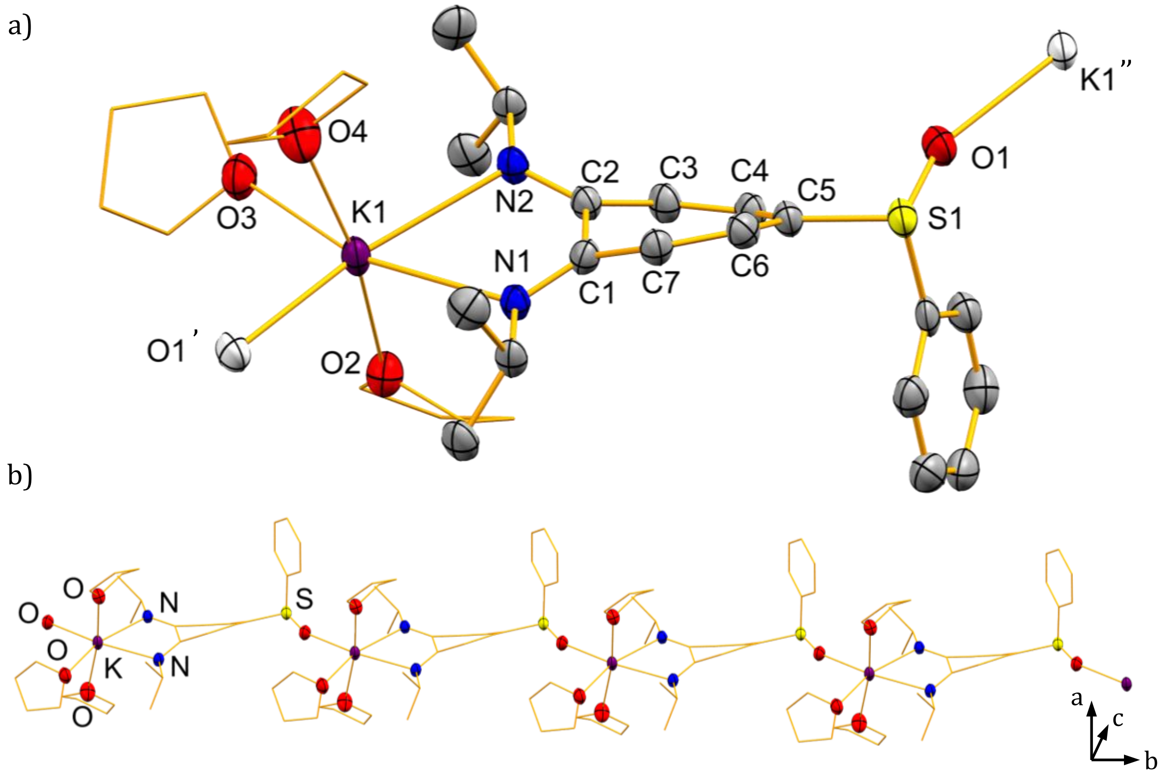

Abbildung 5: a) Ausschnitt der Struktur von [K(Ph(O)S–ATI$^{iPr/iPr}$)(thf)$_3$]$_\infty$ (**[5-Ph(O)S-(thf)$_3$]$_\infty$**) im Festkörper. Die Ellipsoide repräsentieren 50% der Aufenthaltswahrscheinlichkeit. Wasserstoffatome wurden aus Gründen der Übersichtlichkeit nicht abgebildet. Die Kohlenstoffatome der thf-Liganden wurden Drahtmodell dargestellt. Atome, die eine Formeleinheit überschreiten, sind als weiße Ellipsoide dargestellt. b) Eindimensionales Koordinationspolymer von **[5-Ph(O)S-(thf)$_3$]$_\infty$** im Festkörper, wobei Kohlenstoffatome im Drahtmodell dargestellt sind. Ausgewählte Bindungslängen (Å) und -winkel (°): K1–O1‘, 2.637(3); K1–O2, 2.727(3); K1–O3, 2.759(3); K1–O4, 2.682(3); K1–N1, 2.807(3); K1–N2, 2.843(3); N1–C1, 1.291(4); N2–C2, 1.295(4); C1–C2, 1.518(4); C2–C3, 1.456(4); C3–C4, 1.367(4); C4–C5, 1.399(4); C5–C6, 1.400(4); C6–C7, 1.369(4); C1–C7, 1.456(4); N1–K1–N2, 58.43(8); O(1‘–4)–K1–O(1‘–4), 83.10(8)–93.21(7); O2–K1–O4, 169.17(8); O(1‘/3)–K1–N1/2, 101.72(8)–165.05(7); O(2/4)–K1–N1/2, 90.12(7)–100.70(8).

Die K1–N Bindungslängen (K1–N1, 2.807(3) Å; K1–N2, 2.843(3) Å) unterscheiden sich um 0.02 Å und auch die K1–O Bindungslängen bewegen sich mit 2.64 Å bis 2.76 Å in unterschiedlichen

Bereichen. In Übereinstimmung mit dem größeren *trans*-Einfluss der Sulfinyl-Gruppe im Vergleich zu einem thf-Liganden ist die K1−N1 Bindung kürzer als die K1−N2 Bindung und entsprechend die K1−O3 Bindung zum thf-Liganden länger als die K1−O1' Bindung zum Sulfinyl-Rest (K1−O1', 2.637(3) Å; K1−O3, 2.759(3) Å). Die im Rückgrat unsubstituierte Stammverbindung [K(ATI$^{iPr/iPr}$)(thf)]$_\infty$ (**[5-thf]$_\infty$**), welche ebenfalls als thf-Addukt kristallisiert, zeigt zusätzlich zur Koordination eines thf-Liganden eine Metall-Aren-Wechselwirkung in Form einer Koordination des Kaliumatoms an das C$_7$-Rückgrat einer benachbarten Monomereinheit.[63] In **[5-Ph(O)S-(thf)$_3$]$_\infty$** wird keine Wechselwirkung dieser Art beobachtet, was durch die höhere Donorstärke der Sulfinyl-Gruppe in Konkurrenz zur schwächeren Kation-π-Wechselwirkung bedingt ist. Zudem sollte der elektronenziehende Effekt der Sulfinyl-Gruppe im Vergleich zum unsbustituierten Komplex zu einer verringerten π-Elektronendichte im C$_7$-Rückgrat führen. Die Tendenz zur Ausbildung einer Kation-π-Wechselwirkung wird somit zusätzlich verringert. Im Vergleich zum Lithium-Komplex **[3-Ph(O)S-py]$_\infty$** zeigt **[5-Ph(O)S-(thf)$_3$]$_\infty$** eine deutliche Verdrehung der C$_7$N$_2$-Einheit aus der Ebene ([C1−7]−[C1−2,N1−2,M]: **[3-Ph(O)S-py]$_\infty$**, 7.73°; **[5-Ph(O)S-(thf)$_3$]$_\infty$**, 33.3°). Diese liegt in einem ähnlichen Bereich wie die für den Benzoyl-substituierten Komplex **[5-Ph(O)C-py]$_\infty$** gefundene Abwinkelung ([C1−7]−[C1−2,N1−2,M]: 27.9−35.0°).[77] Der Benzoyl-Komplex **[5-Ph(O)C-py]$_\infty$** zeigt allerdings aufgrund der Koordination des Kaliumatoms an die Sauerstoffatome zweier weiterer Monomereinheiten eine maschendrahtartige zweidimensionale Polymerstruktur im Festkörper. Im Vergleich zu literaturbekannten (Halb-)Metall-ATI-Komplexen, deren Winkel zwischen den Ebenen [C1−C7] und [C1−2,N1−2,M] sich im Bereich von 0° bis 23° befinden, besitzt **[5-Ph(O)S-(thf)$_3$]$_\infty$** somit eine deutlich größere Verdrehung aus der Ebene.[65, 78] Dies ist vermutlich auf den Einfluss des Rückgartsubstituenten auf die elektronische Struktur des Liganden zurückzuführen.

2 Alkalimetall-NO$_2$–ATI$^{iPr/iPr}$-Komplexe

2.1 Synthese

Ausgehend von **1-NO$_2$** wurden, in Anlehnung an die in Kapitel XII, 1.1 beschriebenen und literaturbekannten Syntheserouten, die Alkalimetall-Komplexe [Li(NO$_2$–ATI$^{iPr/iPr}$)] (**3-NO$_2$**), [Na(NO$_2$–ATI$^{iPr/iPr}$)] (**4-NO$_2$**) und [K(NO$_2$–ATI$^{iPr/iPr}$)] (**5-NO$_2$**) dargestellt (Abbildung 6). Dabei erwiesen sich die Komplexe der höheren Homologen Natrium und Kalium als schwer löslich in THF. Rückstände von Pentan und Donorsolvenzien wie THF und Et$_2$O konnten auch nach mehreren Stunden Trocknungszeit im Vakuum nicht vollständig entfernt werden.

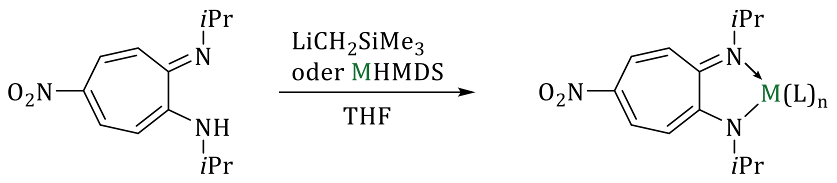

1-NO$_2$

3-NO$_2$ M = Li 72%[a]
4-NO$_2$ M = Na L = thf, Et$_2$O n = 0.06 79%
5-NO$_2$ M = K 75%[a]

Abbildung 6: Synthese der Alkalimetall-Aminotroponiminat-Komplexe [Li(NO$_2$–ATI$^{iPr/iPr}$)] (**3-NO$_2$**), [Na(NO$_2$–ATI$^{iPr/iPr}$)] (**4-NO$_2$**) und [K(NO$_2$–ATI$^{iPr/iPr}$)] (**5-NO$_2$**). [a] Spuren von Pentan (**3-NO$_2$** = 0.3 Äq., **5-NO$_2$** = 0.2 Äq.) wurden ^{1}H-NMR-spektroskopisch detektiert.

Die ^{1}H- und ^{13}C-NMR-spektroskopische Charakterisierung des Lithium-Komplexes **3-NO$_2$** zeigt einen Satz an Signalen für die Protonen des Liganden, der mit einem C_{2v}-symmetrischen Molekül in Lösung in Einklang ist. Im ^{1}H-NMR-Spektrum der Natrium- und Kalium-Komplexe wird direkt nach dem Lösen in Pyridin-d_5 ebenfalls eine C_{2v}-symmetrische Verbindung beobachtet. Nach einigen Stunden in Lösung wird ein weiter Signalsatz detektiert, der separate Signale für alle Protonen zeigt und somit C_1-symmetrischen Verbindungen zugeordnet werden kann. ^{15}N-NMR-spektroskopische Messungen einer Lösung von **5-NO$_2$** in Pyridin-d_5 zeigen Signale bei $\delta = -53.9$ ppm für die Stickstoffatome der C_{2v}-symmetrischen Verbindung, sowie Signale bei $\delta = -41.2$ ppm und $\delta = -32.6$ ppm für die C_1-symmetrische Verbindung. Die drei Signale liegen in einem typischen Bereich für Imino-Gruppen,[79] was auf eine Verschiebung der π-Elektronen in Richtung der Nitro-Gruppe schließen lässt (Schema 13). Geht man davon aus, dass die Verbindungen in Lösung als solvatisierte, monomere Komplexe vorliegen, besitzt der ATI-Ligand mehrerer mögliche Koordinationsstellen für Metall-Atome. Formal wäre neben der Koordination an die *N,N*-Bindungstasche auch eine Koordination an ein bzw. beide Sauerstoffatome der Nitro-Gruppe denkbar. Somit ergeben sich für die ATI-Komplexe zwei mögliche Isomere, in welchen das Metall-Atom entweder an die ATI-Bindungstasche (**N-*E,E***) oder an den Rückgratsubstituenten (**O-*E,E***) koordiniert, wobei die beiden stickstoffgebundenen *Iso*propyl-Gruppen jeweils entgegengesetzt zueinander (*E*,*E*) orientiert sind (Schema 13, links und Mitte). Zusätzlich ist für einen Komplex mit einem über die NO_2-Gruppe koordinierten Metall-Atom ein weiteres Isomer möglich, in welchem die *Iso*propyl-Reste an den Stickstoffatomen eine *E*,*Z*-Konfiguration zeigen (**O-*E,Z***) (Schema 13, rechts). Letzteres wäre im Einklang mit den im ^1H-NMR-Spektrum beobachteten Signalen für eine C_1-symmetrische Verbindung.

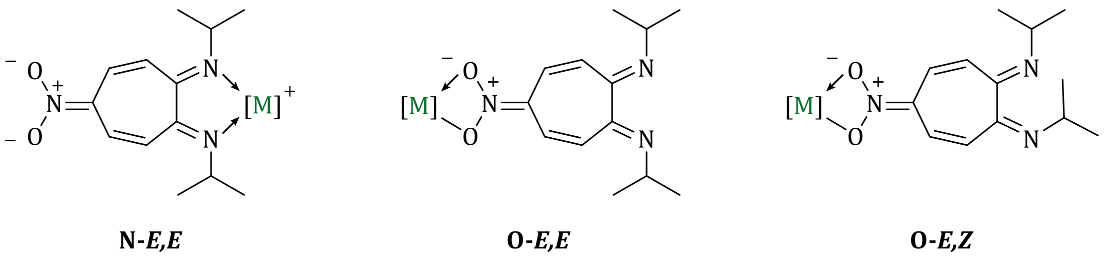

Schema 13: Schematische Darstellung möglicher Isomere der Alkalimetall-ATI-Komplexe mit Nitrofunktionalität. [M] = Li, Na, K.

Nach drei Tagen bei Raumtemperatur in Lösung stellt sich für **4-NO₂** ein Gleichgewicht zwischen den beiden beobachteten Spezies von 1.0:1.5 von C_{2v}-symmetrischem (**N-*E,E*** oder **O-*E,E***) zu C_1-symmetrischem (**O-*E,Z***) Isomer ein. Versuche, eine Isomerisierung in Lösung durch Erhitzen der Verbindung auf 60 °C bzw. 80 °C über vier bis sieben Tage thermisch zu induzieren, führte zu keiner signifikanten Änderung des Isomerenverhältnisses und nach mehreren Tagen bei 80 °C lediglich zu zunehmender Zersetzung der Verbindung zu protoniertem Liganden **1-NO₂**. Die ^1H-NMR-spektroskopische Verfolgung der Umsetzung von **1-NO₂** mit KHMDS zum entprechendne Kalium-Komplex zeigt nach vollständigem Umsatz des Liganden ein Verhältnis von 1.0:1.0 von **N-*E,E*/O-*E,E***- zu **O-*E,Z***-Isomer. Nach drei Tagen bei Raumtemperatur in Lösung verschiebt sich dieses Verhältnis auf 1.0:1.6. Zudem war ein kristalliner Feststoff ausgefallen, welcher röntgendiffraktometrisch als Polymer **[5-NO₂-py]$_\infty$** mit einer *E*,*E*-Konfiguration identifiziert werden konnte (siehe Kapitel XII 2.2). Das Heizen einer Probe auf 60 °C für zwei Tage führte zu einem Verhältnis von 1.0:2.0 von **N-*E,E*/O-*E,E***- zu **O-*E,Z***-Isomer. Eine VT-NMR-spektroskopische Untersuchung von **5-NO₂** in Pyridin-d_5 mit einem Isomerenverhältnis von 1.0:2.6 zu Beginn der Messung zeigte über einen Temperaturbereich von −40 °C bis +40 °C keine Änderung dieses Verhältnisses. Im Bereich von +40 °C bis +70 °C kann eine Verschiebung des Verhältnisses auf 1.0:2.0 beobachtet werden. Dabei können sowohl thermodynamische Effekte eine Rolle spielen als auch eine Verbesserung der Löslichkeit des kristallinen Feststoffes, die mit einer Erhöhung des Gehalts an *E*,*E*-Isomer einhergehen sollte. Um ausschließen zu können, dass eine Bildung von Monomer/Polymergemischen der Grund für die beobachteten Signalaufspaltungen ist, wurde für **5-NO₂** ein ^1H-^1H-DOSY-NMR-Spektrum aufgenommen. Die ermittelten Diffusionskoeffizienten von $4.14 \cdot 10^{-10}\ m^2 \cdot s^{-1}$ für die C_{2v}-symmetrische und $4.34 \cdot 10^{-10}\ m^2 \cdot s^{-1}$ für die C_1-symmetrische

Verbindung zeigen, dass es sich in Lösung um Verbindungen mit sehr ähnlicher bis identischer Molmasse handelt. Dies unterstützt die Annahme einer *E*,*E*-/*E*,*Z*-Isomerisierung.

Da sowohl der Natrium- als auch der Kalium-Komplex in polaren Lösungsmitteln wie THF und Pyridin schwer löslich ist, wurde versucht, die Löslichkeitseigenschaften durch Komplexierung mit neutralen Donorliganden in Form von Kronenethern zu verbessern. Dazu wurde **4-NO₂** mit zwei Äquivalenten 12-Krone-4 bzw. einem Äquivalent 15-Krone-5 in THF umgesetzt. Dies führte nach einer Stunde zu einer vollständigen Lösung aller zuvor festen Bestandteile in THF. Somit kann die Bildung der entsprechenden Kronenether-Komplexe $[Na(12\text{-Krone-}4)_2][NO_2{-}ATI^{iPr/iPr}]$ (**4-NO₂-(12K4)₂**) und $[Na(15\text{-Krone-}5)(NO_2{-}ATI^{iPr/iPr})]$ (**4-NO₂-(15K5)**) angenommen werden. Analog wurde **5-NO₂** mit 18-Krone-6 umgesetzt und ebenfalls eine vollständige Lösung in THF nach Bildung des Kronenether-Komplexes $[K(18\text{-Krone-}6)(NO_2{-}ATI^{iPr/iPr})]$ (**5-NO₂-(18K6)**) beobachtet (Schema 14). Alle Kronenether-Komplexe zeigen, wie ihre Stammverbindungen, zwei Signalsätze in den ^{1}H- und ^{13}C-NMR-Spektren, die *E*,*E*- und *E*,*Z*-Isomeren zugeordnet werden können. Die chemische Verschiebung der ^{15}N-NMR-Signale von **4-NO₂-(15K5)**, welche mit Hilfe von 2D ^{1}H-^{15}N-HMBC-NMR-Spektroskopie zugeordnet werden konnten, deutet wiederum auf das Vorhandensein von zwei Imino-Gruppen hin (*E*,*E*-Isomer: $\delta = -63.2$ ppm, *E*,*Z*-Isomer: $\delta = -51.0$ ppm, -42.3 ppm). Außerdem konnten die Signale der Nitro-Gruppe bei $\delta = -25.6$ (*E*,*E*-Isomer) bzw. -31.6 ppm (*E*,*Z*-Isomer) detektiert werden.

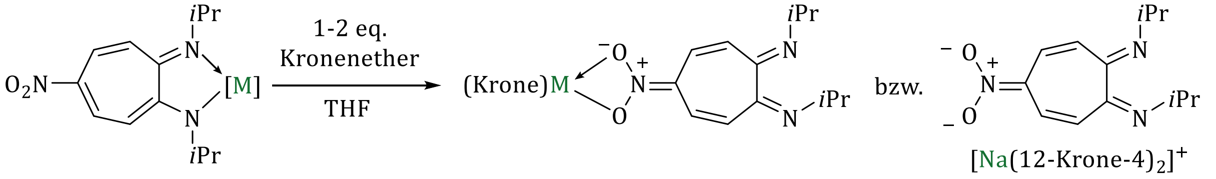

4-NO₂ M = Na
5-NO₂ M = K

4-NO₂-(15K5) M = Na 85%[a]
5-NO₂-(18K6) M = K 83%[a]

4-NO₂-(12K4)₂ 90%[a]

Schema 14: Synthese der Kronenether-Komplexe Komplexe $[Na(12\text{-Krone-}4)_2][NO_2{-}ATI^{iPr/iPr}]$ (**4-NO₂-(12K4)₂**), $[Na(15\text{-Krone-}5)(NO_2{-}ATI^{iPr/iPr})]$ (**4-NO₂-(15K5)**) und $[K(18\text{-Krone-}6)(NO_2{-}ATI^{iPr/iPr})]$ (**5-NO₂-(18K6)**). [a] Spuren von Lösungsmittel (**4-NO₂-(12K4)₂** = 0.05 Äq. THF, **4-NO₂-(15K5)** = 0.2 Äq. Pentan, **5-NO₂-(18K6)** = 0.2 Äq. THF) wurden ^{1}H-NMR-spektroskopisch detektiert.

Aus sterischen Gründen würde man für **4-NO₂-(15K5)** eine Koordination der $[Na(15\text{-Krone-}5)]^{+}$-Einheit über die Nitro-Gruppe erwarten. Für **O-*E*,*E*-** bzw. **O-*E*,*Z*-**Isomere sollten aufgrund der räumlichen Nähe Kreuzsignale zwischen den Protonen der Ethyleneinheiten des Kronenethers und den Protonen an C4- und C6-Position des ATI-Rückgrats im ^{1}H-^{1}H-NOESY-NMR-Spektrum zu beobachten sein. Zusätzlich zu den erwarteten Signalen werden für **4-NO₂-(15K5)** allerdings auch Kreuzsignale des Kronenethers zu den CH_3-Gruppen der *Iso*propyl-Reste im

^{1}H-^{1}H-NOESY-NMR-Spektrum detektiert. Dies lässt auf eine Migration des kronenether-komplexierten Metall-Atoms von der Nitro-Gruppe in Richtung der *N*,*N*-Bindungstasche schließen. Es wird eine halbsandwichartige Koordination der [Na(15-Krone-5)]$^+$-Einheit an das ATI-Rückgrat vorgeschlagen (Schema 15 und Kapitel XII 2.3). Diese Migration kann auf der Zeitskala des NMR-Experiments nicht aufgelöst werden.

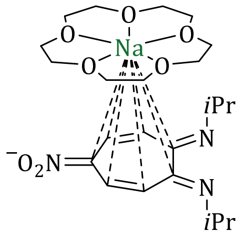

Schema 15: Mögliche halbsandwichartige Struktur von **4-NO$_2$-(15K5)** in Pyridin-*d*$_5$.

2.2 Struktur

Die Struktur der Alkalimetall-Komplexe $[Li(NO_2{-}ATI^{iPr/iPr})(py)]_\infty$ (**$[3\text{-}NO_2\text{-}py]_\infty$**), $[Na(NO_2{-}ATI^{iPr/iPr})(py)]_\infty$ (**$[4\text{-}NO_2\text{-}py]_\infty$**) und $[K(NO_2{-}ATI^{iPr/iPr})(py)]_\infty$ (**$[5\text{-}NO_2\text{-}py]_\infty$**) im Festkörper konnte mit Hilfe von Einkristallröntgenstrukturanalyse aufgeklärt werden. Alle Verbindungen wurden aus Pyridin/*n*-Pentan Lösungsmittel-Systemen kristallisiert.

$[3\text{-}NO_2\text{-}py]_\infty$ kristallisiert in der monoklinen Raumgruppe $P2_1/c$ mit $Z = 4$ (Abbildung 7). Das Lithiumatom ist aufgrund der Koordination eines ATI-Liganden über die *N*,*N*-Bindungstasche, eines Pyridin-Moleküls sowie die Koordination an die beiden Sauerstoffatome der Nitro-Gruppe einer benachbarten Moleküleinheit verzerrt trigonal bipyramidal koordiniert ($\tau = 0.63$, mit N1 und O1' in axialen Positionen, Abbildung 7a). Die Verzerrung ist dabei auf den kleinen Bisswinkel des ATI-Liganden (N1−Li1−N2, 78.9°) und der Nitro-Gruppe (O1'−Li1−O2', 62.1°), sowie die Verdrehung des C_2N_2Li-Fünfrings zum NO_2Li-Vierring, welcher durch die Koordination an die Nitro-Gruppe aufgespannt wird, zurückzuführen ($[C_2N_2Li]-[NO_2Li] = 45.8°$). Die Koordination an den Rückgartsubstituenten führt, wie bereits für die Sulfinyl-substituierte Verbindung **$[3\text{-}Ph(O)S\text{-}py]_\infty$** beobachtet (siehe Abbildung 3), zur Ausbildung eines eindimensionalen Koordinationspolymers im Festkörper, welches sich entlang einer 2_1-Schraubenachse in Richtung der kristallographischen *b*-Achse ausbreitet (Abbildung 7b). Es ergibt sich somit ein μ_2-(M-κ^2*N*)-(M'-κ^2*O*)-Koordinationsmodus. Die Li1−N Bindungslängen sowohl zum ATI-Liganden (2.07−2.10 Å) als auch zum Pyridin-Liganden (2.12 Å) sind im Vergleich zu **$[3\text{-}Ph(O)S\text{-}py]_\infty$** (Li−N = 2.03−2.06 Å) länger, was auf die erhöhte Koordinationszahl des Lithiumatoms zurückgeführt werden kann (**$[3\text{-}Ph(O)S\text{-}py]_\infty$** KZ = 4, **$[3\text{-}NO_2\text{-}py]_\infty$** KZ = 5). Die N1/2−C1/2 Bindungslängen sind im Rahmen der Fehlergrenzen identisch (1.29 Å) und liegen im Bereich von C−N Doppelbindungen von an Aromaten gebundenen Imino-Gruppen.[74] Die N3−C5 Bindung ist mit 1.37 Å deutlich kürzer als im unmetallierten Liganden **$1\text{-}NO_2$** (1.45 Å) und kürzer als typische N−C-Bindungslängen von nitro-substituierten Aromaten.[74] Betrachtet man die C−C Bindungslängen im ATI-Rückgrat, liegen diese zwischen typischen Bindungslängen für C−C Einfach- und Doppelbindungen. Es kann allerdings eine höhere Bindungslängenalternanz als in **$1\text{-}NO_2$** mit einer maximalen Differenz von $\Delta_{max}(C{-}C) = 0.11$ Å zweier benachbarter C−C Bindungen festgestellt werden (**$1\text{-}NO_2$**: $\Delta_{max}(C{-}C) = 0.09$ Å). Die bereits aufgrund der NMR-spektroskopischen Daten vermutete Verschiebung der π-Elektronendichte in Richtung der elektronenziehenden Nitro-Gruppe kann auch im Festkörper bestätigt werden.

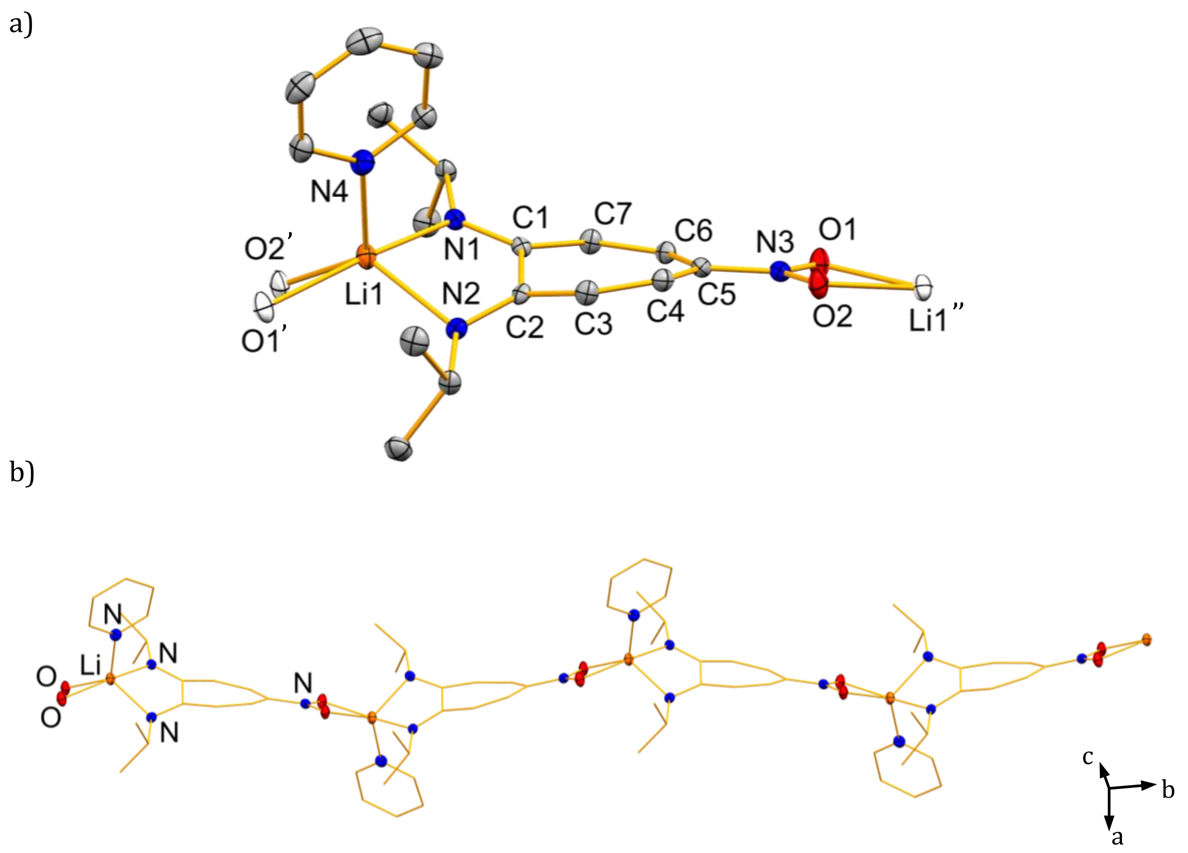

Abbildung 7: a) Ausschnitt der Struktur von [Li(NO$_2$–ATI$^{iPr/iPr}$)(py)]$_\infty$ (**[3-NO$_2$-py]$_\infty$**) im Festkörper. Die Ellipsoide repräsentieren 50% der Aufenthaltswahrscheinlichkeit. Wasserstoffatome sowie zwei in der Elementarzelle enthaltene Pyridin-Moleküle wurden aus Gründen der Übersichtlichkeit nicht abgebildet. Atome, die eine Formeleinheit überschreiten, sind als weiße Ellipsoide dargestellt. b) Eindimensionales Koordinationspolymer von **[3-NO$_2$-py]$_\infty$** im Festkörper, wobei Kohlenstoffatome im Drahtmodell dargestellt sind. Ausgewählte Bindungslängen (Å) und -winkel (°): Li1–N1, 2.067(3); Li1–N2, 2.103(3); Li1–O1‘, 2.104(3); Li1–O2‘, 2.113(3); Li1–N4, 2.123(3); C1–N1, 1.2889(18); C2–N2, 1.2908(18); O1–N3, 1.2783(16); O2–N3, 1.2797(16); N3–C5, 1.3669(19); C1–C7, 1.457(2); C1–C2, 1.519(2); C2–C3, 1.460(2); C3–C4, 1.349(2); C4–C5, 1.430(2); C5–C6, 1.425(2); C6–C7, 1.351(2); N1–Li1–N2, 78.92(10); O1–N3–O2, 116.57(12); O1‘–Li1–O2‘, 62.12(8); N1–Li1–N4, 99.72(11); N2–Li1–N4, 106.70(12); N(1–2, 4)–Li1–O(1–2)‘, 94.18(10)–163.36(14).

Ähnlich wie in den sulfinyl-substituierten Komplexen zeigt das ATI-Rückgrat eine deutliche Verdrehung aus der Ebene. Mit einem Winkel von 23.3° zwischen der Ebene des C$_7$-Rings und der des C$_2$N$_2$Li-Fünfrings ist die Abwinkelung noch deutlich höher als für die Sulfinyl- und Benzoyl-Spezies ([C1−7]−[C1−2,N1−2,M]: **[3-Ph(O)S-py]$_\infty$**, 7.73°; **[3-Ph(O)C-py]$_\infty$**, 19.6°), was auf eine Abnahme der Aromatizität aufgrund des zunehmenden –I- und –M-Effekts der Nitro-Gruppe hindeutet. Die Nitro-Gruppe zeigt einen Torsionswinkel von 1.6(2)° zwischen C6–C5 und N3–O1 und ist damit weniger verdreht als im unmetallierten Liganden. Dies ist im Einklang mit einem erhöhten N–C Mehrfachbindungsanteil in **[3-NO$_2$-py]$_\infty$** im Vergleich zu **1-NO$_2$**.

[4-NO$_2$-py]$_\infty$ kristallisiert in der monoklinen Raumgruppe $P2_1/c$ mit $Z = 8$ (Abbildung 8). Die asymmetrische Einheit enthält zwei kristallographisch unabhängige, chemisch identische Formeleinheiten, von welchen nur eine Einheit diskutiert wird. Analog zum Lithium-Komplex **[3-NO$_2$-py]$_\infty$** wird ein μ_2-(M-κ^2N)-(M‘-κ^2O)-Koordinationsmodus beobachtet, in welchem sich das eindimensionale Koordinationspolymer entlang einer 2_1-Schraubenachse in Richtung der kristallographischen *b*-Achse ausbreitet.

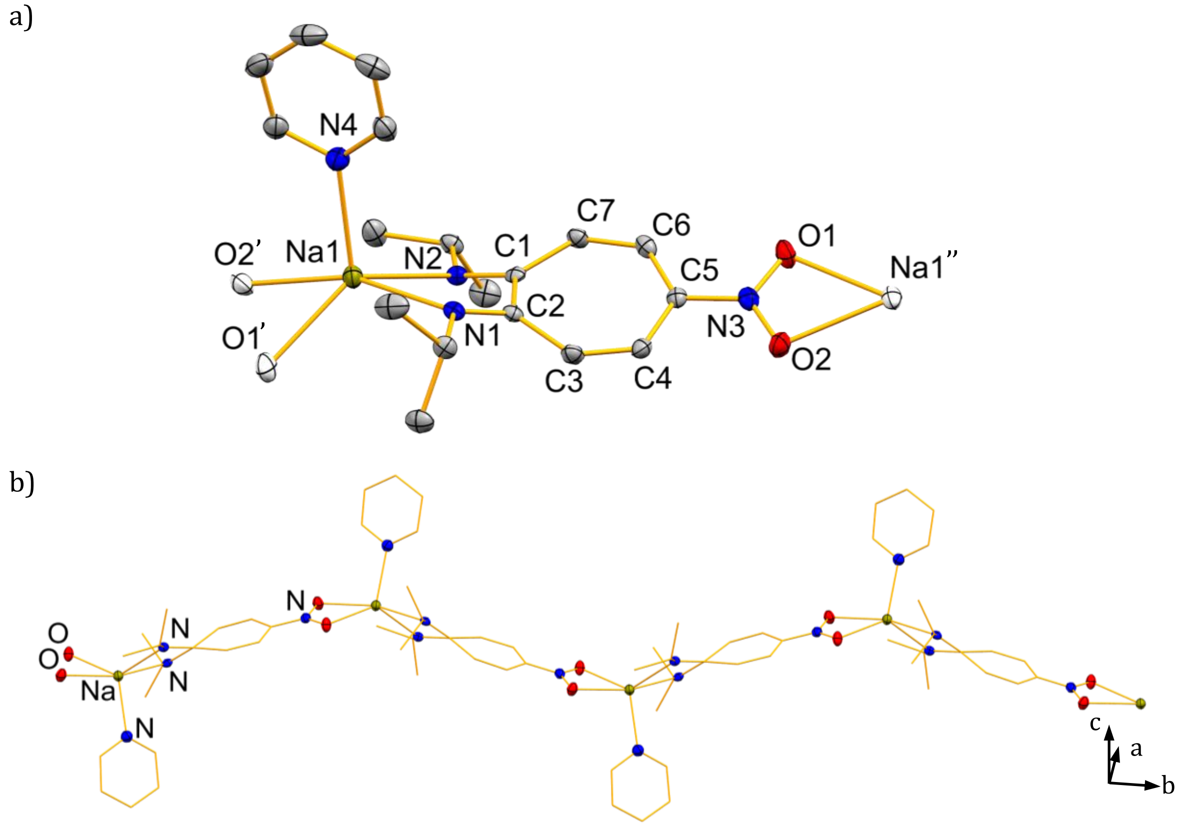

Abbildung 8: a) Ausschnitt der Struktur von $[\mathrm{Na(NO_2{-}ATI}^{i\mathrm{Pr}/i\mathrm{Pr}})(\mathrm{py})]_\infty$ (**[4-NO$_2$-py]$_\infty$**) im Festkörper. Die Ellipsoide repräsentieren 50% der Aufenthaltswahrscheinlichkeit. Die asymmetrische Einheit enthält zwei kristallographisch unabhängige, chemisch identische Formeleinheiten, von welchen nur eine Einheit diskutiert wird. Wasserstoffatome wurden aus Gründen der Übersichtlichkeit nicht abgebildet. Atome, die eine Formeleinheit überschreiten, sind als weiße Ellipsoide dargestellt. b) Eindimensionales Koordinationspolymer von **[4-NO$_2$-py]$_\infty$** im Festkörper, wobei Kohlenstoffatome im Drahtmodell dargestellt sind. Ausgewählte Bindungslängen (Å) und -winkel (°): Na1–N1, 2.4408(15); Na1–N2, 2.3777(16); Na1–N4, 2.4252(18); Na1–O1‘, 2.4355(15); Na–O2‘, 2.3386(14); N1–C1, 1.293(2); N2–C2, 1.286(2); N3–O1, 1.2731(19); N3–O2, 1.2757(19); N3–C5, 1.378(2); C1–C2, 1.525(2); C2–C3, 1.455(2); C3–C4, 1.349(2); C4–C5, 1.417(2); C5–C6, 1.415(3); C6–C7, 1.357(2); C1–C7, 1.452(2); N1–Na1–N2, 67.75(5); O1‘–Na1–O2‘, 54.40(5); O(1–2)‘–Na–N(1–2,4), 95.58(5)–159.39(6); N(1–2)–Na1–N4, 100.18(6)–106.82(6).

Das Natriumatom ist verzerrt quadratisch pyramidal koordiniert (τ = 0.46 mit O1‘ in der apikalen Position[a]), wobei die Verzerrung wiederum durch die Bisswinkel des ATI-Liganden (N1−Na1−N2, 67.75(5)°) und der Nitrofunktionalität (O1‘−Na1−O2‘, 54.40(5)°) sowie die Verdrehung der durch die Koordination aufgespannten Vier- bzw. Fünfringe ([C_2N_2Na]−[NO_2Na] = 45.9°) zueinander bedingt ist. Auch die für **[3-NO$_2$-py]$_\infty$** bereits diskutierten Bindungsparameter, welche für eine Verschiebung der π-Elektronendichte in Richtung der Nitrofunktionalität sprechen, deuten eine analoge Struktur für die Natrium-Verbindung **[4-NO$_2$-py]$_\infty$** an (N−C, 1.29 Å; N3−C5, 1.38 Å; Δ_{max}(C−C), 0.11 Å). Der Einfluss des Metall-Atoms auf die Verdrehung des ATI-Gerüst aus der Ebene zeigt sich an einem leicht vergrößerten Winkel zwischen dem C_7-Ring und dem C_2N_2Na-Fünfring von 27.5° (**[3-NO$_2$-py]$_\infty$**: 23.3°). Im Vergleich zum benzoyl-substituierten Natrium-Komplex **[4-Ph(O)C-py]$_\infty$** ([C1−7]−[C1−2,N1−2,Na], 23.9°) wird der steigende Einfluss des induktiven und mesomeren Effekts der Nitro-Gruppe in **[4-NO$_2$-py]$_\infty$** auf die Verdrehung des ATI-Gerüsts deutlich. Die Nitro-Gruppe zeigt außerdem eine ähnlich geringe Verdrehung wie im Lithium-Komplex (θ(O2−N3−C5−C4) = 2.2(2)°).

[5-NO$_2$-py]$_\infty$ kristallisiert in der triklinen Raumgruppe $P\bar{1}$ mit $Z = 2$ (Abbildung 9). Das Kaliumatom ist, wie seine niedrigeren Homologen in **[3-NO$_2$-py]$_\infty$** und **[4-NO$_2$-py]$_\infty$**, fünffach koordiniert. Die verzerrt quadratisch pyramidale Koordinationsgeometrie (τ = 0.30 mit N1 in der apikalen Position)[a] wird dabei durch Koordination des Metall-Atoms an die *N*,*N*-Bindungstasche eines ATI-Liganden, an ein Pyridin-Molekül sowie an je ein Sauerstoffatom der Nitro-Gruppe von zwei verschiedenen benachbarten Monomereinheiten erhalten (Abbildung 9a). Zwei Monomereinheiten bilden eine dimere Struktur aus, welche über eine Koordination des jeweiligen Zentralmetalls an ein Sauerstoffatom der Nitro-Gruppe des jeweils entgegengesetzt orientierten Monomers verknüpft ist (Abbildung 9b). Durch die Koordination des zweiten Sauerstoffatoms der Nitro-Gruppe an das Kaliumatom eines benachbarten Dimers wird ein eindimensionales Koordinationspolymer gebildet, dass sich durch Translation in Richtung der kristallographischen *c*-Achse ausbreitet. Man erhält zwei entgegengesetzt verlaufende Stränge von Polymerketten, die durch die K−O Bindungen, die zur Bildung der dimeren Untereinheiten führt, verknüpft sind (Abbildung 9c). Ein Ligand nimmt somit eine verbrückende Position zwischen drei Kaliumatomen ein, weshalb von einem μ_3-(M-κ^2*N*)-(M‘-κ^1*O*)-(M“-κ^1*O*)-Koordinationsmodus gesprochen werden kann.

---

[a] Bestimmung des Atoms in der apikalen Position: Aufsummierung aller Winkel des koordinierenden Atoms eines Liganden zu den koordinierenden Atomen aller anderen Liganden. Das Atom, für welches sich die kleinste Winkelsumme ergibt, nimmt die apikale Position ein.

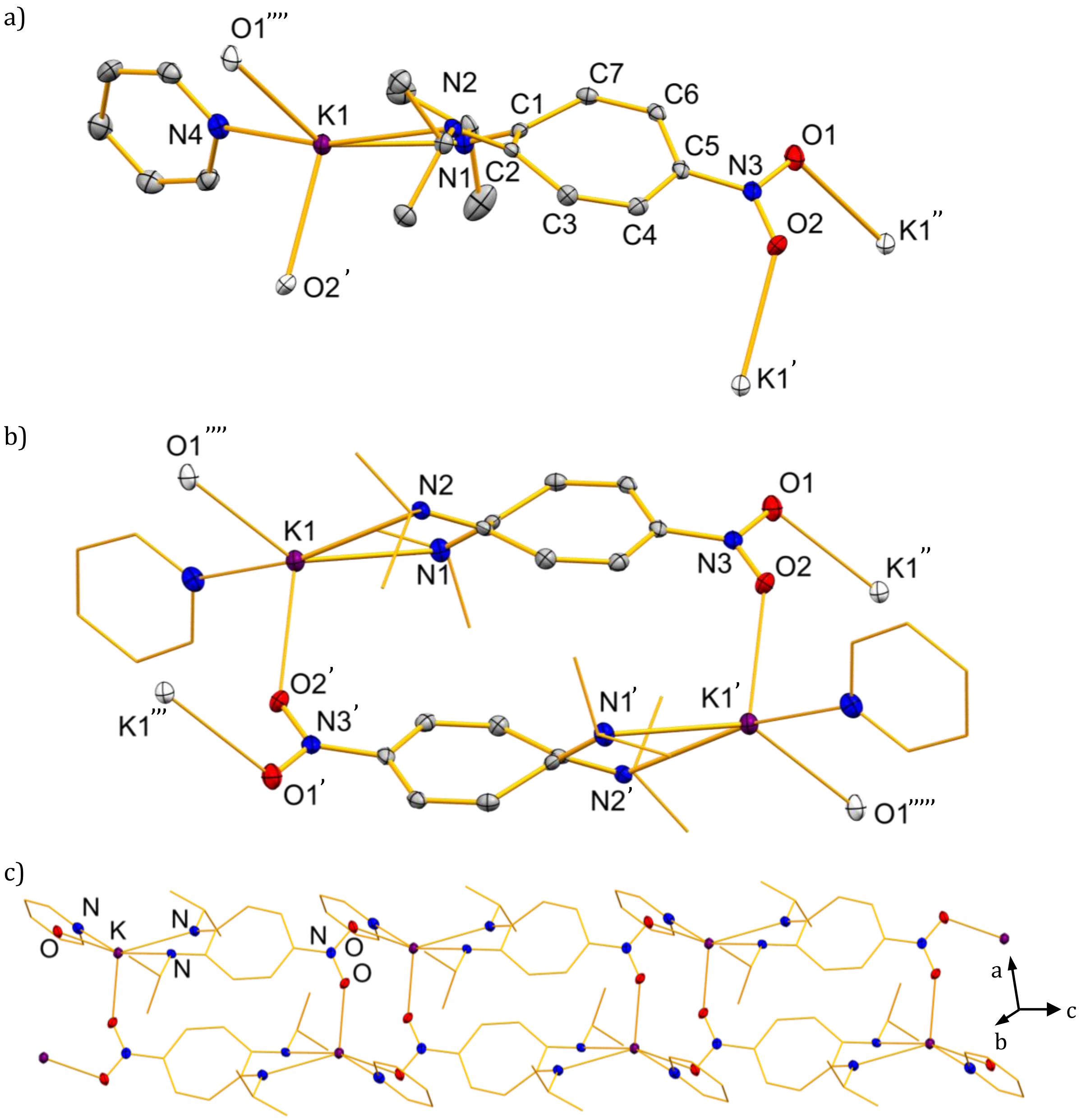

Abbildung 9: a) Ausschnitt der Struktur von [K(NO$_2$–ATI$^{iPr/iPr}$)(py)]$_\infty$ (**[5-NO$_2$-py]$_\infty$**) im Festkörper. Die Ellipsoide repräsentieren 50% der Aufenthaltswahrscheinlichkeit. Wasserstoffatome wurden aus Gründen der Übersichtlichkeit nicht abgebildet. Atome, die eine Formeleinheit überschreiten, sind als weiße Ellipsoide dargestellt. b) Dimere Untereinheit des Koordinationspolymers von **[5-NO$_2$-py]$_\infty$**. Atome, die eine Dimereinheit überschreiten, sind als weiße Ellipsoide dargestellt. Ein Pyridin-Molekül sowie die *Iso*propyl-Reste an den Stickstoffatomen sind im Drahtmodell dargestellt. c) Eindimensionales Koordinationspolymer von **[5-NO$_2$-py]$_\infty$** im Festkörper, wobei Kohlenstoffatome im Drahtmodell dargestellt sind. Ausgewählte Bindungslängen (Å) und -winkel (°): K1–N1, 2.9323(14); K1–N2, 2.8325(14); K1–N4, 2.8495(16); K1–O1‘‘‘‘, 2.6694(13); K1–O2‘, 2.6781(15); N1–C1, 1.283(2); N2–C2, 1.291(2); N3–C5, 1.375(2); N3–O1, 1.2721(18); N3–O2, 1.2807(19); C1–C2, 1.509(2); C2–C3, 1.460(2); C3–C4, 1.355(2); C4–C5, 1.421(2); C5–C6, 1.431(2); C6–C7, 1.346(2); C1–C7, 1.474(2); N2–K1–N1, 58.42(4); O1‘‘‘‘–K1–O2‘, 110.98(4); O(1‘‘‘‘–2‘)–K1–N(1–2,4), 82.92(4)–141.40(4); N(1–2)–K1–N4, 105.14(4)–159.20(4).

Aufgrund des dreifach verbrückenden Charakters des ATI-Liganden zeigt die Nitro-Gruppe im Vergleich zu den Komplexen der niedrigeren Homologen einen geringfügig größeren Torsionswinkel von 4.8(2)° zwischen C6–C5 und N3–O1. Bindungsparameter wie die N–C Bindungslängen (N1/2–C1/2, 1.28–1.29 Å, N3–C5, 1.38 Å) und die maximale Differenz von C–C Bindungslängen im ATI-Rückgrat (Δ_{max}(C–C) = 0.12 Å) lassen wiederum auf die Verschiebung der π-Elektronen in Richtung der Nitro-Gruppe schließen. Die damit verbundene verringerte Aromatizität zeigt sich in der Verdrehung des ATI-Gerüsts von 39.3°. Die Verdrehung des ATI-Gerüsts rückgrat-substituierter Kalium-Komplexe steigt in der die Reihe **[5-Ph(O)S-(thf)$_3$]$_\infty$** < **[5-Ph(O)C-py]$_\infty$** < **[5-NO$_2$-py]$_\infty$** ([C1–7]–[C1–2,N1–2,M]: **[5-Ph(O)S-(thf)$_3$]$_\infty$**, 33.3°; **[5-Ph(O)C-py]$_\infty$**, 27.9–35.0°).[77] Dies kann auf die Zunahme des –I- und –M-Effekts in dieser Reihe zurückgeführt werden. Im Vergleich mit literaturbekannten Komplexen besitzt **[5-NO$_2$-py]$_\infty$** die größte für (Halb-)Metall-ATI-Komplexe beobachtete Verdrehung des ATI-Gerüsts.[65, 78] Die Einführung eines (elektronenziehenden) Substituenten im ATI-Rückgrat kann somit neben dem Substitutionsmuster an den Stickstoffatomen sowie dem (Halb-)Metall in der ATI-Bindungstasche als weiterer Faktor für die Beeinflussung der Flexibilität des ATI-Gerüsts genutzt werden.

Auch die Festkörperstrukturen der Kronenether-Verbindungen **4-NO$_2$-(15K5)**, **4-NO$_2$-(12K4)$_2$** und **5-NO$_2$-(18K6)** konnten durch Einkristallröntgenstrukturanalyse von Einkristallen, welche aus Pyridin/*n*-Pentan (**4-NO$_2$-(15K5)**, **4-NO$_2$-(12K4)$_2$**) oder THF/*n*-Pentan (**5-NO$_2$-(18K6)**) Lösungsmittel-Systemen gewonnen wurden, aufgeklärt werden. Verwendet man die für das entsprechende Alkalimetall-Kation passenden Kronenether, beobachtet man die erwartete Adduktbildung (**4-NO$_2$-(15K5)**: monoklin, $P2_1/c$, $Z = 4$, Abbildung 10; **5-NO$_2$-(18K6)**: monoklin, $C2/c$, $Z = 8$, Abbildung 11).

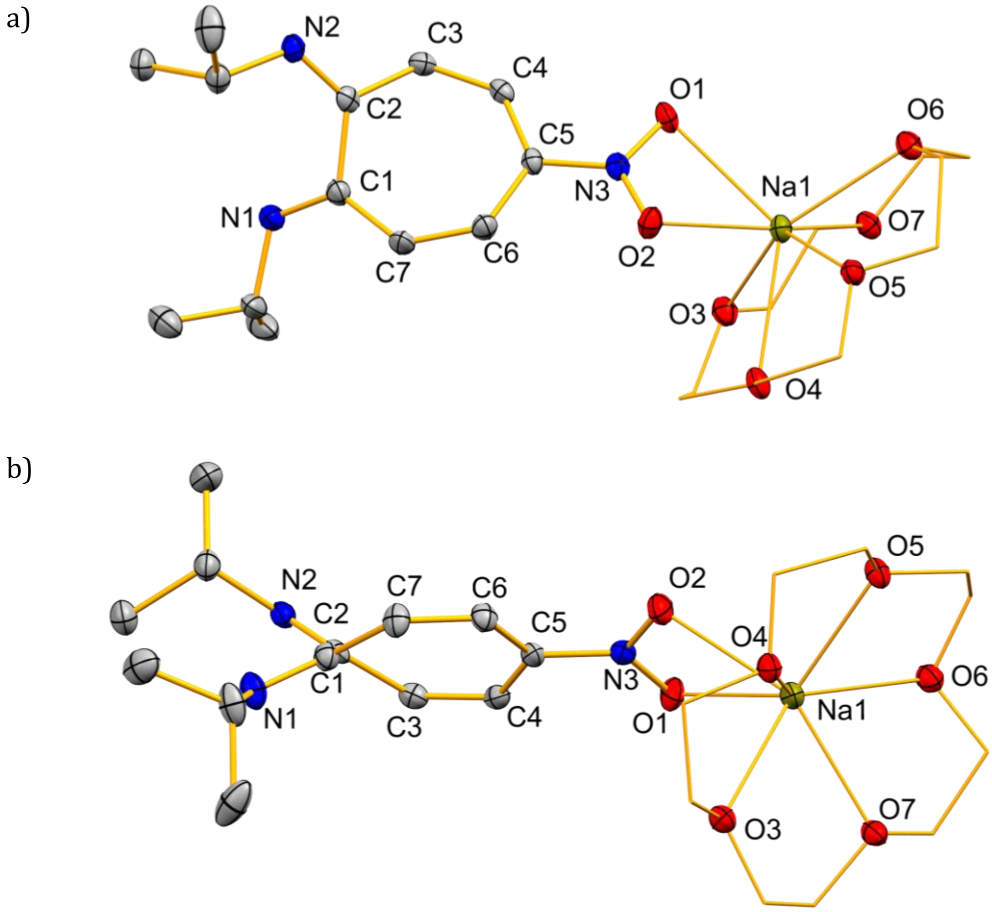

Abbildung 10: a) Struktur von [Na(NO$_2$–ATI$^{iPr/iPr}$)(15-Krone-5)] (**4-NO$_2$-(15K5)**) im Festkörper in der Draufsicht. b) Struktur von **4-NO$_2$-(15K5)** entlang der C1–C2 Bindung liegend. Die Ellipsoide repräsentieren 50% der Aufenthaltswahrscheinlichkeit. Wasserstoffatome wurden aus Gründen der Übersichtlichkeit nicht abgebildet. Die Ethyleneinheiten des Kronenethers sind im Drahtmodell dargestellt. Ausgewählte Bindungslängen (Å) und -winkel (°): Na1–O1, 2.5704(12); Na1–O2, 2.3953(12); Na1–O(3–6), 2.4106(13)–2.5634(12); N1–C1, 1.2860(18); N2–C2, 1.2874(18); N3–C5, 1.3779(18); N3–O2, 1.2838(15); C1–C2, 1.505(2); C2–C3, 1.4626(19); C3–C4, 1.3502(19); C4–C5, 1.435(2); C5–C6, 1.425(2); C6–C7, 1.354(2); C1–C7, 1.4681(19); O2–Na1–O1, 52.11(4); O(1–2)–Na1–O(3–7), 79.58(4)–153.79(4); O(3–7)–Na1–O(3–7), 66.46(4)–134.50(4).

4-NO$_2$-(15K5) und **5-NO$_2$-(18K6)** zeigen somit im Festkörper monomere Strukturen, wobei das Metall-Atom durch das Kronenether-Molekül sowie die beiden Sauerstoffatome der Nitrofunktionalität des Liganden koordiniert wird. Dies führt zu stark verzerrten Koordinationsgeometrien mit Koordinationszahlen von KZ = 7 (**4-NO$_2$-(15K5)**) und KZ = 8 (**5-NO$_2$-(18K6)**) für das Alkalimetall.

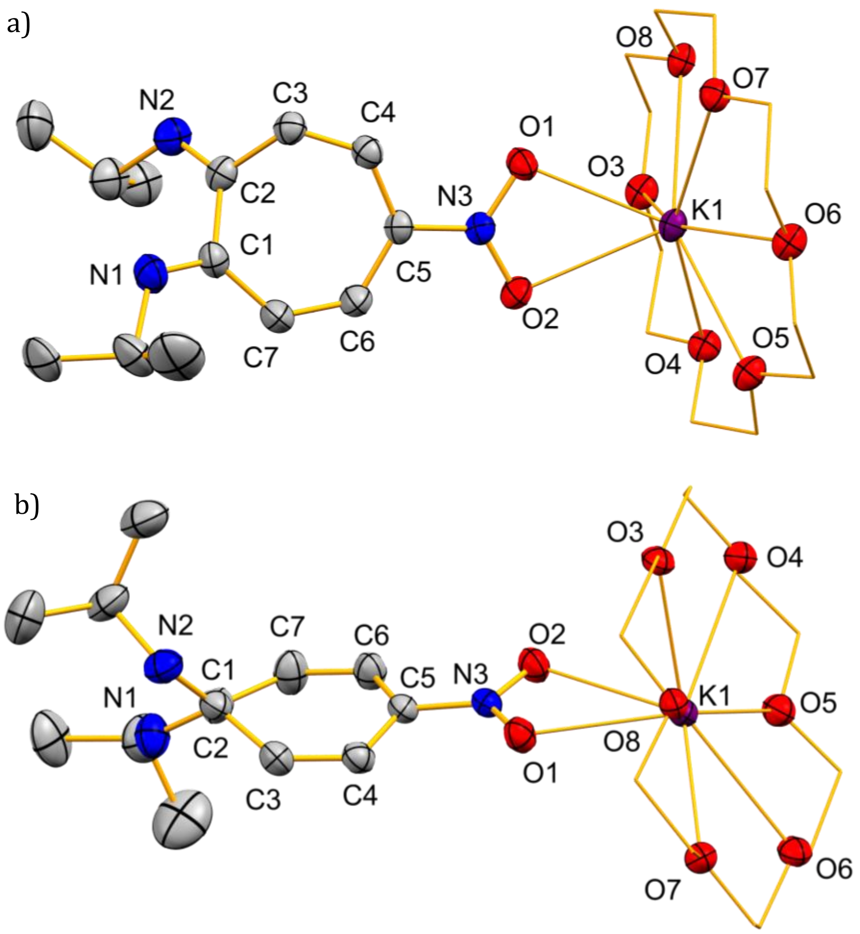

Abbildung 11: a) Struktur von [K(NO$_2$–ATI$^{iPr/iPr}$)(18-Krone-6)] (**5-NO$_2$-(18K6)**) im Festkörper in der Draufsicht. b) Struktur von **5-NO$_2$-(18K6)** entlang der C1–C2 Bindung liegend. Die Ellipsoide repräsentieren 50% der Aufenthaltswahrscheinlichkeit. Wasserstoffatome wurden aus Gründen der Übersichtlichkeit nicht abgebildet. Die Ethyleneinheiten des Kronenethers sind im Drahtmodell dargestellt. Ausgewählte Bindungslängen (Å) und -winkel (°): K1–O1, 2.7255(9); K1–O2, 2.8371(10); K1–O(3–8), 2.8111(9)–2.9682(9); N1–C1, 1.2820(18); N2–C2, 1.2782(18); N3–C5, 1.3710(16); N3–O1, 1.2840(14); N3–O2, 1.2787(13); C1–C2, 1.5056(19); C2–C3, 1.4712(19); C3–C4, 1.3410(18); C4–C5, 1.4419(17); C5–C6, 1.4234(18); C6–C7, 1.356(2); C1–C7, 1.462(2); O1–K1–O2, 46.49(3); O(1–8)–K1–O(1–8), 57.24(3)–154.44(3).

Die Koordination des Metalls über die Nitro-Gruppe im Festkörper lässt annehmen, dass auch in Lösung Strukturen dieser Koordinationsform vorliegen können. Außerdem zeigen die *Iso*propyl-Substituenten in beiden Strukturen eine für ATI-Komplexe untypische

E,*Z*-Konfiguration, was die bereits aufgrund der NMR-spektroskopischen Daten vermutete *E*,*E*-/*E*,*Z*-Isomerie bestätigt. Analog zu den kronenetherfreien Stammverbindungen deuten die Bindungsparameter des Ligandgerüsts für beide Verbindungen eine in Richtung der Nitro-Gruppe verschobene π-Elektronendichte an (Tabelle 2). Dabei kann eine zunehmende Lokalisierung der π-Elektronen ähnlich wie in Schema 13 (**O-*E*,*Z***) dargestellt angenommen werden.

Tabelle 2: Bindungsparameter der Kronenether-Komplexe **4-NO$_2$-(12K4)$_2$**, **4-NO$_2$-(15K5)** und **5-NO$_2$-(18K6)**.

Bindungsparameter [Å]bzw. [°]	**4-NO$_2$-(12K4)$_2$**	**4-NO$_2$-(15K5)**	**5-NO$_2$-(18K6)**
N1–C1	1.279(3)	1.2860(18)	1.2820(18)
N2–C2	1.284(3)	1.2874(18)	1.2782(18)
N3–C5	1.395(3)	1.3779(18)	1.3710(16)
Δ_{max}(C–C)	0.12	0.12	0.13
[C1–C7]–[C1–2,N1–2]	41.7	40.2	43.6
θ (C4/6–C5–N3–O1/2)	0.6(3)	7.7(2)	0.0(2)

Die Komplexierung von **4-NO$_2$** mit zwei Äquivalenten 12-Krone-4 führt zur Bildung eines freien Ligand-Anions, das keine gerichtete Bindungswechselwirkung zum [Na(12-Krone-4)$_2$]-Kation eingeht (**4-NO$_2$-(12K4)$_2$**: monoklin, $P2_1/c$, $Z = 4$, Abbildung 12). Eine ligandinduzierte Disproportionierung wie sie für die vorher diskutierte Bildung von **6-Ph(O)S** beobachtet wird (siehe Abbildung 4), findet nicht statt, was durch die steigende Tendenz zur Koordination an die NO$_2$-Gruppe im Gegensatz zur *N*,*N*-Bindungstasche bedingt ist. Trotz fehlender Koordination des Metall-Atoms an den Liganden zeigt **4-NO$_2$-(12K4)$_2$** eine Verdrehung von 41.7° für das ATI-Gerüst, was auf den anionischen Charakter des Liganden sowie die Verschiebung der π-Elektronendichte in Richtung der Nitro-Gruppe zurückzuführen ist. Diese Verschiebung bestätigen auch die Längen der N–C bzw. C–C Bindungen (Tabelle 2). **4-NO$_2$-(12K4)$_2$** ist somit der erste kristallographisch charakterisierte ATI-Komplex, in welchem Komplexanion und -Kation vollständig voneinander separiert vorliegen.

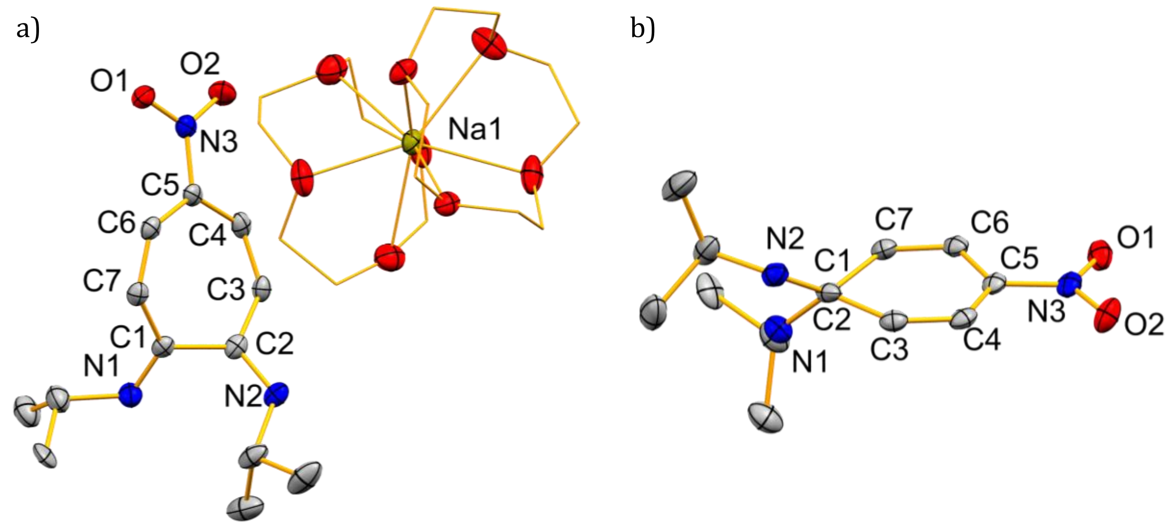

Abbildung 12: a) Struktur von [Na(12-Krone-4)$_2$][(NO$_2$–ATI$^{iPr/iPr}$)] (**4-NO2-(12K4)$_2$**) im Festkörper in der Draufsicht. b) Struktur von **4-NO$_2$-(12K4)$_2$** mit Blickrichtung entlang der C1–C2 Bindung liegend. Die Ellipsoide repräsentieren 50% der Aufenthaltswahrscheinlichkeit. Wasserstoffatome und das [Na(12-Krone-4)$_2$]$^+$-Fragment in b) wurden aus Gründen der Übersichtlichkeit nicht abgebildet. Die Ethyleneinheiten des Kronenethers sind im Drahtmodell dargestellt. Ausgewählte Bindungslängen (Å) und -winkel (°): N1–C1, 1.279(3); N2–C2, 1.284(3); N3–C5, 1.395(3); N3–O1, 1.264(3); N3–O2, 1.267(3); C1–C2, 1.507(4); C2–C3, 1.465(4); C3–C4, 1.354(4); C4–C5, 1.428(4); C5–C6, 1.428(4); C6–C7, 1.354(4); C1–C7, 1.470(4).

2.3 DFT-Rechnungen

Zur Verifizierung der *E,E*-/*E,Z*-Isomerisierung der Alkalimetall-Aminotroponiminat-Komplexe mit Nitrofunktionalität in Lösung wurden von *Dr. Crispin Lichtenberg* DFT-Rechnungen im polarisierbaren Kontinuumsmodell (Lösungsmittelmodell Pyridin) durchgeführt.[b] Dabei wurden die Energien für Modellverbindungen mit je zwei zusätzlichen Pyridin-Liganden **3-NO$_2$-(py)$_2$**, **4-NO$_2$-(py)$_2$** und **5-NO$_2$-(py)$_2$** berechnet. Für die Lithium-Verbindung **3-NO$_2$-(py)$_2$,** welche in Lösung nur einen Signalsatz für eine C_{2v}-symmetrische Verbindung im ^{1}H-NMR-Spektrum zeigt, erhält man das *E,E*-Isomer, bei welchem das Lithiumatom in der *N,N*-Bindungstasche sitzt, als energetisch günstigeres Isomer (**N-*E,E*→O-*E,E***: $\Delta H = 10.8$ kcal·mol^{-1}, $\Delta G = 8.2$ kcal·mol^{-1}). Es kann somit von einem **N-*E,E***-Koordinationsmodus in Lösung ausgegangen werden. Analog erhält man für die Natrium-Verbindung **4-NO$_2$-(py)$_2$** das **N-*E,E***-Isomer mit niedrigster Energie (Abbildung 13). Eine Koordination über die Nitro-Gruppe sowie eine *E,E*-Konfiguration der *Iso*propyl-Reste, welche ebenfalls Signale einer C_{2v}-symmetrischen Verbindung im NMR-Spektrum bedingen würde, ist mit Energieunterschieden von $\Delta H = 7.7$ kcal·mol^{-1} bzw. $\Delta G = 4.4$ kcal·mol^{-1} energetisch nur wenig ungünstiger, ein **O-*E,E***-Koordinationsmodus ist also durchaus denkbar. Eine mögliche Migration des Metall-Atoms von der *N,N*- nur *O,O*-Bindungstasche konnte allerdings NMR-spektroskopisch nicht aufgelöst werden. Die Bildung des *E,Z*-Isomers in Lösung ist schließlich ausgehend von einer **N-*E,E***-Konfiguration nur schwach endergon ($\Delta G = 1.4$ kcal·mol^{-1}) bzw. von einer **O-*E,E***-Konfiguration schwach exergon ($\Delta G = -3.0$ kcal·mol^{-1}). Da in Lösung die Einstellung eines Gleichgewichts zwischen *E,E*- und *E,Z*-Isomer beobachtet wird, sollte die Energiebarriere zwischen den C_{2v}-symmetrischen und C_1-symmetrischen Isomeren bei Raumtemperatur überwindbar sein. Ähnliche Ergebnisse sind auch für die Kalium-Verbindung zu erwarten. Wie in der Festkörperstruktur von **[5-NO$_2$-py]$_\infty$** gefunden (Abbildung 9), zeigen auch die Rechnungen, dass die Bildung von dimeren Strukturen exotherm und exergon ($\Delta H = -35.0$ kcal·mol^{-1}, $\Delta G = -20.3$ kcal·mol^{-1}) ist.

---

[b] Das Funktional B3LYP mit Grimme-Dispersionskorrektur (GD3) und die Basissätze 6-31G(d,p) [H, Li, C, N, O] und 6-311G(d,p) [Na, K] wurden genutzt. Frequenzanalysen zeigten null imaginäre Frequenzen für Grundzustände und eine imaginäre Frequenz für Übergangszustände.

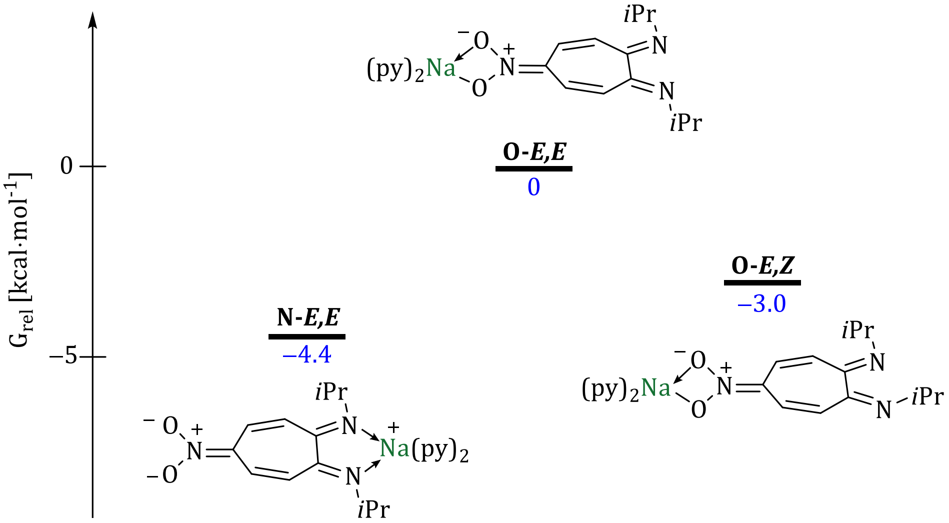

Abbildung 13: Schematische Darstellung der relativen Gibbs-Energien der berechneten Isomere von [Na(NO_2–ATI$^{iPr/iPr}$)(py)$_2$].

Die Natrium-Kronenether-Komplexe wurden ebenfalls mit Hilfe von DFT-Rechnungen untersucht. Für beide zeigt sich, dass deren Bildung aus der Stammverbindung durch Komplexierung mit dem entsprechenden Kronenether energetisch stark begünstigt ist (Schema 16). Dabei liegt das **O-*E*,*Z***-Isomer für **4-NO_2-(15K5)** energetisch am tiefsten, was im Einklang mit der Festkörperstruktur ist (Abbildung 10). In Lösung dagegen werden im NMR-Spektrum wiederum das C_{2v}-symmetrische und C_1-symmetrische Isomer detektiert, was mit einem sehr geringen Energieunterschied der beiden Isomere von ΔG = 1.09 kcal·mol^{-1} einhergeht. Die Beobachtung von Kreuzsignalen zwischen den Protonen des Kronenethers und denen der *Iso*propyl-Substituenten an den Stickstoffatomen im ^{1}H-^{1}H-NOESY-NMR-Spektrum kann durch eine Migration der [Na(15-Krone-5]$^+$-Einheit von der Nitro-Gruppe auf das ATI-Rückgrat erklärt werden. Die dabei gebildete halbsandwichartige Verbindung liegt um ΔG = 3.67 kcal·mol^{-1} höher in der Energie, als das **O-*E*,*Z***-Isomer (siehe Schema 15).

	ΔH (ΔG) [kcal·mol^{-1}]
4-NO_2-(py)$_2$ + 2 (12-Krone-4) ⟶ ***E*,*Z*-4-NO_2-(12K4)$_2$** + 2 (Py)	−27.8 (−24.5)
4-NO_2-(py)$_2$ + (15-Krone-5) ⟶ **O-*E*,*Z*-4-NO_2-(15K5)** + 2 (Py)	−11.2 (−18.7)

Schema 16: Thermodynamische Daten für die Bildung der Kronenether-Komplexe ***E*,*Z*-4-NO_2-(12K4)$_2$** und **O-*E*,*Z*-4-NO_2-(15K5)**.

Die energetischen Lagen der Isomere von **4-NO_2-(12K4)$_2$** stehen ebenfalls im Einklang mit der im Festkörper gefundenen *E*,*Z*-Konfiguration. ***E*,*Z*-4-NO_2-(12K4)$_2$** liegt um ΔG = −3.69 kcal·mol^{-1} niedriger als das C_{2v}-symmetrische *E*,*E*-Isomer. Die *E*/*Z*-Isomerisierung der C−N-Doppelbindung kann sowohl über einen Inversionsmechanismus, einen Rotationsmechanismus als auch über eine Vielzahl von Mechanismen, die zwischen den beiden Extremen liegen, ablaufen.[80] Welcher Pfad beschritten wird, hängt dabei z. B. vom Lösungsmittel und von der Art der Substituenten an der C−N Doppelbindung ab. Rechnungen konnten zeigen, dass Isomerisierungen eher über einen Inversionsmechanismus ablaufen, wenn die Doppelbindung Substituenten mit positiven Hammett Parametern (σ_m) trägt.[80a] Für Verbindung **4-NO_2-(12K4)$_2$** wurde ein linearer Übergangszustand für eine Konfigurationsänderung von *E*,*Z* zu *E*,*E* mit einer Energiebarriere von ΔG‡ = 26.6 kcal·mol^{-1} berechnet (Abbildung 14). Dies deutet an, dass die elekronenziehenden Eigenschaften des Nitro-Substituenten den Isomerisierungsmechanismus maßgeblich beeinflussen, da dem stickstoffgebundenen *Iso*propyl-Substituenten aufgrund seiner elektronenschiebenden Eigenschaften ein leicht negativer Hammett Parameter zugeschrieben wird.[81]

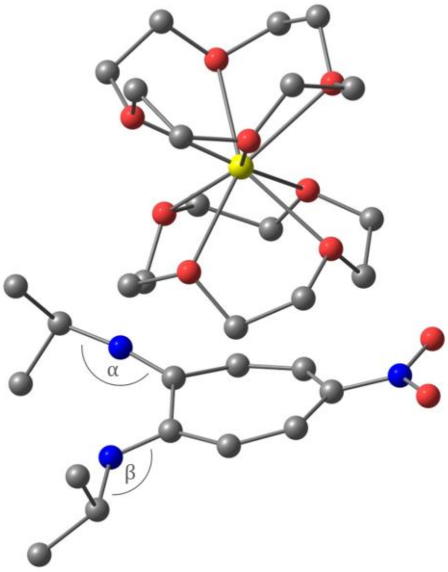

Abbildung 14: Berechneter linearer Übergangszustand der *E*,*Z*-Isomerisierung von **4-NO_2-(12K4)$_2$** in Lösung (α = 169.5°, β = 122.0°).

XIII Elektrochemie rückgratsubstituierter Liganden und Alkalimetall-Komplexe

1 Ph(O)S–ATI$^{iPr/iPr}$

Um Aussagen über die elektrochemischen Eigenschaften zu treffen, wurde sowohl der neutrale ATI-Ligand **1-Ph(O)S** als auch die Alkalimetall-Komplexe **3-Ph(O)S**, **4-Ph(O)S** und **5-Ph(O)S** cyclovoltammetrisch untersucht. Alle Messungen wurden in THF (0.1 M [(nBu)$_4$N][PF$_6$] in THF) bei Raumtemperatur durchgeführt und die erhaltenen Redoxpotentiale gegen Ferrocen/Ferrocenium referenziert. Im Bereich von 0.42 V bis 0.46 V kann für alle Verbindungen die für ATI-Verbindungen typische irreversible Oxidation des Liganden gefunden werden (Tabelle 3, Einträge I, II, IV, VI).[39] Für die Alkalimetall-Komplexe zeigen sich zudem irreversible Oxidationen bei −0.26 V (**3-Ph(O)S**), −0.55 V (**4-Ph(O)S**) bzw. −0.77 V (**5-Ph(O)S**), welche möglicherweise einer Oxidation der Sulfinyl-Gruppe zuzuordnen sind (Tabelle 3, Einträge III, V, VII).

Tabelle 3: Aus cyclovoltammetrischen Messungen in THF (0.1 M [(nBu)$_4$N][PF$_6$] in THF) bei Raumtemperatur ermittelte Redoxeigenschaften der sulfinyl-substituierten Verbindungen **1-Ph(O)S**, **3-Ph(O)S**, **4-Ph(O)S** und **5-Ph(O)S** unter oxidativen Bedingungen.

Eintrag	Vbd.	E_{pa} oder E_{pa}/E_{pc} [V]	Klassifizierung[a]	Reversibilität[b]
I	**1-Ph(O)S**	0.46	E	irrev
II	**3-Ph(O)S**	0.45	E	irrev
III	**3-Ph(O)S**	−0.26	E	irrev
IV	**4-Ph(O)S**	0.42	E	irrev
V	**4-Ph(O)S**	−0.55/−1.96	ECEC	pr
VI	**5-Ph(O)S**	0.45	E	irrev
VII	**5-Ph(O)S**	−0.77	E	irrev

[a] E = Elektronentransfer, C = chemische Reaktion, [b] irrev = irreversibel, pr = partiell reversibel.

Für **3-Ph(O)S** kann durch das Starten der Messung bei −0.68 V und anschließendem Potentialvorschub in oxidative Richtung (Abbildung 15, links, gestrichelte Linie) gezeigt werden, dass die irreversible Oxidation bei −0.26 V durch weitere Oxidationsereignisse überlagert wird, die in Folge einer Reduktion bei sehr niedrigen Potentialen (<3 V) auftreten (Abbildung 15, links, durchgezogene Linie).

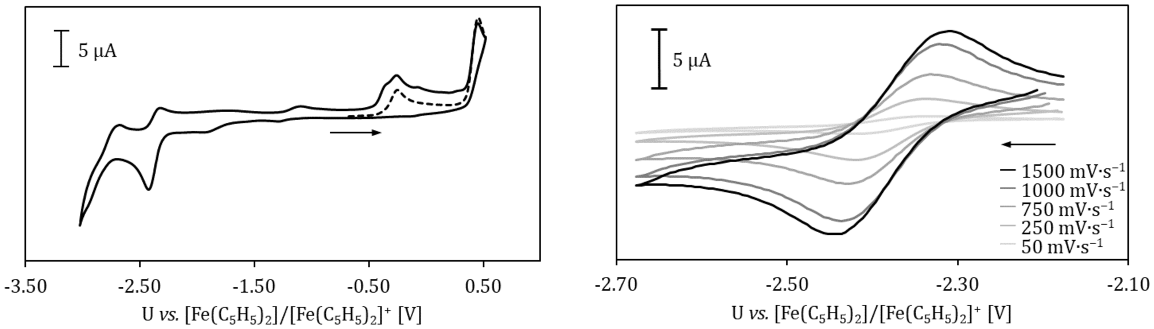

Abbildung 15: Cyclovoltammogramm von [Li(Ph(O)S–ATI$^{iPr/iPr}$)] (**3-Ph(O)S**) in THF (0.1 M [(*n*Bu)$_4$N][PF$_6$] in THF) bei Raumtemperatur und einer Vorschubgeschwindigkeit von 250 mV·s^{-1} über das gesamte Potentialfenster (links, gestrichelte Linie: Oxidation separat abgefahren) und für einen Ausschnitt von −2.67 bis −2.18 V mit Vorschubgeschwindigkeiten von 50 bis 1500 mV·s^{-1} (rechts).

In Folge der Oxidation von **4-Ph(O)S** bei −0.55 V ist eine Reduktionswelle bei −1.96 V zu beobachten, die keinem definierten Ereignis zugeordnet werden konnte (Abbildung 16, rechts). Für den Liganden **1-Ph(O)S** wird unter elektrochemischen Bedingungen kein Redoxereignis gefunden, welches einer Oxidation der Sulfinyl-Gruppe zugeordnet werden könnte (Abbildung 17).

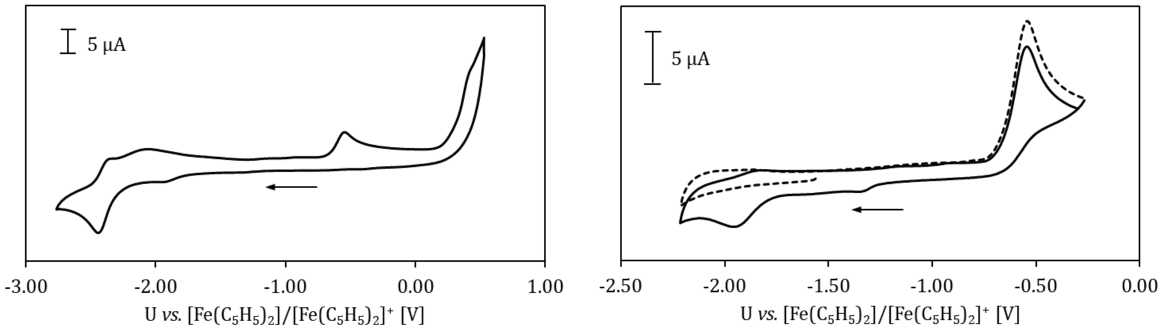

Abbildung 16: Cyclovoltammogramm von [Na(Ph(O)S–ATI$^{iPr/iPr}$)] (**4-Ph(O)S**) in THF (0.1 M [(*n*Bu)$_4$N][PF$_6$] in THF) bei Raumtemperatur und einer Vorschubgeschwindigkeit von 250 mV·s^{-1} über das gesamte Potentialfenster (links) und für einen Ausschnitt von −2.21 bis −0.26 V (rechts, gestrichelte Linie: Reduktion separat abgefahren).

Unter reduktiven Bedingungen zeigt **1-Ph(O)S** eine reversible Reduktion bei −2.38 V (Abbildung 17, Tabelle 4, Eintrag I).

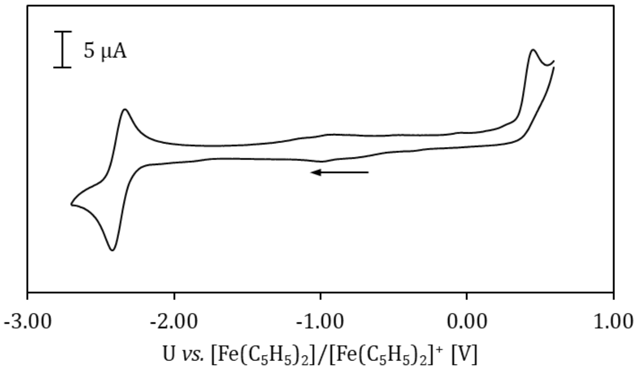

Abbildung 17: Cyclovoltammogramm von Ph(O)S–ATI$^{iPr/iPr}$ (**1-Ph(O)S**) in THF (0.1 M [(nBu)$_4$N][PF$_6$] in THF) bei Raumtemperatur und einer Vorschubgeschwindigkeit von 250 mV·s^{-1}.

Die Alkalimetall-Komplexe zeigen irreversible (**4-Ph(O)S**, Abbildung 16, links), quasireversible (**3-Ph(O)S**, Abbildung 15) bzw. reversible (**5-Ph(O)S**, Abbildung 18) Reduktionsereignisse bei ähnlichen stark negativen Potentialen (Tabelle 4, Eintrag II–IV). Die Quasireversibilität der Reduktion von **3-Ph(O)S** bei −2.38 V kann anhand von Messungen mit unterschiedlichen Vorschubgeschwindigkeiten gezeigt werden (Abbildung 15, rechts). Außerdem wird für **3-Ph(O)S** ein weiteres Reduktionsereignis bei sehr niedrigen Potentialen (<3 V) detektiert. Aufgrund der Nähe zum Rand des Potentailfensters konnte dieses Ereignis nicht klassifiziert werden. Wie bereits erwähnt zeigt sich, dass in Folge dieser Reduktion zusätzliche Oxidationsereignisse im Bereich der irreversiblen Oxidation bei −0.26 V auftreten (Abbildung 15, links).

Tabelle 4: Aus cyclovoltammetrischen Messungen in THF (0.1 M [(nBu)$_4$N][PF$_6$] in THF) bei Raumtemperatur ermittelte Redoxeigenschaften der sulfinyl-substituierten Verbindungen **1-Ph(O)S**, **3-Ph(O)S**, **4-Ph(O)S** und **5-Ph(O)S** unter reduktiven Bedingungen.

Eintrag	Vbd.	$E_{1/2}$ oder E_{pc}/E_{pa} oder E_{pc} [V][a]	Klassifizierung[b]	Reversibilität[c]
I	**1-Ph(O)S**	−2.38	EE	rev
II	**3-Ph(O)S**	−2.38	E	qr
III	**4-Ph(O)S**	−2.44	E	irrev
IV	**5-Ph(O)S**	−2.37	EE	rev

[a] $E_{1/2}$ für Eintrag I und IV, E_{pc}/E_{pa} für Eintrag II, [b] E = Elektronentransfer, C = chemische Reaktion, [c] rev = reversibel, irrev = irreversibel, qr = quasireversibel.

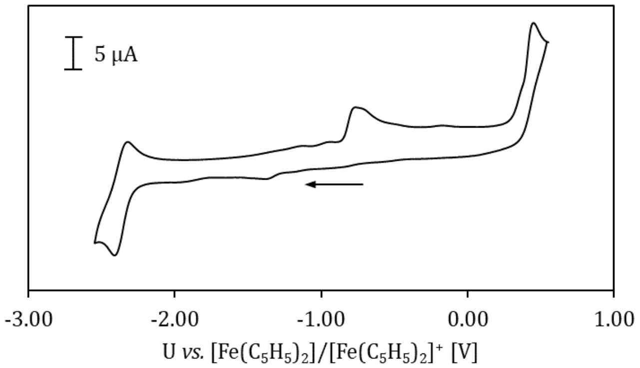

Abbildung 18: Cyclovoltammogramm von [K(Ph(O)S–ATI$^{iPr/iPr}$)] (**5-Ph(O)S**) in THF (0.1 M [(*n*Bu)$_4$N][PF$_6$] in THF) bei Raumtemperatur und einer Vorschubgeschwindigkeit von 250 mV·s^{-1}.

In Übereinstimmung mit bekannten Alkalimetall-ATI-Komplexen ohne Rückgratsubstituent wird angenommen, dass es sich bei den Reduktionsereignissen der sulfinylsubstituierten Komplexe um ligandzentrierte Redox-Ereignisse handelt.[39, 66] Die für den Lithium-Komplex **3-Ph(O)S** auftretenden Reduktions-Ereignisse können nicht alle eindeutig klassifinziert werden, weshalb eine Separation von Reduktions- und zugehöriger Oxidationswellen, wie sie für literaturbekannte Komplexe gefunden wurde, nicht ausgeschlossen werden kann.[39] Für die sulfinyl-substituierten Natrium- und Kalium-Komplexe **4-Ph(O)S** und **5-Ph(O)S** wird keine Separation von Redox-Ereignissen beobachtet

2 NO_2–ATI$^{i\text{Pr}/i\text{Pr}}$

Die nitro-substituierten Verbindungen **1-NO_2**, **3-NO_2**, **4-NO_2** und **5-NO_2** wurden ebenfalls mit Hilfe von Cyclovoltammerie auf ihre Redoxeigenschaften hin untersucht. Alle Messungen wurden in THF (0.1 M $[(n\text{Bu})_4\text{N}][\text{PF}_6]$ in THF) bei Raumtemperatur durchführt und die erhaltenen Potential gegen Ferrocen/Ferrocenium referenziert. Die Lithium-Verbindung **3-NO_2** zeigt dabei als einzige Verbindung bei +0.14 V ein Ereignis, das einer irreversiblen Ligandoxidation zugeordnet werden könnte (Tabelle 5, Eintrag I, Abbildung 19). Es wird davon ausgegangen, dass analoge Oxidationsereignisse für alle anderen Verbindungen außerhalb des in THF zugängigen Potentialfensters liegen. Die Komplexe **4-NO_2** und **5-NO_2** zeigen irreversible Oxidationsereignisse bei negativen Potentialen, die keinen definierten Ereignissen zugeordnet werden konnten (Tabelle 5, Abbildung 21 und Abbildung 22).

Tabelle 5: Aus cyclovoltammetrischen Messungen in THF (0.1 M $[(n\text{Bu})_4\text{N}][\text{PF}_6]$ in THF) bei Raumtemperatur ermittelte Redoxeigenschaften der nitro-substituierten Verbindungen **3-NO_2**, **4-NO_2** und **5-NO_2** unter oxidativen Bedingungen.

Eintrag	Vbd.	E_{pa} [V]	Klassifizierung[a]	Reversibilität[b]
I	**3-NO_2**	+0.14	E	irrev
II	**4-NO_2**	−0.27	E	irrev
III	**5-NO_2**	−0.33	E	irrev

[a] E = Elektronentransfer; [b] irrev = irreversibel.

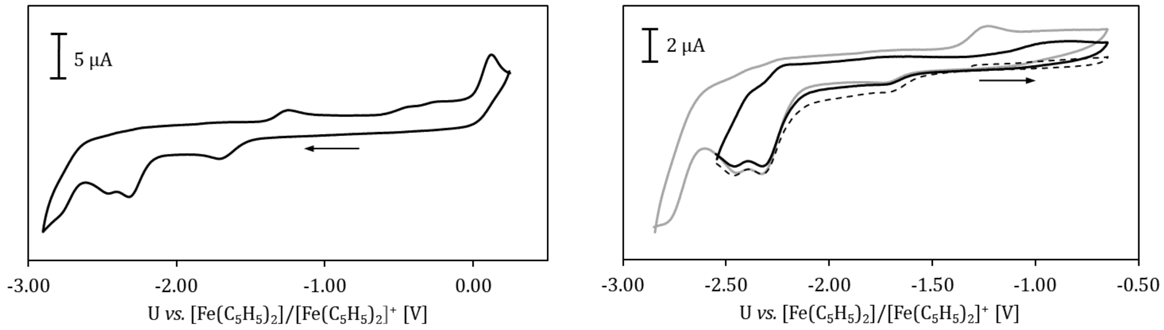

Abbildung 19: Cyclovoltammogramm von [Li(NO_2–ATI$^{i\text{Pr}/i\text{Pr}}$)] (**3-NO_2**) in THF (0.1 M $[(n\text{Bu})_4\text{N}][\text{PF}_6]$ in THF) bei Raumtemperatur und einer Vorschubgeschwindigkeit von 250 $\text{mV}\cdot\text{s}^{-1}$ über das gesamte Potentialfenster (links) und für zwei Ausschnitte separat gemessen (rechts, von −2.84 bis −0.65 V: graue Linie; und −2.55 bis −0.65 V (bei −1.31 V gestartet und in oxidative Richtung gemessen): gestrichelte und schwarze Linie).

Unter reduktiven Bedingungen sind für **1-NO$_2$** zwei irreversible Redoxereignisse zu beobachten (Tabelle 6, Einträge II und III). Außerdem zeigt sich eine Reduktionswelle bei −1.93 V, welche ab einer Vorschubgeschwindigkeit von 250 mV·s^{-1} partiell reversibel ist, wobei die zugehörigen Oxidationswellen zu einem Potential von −1.72 V und −1.24 V verschoben sind (Abbildung 20, rechts; Tabelle 6, Eintrag I). Es kann somit vermutet werden, dass es zu einer chemischen Transformation zwischen Reduktion und anschließender Oxidation kommt, die über den Elektronentransfer hinausgeht.

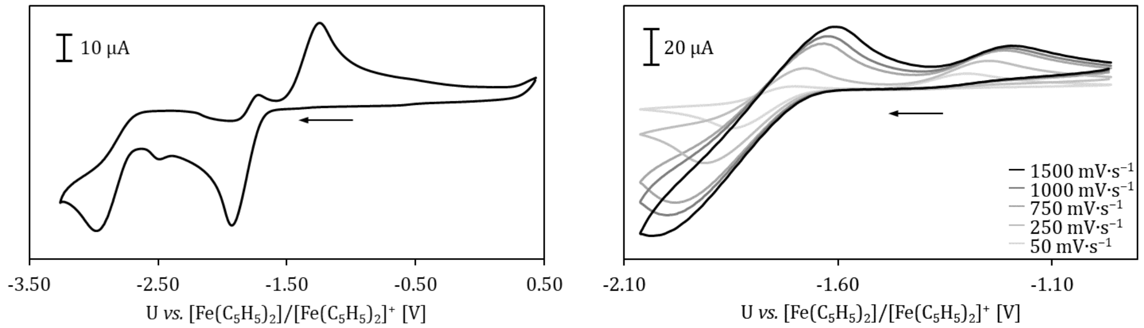

Abbildung 20: Cyclovoltammogramm von NO$_2$–ATI$^{iPr/iPr}$ (**1-NO$_2$**) in THF (0.1 M [(nBu)$_4$N][PF$_6$] in THF) bei Raumtemperatur und einer Vorschubgeschwindigkeit von 250 mV·s^{-1} über das gesamte Potentialfenster (links) und für einen Ausschnitt von −2.06 bis −0.97 V mit Vorschubgeschwindigkeiten von 50 bis 1500 mV·s^{-1} (rechts).

3-NO$_2$ zeigt drei irreversible Reduktionswellen im Bereich von −1.71 bis −2.46 V (Abbildung 19; Tabelle 6, Einträge IV−VI). Außerdem zeigt sich eine Reduktionswelle bei stark negativen Potentialen mit einer um 1.52 V zu positiveren Potentialen verschobenen zugehörigen Oxidationswelle. Die Zugehörigkeit konnte dabei durch das erstmalige Auftreten der Oxidationswelle nach zuvor erfolgter Reduktion verifiziert werden (Abbildung 19, rechts).

Tabelle 6: Aus cyclovoltammetrischen Messungen in THF (0.1 M $[(n\mathrm{Bu})_4\mathrm{N}][\mathrm{PF}_6]$ in THF) bei Raumtemperatur ermittelte Redoxeigenschaften der nitro-substituierten Verbindungen **1-NO$_2$**, **3-NO$_2$**, **4-NO$_2$** und **5-NO$_2$** unter reduktiven Bedingungen.

Eintrag	Vbd.	E_{pc} oder E_{pc}/E_{pa} [V]	Klassifizierung[a]	Reversibilität[b]
I	**1-NO$_2$**	−1.93/−1.72 und −1.24	ECEC	pr
II	**1-NO$_2$**	−2.49	E	irrev[c]
III	**1-NO$_2$**	−2.98	E	irrev[c]
IV	**3-NO$_2$**	−1.71	E	irrev
V	**3-NO$_2$**	−2.32	E	irrev
VI	**3-NO$_2$**	−2.46	E	irrev
VII	**3-NO$_2$**	−2.76/−1.24	ECEC	pr
VIII	**4-NO$_2$**	−1.77/−1.05	ECEC	pr
IX	**4-NO$_2$**	−2.00/−1.78	ECEC	pr
X	**4-NO$_2$**	−2.49	E	irrev
XI	**4-NO$_2$**	−3.05	E	irrev
XII	**5-NO$_2$**	−1.81/−1.69	ECEC	pr
XIII	**5-NO$_2$**	−2.96/−2.45	ECEC	pr

[a] E = Elektronentransfer, C = chemische Reaktion, [b] irrev = irreversibel, pr = partiell reversibel, [c] anhand eins Vergleichs der Spitzenströme von zu positiveren Potentialen verschobenen Oxidationswellen kann nicht ausgeschlossen werden, dass ein partiell reversibles Ereignis mit separierten Redox-Wellen vorliegt.

Die Natrium-Verbindung **4-NO$_2$** zeigt zwei irreversible Reduktionswellen bei stark negativen Potentialen (Abbildung 21, links; Tabelle 6, Einträge X, XI). Außerdem können zwei partiell reversible Ereignisse mit zugehörigen Oxidationswellen, die vom jeweiligen Reduktionsereignis separiert sind, gefunden werden (Abbildung 21, rechts; Tabelle 6, Einträge VIII, IX). Durch Starten einer Messung bei −1.46 V und anschließendem Potentialvorschub in oxidative Richtung kann die Abhängigkeit der Oxidationswelle bei −1.05 V von der zuvor erfolgten Reduktion bei −1.77 V, sowie die Irreversibilität der Oxidation bei −0.27 V gezeigt werden (Abbildung 21, rechts).

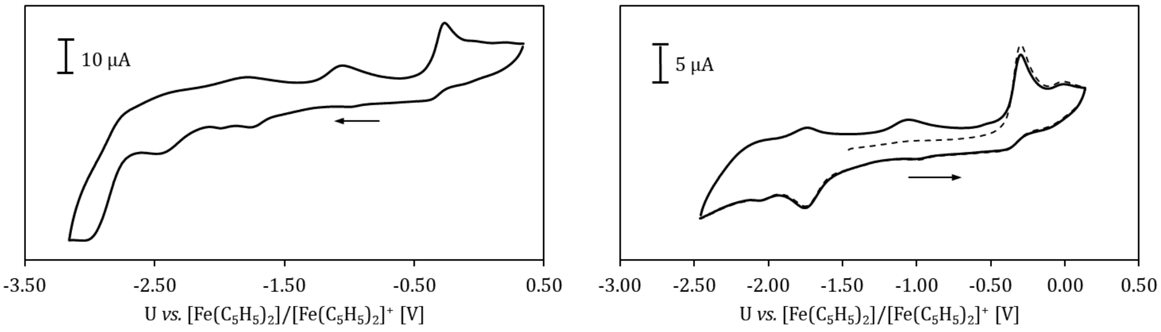

Abbildung 21: Cyclovoltammogramm von $[Na(NO_2{-}ATI^{iPr/iPr})]$ (**4-NO₂**) in THF (0.1 M $[(n\text{Bu})_4N][PF_6]$ in THF) bei Raumtemperatur und einer Vorschubgeschwindigkeit von 250 mV·s⁻¹ über das gesamte Potentialfenster (links) und für einen Ausschnitt gemessen (rechts, von −2.46 bis +0.13 V: schwarze Linie; und −1.46 bis +0.13 V (bei −1.46 V gestartet und in oxidative Richtung gemessen): gestrichelte Linie.

Die Kalium-Verbindung **5-NO₂** besitzt zwei Redoxereignisse für die eine Separation der Reduktions- und der zugehörigen Oxidationswelle beobachtet wird (Tabelle 6, Einträge XII, XIII). Das Ereignis bei sehr niedrigen Potentialen (Eintrag XIII) ist bei geringen Vorschubgeschwindigkeiten (50 mV·s⁻¹) irreversibel, geht allerdings mit zunehmender Vorschubgeschwindigkeit in ein partiell reversibles Ereignis über (Abbildung 22b, links). Die Reduktion bei −1.81/−1.69 V stellt ein partiell reversibles Ereignis dar (Abbildung 22b, rechts).

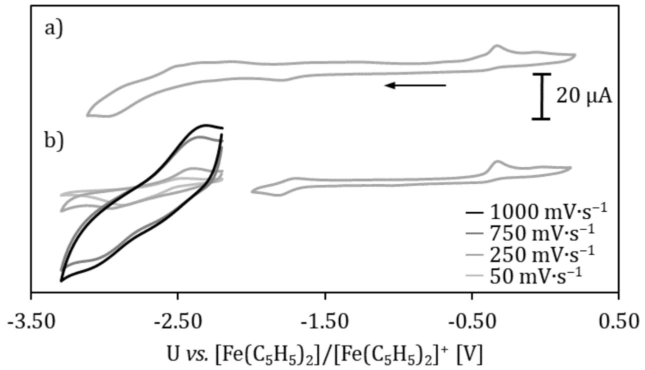

Abbildung 22: Cyclovoltammogramm von $[K(NO_2{-}ATI^{iPr/iPr})]$ (**5-NO₂**) in THF (0.1 M $[(n\text{Bu})_4N][PF_6]$ in THF) bei Raumtemperatur a) bei einer Vorschubgeschwindigkeit von 250 mV·s⁻¹ über das gesamte Potentialfenster b) für einen Ausschnitt von −3.30 bis −2.20 V bei Vorschubgeschwindigkeiten von 50 bis 1000 mV·s⁻¹ gemessen (links) und für einen Ausschnitt von −2.00 V bis +0.20 V bei einer Vorschubgeschwindigkeit von 250 mV·s⁻¹ gemessen (rechts).

Aufgrund der erhaltenen elektrochemischen Daten scheinen alle Komplexe potentiell reduzierbar, wobei vermutlich keine stabilen Radikale gebildet werden, sondern nach Übertragung eines Elektrons eine chemische Transformation stattfindet.

XIV Chemische Redoxstudien

1 Reduktionsexperimente der Alkalimetall-Ph(O)S–ATI$^{iPr/iPr}$-Komplexe

1.1 Lithium- und Natrium-Ph(O)S–ATI$^{iPr/iPr}$

[Li(Ph(O)S–ATI$^{iPr/iPr}$)] (**3-Ph(O)S**) und [Na(Ph(O)S-ATI$^{iPr/iPr}$)] (**4-Ph(O)S**) wurden aufgrund der erhaltenen Daten aus elektrochemischen Untersuchungen mit starken Reduktionsmitteln wie elementarem Lithium bzw. KC_8 oder elementarem Natrium umgesetzt. Die Experimente wurden in THF-d_8 bzw. Pyridin-d_5 durchgeführt und mittels ^{1}H-NMR-Spektroskopie verfolgt. In THF konnte ^{1}H-NMR-spektroskopisch kein Umsatz der Edukte beobachtet werden. In Pyridin ließ eine Farbänderung der Reaktionslösung von gelb zu dunkelbraun für die Umsetzung von **3-Ph(O)S** mit Lithium oder KC_8 eine Reaktion vermuten. ^{1}H-NMR-spektroskopisch wurde kein Umsatz des Edukts beobachtet werden. Es kann davon ausgegangen werden, dass eine Reduktion des Lösungsmittels für die beobachtete Farbänderung verantwortlich ist. Die Generierung zeitweise stabiler radikalischer Spezies wurde aufgrund gleichbleibender Signalintensitäten ohne signifikante Signalverbreiterungen und Änderungen der chemischen Verschiebung über den gesamten Reaktionszeitraum ausgeschlossen. Auch verlängerte Reaktionszeiten und Behandlung mit Ultraschall, um eine eventuelle Passivierung der Alkalimetalle zu verhindern, führten nicht zu einer Reaktion.

1.2 Kalium-Ph(O)S–ATI$^{iPr/iPr}$

[K(Ph(O)S–ATI$^{iPr/iPr}$)] (**5-Ph(O)S**) wurde mit elementarem Kalium in THF-d_8 umgesetzt und die Reaktion ^{1}H-NMR-spektroskopisch verfolgt. Nach sechs Tagen ist ein vollständiger Reaktionsumsatz zu beobachten und man detektiert Signale, die auf die Bildung einer diamagnetischen Spezies **5-red** hindeuten. Im Hinblick auf die in der Literatur für im Rückgrat unsubstituierte Lithium- und Natrium-ATI-Komplexe beobachtete reduktive Dimerisierung könnte für **5-Ph(O)S** ein ähnliches Verhalten angenommen werden.[39, 66] Im ^{1}H-NMR-Spektrum konnten allerdings keine Signale für Protonen an neu gebildeten sp^3-hybridisierten Kohlenstoffatomen, wie sie für eine über das C_7-Rückgrat dimerisierte Verbindung zu erwarten wären, gefunden werden. Mit Hilfe von 2D-NMR-spektroskopischen Methoden konnte eine Signalzuordnung vorgenommen werden. Die Protonen des Rückgrats zeigen vier separate Signale, wobei eines ein Singulett ist. Da ein solches Aufspaltungsmuster nur auftritt, wenn der Rückgratsubstituent an C4- oder C6-Position des C_7-Rings sitzt, wird eine Wanderung des Sulfinyl-Rests an diese Position angenommen. Zusätzlich zu den vier Signalen für das ATI-Rückgrat detektiert man sieben weitere Signale in einem Bereich, der typisch für die chemische Verschiebung von aromatischen Protonen ist. Da für die Phenyl-Gruppe des Sulfinyl-Rests allerdings nur drei Signale erwartet werden, wird eine einfache Wanderung des Rests ausgeschlossen.

Eine Reduktion in Anwesenheit von 18-Krone-6 führte zur Bildung einer analogen vermutlich kronenetherkomplexierten Spezies. Allerdings konnte in THF-d_8 nach einem Tag die Bildung eines Niederschlags beobachtet werden. ^{1}H-NMR-spektroskopisch konnte in Lösung nur noch eine Spezies, die lediglich die charakteristischen Signale einer Phenyl-Gruppe zeigt, detektiert werden. Durch Kristallisation aus einem THF/*n*-Pentan Lösungsmittel-System konnte diese Spezies als 18-Krone-6-Addukt von Kaliumthiophenolat identifiziert werden. Der in THF-d_8 ausgefalle Feststoff wurde in Pyridin-d_5 NMR-spektroskopisch untersucht (Abbildung 23). Für die Protonen der *Iso*propyl-Reste detektiert man zwei Dubletts für die CH_3-Gruppen sowie zwei Septetts für die CH-Gruppen. Die beiden Dubletts bei $\delta = 6.03$ und 6.33 ppm werden dem 7-H und dem 5-H zugeordnet. Das Singulett bei $\delta = 6.57$ ppm repräsentiert das 3-H und ein Dublett vom Dublett von $\delta = 6.73–6.79$ ppm das 6-H.

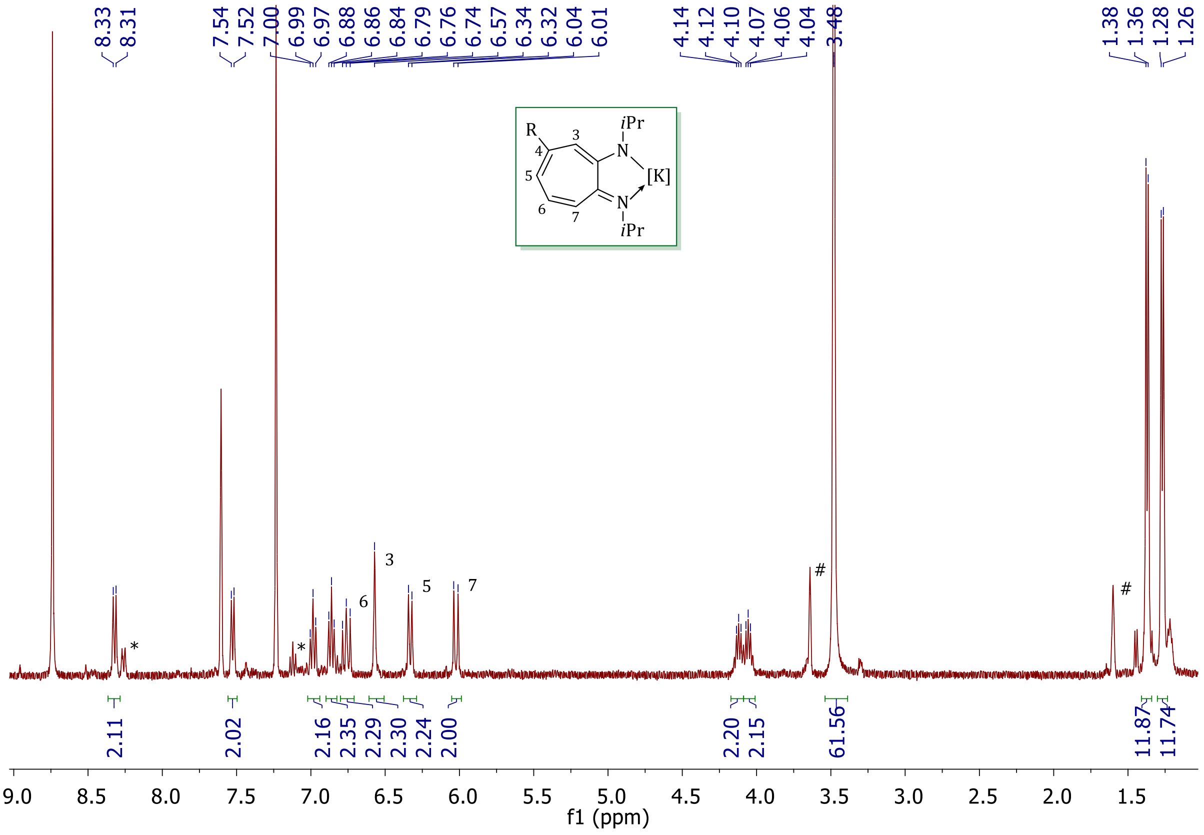

Abbildung 23: ^{1}H-NMR-Spektrum von **5-red** in Pyridin-d_5. * Restsignale von 18-Krone-6-Kaliumthiophenolat, # Restsignale von THF-d_8.

Die restlichen vier Signale sollten somit zu dem an C4-Position gebundenen Rest gehören. Aufgrund der Anzahl und den jeweiligen Intensitäten der Signale kann es sich dabei nicht um einen einzelnen Phenylsulfinyl-Rest handeln. Auf Grundlage des gefundenen Kaliumthiolats kann allerdings eine Generierung von Phenylsulfanyl-Einheiten während der Reduktion angenommen werden. Es wird deshalb vermutet, dass **5-red** mindestens eine solche phenyltragende Einheit enthält. Da andernfalls keine sinnvollen Integralverhältnisse für einen Phenyl-Rest gefunden werden, wird eine symmetrische Struktur vorgeschlagen, welche zwei ATI-Einheiten enthält und über die C4-Position verknüpft ist (Schema 17). Eine Brücke, die eine Phenylsulfanyl-Einheit enthält, wäre dann mit einer stöchiometrischen Reaktionsbilanz sowie den NMR-spektroskopischen Daten im Einklang. Allerdings können zwei zusätzliche Signale im aromatischen Bereich (ein Dublett bei $\delta = 7.53$ und ein überlagertes Signal bei 6.84−6.88 ppm), welche vermutlich weitere Bestandteile der Brücke repräsentieren, nur unzufriedenstellend zugeordnet werden. Eine zu den NMR-Daten passende Möglichkeit wäre die in Schema 17 gezeigte Struktur der Brücke, wobei diese nicht mit einer ausgeglichenen Atombilanz in Einklang stehen würde.

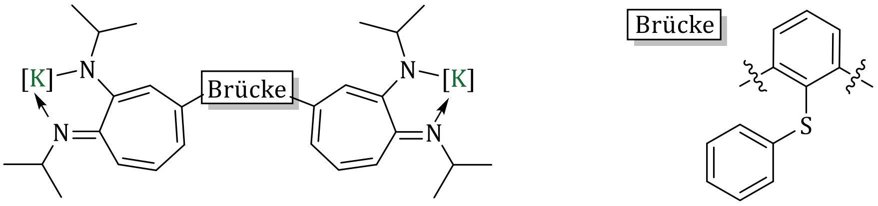

Schema 17: Strukturvorschlag für Verbindung **5-red**.

DFT-Rechnungen von *Dr. Crispin Lichtenberg* für das im Rückgrat unsubstituierte Fragment [K$_2$(ATI$^{iPr/iPr}$)(thf)$_4$]$^\bullet$ konnten zeigen, dass die Spindichte des ungepaarten Elektrons im Vergleich zu den restlichen Kohlenstoffatomen im C$_7$-Rückgrat an C4- und C6-Position am größten ist (0.36 bzw. 0.37;[c] Abbildung 24).[82] Da während der Reduktion von **5-Ph(O)S** vermutlich ein ähnliches Fragment auftritt, wird angenommen, dass eine Radikalrekombination zur Bildung von **5-red** geführt hat. Warum keine Dimerisierung zweier ATI-Radikalfragmente stattgefunden hat, konnte nicht abschließend geklärt werden.

---

[c] Das Funktional UB3LYP mit Grimme-Dispersionskorrektur (GD3) und die Basissätze 6-31G(d,p) [H, C, N, O] und 6-311G(d,p) [K] sowie das Lösungsmittelmodell THF wurden genutzt. Frequenzanalysen zeigten null imaginäre Frequenzen für Grundzustände und eine imaginäre Frequenz für Übergangszustände.

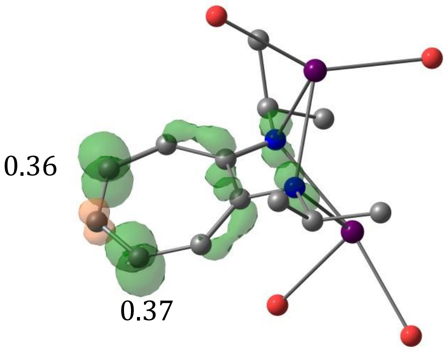

Abbildung 24: Berechnete Struktur von $[K_2(ATI^{iPr/iPr})(thf)_4]^{\bullet}$. Die Kohlenstoffatome der vier thf-Liganden sind nicht dargestellt.

2 Reduktionsexperimente der Alkalimetall-NO_2–ATI$^{iPr/iPr}$-Komplexe

Die Alkalimetall-Komplexe [Li(NO_2–ATI$^{iPr/iPr}$)] (**3-NO_2**), [Na(NO_2–ATI$^{iPr/iPr}$)] (**4-NO_2**) und [K(NO_2–ATI$^{iPr/iPr}$)] (**5-NO_2**) wurden aufgrund der aus cyclovoltammetrischen Messung erhaltenen Daten mit starken Reduktionsmitteln in Form der entsprechenden elementaren Alkalimetalle als Metallsand, als Metall auf Salzverbindungen (Na/NaCl, K/KI), als Metallspiegel oder als Metallnaphthalid (Lithium- bzw. Natrium-Naphthalid in THF) umgesetzt. Alle Experimente wurden in THF durchgeführt. Nach Reaktionszeiten von einer Stunde bis sechs Tagen wurde das Reduktionsmittel durch Filtration entfernt. Es wurde versucht, durch Überschichten mit *n*-Pentan, Reaktionsprodukte aus der Lösung auszukristallisieren. Um die Löslichkeit von **4-NO_2** und **5-NO_2** in THF zu erhöhen und somit eine vollständige Reduktion zu ermöglichen, wurden neutrale Donoren in Form von TMEDA (*N,N,N‘,N‘*-Tetramethylethylendiamin) und PMDTA (*N,N,N‘,N‘‘,N‘‘*-Pentamethyldiethylentriamin) sowie die Kronenether 15-Krone-5 und 18-Krone-6 zugegeben. In allen Versuchen konnten jedoch keine radikalischen oder dimeren Reduktionsprodukte isoliert werden. Die Zugabe der Kronenether führte lediglich zur Bildung der entsprechenden Kronenether-Komplexe **4-NO_2-(15K5)** und **5-NO_2-(18K6)**, welche mit Hilfe von NMR-Spektroskopie bzw. Einkristallröntgenstrukturanalyse identifiziert werden konnten.

3 Oxidationsexperimente der Alkalimetall-NO_2–ATI$^{iPr/iPr}$-Komplexe

Sowohl das Auftreten der irreversiblen Oxidationswelle im Cyclovoltammogramm von **4-NO_2**, als auch das freie ATI-Anion in der Struktur von **4-NO_2-(12K4)$_2$**, veranlasste zu einer Untersuchung des Verhaltens der Natrium-Verbindungen **4-NO_2**, **4-NO_2-(12K4)$_2$** und **4-NO_2-(15K5)** unter oxidativen Bedingungen. Hierfür wurden das starke Oxidationsmittel Nitrosylhexafluorantimonat(V), aber auch das mäßig starke Oxidationsmittel Silbertetrafluoroborat sowie milde Oxidationsmittel wie Ferroceniumchlorid ($[Fe(Cp)_2]Cl$), Tropylium-BAr^F ($[C_7H_7][BAr^F]$, $BAr^F = B(3,5\text{-}(CF_3)_2\text{-}C_6H_3)_4$)) und Tritylchlorid bzw. Trityltetrafluoroborat ($Ph_3CCl/[Ph_3C][BF_4]$) verwendet (Tabelle 7). Für alle Umsetzungen mit $NOSbF_6$ konnte ^{1}H-NMR-spektroskopisch lediglich der neutrale Ligand **1-NO_2** als Reaktionsprodukt identifiziert werden (Tabelle 7, Einträge I–V). Durch Röntgenstrukturanalyse von Einkristallen, welche aus einem Reaktionsansatz in Pyridin-*d*$_5$ gewonnen wurden, konnte außerdem die Bildung von $[Na(12\text{-Krone-}4)_2][SbF_6]$ unter diesen Bedingungen nachgewiesen werden (Tabelle 7, Eintrag II). Eine Verringerung der Reaktionstemperatur von Raumtemperatur auf bis zu −45° C sowie die Zugabe von Abfangreagenzien wie Si_2Me_6 oder Sn_2nBu_6 führte nicht zur Isolierung möglicher Radikalspezies oder anderer Oxidationsprodukte (Tabelle 7, Einträge I, IV, V). Durch die Verwendung milderer Oxidationsmittel konnte ebenfalls keine Isolierung von Radikalspezies ermöglicht werden. ^{1}H-NMR-spektroskopische Verfolgung der Reaktion von **4-NO_2** mit $AgBF_4$ zeigte die Entstehung einer neuen, ATI-haltigen Spezies an, welche durch

Kristallisation und röntgendiffraktometrische Untersuchung der erhaltenen Kristalle als [Ag(NO$_2$–ATI$^{iPr/iPr}$)(py)] (**6-NO$_2$-py**) identifiziert werden konnte (Tabelle 7, Eintrag VI, siehe Kapitel XV). Umsetzungen mit Ferroceniumchlorid sowie der Einsatz von TEMPO (2,2,6,6-Tetramethylpiperidinyloxyl) und Diphenylditellurid als Abfangreagenzien zeigten den Neutralliganden als einziges identifizierbares Produkt (Tabelle 7, Einträge VII, VIII). Für die Oxidation von **4-NO$_2$-(12K4)$_2$** mit Tropylium-BAr^F konnte ^{1}H-NMR-spektroskopisch zunächst die Bildung verschiedener Spezies beobachtet werden, wobei **1-NO$_2$** als Hauptprodukt identifiziert werden konnte. Nach 12 Stunden in Lösung konnte ausschließlich **1-NO$_2$** im ^{1}H-NMR-Spektrum detektiert werden, was auf eine geringe Stabilität der intermediär gebildeten Spezies hindeutet (Tabelle 7, Eintrag IX).

Tabelle 7: Übersicht der Oxidationsexperimente.

Eintrag	Reagenz	Oxidations-mittel	Reaktions-bedingungen	Abfang-reagenz	Produkt
I	**4-NO$_2$**	NOSbF$_6$	py-d_5	Si$_2$Me$_6$	**1-NO$_2$**
II	**4-NO$_2$-(12K4)$_2$**	NOSbF$_6$	py-d_5	-	**1-NO$_2$** + [Na(12-K-4)$_2$][SbF$_6$]
III	**4-NO$_2$-(12K4)$_2$**	NOSbF$_6$	C$_6$D$_6$	-	**1-NO$_2$**
IV	**4-NO$_2$-(12K4)$_2$**	NOSbF$_6$	MeCN, −45 °C	Sn$_2$*n*Bu$_6$	-
V	**4-NO$_2$-(15K5)**	NOSbF$_6$	MeCN, −21 °C	Si$_2$Me$_6$	**1-NO$_2$**
VI	**4-NO$_2$**	AgBF$_4$	py-d_5	-	**6-NO$_2$**
VII	**4-NO$_2$-(12K4)$_2$**	[FeCp$_2$]Cl	MeCN-d_3	Ph$_2$Te$_2$	**1-NO$_2$**
VIII	**4-NO$_2$-(12K4)$_2$**	[FeCp$_2$]Cl	THF	TEMPO	-
IX	**4-NO$_2$-(15K5)**	[C$_7$H$_7$][BAr^F]	THF-d_8	-	**1-NO$_2$**
X	**4-NO$_2$-(12K4)$_2$**	[Ph$_3$C][BF$_4$]	py-d_5	-	**1-NO$_2$** + **4-NO$_2$-Ph$_3$C-(12K4)$_2$**
XI	**4-NO$_2$-(12K4)$_2$**	Ph$_3$CCl	THF	-	**1-NO$_2$** + **4-NO$_2$-Ph$_3$C-(12K4)$_2$**

BAr^F = B(3,5-(CF$_3$)$_2$-C$_6$H$_3$)$_4$), py = Pyridin, TEMPO = 2,2,6,6-Tetramethylpiperidinyloxyl

Die NMR-spektroskopische Verfolgung der Umsetzung von **4-NO$_2$-(12K4)$_2$** mit Trityl-BF$_4$ in Pyridin-d_5 zeigte im ^{1}H-NMR-Spektrum Signale für **1-NO$_2$** sowie Signale einer weiteren, ATI-haltigen Spezies (Tabelle 7, Eintrag X). Aufgrund des Signalmusters kann auf eine im Rückgrat unsymmetrisch substituierte Verbindung geschlossen werden. Eine analoge Reaktion von **4-NO$_2$-(12K4)$_2$** mit Tritylchlorid in THF und anschließende Kristallisation mit *n*-Pentan lieferte Einkristalle zur Röntgenstrukturanalyse (Tabelle 7, Eintrag XI, Abbildung 25). Damit konnte die gebildete Spezies als [Na(12-Krone-4)$_2$][(3-Ph$_3$C–5-NO$_2$–ATI$^{iPr/iPr}$)] (**4-NO$_2$-Ph$_3$C-(12K4)$_2$**)

identifiziert werden. Das Tritylsalz fungiert somit nicht als Oxidationsmittel, sondern reagiert als Carbo-Kation in einer elektrophilen aromatischen Substitution mit dem ATI-Komplex (Schema 18).

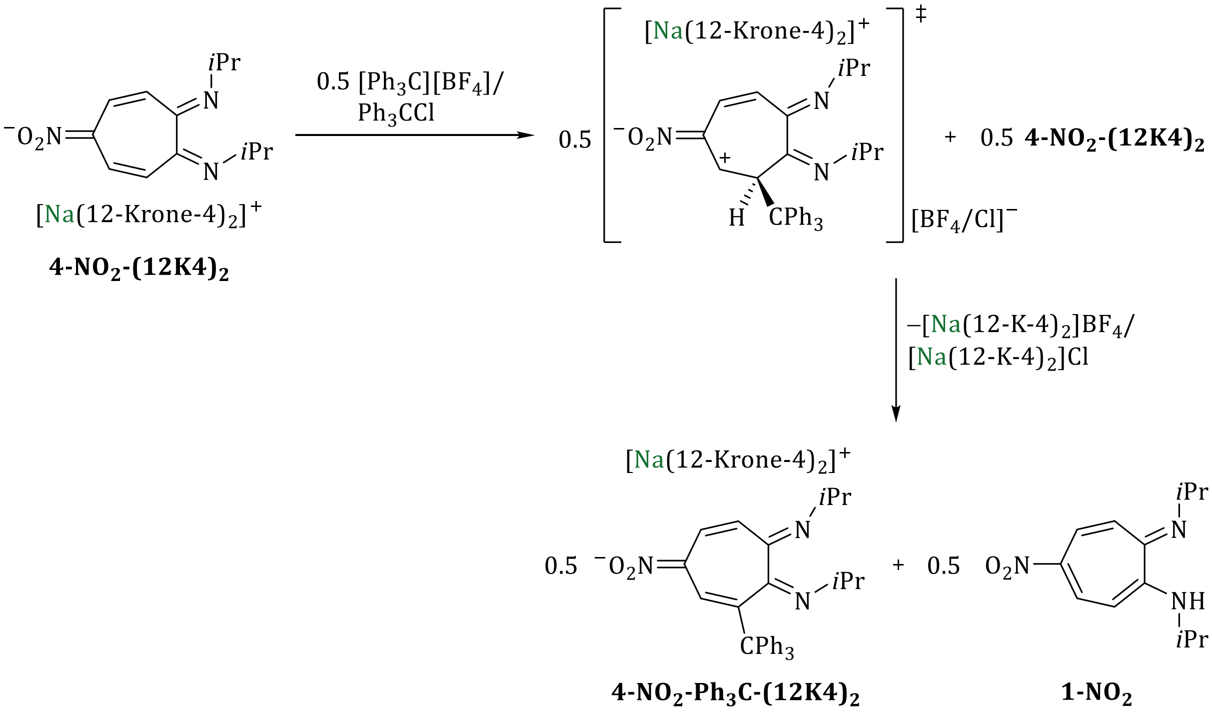

Schema 18: Elektrophile aromatische Substitution von **$4\text{-}NO_2\text{-}(12K4)_2$** unter Bildung von **$4\text{-}NO_2\text{-}Ph_3C\text{-}(12K4)_2$** und **$1\text{-}NO_2$**.

Die Einführung einer Triphenylmethyl-Gruppe in das ATI-Rückgrat konnte von der Gruppe um *Jordan* bei der Umsetzung von Gruppe 13 Metall-ATI-Komplexen $[M(ATI^{iPr/iPr})R_2]$ mit einem Tritylsalz beobachtet werden (M = Al–In, R = Alkyl).[65, 83] Dabei wird eine elektrophile Addition des Carbo-Kations an die C5-Position unter Bildung eines neutralen Diimin-Ligandgerüsts beobachtet (Schema 19). Eine Temperaturerhöhung (auf –30 bis –40 °C für M = Al bzw. auf 80 °C für M = Ga, In) führt allerdings zur Eliminierung von $RCPh_3$ (bzw. $HCPh_3$ und einem Olefin, wenn R β-H-Atome besitzt) und der Bildung eines im Rückgrat unsubstituierten kationischen ATI-Komplexes.

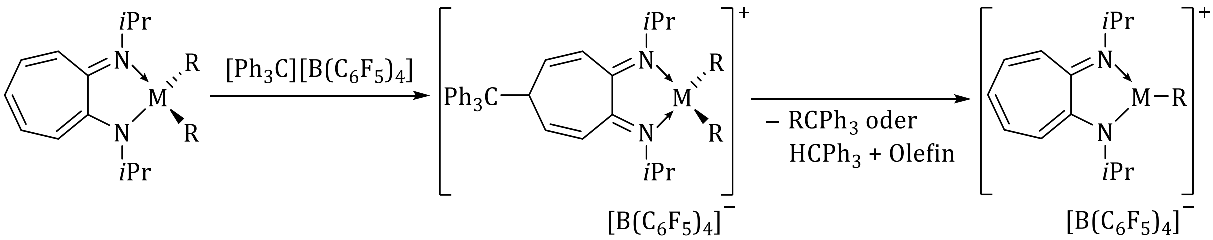

Schema 19: Kooperatives Verhalten des ATI-Liganden in Gruppe 13 Metall-Komplexen. M = Al–In, R = Me, Et, Pr, *i*Bu, Cyclohexyl, Benzyl.[83]

Im Gegensatz zu dem in der Literatur beobachteten, kooperativen Verhalten des ATI-Liganden, wird bei der Umsetzung von **4-NO_2-(12K4)$_2$** mit dem Trityl-Salz ein im Rückgrat triphenylmehtyl-substituierter Komplex erhalten. 0.5 Äquivalente des eingesetzten Kronenether-Komplexes fungieren im Reaktionsverlauf als Base, die zur Abstraktion des Protons am intermediär gebildeten, nicht detektierten σ-Komplex nötig ist. Dies führt zur Bildung des triphenylmethylierten Kronenetherkomplexes **4-NO_2-Ph_3C-(12K4)$_2$** sowie des protonierten Ligand **1-NO_2** (Tabelle 7, Eintrag IX; Schema 18). Prinzipiell wäre auch ein radikalischer Reaktionspfad denkbar, in welchem zuerst ein Elektron vom ATI-Liganden auf das Tritylsalz übertragen wird und anschließend durch Radikalrekombination der σ-Komplex generiert wird.

4-NO_2-Ph_3C-(12K4)$_2$ kristallisiert in der monoklinen Raumgruppe $P2_1/n$ (Z = 4, Abbildung 25). Analog zur Struktur des Edukts **4-NO_2-(12K4)$_2$** liegt der substituierte ATI-Ligand als freies Komplex-Anion vor, das keine gerichtete Bindungswechselwirkung zum Komplex-Kation eingeht. Das Natriumatom ist durch zwei Kronenethermoleküle verzerrt antiprismatisch koordiniert. Die N1/2−C1/2 Bindungslängen liegen mit 1.27−1.29 Å im gleichen Bereich wie die des Edukts, die N3−C5 Bindung ist mit 1.38 Å im Vergleich leicht verkürzt (**4-NO_2-(12K4)$_2$**: N3−C5, 1.40 Å). Auch die maximale Bindungslängendifferenz zweier benachbarter C−C Bindungen ist geringfügig höher (Δ_{max}(C−C): 0.15 Å, **4-NO_2-(12K4)$_2$**: Δ_{max}(C−C): 0.12 Å) und die Abwinkelung aus der Ebene mit 45.0° stärker (**4-NO_2-(12K4)$_2$**: [C1−C7]−[C1−2,N1−2], 41.7°) als in der Ausgangsverbindung. Die Verschiebung der π-Elektronendichte in Richtung der Nitro-Gruppe wird somit durch den +I-Effekt des Triphenylmethyl-Substituenten begünstigt. Außerdem kann angenommen werden, dass die starke Verdrehung des ATI-Gerüsts zusätzlich durch die räumliche Nähe des sterisch anspruchsvollen Trityl-Substituenten zur *Iso*propyl-Gruppe bedingt ist.

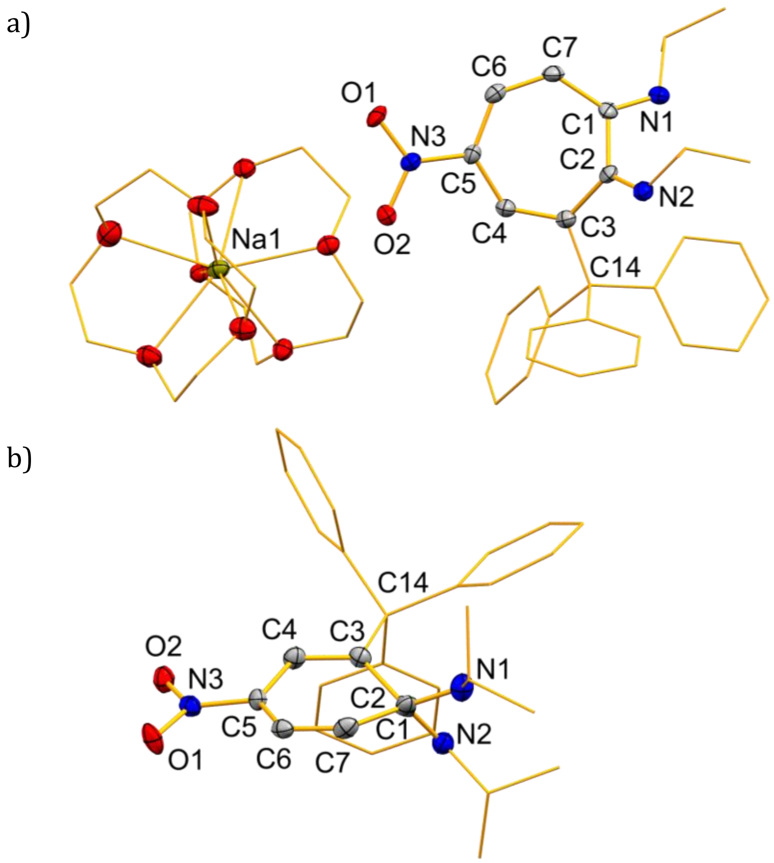

Abbildung 25: a) Struktur von [Na(12-Krone-4)$_2$][(3-Ph$_3$C–5-NO$_2$–ATI$^{iPr/iPr}$)] (**4-NO$_2$-Ph$_3$C-(12K4)$_2$**) im Festkörper in der Draufsicht. b) Struktur von **4-NO$_2$-Ph$_3$C-(12K4)$_2$** mit Blickrichtung entlang der C1–C2-Bindung liegend. Die Ellipsoide repräsentieren 50% der Aufenthaltswahrscheinlichkeit. Wasserstoffatome und [Na(12-Krone-4)$_2$]$^+$ in b) wurden aus Gründen der Übersichtlichkeit nicht abgebildet. Die Ethyleneinheiten des Kronenethers, die Kohlenstoffatome der *Iso*propyl-Reste und der Triphenylmethyl-Einheit sind im Drahtmodell dargestellt. Ausgewählte Bindungslängen (Å) und -winkel (°): N1–C1, 1.290(3); N2–C2, 1.273(3); N3–C5, 1.375(3); N3–O1, 1.280(2); N3–O2, 1.279(2); C1–C2, 1.520(3); C2–C3, 1.493(3); C3–C4, 1.341(3); C4–C5, 1.446(3); C5–C6, 1.422(3); C6–C7, 1.353(3); C1–C7, 1.454(3).

Die gezielte Oxidation der Natrium-ATI-Komplexe zu isolierbaren Radikalspezies oder Dimerisierungsprodukten war unter den gewählten Bedingungen sowie unter Verwendung der genannten Oxidationsmittel nicht möglich. Dabei könnte die mangelnde Stabilität radikalischer Spezies ein limitierender Faktor sein. Außerdem scheinen alternative Reaktionspfade wie eine Salzeliminierung sowie eine elektrophile aromatische Substitution bevorzugt abzulaufen.

XV Synthese und Struktur monometallischer Silber- und heterobimetallischer Alkalimetall-Argentat-ATI-Komplexe

1 [Ag(NO_2–ATI$^{iPr/iPr}$)]

1.1 Synthese

Da die Umsetzung des Natrium-Komplexes **4-NO_2** mit Silbertetrafluoroborat nicht zu einer Oxidation sondern über eine Salzeliminierung zur Bildung des ersten Silber-ATI-Komplexes [Ag(NO_2–ATI$^{iPr/iPr}$)] (**6-NO_2**) führte, wurde diese Route genutzt, um den Silber-Komplex gezielt herzustellen (Schema 20).

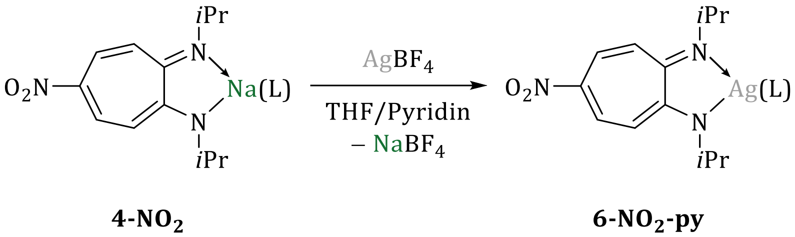

Schema 20: Synthese von [Ag(NO_2–ATI$^{iPr/iPr}$)(L)] (**6-NO_2-(L)**) in THF/Pyridin. L = Et_2O, THF, Pyridin.

Dabei wurde ein Äquivalent Pyridin zu einer THF-Reaktionslösung zugegeben, oder Pyridin als Lösungsmittel verwendet, um eine ausreichende Löslichkeit des Edukts, sowie eine ausreichende Stabilität des Silber-Komplexes zu gewährleisten. Trotz quantitativer Umsetzung zum gewünschten Komplex konnte dieser nicht analysenrein erhalten werden, da auch mehrmaliges Umkristallisieren nicht ausreichte, um während der Reaktion gebildetes $NaBF_4$ zu entfernen. **6-NO_2-py** zeigt im ^{1}H-NMR-Spektrum einen Signalsatz von Protonen, der einer C_{2v}-symmetrischen Verbindung zugeordnet werden kann, welche über mehrere Tage in Lösung stabil ist. Eine Isomerisierung, wie sie für **4-NO_2** gefunden wird, kann nicht beobachtet werden. Eine Koordination über die Nitro-Gruppe kann mit Hilfe NMR-spektroskopischer Methoden nicht aufgelöst und deshalb nicht ausgeschlossen werden. Im Hinblick auf den weichen Charakter des Silberatoms scheint allerdings eine Koordination über die Stickstoffatome plausibel.[84]

1.2 Struktur

Die Struktur von [Ag(NO_2–ATI$^{iPr/iPr}$)] im Festköper konnte durch Einkristallröntgenstrukturanalyse aufgeklärt werden. Hierfür wurden Kristalle durch Grenzphasendiffusion von *n*-Pentan in eine Lösung von **6-NO_2** in Pyridin gewonnen. **6-NO_2-py** kristallisiert in der triklinen Raumgruppe $P\bar{1}$ mit $Z = 2$ (Abbildung 26).

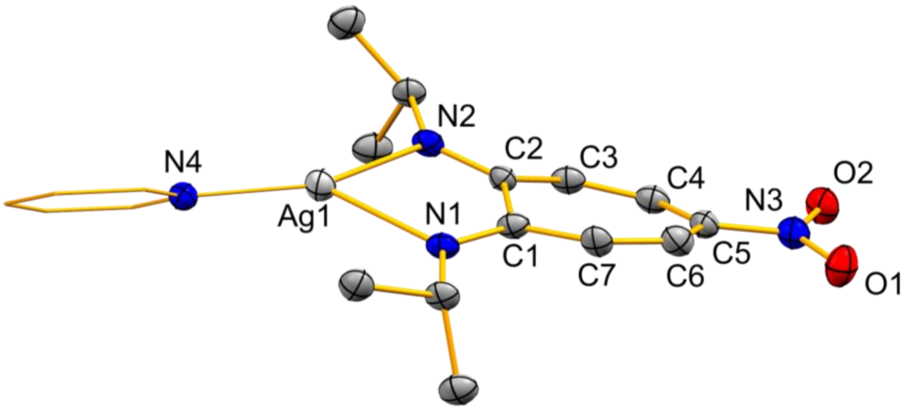

Abbildung 26: Struktur von [Ag(NO_2–ATI$^{iPr/iPr}$)(py)] (**6-NO$_2$-py**) im Festkörper. Die Ellipsoide repräsentieren 50% der Aufenthaltswahrscheinlichkeit. Wasserstoffatome wurden aus Gründen der Übersichtlichkeit nicht abgebildet. Die Kohlenstoffatome des Pyridin-Liganden sind im Drahtmodell dargestellt. Ausgewählte Bindungslängen (Å) und -winkel (°): Ag1–N1, 2.273(3); Ag1–N2, 2.249(3); Ag1–N4, 2.165(3); N1–C1, 1.294(5); N2–C2, 1.303(5); N3–C5, 1.425(5); N3–O1, 1.241(5); N3–O2, 1.257(5); C1–C2, 1.536(5); C2–C3, 1.445(5); C3–C4, 1.356(6); C4–C5, 1.399(6); C5–C6, 1.410(6); C6–C7, 1.360(6); C1–C7, 1.451(6); N1–Ag1–N2, 71.99(2); N(1/2)–Ag1–N4, 140.13(12)–145.71(13).

6-NO$_2$-py zeigt den für ATI-Komplexe am häufigsten gefundenen κ^2*N*-Koodrdinationsmodus. Das Silberatom ist durch Koordination an die ATI-Bindungstasche sowie durch die Koordination eines Pyridin-Moleküls verzerrt trigonal-planar koordiniert. Die Verzerrung ist durch den Bisswinkel der ATI-Bindungstasche bedingt (N1–Ag1–N2, 72°). Die Ag–N Bindungslängen liegen mit 2.17–2.27 Å in einem ähnlichen Bereich wie analoge Bindungen in strukturell verwandten Pyridylpyrrolid-[85] und 2,2'-Bipyridin-Silber-Komplexen[86] sowie Silber-β-diketaminaten,[87] in welchen das Silberatom dreifach koordiniert vorliegt. Im Vergleich zu den Alkalimetall-Komplexen deuten die Bindungsparameter des Liganden auf eine geringere Verschiebung der π-Elektronendichte in Richtung der Nitro-Gruppe hin. Die N3–C5 Bindung hat mit einer Länge von 1.43 Å eher Einfachbindungscharakter (Alkalimetall-ATI-Komplexe: N3–C5, 1.37–1.40 Å) und auch die maximale Bindungslängendifferenz zweier benachbarter C–C-Bindungen ist für **6-NO$_2$-py** ein wenig geringer (Δ_{max}(C–C), 0.10 Å) als in den Alkali-Metall-Derivaten (Δ_{max}(C–C), 0.11–0.13 Å). Die gesteigerte Delokalisierung der π-Elektronen spiegelt sich auch in der weniger ausgeprägten Abwinkelung der [C1–2,N1–2,Ag]-Ebene gegenüber der [C1–7]-Ebene wider (17.1°). Literaturbeispiele für Silber enthaltende ATI-Komplexe sind selten und beschränken sich auf Germanium- und Zinn-Komplexe [M(ATI$^{R/R}$)X][Ag(HB(3,5-(CF_3Pz)$_3$] (M = Ge, Sn; X = Cl, I, N_3, O_3SCF_3; R = Me, *n*Pr; HB(3,5-(CF_3Pz)$_3$ = Hydrotris(3,5-bis(trifluoromethyl)pyrazolyl)borat),[78a, 88] sowie thio- und selenogermanonkoordinierte Silber-Komplexe [(Ph–EGe(ATI$^{tBu/tBu}$)(AgI)]$_2$ (E = S, Se; Schema 21).[89] Der ATI-Ligand koordiniert in all diesen Beispielen nicht an das Silberatom, sondern es kommt zur Ausbildung von Ge/Sn-Silber-Bindungen, bzw. Adduktbildung mit Ge=E→AgI Einheiten.

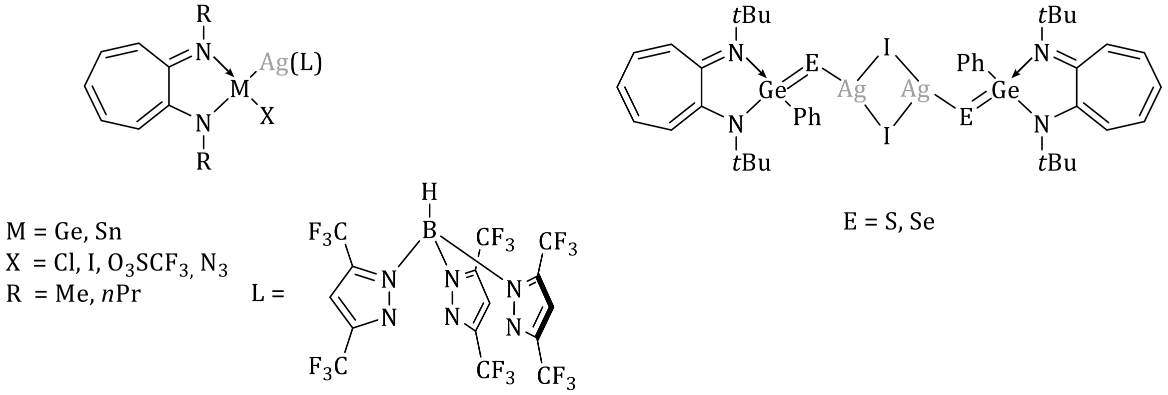

Schema 21: Literaturbekannte Silber enthaltende ATI-Komplexe.

6-NO₂ ist somit der erste Vertreter eines Silber-ATI-Komplexes, in dem das Silberatom als Zentralmetall durch die *N*,*N*-Bindungstasche koordiniert wird. Die Ausbildung einer polymeren Struktur durch Koordination des Metall-Atoms an die Nitro-Gruppe einer benachbarten Monomereinheit, wie sie bei den Alkalimetall-Komplexen gefunden wurde, wird nicht beobachtet. Der strukturell verwandte, nitro-substituierte β-Diketiminat-Komplex $[Ag(NO_2{-}C(CHN(Dipp))_2]$ (Dipp = Di*iso*propylphenyl) dagegen bildet im Festkörper eine lineare, über Ag–O-Wechselwirkungen verknüpfte, polymere Struktur aus (Abbildung 27).[87b] DFT-Rechnungen zur Bildung von Lewis-Säure-Base-Addukten von AgCl und ungesättigten Aldehyden und Iminen konnten zeigen, dass eine Koordination des Silberatoms an das Stickstoffatom günstiger ist als an das Sauerstoffatom.[90] Ähnlich dazu könnte bei der Kristallisation von **6-NO₂-py** die Koordination von Pyridin als Stickstoffdonor in Konkurrenz zur Nitro-Gruppe bevorzugt sein.

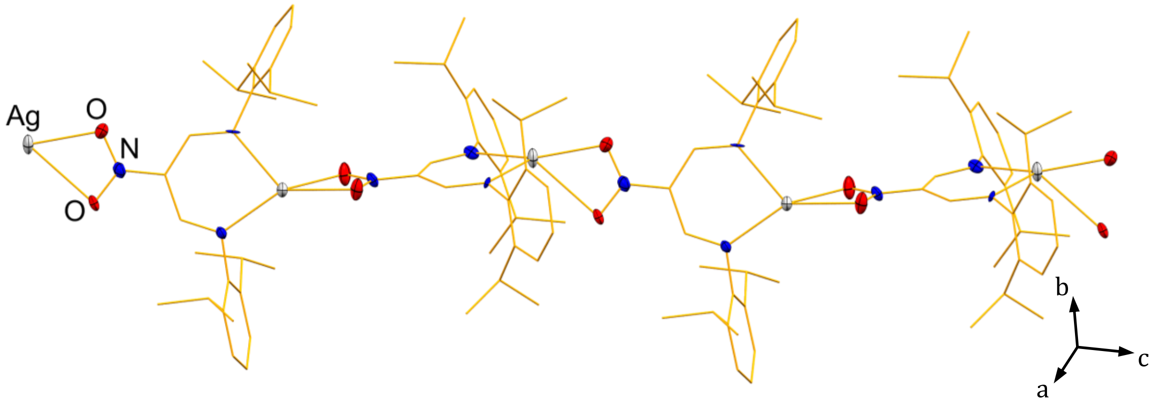

Abbildung 27: Literaturbekanntes, lineares Koordinationspolymer von $[Ag(NO_2{-}C(CHN(Dipp))_2]$ (Dipp = Di*iso*propylphenyl) im Festkörper, welches als Vergleich zur Monomer-Struktur von **6-NO₂-py** dient.[87b]

2 [Na(Krone)][Ag(NO_2–ATI$^{iPr/iPr}$)$_2$]

2.1 Synthese

Analog zur zuvor beschriebenen Synthese des ersten Silber-ATI-Komplexes wurden je zwei Äquivalente der Natrium-Kronenether-Komplexe **4-NO_2-(12K4)$_2$** und **4-NO_2-(15K5)** mit $AgBF_4$ umgesetzt. Es konnte die Bildung von heterobimetallischen Natrium-Argentat-Komplexen beobachtet werden (Schema 22).

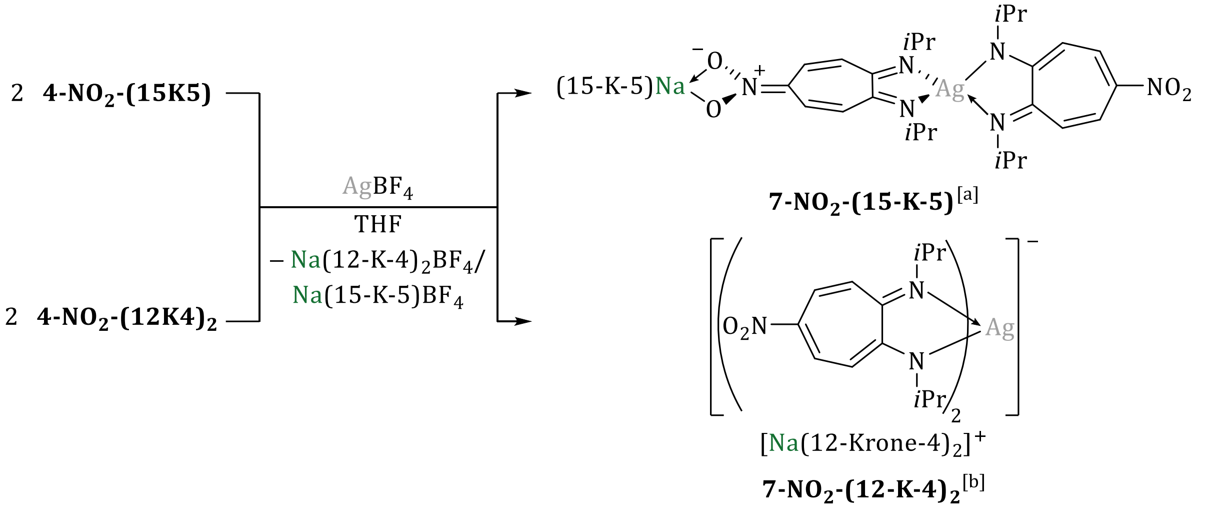

Schema 22: Synthese der Komplexe [Na(15-Krone-5)Ag(NO_2–ATI$^{iPr/iPr}$)$_2$] (**7-NO_2-(15K5)**) und [Na(12-Krone-4)$_2$][NO_2–Ag(ATI$^{iPr/iPr}$)$_2$] (**7-NO_2-(12K4)$_2$**), [a] Rohausbeute, die isolierte Verbindung enthält eine nicht quantifizierte Menge [Na(15-Krone-5)][BF_4]; [b] die isolierte Verbindung enthält 0.9mol% [Na(12-Krone-4)$_2$][BF_4].

Um die während der Reaktion entstandenen Natrium-Kronenether-Boratsalze zu entfernen, wurden auch die Kronenether-Verbindungen mehrfach umkristallisiert. Die Verbindungen konnten jedoch nicht analysenrein erhalten werden. Quantifizierung mittels ^{19}F-NMR-Spektroskopie unter Verwendung von K[BF(CN)$_3$] als internem Standard zeigte, dass die isolierte Charge von **7-NO_2-(12K4)$_2$** 0.9mol% [Na(12-Krone-4)$_2$][BF_4] enthält. Eine ^{1}H- und ^{13}C-NMR-spektroskopische Charakterisierung der isolierten Chargen für die Argentat-Komplexe zeigte in Analogie zum monometallischen Silber-Komplex **6-NO_2** für beide Verbindungen je einen Satz an Resonanzen sowohl im ^{1}H- als auch im ^{13}C-NMR-Spektrum. Es konnten keine Signale detektiert werden, die auf eine *E,Z*-Isomerisierung hindeuten. Die Bildung von Natrium-Natriat-Komplexen wird für die im Rückgrat unsubstituierten Komplexe [Na(ATI$^{R/R}$)(L)] (R = *i*Pr, Ph, L = thf) bereits bei Zugabe von 12-Krone-4 zum monometallischen Alkalimetall-Komplex beobachtet.[63] Aufgrund der veränderten elektronischen Struktur des Liganden durch die Verschiebung der π-Elektronendichte in Richtung der Nitro-Gruppe, sowie ihre Funktion als zusätzliche Koordinationsstelle, wird für den nitro-substituierten Natriumkomplex **4-NO_2** die

Bildung einkerniger monometallischer Kronenether-Komplexe beobachtet (siehe Kapitel XII, 2). Die Zugabe des Silbersalzes initiiert schließlich eine Koordination zweier ATI-Liganden über die *N*,*N*-Bindungstasche an das weiche Silberatom.

2.2 Struktur

Durch Kristallisation aus THF/*n*-Pentan Lösungsmittel-Systemen konnten für die Komplexe **7-NO_2-(15K5)** und **7-NO_2-(12K4)$_2$** die Strukturen im Festkörper mit Hilfe von Einkristallröntgenstrukturanalyse bestimmt werden. **7-NO_2-(15K5)** kristallisiert in der triklinen Raumgruppe $P\bar{1}$ mit $Z = 2$ (Abbildung 28) und **7-NO_2-(12K4)$_2$** in der monoklinen Raumgruppe $P2_1/n$ mit $Z = 4$ (Abbildung 29).

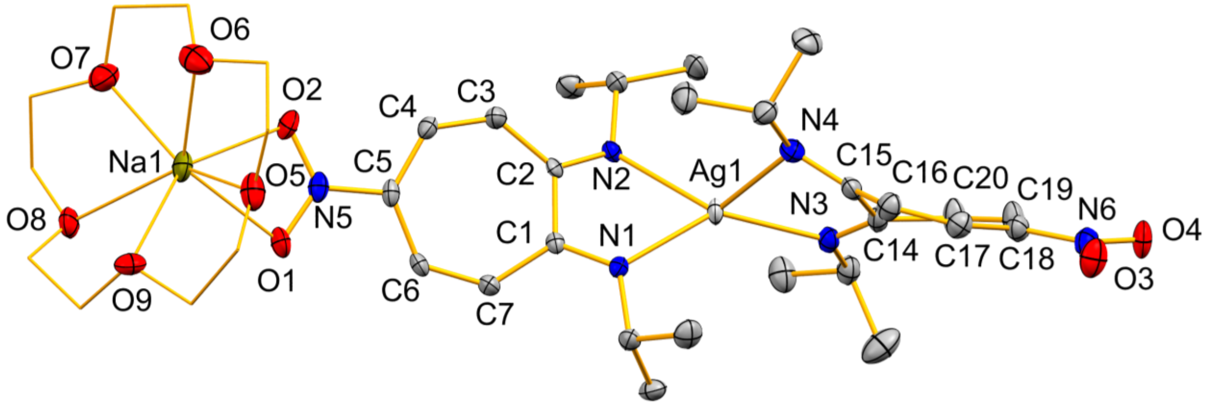

Abbildung 28: Struktur von [Na(15-Krone-5)Ag(NO_2–ATI$^{iPr/iPr}$)$_2$] (**7-NO_2-(15K5)**) im Festkörper. Die Ellipsoide repräsentieren 50% der Aufenthaltswahrscheinlichkeit. Wasserstoffatome und ein in der Elementarzelle enthaltenes Pyridin-Molekül wurden aus Gründen der Übersichtlichkeit nicht abgebildet. Die Kohlenstoffatome der Ethyleneinheiten des Kronenether-Moleküls sind im Drahtmodell dargestellt. Ausgewählte Bindungslängen (Å) und -winkel (°): Ag1–N1, 2.284(3); Ag1–N2, 2.297(2); Ag1–N3, 2.211(3); Ag1–N4, 2.437(3); Na1–O1, 2.477(3); Na1–O2, 2.399(3); Na1–(O5–O9), 2.341(6)–2.526(5); N1–C1, 1.295(3); N2–C2, 1.297(4); N3–C14, 1.303(4); N4–C15, 1.303(4); N5–C5, 1.387(4); N6–C18, 1.400(4); C1–C2, 1.521(4); C2–C3, 1.449(4); C3–C4, 1.361(4); C4–C5, 1.414(4); C5–C6, 1.427(4); C6–C7, 1.357(4); C1–C7, 1.456(4); C14–C15, 1.518(5); C15–C16, 1.458(4); C16–C17, 1.365(4); C17–C18, 1.407(5); C18–C19, 1.412(5); C19–C20, 1.364(4); C20–C14, 1.450(4); N1–Ag1–N2, 71.80(9); N3–Ag1–N4, 72.69(10); N(1/2)–Ag1–(N3/4), 111.81(10)–147.22(10).

Die Silberatome liegen durch Koordination zweier ATI-Liganden über die *N*,*N*-Bindungstasche in beiden Komplexen vierfach koordiniert vor und sind aufgrund des kleinen Bisswinkels das ATI-Liganden (**7-NO_2-(15K5)**: N1/3–Ag1–N2/4, 71.80(9)–72.69(10); **7-NO_2-(12K4)$_2$** N1/3–Ag1–N2/4, 71.31(9)–71.58(8)) verzerrt tetraedrisch umgeben. Im Unterschied zu **7-NO_2-(12K4)$_2$**, in dem keine gerichtete Bindungswechselwirkung zwischen dem Komplex-Kation und -Anion vorliegt, koordiniert in **7-NO_2-(15K5)** die [Na(15-Krone-5)]$^+$-Einheit an die

Nitro-Gruppe eines Liganden. Die Ag–N Bindungslängen liegen mit 2.21 bis 2.44 Å in einem ähnlichen Bereich wie die analogen Bindungen in Silber-Komplexen mit Stickstoff-Donorliganden und einer Koordinationszahl von vier für die Silberatome.[91]

Tabelle 8: Bindungsparameter der Kronenether-Komplexe **7-NO$_2$-(15K5)** und **7-NO$_2$-(12K4)$_2$**.

Bindungsparameter [Å]bzw. [°]	**7-NO$_2$-(15K5)**	**7-NO$_2$-(12K4)$_2$**
N1–C1/ N2–C2	1.295(3)/ 1.297(4)	1.299(4)/ 1.296(4)
N3–C14/ N4–C15	1.303(4)/ 1.303(4)	1.292(4)/ 1.303(4)
N5–C5/ N6–C18	1.387(4)/ 1.400(4)	1.407(4)/ 1.403(4)
Δ_{max}(C–C)	0.10	0.09
[C1–C7]–[C1–2,N1–2,Ag1]	26.3	24.0
[C14–C20]–[C14–15,N3–4,Ag1]	31.5	26.2
θ (C4–C5, N5–O1/2)	0.2(4)	5.4(4)
θ (C17–C18, N6–O3)	7.0(5)	7.0(4)

Im Vergleich zum monometallischen einkernigen Komplex **6-NO$_2$-py** (Ag–N^{ATI}, 2.25–2.27 Å) sind die Ag–N Bindungen leicht verlängert, was auf die höhere Koordinationszahl des Silberatoms sowie die negative Ladung der [Ag(NO$_2$–ATI$^{iPr/iPr}$)$_2$]$^-$-Einheit in den heterobimetallischen Komplexen zurückgeführt werden kann. Dabei zeigt sich in **7-NO$_2$-(15K5)** ein deutlicher Unterschied der Ag–N Bindungslängen der jeweiligen Liganden zueinander. Für den an der Nitro-Gruppe durch die [Na(15-Krone-5)]$^+$-Einheit koordinierten ATI-Liganden sind die Bindungslängen im Rahmen der Fehlergrenzen identisch (Ag–N, 2.30 Å). Für den ATI-Liganden mit der freien Nitro-Gruppe unterscheiden sich die Bindungslängen dagegen deutlich (Ag–N, 2.21–2.44 Å). Dies wirkt sich allerdings nicht auf die N–C Bindungslängen aus. Betrachtet man die N3/4–C14/15 Bindungslängen, sind diese identisch, sowohl zueinander als auch im Vergleich zu den N1/2–C1/2 Bindungslängen des [Na(15-Krone-5)(NO$_2$–ATI$^{iPr/iPr}$)]-Fragments (Tabelle 8). Die N5/6–C5/18 Bindungslängen des ATI-Rückgrats zur Nitro-Gruppe sind im Rahmen der Fehlergrenzen ebenfalls für beide Fragmente identisch und besitzen partiellen Doppelbindungscharakter. Diese Befunde deuten auf eine analoge elektronische Struktur beider Liganden hin. Die Unterschiede in den Ag–N Bindungslängen scheinen somit auf sterische Effekte zurückzuführen zu sein. Die Verdrehung des ATI-Gerüsts, welche anhand des Winkels zwischen der Ebene des ATI-Rückgrats ([C1–C7]) zur Ebene [C1–C2,N1–N2,Ag] quantifiziert wird, ist vermutlich aufgrund von Packungseffekten für den Liganden ohne zusätzliche Koordination über die Nitro-Gruppe größer, als für den Liganden mit zusätzlicher Koordination (Tabelle 8).

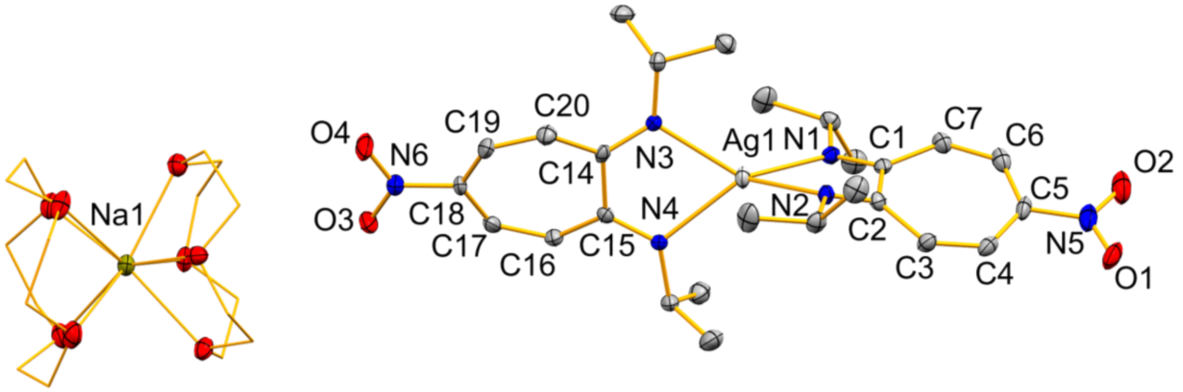

Abbildung 29: Struktur von $[Na(12\text{-Krone-}4)_2][Ag(NO_2\text{–}ATI^{iPr/iPr})_2]$ (**7-NO$_2$-(12K4)$_2$**) im Festkörper. Die Ellipsoide repräsentieren 50% der Aufenthaltswahrscheinlichkeit. Wasserstoffatome wurden aus Gründen der Übersichtlichkeit nicht abgebildet. Die Kohlenstoffatome der Ethyleneinheiten der Kronenether-Moleküle sind im Drahtmodell dargestellt. Ausgewählte Bindungslängen (Å) und -winkel (°): Ag1–N1, 2.261(3); Ag1–N2, 2.344(2); Ag1–N3, 2.304(2); Ag1–N4, 2.299(3); N1–C1, 1.299(4); N2–C2, 1.296(4); N3–C14, 1.292(4); N4–C15, 1.303(4); N5–C5, 1.407(4); N6–C18, 1.403(4); C1–C2, 1.526(4); C2–C3, 1.446(4); C3–C4, 1.360(4); C4–C5, 1.404(4); C5–C6, 1.411(4); C6–C7, 1.358(4); C1–C7, 1.454(4); C14–C15, 1.513(4); C15–C16, 1.444(4); C16–C17, 1.366(4); C17–C18, 1.408(4); C18–C19, 1.409(4); C19–C20, 1.360(4); C20–C14, 1.451(4); N1–Ag1–N2, 71.58(8); N3–Ag1–N4, 71.31(9); N(1/2)–Ag1–(N3/4), 125.13(8)–137.86(9).

In **7-NO$_2$-(12K4)$_2$** unterscheiden sich die Ag1–N1/2 Bindungslängen deutlich (2.26–2.34 Å), wohingegen die Ag1–N3/4 Bindungslängen des anderen ATI-Liganden im Rahmen der Fehlergrenzen identisch sind (2.30 Å). Da hier keine Koordination über die Nitro-Gruppe stattfindet, unterstützt dies die Vermutung, dass die Ag–N Bindungslängen durch sterische Faktoren beeinflusst werden. Bindungsparameter wie die N–C Bindungslängen, die maximale Bindungslängendifferenz zweier benachbarter C–C Bindungen sowie die Winkel für die Verdrehung aus der Ebene beider ATI-Liganden unterscheiden sich für **7-NO$_2$-(15K5)** und **7-NO$_2$-(12K4)$_2$** nicht, beziehungsweise nur gering (Tabelle 8). Die Torsionswinkel der Nitro-Gruppen liegen in beiden Argentat-Komplexen in einem ähnlichen Bereich wie die für die Vorläuferkomplexe (0.0–7.7°, Tabelle 8). Aufgrund ihres möglichen Einsatzes in Kreuzkupplungsreaktionen fanden Organoargentate Aufmerksamkeit in der Literatur.[92] Außerdem konnte kürzlich gezeigt werden, dass sich das Lithium-bis(amido)argentat-Derivat $[(TMP)_2Ag(CN)Li_2]$ (TMP = 2,2,6,6-Tetramethylpiperidido) als Base für die direkte *ortho*-Argentierung von (Hetero)-Arenen eignen.[93] In der Literatur beschriebene Natrium-Argentat-Verbindungen sind beispielsweise Cyanoargentate,[94] Nitroargentate[95] sowie Amidoargentate.[96] Die Komplexe **7-NO$_2$-(12K4)$_2$** und **7-NO$_2$-(15K5)** sind die ersten strukturell charakterisierten Natrium-Argentat-ATI-Komplexe.

XVI Elektrophile aromatische Substitution an Natrium-ATI-Komplexen

1 Synthese von Ph$_3$C-substituierten ATI-Komplexen

Funktionalisierungen der C5-Position im ATI-Rückgrat sind über eine elektrophile aromatische Substitution am protonierten Liganden möglich und führten zu einer Vielzahl von Aminotroponiminen.[70, 97] Durch weitere Umsetzung des C5-Brom-substituierten Liganden in einer nukleophilen aromatischen Substitution konnte die Bibliothek der rückgartsubstituierten ATI-Liganden zusätzlich erweitert werden.[70] Die Übertragung eines sterisch anspruchsvollen Triphenylmethyl-Rests durch Umsetzung des 5-Nitro–ATI-Komplexes **4-NO$_2$-(12K4)$_2$** mit Ph$_3$CCl beschreibt die erste direkte elektrophile aromatische Substitution an einem ATI-Komplex (siehe Kapitel XIV, 3). Um eine Allgemeingültigkeit dieses Reaktionsverhaltens für ATI-Komplexe zu überprüfen und so einen Zugang zu weiteren funktionalisierten Verbindungen zu ermöglichen, wurde dieser Reaktionspfad weiter untersucht. Da zur Abstraktion eines Protons aus dem intermediär gebildeten σ-Komplex eine Base nötig ist, wurden in den gezielten Syntheseversuchen triphenylmethyl-substituierter Natrium-ATI-Komplexe die Natrium-Basen NaH oder NaHMDS eingesetzt. NMR-spektroskopische Verfolgung der Umsetzung der bereits in C5-Postition substituierten Komplexe [Na(12-Krone-4)$_2$][(NO$_2$–ATI$^{iPr/iPr}$)] (**4-NO$_2$-(12K4)$_2$**) und [Na(Ph(O)C–ATI$^{iPr/iPr}$)] (**4-Ph(O)C**) mit Ph$_3$CCl zeigte nach drei Tagen einen vollständigen Umsatz zu substituierten Produkten an (Schema 23).

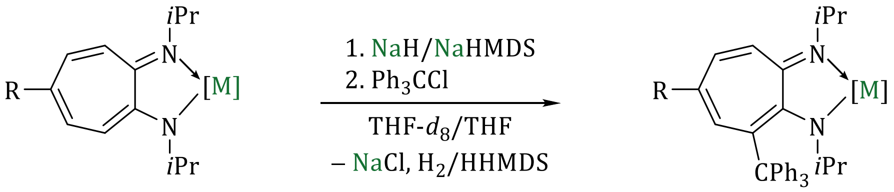

[M] = Na, Na(12-Krone-4)$_2$
R = NO$_2$, Ph(O)C

[M] = Na(12-Krone-4)$_2$, R = NO$_2$ **4-NO$_2$-Ph$_3$C-(12K4)$_2$** 18%[a]
[M] = Na, R = Ph(O)C **4-Ph(O)C-Ph$_3$C** n.b.

Schema 23: Synthese der rückgratsubstituierten Komplexe [Na(12-Krone-4)$_2$][(3-Ph$_3$C–5-NO$_2$–ATI$^{iPr/iPr}$)] (**4-NO$_2$-Ph$_3$C-(12K4)$_2$**) und [Na(3-Ph$_3$C–5-Ph(O)C–ATI$^{iPr/iPr}$)] (**4-Ph(O)C-Ph$_3$C**). [a] Isolierte Ausbeute. ^{1}H-NMR-spektroskopische Reaktionskontrolle zeigte für Umsetzungen im NMR-Maßstab quantitativen Umsatz an.

Die ^{1}H-NMR-Spektren von **4-Ph(O)C-Ph$_3$C** und **4-NO$_2$-Ph$_3$C-(12K4)$_2$** zeigen die erwarteten Resonanzen. Der Aufbruch der C_{2v}-Symmetrie wird durch die Detektion von zwei (**4-NO$_2$-Ph$_3$C-(12K4)$_2$**) bzw. vier Signalen (**4-Ph(O)C-Ph$_3$C**) für die CH$_3$- sowie von je zwei Signalen für die CH-Protonen der *Iso*propyl-Reste und von drei Signalen für die CH-Protonen des

ATI-Rückgrats deutlich. Aus dem Versuchsansatz zur Synthese von **4-Ph(O)C-Ph_3C** im NMR-Maßstab konnten zudem Einkristalle zur Röntgenstrukturanalyse gewonnen werden, welche die Bildung der gewünschten Verbindung ebenfalls bestätigen (siehe Kapitel XVI, 2). Versuche, die Rückgratsubstitutionen in größerem Maßstab in THF zu wiederholen, führten für die Ph(O)C-Spezies lediglich zur Reisolation des Edukts **4-Ph(O)C**. Es wird angenommen, dass hier eine zu kurze Reaktionszeit zu einem unvollständigen Umsatz geführt hat. Da für die Zielverbindung außerdem eine bessere Löslichkeit in weniger stark polaren Lösungsmitteln erwartet wird als für das Edukt, könnte diese beim Waschen des Rohprodukts mit Toluol und Et_2O entfernt worden sein. ^{1}H-NMR-spektroskopische Untersuchungen der Waschlösung waren jedoch aufgrund der geringen Menge des untersuchten Materials nicht aussagekräftig. **4-NO_2-Ph_3C-(12K4)$_2$** konnte in geringen Ausbeuten von 18% synthetisiert werden. Auch hier könnte die partielle Löslichkeit der Zielverbindung in zum Waschen verwendetem Et_2O zu Ausbeuteverlusten geführt haben.

Um Aussagen darüber treffen zu können, ob eine elektrophile aromatische Substitution mit Tritylchlorid durch die bereits veränderte Elektronik des ATI-Liganden in Form der Rückgratsubstituenten in C5-Position ermöglicht wird, wurde auch der im Rückgrat unsubstituierte Natrium-Komplex $[Na(ATI^{iPr/iPr})]$ untersucht. Dafür wurde der Neutralligand **1** *in situ* zum entsprechenden Natrium-Komplex umgesetzt und ein bzw. drei Äquivalente Tritylchlorid zugegeben (Schema 24).

1

x = 2; y = 1; R^1 = Ph_3C; R^2 = H **4-Ph_3C** n = 1.4 73%

x = 4; y = 3; R^1, R^2 = Ph_3C **4-(Ph_3C)$_2$** n = 2.8 30%

Schema 24: Synthese der Komplexe $[Na(Ph_3C–ATI^{iPr/iPr})]$ (**4-Ph_3C**) und $[Na(3,5\text{-bis}(Ph_3C)–ATI^{iPr/iPr})]$ (**4-(Ph_3C)$_2$**).

Der Komplex $[Na(Ph_3C–ATI^{iPr/iPr})]$ (**4-Ph_3C**) wurde in guten Ausbeuten isoliert. Die NMR-spektroskopische Charakterisierung steht mit der Bildung eines in C5-Position substituierten Komplexes in Einklang. Die Umsetzung mit drei Äquivalenten führte allerdings nicht zur dreifach substituierten Spezies. Stattdessen wird der Komplex $[Na(3,5\text{-bis}(Ph_3C)–ATI^{iPr/iPr})]$ (**4-(Ph_3C)$_2$**) erhalten. Durch die Anzahl sowie das Signalmuster der ATI-Rückgratprotonen im ^{1}H-NMR-Spektrum kann die zweifache Substitution bestätigt werden. Auch die Detektion von je zwei Signalen für die CH_3- und CH-Protonen der *Iso*propyl-Reste deutet an, dass es sich nicht um eine C_{2v}-symmetrische Verbindung handelt. Die Resonanzen für die Phenyl-Protonen eines Trityl-

Substituenten zeigen eine starke Verbreiterung bei Raumtemperatur, was vermutlich auf eine gehinderte Rotation der Phenyl-Gruppen zurückzuführen ist. Der unvollständige Umsatz kann auf die nicht ausreichend lange Reaktionszeit von zwei Stunden zurückgeführt werden. Es kann angenommen werden, dass durch eine Optimierung der Reaktionsbedingungen für alle untersuchten Umsetzungen mit Tritylchlorid die Zielverbindungen in adäquater Ausbeute und Reinheit zugänglich gemacht werden können. Die elektrophile aromatische Substitution von Natrium-ATI-Komplexen bzw. die Darstellung der rückgartsubstituierten Komplexe in einer Eintopfsynthese ausgehend vom im Rückgrat unsubstituierten Neutralliganden stellt somit einen einfachen Weg zu funktionalisierten Komplexen ohne aufwändige Reinigungsschritte dar.

2 Struktur von Ph_3C-substituierten ATI-Komplexen

Durch Diffusion von *n*-Pentan in eine Lösung von $[\text{Na}(3\text{-Ph}_3\text{C–5-Ph(O)C–ATI}^{i\text{Pr}/i\text{Pr}})]$ (**4-Ph(O)C-Ph$_3$C**) in THF-d_8 konnten Einkristalle zur Röntgenstrukturanalyse erhalten werden. $[\text{Na}(3\text{-Ph}_3\text{C–5-Ph(O)C–ATI}^{i\text{Pr}/i\text{Pr}})(\text{thf})_2]_2$ (**[4-Ph(O)C-Ph$_3$C-(thf)$_2$]$_2$**) kristallisiert in der monoklinen Raumgruppe $P2_1/n$ als Koordinationsdimer (Z = 2, Abbildung 30).

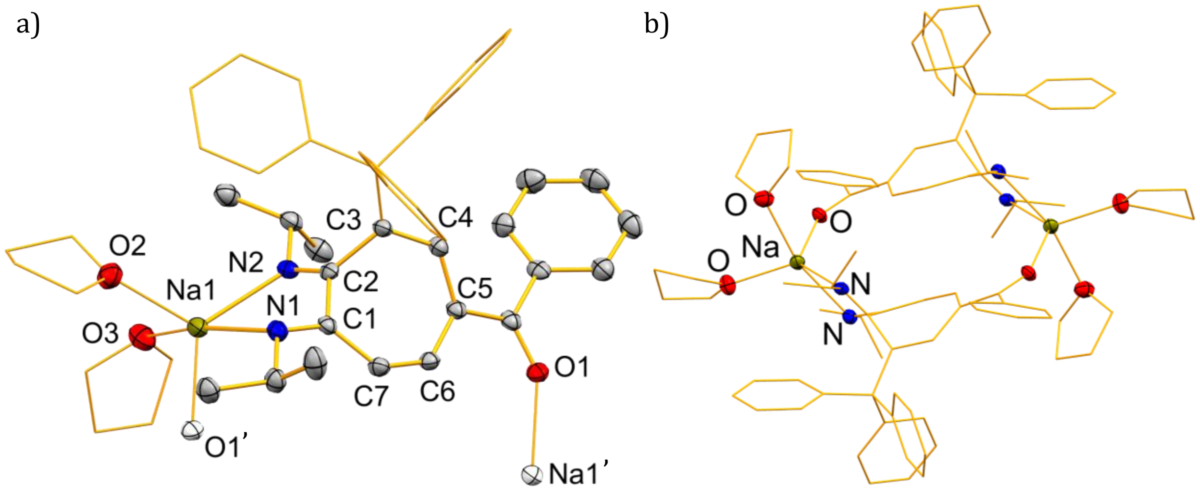

Abbildung 30: a) Ausschnitt der Struktur von $[\text{Na}(3\text{-Ph}_3\text{C–5-Ph(O)C–ATI}^{i\text{Pr}/i\text{Pr}})(\text{thf})_2]_2$ (**[4-Ph(O)C-Ph$_3$C-(thf)$_2$]$_2$**) im Festkörper. Die Ellipsoide repräsentieren 50% der Aufenthaltswahrscheinlichkeit. Wasserstoffatome wurden aus Gründen der Übersichtlichkeit nicht abgebildet. Die Ethyleneinheiten der thf-Liganden sowie die Kohlenstoffatome des Trityl-Substituenten sind im Drahtmodell dargestellt. Atome, die eine Formeleinheit überschreiten, sind als weiße Ellipsoide dargestellt. b) Dimere Einheit von **[4-Ph(O)C-Ph$_3$C-(thf)$_2$]$_2$**. Kohlenstoffatome sind im Drahtmodell dargestellt. Ausgewählte Bindungslängen (Å) und -winkel (°): Na1–N1, 2.535(3); Na1–N2, 2.432(2); Na1–O1‘, 2.227(2); Na1–O2, 2.295(2); Na1–O3, 2.480(3); N1–C1, 1.300(3); N2–C2, 1.276(3); C1–C2, 1.505(4); C2–C3, 1.493(3); C3–C4, 1.351(3); C4–C5, 1.452(3); C5–C6, 1.421(3); C6–C7, 1.363(3); C1–C7, 1.438(3); N2–Na1–N1, 71.71(8); O1‘–Na1–O(2/3), 84.72(8)–115.63(8); O(1‘–3)–Na1–N(1/2), 89.39(8)–164.63(8).

Das Natriumatom ist aufgrund der Koordination des ATI-Liganden über die *N,N*-Bindungstasche und der Koordination zweier thf-Liganden sowie des Benzoyl-Sauerstoffatoms einer benachbarten monomeren Einheit verzerrt trigonal bipyramidal umgeben ($\tau = 0.67$, mit O3 und N1 in axialen Positionen). Die Verzerrung ist dabei auf den kleinen Bisswinkel des ATI-Liganden (N2−Na1−N1, 71.71(8)°) zurückzuführen. Die Na−N Bindungslängen unterscheiden sich mit einer Differenz von 0.11 Å deutlich, was auf eine Abwinkelung (quantifiziert durch den Winkel zwischen den Ebenen [C3−C7] und [C1−3,C7]) des ATI-Gerüsts entlang der C3/C7-Achse von 36.4° zurückzuführen ist. Eine solche Faltung ist für ATI-Liganden seltener als die für die Nitro-substituierten Verbindungen beschriebene Verdrehung und konnte für den Komplex $[\mathrm{Rh(C_5Me_5)(H{-}ATI^{\mathit{i}Pr/\mathit{i}Pr})}]^+$, in welchem der ATI-Ligand in seiner protonierten Form vorliegt, beobachtet werden.[98] In **4-Ph(O)C-Ph$_3$C** ist vermutlich der sterische Anspruch des Trityl-Substituenten für diese Geometrieänderung verantwortlich. Eine leichte Auswirkung der Verdrehung wird auch auf die N−C Bindungslängen (1.28−1.30 Å) beobachtet. Sowohl die N−C (1.28−1.30 Å) also auch die C−C Bindungslängen (1.35−1.51 Å) liegen in einem sehr ähnlichen Bereich wie die analoger Bindungen in der Stammverbindung **[4-Ph(O)C-py]$_\infty$** (N−C, 1.30 Å; C−C, 1.36−1.52 Å)[77] und deuten auf eine stärkere Lokalisierung der π-Elektronendichte als im unsubstituierten Komplex $[\mathrm{Na(ATI^{\mathit{i}Pr/\mathit{i}Pr})(thf)}]$ hin. Dies ist auf den elektronenziehenden Charakter der Benzoyl-Gruppe zurückzuführen. Die Na−O Bindungslänge zum Benzoyl-Sauerstoffatom einer benachbarten Monomereinheit ist mit 2.23 Å kürzer als die zu den neutralen thf-Donor-Liganden (2.30−2.48 Å) und im Rahmen der Fehlergrenzen identisch zur Länge der analogen Bindung in **[4-Ph(O)C-py]$_\infty$**. Im Unterschied zu **[4-Ph(O)C-py]$_\infty$** führt die Koordination an die Benzoyl-Gruppe nicht zur Ausbildung eines Koordinationspolymers sondern eines Koordinationsdimers (Abbildung 30b).

4-Ph_3C-(thf)$_2$ kristallisiert aus einem THF/*n*-Pentan Gemisch bei −30 °C in der triklinen Raumgruppe $P\bar{1}$ (Z = 8, Abbildung 31).

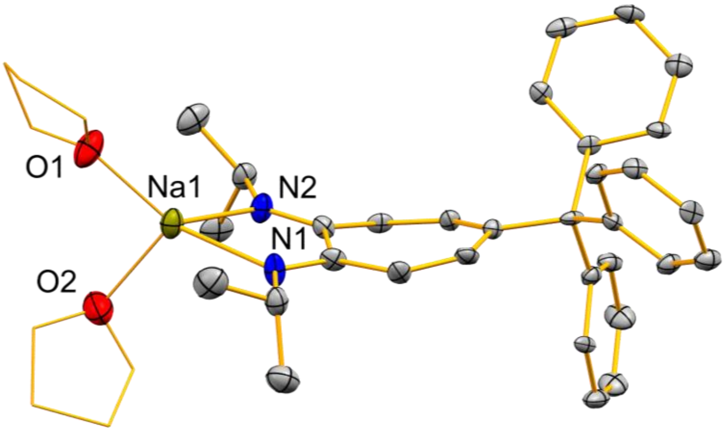

Abbildung 31: Struktur von [Na(Ph_3C–$ATI^{iPr/iPr}$)$(thf)_2$] (**4-Ph_3C-(thf)$_2$**) im Festkörper. Die Ellipsoide repräsentieren 50% der Aufenthaltswahrscheinlichkeit. Wasserstoffatome wurden aus Gründen der Übersichtlichkeit nicht abgebildet. Die Ethyleneinheiten der thf-Liganden sind im Drahtmodell dargestellt.

Allerdings ist die Qualität der erhaltenen Daten nicht ausreichend, um Bindungslängen und -winkel zu diskutieren. Die Struktur dient deshalb als Konnektivitätsbeweis. Im Unterschied zur unsubstituierten Stammverbindung [Na($ATI^{iPr/iPr}$)(thf)] wird keine Kation-π-Wechselwirkung mit dem ATI-Rückgrat beobachtet, sondern eine monomere Struktur in der die Koordinationssphäre des Natriumatoms durch Koordination zweier thf-Liganden abgesättigt ist.[63] Grund hierfür könnte der sterische Anspruch des Trityl-Substituenten sein, der das Rückgrat abschirmt.

4-(Ph_3C)$_2$-(thf)$_2$kristallisiert ebenfalls aus einem THF/*n*-Pentan Lösungsmittel-System in der monoklinen Raumgruppe $P2_1/n$ (Z = 4, Abbildung 32). Das Natriumatom ist aufgrund der κ^2N-Koodrination des ATI-Liganden sowie der Koordination zweier thf-Liganden verzerrt tetraedrisch koordiniert, wobei die Verzerrung auf den Bisswinkel des ATI-Liganden (N1−Na1−N2, 75.4°) zurückzuführen ist. Die Na−N Bindungslängen sind identisch (2.38 Å) und nur geringfügig länger als in der unsubstituierten Stammverbindung (2.36 Å).[63] Die Na−O Bindungslängen (2.29−2.32 Å) liegen in einem ähnlichen Bereich wie die der analogen Bindung in [Na($ATI^{iPr/iPr}$)(thf)]. Im Gegensatz zur Stammverbindung wird in **4-(Ph_3C)$_2$-(thf)$_2$** keine Kation-π-Wechselwirkung beobachtet, was auf den hohen sterischen Anspruch den beiden Trityl-Substituenten zurückzuführen ist.

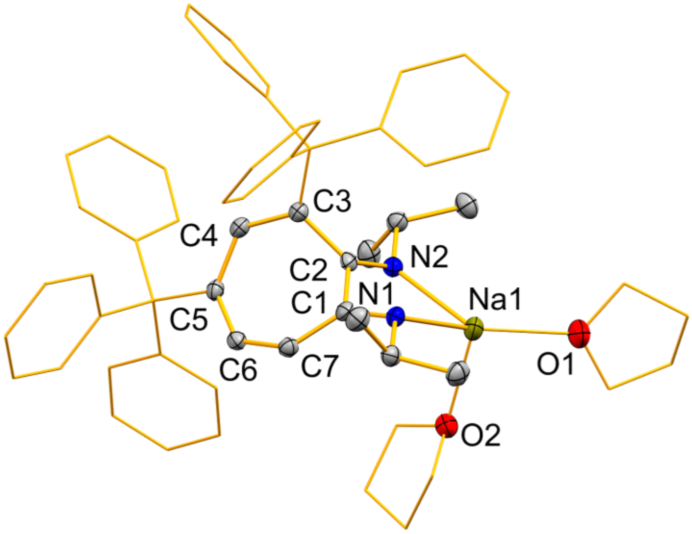

Abbildung 32: Struktur von [Na(3,5-bis(Ph$_3$C)–ATI$^{iPr/iPr}$)(thf)$_2$] (**4-(Ph$_3$C)$_2$-(thf)$_2$**) im Festkörper. Die Ellipsoide repräsentieren 50% der Aufenthaltswahrscheinlichkeit. Wasserstoffatome sowie ein in der Elementarzelle enthaltenes THF-Molekül wurden aus Gründen der Übersichtlichkeit nicht abgebildet. Die Kohlenstoffatome der thf-Liganden, der Trityl-sowie der *Iso*propyl-Substituenten sind im Drahtmodell dargestellt. Ausgewählte Bindungslängen (Å) und -winkel (°): Na1–N1, 2.3780(16); Na1–N2, 2.3806(16); Na1–O1, 2.285(13); Na1–O2, 2.3188(15); N1–C1, 1.324(2); N2–C2, 1.283(2); C1–C2, 1.504(2); C2–C3, 1.491(2); C3–C4, 1.363(2); C4–C5, 1.430(2); C5–C6, 1.390(2); C6–C7, 1.405(2); C1–C7, 1.414(2); N1–Na1–N2, 75.41(5); N(1/2)–Na1–O(1/2), 98.01(5)–146.9(9), O1–Na1–O2, 96.5(4).

XVII Synthese und Struktur von Bismut-Aminotroponiminaten

1 Homo- und heteroleptische $[\mathrm{Bi}(\mathrm{ATI}^{i\mathrm{Pr}/i\mathrm{Pr}})_n\mathrm{Cl}_{3-n}]$ Komplexe

1.1 Synthese

Die heteroleptischen Bismut-Komplexe $[\mathrm{Bi}(\mathrm{ATI}^{i\mathrm{Pr}/i\mathrm{Pr}})_2\mathrm{Cl}]$ (**8**) und $[\mathrm{Bi}(\mathrm{ATI}^{i\mathrm{Pr}/i\mathrm{Pr}})\mathrm{Cl}_2]$ (**9**) wurden in Anlehnung an die Literatur über eine Salzeliminierung dargestellt.[62] Hierfür wurde der Ligand **1** in einer Eintopfsynthese mit NaHMDS und der entsprechenden Anzahl an Äquivalenten BiCl_3 in THF umgesetzt (Schema 25).

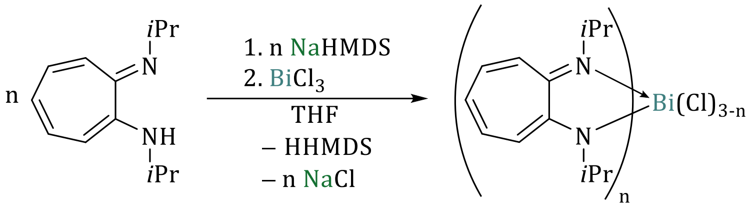

1

8 n = 2
9 n = 1

Schema 25: Synthese der heteroleptischen Bismut-Komplexe $[\mathrm{Bi}(\mathrm{ATI}^{i\mathrm{Pr}/i\mathrm{Pr}})_2\mathrm{Cl}]$ (**8**) und $[\mathrm{Bi}(\mathrm{ATI}^{i\mathrm{Pr}/i\mathrm{Pr}})\mathrm{Cl}_2]$ (**9**).

Direkt nach Zugabe einer Lösung von BiCl_3 zum *in situ* synthetisierten Natrium-Komplex konnte die Bildung einer großen Menge orangen Niederschlags beobachtet werden. Aus diesem Grund wurde auf eine Filtration zur Entfernung von Natriumchlorid verzichtet, da vermutet wurde, dass der gewünschte Komplex in THF ebenfalls schwer löslich ist. Aufgrund der mäßigen Löslichkeit der heteroleptischen Bismut-Komplexe in Pyridin waren weder Versuche einer fraktionierenden Kristallisation noch Waschen des Feststoffes mit Pyridin erfolgreich, um NaCl aus dem Rohprodukt vollständig zu entfernen und die Komplexe in ausreichender Menge und Reinheit für eine vollständige Charakterisierung zu erhalten. Zudem konnten für die Monochloro-Spezies **8** außerdem ^{1}H-NMR-spektroskopisch 8% der Dichloro-Spezies **9** sowie 16% des Liganden **1** im Rohprodukt nachgewiesen werden. Die Bismut-Komplexe zeigen somit ein ähnliches Verhalten wie die ersten literaturbeschriebenen heteroleptischen Bismut-ATI-Komplexe, in welchen ein *Iso*propyl-Substituent am Liganden gegen einen Ferrocenyl-Substituenten ausgetauscht ist. $[\mathrm{Bi}(\mathrm{ATI}^{\mathrm{Fc}/i\mathrm{Pr}})\mathrm{Cl}_2]$ konnte in guten Ausbeuten isoliert werden. Die Bildung von $[\mathrm{Bi}(\mathrm{ATI}^{\mathrm{Fc}/i\mathrm{Pr}})_2\mathrm{Cl}]$ konnte NMR-spektroskopisch gezeigt werden, Isolationsversuche führten jedoch zu Gemischen der Mono- und Dichloro-Spezies sowie protoniertem Liganden.[62] Dies deutet auf eine zunehmende Instabilität von Bismut-ATI-Komplexen mit zunehmender Anzahl koordinierender ATI-Liganden hin. Diese Vermutung bestätigen Beobachtungen bei der Synthese des homoleptischen $[\mathrm{Bi}(\mathrm{ATI}^{i\mathrm{Pr}/i\mathrm{Pr}})_3]$ (**10**) durch Umsetzung von $[\mathrm{Na}(\mathrm{ATI}^{i\mathrm{Pr}/i\mathrm{Pr}})]$ und BiCl_3 in einer 3:1 Stöchiometrie in deuterierten Lösungsmitteln wie $\mathrm{C}_6\mathrm{D}_6$, THF-d_8 oder $\mathrm{CD}_3\mathrm{CN}$. Hier kann die quantitative Bildung von **10** ^{1}H-NMR-spektroskopisch verfolgt werden, allerdings zeigt sich bereits nach zehn Minuten eine Zersetzung in den protonierten Liganden **1** sowie elementares Bismut in Form eines schwarzen Niederschlags. Sowohl die Verwendung silanisierter Glasgeräte und verschiedener Lösungsmittel (THF, Pyridin, Acetonitril) als auch die Verringerung der Reaktionstemperatur von Raumtemperatur auf −78 °C führten zu keiner signifikanten Erhöhung der Stabilität der *in situ* generierten Bismut-Verbindung. Aufgrund der Tendenz von Bismut(III)-Diarylamiden $[\mathrm{Bi(NAr_2)_3}]$ (Ar = Ph, $C_6H_4CH_3$, $C_6H_4OCH_3$, C_6H_4Br, $C_6H_4C_6H_5$) zur homolytischen Bindungsspaltung wurde versucht,[99] eventuell gebildete Radikalspezies bei der Synthese von **10** mit Hilfe von $n\mathrm{Bu_6Sn_2}$ abzufangen.[100] Es konnten jedoch keine Hinweise auf die Bildung von Kopplungsprodukten gefunden werden. Somit war eine Isolierung von Komplex **10** in einer ausreichenden Menge und Reinheit für eine vollständige Charakterisierung nicht möglich. Dagegen sind die literaturbekannten homoleptischen Bismut-Komplexe der Liganden H−ATI$^{\mathrm{Fc}/i\mathrm{Pr}}$ sowie H−ATI$^{\mathrm{Ph}/i\mathrm{Pr}}$ in guten Ausbeuten synthetisierbar.[62, 69] Der Austausch des Fc- bzw. Ph-Substituenten durch *i*Pr scheint somit eine zunehmende Destabilisierung zu bewirken, was auf den +I-Effekt des Substituenten zurückzuführen sein könnte.

1.2 Struktur

Durch Lösungsmitteldiffusion von *n*-Pentan in einen Reaktionsansatz in THF konnten geringe Mengen einkristallinen Materials von **10** zur Einkristallröntgenstrukturanalyse erhalten werden. [Bi(ATI$^{i\mathrm{Pr}/i\mathrm{Pr}}$)$_3$] (**10**) kristallisiert in der monoklinen Raumgruppe $P2_1/c$ mit $Z = 4$ (Abbildung 33). **10** ist das dritte, strukturell charakterisierte Beispiel eines homoleptischen Bi(ATI)$_3$ Komplexes und das erste Beispiel mit einem symmetrischen Substitutionsmuster an den Stickstoffatomen des ATI-Liganden.[62, 69] Ebenso wie bei den literaturbekannten Vertretern ist das Bismutatom stark verzerrt oktaedrisch umgeben, wobei die Verzerrung durch den Bisswinkel des ATI-Liganden (N−Bi−N(chelatisierend), 64.96(15)−65.64(14)°) und ein möglicherweise stereochemisch aktives bismut-zentriertes freies Elektronenpaar bedingt ist.[62] Die Bi−N Bindungslängen innerhalb eines ATI-Liganden unterscheiden sich deutlich (0.15−0.23 Å). Die kürzeren Bi−N Bindungen repräsentieren dabei Bindungen mit kovalentem Charakter (2.36−2.38 Å), den längeren Bindungen wird ein dativer Charakter zugeschrieben (2.52−2.62 Å).[101] Diese Alternanz zeigt sich allerdings nicht in den N−C Bindungslängen, welche im Rahmen der Fehlergrenzen identisch sind und in einem Bereich zwischen Bindungslängen typischer N−C-Einfach- bzw. Doppelbindungen liegen.[74] Dies deutet auf eine Delokalisierung der π-Elektronen im ATI-Liganden hin.

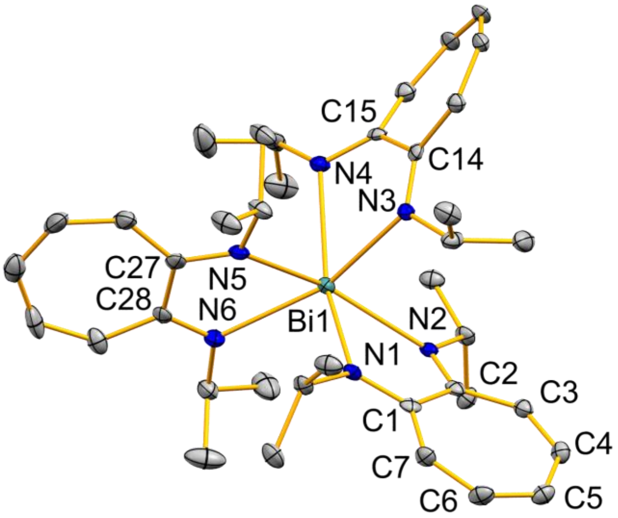

Abbildung 33: Struktur von [Bi(ATI$^{i\mathrm{Pr}/i\mathrm{Pr}}$)$_3$] (**10**) im Festkörper. Die Ellipsoide repräsentieren 50% der Aufenthaltswahrscheinlichkeit. Wasserstoffatome wurden aus Gründen der Übersichtlichkeit nicht abgebildet. Ausgewählte Bindungslängen (Å) und -winkel (°): Bi1–N1 2.357(4); Bi1–N2, 2.512(4); Bi1–N3, 2.386(4); Bi1–N4, 2.624(4); Bi1–N5, 2.376(4); Bi1–N6, 2.537(4); C1–N1, 1.352(6); N2–C2, 1.315(6); N3–C14, 1.323(7); N4–C15, 1.310(6); N5–C27, 1.329(6); N6–C28, 1.311(7); C1–C2, 1.491(7); C2–C3, 1.424(7); C3–C4, 1.366(7); C4–C5, 1.378(7); C5–C6, 1.372(8); C6–C7, 1.389(7); C7–C1, 1.413(7); N–Bi–N (chelatisierend), 64.96(15)–65.64(14); N–Bi–N (nicht chelatisierend), 81.99(14)–159.15(15).

Durch Lösungsmitteldiffusion von *n*-Pentan in THF-Lösungen der heteroleptischen Bismut-Komplexe konnten ebenfalls geringe Mengen kristallinen Materials zur Einkristallröntgenstrukturanalyse gewonnen werden. [Bi(ATI$^{i\mathrm{Pr}/i\mathrm{Pr}}$)$_2$Cl]$_\infty$ (**8**$_\infty$) kristallisiert in der monoklinen Raumgruppe $P2_1/n$ mit $Z = 4$ und [Bi(ATI$^{i\mathrm{Pr}/i\mathrm{Pr}}$)Cl$_2$]$_\infty$ (**9**$_\infty$) in der triklinen Raumgruppe $P\bar{1}$ mit $Z = 1$ (Abbildung 34 und Abbildung 35). Aufgrund der Ausbildung von intermolekularen Bi···Cl Wechselwirkung sind die Bismutatome in beiden Verbindungen verzerrt oktaedrisch koordiniert, wobei die Verzerrung auf den ATI-Bisswinkel (**8**$_\infty$: 67.2–69.1°; **9**$_\infty$: 73.6°) zurückzuführen ist. In **8**$_\infty$ wechselwirkt das Bismutatom mit dem Chlor-Substituenten einer weiteren monomeren Einheit, was zur Ausbildung eines eindimensionalen Koordinationspolymers entlang einer 2$_1$-Schraubenachse in Richtung der kristallographischen *b*-Achse führt (Abbildung 34b). Die intermolekularen Bi···Cl Abstände sind dabei nur marginal länger als die intramolekularen Bindungen und liegen 22% unterhalb der Summe der van-der-Waals Radien (3.82 Å[102], Tabelle 9). In **9**$_\infty$ dagegen geht das Bismutatom intermolekulare Wechselwirkungen mit je einem Chlor-Substituenten zweier weiterer Monomereinheiten ein. Dies führt ebenfalls zur Ausbildung eines eindimensionalen Koordinationspolymers entlang der kristallographischen *a*-Achse (Abbildung 35b). Durch die Bi···Cl Wechselwirkungen bilden sich zwei Bi$_2$Cl$_2$-Vierringe, die um 69.1° zueinander verkippt sind. Die intramolekularen Bi–Cl Bindungen sind in **9**$_\infty$ kürzer als in der Monochloro-Spezies **8**$_\infty$, was auf den Austausch eines ATI-Liganden gegen einen Chlor-

Substituenten zurückzuführen ist (Tabelle 9). Im Vergleich zur einzigen literaturbekannten Bismut-ATI-Chlorospezies [Bi(ATI$^{Fc/i\mathrm{Pr}}$)Cl$_2$] sind die intramolekularen Bi–Cl Bindungen leicht verlängert (2.70–2.76 Å), da die Koordinationszahl in **9$_\infty$** größer ist und außerdem beide Chloratome eine verbrückende Funktion besitzen ([Bi(ATI$^{Fc/i\mathrm{Pr}}$)Cl$_2$]: KZ = 5, Bi–Cl(terminal), 2.64–2.67 Å, Bi–Cl(verbrückend), 2.71–2.74 Å).[62] Eine zu **9$_\infty$** analoge Polymerstruktur zeigt dagegen das strukturell verwandte Bismut-amidinat [Bi(*t*BuC(N*i*Pr)$_2$)Cl$_2$].[103] Sowohl inter- (3.17–3.21 Å) als intramolekulare Bi–Cl Bindungslängen (2.69–2.74 Å) sind deshalb in einem ähnlichen Bereich.[103]

Tabelle 9: Bindungsparameter der heteroleptischen Bismut-Komplexe [Bi(ATI$^{i\mathrm{Pr}/i\mathrm{Pr}}$)$_2$Cl]$_\infty$ (**8$_\infty$**) und [Bi(ATI$^{i\mathrm{Pr}/i\mathrm{Pr}}$)Cl$_2$]$_\infty$ (**9$_\infty$**).

Bindungsparameter [Å]	**8$_\infty$**	**9$_\infty$**
Bi–N	2.276(2)–2.422(2)	2.184(2)–2.203(2)
N1–C1/ N2–C2	1.320(3)–1.336(3)	1.343(4)–1.344(4)
N3–C14/ N4–C15	1.321(3)–1.335(3)	-
Bi–Cl	2.9433(9)	2.7008(8)–2.7630(8)
Bi⋯Cl	2.9879(9)	3.2234(8)–3.436(1)

Die Bi–N Bindungslängen sind für beide Verbindungen aufgrund der elektronegativen Chlor-Substituenten und der intermolekularen Bi⋯Cl Wechselwirkungen kürzer als im homoleptischen Komplex **10**. In **8$_\infty$** sind die Bi–N Bindungen, die Chlor-Substituenten in *trans*-Position besitzen, kürzer (2.28–2.31 Å) als die mit einem Stickstoffatom in *trans*-Position (2.36–2.42 Å). Im Vergleich dazu sind die Bi–N Bindungslängen in **9$_\infty$** im Rahmen der Fehlergrenzen identisch und aufgrund des Einflusses der zwei gebundenen Chlor-Substituenten kürzer als in **8$_\infty$** (Tabelle 9).

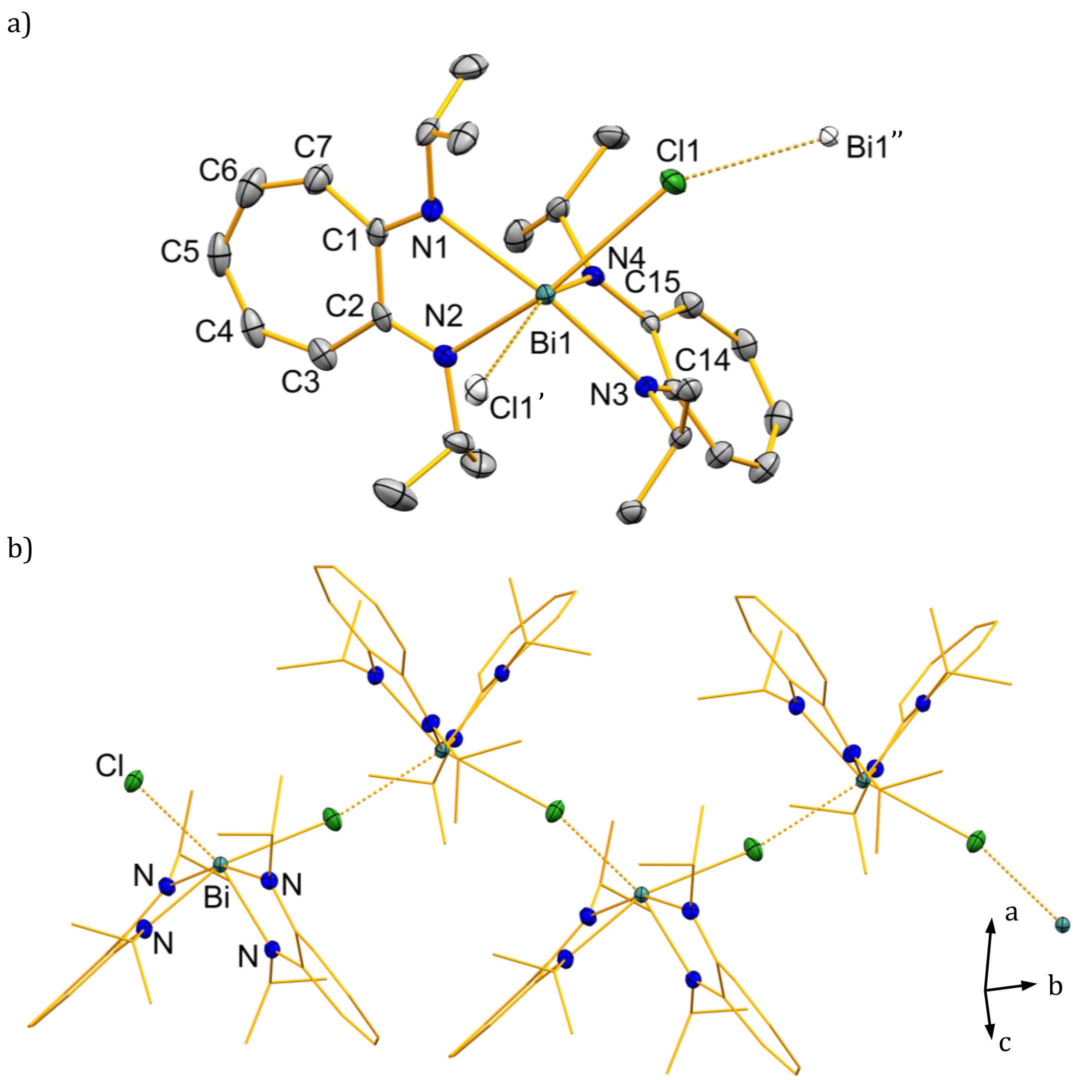

Abbildung 34: a) Ausschnitt der Struktur von $[\mathrm{Bi(ATI}^{i\mathrm{Pr}/i\mathrm{Pr}})_2\mathrm{Cl}]_\infty$ (**8_∞**) im Festkörper. Die Ellipsoide repräsentieren 50% der Aufenthaltswahrscheinlichkeit. Wasserstoffatome wurden aus Gründen der Übersichtlichkeit nicht abgebildet. Atome, die eine Formeleinheit überschreiten, sind als weiße Ellipsoide dargestellt. b) Eindimensionales Koordinationspolymer von **8_∞** im Festkörper, wobei Kohlenstoffatome im Drahtmodell dargestellt sind. Ausgewählte Bindungslängen (Å) und -winkel (°): Bi1–N1, 2.422(2); Bi1–N2, 2.308(2); Bi–N3, 2.364(2); Bi1–N4, 2.276(2); Bi1–Cl1, 2.9433(9); Bi1···Cl1', 2.9879(9); N1–C1, 1.320(3); N2–C2, 1.336(3); N3–C14, 1.321(3); N4–C15, 1.335(3); C1–C2, 1.495(4); C2–C3, 1.421(4); C3–C4, 1.387(4); C4–C5, 1.368(4); C5–C6, 1.378(4); C6–C7, 1.376(4); C7–C1, 1.424(4); N–Bi1–N (chelatisierend), 67.21(7)–69.14(7); N–Bi1–N (nicht chelatisierend), 81.64(8)–159.06(7); N(1-4)–Bi1–Cl(1/1'), 80.67(6)–159.19(6); Cl1–Bi1–Cl1', 118.986(16).

Wie aufgrund der Tendenz des ATI-Liganden zur Delokalisation von π-Elektronen über das C_7-Rückgrat sowie die beiden Stickstoffatome zu erwarten, sind die C–N Bindungslängen eines ATI-Liganden sowohl in **8_∞** als auch in **9_∞** im Rahmen der Fehlergrenzen identisch und liegen in einem Bereich zwischen typischen C–N Einfach- und Doppelbindungen (Tabelle 9). Eine Aren-Aren Wechselwirkung, wie sie in $[\mathrm{Bi(ATI}^{\mathrm{Fc}/i\mathrm{Pr}})\mathrm{Cl}_2]$ beobachtet wird, tritt nicht auf.[62]

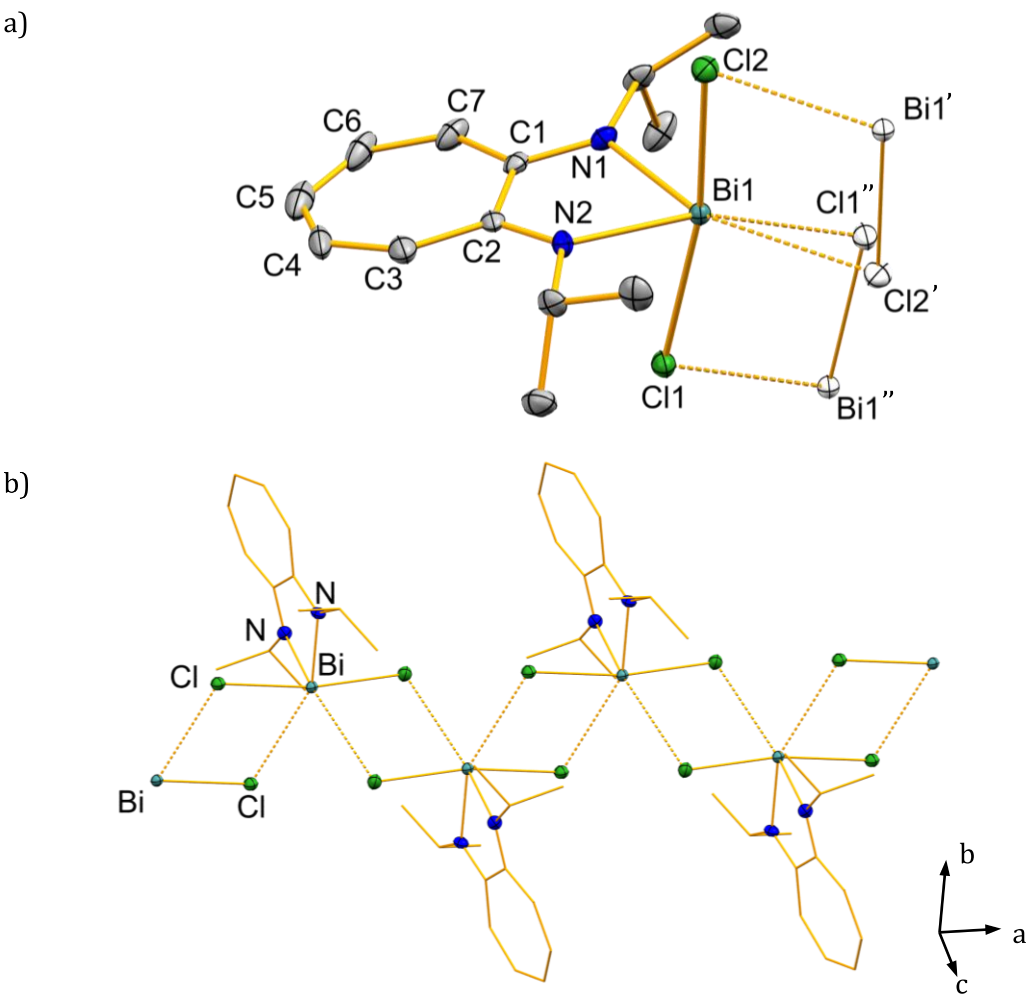

Abbildung 35: a) Ausschnitt der Struktur von $[Bi(ATI^{iPr/iPr})Cl_2]_\infty$ (**9**$_\infty$) im Festkörper. Die Ellipsoide repräsentieren 50% der Aufenthaltswahrscheinlichkeit. Wasserstoffatome wurden aus Gründen der Übersichtlichkeit nicht abgebildet. Atome, die eine Formeleinheit überschreiten, sind als weiße Ellipsoide dargestellt. b) Eindimensionales Koordinationspolymer von **9**$_\infty$ im Festkörper, wobei Kohlenstoffatome im Drahtmodell dargestellt sind. Ausgewählte Bindungslängen (Å) und -winkel (°): Bi1–Cl1, 2.7630(8); Bi1···Cl1“, 3.2234(8); Bi–Cl2, 2.7008(8); Bi···Cl2‘, 3.436(1); Bi1–N1, 2.184(2); Bi1–N2, 2.203(2); N1–C1, 1.344(4); N2–C2, 1.343(4); C1–C2, 1.472(4); C2–C3, 1.421(5); C3–C4, 1.381(5); C4–C5, 1.378(6); C5–C6, 1.379(6); C6–C7, 1.378(5); C7–C1 1.416(4); Cl(1–2’)–Bi1–Cl(1–2’), 71.97(2)–170.06(2); N(1/2)–Bi1–Cl(1–2’), 82.22(7)–164.29(8); N1–Bi1–N2, 73.58(10).

2 Heteroleptische $[Bi(Ph(O)S{-}ATI^{iPr/iPr})_nX_{3-n}]$ Komplexe

2.1 Synthese

Die Synthese heteroleptischer Bismut-Ph(O)S–ATI-Komplexe wurde in Anlehnung an die Literatur aus den Natrium- und Kalium-ATI-Komplexen durch Salzeliminierungen mit $BiCl_3$ bzw. BiI_3 durchgeführt (Schema 26).[62] Eine Lösung des ATI-Komplexes wurde unter Rühren zu einer Lösung des Bismut-Salzes getropft. Durch Filtration wurde anschließend das entstandene Alkalimetallsalz abgetrennt. Die Bismut-Verbindungen $[Bi(Ph(O)S{-}ATI^{iPr/iPr})_2Cl]$ (**8-Ph(O)S**), $[Bi(Ph(O)S{-}ATI^{iPr/iPr})Cl_2]$ (**9-Ph(O)S**) und $[Bi(Ph(O)S{-}ATI^{iPr/iPr})I_2]$ (**11-Ph(O)S**) konnten nach Waschen mit *n*-Pentan und Trocknen im Vakuum als rote (**8-Ph(O)S**), orange (**9-Ph(O)S**) bzw. violette (**11-Ph(O)S**) Feststoffe in moderaten Ausbeuten erhalten werden.

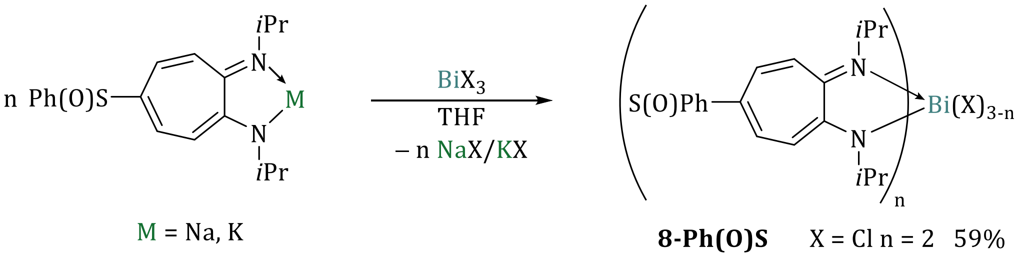

8-Ph(O)S	X = Cl	n = 2	59%
9-Ph(O)S	X = Cl	n = 1	54%[a]
11-Ph(O)S	X = I	n = 1	62%[b]

Schema 26: Synthese der heteroleptischen Bismut-Komplexe $[Bi(Ph(O)S{-}ATI^{iPr/iPr})_2Cl]$ (**8-Ph(O)S**), $[Bi(Ph(O)S{-}ATI^{iPr/iPr})Cl_2]$ (**9-Ph(O)S**) und $[Bi(Ph(O)S{-}ATI^{iPr/iPr})I_2]$ (**11-Ph(O)S**), [a] 1.00 Äq. Pyridin bzw. [b] 0.45 Äq THF wurden ^1H-NMR-spektroskopisch detektiert.

Alle Versuche, die Monoiodo-Verbindung $[Bi(Ph(O)S{-}ATI^{iPr/iPr})_2I]$ auf analoge Weise darzustellen, führten zur Isolierung von Gemischen der gewünschten Verbindung und $[Bi(Ph(O)S{-}ATI^{iPr/iPr})I_2]$ (**11-Ph(O)S**) (16–23%) sowie des protonierten Liganden **1-Ph(O)S** (17–31%). Alle isolierten Verbindungen zeigen die erwarteten Signale im ^1H- und ^{13}C-NMR-Spektrum, wobei für **9-Ph(O)S** und **11-Ph(O)S** im ^1H-NMR-Spektrum je zwei Dubletts für die CH_3-Gruppen der *Iso*propyl-Reste detektiert werden. Dies könnte, ebenso wie für den Lithium-Komplex **3-Ph(O)S**, auf das Vorhandensein eines Stereozentrums am Schwefelatom oder wahrscheinlicher auf eine eingeschränkte Rotation der *Iso*propyl-Reste zurückgeführt werden.

2.2 Struktur

Durch Lösungsmitteldiffusion von *n*-Pentan oder *n*-Hexan in Pyridin-Lösungen von **9-Ph(O)S** und **11-Ph(O)S** konnten Kristalle zur Einkristallröntgenstrukturanalyse erhalten werden.

[9-Ph(O)S]$_\infty$ kristallisiert in der orthorombischen Raumgruppe *Pbca* ($Z = 4$, Abbildung 36). Die Qualität der erhaltenen Daten ist nicht ausreichend, um Bindungslängen und -winkel zu diskutieren, die Struktur dient deshalb als Konnektivitätsbeweis. Aufgrund der Koordination eines ATI-Liganden, zweier Chlor-Substituenten und eines Pyridin-Moleküls an das Bismutatom sowie der Ausbildung einer intermolekularen Bi···Cl Wechselwirkung ist das Bismutatom oktaedrisch koordiniert. Die intermolekulare Wechselwirkung führt zur Ausbildung eines linearen Koordinationspolymers entlang einer 2_1-Schraubenachse in Richtung der kristallographischen *b*-Achse, wie es auch für die im Rückgrat unsubstituierte Monochloro-Verbindung **8$_\infty$**, die ebenfalls eine intermolekulare Bi···Cl Wechselwirkung besitzt, beobachtet wird (vgl. Abbildung 34).

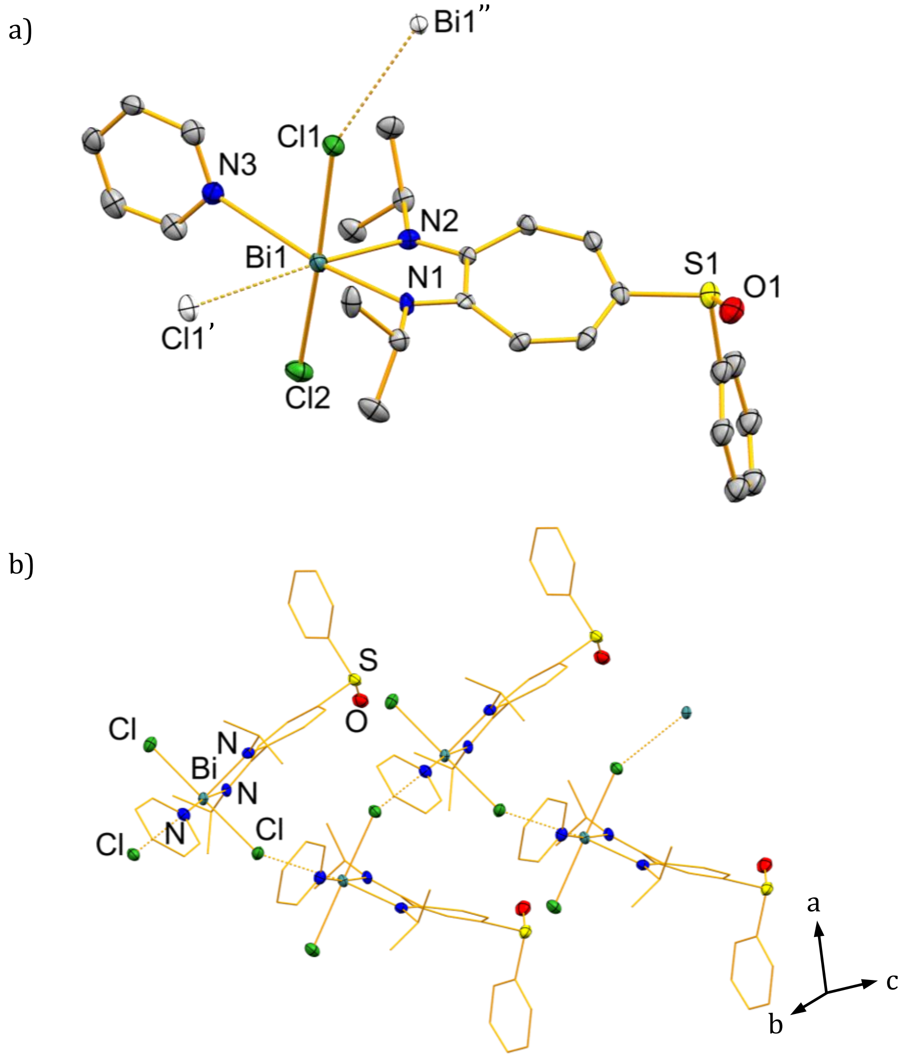

Abbildung 36: a) Ausschnitt der Struktur von $[\mathrm{Bi(Ph(O)S{-}ATI}^{i\mathrm{Pr}/i\mathrm{Pr}})\mathrm{Cl}_2]_\infty$ (**[9-Ph(O)S]$_\infty$**) im Festkörper. Die Ellipsoide repräsentieren 50% der Aufenthaltswahrscheinlichkeit. Wasserstoffatome wurden aus Gründen der Übersichtlichkeit nicht abgebildet. Atome, die eine Formeleinheit überschreiten, sind als weiße Ellipsoide dargestellt. b) Eindimensionales Koordinationspolymer von **[9-Ph(O)S]$_\infty$** im Festköper, wobei Kohlenstoffatome im Drahtmodell dargestellt sind.

[11-Ph(O)S]$_\infty$ kristallisiert in der orthorombischen Raumgruppe *Pnna* ($Z = 8$, Abbildung 37). Analog wie in der zuvor beschriebenen Struktur der Dichloro-Verbindung **[9-Ph(O)S]$_\infty$** ist das Bismutatom verzerrt oktaedrisch koordiniert, wobei die Verzerrung durch den kleinen ATI-Bisswinkel bedingt ist (N1–Bi1–N2, 71.6°).

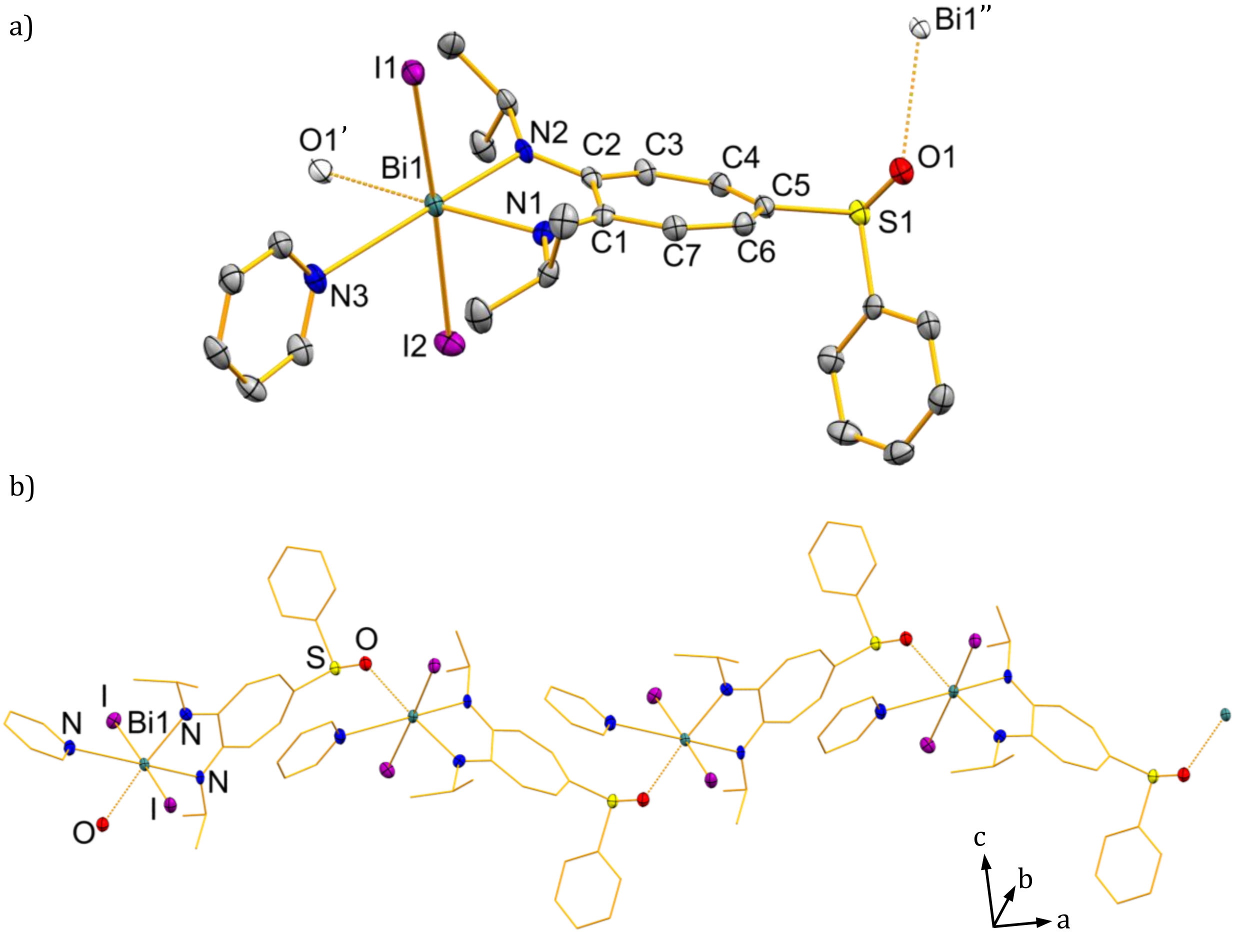

Abbildung 37: a) Ausschnitt der Struktur von [Bi(Ph(O)S–ATI$^{iPr/iPr}$)I$_2$]$_\infty$ (**[11-Ph(O)S]$_\infty$**) im Festkörper. Die Ellipsoide repräsentieren 50% der Aufenthaltswahrscheinlichkeit. Wasserstoffatome und ein in der Elementarzelle enthaltenes Pyridin-Molekül wurden aus Gründen der Übersichtlichkeit nicht abgebildet. Atome, die eine Formeleinheit überschreiten, sind als weiße Ellipsoide dargestellt. b) Eindimensionales Koordinationspolymer von **[11-Ph(O)S]$_\infty$** im Festkörper, wobei Kohlenstoffatome im Drahtmodell dargestellt sind. Ausgewählte Bindungslängen (Å) und -winkel (°): Bi1–I1, 3.0642(7); Bi–I2, 3.0472(7); Bi···O1‘, 2.652(3); Bi1–N1, 2.277(4); Bi1–N2, 2.260(3); Bi1–N3, 2.950(4); N1–C1, 1.328(6); N2–C2, 1.339(5); C1–C2, 1.476(6); C2–C3, 1.427(6); C3–C4, 1.383(6); C4–C5, 1.375(6); C5–C6, 1.398(6); C6–C7, 1.377(6); C7–C1 1.434(6); I(1/2)–Bi1–N(1–3), 87.36(8)–93.93(9); I(1/2)–Bi1–O1‘, 87.28(7)–93.53(7); I1–Bi1–I2, 175.448(10); N(1–3)–Bi1–O1‘, 79.34(11)–169.34(11); N1–Bi1–N2, 71.60(13).

Allerdings besteht in **[11-Ph(O)S]$_\infty$** keine intermolekulare Bismut–Halogen Wechselwirkung, sondern das Bismutatom koordiniert über das Sauerstoffatom an den Sulfinyl-Rest einer benachbarten Monomereinheit, was auch hier zur Ausbildung eines linearen Koordinationspolymers entlang einer 2_1-Schraubenachse in Richtung der kristallographischen *a*-Achse führt (Abbildung 37b). Die Bi–O Wechselwirkung ist dabei gegenüber einer Bi–I Wechselwirkung bevorzugt, was auf den größeren Ionenradius des Iodatoms (2.20 Å)[104] im Vergleich zum Sauerstoffatom (1.35 Å),[104] sowie die stärkere Donorfähigkeit der Sulfinyl-Einheit, zurückgeführt werden kann. Die Bi1–O1‘ Bindungslänge liegt mit 2.65 Å 26% unterhalb der Summe der van der Waals Radien (3.59 Å)[102] und ist nur geringfügig länger als die Bi–O Bindungen in DMSO-solvatisierten Bismut-Phenantrolin- bzw. -Bipyridin-Halogeniden (2.46–2.59 Å).[105] Auch die Längen der Bi–I Bindungen (3.05–3.06 Å) liegen in einen ähnlichen Bereich wie die der analogen Bindungen des strukturell verwandten β-Dialdiminato-Bismut-Komplex $[BiI_2((N(2,6\text{-}i\mathrm{Pr}_2\text{-}C_6H_3)CH)_2C(C_6H_5))_2]$ (Bi–I, 2.82–3.24 Å).[54a] Die Bi–N^{ATI} Bindungslängen sind im Rahmen der Fehlergrenzen identisch (2.26–2.28 Å) und kürzer als die Bi1–N3 Bindungslänge (2.95 Å) zu dem als neutraler Donor-Ligand fungierenden Pyridin-Molekül. Bedingt durch den Austausch von Chlor-Substituenten zu Iod-Substituenten sowie das Einbringen der elektronenziehenden Sulfinyl-Gruppe sind Bi–N^{ATI} Bindungslängen in **[11-Ph(O)S]$_\infty$** im Vergleich zur im Rückgrat unsubstituierten Dichloro-Verbindung **9$_\infty$** um 0.08–0.10 Å länger.

3 Heteroleptische [Bi(NO$_2$–ATI$^{iPr/iPr}$)$_n$Cl$_{3-n}$] Komplexe

3.1 Synthese

In Anlehnung an die zuvor beschriebenen und literaturbekannten Synthesen wurde der Komplex [Bi(NO$_2$–ATI$^{iPr/iPr}$)Cl$_2$] (**9-NO$_2$**) in einer Salzeliminierung ausgehend vom Natrium-ATI-Komplex in THF dargestellt (Schema 27). Sowohl das ^{1}H- als auch das ^{13}C-NMR-Spektrum zeigte die erwarteten Resonanzen einer C_{2v}-symmetrischen Verbindung. Versuche, den Monochloro-Komplex [Bi(NO$_2$–ATI$^{iPr/iPr}$)$_2$Cl] (**8-NO$_2$**) in analoger Weise herzustellen, führten lediglich zur Isolierung kleiner Mengen einkristallinen Materials, welches mit Hilfe von Einkristallröntgenstrukturanalyse als Dichloro-Spezies **9-NO$_2$** identifiziert werden konnte (Abbildung 38). Eine ^{1}H-NMR-spektroskopische Verfolgung der Umsetzung des Natrium-Komplexes mit einem halben Äquivalent BiCl$_3$ in Pyridin-d_5 zeigte zuerst die Bildung der Dichloro-Spezies **9-NO$_2$** an. Nach zwölf Stunden in Lösung konnte die Bildung einer weiteren ATI-haltigen Spezies beobachtet werden, die jedoch nicht weiter charakterisiert bzw. isoliert werden konnte. Ein Grund für die unvollständige Salzeliminierung könnte die schlechte Löslichkeit des Natrium-Komplexes in THF und Pyridin und die damit verbundene veränderte Stöchiometrie sein.

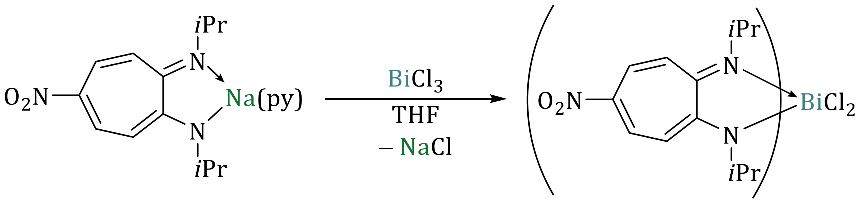

4-NO$_2$(py)

9-NO$_2$ 39%

Schema 27: Synthese von [Bi(NO$_2$–ATI$^{iPr/iPr}$)Cl$_2$] (**9-NO$_2$**) in THF.

3.2 Struktur

9-NO$_2$ kristallisiert aus einer THF/*n*-Pentan Mischung in der triklinen Raumgruppe $P\bar{1}$ mit $Z = 2$ (Abbildung 38). Die asymmetrische Einheit enthält je zwei mono- und zwei dinukleare, kristallographisch unabhängige aber chemisch identische Formeleinheiten, von welchen jeweils nur eine diskutiert wird. In der mononuklearen Einheit ist das Bismutatom aufgrund der Koordination des Liganden über die *N*,*N*-Bindungstasche sowie zweier Chlor-Substituenten bisphenoidal koordiniert (Abbildung 38a). Die zusätzliche Wechselwirkung des Bismutatoms mit dem Chlor-Substituenten einer benachbarten Formeleinheit in der dinuklearen Einheit führt zu einer verzerrt quadratisch-pyramidalen Koordinationsgeometrie des Bismutatoms ($\tau = 0.14$ mit N4 in der apikalen Position; Abbildung 38b).

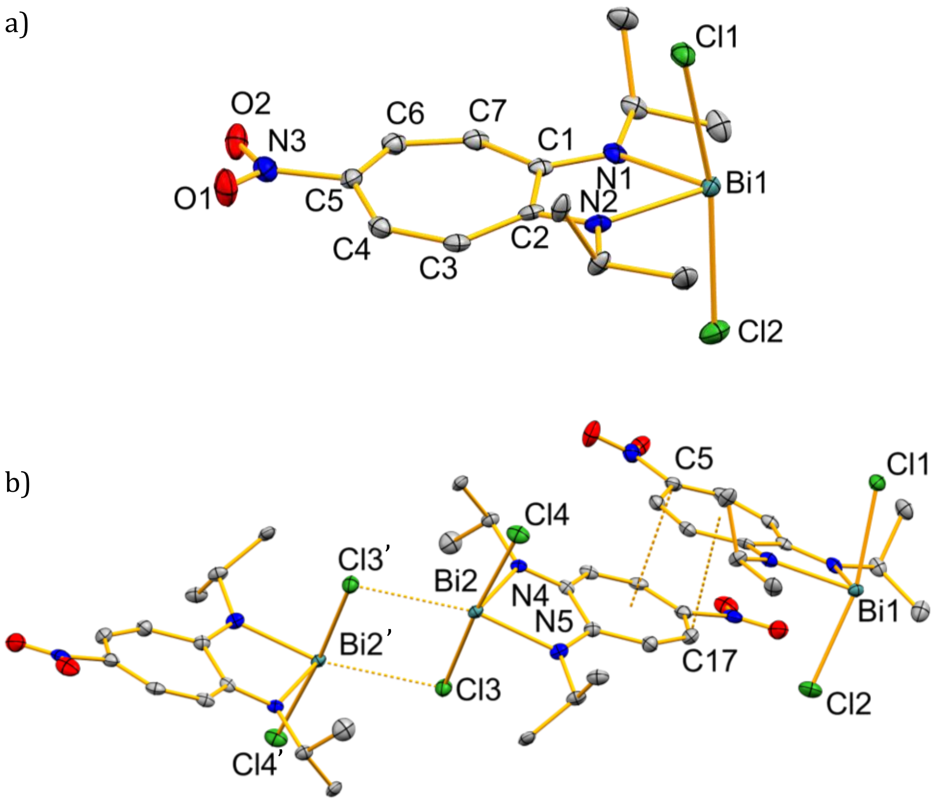

Abbildung 38: a) Mononukleare Einheit von [Bi(NO$_2$–ATI$^{i\mathrm{Pr}/i\mathrm{Pr}}$)Cl$_2$] (**9-NO$_2$**) im Festkörper. Die Ellipsoide repräsentieren 50% der Aufenthaltswahrscheinlichkeit. Wasserstoffatome wurden aus Gründen der Übersichtlichkeit nicht abgebildet. b) Mono- und dinukleare Einheit von **9-NO$_2$** mit Aren-Aren Wechselwirkungen im Festkörper. Ausgewählte Bindungslängen (Å) und -winkel (°): Bi1–Cl1, 2.705(3); Bi–Cl2, 2.648(3); Bi1–N1, 2.201(8); Bi1–N2, 2.210(9); N1–C1, 1.326(13); N2–C2, 1.330(14); N3–C5, 1.462(14); C1–C2, 1.502(14); C2–C3, 1.437(14); C3–C4, 1.365(14); C4–C5, 1.401(14); C5–C6, 1.357(15); C6–C7, 1.395(15); C7–C1 1.424(14); Bi2–Cl4, 2.648(3); Bi2–Cl3, 2.752(3); Bi2···Cl3‘, 3.077(3); Bi2–N4, 2.238(8); Bi2–N5, 2.235(9); N4–C14, 1.331(13); N5–C15, 1.326(12); Cl1–Bi1–Cl2, 165.91(8); N(1–2)–Bi1–Cl(1–2), 81.9(2)–91.1(2); N1–Bi1–N2, 72.9(3); Cl3–Bi2–Cl4, 171.73(8); N(3/4)–Bi2–Cl(3/4), 83.1(2)–91.7(2); N3–Bi2–N4, 72.8(3); N(3/4)–Bi2–Cl3‘, 107.9(2)–163.2(2); Cl(3/4)–Bi2–Cl3‘, 80.18(8)–105.04(8);. C5–[C14–C20], 3.5691(12); C5–Centroid(C14–C20), 3.571; C17–[C1–C7], 3.4924(13); C17–Centroid(C1–C7), 3.687.

Die intramolekularen Bi–Cl Bindungslängen liegen für beide Einheiten in einem ähnlichen Bereich, wobei die Bindung zu dem Chlor-Substituenten, welcher in der dinuklearen Einheit verbrückend wirkt, mit 2.75 Å deutlich länger ist, als die zu den terminal gebundenen Chloratomen (Bi1/2–Cl1/2/4, 2.65–2.71 Å). Der intermolekulare Bi···Cl3‘ Abstand (3.10 Å) in **9-NO$_2$** liegt unterhalb der Summen der van der Waals Radien (3.82 Å)[102] und ist kürzer als die entsprechenden Abstände der im Rückgrat unsubstituierten Dichloro-Spezies **9**$_\infty$ (3.22–3.44 Å), was auf die Wechselwirkung mit zwei weiteren Formeleinheiten in **9**$_\infty$ (anstatt mit einer Einheit in **9-NO$_2$**) zurückzuführen ist. Die Bi–N Bindungslängen sind im Vergleich zu **9**$_\infty$ aufgrund des elektronenziehenden Charakters der Nitro-Gruppe am Liganden länger und unterscheiden sich für die mono- und dinukleare Einheit (2.20–2.21 Å bzw. 2.24 Å) bedingt durch die unterschiedliche Umgebung der Bismutatome. Dies wirkt sich jedoch nicht auf die N–C Bindungslängen aus, die im Rahmen der Fehlergrenzen für beide Einheiten identisch sind (1.33 Å). Zusätzlich zur intermolekularen Bi⋯Cl Wechselwirkung werden außerdem Aren-Aren Wechselwirkungen zwischen dem Ligandrückgrat der mono- und dinuklearen Einheit beobachtet (Abbildung 38b). **9-NO$_2$** ist damit das zweite Beispiel eines Bismut-ATI-Halogenid-Komplexes, der eine solche Wechselwirkung eingeht.[62] In [Bi(ATI$^{Fc/iPr}$)Cl$_2$] führen diese Wechselwirkungen zur Ausbildung eines anorganisch/organischen Koordinationspolymers im Festkörper. Dies wird aufgrund der Wechselwirkung einer mononuklearen mit einer dinuklearen Einheit in **9-NO$_2$** nicht beobachtet. Die C5/C17–Centroid-Abstände (3.57–3.67 Å) liegen in einem ähnlichen Bereich wie die für [Bi(ATI$^{Fc/iPr}$)Cl$_2$] gefundenen C^{ATI}–Centroid Abstände (3.37–3.76 Å)[62] und sind maximal um 0.47 Å länger als der Abstand der Benzol-Ebenen in einem antiparallel verschobenen Nitro-Benzol Dimer (3.2 Å).[106] Die Verschiebung der π-Elektronendichte im ATI-Liganden in Richtung der Nitro-Gruppe ist in der Bismut-Verbindung, ähnlich wie im Silber-Komplex **6-NO$_2$-py**, weniger stark ausgeprägt als in den Alkalimetall-Komplexen. Dies bestätigen die N–C Bindungslängen sowie die maximale Bindungslängendifferenz zweier benachbarter C–C Bindungen im ATI-Liganden (Δ_{max}(C–C) = 0.08 Å). Auch die Verdrehung des ATI-Rückgrats ist im Vergleich zu den Alkalimetall-Komplexen gering, was auf eine gesteigerte Aromatizität hindeutet ([C1–C7]–[C1–2,N1–2,Bi1], 7.54°, [C14–C20]–[C14–15,N4–5,Bi2], 15.41°).

XVIII Zusammenfassung und Ausblick/Summary and outlook

Ein Teil der Ergebnisse in dieser Zusammenfassung wurde bereits in den Veröffentlichungen [62]–[69] publiziert.

Die Untersuchung der Koordinationschemie von Alkalimetall-Komplexen mit dem Aminotroponiminat(ATI)-Liganden H−ATI$^{\mathrm{Ph}/i\mathrm{Pr}}$ hat gezeigt, dass diese über den häufig auftretenden κ^2*N*-Koordinationsmodus (Schema 32, **A**) hinausreicht.[61] Außerdem konnte anhand elektrochemischer und chemischer Redoxstudien am Liganden H−ATI$^{\mathrm{Ph}/i\mathrm{Pr}}$ sowie an dessen Natrium- und Rhodium-Komplex die Redox-Aktivität des ATI-Liganden aufgezeigt werden.[39] Diese Befunde motivierten zu einer erweiterten Untersuchung der Koordinations- und Redox-Eigenschaften von Metall-Komplexen dieser Ligandklasse. Im Rahmen dieser Arbeit lag der Fokus nicht nur auf der Untersuchung des Einflusses des Substitutionsmusters (Substituenten an den Stickstoffatomen sowie im C_7-Rückgrat) des Liganden mit unterschiedlichen sterischen und elektronischen Parametern, sondern auch auf der Untersuchung des Einflusses des Metall-Atoms. Zudem wurden redox-aktive ATI-Liganden auf ein Bismut-Metallzentrum übertragen und die Redox-Eigenschaften der Komplexe untersucht.

Ligandsynthese. Es wurde eine Reihe an literaturbekannten (H−ATI$^{i\mathrm{Pr}/i\mathrm{Pr}}$ (**1**), H−ATI$^{\mathrm{Ph}/i\mathrm{Pr}}$ (**12**), H−ATI$^{\mathrm{Ph}/\mathrm{Ph}}$ (**13**))[71, 107] und neuen (AT$^{\mathrm{Fc}}$ (**14**), H−ATI$^{\mathrm{Fc}/i\mathrm{Pr}}$ (**15**), H−ATI$^{\mathrm{PhSMe}/i\mathrm{Pr}}$ (**16**)) Aminotropon(AT)- und Aminotroponimin(ATI)-Liganden mit unterschiedlichen Substituenten an den Stickstoffatomen und literaturbekannte ATI-Liganden mit Substituenten in C5-Position am C_7-Ring (Ph(O)S−ATI$^{i\mathrm{Pr}/i\mathrm{Pr}}$ (**1-Ph(O)S**), NO_2−ATI$^{i\mathrm{Pr}/i\mathrm{Pr}}$ (**1-NO$_2$**))[70] synthetisiert. Eine Standardroute für im Rückgrat unsubstituierte ATIs stellt die zweistufige Synthese ausgehend von Tosyloxytropon dar (Schema 28, oben).

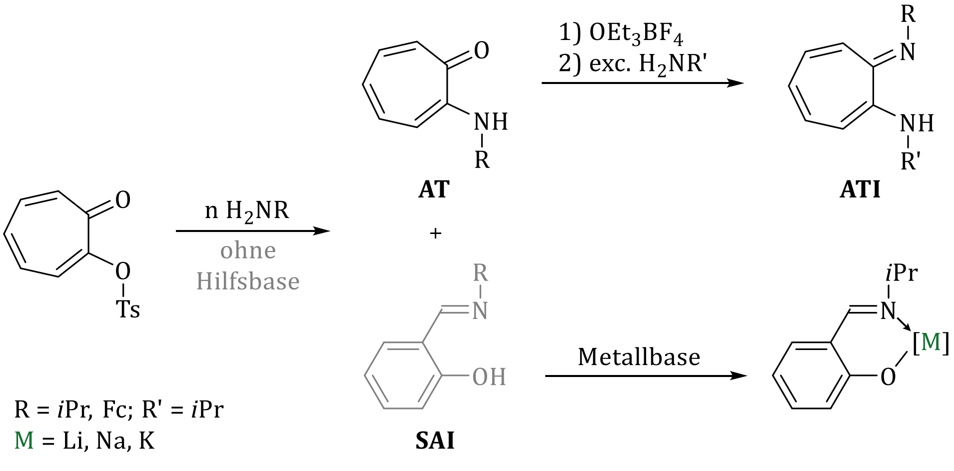

Schema 28: Syntheseroute zur Darstellung von Aminotroponiminen (ATIs) (oben). Für R = *i*Pr und n = 10 sowie R = Fc und n = 1 und ohne Verwendung einer zusätzlichen Hilfsbase wird das Salicylaldimin (SAI)-Derivat als Nebenprodukt isoliert. Metallierung des Salicylaldimin-Derivats (unten). Ts = SO_2-*p*-(C_6H_4Me).

Bei der Synthese von *Iso*propylaminotropon und Ferrocenylaminotropon konnten unter Standardbedingungen die Salicylaldimin(SAI)-Derivate SAI^{iPr} und SAI^{Fc} als Nebenprodukte in geringen Ausbeuten von 3−4% isoliert werden. Durch Anpassung der Reaktionsbedingungen konnte die Ringkontraktion, welche zur Bildung der SAIs führte, signifikant erhöht, bevorzugt adressiert und bis hin zum Hauptreaktionspfad ausgebaut werden. Die Umsetzung von SAI^{iPr} mit der entsprechenden Metallbase führte zu den Alkalimetall-SAI-Komplexen. Der Natrium-Komplex **Na-SAI**$^{\mathbf{iPr}}$ zeigte im Festkörper eine für Natrium SAI-Komplexe seltene, doppelte Heterocuban-Struktur und ist das erste Beispiel, in welchem eine solche Struktur ohne zusätzliche Donor-Substituenten in der Ligandperipherie ausbildet wurde (Abbildung 39a). Die Struktur des Kalium-Komplexes konnte in Form der 18-Krone-6 komplexierten Spezies **K(18K6)-SAI**$^{\mathbf{iPr}}$ aufgeklärt werden (Abbildung 39b). Zudem konnte gezeigt werden, dass die Komplexierung mit dem Kronenether in Lösung eine reversible *E*/*Z*-Isomerisierung der Aldimin C−N Doppelbindung induziert. Stöchiometrische Umsetzungen zweier Alkalimetallkomplexe bzw. die Umsetzung der Lithium- und Natrium-Komplexe in einem Verhältnis von 1:1, 1:3 und 3:1 führte zu gemischtmetallischen SAI-Komplexen. Der Komplex $[Li_3Na(SAI)_4(thf)_2]$ (**Li**$_3$**Na-SAI**$^{\mathbf{iPr}}$**-(thf)**$_2$) konnte als erster s-Block Metall-SAI-Komplex dieser Art strukturell charakterisiert werden (Abbildung 39c). Anhand NMR-spektroskopischer, massenspektrometrischer und einkristall-röntgenstrukturanalytischer Untersuchungen sowie durch DFT-Rechnungen zeigte sich, dass die Komplexe bei Raumtemperatur in Lösung in Gleichgewichten unterschiedlich stark aggregierter, schnell ineinander umwandelbarer Spezies vorliegen.

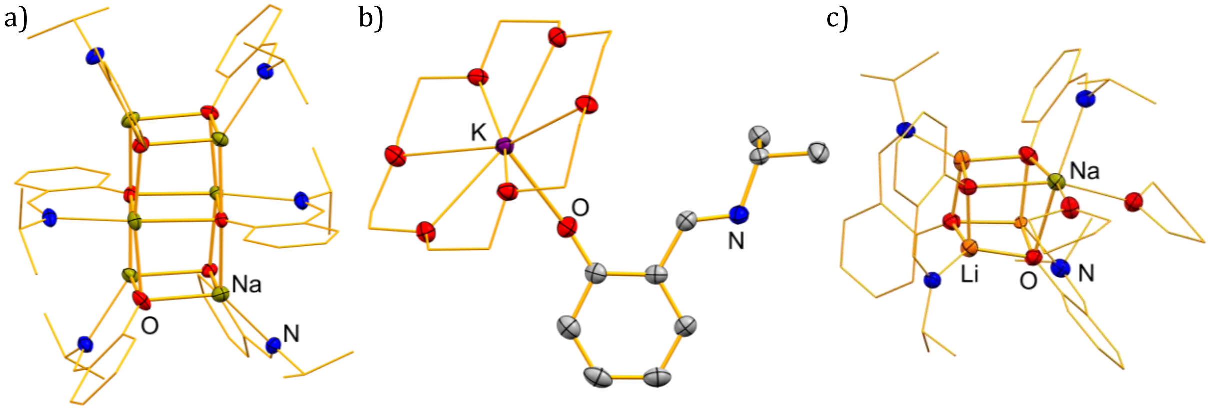

Abbildung 39: Strukturen im Festkörper von **Na-SAI**$^{\mathbf{iPr}}$, **K(18K6)-SAI**$^{\mathbf{iPr}}$ und **Li**$_3$**Na-SAI**$^{\mathbf{iPr}}$**-(thf)**$_2$. Die Kohlenstoffatome der SAI-Einheiten in a) und c), sowie die Kohlenstoffatome des Kronenethers in b) und der THF-Moleküle in c) sind im Drahtmodell dargestellt.

Die literaturbekannte Synthese der im Rückgrat substituierten Liganden verläuft entweder in einer einstufigen Synthese ausgehend vom unsubstituierten ATI über eine elektrophile aromatische Substitution für **1-NO**$_2$, oder dreistufig über **1-Br** mit anschließender nukelophiler aromatischer Substitution und Oxidation zu **1-Ph(O)S**.[70] **1-NO$_2$** konnte über die Literaturroute (und in Einklang mit der Literatur) nur in geringen Ausbeuten von 19% dargestellt werden. Eine Veränderung der Reaktionsbedingungen durch Verwendung verschiedener Lösungsmittel, Reaktionstemperaturen und -zeiten führte zu keiner Steigerung der Ausbeute. Eine Darstellung von **1-NO$_2$** über **1-Br** in Anlehnung an die Synthese von **1-Ph(O)S** wurde untersucht und stellt für zukünftige Synthesen dieser Art einen interessanten Ausgangspunkt dar. Die Produktverteilung variierte allerdings stark mit unterschiedlichen Reaktionsbedingungen (Schema 29). Der Einfluss veränderter Reaktionsbedingungen zeigte sich auch in der Isolierung des ringkontrahierten Nebenprodukts **2** als einzige isolierbare Spezies aus einem Reaktionsansatz mit erhöhter Reaktionstemperatur und verlängerter Reaktionszeit (Schema 29).

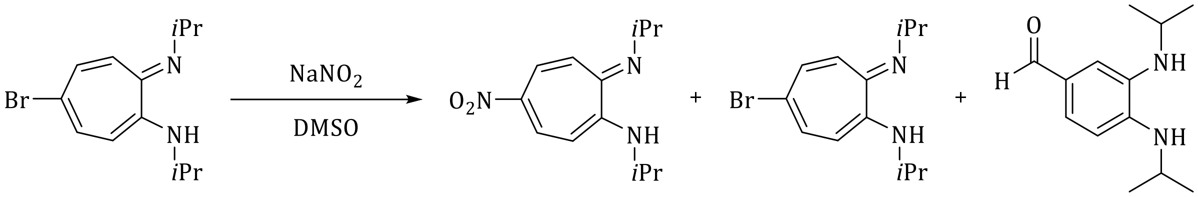

1-Br		**1-NO$_2$**	**1-Br**	**2**
	110 °C, 7 d:	≤42%[a]	≥21%	nicht gefunden
	150 °C 16 d:	<5%	<5%	5%

Schema 29: Synthese von **1-NO$_2$** ausgehend von **1-Br** unter verschiedenen Reaktionsbedingungen. [a] für verschiedene Reaktionsansätze wird eine schwankende Ausbeute erhalten.

Synthese der Alkalimetall-Komplexe. Ausgehend von den neutralen ATI (und AT) Liganden wurden die Alkalimetall-Komplexe durch Umsetzung mit der entsprechenden Metallbase dargestellt (Schema 30). Wird *n*-Butyllithium als Lithiierungsreagenz verwendet, erhält man den gewünschten Komplex [Li(ATI$^{Ph/Ph}$)(Et$_2$O)$_2$] (**Li-13**) sowie ein Nebenprodukt, das durch Addition von *n*-Butyllithium am C$_7$-Ring entsteht. Im Additionsprodukt ist der *n*-Butyl-Rest an C1-Postiton gebunden und das Lithiumatom liegt in der *N*,*N*-Bindungstasche vor.

Die NMR-spektroskopische Charakterisierung aller im Rückgrat unsubstituierten Komplexe steht im Einklang mit den erwarteten Resonanzen für an den Stickstoffatomen symmetrisch ($R^1 = R^2$) bzw. unsymmetrisch ($R^1 \neq R^2$) substituierten ATI-Komplexen.

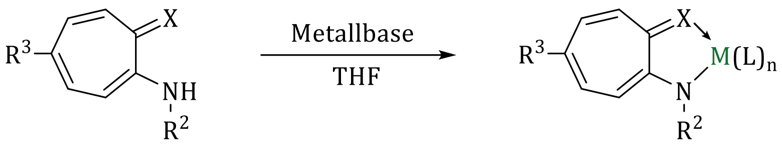

X = O, NR^1; R^1 = *i*Pr, Ph;
R^2 (für X = O) = *i*Pr, Fc (Ferrocenyl);
R^2 (für X = NR^1) = *i*Pr, Fc, Ph, PhSMe;
R^3 = H, Ph(O)S, NO_2; L = Neutralligand; M = Li, Na, K

Schema 30: Synthese der Alkalimetall-ATI und AT-Komplexe.

Die Natrium- und Kalium-Komplexe **4-NO₂** und **5-NO₂** mit Nitro-Funktionalität in C5-Position zeigten in ihren NMR-Spektren eine für ATI-Komplexe bisher unbeschriebene *E*,*E*/*E*,*Z*-Isomerisierung. Aufgrund der elektronenziehenden Eigenschaften der Nitro-Gruppe kann von einer Verschiebung der π-Elektronendichte in Richtung des Rückgratsubstituenten ausgegangen werden. Außerdem kann die Nitro-Gruppe als zusätzliche Koordinationsstelle für ein Metall-Atom fungieren. Damit ergeben sich drei mögliche Isomere für die Komplexe (Schema 31). NMR-spektroskopische Untersuchungen sowie DFT-Rechnungen unterstützten die Annahme einer Isomerisierung dieser Art in Lösung.

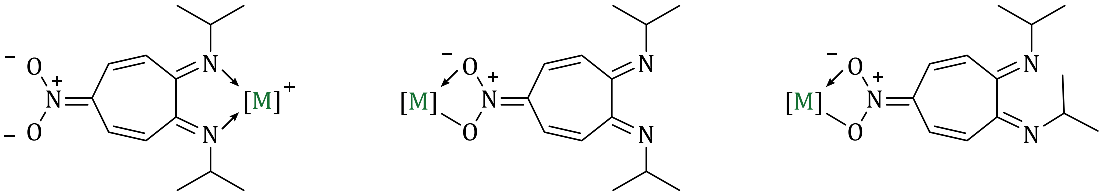

N-*E,E* **O-*E,E*** **O-*E,Z***

Schema 31: Schematische Darstellung möglicher Isomere der Alkalimetall-ATI-Komplexe mit Nitrofunktionalität. [M] = Li, Na, K.

Koordinationschemie der Alkalimetall-Komplexe. Die strukturelle Charakterisierung der ATI-Komplexe zeigte eine Vielzahl möglicher Koordinationsmodi auf. Neben einem Komplex mit dem für ATI-Komplexe bisher dominierenden κ²*N*-Kooridnationsmodus (Schema 32; **A**, für [Na(ATI$^{Ph/Ph}$)(Et$_2$O)$_2$] (**Na-13**)), wurden weitere Beispiele für Komplexe gefunden, in welchen eine Wechselwirkung des Metall-Atoms mit dem C$_7$-Rückgrat einer benachbarten Einheit auftritt, die in der Literatur erstmals für den Natrium-Komplex [Na(ATI$^{Ph/iPr}$)(thf)]$_\infty$ (**[Na-12-thf]$_\infty$**) diskutiert wurde (Schema 32, **B**, für [Na(ATI$^{iPr/iPr}$)(thf)] (**[4-thf]$_\infty$**) und [K(ATI$^{iPr/iPr}$)(thf)] (**[5-thf]$_\infty$**)). DFT-Rechnungen konnten zeigen, dass die Tendenz zur Ausbildung von Kation-π-Wechselwirkungen mit zunehmendem elektronenziehenden Charakter der Substituenten am Stickstoffatom aufgrund der damit einhergehenden Absenkung des HOMOs der Komplexe abnimmt. Auch die energetische Lage der LUMOs sinkt mit steigender Gruppenelektronegativität der Substituenten an den Stickstoffatomen, was das Potential für M→ATI Rückbindungen erhöht. Aufgrund der Ausbildung von Metall-Aren Wechselwirkungen konnten zwei weitere Koordinationsmodi gefunden werden (Schema 32, **C** für [K(ATI$^{\mathrm{Ph/Ph}}$)]$_\infty$ und **D** für [Li(ATI$^{\mathrm{Ph/Ph}}$)]$_\infty$). Alle Komplexe, die die Koordinationsmodi **B**–**D** zeigten, bildeten aufgrund der verbrückenden Eigenschaften der Liganden Koordinationspolymere im Festkörper aus.

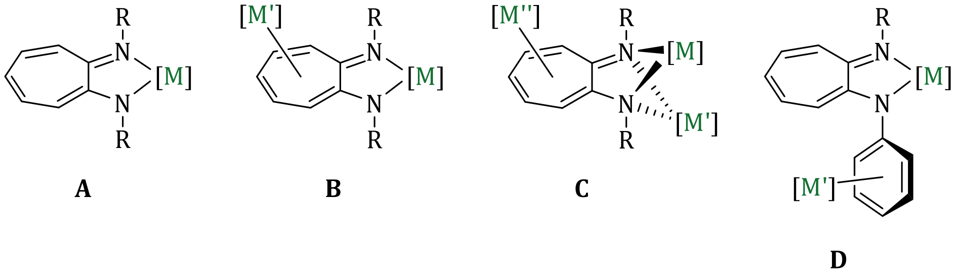

Schema 32: Koordinationsmodi von Alkalimetall-ATI-Komplexen ohne Rückgratsubstituent.

Wie es aufgrund des elektronenziehenden Charakters der Rückgratsubstituenten zu erwarten war, zeigten die Sulfinyl- und Nitro-substituierten Komplexe keine Metall-Aren Wechselwirkung mit dem C$_7$-Rückgrat. Stattdessen fungierten die Rückgratsubstituenten als Donoren, die die Koordinationssphäre des Metall-Atoms benachbarter Moleküleinheiten absättigten (Schema 33). Der verbrückende Charakter der Liganden führte ebenfalls zur Ausbildung von Koordinationspolymeren im Festkörper.

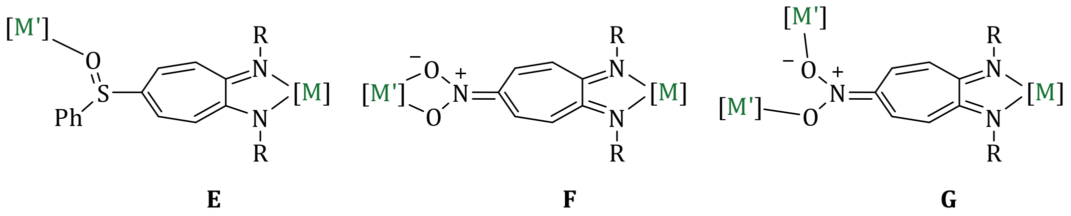

Schema 33: Koordinationsmodi von Alkalimetall-ATI-Komplexen mit Rückgratsubstituent.

Eine Verschiebung der π-Elektronen in Richtung der Nitro-Gruppe konnte für die Alkalimetall-Komplexe [Li(NO$_2$–ATI$^{i\mathrm{Pr}/i\mathrm{Pr}}$)(py)] (**[3-NO$_2$-py]$_\infty$**), [Na(NO$_2$–ATI$^{i\mathrm{Pr}/i\mathrm{Pr}}$)(py)] (**[4-NO$_2$-py]$_\infty$**) und [K(NO$_2$–ATI$^{i\mathrm{Pr}/i\mathrm{Pr}}$)(py)] (**[5-NO$_2$-py]$_\infty$**) anhand von C–N Bindungen mit Doppelbindungscharakter sowie stärker lokalisierten C–C Doppelbindungen im Vergleich zu im Rückgrat unsubstituierten Stammverbindungen bestätigt werden. Die verringerte Delokalisation der π-Elektronen spiegelte sich auch in einer Verdrehung des Rückgrates aus der Ebene wider. Verdrehungswinkel von bis zu 39° überstiegen die Winkel für literaturbekannte (Halb-)Metall-ATI-Komplexe deutlich.[78]

Der Einfluss neutraler Donorliganden auf die Koordinationschemie der Alkalimetall-Komplexe und damit die Beständigkeit von ausgebildeten Kation-π-Wechselwirkungen wurde durch Umsetzung ausgewählter Komplexe mit PMDTA und Kronenethern untersucht. Für $[\mathrm{Na(ATI^{Ph/\mathit{i}Pr})(thf)}]$ (**$[\mathbf{Na\text{-}12\text{-}thf}]_\infty$**) wurde durch den dreizähnigen Stickstoffdonor-Liganden PMDTA, wie erwartet, ein Aufbruch der Polymerstruktur und die Bildung eines Monomeren Komplexes induziert. Die Umsetzung von **$[\mathbf{4\text{-}thf}]_\infty$** und **$[\mathbf{Na\text{-}12\text{-}thf}]_\infty$** mit Kronenethern führte dagegen zu einer ligandinduzierten Disproportionierung unter Ausbildung der Natrium-Natriat-Komplexe $[\mathrm{Na(12\text{-}Krone\text{-}4)_2}][\mathrm{Na(ATI^{\mathit{i}Pr/\mathit{i}Pr})_2}]$ (**$\mathbf{4\text{-}(12K4)_2}$**) und $[\mathrm{Na(12\text{-}Krone\text{-}4)_2}][\mathrm{Na(ATI^{Ph/\mathit{i}Pr})_2}]$ (**$\mathbf{Na(12K4)_2\text{-}12}$**) (Abbildung 40a). Die stöchiometrische Reaktion eines Natrium- und eines Kalium-Komplexes führte zu den ersten gemischtmetallischen Kalium-Natriat-Komplexen, in welchen das weichere Kalium-Kation eine Wechselwirkung mit dem C_7-Rückgrat zweier $[\mathrm{Na(ATI)_2}]^-$-Einheiten eingeht, was die Ausbildung einer polymeren Struktur im Festkörper zur Folge hat (Abbildung 40b).

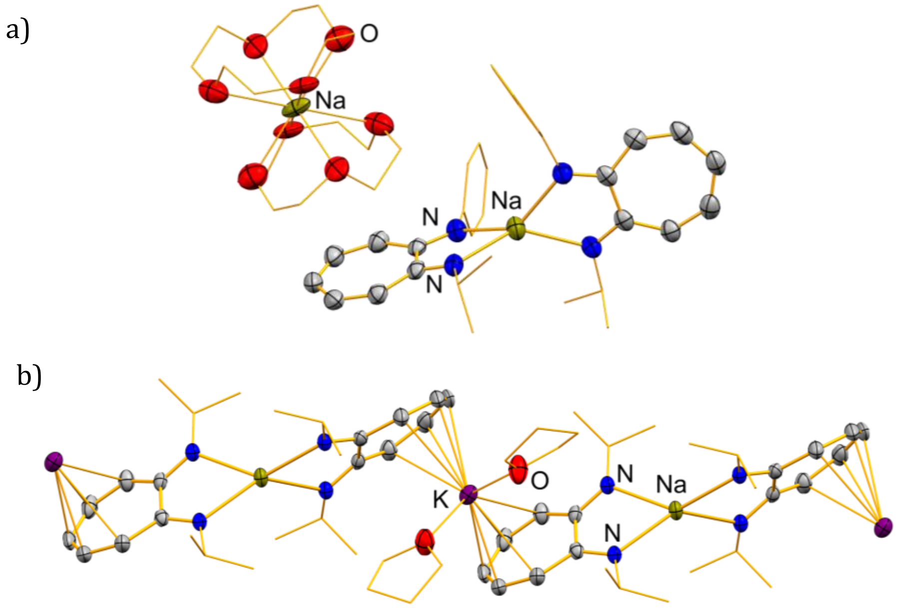

Abbildung 40: a) Struktur von $[\mathrm{Na(12\text{-}Krone\text{-}4)_2}][\mathrm{Na(ATI^{Ph/\mathit{i}Pr})_2}]$ (**$\mathbf{Na(12K4)_2\text{-}12}$**) im Festkörper. b) Auschnitt der Struktur von $[\mathrm{KNa(ATI^{\mathit{i}Pr/\mathit{i}Pr})_2(thf)_2}]_\infty$ im Festkörper. Die Kohlenstoffatome des Kronenethers in a) und die Kohlenstoffatome der THF-Moleküle in b) sowie die Kohlenstoffatome der sticktoffgebundenen Substituenten in a) und b) sind im Drahtmodell dargestellt.

Der Zusammenhang zwischen Struktur und Reaktivität wurde für die Natrium- und gemischtmetallischen Komplexe anhand ihrer Aktivität als Initiatoren der Ringöffnungspolymerisation von ε-Caprolacton untersucht. Es konnte gezeigt werden, dass die Komplexe mit $[\mathrm{Na(ATI)_2}]^-$-Einheit aktivere Initiatoren sind, als Komplexe mit einer neutralen $[\mathrm{Na(ATI)}]$-Einheit. Es wurde allerdings eine geringe Molekulargewichtskontrolle in THF beobachtet. Der in Toluol lösliche Komplex $[\mathrm{Na(ATI^{Ph/\mathit{i}Pr})(thf)}]$ vereinte eine gute

Katalysatoraktivität mit hervorragender Molekulargewichtskontrolle für Polymerisationen in Toluol. In Kombination sind diese Eigenschaften jenen literaturbekannter Alkalimetall-Initiatoren für die Polymerisation von ε-Caprolacton überlegen.

Für [Na(Ph(O)S–ATI$^{iPr/iPr}$)] (**4-Ph(O)S**) führte die Umsetzung mit 12-Krone-4 in Analogie zu der im Rückgrat unsubstituierten Stammverbindung zum Natrium-Natriat-Komplex [Na(12-Krone-4)$_2$][Na(Ph(O)S–ATI$^{iPr/iPr}$)$_2$] (**6-Ph(O)S**). Der Nitro-substituierte Komplex **4-NO$_2$** dagegen zeigte die Bildung eines Adduktkomplexes [Na(NO$_2$–ATI$^{iPr/iPr}$)(15-Krone-5)] (**4-NO$_2$-(15K5)**) für eine Umsetzung mit 15-Krone-5 bzw. die Bildung eines ATI-Anions, das keine gerichtete Bindungswechselwirkung zum [Na(12-Krone-4)$_2$]-Kation eingeht für die Umsetzung mit zwei Äquivalenten 12-Krone-4 (Abbildung 41). **4-NO$_2$-(12K4)$_2$** ist damit die erste strukturell charakterisierte ATI-Verbindung mit einem freien Ligandanion. Die Umsetzung von [K(NO$_2$–ATI$^{iPr/iPr}$)] (**5-NO$_2$**) mit 18-Krone-6 lieferte den zu **4-NO$_2$-(15K5)** analogen Kalium-Komplex [K(NO$_2$–ATI$^{iPr/iPr}$)(18-Krone-6)] (**5-NO$_2$-(18K6)**). Die Verdrehung des ATI-Gerüts ist für die Kronenether-Komplexe noch deutlicher ausgeprägt, als für die unkomplexierten Stammverbindungen.

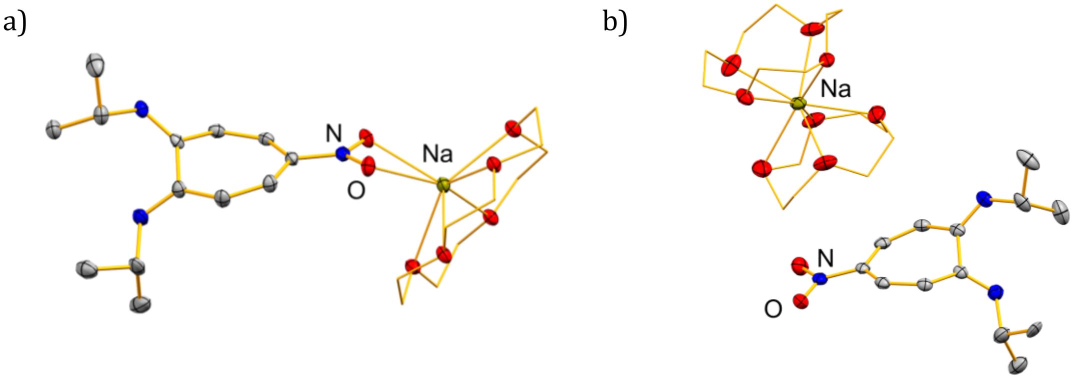

Abbildung 41: Strukturen im Festkörper von a) [Na(NO$_2$–ATI$^{iPr/iPr}$)(15-Krone-5)] (**4-NO$_2$-(15K5)**) und b) [Na(12-Krone-4)$_2$][Na(NO$_2$–ATI$^{iPr/iPr}$)] (**4-NO$_2$-(12K4)$_2$**). Die Kohlenstoffatome der Kornenether sind im Drahtmodell dargestellt.

Für **4-NO$_2$-(15K5)**, **4-NO$_2$-(12K4)$_2$** und **5-NO$_2$-(18K6)** kann in Lösung, ebenso wie für die Stammverbindungen, eine *E*,*E*/*E*,*Z*-Isomerisierung beobachtet werden, jedoch konnten im Festköper ausschließlich die *E*,*Z*-Isomere gefunden werden. DFT-Rechnungen bestätigten diese als energetisch günstigste Isomere der Kronenether-Komplexe. Für **4-NO$_2$-(12K4)$_2$** konnte durch DFT-Rechnungen ein linearer Übergangszustand mit einer Energiebarriere von $\Delta G^{\ddagger} = 26.6\ \mathrm{kcal \cdot mol^{-1}}$ von *E*,*Z*- zu *E*,*E*-Konfiguration bestimmt werden.

Die Flexibilität, Koordinationschemie und Reaktivität von ATI-Komplexen kann somit durch die folgenden Parameter signifikant beeinflusst werden: i) Wahl der Substituenten an den Stickstoffatomen und am C_7-Rückgrat des Liganden, ii) Wahl des Zentral-Atoms in der *N*,*N*-Bindungstasche oder am Rückgratsubstituenten, und iii) durch die Komplexierung mit neutralen Donor-Liganden. Durch Kenntnis der einflussnehmenden Faktoren sollte es in der Zukunft möglich sein, Komplexe mit den gewünschten Eigenschaften für Anwendungen in der Koordinationschemie, Redox-Chemie und der Katalyse zu synthetisieren.

Redox-Verhalten der Alkalimetall-Komplexe. Elektrochemische Untersuchungen der ATI-Liganden und Alkalimetall-ATI-Komplexe mittels Cyclovoltammetrie bestätigten deren Redox-Aktivität. Unter oxidativen Bedingungen fanden sich für im Rückgrat unsubstituierte und substituierte Verbindungen Redoxereignisse, welche einer irreversiblen Oxidation des Liganden zugeschrieben wurden. Das Einbringen des redox-aktiven Ferrocenyl-Substituenten führte erstmal zu ATI-Verbindungen mit reversiblen, ligandzentrierten Redox-Ereignissen unter oxidativen Bedingungen. Komplexe mit Sulfinyl-Substituent im Rückgrat zeigten außerdem irreversible Oxidationsereignisse, die möglicherweise einer Oxidation der Sulfinyl-Gruppe entsprechen. Im Allgemeinen wird für die Oxidationspotentiale eine Verschiebung zu positiveren Potentialen mit zunehmendem elektronenziehenden Charakter der Liganden an den Stickstoffatomen und dem ATI-Rückgrat beobachtet. Unter reduktiven Bedingungen konnte für die im Rückgrat unsubstituierten Komplexe $[\mathrm{Li}(\mathrm{ATI}^{i\mathrm{Pr}/i\mathrm{Pr}})]$ (**3**) und $[\mathrm{Li}(\mathrm{ATI}^{\mathrm{Ph}/i\mathrm{Pr}})]$ (**Li-12**) im Vergleich zum literaturbekannten Komplex $[\mathrm{Na}(\mathrm{ATI}^{\mathrm{Ph}/i\mathrm{Pr}})(\mathrm{thf})]$ (**[Na-12-thf]**$_\infty$) sowohl ein Einfluss der Substituenten an den Stickstoffatomen als auch des Zentralmetalls auf die Redox-Potentiale von ligandzentrierten Reduktionsereignissen festgestellt werden. Beide Lithium-Komplexe zeigten unter elektrochemischen Bedingungen ein ähnliches Verhalten wie der literaturbekannte Komplex **[Na-12-thf]**$_\infty$. Eine Separation von Reduktions- und zugehöriger Oxidationswelle deutete auf eine reduktiv induzierte Dimerisierung hin.[39] Die im Rückgrat substituierten Komplexe weisen Redox-Ereignisse auf, die weniger eindeutig auf reduktive Dimerisierungen hinwiesen, da sowohl irreversible Reduktionswellen als auch eine Vielzahl von Ereignissen, für die die Zusammengehörigkeit von Redox-Wellen nicht immer eindeutig bestimmt werden konnte, gefunden wurden.

Auf Grundlage der Daten aus elektrochemischen Untersuchungen wurden chemische Redox-Studien an den ATI-Komplexen durchgeführt. Die Reduktion von **3** und **Li-12** mit starken Reduktionsmitteln in Form der entsprechenden Alkalimetalle führte, wie in der Literatur für **[Na-12-thf]**$_\infty$ beschrieben, zur chemoselektiven, chemisch reversiblen Bildung von Dimeren (Schema 34).[39] Die Regioselektivität der Dimerisierung wurde maßgeblich durch die Art des Zentral-Atoms sowie das Substitutionsmuster an den Stickstoffatomen des Liganden und die damit zusammenhängende Spindichteverteilung in Radikalintermediaten beeinflusst. Zudem schienen Aggregationsprozesse der Radikalspezies in Lösung eine Rolle zu spielen. Die Diastereoselektivität stand im Zusammenhang mit den gewählten Reaktionsbedingungen. Für das Dimerisierungsprodukt von **3** lagen das *rac*- und *meso*-Isomer in einem Gleichgewicht vor.

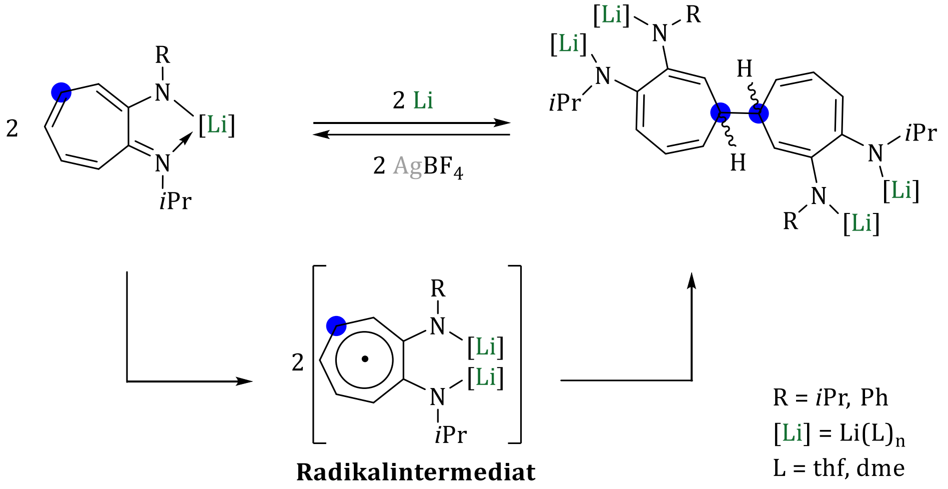

Schema 34: Reversible, reduktive Dimerisierung von [Li(ATI$^{iPr/iPr}$)] (**3**) und [Li(ATI$^{Ph/iPr}$)] (**Li-12**). dme = Dimethoxyethan.

Bei Reduktionsversuchen der Nitro-substituierten sowie der Lithium- und Natrium-sulfinyl-substituierten Komplexe mit starken Reduktionsmitteln konnten keine Reduktionsprodukte, sondern lediglich unverbrauchtes Edukt isoliert werden. Die Umsetzung von [K(Ph(O)S–ATI$^{iPr/iPr}$)] (**5-Ph(O)S**) mit elementarem Kalium führte zum Reduktionsprodukt **5-red**, für welches mit Hilfe NMR-spektroskopischer Daten ein Strukturvorschlag gemacht werden konnte. Eine abschließende Klärung der Struktur von **5-red** mit Hilfe von Einkristallröntgenstrukturanalyse ist noch ausstehend.

Um eine Stabilisierung ligandzentrierter Radikale und damit eine Isolierung von radikalischen ATI-Spezies zu ermöglichen, könnten die Substituenten an den Stickstoffatomen der bereits untersuchten rückgartsubstituierten ATI-Komplexe bzw. der Rückgratsubstituent selbst variiert werden. Eine Kombination aus mesomeren und induktiven Effekten, die zu einer Verringerung der Elektronendichte im ATI-Rückgrat führt, scheint für die Wahl der Liganden sinnvoll. Beispielsweise könnten Phenyl- anstatt *Iso*propyl-Substituenten an den Stickstoffatomen und Substituenten mit elektronenziehenden CF$_3$-Gruppen am ATI-Rückgrat verwendet werden.

Das Auftreten eines unter elektrochemischen Bedingungen irreversiblen Oxidationsereignisses für den Natrium-Komplex **4-NO$_2$**, sowie die einzigartige Struktur der Kronenetherverbindung [Na(12-Krone-4)$_2$][Na(NO$_2$–ATI$^{iPr/iPr}$)] (**4-NO$_2$-(12K4)$_2$**), veranlasste zu einer Untersuchung des

Verhaltens der Nitro-Komplexe unter oxidativen Bedingungen. Unter Verwendung der Oxidationsmittel $NOSbF_6$, Ferroceniumchlorid und Tropylium-BAr^F (BAr^F = $B(3,5-(CF_3)_2-C_6H_3)_4$)) konnten allerdings keine Produkte einer Einelektronenoxidation isoliert werden. Die Umsetzung von **4-NO₂**, **4-NO₂-(12K4)₂** und **4-NO₂-(15K5)** mit dem Oxidationsmittel Silbertetrafluoroborat lieferte die ersten monometallischen Silber- sowie gemischtmetallischen Natrium-Argentat-ATI-Komplexe (Abbildung 42). Schwierigkeiten bei der Entfernung von während der Salzeliminierung gebildeten Boratsalzen erschwerte allerdings eine vollständige Charakterisierung der Komplexe.

Durch die Darstellung des Silber-Komplexes **6-NO₂** über eine alternative Syntheseroute, beispielsweise ausgehend vom Kalium-Komplex durch Umsetzung mit AgCl oder $AgNO_3$, könnte die Bildung schwer zu entfernender Borat-Salze vermieden werden, was die selektive Synthese der Silber-Verbindung, sowie deren vollständige Charakterisierung ermöglichen würde. Ausgehend davon wären die Argentat-Komplexe durch Umsetzung von **6-NO₂** mit den entsprechenden Alkalimetall-Kronenether-Komplexen zugänglich. Außerdem könnte **6-NO₂** zur Synthese Nitro-substituierter Bismut-ATI-Spezies in Salzeliminierungen genutzt werden. Die ATI-Argentate könnten zum Beispiel auf ihre Eignung als Argentierungsreagenzien, für funktionalisierte Aromaten hin untersucht werden. Ähnlich zu Organocupraten könnten die funktionalisierten Organoargentate, die nicht über die klassischen Syntheserouten ihrer Kupferanaloga, wie Oxidation, Hydrometallierung oder Halogen-Metall-Austausch dargestellt werden können, in der organischen Synthese eingesetzt werden.

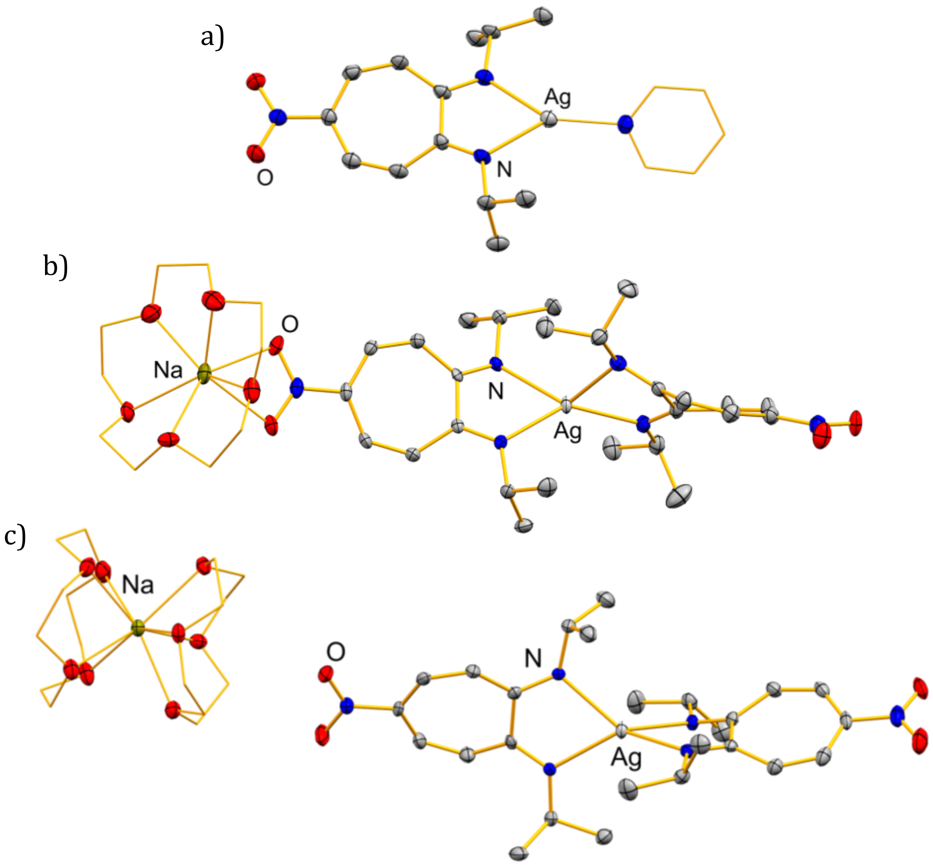

Abbildung 42: Strukturen im Festkörper von a) [Ag(NO$_2$–ATI$^{i\mathrm{Pr}/i\mathrm{Pr}}$)(py)] (**6-NO$_2$-py**), b) [Na(15-Krone-5)Ag(NO$_2$–ATI$^{i\mathrm{Pr}/i\mathrm{Pr}}$)$_2$] (**7-NO$_2$-(15K5)**) und c) [Na(12-Krone-4)$_2$][Ag(NO$_2$–ATI$^{i\mathrm{Pr}/i\mathrm{Pr}}$)$_2$] (**7-NO$_2$-(12K4)$_2$**). Die Kohlenstoffatome des Pyridin-Moleküls in a) und die Kohlenstoffatome der Kronenether-Moleküle in b) und c) sind im Drahtmodell dargestellt.

Oxidationsversuche von **4-NO$_2$-(12K4)$_2$** mit Ph$_3$CCl führten ebenfalls nicht zu oxidierten Spezies, sondern zu dem triphenylmethyl-substituierten Komplex [Na(12-Krone-4)$_2$(3-Ph$_3$C–5-NO$_2$–ATI$^{i\mathrm{Pr}/i\mathrm{Pr}}$)] (**4-NO$_2$-Ph$_3$C-(12K4)$_2$**). Während elektrophile aromatische Substitutionen an ATI-Liganden bereits literaturbekannt sind,[83] wurde diese Art der Reaktion an ATI-Komplexen hier erstmals beobachtet. Das neuartige Reaktionsverhalten konnte auf weitere, im Rückgrat substituierte und unsubstituierte Natrium-ATI-Komplexe übertragen werden. Die Komplexe **4-NO$_2$-Ph$_3$C-(12K4)$_2$** sowie [Na(3-Ph$_3$C–5-Ph(O)C–ATI$^{i\mathrm{Pr}/i\mathrm{Pr}}$)] (**4-Ph(O)C-Ph$_3$C**) konnten unter den gewählten Reaktionsbedingungen nur in geringen Ausbeuten isoliert werden. Die Synthese der einfach und zweifach Ph$_3$C-substituierten Komplexe [Na(Ph$_3$C–ATI$^{i\mathrm{Pr}/i\mathrm{Pr}}$)] (**4-Ph$_3$C**) und [Na(3,5-bis(Ph$_3$C)–ATI$^{i\mathrm{Pr}/i\mathrm{Pr}}$)] (**4-(Ph$_3$C)$_2$**) lieferte unter ähnlichen Reaktionsbedingungen gute Ausbeuten (Abbildung 43).

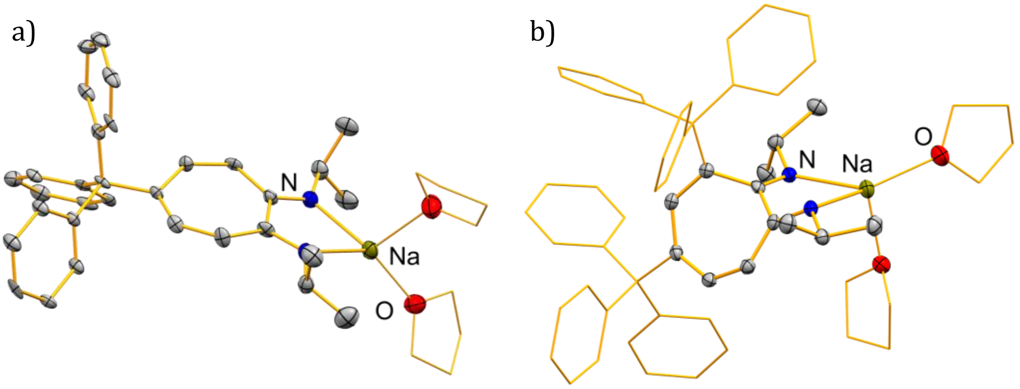

Abbildung 43: Struktur im Festkörper von a) [Na(Ph$_3$C–ATI$^{iPr/iPr}$)(thf)$_2$] (**4-Ph$_3$C-(thf)$_2$**) und b) [Na(3,5 bis(Ph$_3$C)–ATI$^{iPr/iPr}$)(thf)$_2$] (**4-(Ph$_3$C)$_2$-(thf)$_2$**). Die Kohlenstoffatome der Ph$_3$C-Substituenten in b) und die Kohlenstoffatome der THF-Moleküle in a) und b) sind im Drahtmodell dargestellt.

Eine selektive Darstellung von **4-NO$_2$-Ph$_3$C-(12K4)$_2$** und **4-Ph(O)C-Ph$_3$C** sollte durch eine Optimierung der Reaktionsbedingungen der Synthese möglich sein. Die Oxidationsversuche mit den gewählten Oxidationsmitteln zeigen auf, dass, je nach Reagenz, bevorzugt Salzeliminierungen bzw. elektrophile aromatische Substitutionen stattfinden. Die elektrophile aromatische Substitution bietet Zugang zu Komplexen mit sterisch stark abgeschirmtem Rückgrat. Durch Verwendung unterschiedlicher Elektrophile könnte die Synthese weiterer rückgratsubstituierter ATI-Komplexe, die nicht über konventionelle Syntheserouten dargestellt werden können, zum Beispiel weitere alkyl- oder arylmethyl-funktionalisierte ATI-Komplexe, möglich sein. Der sterische Einfluss der Triphenylmethyl-Reste sowie ein verändertes Kristallisationsverhalten der Ph$_3$C-substituierten Komplexe im Vergleich zu den Stammverbindungen könnte dazu beitragen, reduktiv generierte Radikalspezies zu stabilisieren und somit eine Isolierung dieser zu ermöglichen.

Synthese der Bismut-Komplexe. Ausgehend von den Alkalimetall-ATI-Komplexen wurden Bismut-ATI-Komplexe in Salzeliminierungsreaktionen dargestellt (Schema 35). Die homoleptischen Komplexe [Bi(ATI$^{Fc/iPr}$)$_3$] (**Bi-15**) und [Bi(ATI$^{Ph/iPr}$)$_3$] (**Bi-12**) konnten in guten Ausbeuten isoliert werden. [Bi(ATI$^{iPr/iPr}$)$_3$] (**10**) dagegen konnte aufgrund seiner geringen Stabilität in Lösung nur in sehr geringen Mengen erhalten werden, die keine vollständige Charakterisierung zuließen. Heteroleptische Bismut-Chloro-Komplexe des im Rückgrat unsubstituierten Liganden H–ATI$^{iPr/iPr}$ (**1**) konnten aufgrund ihrer schlechten Löslichkeit in gängigen organischen Lösungsmitteln nicht in analysenreiner Form isoliert werden. Außerdem wurde bei der Synthese von [Bi(ATI$^{iPr/iPr}$)$_2$Cl] (**8**), [Bi(ATI$^{Fc/iPr}$)$_2$Cl] (**BiCl-15**), [Bi(Ph(O)S–ATI$^{iPr/iPr}$)$_2$I] (**11-Ph(O)S**) und [Bi(NO$_2$–ATI$^{iPr/iPr}$)$_2$Cl] (**8-NO$_2$**) die Entstehung signifikanter Mengen der jeweiligen Dihalogenid-Spezies und des protonierten Liganden beobachtet. Aufgrund der Stabilität von Bismut-Komplexen mit dem Liganden H−ATI$^{\mathrm{Ph}/i\mathrm{Pr}}$ im Vergleich zu den zuvor beschriebenen Beobachtungen, kann vermutet werden, dass ein höherer sterischer Anspruch der stickstoff-gebundenen Substituenten (*i*Pr bzw. Fc im Gegensatz zu Ph) sowie die elektronenziehenden Eigenschaften des NO_2- bzw. S(O)Ph-Substituenten die Stabilität der Bismut-Komplexe beeinflussen. Die Bildung der heteroleptischen Komplexe ([Bi(ATI)$_2$X] vs. [Bi(ATI)X$_2$]; X = Halogen) scheint zudem überwiegend thermodynamisch kontrolliert zu sein.

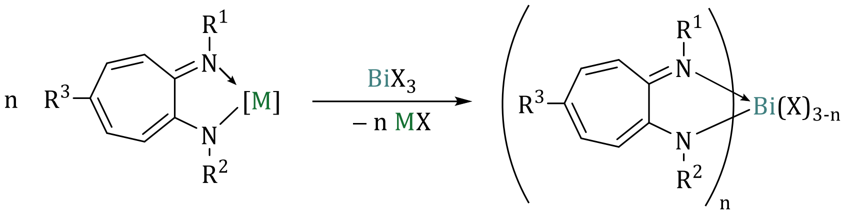

R^1 = *i*Pr; R^2 = *i*Pr, Ph, Fc; R^3 = H, Ph(O)S, NO$_2$
[M] = Na(L)$_n$, K(L)$_n$; L = Neutralligand

Schema 35: Synthese von homo- und heteroleptischen Bismut-ATI-Komplexen.

Die selektiv synthetisierbaren heteroleptischen Bismut-ATI-Komplexe [Bi(ATI$^{\mathrm{Fc}/i\mathrm{Pr}}$)Cl$_2$] (**BiCl$_2$-15**), [Bi(Ph(O)S−ATI$^{i\mathrm{Pr}/i\mathrm{Pr}}$)$_2$Cl] (**8-Ph(O)S**), [Bi(Ph(O)S−ATI$^{i\mathrm{Pr}/i\mathrm{Pr}}$)Cl$_2$] (**9-Ph(O)S**), [Bi(S(O)Ph−ATI$^{i\mathrm{Pr}/i\mathrm{Pr}}$)I$_2$] (**11-Ph(O)S**) und [Bi(NO$_2$−ATI$^{i\mathrm{Pr}/i\mathrm{Pr}}$)Cl$_2$] (**9-NO$_2$**) könnten zukünftig als Vorläufer für niedervalente Bismut-Spezies dienen.

Koordinationschemie der Bismut-Komplexe. [Bi(ATI$^{\mathrm{Fc}/i\mathrm{Pr}}$)$_3$] (**Bi-15**) zeigte im Festkörper eine *mer*-Konfiguration, für [Bi(ATI$^{\mathrm{Ph}/i\mathrm{Pr}}$)$_3$] (**Bi-12**) konnte dagegen das *fac*-Isomer gefunden werden. Die strukturell charakterisierten Bismut-Chloro-Spezies zeigten intermolekulare Bismut-Chlor-Wechselwirkungen, die eine Lewis-Acidität der Verbindungen andeuten und zu Koordinationspolymeren führten. In [Bi(ATI$^{\mathrm{Fc}/i\mathrm{Pr}}$)Cl$_2$]$_\infty$ (**[BiCl$_2$-15]$_\infty$**) und [Bi(NO$_2$−ATI$^{i\mathrm{Pr}/i\mathrm{Pr}}$)Cl$_2$] (**9-NO$_2$**) wurden zudem erstmals π-π-Wechselwirkungen des ATI-Rückgrats zweier benachbarter Molekül-Einheiten beobachtet (Abbildung 44). Die ditopen Eigenschaften des ATI-Liganden, welche zuerst in Form von Metall-Aren Wechselwirkungen beobachtet wurden, konnten damit um Aren-Aren-Wechselwirkungen erweitert werden.

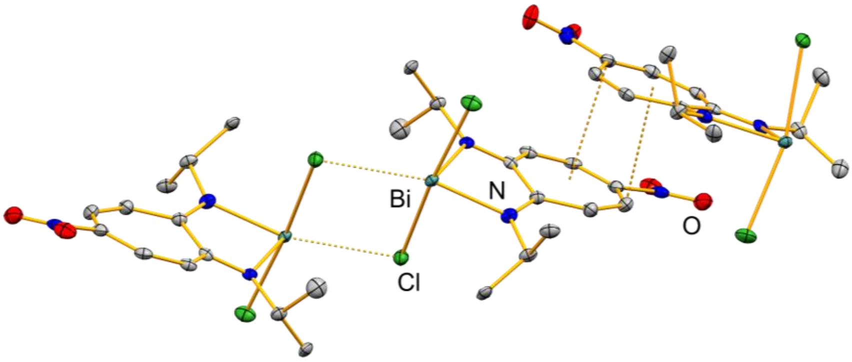

Abbildung 44: Struktur im Festkörper von [Bi(NO$_2$–ATI$^{iPr/iPr}$)Cl$_2$] (**9-NO$_2$**) mit intermolekularen Bi···Cl und Aren-Aren Wechselwirkungen.

In Anlehnung an die Synthese von neutralen Bismut-ATI-Komplexen konnten auch kationische Verbindungen in Salzeliminierungen dargestellt werden. Komplexe mit Triflat-Gegenion kristallisierten als Kontaktionenpaare, Verbindungen mit [SbF$_6$]$^-$ als Gegenion als solvensseparierte Ionenpaare und unter Verwendung des schwach koordinierenden [BAr^F]$^-$-Gegenions erhielt man freie Bi-ATI-Kationen mit schwachen Bi···Fluor Wechselwirkungen zum Gegenion (Abbildung 45). VT-NMR-spektroskopische Untersuchungen sowie eine Linienformanalyse ließen annehmen, dass die sterische Umgebung in neutralen und den entsprechenden kationischen Komplexen mit dem Liganden H–ATI$^{Ph/iPr}$ ähnlich ist, was auf orbitalbasierte Bismut-Ligand Wechselwirkung hindeutet. Mit Hilfe der Gutmann-Beckett Methode konnte gezeigt werden, dass die Lewisacidität der kationischen Komplexe mit Akzeptornummern von 21–29 gering ist.

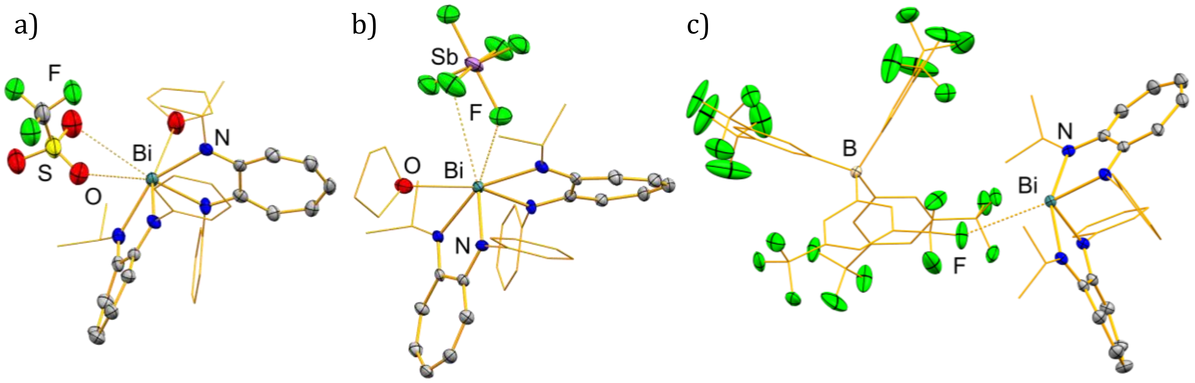

Abbildung 45: Strukturen im Festkörper der Bismut-Kationen a) [Bi(ATI$^{Ph/iPr}$)$_2$(thf)][OTf] b) [Bi(ATI$^{Ph/iPr}$)$_2$(thf)][SbF$_6$] und c) [Bi(ATI$^{Ph/iPr}$)$_2$][BAr^F], OTf = O$_3$SCF$_3$; BAr^F = B(3,5-(CF$_3$)$_2$-C$_6$H$_3$)$_4$. Die Kohlenstoffatome der THF-Moleküle in a) und b), die Kohlenstoffatome des BAr^F-Gegenions in c) sowie die Kohlenstoffatome aller stickstoffgebunden *Iso*propyl- und Phenyl-Reste sind im Drahtmodell dargestellt.

Redox-Verhalten der Bismut-Komplexe. Die Redox-Eigenschaften ausgewählter Bismut-ATI-Komplex wurde mit Hilfe cyclovoltammetrischer Messungen untersucht. Der homoleptische Bismut-Komplex **Bi-15** zeigte unter oxidativen Bedingungen drei reversible, ferrocenyl-basierte und damit ligandzentrierte Redox-Ereignisse. Die Separierung der Redox-Wellen ließ auf eine elektronische Kommunikation der drei Ferrocenyl-Reste schließen. Diese Annahme konnte durch DFT-Rechnung unterstützt werden. Unter reduktiven Bedingungen zeigten die homoleptischen Komplexe **Bi-15** und **Bi-12** ligandzentrierte Ereignisse, die ähnliches, wie das für den Natrium-Komplex **[Na-12-thf]$_\infty$** gefundene, Verhalten der Komplexe vermuten lassen. Für die Bismut-Kationen dagegen konnten partiell reversible bzw. quasireversible Redox-Ereignisse gefunden werden. DFT-Rechnungen an einer reduzierten $[\mathrm{Bi(ATI)_2}]^{\bullet}$-Radikalspezies zeigten die Lokalisierung eines signifikanten Anteils an Spindichte auf dem Bismutatom. Es konnte somit von einem Bismut-zentrierten Radikal gesprochen werden. Anhand des Vergleichs neutraler und kationischer Bismut-ATI-Komplexe konnte gezeigt werden, dass die Redox-Eigenschaften durch die Ladung der Komplexe kontrollierbar sind.

Die Generierung isolierbarer Bismut-ATI-Radikalspezies war bisher nicht möglich, sollte aber durch die Wahl geeigneter Substituenten am ATI-Liganden sowie die Ladung der Komplexe realisierbar sein. Dabei sollten, ähnlich wie bei den Alkalimetall-Komplexen, Substituenten mit elektronenziehenden Eigenschaften und hohem sterischen Anspruch vorteilhaft sein.

Summary and outlook

Some of the results in this summary have already been published in references [62]–[69].

The structural investigation of alkali metal complexes of the aminotroponimine (ATI) ligand H–ATI$^{\mathrm{Ph}/i\mathrm{Pr}}$ revealed that its coordination chemistry reaches beyond the commonly observed κ^2N coordination mode.[61] Electrochemical and chemical redox studies of the H–ATI$^{\mathrm{Ph}/i\mathrm{Pr}}$ ligand and its sodium and rhodium complexes demonstrated the redox activity of the ATI system.[39] These findings motivated an extended exploration of the coordination and redox properties of this ligand class and their metal complexes. In the context of this work, the focus was not only on the investigation of the influence of the substitution pattern at the nitrogen atoms and at the C_7 backbone of the ligand with different steric and electronic parameters, but also on studying the influence of the metal centre. In addition, bismuth ATI complexes were synthesised and their redox properties were analysed.

Ligand synthesis. A series of literature-known (H–ATI$^{i\mathrm{Pr}/i\mathrm{Pr}}$ (**1**), H–ATI$^{\mathrm{Ph}/i\mathrm{Pr}}$ (**12**), H–ATI$^{\mathrm{Ph}/\mathrm{Ph}}$ (**13**))[71, 107] and new (AT$^{\mathrm{Fc}}$ (**14**), H–ATI$^{\mathrm{Fc}/i\mathrm{Pr}}$ (**15**), H–ATI$^{\mathrm{PhSMe}/i\mathrm{Pr}}$ (**16**)) aminotropone (AT) and aminotroponimine (ATI) ligands with different substituents at the nitrogen atoms and literature-known ATI ligands with substituents at the C5 position at the C_7 ring (Ph(O)S–ATI$^{i\mathrm{Pr}/i\mathrm{Pr}}$ (**1-Ph(O)S**), NO_2–ATI$^{i\mathrm{Pr}/i\mathrm{Pr}}$ (**1-NO$_2$**))[70] were synthesised. The standard procedure is a two-step synthetic route, starting with tosyloxytropone (Scheme 28, top).

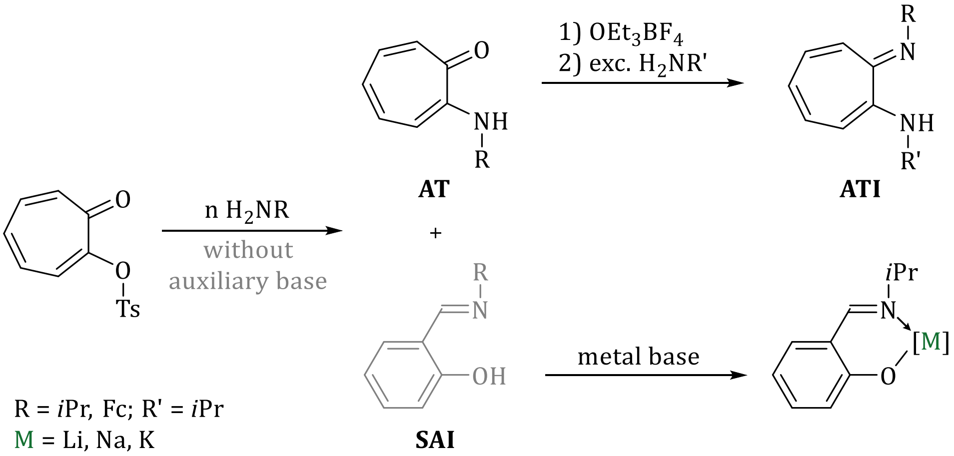

Scheme 28: Synthetic route to aminotroponimines (ATIs) (top). For R = *i*Pr and n = 10 or R = Fc and n = 1 and without adding an additional auxiliary base, the salicylaldimine (SAI) derivative was isolated as a by-product. Metalation of the SAI derivative (bottom). Ts = SO_2-*p*-(C_6H_4Me).

In the synthesis of *iso*propyl aminotropone and ferrocenyl aminotropone under standard conditions, the salicylaldimine (SAI) derivatives SAI$^{i\mathrm{Pr}}$ and SAI$^{\mathrm{Fc}}$ were isolated as by-products in low yields of 3–4%. Modification of the reaction conditions resulted in a significant increase of ring contraction, which led to the formation of the SAI ligands. This reaction pathway was explicitly addressed and turned into the main pathway. The reaction of the SAI^{iPr} ligand with the corresponding metal base yielded the alkali metal complexes. The sodium complex **Na-SAI^{iPr}** showed a double heterocubane structure in the solid state and represents the first example in which this structural motif was realised in complexes without further donor substituents in the ligand periphery (Figure 39a). The structure in the solid state of the potassium complex was elucidated as the 18-crown-6 adduct **K(18K6)-SAI^{iPr}** (Figure 39b). It has been shown, that in solution the complexation with the neutral donor 18-crown-6 induces a reversible *E*/*Z* isomerisation of the aldimine C–N double bond. Stoichiometric reaction of two alkali metal complexes or the reaction of the lithium and sodium complexes in a ratio 1:1, 1:3 and 3:1 led to the mixed metal SAI complexes. Complex [$Li_3Na(SAI)_4(thf)_2$] (**Li$_3$Na-SAI^{iPr}-(thf)$_2$**) was the first structurally characterised s-block metal SAI complex of this type (Figure 39c). It was shown by NMR spectroscopy, mass spectrometry, single-crystal X-ray diffraction analysis as well as DFT calculations that these complexes exist in an equilibrium of species with different degrees of aggregation.

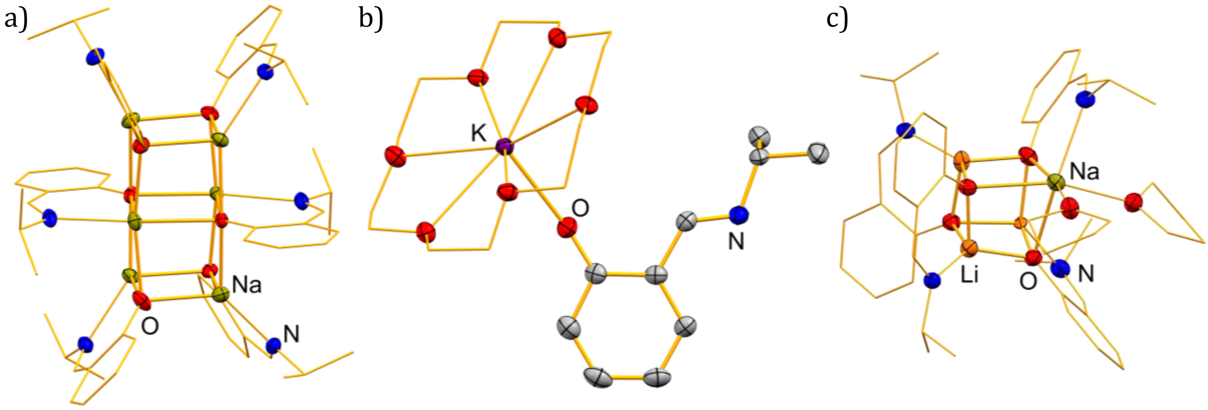

Figure 39: Molecular structures of **Na-SAI^{iPr}**, **K(18K6)-SAI^{iPr}** and **Li$_3$Na-SAI^{iPr}-(thf)$_2$** in the solid state. The carbon atoms of the SAI units in a) and c), as well as the carbon atoms of the crown ether in b) and of the THF molecules in c) are shown in the wire frame model.

The literature-known synthesis of the backbone substituted ATI ligands proceeds either in a one-step reaction starting with the unsubstituted ligand via an electrophilic aromatic substitution for **1-NO$_2$** or in a three-step synthesis with **1-Br** as an isolated intermediate, followed by a nucleophilic aromatic substitution and oxidation yielding **1-Ph(O)S**.[70] In accordance with the literature, **1-NO$_2$** could only be isolated in yields of 19% using the literature-known synthetic route. Variation of the reaction conditions in terms of the choice of solvent, the reaction temperature and time did not increase the yield. However, the synthesis of **1-NO$_2$** via ligand **1-Br** following the synthesis of **1-Ph(O)S** was investigated and represents an interesting starting point for future syntheses. However, the observed product distribution was strongly varying with different reaction conditions, which was further emphasised by the isolation of the ring contracted by-product **2**, which was the only isolable species from a reaction with increased temperature and prolonged reaction time (Scheme 29).

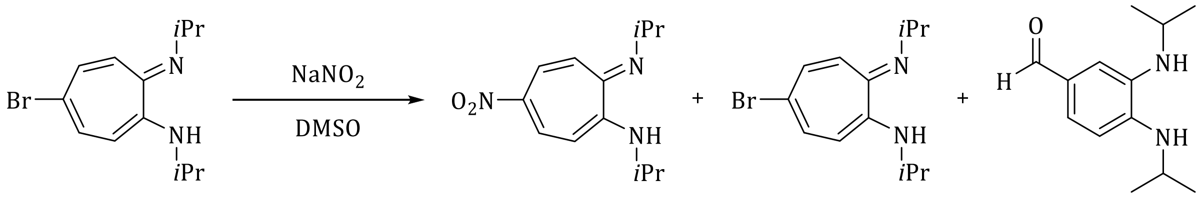

1-Br **1-NO$_2$** **1-Br** **2**

	1-NO$_2$	**1-Br**	**2**
110 °C, 7 d:	≤42%[a]	≥21%	not found
150 °C 16 d:	<5%	<5%	5%

Scheme 29: Synthesis of **1-NO$_2$** starting with **1-Br** under different conditions. [a] Varying yields were received for different reaction approaches.

Synthesis of the alkali metal complexes. The neutral ATI (and AT) ligands were reacted with alkali metal bases to synthesise the corresponding alkali metal complexes (Scheme 30). The use of *n*-butyllithium as lithiating agent led to the desired complex $[Li(ATI^{Ph/Ph})(Et_2O)_2]$ (**Li-13**) as well as a by-product resulting from an addition of *n*-butyllithium to the C_7 backbone. In the addition product, the *n*-butyl group is located at the C1 position of the ligand and the lithium atom located in the *N*,*N* binding pocket.

The NMR spectroscopic characterisation of the complexes without substituents in the backbone was in accordance with the expected resonances for complexes with a symmetric ($R^1 = R^2$) or an unsymmetric ($R^1 \neq R^2$) substitution pattern at the nitrogen atoms of the ligand.

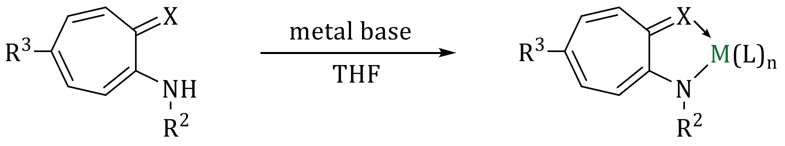

X = O, NR^1; R^1 = *i*Pr, Ph;
R^2 (for X = O) = *i*Pr, Fc (ferrocenyl);
R^2 (for X = NR^1) = *i*Pr, Fc, Ph, PhSMe;
R^3 = H, Ph(O)S, NO$_2$; L = neutral ligand; M = Li, Na, K

Scheme 30: Synthesis of the alkali metal ATI and AT complexes.

In their NMR spectra, the sodium and potassium complexes **4-NO$_2$** and **5-NO$_2$** with the nitro group in the C5 position revealed an *E*,*E*/*E*,*Z* isomerisation, which is a new phenomenon in ATI chemistry. Due to the electron withdrawing effect of the nitro group, a shift of the π-electron density towards the backbone substituent is suggested. Furthermore, the nitro group can act as a binding site for metal atoms. As a consequence there are three different isomers possible for the complexes (Scheme 31). NMR spectroscopic investigations as well as DFT calculations give evidence of this type of isomerisation to be relevant in solution.

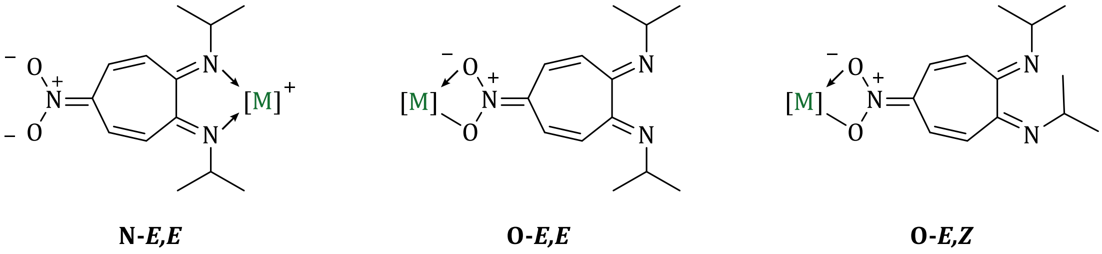

Scheme 31: Schematic representation of possible isomers of the alkali metal ATI complexes with a nitro group. [M] = Li, Na, K.

Coordination chemistry of alkali metal complexes. The structural characterisation of the alkali metal complexes revealed a variety of possible coordination modes. Besides one complex with the so far predominantly observed κ^2*N* coordination mode (Scheme 32, **A**, for [Na(ATI$^{Ph/Ph}$)(Et$_2$O)$_2$] (**Na-13**)), further examples of complexes were found in which an interaction of the metal atom with the C$_7$ backbone of a neighbouring monomer unit occurs, which was first discussed in the literature for the sodium complex [Na(ATI$^{Ph/iPr}$)(thf)]$_\infty$ (**[Na-12-thf]$_\infty$**) (Scheme 32, **B**, for [Na(ATI$^{iPr/iPr}$)(thf)] (**[4-thf]$_\infty$**) and [K(ATI$^{iPr/iPr}$)(thf)] (**[5-thf]$_\infty$**)). DFT calculations showed, that the tendency towards the formation of cation π-interactions decreases with increasing electron withdrawing character of the substituents at nitrogen due to a concomitant lowering of the HOMO of the complex. A decrease of the LUMO level with increasing group electronegativity of the substituents at nitrogen rises the potential for M→ATI backbonding. Due to metal-arene interactions, two additional structural motifs were observed (Scheme 32, **C** for [K(ATI$^{Ph/Ph}$)]$_\infty$ and **D** for [Li(ATI$^{Ph/Ph}$)]$_\infty$). The bridging properties of the ligands in coordination modes **B**–**D** led to the formation of coordination polymers in the solid state.

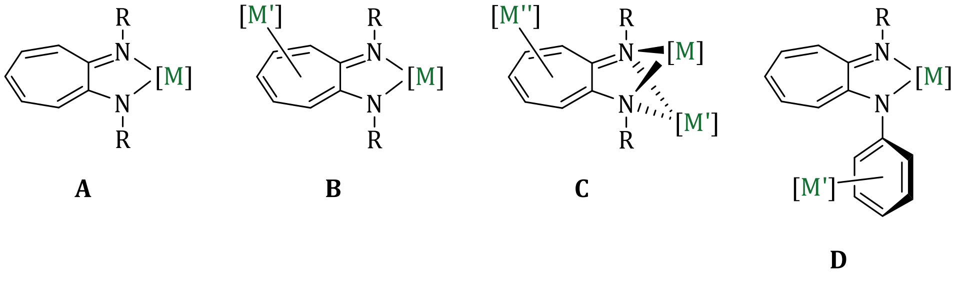

Scheme 32: Coordination modes of alkali metal complexes without substituents in the backbone.

As expected due to the electron withdrawing nature of the backbone substituents, the complexes with sulfinyl and nitro substituents did not show any metal arene interactions with the C$_7$ backbone. Instead, these groups acted as donors saturating the coordination sphere of the metal atom of adjacent units (Scheme 33). The bridging character of the ligands again led to the formation of coordination polymers in the solid state.

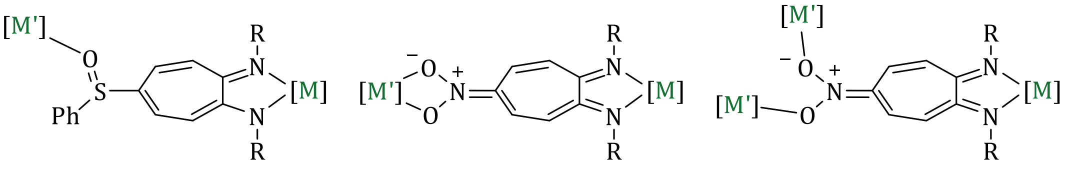

E **F** **G**

Scheme 33: Coordination modes of alkali metal ATI complexes with substituents in the ligand backbone.

The more pronounced double bond character of C–N bonds as well as more localised C–C double bonds in the complexes [Li(NO_2–ATI$^{iPr/iPr}$)(py)] (**[3-NO$_2$-py]$_\infty$**), [Na(NO_2–ATI$^{iPr/iPr}$)(py)] (**[4-NO$_2$-py]$_\infty$**) and [K(NO_2–ATI$^{iPr/iPr}$)(py)] (**[5-NO$_2$-py]$_\infty$**) as compared to the unsubstituted parent compounds corroborates a shift of π-electron density towards the nitro group. The reduced delocalisation of π-electron density was also reflected in an out of plane twisting of the ATI backbone. Twist angles of up to 39° significantly exceeded the angles for literature known (semi-)metal complexes.[78]

The influence of neutral donor ligands on the coordination chemistry of alkali metal complexes and thus on the stability of cation-π-interactions was investigated in reactions of selected complexes with PMDTA and crown ethers. As expected, a break-up of the polymeric structure and the formation of a monomeric complex was induced for [Na(ATI$^{Ph/iPr}$)(thf)] (**[Na-12-thf]$_\infty$**) when reacted with the tridentate donor ligand PMDTA. In contrast, the reaction of **[4-thf]$_\infty$** and **[Na-12-thf]$_\infty$** with crown ethers led to a ligand induced disproportionation and the formation of the sodium sodiate complexes [Na(12-crown-4)$_2$][Na(ATI$^{iPr/iPr}$)$_2$] (**4-(12K4)$_2$**) and [Na(12-crown-4)$_2$][Na(ATI$^{Ph/iPr}$)$_2$] (**Na(12K4)$_2$-12**) (Figure 40a). The stoichiometric reaction of a sodium and a potassium complex led to the first mixed metal potassium sodiate ATI complexes, where the softer potassium cation interacts with the C_7 backbone of two neighbouring [Na(ATI)$_2$]$^-$ units, resulting in a polymeric structure in the solid state (Figure 40b).

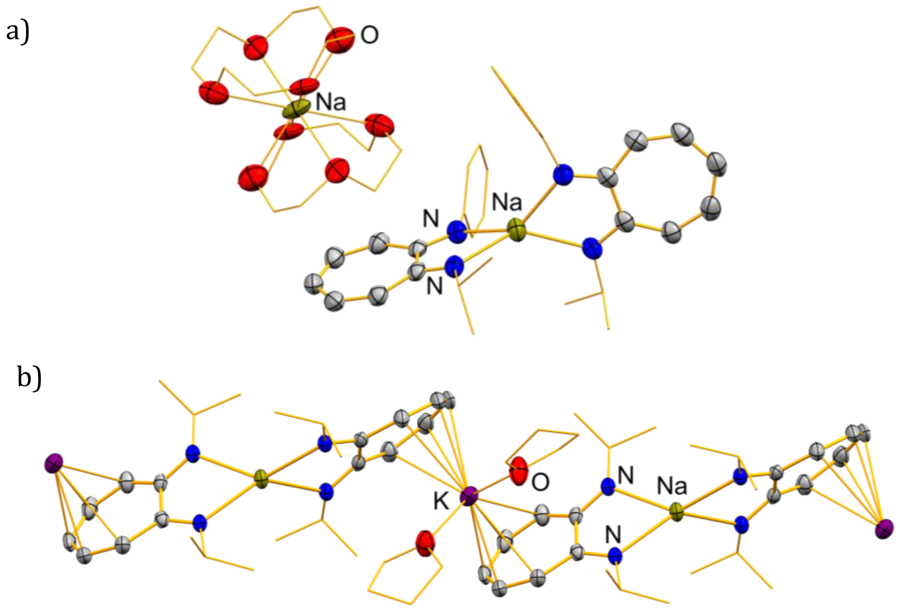

Figure 40: a) Molecular structure of $[\mathrm{Na(12\text{-}crown\text{-}4)_2}][\mathrm{Na(ATI^{Ph/\mathit{i}Pr})_2}]$ (**Na(12K4)₂-12**) in the solid state. b) Cutout of the solid-state structure of $[\mathrm{KNa(ATI^{\mathit{i}Pr/\mathit{i}Pr})_2(thf)_2}]_\infty$. The carbon atoms of the crown ether in a) and the carbon atoms of the THF molecules in b) as well as the carbon atoms of nitrogen-bound substituents in a) and b) are shown as wire frame.

The relationship between structure and reactivity was analysed for the sodium and the mixed metal complexes on the basis of their activity as initiators in the ring opening polymerisation of ε-caprolactone. The complexes with a $[\mathrm{Na(ATI)_2}]^-$ moiety are more active initiators than complexes with a neutral [Na(ATI)] moiety. However, a poor molecular weight control was observed in THF. The toluene soluble complex $[\mathrm{Na(ATI^{Ph/\mathit{i}Pr})(thf)}]$ combined a good catalytic activity with an excellent molecular weight control for polymerisations in this solvent. In combination, these results are superior to those of literature established alkali metal initiators for the polymerisation of ε-caprolactone.

In analogy to the unsubstituted parent compounds, the reaction of $[\mathrm{Na(Ph(O)S{-}ATI^{\mathit{i}Pr/\mathit{i}Pr})}]$ (**4-Ph(O)S**) with 12-crown-4 resulted in the formation of the sodium sodiate complex $[\mathrm{Na(12\text{-}crown\text{-}4)_2}][\mathrm{Na(Ph(O)S{-}ATI^{\mathit{i}Pr/\mathit{i}Pr})_2}]$ (**6-Ph(O)S**). The complex **4-NO₂** with a nitro substituent, on the other hand, led to the formation of the adduct $[\mathrm{Na(NO_2{-}ATI^{\mathit{i}Pr/\mathit{i}Pr})(15\text{-}crown\text{-}5)}]$ (**4-NO₂-(15K5)**), when reacted with 15-crown-5. For the reaction with two equivalents of 12-crown-4 the formation of an ATI anion, which does not undergo any directional bonding interactions with the $[\mathrm{Na(12\text{-}crown\text{-}4)_2}]$ cation was observed (Figure 41). **4-NO₂-(12K4)₂** is thus the first structurally characterised ATI compound with a free ligand anion. The reaction of $[\mathrm{K(NO_2{-}ATI^{\mathit{i}Pr/\mathit{i}Pr})}]$ (**5-NO₂**) with 18-crow-6 yielded the potassium complex $[\mathrm{K(NO_2{-}ATI^{\mathit{i}Pr/\mathit{i}Pr})(18\text{-}crown\text{-}6)}]$ (**5-NO₂-(18K6)**) analogous to **4-NO₂-(15K5)**. The twist of the ATI sceleton is even more pronounced for the crown ether complexes than for the parent compounds without crown ethers.

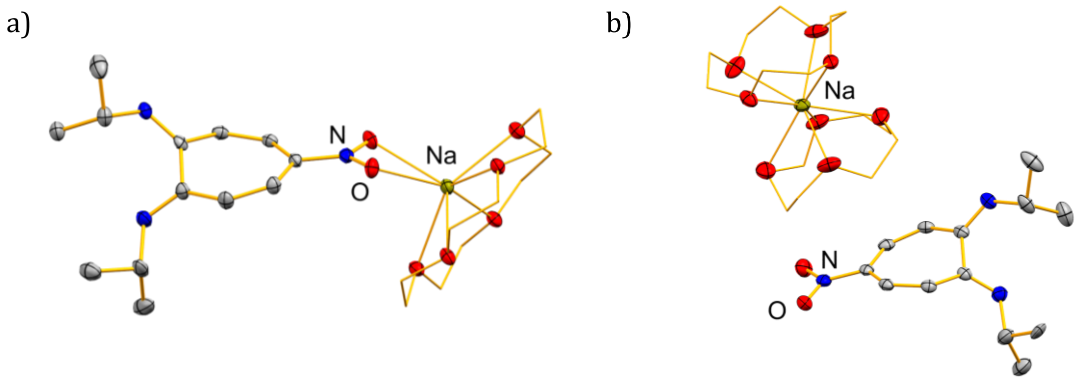

Figure 41: Molecular structures of a) [Na(NO_2–ATI$^{iPr/iPr}$)(15-crown-5)] (**4-NO_2-(15K5)**) and b) [Na(12-crown-4)$_2$][Na(NO_2–ATI$^{iPr/iPr}$)] (**4-NO_2-(12K4)$_2$**) in the solid state. The carbon atoms of the crown ethers are shown as wire frame.

For **4-NO_2-(15K5)**, **4-NO_2-(12K4)$_2$** and **5-NO_2-(18K6)** an *E*,*E*/*E*,*Z* isomerisation was observed in solution, as for their parent compounds, but only the *E*,*Z* isomers were found in the solid state. DFT calculations confirmed these as the energetically most favourable isomers of the crown ether complexes. For **4-NO_2-(12K4)$_2$** a linear transition state with an energy barrier of $\Delta G^{\ddagger} = 26.6\ \mathrm{kcal \cdot mol^{-1}}$ from the *E*,*Z* to the *E*,*E* configuration was determined by DFT calculations.

The flexibility, coordination chemistry, and reactivity of ATI complexes and thus can be significantly influenced by the following parameters: i) choice of the substituents at the nitrogen atoms and at the C_7 backbone of the ligand, ii) choice of the central atom in the *N*,*N* binding pocket or at the backbone substituent, and iii) by the complexation with neutral donor ligands. In the future, these insights will help to enable the synthesis of ATI complexes with desired properties for applications in coordination chemistry, redox chemistry and catalysis.

Redox behaviour of the alkali metal complexes. Electrochemical investigations of ATI ligands and their complexes were conducted using cyclic voltammetry. Under oxidative conditions, redox events were found for compounds with and without substituents in the ligand backbone, which were attributed to an irreversible ligand oxidation. The introduction of the redox-active ferrocenyl substituent at the nitrogen atom led for the first time to ATI compounds with reversible, ligand-centred redox events under oxidative conditions. Complexes with sulfinyl substituent in the backbone showed irreversible oxidation events possibly corresponding to an oxidation of the sulfinyl group. In general, a shift towards more positive potentials was observed for the oxidation potentials with increasing electron-withdrawing character of the substituents at the nitrogen atoms and the ATI backbone. Under reductive conditions, an influence of both the substituents at the nitrogen atoms and the central metal on the redox potentials of ligand-centred reduction events was observed for the complexes [Li(ATI$^{i\mathrm{Pr}/i\mathrm{Pr}}$)] (**3**) and [Li(ATI$^{\mathrm{Ph}/i\mathrm{Pr}}$)] (**Li-12**) compared to the literature known complex [Na(ATI$^{\mathrm{Ph}/i\mathrm{Pr}}$)(thf)] (**[Na-12-thf]**$_{\infty}$). The separation of the reduction wave and the associated oxidation wave indicated a reductively induced dimerization.[39] Complexes with substituents at the ligand backbone show redox events that were less clearly indicative of reductive dimerization, as both irreversible reduction waves and a varying number of ill-defined redox events were observed.

Complementary to electrochemical investigations, chemical redox studies were carried out. The reduction of **3** and **Li-12** with strong reducing agents in the form of the corresponding alkali metals led to the chemoselective and, chemically reversible formation of dimers, as it was described in the literature for **[Na-12-thf]**$_{\infty}$ (Scheme 34).[39] The regioselectivity of the dimerization was significantly influenced by the nature of the central atom as well as the substitution pattern at the nitrogen atoms of the ligand and the associated spin density in radical intermediates. In addition, aggregation processes of the radical species seemed to play a crucial role in solution. The diastereoselectivity was related to the chosen reaction conditions. For the dimerization product of **3**, the *rac* and *meso* isomers engaged in an equilibrium.

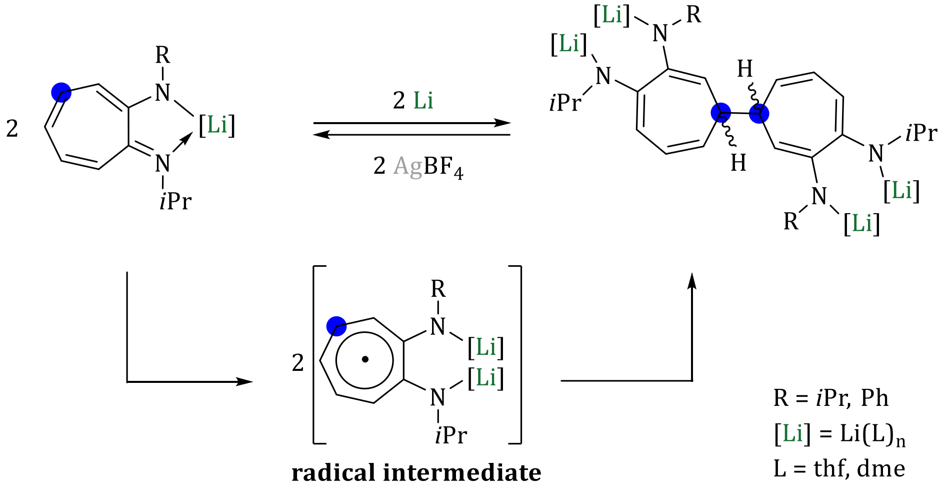

Scheme 34: Reversible, reductive dimerization of [Li(ATI$^{i\mathrm{Pr}/i\mathrm{Pr}}$)] (**3**) and [Li(ATI$^{\mathrm{Ph}/i\mathrm{Pr}}$)] (**Li-12**). dme = dimethoxyethane.

In reduction experiments of complexes with nitro substituent as well as of the lithium and sodium complexes with a sulfinyl substituent, no reduction products, but only starting material was isolated. The reaction of [K(Ph(O)S–ATI$^{i\mathrm{Pr}/i\mathrm{Pr}}$)] (**5-Ph(O)S**) with elemental potassium led to the reduced species **5-red**, for which a structure was proposed based on NMR spectroscopic data. A final structural proof of **5-red** by means of single-crystal X-ray analysis is still pending.

To enable a stabilisation of ligand centred radicals and thus an isolation of radical ATI species, the substituents at the nitrogen atoms of the already investigated backbone-substituted ATI complexes or backbone substituents themselves could be varied. A combination of mesomeric and inductive effects leading to a reduction of the electron density in the ATI backbone seems to be plausible for the choice of appropriate ligands. For example phenyl- instead of *iso*propyl-substituents at nitrogen and substituents with electron-withdrawing CF_3-groups in the ligand backbone could be applied.

The occurrence of an electrochemically irreversible oxidation event for the sodium complex **4-NO₂**, as well as the unique structure of the crown ether compound $[Na(12\text{-Krone-4})_2][Na(NO_2–ATI^{iPr/iPr})]$ (**4-NO₂-(12K4)₂**), prompted an investigation of the behaviour of the nitro complexes under oxidative conditions. However, using the oxidants $NOSbF_6$, ferrocenium chloride, and tropylium-BAr^F ($BAr^F = B(3,5\text{-}(CF_3)_2\text{-}C_6H_3)_4$)), no products of one-electron-oxidation could be isolated. The reaction of **4-NO₂**, **4-NO₂-(12K4)₂** and **4-NO₂-(15K5)** with silver tetrafluoroborate gave the first monometallic silver as well as the first mixed metal sodium argentate ATI complexes (Figure 42). However, difficulties in the removal of borate salts formed during the salt elimination hampered a complete characterisation of the complexes.

The preparation of the silver complex **6-NO₂** via an alternative synthetic route, for example by reacting the potassium complex with AgCl or $AgNO_3$, should avoid the formation of borate salts that are difficult to remove and may allow a selective synthesis as well as complete characterisation of the complex. Based on this, the argentate complexes would be accessible by reaction of **6-NO₂** with the corresponding alkali metal crown ether complexes. In addition, **6-NO₂** could be used to synthesise nitro-substituted bismuth ATI complexes in salt elimination reactions. The ATI argentates could be investigated in view of their suitability as argentation reagents for functionalised aromatics. As their organocopper congeners, the resulting functionalised organoargentates, which are not accessible via common synthetic routs applied for copper derivatives like oxidation, hydrometallation, or halogen-metal exchange, can be used in organic synthesis.

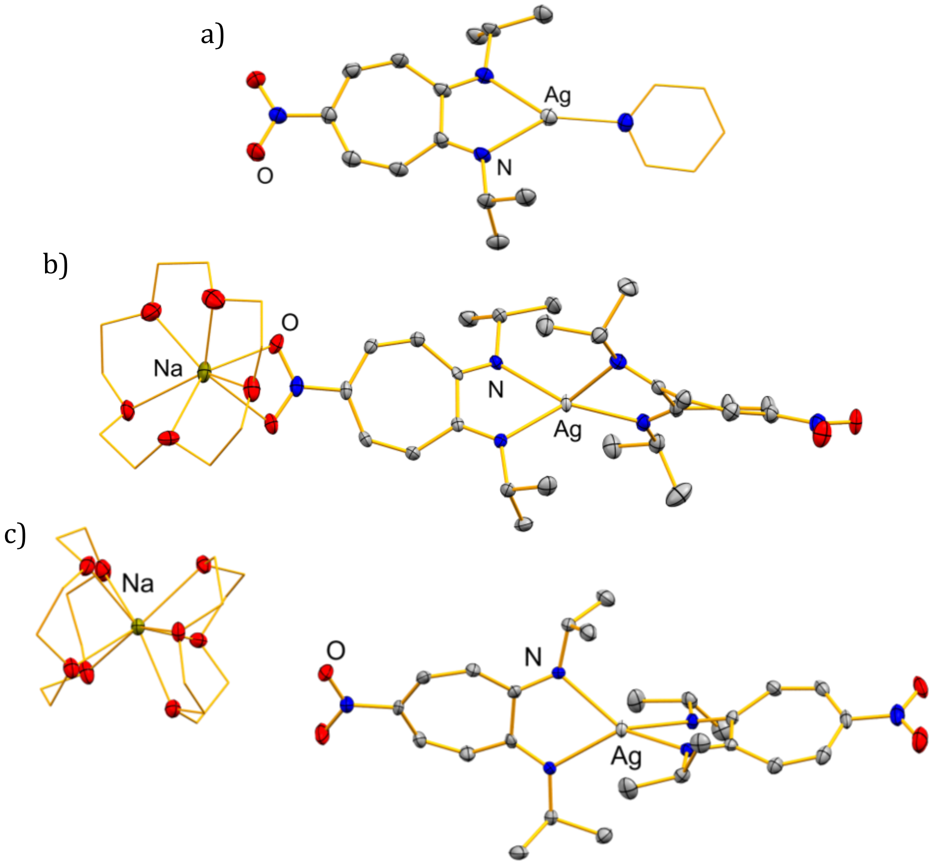

Figure 42: Molecular structures of a) [Ag(NO_2–ATI$^{i\mathrm{Pr}/i\mathrm{Pr}}$)(py)] (**6-$NO_2$-py**), b) [Na(15-crown-5)Ag(NO_2–ATI$^{i\mathrm{Pr}/i\mathrm{Pr}}$)$_2$] (**7-$NO_2$-(15K5)**) and c) [Na(12-crown-4)$_2$][Ag(NO_2–ATI$^{i\mathrm{Pr}/i\mathrm{Pr}}$)$_2$] (**7-$NO_2$-(12K4)$_2$**) in the solid state. The carbon atoms of the pyridine molecules in a) and the carbon atoms of the crown ether molecules in b) and c) are shown as wire frame.

Oxidation experiments of **4-NO_2-(12K4)$_2$** with Ph_3CCl did not lead to oxidised species, but resulted in the triphenylmethyl substituted complex [Na(12-crown-4)$_2$(3-Ph_3C–5-NO_2–ATI$^{i\mathrm{Pr}/i\mathrm{Pr}}$)] (**4-$NO_2$-$Ph_3C$-(12K4)$_2$**). While electrophilic aromatic substitution reactions have been reported for ATI ligands,[83] this type of reaction has now for the first time been observed for ATI complexes. This reaction behaviour was transferred to further backbone substituted and unsubstituted sodium ATI complexes. Complex **4-NO_2-Ph_3C-(12K4)$_2$** and [Na(3-Ph_3C–5-Ph(O)C–ATI$^{i\mathrm{Pr}/i\mathrm{Pr}}$)] (**4-Ph(O)C-$Ph_3C$**) could only be isolated in low yields under the chosen reaction conditions. The single and double Ph_3C-substituted complexes [Na(Ph_3C–ATI$^{i\mathrm{Pr}/i\mathrm{Pr}}$)] (**4-$Ph_3C$**) and [Na(3,5-bis($Ph_3C$)–ATI$^{i\mathrm{Pr}/i\mathrm{Pr}}$)] (**4-($Ph_3C$)$_2$**) could be obtained in good yields under similar reaction conditions (Figure 43).

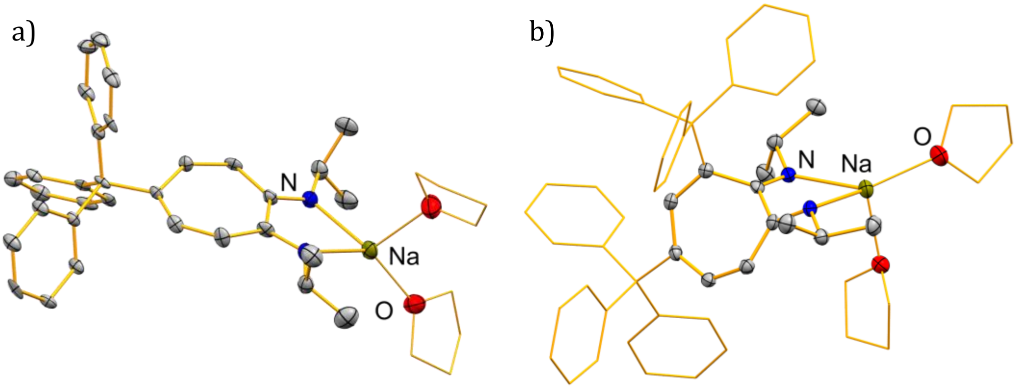

Figure 43: Molecular structures of a) [Na(Ph_3C–ATI$^{iPr/iPr}$)(thf)$_2$] (**4-Ph$_3$C-(thf)$_2$**) and b) [Na(3,5 bis(Ph_3C)–ATI$^{iPr/iPr}$)(thf)$_2$] (**4-(Ph$_3$C)$_2$-(thf)$_2$**) in the solid state. The carbon atoms of the Ph_3C substituents in b) and the carbon atoms of the THF molecules in a) and b) are shown as wire frame.

A selective preparation of **4-NO$_2$-Ph$_3$C-(12K4)$_2$** and **4-Ph(O)C-Ph$_3$C** might be possible by optimising the reaction conditions. The oxidation experiments with the selected oxidising agents show that, depending on the oxidising reagent, salt eliminations or electrophilic aromatic substitutions take place preferably. Electrophilic aromatic substitution provides access to complexes with sterically strongly shielded backbones. By using different electrophiles, the synthesis of further backbone-substituted ATI complexes, for example further alkyl- or arylmethyl-substituted complexes, which cannot be prepared via conventional synthetic routes, might be possible. The steric influence of the triphenylmethyl substituents as well as an altered crystallisation behaviour of the Ph_3C substituted complexes compared to the parent compounds could help to stabilise reductively generated radical species and thus enable their isolation.

Synthesis of the bismuth complexes. Using alkali metal ATI complexes as starting materials, bismuth ATI complexes were prepared in salt elimination reactions (Scheme 35). The homoleptic complexes [Bi(ATI$^{Fc/iPr}$)$_3$] (**Bi-15**) and [Bi(ATI$^{Ph/iPr}$)$_3$] (**Bi-12**) were accessible in good yields. In contrast, [Bi(ATI$^{iPr/iPr}$)$_3$] (**10**) due to its low stability in solution was only obtained in very small amounts, which did not allow for a complete characterisation. Heteroleptic bismuth-chloro complexes with the ligand H–ATI$^{iPr/iPr}$ (**1**) without backbone substituents could not be isolated in analytically pure form due to their poor solubility in common organic solvents. In addition, the synthesis of [Bi(ATI$^{iPr/iPr}$)$_2$Cl] (**8**), [Bi(ATI$^{Fc/iPr}$)$_2$Cl] (**BiCl-15**), [Bi(Ph(O)S–ATI$^{iPr/iPr}$)$_2$I] (**11-Ph(O)S**) and [Bi(NO$_2$–ATI$^{iPr/iPr}$)$_2$Cl] (**8-NO$_2$**) gave rise to significant amounts of the respective dihalogenide species and the protonated ligand. The high stability of complexes with the ligand H–ATI$^{Ph/iPr}$ in comparison to the above mentioned results suggests that the steric demand (*i*Pr/Fc versus Ph) of the nitrogen-bound substituents as well as the electron withdrawing character of the NO$_2$- and the S(O)Ph-groups highly influences the stability of the bismuth complexes. The formation of heteroleptic bismuth complexes ([Bi(ATI)$_2$X] vs. [Bi(ATI)X$_2$; X = halide) seems to be mostly thermodynamically controlled.

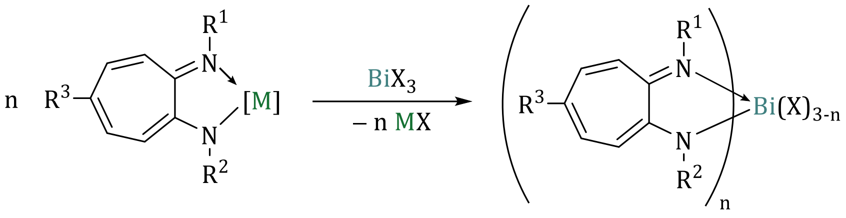

R^1 = *i*Pr; R^2 = *i*Pr, Ph, Fc; R^3 = H, Ph(O)S, NO$_2$
[M] = Na(L)$_n$, K(L)$_n$; L = neutral ligand

Scheme 35: Synthetic route to homo- and heteroleptic bismuth ATI complexes.

The selectively synthesised heteroleptic bismuth ATI complexes [Bi(ATI$^{Fc/iPr}$)Cl$_2$] (**BiCl$_2$-15**), [Bi(Ph(O)S–ATI$^{iPr/iPr}$)$_2$Cl] (**8-Ph(O)S**), [Bi(Ph(O)S–ATI$^{iPr/iPr}$)Cl$_2$] (**9-Ph(O)S**), [Bi(S(O)Ph–ATI$^{iPr/iPr}$)I$_2$] (**11-Ph(O)S**) and [Bi(NO$_2$–ATI$^{iPr/iPr}$)Cl$_2$] (**9-NO$_2$**) could serve as precursors for low-valent bismuth species in the future.

Coordination chemistry of the bismuth complexes. [Bi(ATI$^{Fc/iPr}$)$_3$] (**Bi-15**) showed a *mer* configuration in the solid state, whereas for [Bi(ATI$^{Ph/iPr}$)$_3$] (**Bi-12**) a *fac* isomer was found. The structurally characterised bismuth-chloro species showed intermolecular bismuth-chloro interactions, suggesting a Lewis acidity of the complexes and leading to coordination polymers. For [Bi(ATI$^{Fc/iPr}$)Cl$_2$]$_\infty$ (**[BiCl$_2$-15]$_\infty$**) and [Bi(NO$_2$–ATI$^{iPr/iPr}$)Cl$_2$] (**9-NO$_2$**) π-π interactions of the ATI backbone of two neighbouring units were observed (Figure 44). The ditopic nature of ATI ligands, which were observed in the form of metal-arene interactions first, could thus be extended to include arene-arene interactions.

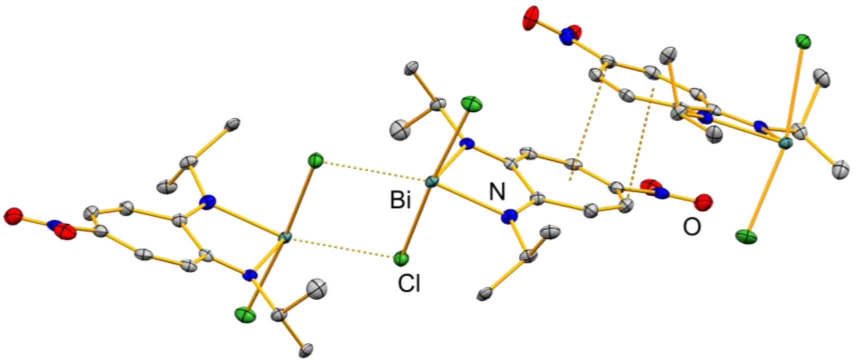

Figure 44: Solid-state structure of [Bi(NO$_2$–ATI$^{iPr/iPr}$)Cl$_2$] (**9-NO$_2$**) with intermolecular Bi···Cl and arene-arene interactions.

Following the synthesis of neutral bismuth ATI complexes, it was possible to prepare cationic compounds in salt elimination reactions. Complexes with triflate as a counteranion crystallised as contact ion pairs, compounds with $[SbF_6]^-$ as counteranion crystallised as solvent-separated ion pairs and using the weakly coordinating $[BArF]^-$ counteranion free bismuth ATI cations with weak Bi···Fluorine interactions to the counterion were obtained (Figure 45). VT NMR spectroscopic studies and line shape analysis suggested a similar steric environment in the neutral and corresponding cationic complexes with the $H{-}ATI^{Ph/iPr}$ ligand, indicating orbital-based bismuth ligand interactions. It was shown by using the Gutmann-Beckett method that the Lewis acidity of the cationic complexes with acceptor numbers of 21–29 is rather low.

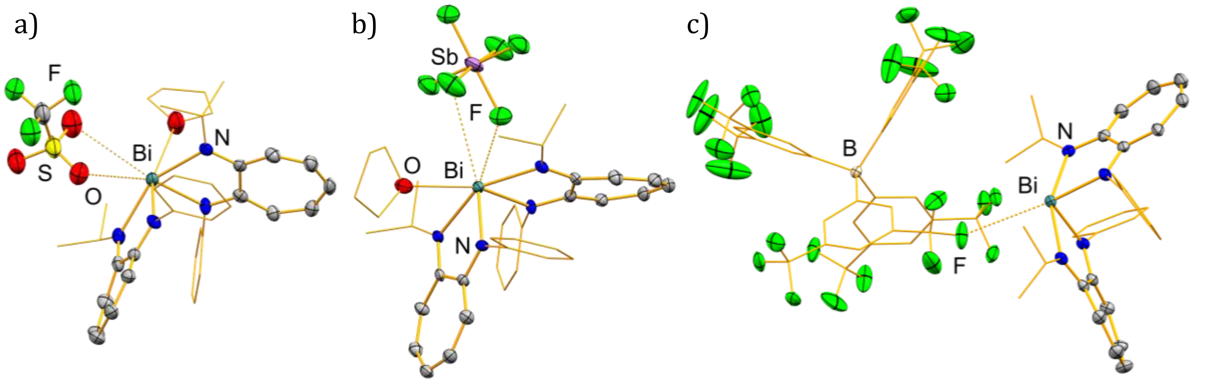

Figure 45: Molecular structures of the bismuth cations a) $[Bi(ATI^{Ph/iPr})_2(thf)][OTf]$ b) $[Bi(ATI^{Ph/iPr})_2(thf)][SbF_6]$ and c) $[Bi(ATI^{Ph/iPr})_2][BAr^F]$ in the solid state, OTf = O_3SCF_3; BAr^F = $B(3,5\text{-}(CF_3)_2\text{-}C_6H_3)_4$. The carbon atoms of the THF molecules in a) and b), the carbon atoms of the BAr^F counterion in c) as well as the carbon atoms of the nitrogen-bound *iso*propyl and phenyl substituents are shown as wire frame.

Redox behaviour of bismuth complexes. The redox properties of selected bismuth ATI complexes were investigated using cyclic voltammetry measurements. The homoleptic bismuth complex **Bi-15** showed three reversible, ferrocenyl based and thus ligand centred redox events under oxidative conditions. The separation of redox waves suggested an electronic communication between the three ferrocenyl substituents. This assumption was supported by DFT calculations. Under reductive conditions, the homoleptic complexes **Bi-15** and **Bi-12** showed ligand-centred redox events, suggesting a behaviour similar to that of the sodium complex **[Na-12-thf]$_\infty$**. In contrast, partially reversible or quasireversible redox events were found for the bismuth cations. DFT calculations on a reduced $[Bi(ATI)_2]^{\bullet}$ radical species showed a localisation of significant parts of spin density on the bismuth atom. By comparing neutral and cationic bismuth ATI complexes, it has been shown that the redox properties can be controlled by the charge of the complexes.

The generation of isolable bismuth ATI radical species has not been successful so far, but should be realisable through the choice of suitable substituents on the ATI ligand as well as through the charge of the complexes. Similar to the alkali metal complexes, substituents with electron withdrawing properties and high steric demand should be advantageous.

XIX Experimentalteil

1 Allgemeines

Alle oxidations- und hydrolyseempfindlichen Umsetzungen wurden mit Hilfe von Schlenktechniken oder in Gloveboxen der Marke MBraun oder GSG unter Argonatmosphäre durchgeführt. Lösungsmittel wurden nach den gängigen Labortechniken getrocknet und entgast.

Die NMR-Spektren wurden an 400 oder 500 MHz NMR-Spektrometern der Marke Bruker aufgenommen. Die ^{1}H- und ^{13}C-Verschiebungen wurden relativ zu $SiMe_4$ angegeben und die ^{1}H- und ^{13}C-Verschiebungen des Lösungsmittels als zweiter Standard genutzt. ^{7}Li-Verschiebungen und ^{23}Na-Verschiebungen wurden relativ zu 1M LiCl in D_2O bzw. 1M NaCl in D_2O und ^{19}F-Verschiebungen wurden relativ zu $CFCl_3$ angegeben. ^{15}N-NMR-Verschiebungen wurden relativ zu CH_3NO_2 (90% in $CDCl_3$) angegeben und mit Hilfe von 2D ^{1}H-^{15}N-NMR-Korrelationsspektren bestimmt. Wenn nicht anders angegeben, wurden alle NMR-Spektren bei 23 °C aufgenommen. Für das quantitative, protonen-gekoppelte ^{19}F-NMR wurde eine spektrale Breite von 212.54 ppm, ein Offset O1P von −200 ppm, eine Aquisitionszeit von 1.98 s, 8 Scans und eine Delay-Zeit von 60 s sowie 90° Puls genutzt. Für die Quantifizierung wurde folgende Formel genutzt

$$m([Na(12\text{-}Krone\text{-}4)_2\,BF_4]) = \frac{M([Na(12\text{-}Krone\text{-}4)_2][BF_4])}{M(K[BF(CN)_3])}\frac{I([Na(12\text{-}Krone\text{-}4)_2\,][BF_4])}{I(K[BF(CN)_3])}$$

$$\frac{N(K[BF(CN)_3])}{N([Na(12\text{-}Krone\text{-}4)_2\,][BF_4])}m(K[BF(CN)_3])$$

m = Masse der Einwaage, M = molare Masse, I = Wert des Integrals, N = Anzahl der Protonen, die das Signal repräsentiert.

Kristalle, die für eine Einkristallröntgenstrukturanalyse geeignet waren, wurden in perfluoriertem Polyetheröl aufgenommen und auf einer Nylon-Schleife auf das Goniometer überführt. Die Einkristallröntgenstrukturanalysen wurden an einem Bruker X8-APEX II Diffraktometer oder einem Bruker D8 Quest Diffraktometer mit Mehrschichtspiegelmonochromatoren unter der Verwendung von MoKα-Strahlung oder an einem Rigaku Oxford Diffraction XtaLAB Synergy Diffraktrometer mit einem Semiconduktor HPA-Detektor (HyPix-6000) und Mehrschichtspiegelmonochromatoren unter der Verwendung von CuKα-Strahlung durchgeführt. Die Strukturen wurden mittels direkter Methoden gelöst, mit dem SHELX-Softwarepaket verfeinert und mit Fourier-Expansion erweitert (G. Sheldrick, Universität Göttingen, 1997). Alle Nichtwasserstoffatome wurden anisotrop verfeinert, und die Wasserstoffatome wurden auf idealisierten Positionen in die Strukturfaktorberechnung einbezogen.

Die Aufnahme der Cyclovoltammogramme wurde mit einem Gamry Instruments Reference 600 Potentiostat unter Argonatmospähre durchgeführt und ein Standard-Messaufbau einer Drei-Elektroden-Zelle mit einer Platin-Arbeitselektrode, einem Platindraht als Gegenelektrode und einem Silberdraht als Referenzelektrode verwendet. Alle Messungen wurden in THF/0.1 M $[N(nBu)_4][PF_6]$ bei 23 °C durchgeführt. Die erhaltenen Redoxpotentiale wurden auf das Redoxpaar Ferrocen/Ferrocenium referenziert.

Die DFT-Rechnungen wurden von *Dr. Crispin Lichtenberg* mit dem Programm Gaussian 09 bzw. Gaussian 16 und dem 6-31G(d,p) (H, Li, C, N, O)[108] bzw. 6-311G(d,p) (Na, K)[109] Basissatz sowie dem B3LYP Funktional durchgeführt.[110] Pyridin und THF Lösungsmittelmodelle wurden angewandt. Die D3-Version von Grimmes Dispersionsmodell mit der ursprünglichen D3 Dämfpungsfunktion wurde angewandt.[111] Frequenzanalysen zeigten null imaginäre Frequenzen für Grundzustände und eine imaginäre Frequenz für Übergangszustände. Thermodynamische Parameter wurden bei einer Temperatur von 298.15 K und einem Druck von 1.00 atm berechnet.

Die Elementaranalysen (C, H, N) erfolgten an einem Vario Micro Cube der Firma Elementar Analysesysteme GmbH.

Die Zuordnung der ^{1}H- und ^{13}C-Signale in den NMR-Spektren wurde nach folgendem Schema vorgenommen.

Schema 36: Zur Signalzuordnung verwendete Nummerierung.

Nomenklatur der ATI-Liganden. X–ATI$^{R/R'}$ mit X = Substituent an C5-Position im ATI-Rückgrat, R/R' = Substituenten an den Stickstoffatomen des Liganden. In Komplexverbindungen wird X = H weggelassen und alle ATI-Liganden liegen in ihrer monoanionischen Form vor.

2 Synthese rückgratsubstituierter Aminotroponimine

Die literaturbekannten Liganden H–ATI$^{i\mathrm{Pr}/i\mathrm{Pr}}$ (**1**), Br–ATI$^{i\mathrm{Pr}/i\mathrm{Pr}}$ (**1-Br**), PhS–ATI$^{i\mathrm{Pr}/i\mathrm{Pr}}$ (**1-PhS**) und Ph(O)S–ATI$^{i\mathrm{Pr}/i\mathrm{Pr}}$ (**1-Ph(O)S**) wurden analog zu den Literaturvorschriften synthetisiert. Ausbeuten und die ^{1}H-NMR-spektroskopische Charakterisierung waren im Einklang mit der Literatur.[70-71]

NO_2–ATI$^{i\mathrm{Pr}/i\mathrm{Pr}}$ (**1-NO$_2$**)

Bis auf die Aufarbeitung wurden alle Schritte unter Argonatmosphäre durchgeführt.

Zu einer Lösung von Br–ATI$^{i\mathrm{Pr}/i\mathrm{Pr}}$ (**1-Br**) (1.00 g, 3.53 mmol) in trockenem DMSO (20 mL) wurde eine Lösung von Natriumnitrit (256 mg, 3.71 mmol) in trockenem DMSO (20 mL) gegeben. Die Mischung wurde bei 110 °C für 7 Tage gerührt. Die Lösung wurde mit einer Mischung aus destilliertem Wasser (150 mL) und MTBE (150 mL) extrahiert. Die wässrige Phase wurde mit MTBE (3 × 100 mL) extrahiert. Die vereinten organischen Phasen wurden mit gesättigter Natriumchloridlösung (40 mL) gewaschen und über Magnesiumsulfat getrocknet. Das Lösungsmittel wurde unter vermindertem Druck entfernt. Das Rohprodukt wurde säulenchromatographisch gereinigt (stationäre Phase: Siliciumdioxid, Laufmittel: *n*-Hexan/MTBE 10:1, 5 Vol% NEt_3). Ausbeute: 365 mg (1.46 mmol, 42%) eines roten, kristallinen Feststoffs.

^{1}H-NMR (400 MHz, $CDCl_3$): δ = 1.28 (d, 12H, $^{3}J_{\mathrm{HH}}$ = 6.3 Hz, CHMe_2), 3.91–4.00 (sept, 2H, $^{3}J_{\mathrm{HH}}$ = 6.2 Hz, CHMe$_2$), 6.23 (d, 2H, $^{3}J_{\mathrm{HH}}$ = 12.0 Hz, 3-H, 7-H), 8.05 (d, 2H, $^{3}J_{\mathrm{HH}}$ = 11.3 Hz, 4-H, 6-H) ppm.

Für eine Synthese unter diesen Bedingungen wurde in Folgesynthesen eine schwankende Ausbeute (5–13%) erhalten.

3,4–Bis(*iso*prpopylamino)benzaldehyd (**2**)

Zu einer Lösung von Br–ATI$^{i\mathrm{Pr}/i\mathrm{Pr}}$ (**1-Br**) (2.93 g, 10.4 mmol) in DMSO (40 mL) wurde Natriumnitrit (750 mg, 10.9 mmol) gegeben. Die Mischung wurde bei 150 °C für 16 Tage gerührt. Die Aufarbeitung wurde analog zur Aufarbeitung bei der Synthese von **1-NO$_2$** durchgeführt. Während der säulenchromatograpischen Reinigung (stationäre Phase: Siliciumdioxid, Laufmittel: *n*-Hexan/MTBE 10:1, 5 Vol% NEt_3) wurde 3,4–Bis(*iso*prpopylamino)benzaldehyd als bräunlicher kristalliner Feststoff isoliert. Ausbeute: 108 mg, 490 µmol (5%).

^{1}H-NMR (400 MHz, $CDCl_3$): δ = 1.23 (d, 6H, $^{3}J_{\mathrm{HH}}$ = 6.2 Hz, 3-NCHMe_2), 1.29 (d, 6H, $^{3}J_{\mathrm{HH}}$ = 6.2 Hz, 4-NCHMe_2), 3.56–3.58 (sept, 1H, $^{3}J_{\mathrm{HH}}$ = 6.2 Hz, 3-NCHMe$_2$), 3.70–3.75 (sept, 1H, $^{3}J_{\mathrm{HH}}$ = 6.3 Hz, 4-NCHMe$_2$), 4.32 (br. s, 2H, NH), 6.65 (d, 1H, $^{3}J_{\mathrm{HH}}$ = 8.2 Hz, 5-H), 7.28 (s, 1H, 2-H), 7.36 (d, 1H, $^{3}J_{\mathrm{HH}}$ = 7.9 Hz, 6-H), 9.71 (s, 1H, COH) ppm.^{13}C-NMR (101 MHz, Pyridin-d_5): δ = 22.97 (s, 4-NCHMe), 23.07 (s, 3-NCHMe), 44.16 (s, NCHMe$_2$), 45.42 (s, NCHMe$_2$), 109.26 (s, 5-C), 114.51 (s, 2-C), 126.66 (s, 3-C), 127.73 (s, 6-C), 133.97 (s, 1-C), 145.04 (s, 4-C), 190.99 (s, COH) ppm.

Elementaranalyse: Ber. (%) für $C_{13}H_{20}N_2O$ (220.32 g/mol): C: 70.87, H: 9.15, N: 12.72, gef.: C: 70.71, H: 9.19, N: 12.73.

3 Synthese rückgratsubstituierter Alkalimetall-Aminotroponiminat-Komplexe

[Li(Ph(O)S–ATI$^{iPr/iPr}$)] (**3-Ph(O)S**)

Trimethylsilyl(methyllithium) ($LiCH_2SiMe_3$, 31.0 mg, 330 µmol) wurde zu einer Lösung aus Ph(O)S–ATI$^{iPr/iPr}$ (**1-Ph(O)S**) (102 mg, 311 µmol) in THF gegeben. Nach 5 Minuten Reaktionszeit wurde das Lösungsmittel im Vakuum entfernt. Der erhaltene gelbe Feststoff wurde mit Pentan und Et_2O (je 4 × 2 mL) gewaschen. Kristalle wurden durch die Diffusion von Pentan (1 mL) in eine Lösung von **3-Ph(O)S** (9.0 mg) in Pyridin (2 mL) erhalten. Ausbeute: 44 mg, 130 µmol (mit n = 0.05 Äq. Et_2O), 42% eines gelben Pulvers.

^{1}H-NMR (500 MHz, Pyridin-d_5): δ = 0.92 (d, 6H, $^3J_{HH}$ = 6.3 Hz, CH*Me₂*), 0.95 (d, 6H, $^3J_{HH}$ = 6.2 Hz, CH*Me₂*), 1.14 (t, n × 6H, Et_2O), 3.34–3.38 (q, n × 4H, Et_2O), 3.81–3.88 (sept, 2H, $^3J_{HH}$ = 6.2 Hz, C*H*Me₂), 6.26 (d, 2H, $^3J_{HH}$ = 11.9 Hz, 3-H, 7-H), 7.32–7.35 (m, 3H, *p*-Ph, 4-H, 6-H), 7.44–7.46 (m, 2H, *m*-Ph), 8.00–8.03 (m, 2H, *o*-Ph) ppm. ^{13}C-NMR (126 MHz, Pyridin-d_5): δ = 15.97 (s, Et_2O), 24.03 (s, CH*Me₂*), 24.17 (s, CH*Me₂*), 49.74 (s, *C*HMe₂), 66.24 (s, Et_2O), 106.16 (s, 3-C, 7-C), 120.79 (s, 5-C), 125.67 (s, *o*-Ph), 129.43 (s, *m*-Ph), 129.84 (s, *p*-Ph), 132.15 (s, 4-C, 6-C), 150.21 (s, überlagert durch Signale von Pyridin-d_5, *ipso*-Ph), 164.07 (s, 1-C, 2-C) ppm. ^{7}Li-NMR (194 MHz, Pyridin-d_5): δ = 3.24 ppm.

Elementaranalyse: Ber. (%) für $C_{19}H_{23}LiN_2OS{\cdot}(C_5H_5N)$ (413.51 g/mol): C 69.71, H 6.83, N 10.16, S 7.75; gef. C 69.59, H 7.17, N 10.45, S 7.40.

Der Anteil an neutralen Donorliganden (Et_2O, THF, Pyridin) muss für jede Charge separat bestimmt werden.

[Na(Ph(O)S–ATI$^{iPr/iPr}$)] (**4-Ph(O)S**)

Zu einer Lösung von Ph(O)S–ATI$^{iPr/iPr}$ (**1-Ph(O)S**) (150 mg, 457 µmol) in THF (3 mL) wurde NaHMDS (84 mg, 457 µmol) gegeben. Nach 10 min wurde das Lösungsmittel im Vakuum entfernt und der beige Feststoff mit Toluol und Pentan (jeweils 2 × 3 mL) sowie mit Et_2O (3 × 3 mL) gewaschen. Das Produkt wurde im Vakuum getrocknet. Ausbeute: 118 mg, 337 µmol, 74% eines beigen Feststoffes.

^{1}H-NMR (400 MHz, THF-d_8): δ = 1.08 (d, 12H, $^3J_{HH}$ = 6.2 Hz, CH*Me₂*), 3.64–3.73 (sept, 2H, $^3J_{HH}$ = 6.2 Hz, C*H*Me₂), 5.61 (d, 2H, $^3J_{HH}$ = 11.9 Hz, 3-H, 7-H), 6.52 (d, 2H, $^3J_{HH}$ = 11.8 Hz, 4-H, 6-H), 7.26–7.29 (m, 1H, *p*-Ph), 7.33–7.37 (m, 2H, *m*-Ph), 7.52–7.53 (m, 2H, *o*-Ph) ppm. ^{13}C-NMR (101 MHz, THF-d_8): δ = 24.04 (s, CH*Me₂*), 24.23 (s, CH*Me₂*), 50.00 (s, *C*HMe₂), 103.97 (s, 3-C, 7-C), 114.20 (s, 5-C), 125.74 (s, *o*-Ph), 128.83 (s, *m*-Ph), 129.25 (s, *p*-Ph), 131.80 (s, 4-C, 6-C), 148.89 (s, *ipso*-Ph), 163.04 (s, 1-C, 2-C) ppm.

Elementaranalyse: Ber. (%) für $C_{19}H_{23}N_2NaOS$ (350.46 g/mol): C 65.12, H 6.62, N 7.99, S 9.15; gef. C 65.06, H 6.68, N 8.03, S 8.83.

[Na(12-Krone-4)$_2$][Na(Ph(O)S–ATI$^{iPr/iPr}$)$_2$] (**6-Ph(O)S**)

12-Krone-4 (14 mg, 80 µmol) wurde zu einer Lösung von **4-Ph(O)S** (28 mg, 80 µmol) in DME (1 mL) gegeben und mit Pentan (1 mL) übersichtet. Der ausgefallene kristalline Feststoff wurde durch Filtration isoliert und im Vakuum getrocknet. Ausbeute: 23 mg, 22 mmol (mit *n* = 0.08 Äq. DME), 28%.

^{1}H-NMR (400 MHz, Pyridin-*d*$_5$): δ = 1.18 (d, 24H, $^3J_{HH}$ = 6.1 Hz, CH*Me$_2$*), 3.28 (s, *n* × 6H, DME-C*H$_3$*), 3.51 (s, *n* × 4H, DME-C*H$_2$*) 3.61 (s, 32H, Kronenether-C*H$_2$*), 3.82–3.91 (sept, 2H, $^3J_{HH}$ = 6.2 Hz, C*H*Me$_2$), 6.00 (d, 2H, $^3J_{HH}$ = 11.9 Hz, 3-H, 7-H), 7.16 (d, 2H, $^3J_{HH}$ = 11.7 Hz, 4-H, 6-H), 7.28–7.32 (dd, 4H, $^3J_{HH}$ = 7.2 Hz, $^3J_{HH}$ = 7.6 Hz, *p*-Ph), 7.38–7.42 (dd, 4H, $^3J_{HH}$ = 7.5 Hz, $^3J_{HH}$ = 7.8 Hz, *m*-Ph), 7.97 (d, 2H, $^3J_{HH}$ = 6.9 Hz, *o*-Ph) ppm. ^{13}C-NMR (101 MHz, Pyridin-*d*$_5$): δ = 24.61 (s, CH*Me$_2$*), 24.72 (s, CH*Me$_2$*), 50.28 (s, *C*HMe), 59.06 (s, DME-*C*H$_3$), 68.04 (s, Kronenether-*C*H$_2$), 72.50 (s, DME-*C*H$_2$), 104.66 (s, 3-C, 7-C), 116.68 (s, 5-C), 125.98 (s, *o*-Ph), 129.23 (s, *m*-Ph), 129.51 (s, *p*-Ph), 132.25 (s, 4-C, 6-C), 150.44 (s, *ipso*-Ph), 163.30 (s, 1-C, 2-C) ppm.

Elementaranalyse: Ber. (%) für $C_{54}H_{78}Na_2N_4O_{10}S_2$ (1053.34 g/mol): C, 61.58; H, 7.46; N, 5.32; S, 6.09; gef.: C, 61.64; H, 7.55; N, 5.37; S, 6.07.

[K(Ph(O)S–ATI$^{iPr/iPr}$)] (**5-Ph(O)S**)

Zu einer Lösung von Ph(O)S–ATI$^{iPr/iPr}$ (**1-Ph(O)S**) (200 mg, 609 µmol) in THF (3 mL) wurde Kaliumhexamethyldisilazid (KHMDS, 134 mg, 672 µmol) gegeben. Nach 5 min wurde das Lösungsmittel im Vakuum entfernt und der gelbe Feststoff jeweils mit Toluol (3 × 2 mL) sowie mit Pentan (4 × 4 mL) gewaschen. Das Produkt wurde im Vakuum getrocknet. Ausbeute: 161 mg, 428 µmol (mit 0.1 Äq. Toluol) 70% eines gelben Feststoffes.

^{1}H-NMR (400 MHz, THF-*d*$_8$): δ = 1.08 (d, 12H, $^3J_{HH}$ = 5.9 Hz, CH*Me$_2$*), 2.30 (s, *n* × 3H, Tol), 3.63–3.69 (sept, 2H, $^3J_{HH}$ = 6.1 Hz, C*H*Me$_2$), 5.38 (d, 2H, $^3J_{HH}$ = 11.8 Hz, 3-H, 7-H), 6.42 (d, 2H, $^3J_{HH}$ = 11.5 Hz, 4-H, 6-H), 7.21–7.25 (m, 1H, *p*-Ph), 7.29–7.33 (t, 2H, $^3J_{HH}$ = 7.4 Hz, *m*-Ph), 7.51–7.52 (d, 2H, $^3J_{HH}$ = 7.3 Hz, *o*-Ph) ppm. ^{13}C-NMR (101 MHz, THF-*d*$_8$): δ = 23.71 (s, CH*Me$_2$*), 24.12 (s, CH*Me$_2$*), 50.73 (s, *C*HMe$_2$), 102.51 (s, 3-C, 7-C), 112.25 (s, 5-C), 125.85 (s, *o*-Ph), 128.55 (s, *m*-Ph), 128.72 (s, *p*-Ph), 131.69 (s, 4-C, 6-C), 150.12 (s, *ipso*-Ph), 163.15 (s, 1-C, 2-C) ppm.

Elementaranalyse: Ber. (%) für $C_{19}H_{23}KN_2OS\cdot(C_4H_{10}O)_{0.33}$ (396.30 g/mol): C 61.58, H 6.69, N 7.06, S 8.08; gef. C 61.71, H 6.82, N 7.17, S 7.90.

Der Anteil an neutralen Donorliganden muss für jede Charge separat bestimmt werden.

Reduktionsprodukt **5-red**

Zu einer Lösung von **5-Ph(O)S** (50 mg, 136 µmol) in THF (2 mL) wurde elementares Kalium (17 mg, 435 µmol) gegeben und die Suspension 3 d bei Raumtemperatur rühren gelassen. Die Suspension wurde filtriert, 18-Krone-6 (36 mg, 136 µmol) zugegeben und die Lösung mit *n*-Pentan (2 mL) überschichtet und bei −30 °C gelagert. Der ausgefallene Feststoff wurde durch Filtration isoliert und im Vakuum getrocknet. Der Feststoff wurde in THF-d_8 gelöst und über Nacht bei Raumtemperatur stehen gelassen. Der ausgefallene Feststoff wurde durch Filtration isoliert und in Pyridin-d_5 gelöst.

^{1}H-NMR (400 MHz, Pyridin-d_5) δ = 1.27 (d, 12H, $^{3}J_{\mathrm{HH}}$ = 5.8 Hz, CH*Me*), 1.37 (d, 12H, $^{3}J_{\mathrm{HH}}$ = 5.7 Hz, CH*Me*), 3.48 (s, n × 24H, Kronenether-C*H*$_2$), 4.03–4.09 (m, 2H, C*H*Me), 4.09–4.15 (m, 2H, C*H*Me), 6.03 (d, 2H, $^{3}J_{\mathrm{HH}}$ = 11.6 Hz, 7-H), 6.33 (d, 2H, $^{3}J_{\mathrm{HH}}$ = 9.1 Hz, 5-H), 6.57 (s, 2H, 3-H), 6.73–6.79 (dd, 2H, , $^{3}J_{\mathrm{HH}}$ = 11.0 Hz, $^{3}J_{\mathrm{HH}}$ = 9.4 Hz, 6-H), 6.84–6.88 (m, 2H, *p*-Ph$_{\mathrm{Brücke}}$, *p*-Ph), 6.97–7.00 (dd, 2H, $^{3}J_{\mathrm{HH}}$ = 7.6 Hz, $^{3}J_{\mathrm{HH}}$ = 6.6 Hz, *m*-Ph), 7.52 (d, 2H, $^{3}J_{\mathrm{HH}}$ = 6.9 Hz, *m*-Ph$_{\mathrm{Brücke}}$), 8.32 (d, 2H, $^{3}J_{\mathrm{HH}}$ = 7.9 Hz, *o*-Ph) ppm. ^{13}C-NMR (101 MHz, Pyridin-d_5) δ = 24.82–25.62 (m, THF-d_8), 25.16 (s, CH*Me*), 50.06 (s, *C*HMe), 50.17 (s, *C*HMe), 67.01–67.91 (m, THF-d_8), 70.82 (s, Kronenether-*C*H$_2$), 102.76 (s, 7-C), 108.59 (s, 5-C), 109.12 (s, 3-C), 117.29 (s, *p*-Ph$_{\mathrm{Brücke}}$, *p*-Ph), 125.23 (s, *m*-Ph), 129.10 (s, *m*-Ph$_{\mathrm{Brücke}}$), 130.75 (s, 6-C), 137.59 (s, *o*-Ph), 150.85 (s, 4-C), 151.84 (s, *o*-Ph$_{\mathrm{Brücke}}$), 159.24 (s, *ipso*-Ph, *ipso*-Ph$_{\mathrm{Brücke}}$), 162.16 (s, 2-C), 162.40 (s, 1-C) ppm.

[Li(NO$_2$–ATI$^{i\mathrm{Pr}/i\mathrm{Pr}}$)] (**3-NO$_2$**)

Zu einer Lösung von NO$_2$–ATI$^{i\mathrm{Pr}/i\mathrm{Pr}}$ (**1-NO$_2$**) (200 mg, 802 µmol) in THF (6 mL) wurde LiCH$_2$SiMe$_3$ (77.1 mg, 818 µmol) gegeben. Das Lösungsmittel wurde unter vermindertem Druck entfernt und der Feststoff wurde mit Diethylether (1 × 3 mL) und Pentan (3 × 3 mL) gewaschen. Kristalle wurden durch die Diffusion von Pentan (1 mL) in eine Lösung von **3-NO$_2$** (9.0 mg) in Pyridin (2 mL) erhalten. Ausbeute: 145 mg, 528 µmol (mit *n* = 0.27 Äq. Pentan), 66% eines orangenen kristallinen Feststoffs.

^{1}H-NMR (400 MHz, Pyridin-d_5): δ = 0.95 (d, 12H, $^{3}J_{\mathrm{HH}}$ = 5.9 Hz, CH*Me$_2$*), 3.88–3.94 (sept, 2H, $^{3}J_{\mathrm{HH}}$ = 6.2 Hz, C*H*Me$_2$), 6.22 (d, 2H, $^{3}J_{\mathrm{HH}}$ = 12.6 Hz, 3-H, 7-H), 8.50 (d, 2H, $^{3}J_{\mathrm{HH}}$ = 12.6 Hz, 4-H, 6-H) ppm. ^{13}C-NMR (101 MHz, Pyridin-d_5): δ = 23.90 (s, Me), 50.29 (s, *C*HMe$_2$), 106.12 (s, 3-C, 7-C), 129.52 (s, 4-C, 6-C), 130.71 (s, 5-C), 164.30 (s, 1-C, 2-C) ppm. ^{7}Li-NMR (156 MHz, Pyridin-d_5): δ = 2.99 (s) ppm.

Elementaranalyse: Ber. (%) für $C_{13}H_{18}LiN_3O_2 \cdot C_5H_5N$ (334.20 g/mol): C: 64.66, H: 6.93, N: 16.76, gef.: C: 64.46, H: 6.99, N: 16.93.

[Na(NO$_2$–ATI$^{i\mathrm{Pr}/i\mathrm{Pr}}$)] (**4-NO$_2$**)

Zu einer Lösung von NO$_2$–ATI$^{i\mathrm{Pr}/i\mathrm{Pr}}$ (**1-NO$_2$**) (93 mg, 373 µmol) in THF (2 mL) wurde NaHMDS (69 mg, 373 µmol) gegeben. Das Lösungsmittel wurde unter vermindertem Druck entfernt und der Feststoff wurde mit Toluol, Diethylether und Pentan (je 3 × 3 mL) gewaschen. Kristalle wurden über die Diffusion von Pentan (1 mL) in eine Lösung von **4-NO$_2$** (10.0 mg) in Pyridin (2 mL) erhalten. Ausbeute: 83 mg, 296 µmol, (mit je 0.06 Äq. THF und Et$_2$O), 79% eines orangenen kristallinen Feststoffs.

Nach 3 d in Lösung werden zwei Signalsätze für das *E,E*-Isomer und das *E,Z*-Isomer im Verhältnis 1.0:1.5 im ^{1}H-NMR-Spektrum detektiert.

E,E-Isomer: ^{1}H-NMR (400 MHz, Pyridin-*d$_5$*): δ = 1.15 (d, 12H, $^3J_{HH}$ = 6.3 Hz, CH*Me$_2$*), 3.92–3.95 (sept, 2H, $^3J_{HH}$ = 6.2 Hz, C*H*Me$_2$), 6.08 (d, 2H, $^3J_{HH}$ = 12.6 Hz, 3-H, 7-H), 8.34 (d, 2H, $^3J_{HH}$ = 12.7 Hz, 4-H, 6-H) ppm. ^{13}C-NMR (101 MHz, Pyridin-*d$_5$*): δ = 24.16 (s, Me), 51.16 (s, *C*HMe$_2$), 109.14 (s, 3-C, 7-C), 124.19 (s, 5-C), 128.53 (s, 4-C, 6-C), 163.68 (s, 1-C, 2-C) ppm.

E,Z-Isomer: ^{1}H-NMR (400 MHz, Pyridin-*d$_5$*): δ = 1.22 (d, 6H, $^3J_{HH}$ = 6.2 Hz, 1-NCH*Me$_2$*), 1.37 (d, 6H, $^3J_{HH}$ = 6.2 Hz, 2-NCH*Me$_2$*), 4.01–4.04 (sept, 1H, $^3J_{HH}$ = 6.1 Hz, 1-NC*H*Me$_2$), 4.53–4.56 (sept, 1H, $^3J_{HH}$ = 6.4 Hz, 2-NC*H*Me$_2$), 6.11 (d, 1H, $^3J_{HH}$ = 13.3 Hz, 7-H), 6.51 (d, 1H, $^3J_{HH}$ = 12.7 Hz, 3-H), 8.22 (m, 2H, 4-C, 6-C) ppm. ^{13}C-NMR (101 MHz, Pyridin-*d$_5$*): δ = 24.30 (s, 1-NCH*Me$_2$*), 25.10 (s, 2-NCH*Me$_2$*), 51.27 (s, 1-N*C*HMe$_2$), 51.68 (s, 2-N*C*HMe$_2$), 111.64 (s, 7-C), 122.51 (s, 3-C), 124.43 (s, 5-C), 126.43 (s, 4-C/6-C), 128.76 (s, 4-C/6-C), 160.78 (s, 1-C), 162.92 (s, 2-C) ppm.

Elementaranalyse: Ber. (%) für $C_{13}H_{18}NaN_3O_2{\cdot}(C_5H_5N)$ (350.17 g/mol): C: 61.70, H: 6.62, N: 15.99, gef.: C: 61.57, H: 6.45, N: 15.65.

[K(NO$_2$–ATI$^{iPr/iPr}$)] (**5-NO$_2$**)

Zu einer Lösung von NO$_2$–ATI$^{iPr/iPr}$ (**1-NO$_2$**)(100 mg, 401 µmol) in THF (2 mL) wurde KHMDS (84.0 mg, 421 µmol) und THF (2 mL) gegeben. Das Lösungsmittel wurde unter vermindertem Druck entfernt, und der Feststoff wurde mit Diethylether (2 × 2 mL) und Pentan (3 × 2 mL) gewaschen. Kristalle wurden über die Diffusion von Pentan (2 mL) in eine Lösung von **5-NO$_2$** in Pyridin (4 mL) erhalten. Ausbeute: 91 mg (301 µmol, mit 0.21 Äq. Pentan, 75%) eines braun-orangenen, kristallinen Feststoffs.

Es konnten zwei Signalsätze für das *E,E*-Isomer und das *E,Z*-Isomer im ^{1}H-NMR-Spektrum detektiert werden. Nach 3 d stellte sich ein festes Verhältnis von 1.0:1.6 ein.

E,E-Isomer: ^{1}H-NMR (400 MHz, Pyridin-*d$_5$*): δ = 1.16 (d, 12H, $^3J_{HH}$ = 6.1 Hz, CH*Me$_2$*), 3.91–4.00 (sept, 2H, $^3J_{HH}$ = 6.1 Hz, C*H*Me$_2$), 6.01 (d, 2H, $^3J_{HH}$ = 12.7 Hz, 3-H, 7-H, überlagert durch 7-H von *E,Z*-Isomer), 8.34 (d, 1H, $^3J_{HH}$ = 12.6 Hz, 4-H, 6-H) ppm. ^{13}C-NMR (101 MHz, Pyridin-*d$_5$*): δ = 24.26 (s, CH*Me$_2$*), 51.34 (s, *C*HMe$_2$), 109.16 (s, 3-C, 7-C), 126.35 (s, 5-C), 128.40 (s, 4-C, 6-C), 163.76 (s, 1--C, 2-C) ppm. ^{15}N-^{1}H-HMBC-NMR (50 MHz, 500 MHz, Pyridin-*d$_5$*): δ = −53.9 (s, 1-N, 2-N) ppm.

E,Z-Isomer: ^{1}H-NMR (400 MHz, Pyridin-*d$_5$*): δ = 1.24 (d, 6H, $^3J_{HH}$ = 6.1 Hz, 1-NCH*Me$_2$*), 1.39 (d, 6H, $^3J_{HH}$ = 6.2 Hz, 2-NCH*Me$_2$*), 4.00–4.07 (sept, 1H, $^3J_{HH}$ = 6.2 Hz, 1-NC*H*Me$_2$), 4.56–4.62 (sept, 1H, $^3J_{HH}$ = 6.1 Hz, 2-NC*H*Me$_2$), 6.02 (d, 1H, $^3J_{HH}$ = 13.1 Hz, 7-H, überlagert durch 3-H, 7-H von *E,E*-Isomer), 6.46 (d, 1H, $^3J_{HH}$ = 13.0 Hz, 3-H), 8.25 (d, 2H, $^3J_{HH}$ = 12.4 Hz, 4-H), 8.26 (d, 1H,

$^{3}J_{\mathrm{HH}}$ = 13.4 Hz, 6-H) ppm. ^{13}C-NMR (101 MHz, Pyridin-*d$_5$*): *δ* = 24.37 (s, 1-NCH*Me$_2$*), 25.14 (s, 2-NCH*Me$_2$*), 51.18 (s, 1-N*C*HMe$_2$), 51.57 (s, 2-N*C*HMe$_2$), 110.40 (s, 7-C), 121.52 (s, 3-C), 125.90 (s, 5-C), 126.59 (s, 4-C), 128.93 (s, 6-C), 160.82 (s, 1-C), 163.01 (s, 2-C) ppm. ^{15}N-^{1}H-HMBC-NMR (50 MHz, 500 MHz, Pyridin-*d$_5$*): *δ* = −41.2 (s, 2-N), −32.6 (s, 1-N) ppm.

Elementaranalyse: Ber. (%) für $C_{13}H_{18}KN_3O_2{\cdot}C_5H_5N$ (366.15 g/mol): C: 58.99, H: 6.33, N: 15.29, gef.: C: 58.95, H: 6.45, N: 15.52.

[Na(12-Krone-4)$_2$][(NO$_2$–ATI$^{i\mathrm{Pr}/i\mathrm{Pr}}$)] (**4-NO$_2$-(12K4)$_2$**)

Zu einer Suspension von [Na(NO$_2$–ATI$^{i\mathrm{Pr}2}$)] (**4-NO$_2$**) (100 mg, 369 µmol) in THF (3 mL) wurde (12-Krone-4) (129 mg, 738 µmol) gegeben. Das Lösungsmittel wurde im Vakuum entfernt, und der Feststoff wurde mit Pentan (3 × 2 mL) gewaschen und im Vakuum getrocknet. Ausbeute: 209 mg, 333 µmol (mit 0.05 Äq. THF), 90% eines gelben Feststoffs.

Es konnten zwei Signalsätze für das *E,E*-Isomer und das *E,Z*-Isomer im Verhältnis 1.0:1.3 im ^{1}H-NMR-Spektrum detektiert werden.

E,E-Isomer: ^{1}H-NMR (400 MHz, Pyridin-*d$_5$*): *δ* = 1.22 (d, 12H, $^{3}J_{\mathrm{HH}}$ = 6.2 Hz, CH*Me$_2$*), 3.61 (s, 32H, Kronenether-C*H$_2$*), 3.94–4.00 (br. sept, 2H, C*H*Me$_2$), 6.06 (d, 2H, $^{3}J_{\mathrm{HH}}$ = 12.7 Hz, 3-H,7-H), 8.41 (d, 2H, $^{3}J_{\mathrm{HH}}$ = 12.6 Hz, 4-H, 6-H) ppm. ^{13}C-NMR (101 MHz, Pyridin-*d$_5$*): *δ* = 22.95 (s, CH*Me$_2$*), 51.12 (s, *C*HMe$_2$), 68.30 (Kronenether-*C*H$_2$), 107.67 (s, 3-C, 7-C), 125.75 (s, 5-C), 128.79 (s, 4-C, 6-C), 163.65 (s, 1-C, 2-C) ppm.

E,Z-Isomer: ^{1}H-NMR (400 MHz, Pyridin-*d$_5$*): *δ* = 1.24 (d, 6H, $^{3}J_{\mathrm{HH}}$ = 6.2 Hz, 1-NCH*Me$_2$*), 1.38 (d, 6H, $^{3}J_{\mathrm{HH}}$ = 6.2 Hz, 2-NCH*Me$_2$*), 3.61 (s, 32H, Kronenether-C*H$_2$*), 4.01–4.10 (sept, 1H, $^{3}J_{\mathrm{HH}}$ = 6.2 Hz, 1-NC*H*Me$_2$), 4.56–4.65 (sept, 1H, $^{3}J_{\mathrm{HH}}$ = 6.2 Hz, 2-NC*H*Me$_2$), 6.04 (d, 1H, $^{3}J_{\mathrm{HH}}$ = 12.7 Hz, 7-H), 6.47 (d, 1H, $^{3}J_{\mathrm{HH}}$ = 12.9 Hz, 3-H), 8.32 (ddd, 1H, $^{3}J_{\mathrm{HH}}$ = 12.9 Hz, $^{4}J_{\mathrm{HH}}$ = 2.0, 4-H), 8.34 (dd, 1H, $^{3}J_{\mathrm{HH}}$ = 12.8 Hz, $^{4}J_{\mathrm{HH}}$ = 1.9, 6-H) ppm. ^{13}C-NMR (101 MHz, Pyridin-*d$_5$*): *δ* = 24.40 (s, 1-NCH*Me$_2$*), 25.15 (s, 2-NCH*Me$_2$*), 51.15 (s, 1-NCH*Me$_2$*), 51.46 (s, 2-N*C*HMe$_2$), 68.30 (Kronenether-*C*H$_2$), 109.37 (s, 7-C), 120.69 (s, 3-C), 125.75 (s, 5-C), 126.85 (s, 4-C), 129.19 (s, 6-C), 160.88 (s, 1-C), 163.07 (s, 1-C) ppm. ^{23}Na-NMR (106 MHz, Pyridin-*d$_5$*): *δ* = 1.7 (br. s, *Na*) ppm.

Elementaranalyse: Ber. (%) für $C_{29}H_{50}N_3NaO_{10}$ (623.72 g/mol): C: 55.85, H: 8.08, N: 6.74, gef.: C: 56.00, H: 8.25, N: 6.85.

[Na(15-Krone-5)(NO$_2$–ATI$^{i\mathrm{Pr}/i\mathrm{Pr}}$)] (**4-NO$_2$-(15K5)**)

Zu einer Suspension von [Na(NO$_2$–ATI$^{i\mathrm{Pr}/i\mathrm{Pr}}$)] (**4-NO$_2$**) (25.0 mg, 87.0 µmol) in THF (3 mL) wurde (15-Krone-5) (19.2 mg, 87.2 µmol) gegeben. Die orangene Lösung wurde mit Pentan überschichtet und für 6 d stehen gelassen. Der ausgefallene Feststoff wurde durch Filtration isoliert, mit Diethylether (1 × 2 mL) und Pentan (3 × 2 mL) gewaschen und im Vakuum getrocknet. Ausbeute: 37.6 mg, 74.3 µmol (mit 0.20 Äq. Pentan), 85% eines gelben, kristallinen Feststoffs.

Es werden zwei Signalsätze für das *E,E*-Isomer und das *E,Z*-Isomer im Verhältnis 1.0:1.9 im ^{1}H-NMR-Spektrum detektiert.

E,E-Isomer: ^{1}H-NMR (400 MHz, Pyridin-*d*$_5$): δ = 1.20 (d, 12H, $^{3}J_{HH}$ = 6.6 Hz, CH*Me*$_2$), 3.59 (s, 20H, Kronenether-C*H*$_2$), 3.93–3.99 (sept, 2H, $^{3}J_{HH}$ = 5.9 Hz, C*H*Me$_2$), 6.10 (d, 2H, $^{3}J_{HH}$ = 12.6 Hz, 3-H, 7-H), 8.29 (d, 2H, $^{3}J_{HH}$ = 12.8 Hz, 4-H, 6-H) ppm. ^{13}C-NMR (125 MHz, Pyridin-*d*$_5$): δ = 24.33 (s, Me), 51.26 (s, *C*HMe$_2$), 69.78 (Kronenether-*C*H$_2$), 109.59 (s, 3-C, 7-C), 126.11 (s, 5-C), 128.25 (s, 4-C, 6-C), 163.43 (s, 1-C, 2-C) ppm. ^{15}N-^{1}H-HMBC-NMR (50.7 MHz, Pyridin-*d*$_5$): δ = −63.2 (überlagert durch Pyridin-*d*$_5$, 1-N, 2-N), −25.6 (s, *N*O$_2$) ppm.

E,Z-Isomer: ^{1}H-NMR (400 MHz, Pyridin-*d*$_5$): δ = 1.22 (d, 6H, $^{3}J_{HH}$ = 6.33 Hz, 1-NCH*Me*$_2$), 1.37 (d, 6H, $^{3}J_{HH}$ = 6.21 Hz, 2-NCH*Me*$_2$), 3.59 (s, 20H, Kronenether-C*H*$_2$), 3.99–4.05 (sept, 1H, $^{3}J_{HH}$ = 6.19 Hz, 1-NC*H*Me$_2$), 4.52–4.58 (sept, 1H, $^{3}J_{HH}$ = 6.18 Hz, 2-NC*H*Me$_2$), 6.06 (d, 1H, $^{3}J_{HH}$ = 12.8 Hz, 7-H), 6.48 (d, 1H, $^{3}J_{HH}$ = 12.7 Hz, 3-H), 8.19 (dd, 1H, $^{3}J_{HH}$ = 5.03 Hz, $^{4}J_{HH}$ = 1.88, 6-H), 8.23 (dd, 1H, $^{3}J_{HH}$ = 5.03 Hz, $^{4}J_{HH}$ = 1.88, 4-H) ppm. ^{13}C-NMR (101 MHz, Pyridin-*d*$_5$): δ = 24.35 (s, 1-NCH*Me*$_2$), 25.1 (s, 2-NCH*Me*$_2$), 51.20 (s, 1-N*C*HMe$_2$), 51.58 (s, 2-N*C*HMe$_2$), 69.78 (Kronenether-*C*H$_2$), 110.58 (s, 7-C), 121.61 (s, 3-C), 125.40 (s, 5-C), 126.62 (s, 4-C), 128.93 (s, 6-C), 160.81 (s, 1-C), 162.97 (s, 2-C) ppm. ^{15}N-^{1}H-HMBC-NMR (50.7 MHz, Pyridin--*d*$_5$): δ = −51.0 (s, 2-N), −42.3 (s, 1-N), −31.6 (s, *N*O$_2$) ppm. ^{23}Na-NMR (106 MHz, Pyridin-*d*$_5$): δ = 0.94 (br. s) ppm.

Elementaranalyse: Ber. (%) für $C_{23}H_{38}N_3NaO_7$ (491.56 g/mol): C: 56.20, H: 7.79, N: 8.55, gef.: C: 56.21, H: 7.82, N: 8.64.

[K(18-Krone-6)(NO$_2$–ATI$^{iPr/iPr}$)] (**5-NO$_2$-(18K6)**)

Zu einer Lösung von NO$_2$–ATI$^{iPr/iPr}$ (**1-NO$_2$**) (108 mg, 432 µmol) in THF (3 mL) wurden KHMDS (86 mg, 432 µmol) und 18-Krone-6 (114 mg, 432 µmol) gegeben. Das Lösungsmittel wurde im Vakuum entfernt. Der gelbe Feststoff wurde mit Pentan (4 × 15 mL) gewaschen und im Vakuum getrocknet. Ausbeute: 202 mg, 349 µmol (mit *n* = 0.19 Äq. THF), 83% eines gelben Feststoffs.

Es konnten zwei Signalsätze für das *E,E*-Isomer und das *E,Z*-Isomer im Verhältnis 1.0:1.5 im ^{1}H-NMR-Spektrum detektiert werden.

E,E-Isomer: ^{1}H-NMR (400 MHz, Pyridin-*d*$_5$): δ = 1.22 (d, 12H, $^{3}J_{HH}$ = 6.2 Hz, CH*Me*$_2$), 1.61–1.64 (m, *n* × 4H, β-THF), 3.47 (s, 24H, Kronenether-C*H*$_2$), 3.65-3.67 (m, *n* × 4H, α-THF), 3.98–4.12 (br. sept, 2H, $^{3}J_{HH}$ = 6.2 Hz, C*H*Me$_2$, überlagert durch C*H*Me$_2$ von *E*,*Z*-Isomer), 6.04 (br. d, 2H, $^{3}J_{HH}$ = 12.7 Hz, 3-H, 7-H), 8.37-8.44 (m, 2H, 4-H, 6-H, überlagert durch 4-H und 6-H von *E,Z*-Isomer) ppm. ^{13}C-NMR (101 MHz, Pyridin-*d*$_5$): δ = 24.49 (s, CH*Me*$_2$), 26.27 (s, β-THF), 50.98 (s, *C*HMe$_2$), 68.30 (s, α-THF), 70.78 (Kronenether-*C*H$_2$), 108.14 (s, 3-C, 7-C), 126.00 (s, 5-C), 127.22 (s, 4-C, 6-C), 163.44 (s, 1-C, 2-C) ppm.

E,Z-Isomer: ^{1}H-NMR (400 MHz, Pyridin-*d₅*): δ = 1.26 (d, 6H, $^3J_{HH}$ = 6.2 Hz, 1-NCH*Me₂*), 1.39 (d, 6H, $^3J_{HH}$ = 6.2 Hz, 2-NCH*Me₂*), 1.61–1.64 (m, *n* × 4H, β-THF), 3.47 (s, 24H, Kronenether-C*H₂*), 3.65–3.67 (m, *n* × 4H, α-THF), 3.98–4.12 (br. sept, 2H, $^3J_{HH}$ = 6.2 Hz, 1-NC*H*Me₂, überlagert durch C*H* von *E,E*-Isomer), 4.61–4.71 (sept, 1H, $^3J_{HH}$ = 6.2 Hz, 2-NC*H*Me₂), 5.97 (d, 1H, $^3J_{HH}$ = 12.5 Hz, 7-H), 6.45 (d, 1H, $^3J_{HH}$ = 12.6 Hz, 3-H), 8.37–8.44 (m, 2H, 4-H, 6-H, überlagert durch 4-H und 6-H von *E,E*-Isomer) ppm. ^{13}C-NMR (101 MHz, Pyridin-*d₅*): δ = 24.60 (s, 1-NCH*Me₂*), 25.20 (s, 2-NCH*Me₂*), 26.27 (s, β-THF), 51.30 (s, 1-N*C*HMe₂), 51.33 (s, 2-N*C*HMe₂), 68.30 (s, α-THF), 70.78 (Kronenether-*C*H₂), 107.30 (s, 7-C), 119.06 (s, 3-C), 125.83 (s, 5-C), 128.33 (s, 4-C/6-C), 129.55 (s, 4-C/6-C), 160.97 (s, 1-C), 163.19 (s, 2-C) ppm.

Elementaranalyse: Ber. (%) für $C_{25}H_{42}KN_3O_8$ (551.72 g/mol): C: 54.43, H: 7.67, N: 7.62, gef.: C: 54.84, H: 7.76, N: 7.85.

4 Synthese monometallischer Silber- und heterobimetallischer Alkalimetall-Argentat-ATI-Komplexe

[Ag(NO₂–ATI$^{iPr/iPr}$)] (**6-NO₂**)

Zu einer Suspension von [Na(NO₂–ATI$^{iPr/iPr}$)(thf)$_{0.06}$(Et₂O)$_{0.06}$] (10 mg, 36 µmol) in Pyridin (1 mL) wurde AgBF₄ (7 mg, 36 µmol) gegeben. Die rote Suspension wurde für 1 h bei Raumtemperatur stehen gelassen und dann mit Et₂O (1 mL) überschichtet. Nach zwei Tagen wurden die ausgefallenen, roten Kristalle durch Filtration isoliert und im Vakuum getrocknet. Ausbeute: 1 mg. Der isolierte Feststoff enthält eine nicht quantifizierte Menge NaBF₄. Die NMR-spektroskopisch untersuchte Charge enthielt *n* = 0.36 Äq. Et₂O.

^{1}H-NMR (400 MHz, Pyridin-*d₅*): δ = 1.12–1.16 (t, *n* × 3H, Et₂O), 1.25 (d, 12H, $^3J_{HH}$ = 6.2 Hz, CH*Me₂*), 3.34–3.39 (q, *n* × 4H, Et₂O), 3.91–4.00 (sept, 4H, $^3J_{HH}$ = 6.2 Hz, C*H*Me₂), 6.03 (d, 2H, $^3J_{HH}$ = 12.9 Hz, 3-H, 7-H), 8.38 (d, 2H, $^3J_{HH}$ = 12.8 Hz, 4-H, 6-H) ppm. ^{13}C-NMR (101 MHz, Pyridin-*d₅*): δ = 15.96 (s, Et₂O), 24.96 (s, CH*Me₂*), 51.02 (s, *C*HMe₂), 66.23 (s, Et₂O), 106.66 (s, 3-C, 7-C), 128.86 (s, 5-C), 129.78 (s, 4-C, 6-C), 162.23 (s, 1-C, 2-C) ppm.

[Na(12-Krone-4)₂][Ag(NO₂–ATI$^{iPr/iPr}$)₂] (**7-NO₂-(12K4)₂**)

Zu einer Lösung von **4-NO₂-(12K4)₂** (10 mg, 15 µmol) in THF (1 mL) wurde AgBF₄ (1.6 mg, 8.0 µmol) gegeben. Die rote Lösung wurden nach 2 h bei Raumtemperatur mit Hexan (2 mL) überschichtet. Nach 1 d wurde die ausgefallenen, roten Kristalle durch Filtration isoliert. Das Filtrat wurde weiter mit Hexan (2 mL) überschichtet und nach 4 d die ausgefallen roten Kristalle durch Filtration isoliert. Beide Chargen an Kristallen wurden vereinigt und aus THF/Et₂O (1:2) umkristallisiert. Ausbeute: 4.2 mg. Die isolierte Verbindung wurde in Pyridin-*d*₅ (0.5 mL) gelöst und mit K[BF(CN)₃] (1.3 mg, 8.57 µmol) versetzt. Mit Hilfe eines quantitativen ^{19}F-NMR Spektrums wurde der Gehalt an [Na(12-Krone-4)₂][BF₄] auf 0.9mol% bestimmt.

^{1}H-NMR (400 MHz, Pyridin-d_5): δ = 0.81 (t, Pentan), 1.26 (d, 24H, $^3J_{\mathrm{HH}}$ = 6.2 Hz, CHMe_2, Signale von Pentan werden überlagert), 3.60 (s, 32H, Kronenether-CH_2), 3.91–4.00 (sept, 4H, $^3J_{\mathrm{HH}}$ = 6.2 Hz, CHMe$_2$), 6.02 (d, 4H, $^3J_{\mathrm{HH}}$ = 12.8 Hz, 3-H, 7-H), 8.42 (d, 4H, $^3J_{\mathrm{HH}}$ = 12.8 Hz, 4-H, 6-H) ppm. ^{13}C-NMR (101 MHz, Pyridin-d_5): δ = 14.61 (s, Pentan), 22.96 (s, Pentan), 24.99 (s, CHMe_2), 51.00 (s, CHMe$_2$), 67.77 (s, Kronenether-CH$_2$), 106.15 (s, 3-C, 7-C), 129.76 (s, 5-C, überlagert durch 4-C, 6-C), 129.76 (s, 4-C, 6-C), 162.19 (s, 1-C, 2-C) ppm.

Elementanalyse: Ber. (%) für $C_{42}H_{68}AgN_6NaO_{12}$ (979.89 g/mol): C: 51.48, H: 7.00, N: 8.58, gef.: C: 51.89, H: 7.02, N: 8.74.

[Na(15-Krone-5)Ag(NO$_2$–ATI$^{i\mathrm{Pr}/i\mathrm{Pr}}$)$_2$] (**7-NO$_2$-(15K5)**)

Zu einer Suspension aus [Na(NO$_2$–ATI$^{i\mathrm{Pr}/i\mathrm{Pr}}$)] (**4-NO$_2$**) (10 mg, 37 µmol) in Pyridin-d_5 (0.5 mL) wurden AgBF$_4$ (7.2 mg, 37 µmol) und [Na(15-Krone-5)(NO$_2$–ATI$^{i\mathrm{Pr}/i\mathrm{Pr}}$)] (**4-NO$_2$-(15K5)**) (18 mg, 37 µmol) gegeben. Die Lösung wurde mit Et$_2$O (0.5 mL) überschichtet. Nach drei Tagen wurden rote Kristalle durch Filtration isoliert und im Vakuum getrocknet. Ausbeute: 15 mg, 16.2 µmol (mit 1 Äq. Pyridin)[d], 87%.

^{1}H-NMR (400 MHz, Pyridin-d_5): δ = 1.26 (d, 24H, $^3J_{\mathrm{HH}}$ = 6.1 Hz, CHMe_2), 3.59 (s, 20H, Kronenether-CH_2), 3.91–4.00 (sept, 4H, $^3J_{\mathrm{HH}}$ = 6.2 Hz, CHMe$_2$), 6.02 (d, 4H, $^3J_{\mathrm{HH}}$ = 12.5 Hz, 3-H, 7-H), 8.41 (d, 4H, $^3J_{\mathrm{HH}}$ = 12.8 Hz, 4-H, 6-H) ppm. ^{13}C-NMR (101 MHz, Pyridin-d_5): δ = 25.00 (s, CHMe_2), 51.02 (s, CHMe$_2$), 69.35 (s, Kronenether-CH$_2$), 106.18 (s, 3-C, 7-C), 129.05 (s, 5-C), 129.75 (s, 4-C, 6-C), 162.18 (s, 1-C, 2-C) ppm.

Elementanalyse: Ber. (%) für $C_{36}H_{56}AgN_6NaO_9{\cdot}C_5H_5N$ (926.84 g/mol): C: 53.13, H: 6.63, N: 10.58, gef.: C: 53.33, H: 6.73, N: 10.75.

5 Synthese Ph$_3$C-substituierter ATI-Komplexe

[Na(12-Krone-4)$_2$][(3-Ph$_3$C–5-NO$_2$–ATI$^{i\mathrm{Pr}/i\mathrm{Pr}}$)] (**4-NO$_2$-Ph$_3$C-(12K4)$_2$**)

Zu einer Lösung von [Na(12-Krone-4)$_2$][(NO$_2$–ATI$^{i\mathrm{Pr}/i\mathrm{Pr}}$)] (**4-NO$_2$-(12K4)$_2$**) (20 mg, 32 µmol) in THF (1 mL) wurde Ph$_3$CCl (9 mg, 32 µmol) und NaH (1 mg, 32 µmol) gegeben. Die Reaktionslösung wurde 48 h bei Raumtemperatur gerührt, filtriert und das Lösungsmittel im Vakuum entfernt. Der orangene Feststoff wurde mit Et$_2$O (3 × 5 mL) gewaschen und im Vakuum getrocknet. Ausbeute: 5 mg, 6 µmol (mit n = 0.38 Äq. Et$_2$O und m = 0.2 Äq. Pentan), 18%.

^{1}H-NMR (400 MHz, THF-d_8): δ = 0.62 (d, 6H, $^3J_{\mathrm{HH}}$ = 5.6 Hz, 2-NCHMe_2), 0.88 (t, m × 6H, Pentan), 1.10 (t, n × 6H, Et$_2$O), 1.12 (d, 6H, $^3J_{\mathrm{HH}}$ = 6.1 Hz, 1-NCHMe_2), 1.32 (m, Pentan), 3.35–3.40 (q, n × 4H, Et$_2$O), 3.58 (s, 32H, Kronenether-CH_2), 3.59–3.68 (m, 1H, 2-NCHMe$_2$, überlagert durch Signal des Kronenether), 3.85–3.94 (sept, 1H, $^3J_{\mathrm{HH}}$ = 6.2 Hz, 1-NCHMe$_2$), 5.81 (d, 1H, $^3J_{\mathrm{HH}}$ = 12.2 Hz, 7-H),

---

[d] Kristallstruktur- und elementaranalytische Daten deuten an, dass 1 Äq. Pyridin enthalten ist. ^{19}F-NMR-spektroskopisch konnten Spuren von [Na(15-Korne-5)][BF$_4$] nachgewiesen werden.

6.94–6.98 (m, 3H, *p*-Ph), 7.03-7.06 (m, 6H, *m*-Ph), 7.22 (d, 1H, $^{4}J_{\mathrm{HH}}$ = 1.6 Hz, 4-H), 7.41-7.43 (m, 6H, *o*-Ph), 7.61 (dd, 1H, $^{3}J_{\mathrm{HH}}$ = 12.1 Hz, $^{4}J_{\mathrm{HH}}$ = 1.5 Hz, 6-H) ppm. ^{13}C-NMR (101 MHz, THF-*d*$_8$): *δ* = 14.16 (s, Pentan), 15.48 (s, Et$_2$O), 23.00 (s, Pentan), 23.37 (s, 2-NCH*Me*$_2$), 24.08 (s, 1-NCH*Me*$_2$), 34.87 (s, Pentan), 50.95 (s, 1-N*C*HMe$_2$), 51.14 (s, 2-N*C*HMe$_2$), 66.13 (s, Et$_2$O), 70.33 (s, Kronenether-*C*H$_2$), 107.79 (s, 7-C), 124.20 (s, 5-C), 125.07 (s, *p*-Ph), 127.06 (s, *m*-Ph), 128.92 (s, 6-C), 130.81 (s, 4-C), 132.46 (s, *o*-Ph), 134.59 (s, 3-C), 136.28 (s, *C*Ph$_3$), 149.64 (s, *ipso*-Ph), 160.38 (s, 1-C), 163.62 (s, 2-C) ppm.

Elementanalyse: Ber. (%) für $C_{48}H_{64}N_3NaO_{10}$ (866.04 g/mol): C: 66.57, H: 7.45, N: 4.85, gef.: C: 66.33, H: 7.64, N: 4.86.

[Na(3,5-bis(Ph$_3$C)–ATI$^{i\mathrm{Pr}/i\mathrm{Pr}}$)] (**4-(Ph$_3$C)$_2$**)

Zu einer Lösung von H–ATI$^{i\mathrm{Pr}/i\mathrm{Pr}}$ (**1**) (30 mg, 147 µmol) in THF (1 mL) wurde Ph$_3$CCl (123 mg, 441 µmol) und NaHMDS (108 mg, 784 µmol) gegeben. Die Reaktionslösung wurde 2 h bei Raumtemperatur gerührt, filtriert und das Lösungsmittel langsam unter Atmosphärendruck auf ein Drittel verringert. Das kristalline Produkt wurde durch Filtration isoliert und im Vakuum getrocknet. Ausbeute: 40 mg, 44 µmol (mit *n* = 2.75 Äq. THF), 30%.

^{1}H-NMR (400 MHz, C$_6$D$_6$): *δ* = 0.06 (d, 3H, $^{3}J_{\mathrm{HH}}$ = 6.0 Hz, CH*Me*), 0.87 (d, 3H, $^{3}J_{\mathrm{HH}}$ = 6.1 Hz, CH*Me*), 1.00 (d, 3H, $^{3}J_{\mathrm{HH}}$ = 6.1 Hz, CH*Me*), 1.12 (d, 3H, $^{3}J_{\mathrm{HH}}$ = 6.3 Hz, CH*Me*), 1.35–1.39 (m, *n* × 4H, β-THF), 3.45–3.48 (m, *n* × 4H, α-THF), 3.57-3.64 (sept, 1H, $^{3}J_{\mathrm{HH}}$ = 6.1 Hz, C*H*Me$_2$), 4.16-4.26 (sept, 1H, $^{3}J_{\mathrm{HH}}$ = 6.2 Hz, C*H*Me$_2$), 5.39 (d, 1H, $^{3}J_{\mathrm{HH}}$ = 10.5 Hz, 7-H), 6.38 (s, 1H, 4-H), 6.88 (dd, 1H, $^{3}J_{\mathrm{HH}}$ = 9.8 Hz, $^{3}J_{\mathrm{HH}}$ = 0.8 Hz, 6-H), 6.96–7.02 (m, 6H, *p*-Ph/*m*-Ph), 7.02–7.06 (m, 6H, *m*-Ph/*p*-Ph), 7.10–7.14 (m, 6H, *m*-Ph/*p*-Ph), 7.58–7.60 (m, 6H, *o*-Ph) ppm.

In THF-*d*$_8$ werden zwei Isomere im Verhältnis 1.0:0.8 detektiert. Alle Signale, die zu den Phenyl-Ringen der CPh$_3$ Substituenten gehören, konnten nicht eindeutig einem der beiden Isomere zugeordnet werden und wurden deshalb für beide Isomere aufgelistet.

Isomer 1: ^{1}H-NMR (500 MHz, THF-*d*$_8$, −40 °C): *δ* = 0.03 (d, 3H, $^{3}J_{\mathrm{HH}}$ = 6.0 Hz, 2-NCH*Me*), 0.37 (d, 3H, $^{3}J_{\mathrm{HH}}$ = 6.1 Hz, 1-NCH*Me*), 0.87 (d, 3H, $^{3}J_{\mathrm{HH}}$ = 6.8 Hz, 2-NCH*Me*), 0.99 (d, 3H, $^{3}J_{\mathrm{HH}}$ = 6.2 Hz, 1-NCH*Me*), 1.77–1.80 (m, *n* × 4H, β-THF), 3.21–3.27 (m, 1H, 1-NC*H*Me$_2$, überlagert durch 1-NC*H*Me$_2$ von Isomer 2), 3.60–3.63 (m, *n* × 4H, α-THF), 3.95-4.00 (sept, 1H, $^{3}J_{\mathrm{HH}}$ = 6.0 Hz, 2-NC*H*Me$_2$), 4.85 (d, 1H, $^{3}J_{\mathrm{HH}}$ = 9.9 Hz, 7-H), 5.85 (s, 1H, 4-H), 6.12 (d, 1H, $^{3}J_{\mathrm{HH}}$ = 9.8 Hz, 6-H), 6.47 (d, 2H, $^{3}J_{\mathrm{HH}}$ = 7.7 Hz, *o*-Ph), 6.79 (m, 2H, *m*-Ph), 6.87–90 (m, 1H, *p*-Ph), 6.96–7.17 (m, 23H, *m*-Ph/*p*-Ph/*o*-Ph, überlagert durch Ph-Signale von Isomer 2), 7.67 (br. D, 2H, *o*-Ph) ppm. ^{13}C-NMR (125 MHz, THF-*d*$_8$; −40 °C): *δ* = 21.53 (s, 2-NCH*Me*), 23.39 (s, 1-NCH*Me*), 25.21 (s, 1-NCH*Me*, überlagert durch Signal von THF-*d*$_8$), 25.72 (s, 2-NCH*Me*), 26.19 (s, β-THF), 49.17 (s, 1-N*C*HMe$_2$), 50.31 (s, 2-N*C*HMe$_2$), 68.03 (s, α-THF), 66.25 (s, C$_\mathrm{q}$), 67.25 (s, C$_\mathrm{q}$, überlagert durch Signal von THF-*d*$_8$), 92.08 (s, 7-C), 114.65 (s, 3-C), 117.81 (s, 5-C), 125.10 (s, Ph), 125.46 (s, *p*-Ph), 125.90 (s, Ph), 126.01 (s, Ph), 126.08 (s, Ph), 126.41 (s, Ph), 126.55 (s, Ph), 126.80 (s, *m*-Ph), 126.80 (s, Ph), 127.17 (s, Ph), 127.47 (s, Ph), 127.87 (s, Ph), 131.52 (s, *o*-Ph, Ph), 131.77 (s, Ph), 132.04 (s, Ph), 132.58 (s, Ph), 133.85 (s, *o*-Ph), 135.65 (s, 6-C), 137.46 (s, 4-C), 146.97 (s, C_q), 147.17 (s, C_q), 148.63 (s, C_q), 150.74 (s, C_q), 152.31 (s, *ipso*-Ph), 159.90 (s, 1-C), 175.51 (s, 2-C) ppm.

Isomer 2: ^{1}H-NMR (500 MHz, THF-d_8, −40 °C): δ = 0.80 (d, 3H, $^3J_{HH}$ = 6.1 Hz, 1-NCH*Me*), 0.90 (d, 3H, $^3J_{HH}$ = 5.1 Hz, 1-NCH*Me*), 0.92 (d, 3H, $^3J_{HH}$ = 6.3 Hz, 2-NCH*Me*), 1.07 (d, 3H, $^3J_{HH}$ = 6.1 Hz, 2-NCH*Me*), 1.77−1.80 (m, *n* × 4H, β-THF), 3.25−3.31 (m, 1H, 1-NC*H*Me_2, überlagert durch 1-NC*H*Me_2 von Isomer 1), 3.60−3.63 (m, *n* × 4H, α-THF), 3.82-3.87 (sept, 1H, $^3J_{HH}$ = 6.1 Hz, 2-NC*H*Me_2), 5.09 (d, 1H, $^3J_{HH}$ = 7.7 Hz, 7-H), 5.65 (s, 1H, 4-H), 6.41 (d, 1H, $^3J_{HH}$ = 7.5 Hz, 6-H), 6.96−7.17 (m, 23H, *m*-Ph/*p*-Ph/*o*-Ph, überlagert durch Ph-Signale von Isomer 1) ppm. ^{13}C-NMR (125 MHz, THF-d_8, −40 °C): δ = 20.47 (s, 1-NCH*Me*), 22.46 (s, 1-NCH*Me*), 22.68 (s, 2-NCH*Me*), 24.38 (s, 2-NCH*Me*), 26.19 (s, β-THF), 44.03 (s, 1-N*C*HMe_2), 52.54 (s, 2-N*C*HMe_2), 68.03 (s, α-THF), 65.90 (s, C_q), 65.93 (s, C_q), 94.20 (s, 7-C), 125.10 (s, Ph), 125.90 (s, Ph), 126.01 (s, Ph), 126.08 (s, Ph), 126.41 (s, Ph), 126.55 (s, Ph), 126.80 (s, Ph), 127.17 (s, Ph), 127.47 (s, Ph), 127.87 (s, Ph), 128.90 (s, 6-C), 131.52 (s, Ph), 131.77 (s, Ph), 132.04 (s, Ph), 132.58 (s, Ph), 133.85 (s, 3-C), 136.69 (s, 4-C), 137.49 (s, 5-C), 139.06 (s, C_q), 146.97 (s, C_q), 147.17 (s, C_q), 148.63 (s, C_q), 150.74 (s, C_q), 162.33 (s, 2-C) ppm.

Elementanalyse: Ber. (%) für $C_{51}H_{47}N_2Na{\cdot}(C_4H_8O)_2$ (855.15 g/mol): C: 82.87, H: 7.43, N: 3.28, gef.: C: 82.53, H: 7.57, N: 3.19.

[Na(Ph$_3$C−ATI$^{iPr/iPr}$)] (**4-Ph$_3$C**)

Zu einer Lösung von H−ATI$^{iPr/iPr}$ (**1**) (30 mg, 147 µmol) in THF (1 mL) wurde Ph_3CCl (41 mg, 147 µmol) und NaHMDS (54 mg, 294 µmol) gegeben. Die Reaktionslösung wurde 2 h bei Raumtemperatur gerührt, filtriert und das Lösungsmittel im Vakuum entfernt. Das Rohprodukt wurde aus THF/*n*-Pentan (1:2, 4 mL) bei −30 °C umkristallisiert. Ausbeute: 61 mg, 107 µmol (mit *n* = 2 Äq. THF), 73%.

^{1}H-NMR (400 MHz, THF-d_8): δ = 1.08 (d, 12H, $^3J_{HH}$ = 6.2 Hz, CH*Me$_2$*), 1.72−1.79 (m, *n* × 4H, β-THF), 3.60−3.64 (m, *n* × 4H, α-THF), 3.64-3.71 (sept, 2H, $^3J_{HH}$ = 6.2 Hz, C*H*Me_2), 5.69 (d, 2H, $^3J_{HH}$ = 12.2 Hz, 3-H, 7-H), 6.33 (d, 2H, $^3J_{HH}$ = 12.2 Hz, 4-H, 6-H), 7.01−7.05 (m, 3H, *p*-Ph), 7.11−7.15 (m, 6H, *m*-Ph), 7.27-7.29 (m, 6H, *o*-Ph) ppm. ^{13}C-NMR (101 MHz, THF-d_8): δ = 24.49 (s, CH*Me$_2$*), 26.19 (s, β-THF), 48.64 (s, *C*HMe_2), 68.02 (s, α-THF), 104.40 (s, 3-C, 7-C), 123.01 (s, 5-C), 125.38 (s, *p*-Ph), 127.37 (s, *m*-Ph), 132.02 (s, *o*-Ph), 135.66 (s, 4-C, 6-C), 149.85 (s, *ipso*-Ph), 161.99 (s, 1-C, 2-C) ppm.

Elementanalyse: Ber. (%) für $C_{32}H_{33}N_2Na{\cdot}(C_4H_8O)_2$ (612.83 g/mol): C: 78.40, H: 8.06, N: 4.57, gef.: C: 78.42, H: 7.97, N: 4.71.

6 Synthese von Bismut-ATI-Komplexen

$[\mathrm{Bi(ATI}^{i\mathrm{Pr}/i\mathrm{Pr}})_2\mathrm{Cl}]$ (**8**)

H–ATI$^{i\mathrm{Pr}/i\mathrm{Pr}}$ (**1**) (200 mg, 979 µmol) wurde in THF (2 mL) gelöst und mit NaHMDS (179 mg, 979 µmol) versetzt. Zur orangen Lösung wurde eine Lösung von $\mathrm{BiCl_3}$ (155 mg, 490 µmol) in THF (1 mL) getropft. Die rote Suspension wurde filtriert und das Lösungsmittel des Filtrats im Vakuum entfernt. Der orange Feststoff wurde mit Pentan (3 × 3 mL) gewaschen und im Vakuum getrocknet.

Ausbeute: 116 mg (die isolierte Verbindung enthält 6% $[\mathrm{Bi(ATI}^{i\mathrm{Pr}/i\mathrm{Pr}})\mathrm{Cl_2}]$ (**9**) und 16% H–ATI$^{i\mathrm{Pr}/i\mathrm{Pr}}$ (**1**) sowie n = 0.2 Äq. THF)

^{1}H-NMR (400 MHz, Pyridin-d_5): δ = 1.52 (d, 24H, $^3J_{\mathrm{HH}}$ = 6.7 Hz, CHMe_2), 1.82-1.85 (m, n × 4 H, α-THF), 3.65-3.68 (m, n × 4 H, β-THF), 4.89–4.99 (sept, 4H, $^3J_{\mathrm{HH}}$ = 6.7 Hz, C$H_{i\mathrm{Pr}}$), 6.47 (dd, 2H, $^3J_{\mathrm{HH}}$ = 9.8 Hz, $^3J_{\mathrm{HH}}$ = 8.3 Hz, 5-H), 6.73 (d, 4H, $^3J_{\mathrm{HH}}$ = 11.5 Hz, 3-H, 7-H), 7.28 (dd, 4H, $^3J_{\mathrm{HH}}$ = 11.7 Hz, $^3J_{\mathrm{HH}}$ = 9.1 Hz, 4-H, 6-H) ppm. ^{13}C-NMR (101 MHz, Pyridin-d_5): δ = 22.87 (s, CHMe_2), 52.84 (s, CHMe$_2$), 118.30 (s, 3-C, 7-C), 120.15 (s, 5-C), 134.20 (s, 4-C, 6-C), 167.33 (s, 1-C, 2-C) ppm.

$[\mathrm{Bi(ATI}^{i\mathrm{Pr}/i\mathrm{Pr}})\mathrm{Cl_2}]$ (**9**)

H–ATI$^{i\mathrm{Pr}/i\mathrm{Pr}}$ (**1**) (200 mg, 979 µmol) wurde in THF (2 mL) gelöst und mit NaHMDS (179 mg, 979 µmol) versetzt. Zur orangen Lösung wurde eine Lösung von $\mathrm{BiCl_3}$ (309 mg, 979 µmol) in THF (1 mL) getropft. Das Lösungsmittel wurde im Vakuum entfernt. Der orange Feststoff wurde mit Pentan (3 × 3 mL) gewaschen und im Vakuum getrocknet. Ausbeute: 392 mg (die isolierte Verbindung enthält 12% H–ATI$^{i\mathrm{Pr}/i\mathrm{Pr}}$ (**1**) + 1 Äq. NaCl)

^{1}H-NMR (400 MHz, Pyridin-d_5): δ = 1.82 (d, 12H, $^3J_{\mathrm{HH}}$ = 6.4 Hz, CHMe_2), 1.82 (m, n × 4 H, α-THF, überlagert durch Signale von CHMe_2), 5.42–5.51 (sept, 4H, $^3J_{\mathrm{HH}}$ = 6.4 Hz, CHMe$_2$), 3.79–3.82 (m, n × 4 H, β-THF), 6.64 (dd, 1H, $^3J_{\mathrm{HH}}$ = 10.3 Hz, $^3J_{\mathrm{HH}}$ = 8.1 Hz, 5-H), 6.83–6.88 (d, 2H, $^3J_{\mathrm{HH}}$ = 11.5 Hz, 3-H, 7-H), 7.52 (dd, 2H, $^3J_{\mathrm{HH}}$ = 11.4 Hz, $^3J_{\mathrm{HH}}$ = 9.5 Hz, 4-H, 6-H) ppm.

$[\mathrm{Bi(Ph(O)S{-}ATI}^{i\mathrm{Pr}/i\mathrm{Pr}})_2\mathrm{Cl}]$ (**8-Ph(O)S**)

Zu einer Lösung von $\mathrm{BiCl_3}$ (13.3 mg, 0.042 mmol) in THF (2 mL) wurde langsam eine Lösung von $[\mathrm{Na(Ph(O)S{-}ATI}^{i\mathrm{Pr}/i\mathrm{Pr}})]$ (**4-Ph(O)S**) (29.6 mg, 0.084 mmol) in THF (1 mL) getropft. Nach einer Reaktionszeit von 5 Minuten wurde der ausgefallene Feststoff abfiltriert und das Filtrat wurde mit n-Hexan (0.5 mL) überschichtet. Nach 4 Tagen wurde das Produkt durch Filtration isoliert und nach Trocknung im Vakuum als roter Feststoff erhalten. Ausbeute: 23 mg, 0.026 mmol, 59% eines roten Feststoffs.

^{1}H-NMR (500 MHz, Pyridin-d_5): δ = 1.41 (br. s, 24H, CHMe_2), 4.86–4.90 (br. sept, 4H, CHMe$_2$), 6.69 (d, 4H, $^3J_{\mathrm{HH}}$ = 11.9 Hz, 3-H, 7-H), 7.35–7.39 (m, 2H, p-Ph), 7.44–7.47 (m, 4H, m-Ph), 7.75 (d, $^3J_{\mathrm{HH}}$ = 12.2 Hz, 2H, 4-H, 6-H), 7.91–7.93 (m, 4H, o-Ph) ppm. ^{13}C-NMR (125 MHz, Pyridin-d_5):

δ = 22.68 (s, CH*Me₂*), 22.81 (s, CH*Me₂*), 53.41 (s, *C*HMe₂), 116.77 (s, 3-C, 7-C), 125.20 (s, *o*-Ph), 130.07 (s, *m*-Ph), 131.20 (s, *p*-Ph), 131.28 (s, 4-C, 6-C), 133.79 (s, 5-C), 148.37 (s, *ipso*-Ph), 167.42 (s, 1-C, 2-C) ppm.

Elementaranalyse: Ber. (%) für $C_{38}H_{46}BiClN_4O_2S_2$ (899.36 g/mol): C 50.75, H 5.16, N 6.23, S 7.13; gef.: C 50.38, H 5.19, N 6.09, S 7.04.

$[Bi(Ph(O)S–ATI^{iPr/iPr})Cl_2]$ (**9-Ph(O)S**)

Zu einer Lösung von $BiCl_3$ (27 mg, 85.6 µmol) in THF (2 mL) wurde langsam eine Lösung von $[Na(Ph(O)S–ATI^{iPr/iPr})]$ (**4-Ph(O)S**) (30 mg, 85.6 µmol) in THF (1 mL) getropft. Nach 5 Minuten wurde die rote Suspension filtriert und das Lösungsmittel im Vakuum entfernt. Durch Diffusion von Et_2O (3 mL) in eine Lösung des Rohprodukts in Pyridin (3 mL) wurden Kristalle erhalten.

Ausbeute: 32 mg, 46.6 µmol (mit 1 Äq. Pyridin), 54% oranger Nadeln.

^{1}H-NMR (400 MHz, Pyridine-*d₅*): *δ* = 1.61–1.64 (m, *n* × 4H, β-THF) 1.76–1.79 (überlagertes d, 12H, CH*Me₂*), 3.65–3.68 (m, *n* × 4H, α-THF), 5.36–5.42 (sept, 2H, $^3J_{HH}$ = 6.5 Hz, C*H*Me₂), 6.85 (d, 2H, $^3J_{HH}$ = 12.0 Hz, 3-H, 7-H), 7.43–7.46 (m, 1H, *p*-Ph), 7.50–7.58 (m, 2H, *m*-Ph), 7.92–7.97 (m, 4H, 4-H, 6-H, *o*-Ph) ppm. ^{13}C-NMR (101 MHz, Pyridine-*d₅*): *δ* = 23.92 (s, CH*Me₂*), 23.98 (s, CH*Me₂*), 26.26 (s, β-THF), 53.34 (s, *C*HMe₂), 68.29 (s, α-THF), 120.78 (s, 3-C, 7-C), 125.30 (s, *o*-Ph), 130.34 (s, *m*-Ph), 131.73 (s, *p*-Ph), 131.90 (s, 4-C, 6-C), 139.15 (s, 5-C), 148.03 (s, *ipso*-Ph), 171.58 (s, 1-C, 2-C) ppm.

Elementaranalyse: Ber. (%) für $C_{19}H_{23}BiCl_2N_2OS \cdot C_5H_5N$ (684.43 g/mol): C 41.99, H 4.11, N 6.12, S 4.67; gef.: C 41.88, H 4.19, N 5.85, S 4.48.

Der Anteil an neutralen Donorliganden (THF, Pyridin) muss für jede Charge separat bestimmt werden.

$[Bi(Ph(O)S–ATI^{iPr/iPr})_2I]$

Eine Lösung von $[K(Ph(O)S–ATI^{iPr/iPr})]$ (**5-Ph(O)S**) (30 mg, 81.8 µmol) in THF (2 mL) wurde unter Rühren zu einer Lösung von BiI_3 (24.1 mg, 40.9 µmol) in THF (2 mL) getropft. Die Suspension wurde filtriert und mit Pentan (6 mL) versetzt. Der ausgefallene Feststoff wurde durch Filtration isoliert und im Vakuum getrocknet. Das Rohprodukt wurde mit Et_2O (2 × 2 mL) gewaschen und im Vakuum getrocknet. Ausbeute: n.b. (die isolierte Verbindung enthält 23% $[Bi(Ph(O)S–ATI^{iPr/iPr})I_2]$ (**11-Ph(O)S**) und 31% $Ph(O)S–ATI^{iPr/iPr}$ (**1-Ph(O)S**)

^{1}H-NMR (400 MHz, Pyridin-*d₅*): *δ* = 1.41–1.43 (br. m, 24H, CH*Me₂*), 4.80–4.83 (sept, 4H, $^3J_{HH}$ = 6.7 Hz, C*H*Me₂), 6.75 (d, 4H, $^3J_{HH}$ = 12.1 Hz, 3-H, 7-H), 7.33–7.38 (m, 2H, *p*-Ph), 7.43–7.46 (m, 4H, *m*-Ph), 7.77 (d, 4H, $^3J_{HH}$ = 12.0 Hz, 4-H, 6-H), 7.91 (d, 4H, $^3J_{HH}$ = 12.1 Hz, *o*-Ph) ppm.

$[Bi(Ph(O)S–ATI^{iPr/iPr})I_2]$ (**11-Ph(O)S**)

Eine Lösung von $[K(Ph(O)S–ATI^{iPr/iPr})]$ (**5-Ph(O)S**) (20 mg, 54.6 µmol) in THF (2 mL) wurde unter Rühren zu einer Lösung von BiI_3 (32.3 mg, 54.6 µmol) in THF (2 mL) getropft. Die dunkelrote

Suspension wurde filtriert und das Lösungsmittel im Vakuum entfernt. Das Rohprodukt wurde mit Et_2O und Pentan (je 2 × 2 mL) gewaschen und im Vakuum getrocknet. Ausbeute: 28 mg, 34 µmol (mit $n = 0.45$ Äq. THF), 62% eines dunkelvioletten Feststoffes.

^{1}H-NMR (500 MHz, Pyridin-d_5): $\delta = 1.61–1.64$ (m, $n \times 4$H, β-THF), 1.71 (d, 6H, $^3J_{HH} = 5.4$ Hz, CH*Me₂*), 1.73, (d, 6H, $^3J_{HH} = 5.4$ Hz, CH*Me₂*), 3.65–3.68 (m, $n \times 4$H, α-THF), 5.12–5.18 (sept, 2H $^3J_{HH} = 6.5$ Hz, C*H*Me$_2$), 6.95 (d, 2H, $^3J_{HH} = 12.3$ Hz, 3-H, 7-H), 7.41–7.48 (m, 1H, *p*-Ph), 7.50–7.51 (m, 2H, *m*-Ph), 7.92–7.95 (m, 4H, 4-H, 6-H, *o*-Ph) ppm. ^{13}C-NMR (126 MHz, Pyridine-d_5): $\delta = 24.03$ (s, CH*Me₂*), 24.05 (s, CH*Me₂*), 26.26 (s, β-THF), 54.27 (s, *C*HMe$_2$), 68.29 (s, α-THF), 122.19 (s, 3-C, 7-C), 125.30 (s, *o*-Ph), 130.35 (s, *m*-Ph), 131.80 (s, *p*-Ph), 131.98 (s, 4-C, 6-C), 139.55 (s, 5-C), 147.64 (s, *ipso*-Ph), 172.21 (s, 1-C, 2-C) ppm.

Elementaranalyse: Ber. (%) für $C_{19}H_{23}BiI_2N_2OS$ C_5H_5N (869.36 g/mol): C 33.16, H 3.25, N 4.83, S 3.69; gef.: C 33.36, H 3.39, N 4.77, S 3.64.

Der Anteil an neutralen Donorliganden in der isolierten Verbindung muss für jede Charge bestimmt werden.

[Bi(NO$_2$–ATI$^{iPr/iPr}$)Cl$_2$] (**9-NO₂**)

Zu einer Suspension von [Na(NO$_2$–ATI$^{iPr/iPr}$)(py)] (**4-NO₂-py**) (25.0 mg, 92.2 µmol) in THF (1 mL) wurde eine Lösung von $BiCl_3$ (29.1 mg, 92.2 µmol) in THF (1 mL) langsam zugetropft. Der Feststoff wurde abfiltriert, und die Lösung wurde mit *n*-Pentan überschichtet und für 4 d stehen gelassen. Das Produkt wurde durch Filtration isoliert, mit Et_2O (3 × 3 mL) gewaschen und im Vakuum getrocknet.

Ausbeute: 18.8 mg, 35.7 µmol, 39% eines dunkelroten, kristallinen Feststoffs.

^{1}H-NMR (400 MHz, Pyridin-d_5): $\delta = 1.80$ (d, 12H, $^3J_{HH} = 6.5$ Hz, CH*Me₂*), 5.44–5.52 (sept, 2H, $^3J_{HH} = 6.1$ Hz, C*H*Me$_2$), 6.72 (d, 2H, $^3J_{HH} = 12.3$ Hz, 3-H, 7-H), 8.51 (d, 2H, $^3J_{HH} = 12.2$ Hz, 4-H, 6-H) ppm. ^{13}C-NMR (101 MHz, Pyridin-d_5): $\delta = 23.78$ (s, CH*Me₂*), 53.96 (s, *C*HMe$_2$), 117.50 (s, 3-C, 7-C), 130.55 (s, 4-C, 6-C), 141.13 (s, 5-C), 172.10 (s, 1-C, 2-C) ppm.

Elementaranalyse: Ber. (%) für $C_{13}H_{18}BiCl_2N_3O_2$ (528.19 g/mol): C: 29.56, H: 3.44, N: 7.96, gef. C: 29.69, H: 3.62, N: 7.83.

XX Verbindungsverzeichnis

1	H–ATI$^{i\mathrm{Pr}/i\mathrm{Pr}}$
1-Br	Br–ATI$^{i\mathrm{Pr}/i\mathrm{Pr}}$
1-PhS	PhS–ATI$^{i\mathrm{Pr}/i\mathrm{Pr}}$
1-Ph(O)S	Ph(O)S–ATI$^{i\mathrm{Pr}/i\mathrm{Pr}}$
1-NO$_2$	NO$_2$–ATI$^{i\mathrm{Pr}/i\mathrm{Pr}}$
2	3,4-Bis(*iso*propylamino)benzaldehyd
3	[Li(ATI$^{i\mathrm{Pr}/i\mathrm{Pr}}$)]
3-(thf)$_2$	[Li(ATI$^{i\mathrm{Pr}/i\mathrm{Pr}}$)(thf)$_2$]
[4-thf]$_\infty$	[Na(ATI$^{i\mathrm{Pr}/i\mathrm{Pr}}$)(thf)]$_\infty$
4-(12K4)$_2$	[Na(12-Krone-4)$_2$][Na(ATI$^{i\mathrm{Pr}/i\mathrm{Pr}}$)$_2$]
4-Ph$_3$C	[Na(Ph$_3$C–ATI$^{i\mathrm{Pr}/i\mathrm{Pr}}$)]
4-Ph$_3$C-(thf)$_2$	[Na(Ph$_3$C–ATI$^{i\mathrm{Pr}/i\mathrm{Pr}}$)(thf)$_2$]
4-(Ph$_3$C)$_2$	[Na(3,5-bis(Ph$_3$C)–ATI$^{i\mathrm{Pr}/i\mathrm{Pr}}$)]
4-(Ph$_3$C)$_2$-(thf)$_2$	[Na(3,5-bis(Ph$_3$C)–ATI$^{i\mathrm{Pr}/i\mathrm{Pr}}$)(thf)$_2$]
[5-thf]$_\infty$	[K(ATI$^{i\mathrm{Pr}/i\mathrm{Pr}}$)(thf)]$_\infty$
3-Ph(O)S	[Li(Ph(O)S–ATI$^{i\mathrm{Pr}/i\mathrm{Pr}}$)]
[3-Ph(O)S-py]$_\infty$	[Li(Ph(O)S–ATI$^{i\mathrm{Pr}/i\mathrm{Pr}}$)(py)]$_\infty$
4-Ph(O)S	[Na(Ph(O)S–ATI$^{i\mathrm{Pr}/i\mathrm{Pr}}$)]
5-Ph(O)S	[K(Ph(O)S–ATI$^{i\mathrm{Pr}/i\mathrm{Pr}}$)]
[5-Ph(O)S-(thf)$_3$]$_\infty$	[K(Ph(O)S–ATI$^{i\mathrm{Pr}/i\mathrm{Pr}}$)(thf)$_3$]$_\infty$
6-Ph(O)S	[Na(12-Krone-4)$_2$][Na(Ph(O)S–ATI$^{i\mathrm{Pr}/i\mathrm{Pr}}$)$_2$]
5-red	reduzierte Spezies von [K(Ph(O)S–ATI$^{i\mathrm{Pr}/i\mathrm{Pr}}$)]
[3-Ph(O)C-py]$_\infty$	[Li(Ph(O)C–ATI$^{i\mathrm{Pr}/i\mathrm{Pr}}$)(py)]$_\infty$
4-Ph(O)C	[Na(Ph(O)C–ATI$^{i\mathrm{Pr}/i\mathrm{Pr}}$)]
[4-Ph(O)C-py]$_\infty$	[Na(Ph(O)C–ATI$^{i\mathrm{Pr}/i\mathrm{Pr}}$)(py)]$_\infty$
4-Ph(O)C-Ph$_3$C	[Na(3-Ph$_3$C–5-Ph(O)C–ATI$^{i\mathrm{Pr}/i\mathrm{Pr}}$)]
[4-Ph(O)C-Ph$_3$C-(thf)$_2$]$_2$	[Na(3-Ph$_3$C–5-Ph(O)C–ATI$^{i\mathrm{Pr}/i\mathrm{Pr}}$)(thf)$_2$]$_2$
[5-Ph(O)C-py]$_\infty$	[K(Ph(O)C–ATI$^{i\mathrm{Pr}/i\mathrm{Pr}}$)(py)]$_\infty$
3-NO$_2$	[Li(NO$_2$–ATI$^{i\mathrm{Pr}/i\mathrm{Pr}}$)]
[3-NO$_2$-py]$_\infty$	[Li(NO$_2$–ATI$^{i\mathrm{Pr}/i\mathrm{Pr}}$)(py)]$_\infty$
4-NO$_2$	[Na(NO$_2$–ATI$^{i\mathrm{Pr}/i\mathrm{Pr}}$)]
[4-NO$_2$-py]$_\infty$	[Na(NO$_2$–ATI$^{i\mathrm{Pr}/i\mathrm{Pr}}$)(py)]$_\infty$
4-NO$_2$-(12K4)$_2$	[Na(12-Krone-4)$_2$][(NO$_2$–ATI$^{i\mathrm{Pr}/i\mathrm{Pr}}$)]
4-NO$_2$-Ph$_3$C-(12K4)$_2$	[Na(12-Krone-4)$_2$(3-Ph$_3$C–5-NO$_2$–ATI$^{i\mathrm{Pr}/i\mathrm{Pr}}$)]
4-NO$_2$-(15K5)	[Na(15-Krone-5)(NO$_2$–ATI$^{i\mathrm{Pr}/i\mathrm{Pr}}$)]

5-NO$_2$	[K(NO$_2$–ATI$^{i\mathrm{Pr}/i\mathrm{Pr}}$)]
[5-NO$_2$-py]$_\infty$	[K(NO$_2$–ATI$^{i\mathrm{Pr}/i\mathrm{Pr}}$)(py)]$_\infty$
5-NO$_2$-(18K6)	[K(18-Krone-6)(NO$_2$–ATI$^{i\mathrm{Pr}/i\mathrm{Pr}}$)]
6-NO$_2$	[Ag(NO$_2$–ATI$^{i\mathrm{Pr}/i\mathrm{Pr}}$)]
6-NO$_2$-py	[Ag(NO$_2$–ATI$^{i\mathrm{Pr}/i\mathrm{Pr}}$)(py)]
7-NO$_2$-(12K4)$_2$	[Na(12-Krone-4)$_2$][Ag(NO$_2$–ATI$^{i\mathrm{Pr}/i\mathrm{Pr}}$)$_2$]
7-NO$_2$-(15K5)	[Na(15-Krone-5)Ag(NO$_2$–ATI$^{i\mathrm{Pr}/i\mathrm{Pr}}$)$_2$]
8	[Bi(ATI$^{i\mathrm{Pr}/i\mathrm{Pr}}$)$_2$Cl]
8$_\infty$	[Bi(ATI$^{i\mathrm{Pr}/i\mathrm{Pr}}$)$_2$Cl]$_\infty$
9	[Bi(ATI$^{i\mathrm{Pr}/i\mathrm{Pr}}$)Cl$_2$]
9$_\infty$	[Bi(ATI$^{i\mathrm{Pr}/i\mathrm{Pr}}$)$_2$Cl]$_\infty$
10	[Bi(ATI$^{i\mathrm{Pr}/i\mathrm{Pr}}$)$_3$]
8-Ph(O)S	[Bi(Ph(O)S–ATI$^{i\mathrm{Pr}/i\mathrm{Pr}}$)$_2$Cl]
9-Ph(O)S	[Bi(Ph(O)S–ATI$^{i\mathrm{Pr}/i\mathrm{Pr}}$)Cl$_2$]
[9-Ph(O)S]$_\infty$	[Bi(Ph(O)S–ATI$^{i\mathrm{Pr}/i\mathrm{Pr}}$)Cl$_2$]$_\infty$
11-Ph(O)S	[Bi(Ph(O)S–ATI$^{i\mathrm{Pr}/i\mathrm{Pr}}$)I$_2$]
[11-Ph(O)S]$_\infty$	[Bi(Ph(O)S–ATI$^{i\mathrm{Pr}/i\mathrm{Pr}}$)I$_2$]$_\infty$
8-NO$_2$	[Bi(NO$_2$–ATI$^{i\mathrm{Pr}/i\mathrm{Pr}}$)$_2$Cl]
9-NO$_2$	[Bi(NO$_2$–ATI$^{i\mathrm{Pr}/i\mathrm{Pr}}$)Cl$_2$]
12	H–ATI$^{\mathrm{Ph}/i\mathrm{Pr}}$
Li-12	[Li(ATI$^{\mathrm{Ph}/i\mathrm{Pr}}$)]
[Na-12-thf]$_\infty$	[Na(ATI$^{\mathrm{Ph}/i\mathrm{Pr}}$)(thf)]$_\infty$
Na(12K4)$_2$-12	[Na(12-Krone-4)$_2$][Na(ATI$^{\mathrm{Ph}/i\mathrm{Pr}}$)$_2$]
Bi-12	[Bi(ATI$^{\mathrm{Ph}/i\mathrm{Pr}}$)$_3$]
13	H–ATI$^{\mathrm{Ph}/\mathrm{Ph}}$
Li-13-(Et$_2$O)$_2$	[Li(ATI$^{\mathrm{Ph}/\mathrm{Ph}}$)(Et$_2$O)$_2$]
Na-13-(Et$_2$O)$_2$	[Na(ATI$^{\mathrm{Ph}/\mathrm{Ph}}$)(Et$_2$O)$_2$]
14	AT$^{\mathrm{Fc}}$
15	H–ATI$^{\mathrm{Fc}/i\mathrm{Pr}}$
Bi-15	[Bi(ATI$^{\mathrm{Fc}/i\mathrm{Pr}}$)$_3$]
BiCl-15	[Bi(ATI$^{\mathrm{Fc}/i\mathrm{Pr}}$)$_2$Cl]
BiCl$_2$-15	[Bi(ATI$^{\mathrm{Fc}/i\mathrm{Pr}}$)Cl$_2$]
[BiCl$_2$-15]$_\infty$	[Bi(ATI$^{\mathrm{Fc}/i\mathrm{Pr}}$)Cl$_2$]$_\infty$
16	H–ATI$^{\mathrm{PhSMe}/i\mathrm{Pr}}$
Na-SAI$^{i\mathrm{Pr}}$	[Na(SAI$^{i\mathrm{Pr}}$)]
K(18K6)-SAI$^{i\mathrm{Pr}}$	[K(18-Krone-6)(SAI$^{i\mathrm{Pr}}$)]
Li$_3$Na-SAI$^{i\mathrm{Pr}}$-(thf)$_2$	[Li$_3$Na(SAI)$_4$(thf)$_2$]

XXI Literaturverzeichnis

[1] a) M. D. Ward, J. A. McCleverty, *J. Chem. Soc., Dalton Trans.* **2002**, 10.1039/B110131P, 275-288; b) W. Kaim, B. Schwederski, *Coord. Chem. Rev.* **2010**, *254*, 1580-1588; c) W. Kaim, *Inorg. Chem.* **2011**, *50*, 9752-9765; d) W. Kaim, *Eur. J. Inorg. Chem.* **2012**, *2012*, 343-348; e) P. J. Chirik, K. Wieghardt, *Science* **2010**, *327*, 794-795; f) P. J. Chirik, *Inorg. Chem.* **2011**, *50*, 9737-9740; g) A. M. Allgeier, C. A. Mirkin, *Angew. Chem. Int. Ed.* **1998**, *37*, 894-908.

[2] a) H. B. Gray, R. Williams, I. Bernal, E. Billig, *J. Am. Chem. Soc.* **1962**, *84*, 3596-3597; b) A. Davison, N. Edelstein, R. H. Holm, A. H. Maki, *J. Am. Chem. Soc.* **1963**, *85*, 2029-2030.

[3] C. K. Joergensen, *Coord. Chem. Rev.* **1966**, *1*, 164-178.

[4] C. K. Joergensen, *Struct. Bonding (Berlin)* **1966**, *1*, 234-248.

[5] J. A. McCleverty, *Chem. Rev.* **2004**, *104*, 403-418.

[6] J. H. Enemark, R. D. Feltham, *Coord. Chem. Rev.* **1974**, *13*, 339-406.

[7] T. Ampßler, G. Monsch, J. Popp, T. Riggenmann, P. Salvador, D. Schröder, P. Klüfers, *Angew. Chem. Int. Ed.* **2020**, *59*, 12381-12386.

[8] P. Chaudhuri, C. N. Verani, E. Bill, E. Bothe, T. Weyhermueller, K. Wieghardt, *J. Am. Chem. Soc.* **2001**, *123*, 2213-2223.

[9] a) C. C. Scarborough, K. Wieghardt, *Inorg. Chem.* **2011**, *50*, 9773-9793; b) S. Sproules, K. Wieghardt, *Coord. Chem. Rev.* **2011**, *255*, 837-860; c) D. Zhu, I. Thapa, I. Korobkov, S. Gambarotta, P. H. M. Budzelaar, *Inorg. Chem.* **2011**, *50*, 9879-9887; d) K. G. Caulton, *Eur. J. Inorg. Chem.* **2012**, *2012*, 435-443; e) M. M. Khusniyarov, T. Weyhermueller, E. Bill, K. Wieghardt, *J. Am. Chem. Soc.* **2009**, *131*, 1208-1221; f) W. Kaim, *Dalton Trans.* **2019**, *48*, 8521-8529.

[10] a) M. A. Bigi, S. A. Reed, M. C. White, *Nat. Chem.* **2011**, *3*, 216-222; b) W. I. Dzik, J. I. van der Vlugt, J. N. H. Reek, B. de Bruin, *Angew. Chem. Int. Ed.* **2011**, *50*, 3356-3358; c) P. Verma, J. Weir, L. Mirica, T. D. P. Stack, *Inorg. Chem.* **2011**, *50*, 9816-9825; d) V. Lyaskovskyy, B. de Bruin, *ACS Catalysis* **2012**, *2*, 270-279; e) O. R. Luca, R. H. Crabtree, *Chem. Soc. Rev.* **2013**, *42*, 1440-1459; f) V. K. K. Praneeth, M. R. Ringenberg, T. R. Ward, *Angew. Chem. Int. Ed. Engl.* **2012**, *51*, 10228-10234; g) D. L. J. Broere, R. Plessius, J. I. van der Vlugt, *Chem. Soc. Rev.* **2015**, *44*, 6886-6915; h) J. I. van der Vlugt, *Chem. Eur. J.* **2019**, *25*, 2651-2662.

[11] a) P. Chaudhuri, K. Wieghardt, T. Weyhermüller, T. K. Paine, S. Mukherjee, C. Mukherjee, *Biol. Chem.* **2005**, *386*, 1023-1033; b) K. Ouch, M. S. Mashuta, C. A. Grapperhaus, *Inorg. Chem.* **2011**, *50*, 9904-9914; c) K. Wang, E. I. Stiefel, *Science* **2001**, *291*, 106-109.

[12] a) A. I. Olivos Suarez, H. Jiang, X. P. Zhang, B. de Bruin, *Dalton Trans.* **2011**, *40*, 5697-5705; b) D. Intrieri, A. Caselli, E. Gallo, *Eur. J. Inorg. Chem.* **2011**, *2011*, 5071-5081; c) W. I. Dzik, X. Xu, X. P. Zhang, J. N. H. Reek, B. de Bruin, *J. Am. Chem. Soc.* **2010**, *132*, 10891-10902.

[13] a) M. R. Ringenberg, S. L. Kokatam, Z. M. Heiden, T. B. Rauchfuss, *J. Am. Chem. Soc.* **2008**, *130*, 788-789; b) M. R. Ringenberg, T. B. Rauchfuss, *Eur. J. Inorg. Chem.* **2012**, *2012*, 490-495.

[14] a) J. L. Boyer, J. Rochford, M.-K. Tsai, J. T. Muckerman, E. Fujita, *Coord. Chem. Rev.* **2010**, *254*, 309-330; b) B. de Bruin, E. Bill, E. Bothe, T. Weyhermüller, K. Wieghardt, *Inorg. Chem.* **2000**, *39*, 2936-2947; c) A. F. Heyduk, R. A. Zarkesh, A. I. Nguyen, *Inorg. Chem.* **2011**, *50*,

9849-9863; d) A. L. Smith, K. I. Hardcastle, J. D. Soper, *J. Am. Chem. Soc.* **2010**, *132*, 14358-14360.

[15] M. W. Bouwkamp, A. C. Bowman, E. Lobkovsky, P. J. Chirik, *J. Am. Chem. Soc.* **2006**, *128*, 13340-13341.

[16] C. A. Lippert, K. I. Hardcastle, J. D. Soper, *Inorg. Chem.* **2011**, *50*, 9864-9878.

[17] B. Bagh, D. L. J. Broere, V. Sinha, P. F. Kuijpers, N. P. van Leest, B. de Bruin, S. Demeshko, M. A. Siegler, J. I. van der Vlugt, *J. Am. Chem. Soc.* **2017**, *139*, 5117-5124.

[18] a) E. M. Matson, S. M. Franke, N. H. Anderson, T. D. Cook, P. E. Fanwick, S. C. Bart, *Organometallics* **2014**, *33*, 1964-1971; b) B. Bagh, D. L. J. Broere, M. A. Siegler, J. I. van der Vlugt, *Angew. Chem. Int. Ed.* **2016**, *55*, 8381-8385.

[19] a) E. J. Thompson, L. A. Berben, *Angew. Chem. Int. Ed.* **2015**, *54*, 11642-11646; b) F. Lu, R. A. Zarkesh, A. F. Heyduk, *Eur. J. Inorg. Chem.* **2012**, *2012*, 467-470; c) A. Z. Haddad, S. P. Cronin, M. S. Mashuta, R. M. Buchanan, C. A. Grapperhaus, *Inorg. Chem.* **2017**, *56*, 11254-11265; d) T. J. Sherbow, J. C. Fettinger, L. A. Berben, *Inorg. Chem.* **2017**, *56*, 8651-8660; e) L. A. Berben, *Chem. Eur. J.* **2015**, *21*, 2734-2742.

[20] H. Grützmacher, *Angew. Chem. Int. Ed.* **2008**, *47*, 1814-1818.

[21] a) J. I. van der Vlugt, *Eur. J. Inorg. Chem.* **2012**, *2012*, 363-375; b) J. R. Khusnutdinova, D. Milstein, *Angew. Chem. Int. Ed.* **2015**, *54*, 12236-12273; c) L. Greb, F. Ebner, Y. Ginzburg, L. M. Sigmund, *Eur. J. Inorg. Chem.* **2020**, *2020*, 3030-3047.

[22] a) M. M. Whittaker, J. W. Whittaker, *J. Biol. Chem.* **1988**, *263*, 6074-6080; b) B. A. Jazdzewski, W. B. Tolman, *Coord. Chem. Rev.* **2000**, *200-202*, 633-685; c) J. W. Whittaker, *Arch. Biochem. Biophys.* **2005**, *433*, 227-239.

[23] a) V. Subbarayan, J. V. Ruppel, S. Zhu, J. A. Perman, X. P. Zhang, *Chem. Commun.* **2009**, 10.1039/B905727G, 4266-4268; b) G.-Y. Gao, J. E. Jones, R. Vyas, J. D. Harden, X. P. Zhang, *J. Org. Chem.* **2006**, *71*, 6655-6658.

[24] a) R. S. Potember, T. O. Poehler, D. O. Cowan, *Appl. Phys. Lett.* **1979**, *34*, 405-407; b) Y. Guo, J.-M. Langlois, W. A. Goddard, *Science* **1988**, *239*, 896-899; c) H. Zhao, J. Bazile, Mervin J., J. R. Galán-Mascarós, K. R. Dunbar, *Angew. Chem. Int. Ed.* **2003**, *42*, 1015-1018; d) T. D. Harris, C. Coulon, R. Clérac, J. R. Long, *J. Am. Chem. Soc.* **2011**, *133*, 123-130.

[25] T. Tezgerevska, K. G. Alley, C. Boskovic, *Coord. Chem. Rev.* **2014**, *268*, 23-40.

[26] W. Kaim, *Coord. Chem. Rev.* **1987**, *76*, 187-235.

[27] a) E. Waldhoer, B. Schwederski, W. Kaim, *J. Chem. Soc., Perkin Trans. 2* **1993**, 2109-2111; b) S. Samanta, P. Singh, J. Fiedler, S. Zalis, W. Kaim, S. Goswami, *Inorg. Chem.* **2008**, *47*, 1625-1633; c) D. L. J. Broere, B. Q. Mercado, J. T. Lukens, A. C. Vilbert, G. Banerjee, H. M. C. Lant, S. H. Lee, E. Bill, S. Sproules, K. M. Lancaster, P. L. Holland, *Chem. Eur. J.* **2018**, *24*, 9417-9425.

[28] a) G. L. Closs, L. E. Closs, *J. Am. Chem. Soc.* **1963**, *85*, 818-819; b) S. E. J. Rigby, I. P. Muhiuddin, S. Santabarbara, M. C. W. Evans, P. Heathcote, *Chem. Phys.* **2003**, *294*, 319-328.

[29] a) W. Matheis, W. Kaim, *J. Chem. Soc., Faraday Trans.* **1990**, *86*, 3337-3339; b) H. Helten, C. Neumann, A. Espinosa, P. G. Jones, M. Nieger, R. Streubel, *Eur. J. Inorg. Chem.* **2007**, *2007*, 4669-4678.

[30] a) M. Sieger, B. Sarkar, S. Zalis, J. Fiedler, N. Escola, F. Doctorovich, J. A. Olabe, W. Kaim, *Dalton Trans.* **2004**, 1797-1800; b) G. K. Lahiri, W. Kaim, *Dalton Trans.* **2010**, *39*, 4471-4478; c) B. Giri, S. Kumbhakar, K. Selvan K, A. Muley, S. Maji, *New J. Chem.* **2020**, *44*, 18732-18744.

[31] a) J. A. McCleverty, *Progr. Inorg. Chem.* **1968**, *10*, 49-221; b) R. Eisenberg, H. B. Gray, *Inorg. Chem.* **2011**, *50*, 9741-9751; c) S. Sproules, K. Wieghardt, *Coord. Chem. Rev.* **2010**, *254*, 1358-1382.

[32] a) C. G. Pierpont, C. W. Lange, *Prog. Inorg. Chem.* **1994**, *41*, 331-442; b) C. G. Pierpont, *Coord. Chem. Rev.* **2001**, *216-217*, 99-125; c) C. G. Pierpont, *Inorg. Chem.* **2011**, *50*, 9766-9772; d) A. L. Balch, *J. Am. Chem. Soc.* **1973**, *95*, 2723-2724.

[33] a) T. W. Myers, L. A. Berben, *Inorg. Chem.* **2012**, *51*, 1480-1488; b) V. A. Williams, E. B. Hulley, P. T. Wolczanski, K. M. Lancaster, E. B. Lobkovsky, *Chem. Sci.* **2013**, *4*, 3636-3648; c) P. H. M. Budzelaar, N. N. P. Moonen, R. De Gelder, J. M. M. Smits, A. W. Gal, *Eur. J. Inorg. Chem.* **2000**, 753-769; d) S. C. Bart, K. Chlopek, E. Bill, M. W. Bouwkamp, E. Lobkovsky, F. Neese, K. Wieghardt, P. J. Chirik, *J. Am. Chem. Soc.* **2006**, *128*, 13901-13912; e) V. C. Gibson, C. Redshaw, G. A. Solan, *Chem. Rev.* **2007**, *107*, 1745-1776; f) P. J. Chirik, *Angew. Chem. Int. Ed.* **2017**, *56*, 5170-5181.

[34] a) G. Van Koten, K. Vrieze, *Adv. Organomet. Chem.* **1982**, *21*, 151-239; b) S. J. Kraft, U. J. Williams, S. R. Daly, E. J. Schelter, S. A. Kozimor, K. S. Boland, J. M. Kikkawa, W. P. Forrest, C. N. Christensen, D. E. Schwarz, P. E. Fanwick, D. L. Clark, S. D. Conradson, S. C. Bart, *Inorg. Chem.* **2011**, *50*, 9838-9848.

[35] a) R. Gautam, T. M. Chang, A. V. Astashkin, K. M. Lincoln, E. Tomat, *Chem. Commun.* **2016**, *52*, 6585-6588; b) J. R. Pankhurst, N. L. Bell, M. Zegke, L. N. Platts, C. A. Lamfsus, L. Maron, L. S. Natrajan, S. Sproules, P. L. Arnold, J. B. Love, *Chem. Sci.* **2017**, *8*, 108-116.

[36] a) P. Schweyen, K. Brandhorst, R. Wicht, B. Wolfram, M. Bröring, *Angew. Chem. Int. Ed.* **2015**, *54*, 8213-8216; b) C. Römelt, J. Song, M. Tarrago, J. A. Rees, M. van Gastel, T. Weyhermüller, S. DeBeer, E. Bill, F. Neese, S. Ye, *Inorg. Chem.* **2017**, *56*, 4745-4750.

[37] a) P. J. Krusic, U. Klabunde, C. P. Casey, T. F. Block, *J. Am. Chem. Soc.* **1976**, *98*, 2015-2018; b) M. A. Sierra, M. Gomez-Gallego, R. Martinez-Alvarez, *Chem. - Eur. J.* **2007**, *13*, 736-744; c) W. I. Dzik, X. P. Zhang, B. de Bruin, *Inorg. Chem.* **2011**, *50*, 9896-9903.

[38] a) M. M. Khusniyarov , E. Bill, T. Weyhermüller, E. Bothe, K. Wieghardt, *Angew. Chem. Int. Ed.* **2011**, *50*, 1652-1655; b) M. P. Marshak, M. B. Chambers, D. G. Nocera, *Inorg. Chem.* **2012**, *51*, 11190-11197; c) J. Takaichi, Y. Morimoto, K. Ohkubo, C. Shimokawa, T. Hojo, S. Mori, H. Asahara, H. Sugimoto, N. Fujieda, N. Nishiwaki, S. Fukuzumi, S. Itoh, *Inorg. Chem.* **2014**, *53*, 6159-6169; d) P. Ghosh, R. Naastepad, C. F. Riemersma, M. Lutz, M.-E. Moret, R. J. M. Klein Gebbink, *Chem. Eur. J.* **2017**, *23*, 10732-10737; e) C. Camp, J. Arnold, *Dalton Trans.* **2016**, *45*, 14462-14498.

[39] C. Lichtenberg, I. Krummenacher, *Chem. Commun.* **2016**, *52*, 10044-10047.

[40] a) L. Bourget-Merle, M. F. Lappert, J. R. Severn, *Chem. Rev.* **2002**, *102*, 3031-3066; b) N. J. Hill, I. Vargas-Baca, A. H. Cowley, *Dalton Trans.* **2009**, 10.1039/B815079F, 240-253; c) C. Weetman, S. Inoue, *ChemCatChem* **2018**, *10*, 4213-4228; d) T. Chu, G. I. Nikonov, *Chem. Rev.* **2018**, *118*, 3608-3680; e) R. J. Gilliard, C.-W. Chiu, *Organometallics* **2020**, *39*, 4123-4126.

[41] a) C. Cui, H. W. Roesky, H.-G. Schmidt, M. Noltemeyer, H. Hao, F. Cimpoesu, *Angew. Chem. Int. Ed.* **2000**, *39*, 4274-4276; b) S. P. Green, C. Jones, A. Stasch, *Science* **2007**, *318*, 1754-1757.

[42] a) T. W. Myers, L. A. Berben, *J. Am. Chem. Soc.* **2013**, *135*, 9988-9990; b) T. W. Myers, L. A. Berben, *Chem. Sci.* **2014**, *5*, 2771-2777.

[43] I. L. Fedushkin, A. G. Morozov, V. A. Chudakova, G. K. Fukin, V. K. Cherkasov, *Eur. J. Inorg. Chem.* **2009**, *2009*, 4995-5003.

[44] I. L. Fedushkin, A. N. Lukoyanov, G. K. Fukin, M. Hummert, H. Schumann, *Russ. Chem. Bull.* **2006**, *55*, 1177-1183.

[45] G. Szigethy, A. F. Heyduk, *Dalton Trans.* **2012**, *41*, 8144-8152.

[46] B. E. Cole, J. P. Wolbach, W. G. Dougherty, N. A. Piro, W. S. Kassel, C. R. Graves, *Inorg. Chem.* **2014**, *53*, 3899-3906.

[47] T. W. Myers, L. A. Berben, *J. Am. Chem. Soc.* **2011**, *133*, 11865-11867.

[48] C. Lichtenberg, *Chem. Eur. J.* **2020**, *26*, 9674-9687.

[49] I. L. Fedushkin, N. M. Khvoinova, A. A. Skatova, G. K. Fukin, *Angew. Chem. Int. Ed.* **2003**, *42*, 5223-5226.

[50] T. W. Myers, N. Kazem, S. Stoll, R. D. Britt, M. Shanmugam, L. A. Berben, *J. Am. Chem. Soc.* **2011**, *133*, 8662-8672.

[51] a) E. M. Broderick, N. Guo, C. S. Vogel, C. Xu, J. Sutter, J. T. Miller, K. Meyer, P. Mehrkhodavandi, P. L. Diaconescu, *J. Am. Chem. Soc.* **2011**, *133*, 9278-9281; b) J. Wei, P. L. Diaconescu, *Acc. Chem. Res.* **2019**, *52*, 415-424.

[52] M. G. Chegerev, A. V. Piskunov, A. A. Starikova, S. P. Kubrin, G. K. Fukin, V. K. Cherkasov, G. A. Abakumov, *Eur. J. Inorg. Chem.* **2018**, *2018*, 1087-1092.

[53] N. J. Hill, G. Reeske, J. A. Moore, A. H. Cowley, *Dalton Trans.* **2006**, 10.1039/B609737E, 4838-4844.

[54] a) P. B. Hitchcock, M. F. Lappert, G. Li, *Inorg. Chim. Acta* **2010**, *363*, 1230-1235; b) Y. Li, H. Zhu, G. Tan, T. Zhu, J. Zhang, *Eur. J. Inorg. Chem.* **2011**, *2011*, 5265-5272; c) I. Vránová, R. Jambor, A. Růžička, A. Hoffmann, S. Herres-Pawlis, L. Dostál, *Dalton Trans.* **2015**, *44*, 395-400.

[55] a) F. Wang, O. Planas, J. Cornella, *J. Am. Chem. Soc.* **2019**, *141*, 4235-4240; b) O. Planas, F. Wang, M. Leutzsch, J. Cornella, *Science* **2020**, *367*, 313-317.

[56] M. B. Kindervater, K. M. Marczenko, U. Werner-Zwanziger, S. S. Chitnis, *Angew. Chem. Int. Ed.* **2019**, *58*, 7850-7855.

[57] J. Ramler, J. Poater, F. Hirsch, B. Ritschel, I. Fischer, F. M. Bickelhaupt, C. Lichtenberg, *Chem. Sci.* **2019**, *10*, 4169-4176.

[58] a) C. Lichtenberg, *Angew. Chem. Int. Ed.* **2016**, *55*, 484-486; b) C. Helling, S. Schulz, *Eur. J. Inorg. Chem.* **2020**, *2020*, 3209-3221; c) N. Tokitoh, Y. Arai, R. Okazaki, S. Nagase, *Science* **1997**, *277*, 78-80; d) B. Twamley, C. D. Sofield, M. M. Olmstead, P. P. Power, *J. Am. Chem. Soc.* **1999**, *121*, 3357-3367; e) F. Calderazzo, A. Morvillo, G. Pelizzi, R. Poli, *J. Chem. Soc.,*

Chem. Commun. **1983**, 10.1039/C39830000507, 507-508; f) P. Šimon, F. de Proft, R. Jambor, A. Růžička, L. Dostál, *Angew. Chem. Int. Ed.* **2010**, *49*, 5468-5471; g) R. J. Schwamm, J. R. Harmer, M. Lein, C. M. Fitchett, S. Granville, M. P. Coles, *Angew. Chem. Int. Ed.* **2015**, *54*, 10630-10633.

[59] M. Sakagami, T. Sasamori, H. Sakai, Y. Furukawa, N. Tokitoh, *Chem. Asian J.* **2013**, *8*, 690-693.

[60] Z. R. Turner, *Inorg. Chem.* **2019**, *58*, 14212-14227.

[61] C. Lichtenberg, *Organometallics* **2016**, *35*, 894-902.

[62] A. Hanft, C. Lichtenberg, *Dalton Trans.* **2018**, *47*, 10578-10589.

[63] A. Hanft, M. Jürgensen, R. Bertermann, C. Lichtenberg, *ChemCatChem* **2018**, *10*, 4018-4027.

[64] A. Hanft, C. Lichtenberg, *Organometallics* **2018**, *37*, 1781-1787.

[65] A. Hanft, C. Lichtenberg, *Eur. J. Inorg. Chem.* **2018**, *2018*, 3361-3373.

[66] A. Hanft, I. Krummenacher, C. Lichtenberg, *Chem. Eur. J.* **2019**, *25*, 11883-11891.

[67] A. Hanft, C. Lichtenberg, *Zeitschrift für Kristallographie - New Crystal Structures* **2020**, *235*, 963-966.

[68] A. Hanft, M. Jürgensen, L. Wolz, K. Radacki, C. Lichtenberg, *Inorg. Chem.* **2020**, *59*, 17678-17688.

[69] A. Hanft, K. Radacki, C. Lichtenberg, *Chem. Eur. J.*, https://doi.org/10.1002/chem.202005186.

[70] a) M. Dochnahl, K. Lohnwitz, J. W. Pissarek, P. W. Roesky, S. Blechert, *Dalton Trans.* **2008**, 2844-2848; b) M. Dochnahl, K. Loehnwitz, A. Luehl, J.-W. Pissarek, M. Biyikal, P. W. Roesky, S. Blechert, *Organometallics* **2010**, *29*, 2637-2645.

[71] a) H. V. R. Dias, W. Jin, R. E. Ratcliff, *Inorg. Chem.* **1995**, *34*, 6100-6105; b) M. Dochnahl, K. Lohnwitz, J. W. Pissarek, M. Biyikal, S. R. Schulz, S. Schon, N. Meyer, P. W. Roesky, S. Blechert, *Chem. Eur. J.* **2007**, *13*, 6654-6666.

[72] M. Hesse, H. Meier, B. Zeeh, *Spektroskopische Methoden in der organischen Chemie*, Georg Thieme Verlag, Stuttgart, **2005**.

[73] a) T. Nozoe, Y. Kitahara, S. Masamune, S. Yamaguchi, *Proc. Jpn. Acad.* **1952**, *28*, 85-88; b) T. Nozoe, S. Seto, ucirc, ichi, S. Matsumura, *Proc. Jpn. Acad.* **1952**, *28*, 483-487; c) T. Nozoe, S. Seto, ucirc, ichi, H. Takeda, S. Morosawa, K. Matsumoto, *Proc. Jpn. Acad.* **1952**, *28*, 192-197; d) P. L. Pauson, *Chem. Rev.* **1955**, *55*, 9-136; e) T. Mukai, *Bull. Chem. Soc. Jpn.* **1959**, *32*, 272-279; f) T. Toda, *Bull. Chem. Soc. Jpn.* **1967**, *40*, 588-590; g) G. Biggi, A. J. De Hoog, F. Del Cima, F. Pietra, *J. Am. Chem. Soc.* **1973**, *95*, 7108-7113; h) M. Biyikal, K. Löhnwitz, P. W. Roesky, S. Blechert, *Synlett* **2008**, *2008*, 3106-3110.

[74] F. H. Allen, O. Kennard, D. G. Watson, L. Brammer, A. G. Orpen, R. Taylor, *J. Chem. Soc., Perkin Trans. 2* **1987**, S1-S19.

[75] A. Domenicano, G. Schultz, I. Hargittai, M. Colapietro, G. Portalone, P. George, C. W. Bock, *Struct. Chem.* **1990**, *1*, 107-122.

[76] H. V. R. Dias, W. Jin, Z. Wang, *Inorg. Chem.* **1996**, *35*, 6074-6079.

[77] P. Endres, Praktikumsbericht, Julius-Maximilians-Universität Würzburg, **2019**.

[78] a) A. E. Ayers, H. V. R. Dias, *Inorg. Chem.* **2002**, *41*, 3259-3268; b) S. Datta, P. W. Roesky, S. Blechert, *Organometallics* **2007**, *26*; c) R. K. Siwatch, S. Kundu, D. Kumar, S. Nagendran, *Organometallics* **2011**, *30*, 1998-2005; d) S. Sinhababu, R. K. Siwatch, G. Mukherjee, G. Rajaraman, S. Nagendran, *Inorg. Chem.* **2012**, *51*, 9240-9248.

[79] a) A. Ariza-Castolo, J. A. Montalvo-González, R. Montalvo-González, *Magn. Reson. Chem.* **2005**, *43*, 975-978; b) V. A. Semenov, D. O. Samultsev, A. Y. Rulev, L. B. Krivdin, *Magn. Reson. Chem.* **2015**, *53*, 1031-1034.

[80] a) J. Gálvez, A. Guirado, *J. Comput. Chem.* **2010**, *31*, 520-531; b) R. Paetzold, M. Reichenbächer, K. Appenroth, *Z. Chem.* **1981**, *21*, 421-430.

[81] C. Hansch, A. Leo, R. W. Taft, *Chem. Rev.* **1991**, *91*, 165-195.

[82] A. Hanft, Master Thesis, Julius-Maximilians-Universität Würzburg **2017**.

[83] a) A. V. I. Korolev, Eiji; Guzei, Ilia A.; Young, Victor G. Jr.; Jordan Richard F., *J. Am. Chem. Soc.* **2001**, *123*; b) A. V. Korolev, F. Delpech, S. Dagorne, I. A. Guzei, R. F. Jordan, *Organometallics* **2001**, *20*, 3367-3369; c) F. Delpech, I. A. Guzei, R. F. Jordan, *Organometallics* **2002**, *21*, 1167-1177.

[84] R. G. Pearson, *J. Chem. Educ.* **1968**, *45*, 581.

[85] a) J. A. Flores, K. Pal, M. E. Carroll, M. Pink, J. A. Karty, D. J. Mindiola, K. G. Caulton, *Organometallics* **2014**, *33*, 1544-1552; b) S. Durini, G. A. Ardizzoia, B. Therrien, S. Brenna, *New J. Chem.* **2017**, *41*, 3006-3014.

[86] a) H.-Y. Liu, H. Wu, J.-F. Ma, *Acta Crystallogr. Sect. E* **2006**, *62*, m325-m326; b) S. K. Emashova, A. A. Titov, O. A. Filippov, A. F. Smol'yakov, E. M. Titova, L. M. Epstein, E. S. Shubina, *Eur. J. Inorg. Chem.* **2019**, *2019*, 4855-4861.

[87] a) H. V. R. Dias, S. Singh, *Inorg. Chem.* **2004**, *43*, 7396-7402; b) C. Shimokawa, S. Itoh, *Inorg. Chem.* **2005**, *44*, 3010-3012; c) H. A. Chiong, O. Daugulis, *Organometallics* **2006**, *25*, 4054-4057.

[88] a) H. V. R. Dias, Z. Wang, *Inorg. Chem.* **2000**, *39*, 3890-3893; b) H. V. R. Dias, A. E. Ayers, *Polyhedron* **2002**, *21*, 611-618.

[89] D. Yadav, R. K. Siwatch, G. Mukherjee, G. Rajaraman, S. Nagendran, *Inorg. Chem.* **2014**, *53*, 10054-10059.

[90] Y. Yamamoto, *J. Org. Chem.* **2007**, *72*, 7817-7831.

[91] a) S. W. Jaros, U. Śliwińska-Hill, A. Białońska, D. S. Nesterov, P. Kuropka, J. Sokolnicki, B. Bażanów, P. Smoleński, *Dalton Trans.* **2019**, *48*, 11235-11249; b) O. Mamula, A. von Zelewsky, T. Bark, H. Stoeckli-Evans, A. Neels, G. Bernardinelli, *Chem. Eur. J.* **2000**, *6*, 3575-3585.

[92] a) C.-S. Hwang, P. P. Power, *J. Organomet. Chem.* **1999**, *589*, 234-238; b) S. Weske, R. A. Hardin, T. Auth, R. A. J. O'Hair, K. Koszinowski, C. A. Ogle, *Chem. Commun.* **2018**, *54*, 5086-5089; c) J.-M. Weibel, A. Blanc, P. Pale, *Chem. Rev.* **2008**, *108*, 3149-3173.

[93] N. Tezuka, K. Hirano, A. J. Peel, A. E. H. Wheatley, K. Miyamoto, M. Uchiyama, *Chem. Sci.* **2020**, *11*, 1855-1861.

[94] a) K.-J. Range, S. Kühnel, M. Zabel, *Acta Crystallogr. Sect. C* **1989**, *45*, 1419-1420; b) M. Zabel, S. Kühnel, K.-J. Range, *Acta Crystallogr. Sect. C* **1989**, *45*, 1619-1621.

[95] B. Skelton, A. White, *Aust. J. Chem.* **1979**, *32*, 297-300.

[96] a) W. Khayata, D. Baylocq, F. Pellerin, N. Rodier, *Acta Crystallogr. Sect. C* **1984**, *40*, 765-767; b) T. Murai, M. Yamamoto, S. Kondo, S. Kato, *J. Org. Chem.* **1993**, *58*, 7440-7445; c) R. Weber, M. Gilles, G. Bergerhoff, *Z. Kristallorg. Cryst. Mater* **1993**, *206*, 273-274; d) S. W. Ng, *Z. Kristallorg. Cryst. Mater* **1995**, *210*, 206-209; e) V. T. Yilmaz, S. Hamamci, C. Thöne, *Z. Anorg. Allg. Chem.* **2004**, *630*, 1641-1644.

[97] W. R. Brasen, H. E. Holmquist, R. E. Benson, *J. Am. Chem. Soc.* **1961**, *83*, 3125-3135.

[98] M. Pittracher, U. Frisch, H. Kopacka, K. Wurst, T. Müller, L. Oehninger, I. Ott, E. Wuttke, S. Scheerer, R. F. Winter, B. Bildstein, *Organometallics* **2014**, *33*, 1630-1643.

[99] K. Oberdorf, A. Hanft, J. Ramler, I. Krummenacher, M. Bickelhaupt, J. Poater, C. Lichtenberg, *Angew. Chem. Int. Ed.*, https://doi.org/10.1002/anie.202015514.

[100] a) J. Junggebauer, W. P. Neumann, *Tetrahedron* **1997**, *53*, 1301-1310; b) H.-U. Buschhaus, W. P. Neumann, T. Apoussidis, *Liebigs Ann. Chem.* **1981**, *1981*, 1190-1197.

[101] C. L. Raston, B. W. Skelton, V.-A. Tolhurst, A. H. White, *J. Chem. Soc., Dalton Trans.* **2000**, 10.1039/A909338I, 1279-1285.

[102] M. Mantina, A. C. Chamberlin, R. Valero, C. J. Cramer, D. G. Truhlar, *J. Phys. Chem. A* **2009**, *113*, 5806-5812.

[103] B. Lyhs, S. Schulz, U. Westphal, D. Bläser, R. Boese, M. Bolte, *Eur. J. Inorg. Chem.* **2009**, *2009*, 2247-2253.

[104] R. Shannon, *Acta Crystallogr. Sect. A* **1976**, *32*, 751-767.

[105] G. A. Bowmaker, P. C. Junk, A. M. Lee, B. W. Skelton, A. H. White, *Aust. J. Chem.* **1998**, *51*, 317-324.

[106] J.-I. Seo, I. Kim, Y. S. Lee, *Chem. Phys. Lett.* **2009**, *474*, 101-106.

[107] R. M. Claramunt, D. Sanz, M. Perez-Torralba, E. Pinilla, M. R. Torres, J. Elguero, *Eur. J. Org. Chem.* **2004**, 4452-4466.

[108] P. C. Hariharan, J. A. Pople, *Theoretica chimica acta* **1973**, *28*, 213-222.

[109] a) R. Krishnan, J. S. Binkley, R. Seeger, J. A. Pople, *J. Chem. Phys.* **1980**, *72*, 650-654; b) A. D. McLean, G. S. Chandler, *J. Chem. Phys.* **1980**, *72*, 5639-5648.

[110] A. D. Becke, *J. Chem. Phys.* **1993**, *98*, 5648-5652.

[111] S. Grimme, J. Antony, S. Ehrlich, H. Krieg, *J. Chem. Phys.* **2010**, *132*, 154104.

XXII Anhang

1 Zusatzinformationen

1.1 Kapitel III

Zusatzinformationen zu Kapitel III können unter https://doi.org/10.1002/ejic.201800465 eingesehen werden.

1.2 Kapitel IV

Zusatzinformationen zu Kapitel IV können unter https://doi.org/10.1039/C8DT01019F eingesehen werden.

1.3 Kapitel V

Zusatzinformationen zu Kapitel V können unter https://doi.org/10.1002/cctc.201800580 eingesehen werden.

1.4 Kapitel VI

Zusatzinformationen zu Kapitel VI können unter https://doi.org/10.1021/acs.organomet.8b00208 eingesehen werden.

1.5 Kapitel VII

Zusatzinformationen zu Kapitel VII können unter https://doi.org/10.1002/chem.201901962 eingesehen werden.

1.6 Zusatzinformationen Kapitel VIII

Zusatzinformationen zu Kapitel VIII können unter https://doi.org/10.1515/ncrs-2020-0124 eingesehen werden.

1.7 Zusatzinformationen Kapitel IX

Zusatzinformationen zu Kapitel IX können unter https://doi.org/10.1021/acs.inorgchem.0c02920 eingesehen werden.

1.8 Zusatzinformationen Kapitel X

Zusatzinformationen zu Kapitel X können unter https://doi.org/10.1002/chem.202005186 eingesehen werden.